

COMPTES RENDUS DE L'ACADÉMIE DES SCIENCES

1778-7025 (electronic)

Géoscience *Sciences de la Planète*



Volume 355, Special Issue S2, 2023

Special issue / Numéro thématique
Tribute to Jean Dercourt / *Hommage à Jean Dercourt*

Guest editors / Rédacteurs en chef invités
François Baudin, Éric Calais, François Chabaux

Académie des sciences — Paris



INSTITUT DE FRANCE
Académie des sciences



Comptes Rendus

Géoscience

Objective of the journal

Comptes Rendus Géoscience is an internationally peer-reviewed electronic journal covering the full range of earth sciences and sustainable development. It publishes original research articles, review articles, historical perspectives, pedagogical texts, and conference proceedings of unlimited length, in English or French. *Comptes Rendus Géoscience* is published according to a virtuous policy of diamond open access, free of charge for authors (no publication fees) as well as for readers (immediate and permanent open access).

Editorial director: Étienne Ghys

Editors-in-chief: Éric Calais, Michel Campillo, François Chabaux, Ghislain de Marsily

Editorial Board: Jean-Claude André, Pierre Auger, Mustapha Besbes, Sylvie Bourquin, Yves Bréchet, Marie-Lise Chanin, Philippe Davy, Henri Décamps, Sylvie Derenne, Michel Faure, François Forget, Claude Jaupart, Jean Jouzel, Eric Karsenti, Amaëlle Landais, Sandra Lavorel, Yvon Le Maho, Mickaele Le Ravalec, Hervé Le Treut, Benoit Noetinger, Carole Petit, Valérie Plagnes, Pierre Ribstein, Didier Roux, Bruno Scaillet, Marie-Hélène Tusseau-Vuillemin, Élisabeth Vergès

Editorial secretary: Adenise Lopes

About the journal

All journal's information, including the text of published articles, which is fully open access, is available from the journal website at <https://comptes-rendus.academie-sciences.fr/geoscience/>.

Author enquiries

For enquiries relating to the submission of articles, please visit this journal's homepage at <https://comptes-rendus.academie-sciences.fr/geoscience/>.

Contact

Académie des sciences
23, quai de Conti, 75006 Paris, France
Tel: (+33) (0)1 44 41 43 72
CR-Geoscience@academie-sciences.fr



The articles in this journal are published under the license
Creative Commons Attribution 4.0 International (CC-BY 4.0)
<https://creativecommons.org/licenses/by/4.0/deed.en>



Contents / Sommaire

François Baudin A tribute to Jean Dercourt (1935–2019) — Editorial	1-7
Laurent Jolivet Tethys and Apulia (Adria), 100 years of reconstructions	9-28
Sung-Ping Chang, Manuel Pubellier Rifting and seafloor spreading in the South China sea: a subduction-related extension on the down-going plate?	29-52
Taniel Danelian, Maria Triantaphyllou, Monique Seyler, Ghazar Galoyan, Arayik Grigoryan, Marc Sosson Synthesis of micropaleontological age constraints for the reconstruction of the Tethyan realm in the Lesser Caucasus (Armenia, Karabagh)	53-66
Yves-Michel Le Nindre, Denis Vaslet, Bruno Vrielynck, Leopold Krystyn, Jacques Manivit, Abdullah Memesh, Roger Brett Davies The Middle to Late Triassic of Central Saudi Arabia with emphasis on the Jilh Formation. Part I: lithostratigraphy, facies and paleoenvironments, palaeontology and biostratigraphic age calibration from outcrop studies	67-97
Yves-Michel Le Nindre, Roger Brett Davies, Benoit Issautier, Leopold Krystyn, Denis Vaslet, Bruno Vrielynck, Abdullah Memesh The Middle to Late Triassic of Central Saudi Arabia with emphasis on the Jilh Formation. Part II: sequence stratigraphy, depositional and structural history, correlations and paleogeography	99-135
Marc Poujol, Mathilde Mercuzot, Michel Lopez, Sylvie Bourquin, Olivier Bruguier, Erwan Hallot, Laurent Beccaletto Insights on the Permian tuff beds from the Saint-Affrique Basin (Massif Central, France): an integrated geochemical and geochronological study	137-161
Laurent Beccaletto, Sylvie Bourquin The Brécy depocenter as part of a new northern Massif Central Carboniferous–Permian Basin (France)	163-190
Armelle Riboulleau, Melesio Quijada, Alexis Caillaud, François Baudin, Jean-Noël Ferry, Nicolas Tribovillard Molecular fossils of Aptian–Albian blue marls of the Vocontian Basin (France), depositional conditions and connections to the Tethys Ocean	191-212
Nicolas Tribovillard, Viviane Bout-Roumazeilles, Romain Abraham, Sandra Ventalon, Marion Delattre, François Baudin The contrasting origins of glauconite in the shallow marine environment highlight this mineral as a marker of paleoenvironmental conditions	213-228

Anne-Marie Lézine, Masa Kageyama, Franck Bassinot

Data and models reveal humid environmental conditions during MIS 3 in two of the world's largest deserts 229-246

Foreword

Tribute to Jean Dercourt

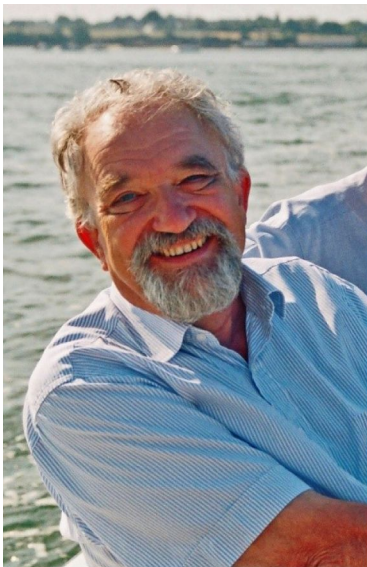
A tribute to Jean Dercourt (1935–2019) — Editorial

François Baudin ^a

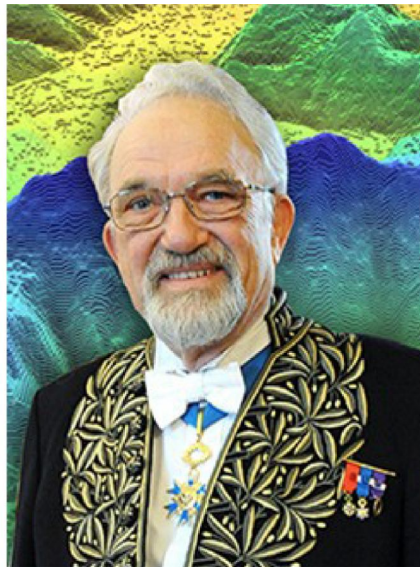
^a Institut des Sciences de la Terre (ISTeP), Sorbonne-Université/CNRS, 4 place Jussieu
75005 Paris, France

E-mail: francois.baudin@sorbonne-universite.fr

Manuscript received 20 October 2023, accepted 25 October 2023.



© Famille Dercourt - Tous droits réservés



© B. Eymann/Académie des sciences - Tous droits réservés

Jean Dercourt was born in Boulogne-Billancourt on March 11th 1935¹. Pressed by his mother to take over the family pharmacy, he began higher studies in pharmacy, and at the same time studied natural sciences, which he found more appealing. He successfully completed this dual training before finally

choosing geology. At university, he met Anne-Marie, who became his wife and they had four children.

He began his career in 1957 as a “stagiaire de recherche” (research fellow) at the National Centre for Scientific Research (CNRS) and he came out first at the “Agrégation de Sciences Naturelles” (the diploma to teach in secondary schools) in 1958. Under the supervision of Jean Aubouin, he worked in Greece to draw up a cross-section of the northern Peloponnese and a 1:200,000 map, while he was an associate professor at Sorbonne from 1959 to 1965.

¹Some elements of Jean Dercourt’s biography summarized here have been translated—with the authors’ agreement—from an article by De Wever and Cadet (2019) published in *Géochronique*, n°150, June 2019, p. 17.

He defended his “Thèse d’Etat” (professoral thesis) in 1964 [Dercourt, 1964].

He was appointed professor of geology at Lille University when he was 29, and was there from 1964 to 1979. This period was interrupted by a sabbatical year in Canada in 1969 where he was a visiting researcher at the University of Edmonton (Alberta). On his return he taught the new revolutionary theory of plate tectonics, being one of the first in France to do so. With his friend Jacques Paquet, he wrote a textbook [Dercourt and Paquet, 1974] which, 50 years later and in its 12th edition, is still a reference for undergraduates. In 1979 Jean Dercourt returned to Paris to teach at Pierre and Marie Curie University (UPMC), where he remained to the end of his career. His dynamic and charismatic personality attracted many students. His qualities as an enthusiastic teacher have left their mark on generations of students training for teaching or research.

Jean Dercourt’s scientific work is marked by the study of sedimentary basins and mountain ranges built over the last 250 million years in the ancient ocean that opened up in Pangea during the Permian and disappeared when the Alps collided. Jean Dercourt directed several international scientific programmes (Tethys and Peri-Tethys) from 1985 to 2004, focusing on the paleodynamics and paleoenvironments of the Tethyan region. Convinced that the paleogeographic map is the ultimate synthesis of an area’s geological knowledge, he set out to map the periods from the opening to the closing of the Tethys Ocean, thereby identifying the marine and terrestrial environments of this important region on a global scale. The programmes have mobilised hundreds of researchers from dozens of countries, generating more than a thousand scientific articles.

Jean Dercourt held many important positions, in the academic world (such as Lille University Vice-President), at the ministry of universities, at the French Geological Society (SGF, as president in 1984–1985) and, of course, at the French Academy of Sciences, where he was a correspondent in 1987, a member in 1991 and then Perpetual Secretary from 1996 to 2010. As Perpetual Secretary, Jean Dercourt was constantly concerned with the transmission of knowledge and the quality of scientific teaching. He was responsible for overseeing the publication of the *Comptes Rendus de l’Académie des sciences*. He supported the development of the Nobel prize

and academician Georges Charpak’s “La main à la pâte” educational activities initiated in 1995. In 2005, he supported the creation of an education and training delegation within the academy. He made the Château-observatory of Abbadie, near Biarritz, owned by the academy, a place open to the public and to teachers.

I have lost count of the number of positions he held on boards of directors and scientific councils in a wide variety of fields, including ocean exploration and exploitation (IFREMER), the French geological survey (BRGM), the French petroleum institute (IFP), radioactive waste (ANDRA), environment and energy management (ADEME), and even Sea fisheries. At international level, his involvement and responsibilities were just as numerous and important. Let me only mention his chairmanship of the Tectonics Commission of the International Union of Geological Sciences (IUGS) and the Commission for the Geological Map of the World (CGMW).

The Society acknowledged the quality of Jean Dercourt’s commitments, as demonstrated the awards he has received: several national and international scientific prizes, membership of six academies in different countries, four honoris causa doctorates, as well as national distinctions (Légion d’honneur, Ordre national du Mérite).

Very much diminished after a stroke, he had retired to his family setting. He closed his eyes on this world on 22th March 2019, aged 84.

Here, we mean to praise him as a colleague and with this special volume of articles as a tribute. But it is the man, the friend, whose lessons and memory we will always remember. Many are aware that it they have been very lucky to cross his path.

I will now briefly introduce the content of the articles of this volume, situating them as regards Jean Dercourt’s research and scientific interests.

“The lost Tethys Ocean was the favourite topic of Jean Dercourt’s research” said Jolivet [2023] as incipit of his paper. Indeed, Jean Dercourt’s first attempts at reconstructing the evolution of the Tethys were carried out with Bernard Biju-Duval and Xavier Le Pichon and presented at the international symposium on the structural history of the Mediterranean basins in 1976 [Biju-Duval et al., 1977]. The series of maps, limited to the Mediterranean domain, caused quite a stir. This attempt was then detailed and completed in the form of 9 maps ex-

tending from Atlantic to Pamir and covering the period from Triassic to the present-day [Dercourt et al., 1985, 1986b]. On the basis of these maps Jean Dercourt built the Tethys programme and its successors (Peri-Tethys, MEBE/Middle-East Basin Evolution), a series of projects organised around large consortia bringing together more than a hundred scientists from academia and industry. The initial paleogeographic maps were extended to all the remains of the Tethys Ocean, from the Caribbean to Indonesia [Rangin et al., 1990, Stéphan et al., 1990], with details to the northern margins of the Tethys [Rakus et al., 1988, 1989, 1990, Dercourt et al., 1990]. Based on these paleogeographic data, depositional paleoenvironments were then reported for the Tethyan realm [Dercourt et al., 1993] and finally for the Peri-Tethyan realm [Dercourt et al., 2000]. Thanks to Jean Dercourt, Tethys joined the collection of books published by Plenum on ocean basins and their margins, as the first to be devoted to an extinct ocean [Nairn et al., 1996]. In addition, this volume introduced the concept of *seuils lithosphériques*, physiographic cratonic barriers that influenced Tethyan ocean dynamics [Vrielynck et al., 1994]. The Apulia, a micro-continent that drifted away from Africa and then shortened to form a part of the Alpine chains, was one of these “*seuils*”.

In his article, entitled “*Tethys and Apulia (Adria), 100 years of reconstructions*”, Jolivet [2023] reviews the main reconstructions of the Mediterranean Tethys published since 1924, following the evolution of concepts and methods. He also discusses the importance of this type of synthesis for understanding large-scale geodynamic processes.

Five years after defending his professoral thesis on the Hellenides, Jean Dercourt spent a sabbatical year in Canada where he travelled through the Rocky Mountains. He went there to study a different orogen model from that of the Mediterranean Alpine ranges. Familiar with the new theory of plate tectonics, proposed the previous year, he quickly understood how this new vision of the dynamics at the surface of Earth accounted for the formation of these two types of orogens. He then wrote two articles, one in French [Dercourt, 1970] and the other in English [Dercourt, 1972], comparing the formation of these two orogens within the framework of plate tectonics. Both articles were successful and won him an international audience. This is probably why he was

elected Member and then Chairman of the Tectonics Commission of the International Union of Geological Sciences (IUGS) from 1980 to 1992, and subsequently Chairman of the Commission for the Geological Map of the World (CGMW) from 1992 to 2000.

In their article, entitled “*Rifting and seafloor spreading in the South China Sea: a subduction related-extension on the down-going plate?*” Chang and Pubellier [2023], the latter being currently Chairman of CGMW, examined the stages of rifting, spreading and termination of activity in the South China Sea basin during the Cenozoic. The rifting-to-drifting history of the South China Sea, which took place between 45 Ma and 16 Ma, may be correlated in terms of stratigraphic boundaries with the subduction-collision history of the Proto South China Sea observed in the NW Borneo and Palawan Island. This evolution illustrates how the process of subduction can have an impact on regional tectonics.

Micropaleontology is particularly useful for establishing a precise biostratigraphic framework in sedimentary basins and for dating geodynamic events. Jean Dercourt quickly realised the value of bringing together tectonicians, geodynamicians and micropaleontologists to propose a timetable for the opening of oceanic domains that are now integrated into mountain ranges. Among microfossils, radiolarians are particularly useful for dating siliceous sediments that are often associated with submarine lavas. In his quest for geodynamic reconstructions of the Tethys, Jean Dercourt led research in this area, in particular with Patrick De Wever [De Wever and Dercourt, 1985] and Luc-Emmanuel Ricou [Knipper et al., 1986]. Such approaches were subsequently pursued and expanded by Jean Dercourt’s disciples, providing valuable information on the geodynamics of complex areas such as the Canadian Rocky Mountains and several parts of the Alpine chain *sensu lato*, from Caribbean to Indonesia.

In their paper, entitled “*Synthesis of micropaleontological age constraints for the reconstruction of the Tethyan realm in the Lesser Caucasus (Armenia, Karabagh)*”, Danelian et al. [2023] provide new biostratigraphic results from two ophiolite outcrops in Armenia. The discovery of the upper Tithonian–lower Berriasian radiolarian allows to date submarine lava eruptions and block sliding from a nearby shallow-water carbonate platform more accurately. Moreover, the discovery of the Upper Coniacian–

Santonian calcareous nannofossils refine the timing of ophiolite obduction in the Lesser Caucasus.

Jean Dercourt was convinced that the geological map is an irreplaceable document that summarises the data acquired on a given study area. Together with Jean Aubouin and Bernard Labesse, they published a handbook for students to introduce them to the geological mapping [Aubouin et al., 1970]. When he became a member of the Academy of Sciences, Jean Dercourt gave up the traditional presentation of a sword by his students and friends to dedicate this fund to the creation of a prize for geological cartography. Jean Dercourt was also convinced that, in sedimentary environments, the stratigraphy of the studied succession should be as detailed as possible. As Chairman of the Committee of the Geological Map of France from 1986 to 1992, then Chairman of the Earth Sciences Council at the Geological Survey of France (BRGM), he met the geologists from this geological survey who were producing the geological maps of the western edge of the Saudi Arabian platform. He convinced them and their supervisors that their work deserved to be widely broadcast and could lead to a doctoral thesis. Thanks to their work, the stratigraphy of the Lower Paleozoic to Upper Jurassic of the Arabian Platform made enormous progress in the late 1980s and early 1990s.

Work has continued since and in their complementary articles, entitled “*The Middle to Late Triassic of Central Saudi Arabia with emphasis on the Jilh Formation. Parts I and II*”, Le Nindre et al. [2023a,b] provide a magnificent stratigraphic and paleoenvironmental synthesis of this formation and discuss both its sequence stratigraphic interpretation and its paleogeographic significance.

Although Jean Dercourt himself did not study much geology of the French territory, with the exception of his postgraduate dissertation (“Diplôme d’Etudes Supérieures”) on the Seine fault in Normandy, he was always keen on French geology. As Chairman of the Scientific Committee for the 6th edition of the geological map of mainland France at 1:1,000,000 scale (published in 1996), he was eager to include the most recent results and innovative concepts, along with Jean Chantaine and the BRGM colleagues involved in the project. Drawing on this experience and the knowledge he has acquired of French geology, he produced an educational book [Dercourt, 1997] in which, following his

guiding principle, he takes the reader on a search for the oceans that have disappeared in mainland France and overseas.

In their paper, entitled “*Insights on the Permian tuff beds from the Saint-Affrique Basin (Massif Central, France): an integrated geochemical and geochronological study*”, Poujol et al. [2023] study several volcanic ash beds of this basin using an integrated petrological, geochemical and geochronological approach. Their results highlight the existence of two different groups of felsic volcanoclastic rocks. Although the first cannot be dated due to the absence of zircon, the second is of late Early Permian age (Cisuralian), demonstrating that the sedimentary filling of the Saint-Affrique Basin is younger than previously assumed.

In their paper, entitled “*The Brécy depocenter as part of a new reference late Variscan basin (northern Massif Central, France)*” Beccalotto and Bourquin [2023] re-interpret 115 km of seismic lines and several deep wells in this Carboniferous-Permian basin covered by Mesozoic deposits in the SW Paris Basin. The geometry, depositional environments and tectonic evolution of the Brécy basin are considerably updated compared with previous work. The alluvial to lacustrine environments, characterising the sedimentary filling, show a transgressive–regressive–transgressive pattern. The current geometry of the Brécy basin is controlled by several east-dipping normal faults, some of which being connected to deep detachment levels active during the late Carboniferous and Permian times.

After returning to Paris as a professor in the early 1980s, Jean Dercourt, together with Eric Fourcade, set up a laboratory devoted to Stratigraphy associating UPMC with the CNRS and the Museum national d’Histoire Naturelle (MNHN). With this new team, they developed integrated stratigraphy combining the most modern approaches of sedimentology, (micro)paleontology, chemostratigraphy, magnetostratigraphy, geochronology and the emerging sequential stratigraphy. Their researches were focused on the Tethyan region, from Turkey [Fourcade et al., 1991] to Spain [Rasplus et al., 1997]. Their results have provided an opportunity to decipher the traces of geodynamic, oceanic or climatic events in the sedimentary series [Dercourt et al., 1986a], in particular the oceanic anoxic events of the Mesozoic. The Toarcian anoxic event that Jean Dercourt spotted

in Greece was clarified [Baudin et al., 1988, 1990].

In their paper, entitled “*Molecular fossils of Aptian–Albian blue marls of the Vocontian Basin (France), depositional conditions and connections to the Tethys Ocean*”, Riboulleau et al. [2023] examine the lipid biomarkers of six organic-rich levels of global or regional extension and discuss their depositional controlling factors. This study demonstrates that, in the Aptian–Albian succession from SE France, organic-matter deposition resulted mostly from local factors and that each level has its own peculiarities. Nevertheless, connections with the Tethys Ocean were critical for the recording of global oceanic anoxic events.

In their paper, entitled “*The contrasting origins of glauconite in the shallow marine environment highlight this mineral as a marker of paleoenvironmental conditions*”, Tribouillard et al. [2023] challenge the paradigm of a constantly slow formation of the authigenic mineral “glauconite” in outer shelf domain. Comparing glauconites formed in contrasting environments from the Jurassic and Cretaceous succession of Boulonnais (NW France), the authors hypothesise that isolated oyster reefs harboured anoxic micro-environments favouring the authigenic formation of glauconite in shallow waters. These results support the idea that the “glauconite factory” is not restricted to outer shelf but may also be formed in very shallow areas of the shelf.

Jean Dercourt himself had never worked on the origin of Man, but he was fascinated by the question. Several major waves of *Homo sapiens* migration from Africa to the Arabian Peninsula and the Levant took place between 59,000 and 29,000 years ago, in the general glacial context of Marine Isotope Stage 3 (MIS 3). However, the environmental conditions at the origin of these migrations are poorly known, and the scarcity of continental data covering this period has been interpreted as reflecting arid conditions. This conclusion has been challenged, as the intense aeolian deflation that occurred during the last glacial maximum (20,000 years ago) could have destroyed or seriously damaged lake or river sediments, which could have reflected humid climatic conditions conducive to the migration of human populations. Another difficulty in studying this period is the methodological limitation of ^{14}C radiocarbon dating, which reaches its limit of use around 50,000 years ago.

In their paper “*Data and models reveal humid environmental conditions during MIS 3 in two of the world’s largest deserts*”, Lézine et al. [2023] compare 245 continental discrete records and 11 long-term continental and marine core records, dated using ^{14}C , U/Th or luminescence methods. These data are compared with results from the Institut Pierre-Simon Laplace (IPSL) general circulation model to discuss hydrological changes between 59,000 and 29,000 years in Northern Tropical Africa, North Africa and the Arabian Peninsula. Despite a general glacial context, wet conditions were widely, creating numerous lakes, rivers and wetlands. This study shows that humid conditions appeared much earlier and were more prevalent in the Arabian Peninsula than in Africa, due to the combination of monsoon rains in summer and Mediterranean rains in winter.

This collection of articles, published as a tribute to Jean Dercourt, includes many useful contributions, which I hope will be of interest to readers. I would like to thank the colleagues who agreed to submit these choice pieces to C. R. Géoscience—Sciences de la Planète, and François Chabaux for supporting and encouraging me in my mission as guest editor of this special issue. Some of these contributions were presented at conferences organised by the Academy of Sciences and the French Geological Society on December 7th and 8th, 2021. Our warmest thanks go to Philippe Taquet, Patrick De Wever and Jean-Paul Cadet, who organised the December 7th event. Special thanks to Françoise Cadet for her careful proof-reading of the English of this editorial.

Declaration of interests

The authors do not work for, advise, own shares in, or receive funds from any organization that could benefit from this article, and have declared no affiliations other than their research organizations.

References

- Aubouin, J., Dercourt, J., and Labesse, B. (1970). *Manuel de travaux pratiques de cartographie*. Dunod, Paris.
- Baudin, F., Dercourt, J., Herbin, J.-P., and Lachkar, G. (1988). Le Lias supérieur de la zone ionienne (Grèce) : une sédimentation riche en carbone organique. *C. R. Acad. Sci. Paris*, 307(II), 985–990.

- Baudin, F., Herbin, J.-P., Bassoullet, J.-P., Dercourt, J., Lachkar, G., Manivit, H., and Renard, M. (1990). Distribution of organic matter during the Toarcian in Mediterranean Tethys and Middle East. In Huc, A.-Y., editor, *Deposition of Organic Facies*, volume 30, pages 73–91. American Association of Petroleum Geologists Studies in Geology, Tulsa.
- Beccaletto, L. and Bourquin, S. (2023). The Brécly depocenter as part of a new northern Massif Central Carboniferous-Permian Basin (France). *C. R. Géosci.*, xx, 000–000. Special issue Tribute to Jean Dercourt.
- Biju-Duval, B., Dercourt, J., and Le Pichon, X. (1977). From the Tethys Ocean to the Mediterranean Sea: a plate tectonic model of the evolution of the western alpine system. In *International Symposium on the Structural History of the Mediterranean Basins, (Split, Yugoslavia)*, pages 143–164. Technip, Paris. 8 maps. <https://archimer.ifremer.fr/doc/00000/51971/>.
- Chang, S.-P. and Pubellier, M. (2023). Rifting and seafloor spreading in the South China Sea: a subduction-related extension on the down-going plate? *C. R. Géosci.*, xx, 000–000. Special issue Tribute to Jean Dercourt.
- Danelian, T., Triantaphyllou, M., Seyler, M., Galoyan, G., Grigoryan, A., and Sosson, M. (2023). Synthesis of micropaleontological age constraints for the reconstruction of the Tethyan realm in the Lesser Caucasus (Armenia, Karabagh). *C. R. Géosci.*, xx, 000–000. Special issue Tribute to Jean Dercourt.
- De Wever, P. and Dercourt, J. (1985). Les radiolaires triasiques-jurassiques comme marqueurs stratigraphiques et paléogéographiques dans les chaînes alpines périméditerranéennes : une revue. *Bull. Soc. Géol. Fr.*, 1(5), 653–662.
- Dercourt, J. (1964). *Contribution à l'étude géologique d'un secteur du Péloponnèse septentrional (Grèce)*, volume 15. Annales géologiques des Pays Helléniques, Athènes.
- Dercourt, J. (1970). L'expansion océanique actuelle et fossile ; ses implications géotectoniques. *Bull. Soc. Géol. Fr.*, 7, 261–317.
- Dercourt, J. (1972). The Canadian Cordillera, the Hellenides and the sea-floor spreading theory. *Can. J. Earth Sci.*, 6, 709–743.
- Dercourt, J. (1997). *Géologie et géodynamique de la France (outremer et européenne)*. Dunod, Paris.
- Dercourt, J., Foucault, A., and Renard, M. (1986a). Liasons entre les phénomènes globaux, les changements du milieu et les grandes crises du monde vivant. *Bull. Cent. Rech. Explor.-Prod. Elf Aquitaine*, 10(2), 285–311.
- Dercourt, J., Gaetani, M., Vrielynck, B., Barrier, E., Biju-Duval, B., Brunet, M.-F., Cadet, J.-P., Crasquin, S., and Sandulescu, M. (2000). *Atlas Peri-Tethys and Explanatory Notes*. CCGM, Paris. 24 maps.
- Dercourt, J. and Paquet, J. (1974). *Géologie. Objets et méthodes*. Dunod, Paris.
- Dercourt, J., Ricou, L.-E., Adamia, S., Csaszar, G., Funk, H., Lefeld, J., Rakus, M., Sandulescu, M., Tollman, A., and Tchoumachenko, P. (1990). *Evolution of the northern margin of the Tethys. Paleogeographic maps 1:10,000,000*, volume 154. Mém. Soc. Géol. France, Paris. 11 maps.
- Dercourt, J., Ricou, L.-E., and Vrielynck, B. (1993). *Atlas Tethys Palaeoenvironmental Maps. Atlas and Explanatory Notes*. Gauthier Villars, CGMW, Paris. 14 maps.
- Dercourt, J., Zonenshain, L. P., Ricou, L. E., Kazmin, V. G., Le Pichon, X., Knipper, A. L., Grandjacquet, C., Sborshchikov, I. M., Boulín, J., Sorokhtin, O., Geysant, J., Lepvrier, C., Biju-Duval, B., Sibuet, J. C., Savostin, L. A., Westphal, M., and Lauer, J.-P. (1985). Présentation de 9 cartes paléogéographiques au 1/20.000.000^{ème} s'étendant de l'Atlantique au Pamir pour la période du Lias à l'Actuel. *Bull. Soc. Géol. Fr.*, 1(5), 637–652.
- Dercourt, J., Zonenshain, L. P., Ricou, L.-E., Kazmin, V. G., Le Pichon, X., Knipper, A. L., Grandjacquet, C., Sborshchikov, I. M., Geysant, J., Lepvrier, C., Pechersky, D. H., Boulín, J., Sibuet, J.-C., Savostin, L. A., Sorokhtin, O., Westphal, M., Bazhenov, M. L., Lauer, J.-P., and Biju-Duval, B. (1986b). Geological evolution of the Tethyan belts from the Atlantic to the Pamir since the Lias. *Tectonophysics*, 123, 241–315.
- Fourcade, E., Dercourt, J., Gunay, Y., Azéma, J., Kozlu, H., Bellier, J.-P., Cordey, F., Cros, P., De Wever, P., Enay, R., Hernandez, J., Lauer, J.-P., and Vrielynck, B. (1991). Stratigraphie et paléogéographie de la marge septentrionale de la plate-forme arabe au Mésozoïque (Turquie du Sud-Est). *Bull. Soc. Géol. Fr.*, 162(1), 27–41.
- Jolivet, L. (2023). Tethys and Apulia (Adria), 100 years of reconstructions. *C. R. Géosci.*, xx, 000–000. Special issue Tribute to Jean Dercourt.
- Knipper, A. L., Ricou, L.-E., and Dercourt, J. (1986).

- Ophiolites as indicators of the geodynamic evolution of the Tethyan Ocean. *Tectonophysics*, 123(1–4), 213–240.
- Le Nindre, Y.-M., Davies, R. B., Issautier, B., Krystyn, L., Vaslet, D., Vrielynck, B., and Memesh, A. (2023a). The middle to late triassic of central Saudi Arabia with emphasis on the Jilh Formation. Part II: sequence stratigraphy, depositional and structural history, correlations and paleogeography. *C. R. Géosci.*, xx, 000–000. Special issue Tribute to Jean Dercourt.
- Le Nindre, Y.-M., Vaslet, D., Vrielynck, B., Krystyn, L., Manivit, J., Memesh, A., and Davies, R. B. (2023b). The middle to late triassic of central Saudi Arabia with emphasis on the Jilh Formation. Part I: lithostratigraphy, facies and paleoenvironments, paleontology and biostratigraphic age calibration from outcrop studies. *C. R. Géosci.*, xx, 000–000. Special issue Tribute to Jean Dercourt.
- Lézine, A. M., Masa, K., and Bassinot, F. (2023). Data and models reveal humid environmental conditions during MIS 3 in two of the world's largest deserts. *C. R. Géosci.*, xx, 000–000. Special issue Tribute to Jean Dercourt.
- Nairn, A. E. M., Ricou, L.-E., Vrielynck, B., and Dercourt, J. (1996). *The Ocean Basins and Margins. The Tethys Ocean*, volume 8. Plenum Press, New York.
- Poujol, M., Mercuzot, M., Lopez, M., Bourquin, S., Bruguier, O., Hallot, E., and Beccaletto, L. (2023). Insights on the Permian tuff beds from the Saint-Affrique Basin (Massif Central, France): an integrated geochemical and geochronological study. *C. R. Géosci.*, xx, 000–000. Special issue Tribute to Jean Dercourt.
- Rakus, M., Dercourt, J., and Nairn, A. E. M. (1988). *Evolution of the Northern Margin of Tethys, Vol. I*. Nouvelle Série No. 154. Mém. Soc. Géol. France, Paris.
- Rakus, M., Dercourt, J., and Nairn, A. E. M. (1989). *Evolution of the Northern Margin of Tethys, Vol. II*. Nouvelle Série No. 154 (II). Mém. Soc. Géol. France, Paris.
- Rakus, M., Dercourt, J., and Nairn, A. E. M. (1990). *Evolution of the Northern Margin of Tethys, Vol. III*. Nouvelle Série No. 154 (III, pt. 1–2). Mém. Soc. Géol. France, Paris. 13 maps.
- Rangin, C., Pubellier, M., Azéma, J., Briais, A., Chotin, P., Fontaine, H., Huchon, P., Jolivet, L., Maury, R., Muller, C., Rampnoux, J.-P., Stephan, J.-F., Tournon, J., Cottureau, N., Dercourt, J., and Ricou, L.-E. (1990). The quest for Tethys in the Western Pacific - 8 paleogeodynamic maps for Cenozoic time. *Bull. Soc. Géol. Fr.*, VI(6), 907–913. 8 maps.
- Rasplus, L., Fourcade, E., Ambroise, D., Andéol, B., Azéma, J., Blanc, P., Busnardo, R., Clerc-Renaud, T., Damotte, R., Dercourt, J., Foucault, A., Galbrun, B., Granier, B., Lachkar, G., Le Hégarat, G., Magné, J., Manivit, H., Mangin, A. M., Masure, E., Mazaud, A., Michaud, E., Morand, F., Renard, M., Schuber, N., and Taugourdeau, J. (1997). Stratigraphie intégrée du sillon citrabétique (Sierra de Fontcalent, province d'Alicante, Espagne). *Geobios*, 20, 337–387.
- Riboulleau, A., Quijada, M., Caillaud, A., Baudin, F., Ferry, J.-N., and Tribouvillard, N. (2023). Molecular fossils of Aptian–Albian blue marls of the Vocontian Basin (France), depositional conditions and connections to the Tethys Ocean. *C. R. Géosci.*, xx, 000–000. Special issue Tribute to Jean Dercourt.
- Stéphan, J.-F., Mercier de Lepinay, B., Calais, E., Tardy, M., Beck, C., Carfantan, J.-C., Olivet, J.-L., Vila, J.-M., Bouysse, P., Mauffret, A., Bourgois, J., Théry, J.-M., Tournon, J., Blanchet, R., and Dercourt, J. (1990). Paleogeodynamic maps of the Caribbean: 14 steps from Lias to Present. *Bull. Soc. Géol. Fr.*, VI(6), 915–919. 14 maps.
- Tribouvillard, N., Bout-Roumazeilles, V., Abraham, R., Ventalon, S., Delattre, M., and Baudin, F. (2023). The contrasting origins of glauconite in the shallow marine environment highlight this mineral as a marker of paleoenvironmental conditions. *C. R. Géosci.*, xx, 000–000. Special issue Tribute to Jean Dercourt.
- Vrielynck, B., Dercourt, J., and Cottureau, N. (1994). Des seuils lithosphériques dans la Téthys. *C. R. Acad. Sci. II*, 318(12), 1677–1685.



Research article

Tribute to Jean Dercourt

Tethys and Apulia (Adria), 100 years of reconstructions

Laurent Jolivet ^{©, a}

^a IStEp, UMR 7193, Sorbonne Université, 4 Place Jussieu, 75252 Paris cedex 05, France

E-mail: laurent.jolivet@sorbonne-universite.fr

Abstract. The lost Tethys Ocean was the favorite topic of Jean Dercourt's research. The Tethys project and his 1986 paper displaying detailed reconstructions in 9 plates from the Triassic to the Present was the beginning of a series of projects organized around large consortia associating scientists from the academic and industrial worlds. The most recent evolutions of these reconstructions show unprecedented images of the evolving geology, including tectonics and paleoenvironments, through time of this complex puzzle. Central to Tethyan tectonics, Apulia, or Adria, has been drawn with different geometries and dimensions from the first concepts by Emile Argand, Kenneth Hsü or John Dewey, to the recent reconstructions by Douwe van Hinsbergen or Paul Angrand. We review here the main reconstructions published since 1924 and the evolution of concepts and methods. We finally discuss the importance of this type of syntheses for understanding large-scale geodynamic processes.

Keywords. Tethys, Mediterranean, Apulia, Adria, Reconstructions.

Manuscript received 1 November 2022, revised and accepted 10 January 2023.

1. Introduction

The past Tethys Ocean was Jean Dercourt's favorite playground. One of his most memorable achievements is the detailed reconstructions he first published with a large group of colleagues in 1986 [Dercourt et al., 1986]. Except for ophiolitic nappes in different sutures zones, this almost entirely lost ocean is only locally preserved in the Eastern Mediterranean, south of Crete, subducting below the Aegean region in the Hellenic trench and in the Gulf of Oman, between Arabia and the Makran subduction zone. Most of it has now been swallowed in the subduction zones fringing the southern margin of Eurasia since the Late Cretaceous. This long period of convergence has seen the formation of major mountain belts, from the Caribbean to Indonesia, some of them still underway such as the Himalayas. Others have collapsed in back-arc regions, as shown by the Hellenides in the Aegean domain.

The younger Mediterranean Sea is the heir of the Tethys and its formation was entirely driven by the behavior of subducting lithospheric slabs in the asthenosphere. In the history of the Mediterranean, it is convenient to distinguish [Jolivet et al., 2021a,b] (1) a Tethyan period, before 30–35 Ma, (2) a Mediterranean period (from 30–35 to 8 Ma) and a Late Mediterranean period (from 8 Ma to the Present). The Tethyan period has seen the opening of the Tethys Ocean and then its subduction underneath Eurasia. The main engine is the large-scale convection driving plate tectonics with slabs and mantle plumes. The Mediterranean period starts because of a complete change of driving mechanism with the prominent role of slab retreat, leading to the opening of back-arc basins (Aegean Sea, Pannonian Basin, Tyrrhenian Sea, Liguro-Provençal Basin, Alboran Sea) at fast rates and the collapse of the mountain belts formed during the Tethyan period (Hellenides, Taurides, Pyrenees). The Late Mediterranean period

sees the progressive cessation of back-arc opening and a return to compressional conditions from the westernmost Mediterranean to the Central Mediterranean. Understanding the dynamics (forces) of this complex puzzle first requires a precise description of the succession of tectonic events in the entire Tethyan realm, with their kinematics and thermal regimes, a goal achieved through reconstructions.

The name of the Tethys Ocean was given by Suess [1883, 1901, 1909] to the ancient deep basin sandwiched between Laurasia and Gondwana, after Neumayr [1885] first proposed its existence for the Jurassic period. Suess [1883, 1901, 1909] further proposed that the observed mountain belts were formed by the contraction of that former ocean, a remarkable intuition at that time. He further understood that the present Mediterranean is an offspring of the Tethys. We have since understood that the ophiolitic belts running from the Caribbean to Indonesia are the remnants of this lost ocean and it has been a challenge to reconstruct its evolution through time since Argand [1924]. This paper presents the various attempts to describe the tectonic evolution of the Tethys since the early work of Argand who had already understood some first order features, among which the major role played by what is now called Apulia, or Adria, in the deformation of the Mediterranean region. The presentation of these successive attempts, until the most recent ones, shows some major steps corresponding to conceptual breakthroughs, such as the discovery of plate tectonics. The core of the paper is focused on the notion of Apulia, a micro-continent drifted away from Africa and then shortened to form a large part of the Alps, the Dinarides and the Hellenides. Apulia, or Adria, is represented as an independent continental block carried by an independent plate during the Mesozoic in most reconstructions. The Apulian continent would have been drifted away from Africa during the early Mesozoic. However, several alternative reconstructions [Argand, 1924, Channell and Horvath, 1976, Angrand and Mouthereau, 2021, Mouthereau et al., 2021, Channell et al., 2022] show it still attached to Africa and the existence of an intervening oceanic tract, known as Mesogea, is thus still debated. The reasons for this disagreement mostly stem from the interpretation of the nature of the lithosphere flooring the deep basins of the Ionian Sea and the Eastern Mediterranean Sea, whether oceanic or con-

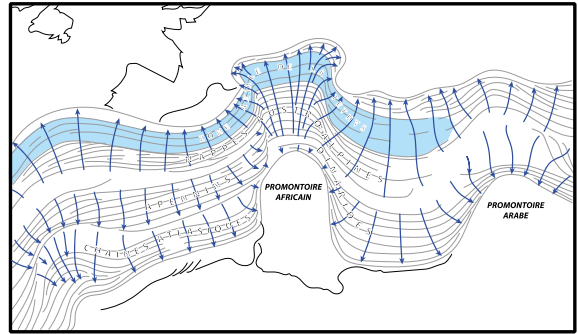


Figure 1. The “promontoire africain” and “promontoire arabe” and direction of crustal flow (“filets d’écoulement”) during Tethys closure in Emile Argand’s conceptions. Redrawn from Argand [1924].

tinental, the continuity of platform deposits from Africa to Apulia and paleomagnetic data that tend to suggest that Apulia had always traveled exactly as Africa during the Mesozoic and the Cenozoic. We come back to this debate and finally discuss the consequences of these reconstructions for the understanding of geodynamic processes.

2. Emile Argand and the “Promontoire Africain”

In *La Tectonique de l’Asie* [Argand, 1924], Emile Argand inferred the direction of a crustal flow (“filets d’écoulement”) from the orientation of folds in mountain belts (Figure 1) introducing a dynamic aspect in continental tectonic studies. He saw the formation of the Mediterranean arcs as the result of such a flow, primarily controlled by the irregular shape of the Gondwanan margin (“vieux bord gondwanien”) and proposed the existence of two promontories impinging the southern margin of Eurasia during the shortening of the Tethys Ocean, the so-called African and Arabian promontories.

This vision is of course outdated nowadays, but it already contained a major ingredient i.e., the complex geometry of the African margin playing a major role in controlling the dynamics of slab retreat in the Eastern and Western Mediterranean, forming the Calabrian and Hellenic arcs. It also contained the germs of the notion of continental blocks between Eurasia and Gondwana, named today Apulia

(or Adria) and Arabia. The separation of these large blocks, we would say “plates” nowadays, away from Gondwana and their evolution during the lifetime of the Tethys until its final closure is still a major scientific question we will discuss at the end of this contribution. Argand [1924] went much further into the description of the Mediterranean region and his reconstructions already showed (Figure 2) the rotation of Iberia opening the Bay of Biscay and the rotation of a rigid block carrying Sardinia and Corsica and the associated formation of extensional basins since the Oligocene. He had thus seen the large picture, the Tethys as an ancestor of the Mediterranean, as first proposed by Suess [1883], and the details of the Mediterranean dynamics without any idea at that time of the importance of subduction dynamics.

3. The first reconstructions incorporating the plate tectonic concepts, the first notion of an Apulian microcontinent

As soon as 1971, a short time after the publication of the new global tectonics [Wilson, 1965, McKenzie and Parker, 1967, Le Pichon, 1968, Morgan, 1968], Hsü [1971] proposed to revised Argand’s scheme (Figure 3) and placed his reasoning in the new framework, although he did not incorporate any precise kinematics.

He suggested the existence of several oceanic basins, still named *geosynclines* in his paper, separating Gondwana from Eurasia, surrounding a so-called *Greco-Italian microcontinent*, the first graphical mention of what will then be named *Apulia* or more recently *Adria*. This is a major shift in Alpine studies with the first implication of the new paradigm. It must be noted, however, that Dewey and Bird [1970], in their seminal paper about mountain belts and the new global tectonics, explicitly already mention the possibility that the complexity of the Mediterranean region is due to the amalgamation of microcontinents with the southern margin of Eurasia during collision.

One important consequence of plate tectonics is also that all the pre-Atlantic kinematic reconstructions of the positions of the large plates leave a vast open space between Africa and Eurasia in the Mesozoic [Bullard et al., 1965, Le Pichon, 1968], a space where the Tethys Ocean had once developed during the Mesozoic (Neo-Tethys). The same year, Smith

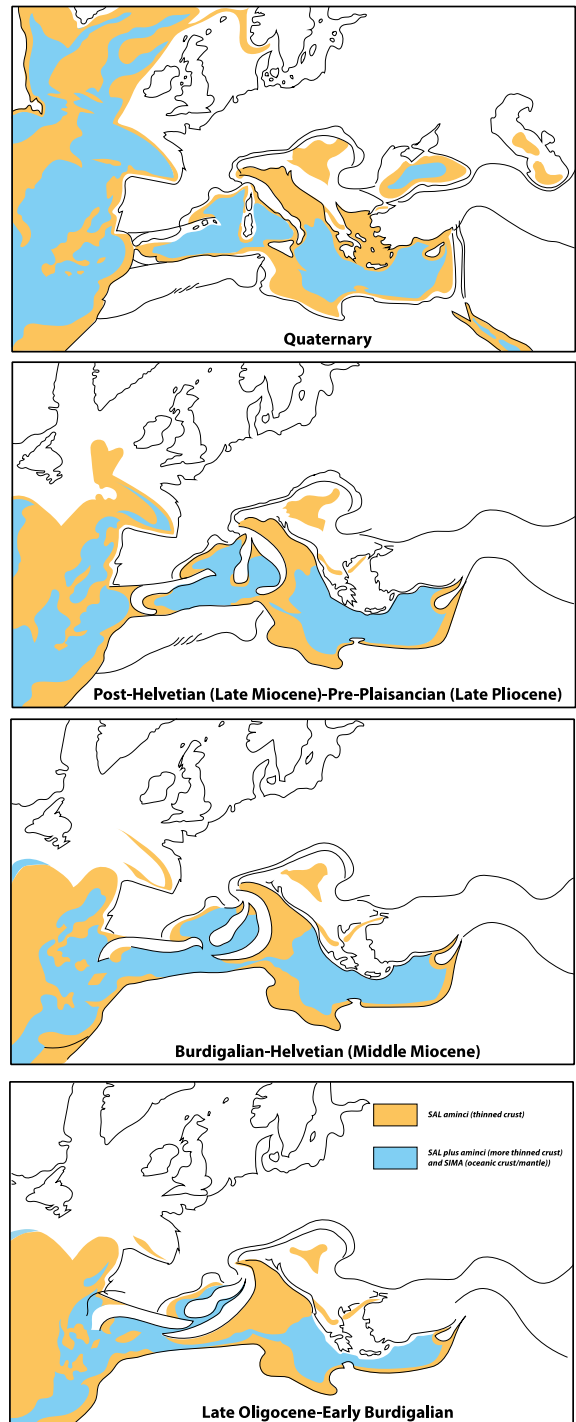


Figure 2. Evolution of the Mediterranean region as viewed by Argand with the rotation of Iberia and Corsica/Sardinia. Redrawn from Argand [1924].

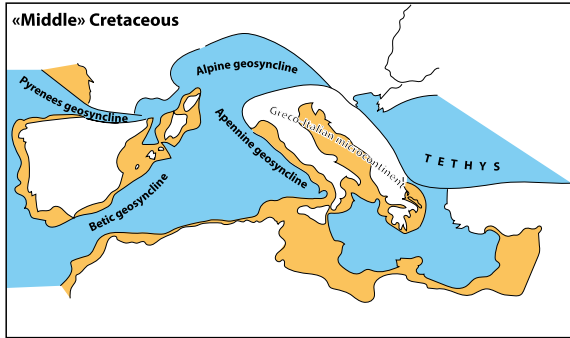


Figure 3. The first reconstruction of the Mediterranean region after the discovery of plate tectonics. The Greco-Italian microcontinent prefigures Apulia/Adria. Redrawn from Hsü [1971].

[1971] published a first attempt of rigorously reconstructing the geometry of the Mediterranean region using the kinematic parameters imposed by the Atlantic magnetic anomalies. This paper does not however show any detail of the temporal evolution of the Tethyan domain between the initial situation and the present-day. A major step is made with the publication of detailed reconstructions by Dewey et al. [1973] (Figure 4), also based on the Atlantic magnetic anomalies with eight stages, from the Late Triassic to the Present, and considering the tectonic evolution within the Tethyan domain.

Figure 4 shows the Late Jurassic (Kimmeridgian) stage of their reconstructions. The intervening domain between Europe and Africa is detailed with several continental blocks and several small oceanic domains. This is the first clear mention of an Apulian block in reconstructions. Apulia represents then the outer zones of the Dinarides, the Hellenides and the Apennines, a carbonate platform deposited on a continental crust. Other independent blocks such as the Carnic block or the Rhodope are shown. This paper is the first modern attempt of reconstructing the Tethys.

The shape and internal geometry of the Apulian or Adriatic block have been drawn very differently through time, as will be obvious in the following. One important constraint on its kinematics comes from paleomagnetic studies. In an important paper, Channell and Horvath [1976] attach the “Adriatic plate” to Africa (Figure 5), the main reason being the ab-

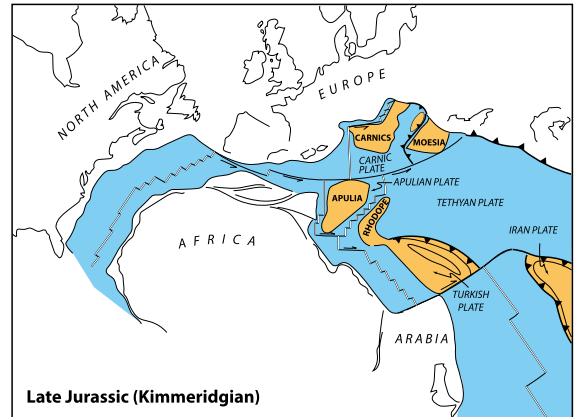


Figure 4. The first reconstruction of the Tethys involving plate tectonics concepts and a kinematics based on oceanic magnetic anomalies. The first explicit mention of an Apulian microcontinent in reconstructions. Redrawn from Dewey et al. [1973].

sence of any significant difference in its apparent polar wander path from that of Africa, as later studies will confirm and precise [Westphal et al., 1986]. The geometry they thus propose is quite similar to Argand’s one with a promontory sticking out from the main body of the African plate. Through much of the Mesozoic Adria has followed a path that did not involve any latitudinal drift away from Africa.

In the same period, Biju-Duval et al. [1977a,b] (Figure 6) show a large Apulia, englobing all the microcontinents shown in older reconstructions, even Channell and Horvath [1976], in a single plate separated from Africa by a narrow oceanic domain, called Mesogea, which remnants are found today in the Eastern Mediterranean. The width of this domain is probably too small to be seen in paleomagnetic data. This reconstruction is constrained by the Africa/Eurasia/North America kinematics deduced from the Atlantic magnetic anomalies. It also involves a palinspastic restoration of the contractional deformation seen in mountain belts, for the first time [Biju-Duval et al., 1977a,b]. This study announces the next step in reconstructing the Tethys, best exemplified by Dercourt et al. [1986].

The new geometrical and kinematic concepts brought to light by the new global tectonics was indeed the starting point for many studies around the world. One important example is the new vision of

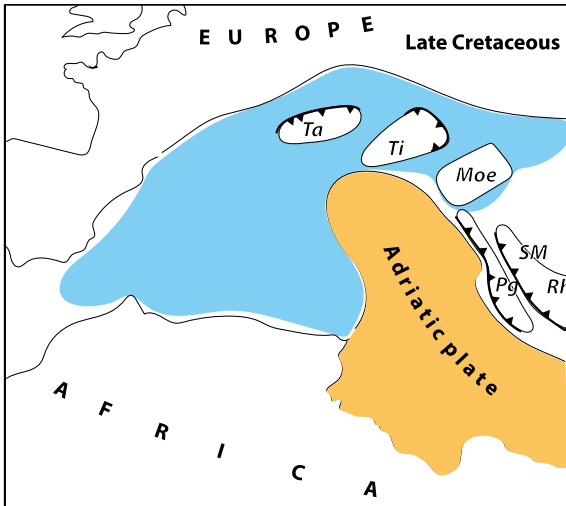


Figure 5. Paleomagnetic data suggest that Adria was always attached to Africa. Redrawn from Channell and Horvath [1976].

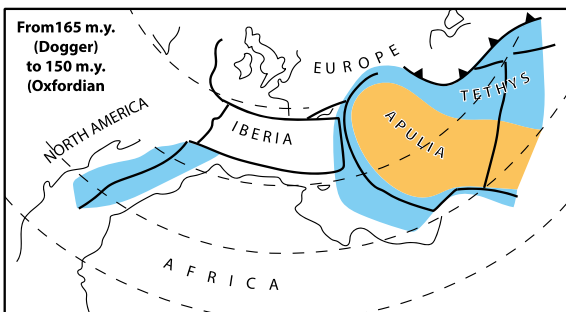


Figure 6. Apulia as a single plate separated from Africa by an oceanic corridor named Mesogea. The reconstruction takes into account oceanic magnetic anomalies and shortening of mountain belts. Redrawn from Biju-Duval et al. [1977a,b].

the tectonic history of Turkey proposed by Şengör and Yilmaz [1981] still serving as the basis of all tectonic studies in this region nowadays (Figure 7). It shows three branches of the NeoTethys and two continental blocks, the Sakarya continent in the north and the Anatolide–Tauride platform in the south, each of the intervening oceanic tracts being represented by ophiolite nappes. The southern branch of the NeoTethys is now represented by the Eastern Mediterranean subducting underneath Crete, simi-

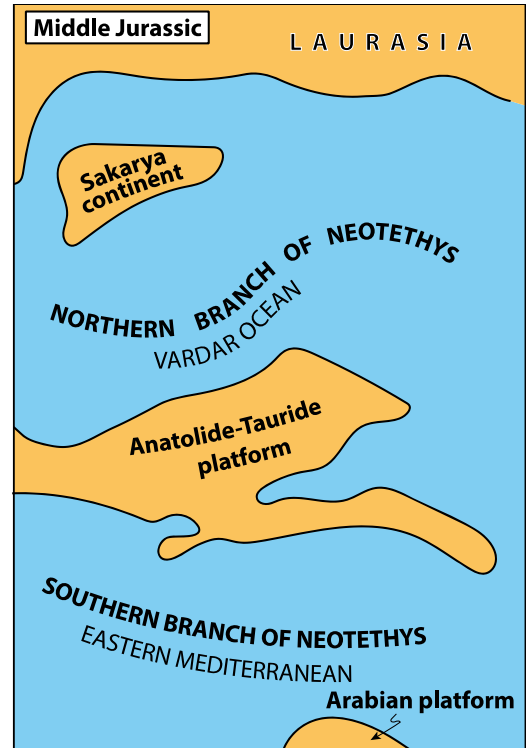


Figure 7. Plate tectonics concepts explain the geological history of Turkey with two continental blocks between Laurasia and the Arabian platform. Redrawn after Şengör and Yilmaz [1981].

lar to the Mesogea of Biju-Duval et al. [1977a,b]. The Vardar Ocean is an extension of the large ophiolitic nappes of continental Greece.

4. Toward modern reconstructions, Tethys project

A major step forward was made through the Tethys Project, a collaborative research venture between French and Russian scientists [Dercourt et al., 1986, Ricou et al., 1986, Dercourt et al., 1993] (Figure 8). We shall not discuss here the details of these reconstructions but only point out a few lines that make it a milestone in tectonic reconstructions in general. The project was achieved through an association between geologists who had a wide experience in the

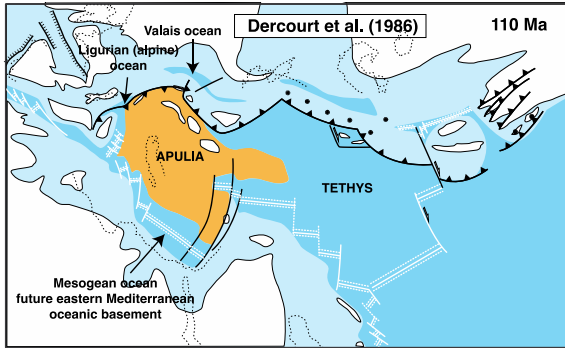


Figure 8. The Tethys Ocean reconstructed in the Tethys project. Apulia is separated from Africa by the Mesogea. Apulia rotates CCW by 30° . Kinematic framework after Savostin et al. [1986]. This reconstruction also shows paleoenvironments (not shown). Redrawn and simplified after Dercourt et al. [1986], paleoenvironments omitted.

geology of the Tethyan realm both onshore and offshore. The reconstructions were based upon a coherent kinematic framework [Savostin et al., 1986] based on the magnetic anomalies in the oceans and on palinspastic restoration of mountain belts and basins, as in Biju-Duval et al. [1977a]. The details of the geological data are published in separate papers [Ricou et al., 1986, Zonenshain and Le Pichon, 1986]. One of the novelties is the interpretation of the Black Sea and the Southern Caspian Sea as back-arc basins formed above the subduction of the main Tethys Ocean underneath the southern margin of Eurasia [Zonenshain and Le Pichon, 1986]. The outcome is a series of 9 maps from 190 Ma (Pliensbachian) to the present, showing continental and oceanic domains, as well as paleo-coastlines and types of sedimentation, thus a first attempt to show paleoenvironmental changes through time.

In Dercourt et al. [1986] Apulia rotates CCW with respect to Africa by 30° from 130 to 80 Ma and the Mesogea does not communicate eastward with the large Tethys Ocean. Oceanic accretion dates back to the Cretaceous in these reconstructions, a point that will be actively debated in later years [Stampfli et al., 1998a,b, Stampfli, 2000]. The reconstructions encompass the entire Tethyan realm from the Caribbean to Indonesia. The position of plate boundaries within the oceanic domains are tentatively

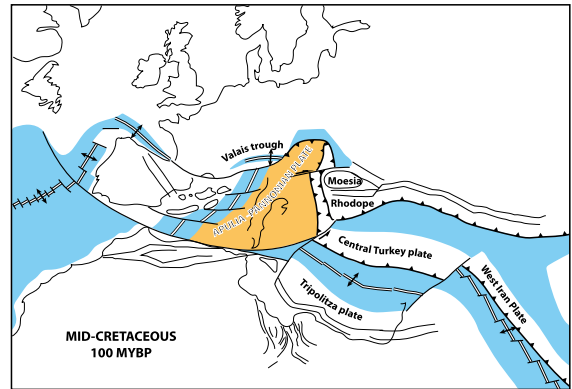


Figure 9. Tethys reconstructed based the kinematic model of Scotese et al. [1988]. Redrawn after Gealey [1988].

shown and kept consistent with the contemporaneous kinematics throughout. This set of maps thus contains many of the recent improvements in paleotectonic reconstructions although it was not made with the convenient softwares available today. The Tethys project was followed by several others involving large international consortia of academics and oil companies, Peri-Tethys, MEBE (Middle-East Basins Evolution), and DARIUS [Ricou, 1994, Dercourt et al., 2000, Gaetani et al., 2003, Barrier and Vrielynck, 2008, Barrier et al., 2018]. Since Peri-Tethys, the emphasis has been on paleoenvironments.

The 80's were a period of fast development of paleo-tectonic reconstructions. The Paleomap project [Scotese et al., 1988] has produced global maps on a long period spanning the last 200 Ma. These maps were used by Gealey [1988] to propose restorations of the Western Tethys (Figure 9) with different kinematic options.

In these reconstructions, Apulia is a unique large block as in Dercourt et al. [1986] with however a different geometry. The equivalent of the Mesogea opens even more recently than in Dercourt et al. [1986] between a Tripolitza plate and the main body of Africa, after the closure of an oceanic basin between this Tripolitza plate and a Central Turkey plate. Toward the east, the Central Turkey plate is relayed by a West Iran plate forming a ribbon of continental blocks detaching from Africa.

Paleomagnetic data, which provided the first independent positive test of continental drift [Irving,

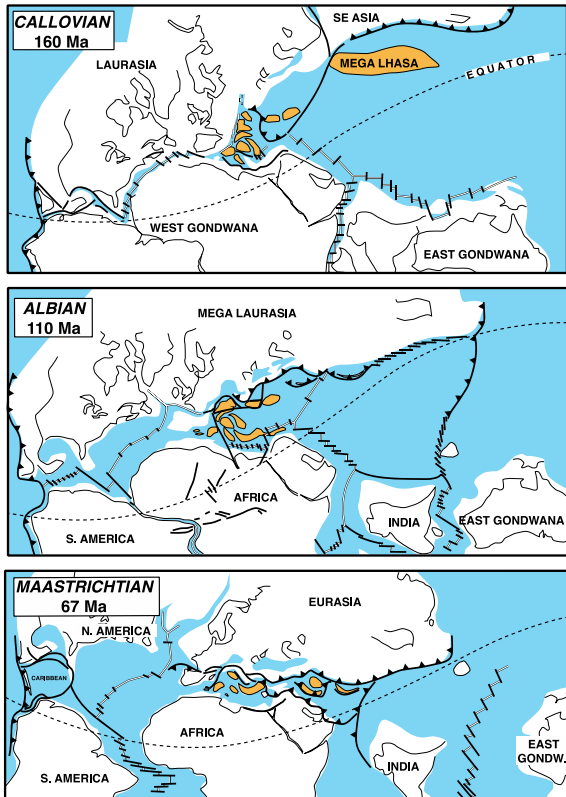


Figure 10. Reconstructions of the Tethys realm in the Peri-Tethys project. Redrawn from Dercourt et al. [1993].

1958, Runcorn, 1962] played a major role in these series of reconstructions when large displacements were involved. The fast displacement of India is constrained by the magnetic anomalies in the Indian Ocean [Patriat and Achache, 1984, Patriat and Ségoufin, 1988] and by paleomagnetic data [Besse et al., 1984, Besse and Courtillot, 1988] that helped assessing intracontinental shortening in the Himalaya.

The question of the small blocks rifting away from Africa and drifting northward to ultimately collide with Eurasia comes into discussion at this period already. Clearly shown in Gealey [1988], they are also emphasized in Ricou [1994] (Figure 10). As will be shown below, this process was not only active in the NeoTethys but also in the PaleoTethys and is still active nowadays, the last of these blocks being Arabia.

The northern connections of the Tethys Ocean were described in details by Ziegler [1999] using the

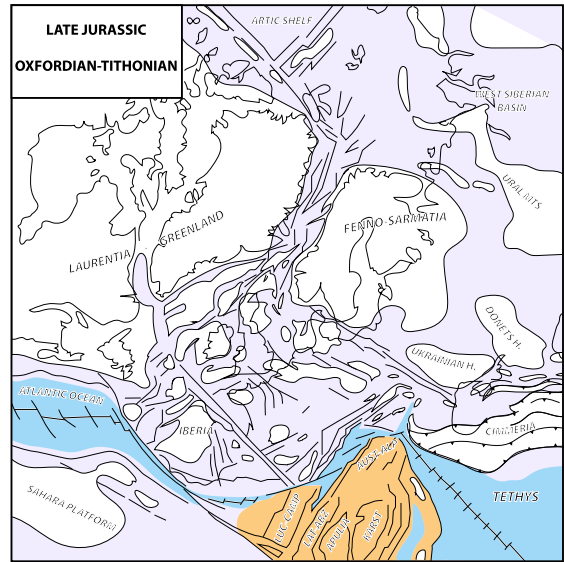


Figure 11. The northern connections of the Tethys. Redrawn after Ziegler [1999].

numerous data acquired offshore and onshore by oil companies. Figure 11 shows one of these maps at the time of opening of the Central Atlantic Ocean, before the formation of the Northern Atlantic in the Late Jurassic. In these reconstructions, Apulia is part of a large block attached to Africa and separated from Europe by an Alpine oceanic basin connected directly to the Atlantic by a system of transform faults.

5. Recent evolutions of paleotectonic reconstructions

Recently made paleotectonic reconstructions take advantage of the development of powerful kinematic softwares such as PaleoMap [Scotese et al., 1988, Schettino and Scotese, 2002] or more recently GPlates [Boyden et al., 2011]. These new methods allow fast and easy tests of various kinematic hypotheses and also to draw the detailed evolution of the intra-oceanic domain based on magnetic anomalies reconstructions. One of the salient examples is the detailed global scale reconstructions of Stampfli and Borel [2002] (Figure 12). Compared to Dercourt et al. [1986], besides some drastically different assumptions on the paleotectonic situation and age of some paleogeographic domains, they also show the details



Figure 12. The global reconstructions of Stampfli and Borel [2002], Anisian stage.

of the intra-oceanic domains and they go way backward in time, back to the early Paleozoic. Figure 12 show the Anisian stage (240 Ma) on the Tethyan side of the globe. It shows the NeoTethys opening at the expense of the PaleoTethys that is closing to the north. A ribbon of continental blocks has detached from Africa and drifts northward toward the subduction zone. The NeoTethys includes part the Mesogea of Dercourt et al. [1986], which thus opens much earlier. The oceanic floor of the eastern Mediterranean in this set of reconstructions is as old as the Triassic, a drastic difference with Dercourt et al. [1986] who assumed a Cretaceous age. This question is not settled yet. Other options have been proposed such as the highly probable Late Jurassic age by Frizon de Lamotte et al. [2011]. The thick sedimentary cover of the oceanic crust between Crete and the North African coast makes all speculations possible but recent studies favor a Jurassic oceanic floor [Tugend et al., 2019].

Figure 13 shows a detail of the Western Tethys 121 Ma ago (Aptian) after Stampfli and Kozur [2006]. The Alpine Tethys is a continuous oceanic domain from the Ligurian Ocean preserved in the Alpine ophiolites and the Maghrebian Tethys between Spain and Morocco, connected with the Central Atlantic. The Vardar and Lycian oceanic domains have de-

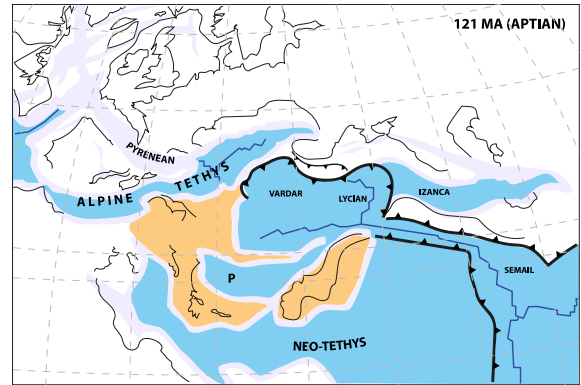


Figure 13. A detailed vision focused on the Tethys realm [Stampfli and Kozur, 2006].

veloped as back-arc basins above the subduction zones, totally consuming the older Maliac and Izanca oceans, a drastic assumption that renders possible the replacement of an ocean by a younger one. In Barrier and Vrielynck [2008] (Figure 14) a full connection of the Atlantic with the Tethys is shown and Apulia forms a large isolated block drifting away from Africa in the Late Jurassic, and the Alpine Ocean is a small tributary of the larger Tethys.

One recent trend of paleotectonic reconstructions is to explore their implications for the amount of slab imaged in the mantle by seismic tomography, orienting the reconstructions toward a 3-D approach. An early attempt was proposed by Faccenna et al. [2001] for the Western Mediterranean, allowing a new description of the history of subduction and slab retreat, which has consequences for the understanding of slab dynamics in the asthenosphere and at the upper/lower mantle discontinuity. A more detailed exercise, on a larger scale, was shown by Hafkenscheid et al. [2006] for the Tethys Ocean based on the reconstructions of Stampfli and Borel [2002] mentioned above and detailed comparison with the tomographic model of the Utrecht Group [Wortel and Spakman, 2000, Spakman and Wortel, 2004]. A reverse approach was later proposed at the scale of the globe to unravel the history of subduction and absolute kinematics for the last 300 Ma by van der Meer et al. [2010]. This study was based on a set of global reconstructions in a paleomagnetic framework [Steinberger and Torsvik, 2008, Torsvik et al., 2008] and the global travel-time tomography model

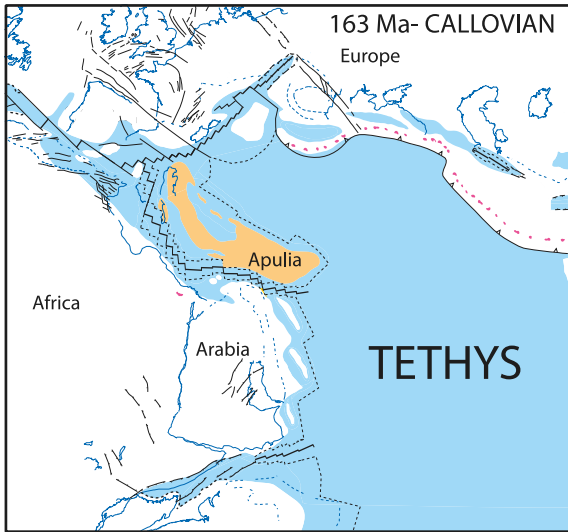


Figure 14. Callovian stage of Tethys reconstructions from the MEBE project. Apulia is totally separated from Africa by the Mesogea Ocean and the Alpine Ocean is a small tributary of the Tethys. Red spots represent active volcanism at the time of the reconstruction. Redrawn from Barrier and Vrielynck [2008].

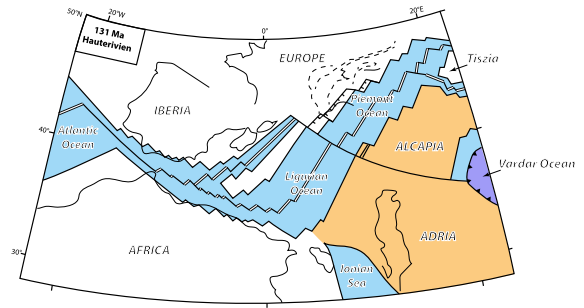


Figure 15. Cretaceous reconstruction of the western Tethys, a wide Ligurian Ocean fully connected to the Atlantic. With these reconstructions the authors estimate the amount of slab swallowed by Tethyan subduction zones. Redrawn from Handy et al. [2010].

of Amaru [2007]. This approach allows pinning the plates with respect to the underlying mantle with some simple assumptions on the behavior of slabs at depth (more or less vertical sinking) and it thus provides a complementary approach to absolute motions. Such a link between slabs at depth and kinematic reconstructions at the surface is proposed by Handy et al. [2010] for the western part of the Tethys (Figure 15).

The geometry of plate boundaries and continental margins in this set of reconstructions is a direct graphic translation of a simple kinematics linking the Ligurian and Piemont Ocean with the Atlantic Ocean. One consequence is the opening of a large Ligurian Ocean west of Adria, a solution that has been recently challenged by Angrand and Mouthereau [Angrand et al., 2020, Angrand and Mouthereau, 2021]. Such a simple kinematic pattern allows an easy calculation of the length of slab subducted in the mantle and facilitates the comparison with the tomographic images. Handy et al. [2010] conclude to a discrepancy between 10 and 30% in the amount of slab subducted deduced from the reconstructions and

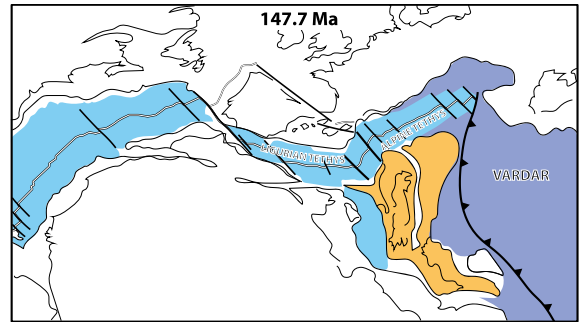


Figure 16. Latest Jurassic reconstruction of the Western Tethys. The Alpine Tethys is a tributary of the Atlantic Ocean. Redrawn from Schettino and Turco [2011].

imaged by tomography. A similar direct kinematic link between the Alpine Ocean and the Atlantic is proposed by Schettino and Turco [2011] (Figure 16) and no direct connection with the large Tethys Ocean is postulated. Apulia remains attached to Africa.

The reference frame of the reconstructions is an important issue. One of the most difficult questions is to reconstruct the paleolatitudes as the whole system of plates may be positioned almost anywhere on the globe if considering only relative kinematics. This question was already addressed in the very first reconstructions by Köppen and Wegener [1924]. They used paleoclimatic proxies such as the presence of tillites, evaporites or coal to test the reliability of Wegener's reconstructions [Wegener, 1912, 1924,

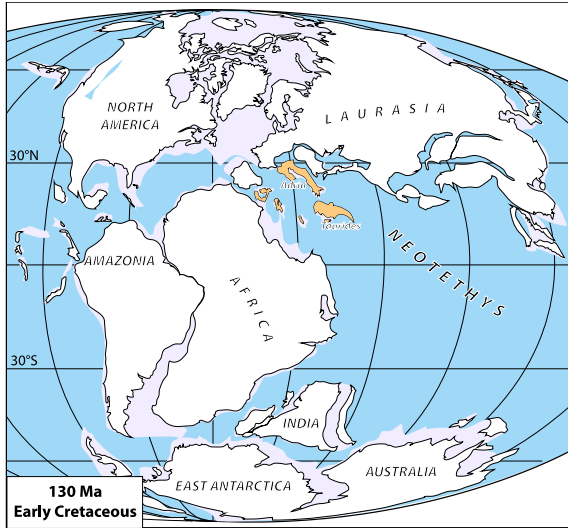


Figure 17. Global reconstruction in the Early Cretaceous and the Adria and Taurides continental blocks in a paleomagnetism-based model. Redrawn from Torsvik and Cocks [2016].

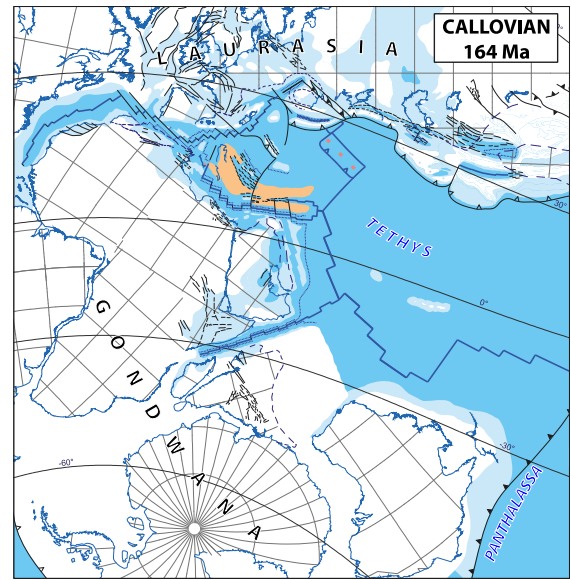


Figure 18. Callovian reconstruction of the Tethys from the DARIUS project. Redrawn from Barrier et al. [2018].

1929] on a globe where the present latitudinal zonation of climates would not change. One powerful tool to determine the paleolatitudinal position of a given plate is through paleomagnetic constraints. Torsvik et al. [2008] and Steinberger and Torsvik [2008] have proposed a set of global reconstructions based on a paleomagnetic framework, assuming little absolute motion of Africa (Figure 17). They thus obtained with an independent approach the paleolatitude and the paleolongitude. The reconstructions are not detailed in the Tethyan realm, but the position of Adria and the Taurides, shown here as two separate blocks in the Early Cretaceous, is mainly based upon paleomagnetic data.

The same kinematic parameters [Torsvik et al., 2008] were used for the large plates for the detailed DARIUS Project reconstructions of Barrier et al. [2018] (Figure 18), but the internal organization of the Tethyan realm is based upon geological data, onshore and offshore. The paleotectonic maps are then decorated with paleoenvironmental conditions based on the observed sedimentary deposits at each stage of the reconstructions (Figure 19) leading to an unprecedented image of the geological changes through time.

6. Discussion: future evolutions of plate models and geodynamic issues

The recent years have seen considerable improvements of tools for reconstructing past plate motions thanks to the development of user-friendly softwares, the most popular of which being certainly GPlates [Torsvik et al., 2008, Boyden et al., 2011, Seton et al., 2012, Müller et al., 2019]. The GPlates group has not only built a very convenient kinematic tool easy to use for geologists, but also a large database of kinematic and geophysical data. The modern reconstructions in addition include the possibility to deform plates along their boundaries, which is also a very useful improvement. These reconstructions can for instance be used for studying the interactions between mantle convection and plate motion at the surface with global numerical models [Rolf et al., 2012, Zahirovic et al., 2016, Coltice et al., 2017] linking in a single coherent tool all the approaches done “by hand” in the previous period. Modern plate reconstructions have reached another dimension and they can be used for discussing the internal dynamics of the Earth based on plate kinematics and geological observations.

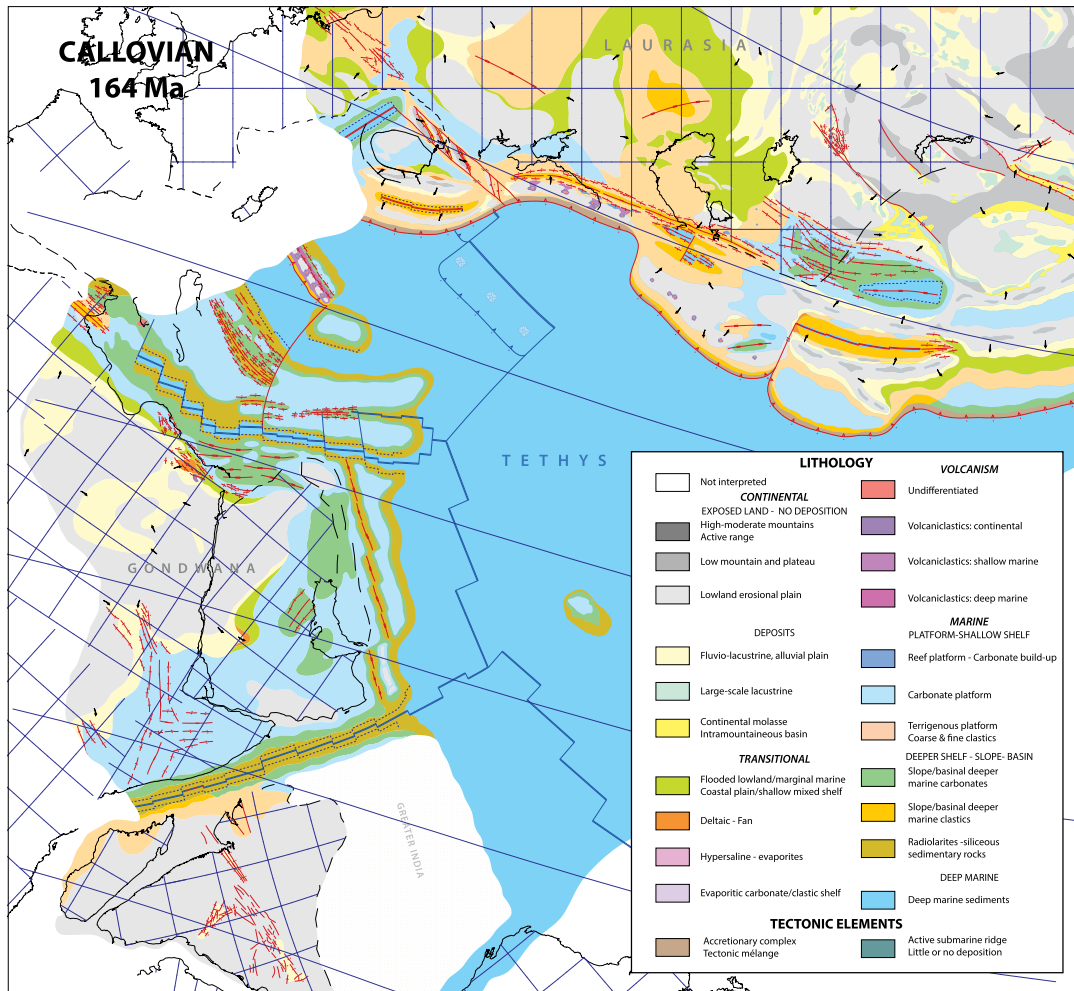


Figure 19. Callovian reconstruction of the Tethys from the DARIUS project with depositional paleoenvironments. Redrawn from Barrier et al. [2018].

This does not mean, however, that a full consensus has been reached in a complex setting such as the Mediterranean and the lost Tethys Ocean. Some debates are still active among geologists working in these regions. The geometry of the micro-continent either named Apulia or Adria is still actively discussed as well as the amount of oceanic crust swallowed by Alpine subduction zones in the Mediterranean, especially in the west where the nature of the crust between Africa and Eurasia is debated. The very existence of Adria as an independent micro-continent is also debated.

Figure 20 is an extract of the detailed reconstructions of the Tethys recently published by van

Hinsbergen et al. [2019] and Figure 21 shows the same region in a set of reconstructions by Angrand and Mouthereau [Angrand et al., 2020, Angrand and Mouthereau, 2021].

The surface covered by oceanic crust is drastically different in the two sets of reconstructions. van Hinsbergen et al. [2019] connect the Alpine Ocean to the Atlantic Ocean [see also Handy et al., 2010] through the Gibraltar Strait and a rather wide oceanic domain is present in the location of the future Pyrenees, while Angrand and Mouthereau [Angrand et al., 2020, Angrand and Mouthereau, 2021] show much less oceanic domains and no continuity of oceanic crust from the Alpine Ocean to the

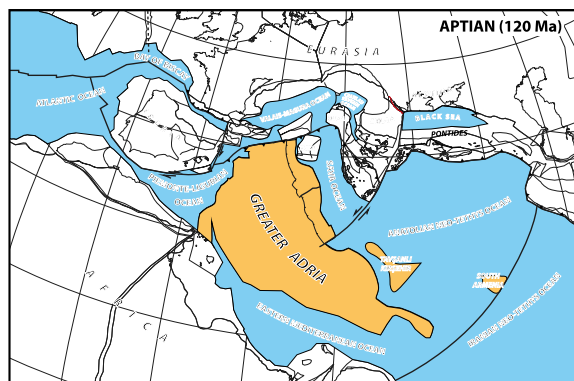


Figure 20. Aptian reconstruction of the Tethys and the Greater Adria, one of GPlates recent applications. Note the oceanic domain in the Pyrenees and the future Alboran Sea. Redrawn from van Hinsbergen et al. [2019]. To be compared with Figure 21.

Atlantic. At the maximum of divergence, only mantle exhumation is shown in the future Betics and the Pyrenees. This is due to drastically different interpretations of the geology of the Pyrenees and the Betics-Rif arc. I shall not show my preference here, but the interested reader can have a look at Romagny et al. [2020] or Bessi re et al. [2021].

As a large majority of reconstructions show a separate micro-continent that has drifted away from Africa, we shall not enter too much into this debate in this paper focused on the different geometries of Apulia/Adria since the first publications. It is however important to mention this still active discussion because the alternative interpretations have drastically different geodynamic implications.

The discussion dates back to the first reconstructions in the 70's. Channell and Horvath [1976] represent Apulia as a promontory of Africa, the main reason being the absence of significant differences in the paleomagnetic drift of Apulia and Africa. This vision is the closest to the original interpretation of Argand [1924]. The recent interpretations of Angrand et al. [2020] and Channell et al. [2022] (Figure 22) come back to a partly similar interpretation without a wide Mesogean Ocean. The Mesogea is instead already present in Biju-Duval et al. [1977a,b] and Dercourt et al. [1986], although they keep a continental bridge between Apulia and Africa. An oceanic domain south

of Apulia was also already present in Dewey et al. [1973].

The debate has been nicely summarized in the recent paper of Channell et al. [2022]. The authors of this paper argue in favor of the original model of Channell and Horvath [1976] and review the available data, in favor or against the existence of the Mesogea. I shall not enter into the details here again and the reader is referred to Channell et al.'s review. I shall only summarize the main points of the debate. The first observation often put forward against the existence of an oceanic domain between Apulia and Africa stems from paleomagnetic data. The paleomagnetic data show that, if an oceanic space ever existed, it could not have been wider than the error on the data that suggest no differential drift. In all reconstructions this oceanic space is not wider than a few hundreds of kilometers, which remain in agreement with the data. The paleomagnetic data alone thus cannot give a definitive answer, even less so because in these reconstructions Apulia is sandwiched between two oceanic spaces, the Mesogean and Alpine oceans, the widths of which being totally unknown. Both are thought to be a few hundreds of kilometers wide, but without any certainty as the only data are (1) the respective paleolatitudes of Africa, Apulia and Eurasia and (2) the reconstructed width of the passive margins, which both come with significant errors. The width of Apulia/Adria is thus largely speculative. Sedimentary facies in Apulian tectonic units show a certain continuity from Africa, which is one more argument against the existence of the Mesogea. The Mesogean Ocean was however narrow and similar depositional environments on either side would not be surprising. Detailed paleoenvironmental reconstructions such as Barrier et al. [2018] (Figure 19) show deep facies south of Apulia on the Mesogean margins. The presence of obducted ophiolites in Cyprus and southern Turkey is another argument in favor of an oceanic basin south of Apulia [Robertson, 1998, Maffione et al., 2017, van Hinsbergen et al., 2019]. The third type of data important in this debate is the nature of the crust in the deep basins of the Central and Eastern Mediterranean, respectively the Ionian Sea and the Herodotus/Levant Basin. Tugend et al. [2019] present a detailed re-assessment of this question. Available seismic data, whether refraction or reflection, suggest an old Mesozoic oceanic basement in both basins, with a Permo-

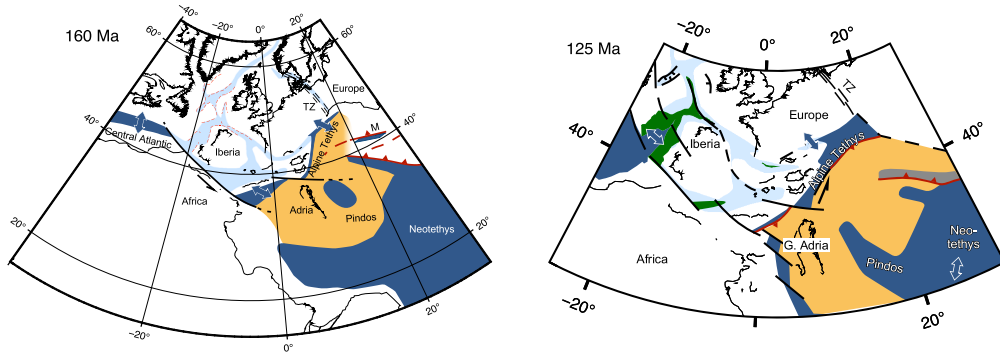


Figure 21. Two stages of the Tethys evolution showing much less oceanic lithosphere in the Western Tethys than in van Hinsbergen et al. [2019]. Compare to Figure 20. Redrawn from Angrand and Mouthereau [Angrand et al., 2020, Angrand and Mouthereau, 2021].

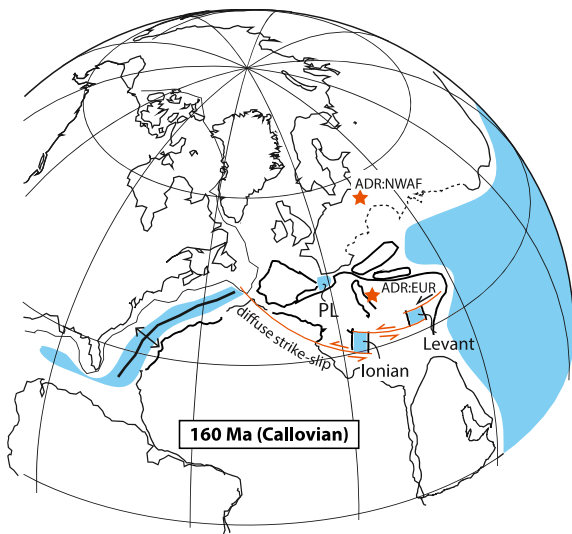


Figure 22. Jurassic reconstruction of Channell et al. [2022] showing no real separation between Africa and Adria. A left-lateral strike-slip fault is represented instead inducing the formation of small oceanic pull-apart basins in the Ionian Sea and Eastern Mediterranean.

Triassic rifting and a Jurassic oceanization. Channell et al. [2022] accept this conclusion and form this oceanic crust within small pull-apart basins, one for the Ionian Sea and one for the Levant Basin, along a left-lateral system of transform faults along which Africa moved with respect to Eurasia during the Mesozoic, a solution already used by Le Pichon et al. [2019]. This kinematic option offers a simple way to accommodate a significant displace-

ment without much latitudinal motion to fit the paleomagnetic data. It however implies that the Ionian Sea and Levant Basin have been separate basins since their formation in the Mesozoic and that the Mediterranean Ridge accretionary wedge that separates them formed there just by chance. An alternative solution is that the two basins are parts of a single deep Mesozoic oceanic basin subducting underneath the Mediterranean Ridge.

The last point of discussion is the engine of the Cenozoic subductions in the Mediterranean realm. It is most of the time considered that convergence and slab retreat in the Calabrian and Hellenic trenches are powered by the weight of the Hellenic and Ionian oceanic lithospheric slabs [Faccenna et al., 1997, 2001, 2014, Carminati et al., 1998a,b, Jolivet and Faccenna, 2000, Spakman and Wortel, 2004, Wortel et al., 2009, Romagny et al., 2020, Jolivet et al., 2021a,b] and that the post-35 Ma dynamics of the Mediterranean is essentially driven by slab behavior in the upper mantle. This widely shared vision is supported by numerical and analogue modeling [Faccenna et al., 2003, Funicello et al., 2003, Sternai et al., 2014, Capitanio, 2014]. In such models, the slabs are considered denser than the continental lithosphere of the overriding plate, and thus oceanic, which agrees with most published reconstructions and geophysical data in the Ionian Sea [Tugend et al., 2019, and references therein]. It also agrees with the presence of a calc-alkaline volcanic arc in Sardinia in the Late Eocene and Oligocene [Lustrino et al., 2009]. Channell et al. [2022] propose the alternative interpretation of a delamination of

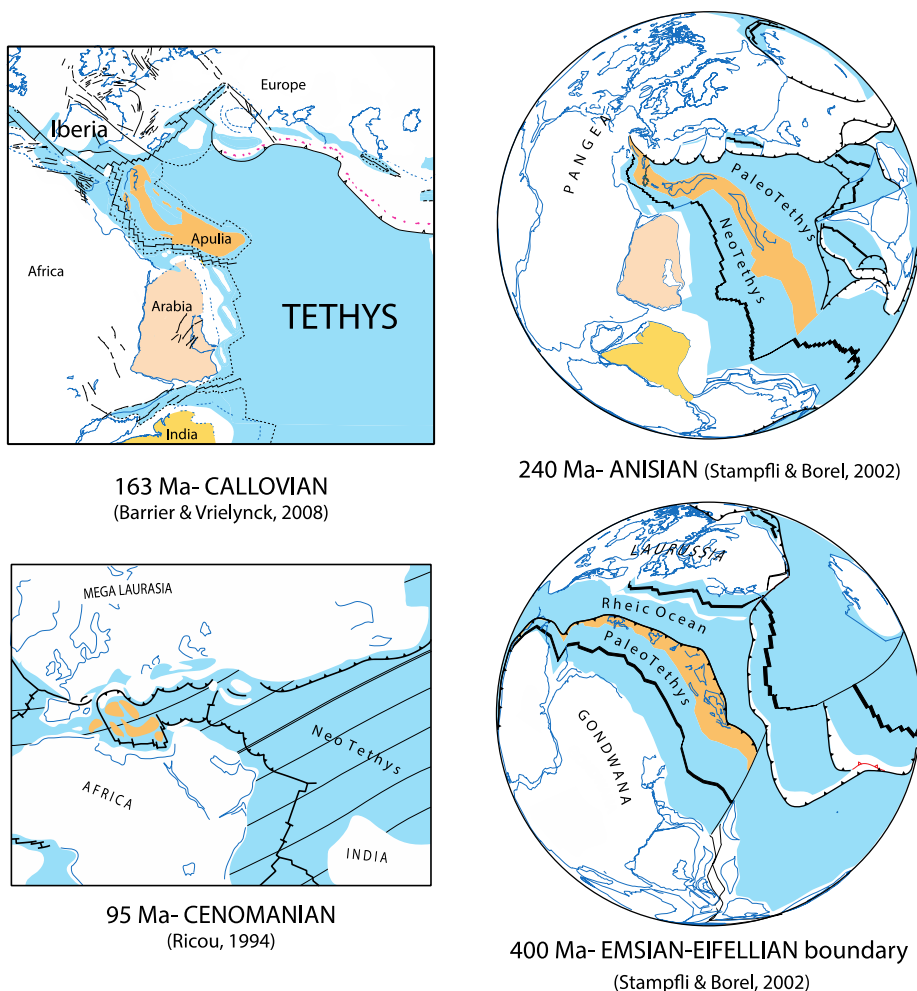


Figure 23. Four stages of the Tethys evolution showing continental blocks rifting away from Gondwana/Africa and drifting northward to ultimately collide with Laurasia/Eurasia. Redrawn from Barrier and Vrielynck [2008], Ricou [1994], Stampfli and Borel [2002].

the continental mantle below a previously thickened crust underneath the back-arc domain that would have similar consequences on the upper plate than the subduction of a retreating oceanic slab. Kinematic reconstructions taking into account paleomagnetic rotations, shortening rates in the Apennines and the amount of extension in the Liguro-Provençal Basin and Tyrrhenian Sea however impose about 600–800 km of maximum southeastward retreat of the Ionian slab since the Late Eocene [Dewey et al., 1989, Rosenbaum et al., 2002, Carminati et al., 2012, Romagny et al., 2020]. 600 or 800 km of shortening cannot be found in the Apennines, even when adding the Pyreneo-Provençal fold-and-thrust belt.

This would then imply that delamination had been triggered by a convective instability below the moderately thickened Pyreneo-Provençal belt and had then been subsequently driven only by the weight of the continental mantle to reach the stage of complete continental break-up in the back-arc domain, first in the Liguro-Provençal Basin and then in the Southern Tyrrhenian Sea. Whether this is physically feasible is still unclear and future studies are required of this alternative geodynamic scenario.

Reading the terms of this debate, one can easily feel that such diverging interpretations will inevitably lead to very different geodynamic interpretations both in mechanical and thermal terms, de-

pending upon whether an oceanic or a continental lithosphere has been consumed in the Mediterranean subduction zones.

Going back to the larger scale, we have seen in the present contribution the various representations of Apulia or Adria through time since Hsü [1971]. Whatever the exact shape and rifting time of these blocks away from Africa or Gondwana, they appear a constant feature of the Tethys geodynamics in most reconstructions considering that Apulia has been drifted away from Africa in the Mesozoic: ribbons of continental blocks rift away from Africa and drift northward faster than their mother continent, to ultimately collide with Eurasia. Before the separation of Apulia, the Cimmerian blocks detached in the Triassic–Liassic and their collision with Eurasia led to the Cimmerian Orogeny in the Jurassic [Şengör, 1979, Gyomlai et al., 2022].

Figure 23 shows four reconstructions by two independent groups of scientists at different periods, from the Devonian (400 Ma) to the Cenomanian (95 Ma). The Anisian stage shows the Cimmerian blocks [Stampfli and Borel, 2002], the Jurassic and Cretaceous stages show Apulia [Ricou, 1994] and the Devonian stage shows another ribbon of blocks drifting away from Gondwana during the opening of the Paleotethys at the expense of the Rheic Ocean [Stampfli and Borel, 2002]. The formation and drift of such blocks thus seems to be a constant scheme of the Tethys Ocean and it requires an explanation.

Figure 24 shows a reconstruction at 250 Ma [Torsvik and Cocks, 2016] highlighting the Cimmerian blocks drifting away from Gondwana. It also shows the projection at the surface of the Large Low Shear Velocity Zones observed by seismologists in the lowermost mantle where all major plumes originate. They represent the source of upwelling branches of whole-mantle convection [Burke, 2011]. The Cimmerian blocks lie to the NE of the Tuzo LLSVP and they migrate toward the main Tethyan subduction zone further northeast. It is thus tempting to conclude that they are carried by the convective flow that is responsible for the breakup of Gondwana. This mechanism has been proposed for the formation and migration of Apulia and Arabia [Faccenna et al., 2013, Jolivet et al., 2016] and tested by numerical modelling [Koptev et al., 2019]. This is only one example of how a first order geodynamic process, not proven yet, can be derived from the observation of

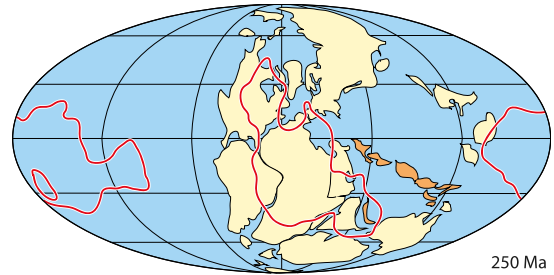


Figure 24. The globe 250 Ma ago. Cimmerian blocks drift northward away from Gondwana to the northeast of the “Tuzo” LLSVP (Large Low Shear Velocity Province). Redrawn from Torsvik and Cocks [2016].

paleotectonic reconstructions. The pioneer work of Jean Dercourt and his colleagues have far-reaching consequences, in terms of large-scale geodynamic processes as well as in terms of paleoenvironments, and thus in terms of prospection of natural resources.

Conflicts of interest

The author has no conflict of interest to declare.

Acknowledgements

I wish to thank the organizing committee of the conference held in the Académie des Sciences dedicated to Jean Dercourt for kindly inviting to present the views of our team on the geodynamics of the Mediterranean region. I feel also indebted to Jean Dercourt who supported me in the early days of my career.

References

- Amaru, M. (2007). *Global Travel Time Tomography With 3-D Reference Models*. PhD thesis, Utrecht University, Utrecht. 174 pages.
- Angrand, P. and Mouthereau, F. (2021). Evolution of the Alpine orogenic belts in the Western Mediterranean region as resolved by the kinematics of the Europe-Africa diffuse plate boundary. *BSGF—Earth Sci. Bull.*, 192, article no. 42.
- Angrand, P., Mouthereau, F., Masini, E., and Asti, R. (2020). A reconstruction of Iberia accounting for W-Tethys/N-Atlantic kinematics since the late Permian-Triassic. *Solid Earth*, 11, 1313–1332.

- Argand, E. (1924). La tectonique de l'Asie. In *Proceedings of the 13th International Geological Congress Brussels*, pages 171–372.
- Barrier, E. and Vrielynck, B. (2008). *Paleotectonic Maps of the Middle East: Atlas of 14 Maps*. CGMW, Paris.
- Barrier, E., Vrielynck, B., Brouillet, J. F., and Brunet, M. F. (2018). Paleotectonic Reconstruction of the Central Tethyan Realm. In *Tectonono-Sedimentary-Palinspastic maps from Late Permian to Pliocene*. CCGM/CGMW, Paris. (Contributors: Angiolini L., Kaveh E., Plunder A., Poisson A., Pourteau A., Robertson A., Shekawat R., Sosson M. and Zanchi A.) <http://www.ccgmm.org>. Atlas of 20 maps (scale: 1/15 000 000).
- Besse, J. and Courtillot, V. (1988). Paleogeographic maps of the Indian ocean bordering continents since the Upper Jurassic. *J. Geophys. Res.*, 94, 2787–2838.
- Besse, J., Courtillot, V., Pozzi, J. P., and Zhou, Y. X. (1984). Paleomagnetic estimates of crustal shortening in the Himalayan thrusts and Zangbo suture. *Nature*, 311, 621–626.
- Bessi re, E., Jolivet, L., Augier, R., Scaillet, S., Pr cigout, J., Aza n, J. M., Crespo-Blanc, A., Masini, E., and Do Couto, D. (2021). Lateral variations of pressure-temperature evolution in non-cylindrical orogens and 3-D subduction dynamics, the Betics-Rif example. *BSGF—Earth Sci. Bull.*, 192, article no. 8.
- Biju-Duval, B., Dercourt, J., and Le Pichon, X. (1977a). From the Tethys Ocean to the Mediterranean Seas: a plate tectonic model of the evolution of the western Alpine system. In Biju-Duval, B. and Montadert, L., editors, *Structural History of the Mediterranean Basins. Proceedings of an International Symposium*, pages 143–164. Editions Technips, Paris.
- Biju-Duval, B., Letouzey, J., and Montadert, L. (1977b). Structure and evolution of the mediterranean sea basins. In *Initial Report of DSDP*, volume 42a, pages 951–984. U.S. Government Printing Office, Washington.
- Boyden, J. A., M ller, R. D., Gurnis, M., Torsvik, T. H., Clark, J. A., Turner, M., Ivey-Law, H., Watson, R. J., and Cannon, J. S. (2011). Next-generation plate-tectonic reconstructions using GPlates. In Keller, G. R. and Baru, C., editors, *Geoinformatics: Cyberinfrastructure for the Solid Earth Sciences*, pages 95–114. Cambridge University Press, Cambridge.
- Bullard, E., Everett, J. E., and Smith, A. G. (1965). The fit of the continents around the Atlantic. *Philos. Trans. R. Soc. Lond., A*, 258(1088), 41–51. A Symposium on Continental Drift.
- Burke, K. (2011). Plate tectonics, the wilson cycle, and mantle plumes: geodynamics from the top. *Annu. Rev. Earth Planet. Sci.*, 39, 1–29.
- Capitanio, F. A. (2014). The dynamics of extrusion tectonics: Insights from numerical modeling. *Tectonics*, 33, 2361–2381.
- Carminati, E., Lustrino, M., and Doglioni, C. (2012). Geodynamic evolution of the central and western Mediterranean: Tectonics vs. igneous petrology constraints. *Tectonophysics*, 579, 173–192.
- Carminati, E., Wortel, M. J. R., Meijer, P. T., and Sabadini, R. (1998a). The two-stage opening of the western-central mediterranean basins: a forward modeling test to a new evolutionary model. *Earth Planet. Sci. Lett.*, 160, 667–679.
- Carminati, E., Wortel, M. J. R., Spakman, W., and Sabadini, R. (1998b). The role of slab detachment processes in the opening of the western-central Mediterranean basins: some geological and geophysical evidence. *Earth Planet. Sci. Lett.*, 160, 651–665.
- Channell, J. E. T. and Horvath, F. (1976). The African-Adriatic promontory as a palaeogeographical premise for Alpine orogeny and playe movements in the Carpatho-Balkan region. *Tectonophysics*, 35, 71–101.
- Channell, J. E. T., Muttoni, G., and Kent, D. V. (2022). Adria in Mediterranean paleogeography, the origin of the Ionian Sea, and Permo-Triassic configurations of Pangea. *Earth-Sci. Rev.*, 230, article no. 104045.
- Coltice, N., G rault, M., and Ulvrova, M. (2017). A mantle convection perspective on global tectonics. *Earth-Sci. Rev.*, 165, 120–150.
- Dercourt, J., Gaetani, M., Vrielynck, B., Barrier, E., Biju-Duval, B., Brunet, M. F., Cadet, J. P., Brasquin, S., and Sandulescu, M. (2000). *Atlas Peri-Tethys, paleogeographical maps*. Commission de la Carte G ologique du Monde, Paris.
- Dercourt, J., Ricou, L. E., and Vrielynck, B. (1993). *Atlas Tethys Palaeo Environmental Maps*. Gauthier-Villars, Paris.
- Dercourt, J., Zonenshain, L. P., Ricou, L. E., Kuzmin, V. G., Le Pichon, X., Knipper, A. L., Grandjacquet,

- C., Sbertshikov, I. M., Geysant, J., Lepvrier, C., Pechersky, D. H., Boulin, J., Sibuet, J. C., Savostin, L. A., Sorokhtin, O., Westphal, M., Bazhenov, M. L., Lauer, J. P., and Biju-Duval, B. (1986). Geological evolution of the Tethys belt from the Atlantic to the Pamir since the Lias. *Tectonophysics*, 123, 241–315.
- Dewey, J. F. and Bird, J. M. (1970). Mountain belts and the new global tectonics. *J. Geophys. Res.*, 75, 2625–2547.
- Dewey, J. F., Helman, M. L., Turco, E., Hutton, D. H. W., and Knott, S. D. (1989). Kinematics of the Western Mediterranean. In Coward, M. P., Dietrich, D., and Park, R. G., editors, *Alpine Tectonics*, volume 45 of *Geological Society, Special Publication*, pages 265–283. Geological Society, London.
- Dewey, J. F., Pitman, W. C. I., Ryan, W. B. F., and Bonnin, J. (1973). Plate tectonics and the evolution of the Alpine system. *Geol. Soc. Am. Bull.*, 84, 137–180.
- Faccenna, C., Becker, T. W., Auer, L., Billi, A., Boschi, L., Brun, J. P., Capitanio, F. A., Funicello, E., Horvath, E., Jolivet, L., Piromallo, C., Royden, L., Rossetti, F., and Serpelloni, E. (2014). Mantle dynamics in the Mediterranean. *Rev. Geophys.*, 52, 283–332.
- Faccenna, C., Becker, T. W., Jolivet, L., and Keskin, M. (2013). Mantle convection in the Middle East: Reconciling Afar upwelling, Arabia indentation and Aegean trench rollback. *Earth Planet. Sci. Lett.*, 375, 254–269.
- Faccenna, C., Becker, T. W., Lucente, F. P., Jolivet, L., and Rossetti, F. (2001). History of subduction and back-arc extension in the Central Mediterranean. *Geophys. J. Int.*, 145, 809–820.
- Faccenna, C., Jolivet, L., Piromallo, C., and Morelli, A. (2003). Subduction and the depth of convection in the Mediterranean mantle. *J. Geophys. Res.*, 108, article no. 2099.
- Faccenna, C., Mattei, M., Funicello, R., and Jolivet, L. (1997). Styles of back-arc extension in the Central Mediterranean. *Terra Nova*, 9, 126–130.
- Frizon de Lamotte, D., Raulin, C., Mouchot, N., Wrobel-Daveau, J. C., Blanpied, C., and Ringenbach, J. C. (2011). The southernmost margin of the Tethys realm during the Mesozoic and Cenozoic: Initial geometry and timing of the inversion processes. *Tectonics*, 30, article no. TC3002.
- Funicello, E., Faccenna, C., Giardini, D., and Regenauer-Lieb, K. (2003). Dynamics of retreating slabs: 2. Insights from three-dimensional laboratory experiments. *J. Geophys. Res.*, 108, article no. 2207.
- Gaetani, M., Dercourt, J., and Vrielynck, B. (2003). The Peri-Tethys Programme: achievements and results. *Episodes*, 26, 79–93.
- Gealey, W. K. (1988). Plate tectonic evolution of the Mediterranean—Middle East region. *Tectonophysics*, 155, 285–306.
- Gyomlai, T., Agard, P., Jolivet, L., Larvet, T., Bonnet, G., Omrani, J., Larson, K., Caron, B., and Noel, J. (2022). Insights from *in-situ* Rb/Sr dating of metamorphic rocks: Evidence of Cimmerian metamorphism and post Mid-Cimmerian exhumation in Central Iran. *J. Asian Earth Sci.*, 233, article no. 105242.
- Hafkenscheid, E., Wortel, M. J. R., and Spakman, W. (2006). Subduction history of the Tethyan region derived from seismic tomography and tectonic reconstructions. *J. Geophys. Res.*, 111, article no. B08401.
- Handy, M. R., Schmid, S. M., Bousquet, R., Kissling, E., and Bernoulli, D. (2010). Reconciling plate-tectonic reconstructions of Alpine Tethys with the geological–geophysical record of spreading and subduction in the Alps. *Earth-Sci. Rev.*, 102, 121–158.
- Hsü, K. J. (1971). Origin of the Alps and Western Mediterranean. *Nature*, 233, 44–48.
- Irving, E. (1958). Palaeogeographic reconstructions from palaeomagnetism. *Geophys. J. Int.*, 1, 224–237.
- Jolivet, L., Baudin, T., Calassou, S., Chevrot, S., Ford, M., Issautier, B., Lasseur, E., Masini, E., Manatschal, G., Mouthereau, F., Thinon, I., and Vidal, O. (2021a). Geodynamic evolution of a wide plate boundary in the Western Mediterranean, near-field versus far-field interactions. *BSGF—Earth Sci. Bull.*, 192, article no. 48.
- Jolivet, L. and Faccenna, C. (2000). Mediterranean extension and the Africa-Eurasia collision. *Tectonics*, 19, 1095–1106.
- Jolivet, L., Faccenna, C., Agard, P., Frizon de Lamotte, D., Menant, A., Sternai, P., and Guillocheau, F. (2016). Neo-Tethys geodynamics and mantle convection: from extension to compression in Africa and a conceptual model for obduction. *Can. J. Earth Sci.*, 53, 1190–1204.

- Jolivet, L., Menant, A., Roche, V., Le Pourhiet, L., Maillard, A., Augier, R., Do Couto, D., Gorini, C., Thinin, I., and Canva, A. (2021b). Transfer zones in Mediterranean back-arc regions and tear faults. *BSGF—Earth Sci. Bull.*, 192, article no. 11.
- Köppen, W. and Wegener, A. (1924). *Die Klimate der Geologischen Vorzeit*. Gebrüder Borntraeger, Berlin.
- Koptev, A., Beniast, A., Gerya, T., Ehlers, T. A., Jolivet, L., and Leroy, S. (2019). Plume-induced breakup of a subducting plate: Microcontinent formation without cessation of the subduction process. *Geophys. Res. Lett.*, 46(7), 3663–3675.
- Le Pichon, X. (1968). Sea-floor spreading and continental drift. *J. Geophys. Res.*, 73, 3661–3667.
- Le Pichon, X., Şengör, A. M. C., and Imren, C. (2019). A new approach to the opening of the Eastern Mediterranean Sea and the origin of the Hellenic Subduction Zone. *Can. J. Earth Sci.*, 56(11), 1119–1143.
- Lustrino, M., Morra, V., Fedele, L., and Franciosi, L. (2009). Beginning of the Apennine subduction system in central western Mediterranean: Constraints from Cenozoic “orogenic” magmatic activity of Sardinia, Italy. *Tectonics*, 28, article no. TC5016.
- Maffione, M., van Hinsbergen, D. J. J., de Gelder, G., van der Goes, F. C., and Morris, A. (2017). Kinematics of Late Cretaceous subduction initiation in the Neo-Tethys Ocean reconstructed from ophiolites of Turkey, Cyprus, and Syria. *J. Geophys. Res. Solid Earth*, 122, 3953–3976.
- McKenzie, D. P. and Parker, D. L. (1967). The North Pacific: an example of tectonics on a sphere. *Nature*, 216, 1276–1280.
- Morgan, W. J. (1968). Rises, trenches, great faults and crustal blocks. *J. Geophys. Res.*, 73, 1959–1982.
- Mouthereau, F., Angrand, P., Jourdon, A., Ternois, S., Fillon, C., Calassou, S., Chevrot, S., Ford, M., Jolivet, L., Manatschal, G., Masini, E., Thinin, I., Vidal, O., and Baudin, T. (2021). Cenozoic mountain building and topographic evolution in Western Europe: impact of billion years lithosphere evolution and plate tectonics. *BSGF—Earth Sci. Bull.*, 192, article no. 56.
- Müller, R. D., Zahirovic, S., Williams, S. E., Cannon, J., Seton, M., Bower, D. J., Tetley, M. G., Heine, C., Le Breton, E., Liu, S., Russell, S. H. J., Yang, T., Leonard, J., and Gurnis, M. (2019). A global plate model including lithospheric deformation along major rifts and orogens since the Triassic. *Tectonics*, 38, 1884–1907.
- Neumayr, M. (1885). Die geographische Verbreitung der Juraformation. *Denkschriften der kaiserlichen Akademie der Wissenschaften (Wien), mathematisch-naturwissenschaftliche Classe*, 50, 57–86.
- Patriat, P. and Achache, J. (1984). India-Asia collision chronology has implications for crustal shortening and driving mechanisms of plates. *Nature*, 311, 615–621.
- Patriat, P. and Ségoufin, J. (1988). Reconstruction of the Central Indian Ocean. *Tectonophysics*, 155, 211–234.
- Ricou, L. E. (1994). Tethys reconstructed: plates, continental fragments and their boundaries since 260 Ma from Central America to South-Eastern Asia. *Geodin. Acta*, 7, 169–218.
- Ricou, L. E., Dercourt, J., Geyssant, J., Grandjacquet, C., Lepvrier, C., and Biju-Duval, B. (1986). Geological constraints on the Alpine evolution of the Mediterranean Tethys. *Tectonophysics*, 123, 83–122.
- Robertson, A. H. F. (1998). Mesozoic-Tertiary tectonic evolution of the easternmost Mediterranean area: integration of marine and land evidence. In Robertson, A. H. F., Emeis, K. C., Richter, C., and Camerlenghi, A., editors, *Proceedings of the Ocean Drilling Program*, volume 160 of *Scientific Results*, pages 723–782. Ocean Drilling Program, College Station, TX.
- Rolf, T., Coltice, N., and Tackley, P. J. (2012). Linking continental drift, plate tectonics and the thermal state of the Earth’s mantle. *Earth Planet. Sci. Lett.*, 351–352, 134–146.
- Romagny, A., Jolivet, L., Menant, A., Bessièrre, E., Maillard, A., Canva, A., and Thinin, I. (2020). Detailed tectonic reconstructions of the Western Mediterranean region for the last 35 Ma, insights on driving mechanisms. *BSGF—Earth Sci. Bull.*, 191, article no. 37.
- Rosenbaum, G., Lister, G. S., and Duboz, C. (2002). Reconstruction of the tectonic evolution of the western Mediterranean since the Oligocene. *J. Virtual Explor.*, 8, 107–126.
- Runcorn, S. K. (1962). Palaeomagnetic evidence for continental drift and its geophysical cause. In Runcorn, S. K., editor, *Continental Drift*, pages 1–40. Academic Press, New York.
- Savostin, L. A., Sibuet, J. C., Zonenshain, L. P., Le Pi-

- chon, X., and Roulet, M. J. (1986). Kinematic evolution of the Tethys belt from the Atlantic Ocean to the Pamir since the Triassic. *Tectonophysics*, 123, 1–35.
- Schettino, A. and Scotese, C. (2002). Global kinematic constraints to the tectonic history of the Mediterranean region and surrounding areas during the Jurassic and Cretaceous, Rosenbaum, G., Lister, G. S. (Eds.), Reconstruction of the evolution of the Alpine-Himalayan orogen. *J. Virtual Explor.*, 8, 149–168.
- Schettino, A. and Turco, E. (2011). Tectonic history of the western Tethys since the Late Triassic. *GSA Bull.*, 123, 89–105.
- Scotese, C. R., Cahagan, L. M., and Larson, R. L. (1988). Plate tectonics reconstructions of the Cretaceous and Cenozoic ocean basins. *Tectonophysics*, 155, 27–48.
- Şengör, A. M. C. (1979). Mid-Mesozoic closure of Permo–Triassic Tethys and its implications. *Nature*, 279, 590–593.
- Şengör, A. M. C. and Yilmaz, Y. (1981). Tethyan evolution of Turkey: a plate tectonic approach. *Tectonophysics*, 75, 181–241.
- Seton, M., Müller, R. D., Zahirovic, S., Gaina, C., Torsvik, T., Shephard, G., Talsma, A., Gurnis, M., Turner, M., Maus, S., and Chandler, M. (2012). Global continental and ocean basin reconstructions since 200 Ma. *Earth-Sci. Rev.*, 113, 212–270.
- Smith, A. G. (1971). Alpine deformation and the oceanic areas of the Tethys, Mediterranean, and Atlantic. *Geol. Soc. Am. Bull.*, 82, 2039–2070.
- Spakman, W. and Wortel, R. (2004). A tomographic view on Western Mediterranean geodynamics. In Cavazza, W., Roure, F. M., Spakman, W., Stampfli, G. M., and Ziegler, P. A., editors, *The TRANSMED Atlas—The Mediterranean Region from Crust to Mantle*, pages 31–52. Springer, Berlin, Heidelberg.
- Stampfli, G. M. (2000). *Tethyan Oceans*, volume 173 of *Special Publications*. Geological Society, London.
- Stampfli, G. M. and Borel, G. D. (2002). A plate tectonic model for the Paleozoic and Mesozoic constrained by dynamic plate boundaries and restored synthetic oceanic isochrons. *Earth Planet. Sci. Lett.*, 196, 17–33.
- Stampfli, G. M. and Kozur, H. W. (2006). Europe from the Variscan to the Alpine cycles. In Gee, D. G. and Stephenson, R. A., editors, *European Lithosphere Dynamics*, volume 32 of *Memoirs*, pages 57–82. Geological Society, London.
- Stampfli, G. M., Mosar, J., De Bono, A., and Vavasis, I. (1998a). Late Paleozoic, Early Mesozoic plate tectonics of the western Tethys. *Bull. Geol. Soc. Greece*, XXXII/1, 113–120.
- Stampfli, G. M., Mosar, J., Marquer, D., Marchant, R., Baudin, T., and Borel, G. (1998b). Subduction and obduction processes in the Swiss Alps. *Tectonophysics*, 296, 159–204.
- Steinberger, B. and Torsvik, T. H. (2008). Absolute plate motions and true polar wander in the absence of hotspot tracks. *Nature*, 452, 620–623.
- Sternai, P., Jolivet, L., Menant, A., and Gerya, T. (2014). Subduction and mantle flow driving surface deformation in the Aegean-Anatolian system. *Earth Planet. Sci. Lett.*, 405, 110–118.
- Suess, E. (1883). *Das Antlitz der Erde*. F. Tempsky, Prague and G. Freytag, Leipzig.
- Suess, E. (1901). *Das Antlitz der Erde*. F. Tempsky, Prag und Wien, and G. Freytag, Leipzig.
- Suess, E. (1909). *Das Antlitz der Erde*. F. Tempsky, Prag und Wien, and G. Freytag, Leipzig.
- Torsvik, T. H. and Cocks, L. R. M. (2016). *Earth History and Palaeogeography*. Cambridge University Press, Cambridge.
- Torsvik, T. H., Müller, R. D., Van der Voo, R., Steinberger, B., and Gaina, C. (2008). Global plate motion frames: Toward a unified model. *Rev. Geophys.*, 46, article no. RG3004.
- Tugend, J., Chamot-Rooke, N., Arsenikos, S., Blanpied, C., and Frizon de Lamotte, D. (2019). Geology of the Ionian Basin and margins: A key to the East Mediterranean geodynamics. *Tectonics*, 38(8), 2668–2702.
- van der Meer, D. G., Spakman, W., van Hinsbergen, D. J. J., Amaru, M. L., and Torsvik, T. H. (2010). Towards absolute plate motions constrained by lower-mantle slab remnants. *Nat. Geosci.*, 3, 36–39.
- van Hinsbergen, D. J. J., Torsvik, T. H., Schmid, S. M., Mañenco, L. C., Maffione, M., Vissers, R. L. M., Gürer, D., and Spakman, W. (2019). Orogenic architecture of the Mediterranean region and kinematic reconstruction of its tectonic evolution since the Triassic. *Gondwana Res.*, 81, 79–229.
- Wegener, A. (1912). Die Entstehung der Kontinente. In *Dr. A. Petermanns Mitteilungen aus Justus Perthes' Geographischer Anstalt*, page 63. Justus Perthes, Gotha.

- Wegener, A. (1924). *The Origin of Continents and Oceans*. E. P. Dutton and Co, New York.
- Wegener, A. (1929). *Die Entstehung der Kontinente und Ozeane*. Auflage, Vieweg, Braunschweig.
- Westphal, M., Bazhenov, M. L., Lauer, J. P., Pechersky, D. H., and Sibuet, J. C. (1986). Paleomagnetic implications on the evolution of the Tethys belt from the Atlantic Ocean to the Pamirs since the Triassic. *Tectonophysics*, 123, 37–82.
- Wilson, J. T. (1965). A new class of faults and their bearing on continental drift. *Nature*, 207, 343–347.
- Wortel, M. J. R. and Spakman, W. (2000). Subduction and slab detachment in the Mediterranean-Carpathian region. *Science*, 290, 1910–1917.
- Wortel, R., Govers, R., and Spakman, W. (2009). Continental collision and the STEP-wise evolution of convergent plate boundaries: From structure to dynamics. In Lallemand, S. and Funicello, F., editors, *Subduction Zone Geodynamics*, pages 47–59. Springer-Verlag, Berlin Heidelberg.
- Zahirovic, S., Matthews, K. J., Flament, N., Müller, R. D., Hill, K. C., Seton, M., and Gurnis, M. (2016). Tectonic evolution and deep mantle structure of the eastern Tethys since the latest Jurassic. *Earth Sci. Rev.*, 162, 293–337.
- Ziegler, P. (1999). Evolution of the Arctic-North Atlantic and the Western Tethys. *AAPG Mem.*, 43, 164–196.
- Zonenshain, L. P. and Le Pichon, X. (1986). Deep basins of the Black Sea and Caspian Sea as remnants of Mesozoic back-arc basins. *Tectonophysics*, 123, 181–240.



Research article

Tribute to Jean Dercourt

Rifting and seafloor spreading in the South China sea: a subduction-related extension on the down-going plate?

Sung-Ping Chang^{Ⓢ,a} and Manuel Pubellier^{Ⓢ,*,b}

^a Ocean Center, National Taiwan University, Taiwan

^b CNRS UMR 8538, Ecole Normale Supérieure, Laboratoire de Géologie, PSL Research University, France

E-mails: chang.sung-ping@gs.ncku.edu.tw (S.-P. Chang),
manupub.pubellier@gmail.com (M. Pubellier)

Abstract. Active margins are sensitive to several subduction-related processes which include rapid opening and closure of neighboring basins. The stages of rifting, spreading and the cessation, of activity the South China Sea basin in Cenozoic appears to be coeval with the progressive closure of the Proto-South China Sea which ended with collision in Borneo and Palawan. The evolution bracketed between 45 Ma and 16 Ma, migrated through time from NE to SW. This dual simultaneous tectonic evolution illustrates how far-field subduction process may impact the regional tectonics in terms of both rifting and contraction of the crust from initiation to termination.

Keywords. South China Sea, Subduction, Proto South China Sea, Rifting, Spreading, Stratigraphic-tectonic correlations.

Manuscript received 30 December 2022, revised 27 May 2023 and 25 July 2023, accepted 17 August 2023.

1. Introduction

The original causes for the opening of large oceans are difficult to decipher because the conditions of their onset is generally obscured by their later development. On the other hand, marginal basins open as a result of mechanisms which can be identified easily, and include several subduction-related processes encompassing back-arc or forearc setting, and often follow gravity collapse of older existing orogens. In Southeast Asia, many basins have formed in convergence setting and most of them are young enough to have it preserved [Pubellier and Morley, 2014, Rangin et al., 1990b], such as the Philippine

Sea [Karig, 1974], the Sulu Sea [Rangin, 1989], the Celebes Sea or the Banda/Damar seas. The extension responsible for the opening is observed on both upper and lower plate, and the rifting/spreading of basins is often coeval with closure of the neighboring ones [Pubellier and Meresse, 2013]. The stages of rifting, spreading and the cessation of activity of the SCS basin in Cenozoic appear to be coeval with the progressive closure of the Proto-South China Sea (PSCS) which ended with collision in Borneo and Palawan [Franke et al., 2014, Hall and Breitfeld, 2017]. However, if the ages of the rifting stages are relatively well constrained, the dating of the closure is blurred and requires a discussion of the successive regional unconformities.

Mature marginal basins are usually underlain by oceanic crust and are semi-isolated from the open

* Corresponding author.

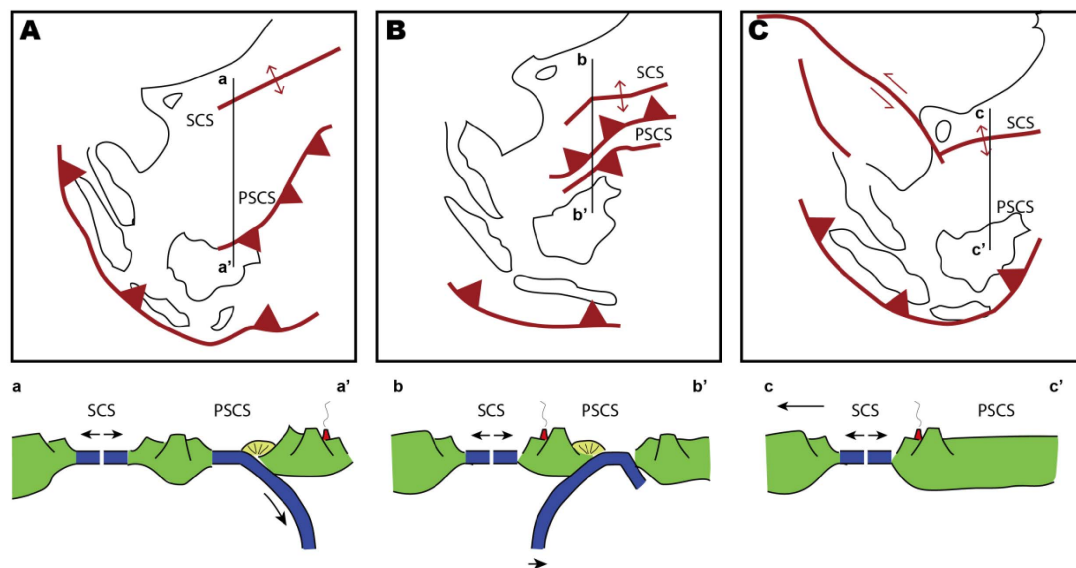


Figure 1. Schematic models illustrating three possible scenarios for the South China Sea opening. (A) Slab-pull model suggesting a southward subduction of the Proto-South China Sea [Taylor and Hayes, 1983, Hall, 2002, Pubellier et al., 2003, Morley, 2016]. (B) Back-arc model suggesting that the South China Sea opened on the overriding plate while Proto-South China Sea either subducted northward, or was undergoing double-sided subduction [Wu and Suppe, 2017, Li et al., 2020, Lin et al., 2020]. A variation of this option is an oceanward subduction followed by a continentward subduction [Larvet et al., 2022]. (C) Block extrusion induced by the India-Eurasia collision which opened the South China Sea along strike-slip fault [Tapponnier et al., 1982, Biais et al., 1993, Leloup et al., 2001].

ocean by a tectonic or volcanic ridge [Zhou, 2014]. They are formed as a result of several processes encompassing back-arc or fore-arc setting, and deformed by adjacent boundary forces, such as for instance, trench retreat, block rotations or collision [Chenin et al., 2017]. The evolution of the basins, and their adjacent structures, can be interpreted from their stratigraphic record. The temporal and spatial variation at regional scale, allows invoking a geodynamic scenario of evolution. Their short-lived cycle also provides easier correlation across short distance between the basin margins and their surrounding tectonic realms.

Many studies had suggested the opening of the SCS, and the closure of the PSCS, took place simultaneously in Cenozoic time [Holloway, 1982, Taylor and Hayes, 1983, Zhou et al., 1995, Pubellier et al., 2003, Franke et al., 2014, Hall and Breiffeld, 2017, Lunt, 2019, Li et al., 2020, Lin et al., 2020]. Different geodynamic and boundary forces have been suggested and debated (Figure 1), such as the India-Eurasia

collision inducing extrusion of the Indo-China Block [Tapponnier et al., 1982, Biais et al., 1993, Leloup et al., 2001], the opening of a supra-subduction basin [Wu and Suppe, 2017, Li et al., 2020, Lin et al., 2020], or a basin opening in the midst of the downgoing plate [Taylor and Hayes, 1983, Hall, 2002, Pubellier et al., 2003, Morley, 2016, Li et al., 2020]. The discussion of the different tectonic models of evolution in East and Southwest South China Sea, although still debated, has been reviewed recently [Morley, 2016, Hennig-Breiffeld et al., 2019, Wang et al., 2020].

The South China Sea, although a far field product of the subduction, is difficult to consider as a back-arc basin, unless involving a double-verging subduction [Wu and Suppe, 2017, Li et al., 2020, Lin et al., 2020], and has been created as the result of tectonics involving either the extrusion of the Indochina block [Tapponnier et al., 1982, Biais et al., 1993, Leloup et al., 2001], or the slab-pull triggered by the southward subduction of the Proto-South China Sea [Taylor and Hayes, 1983, Hall, 2002, Pubellier et al.,

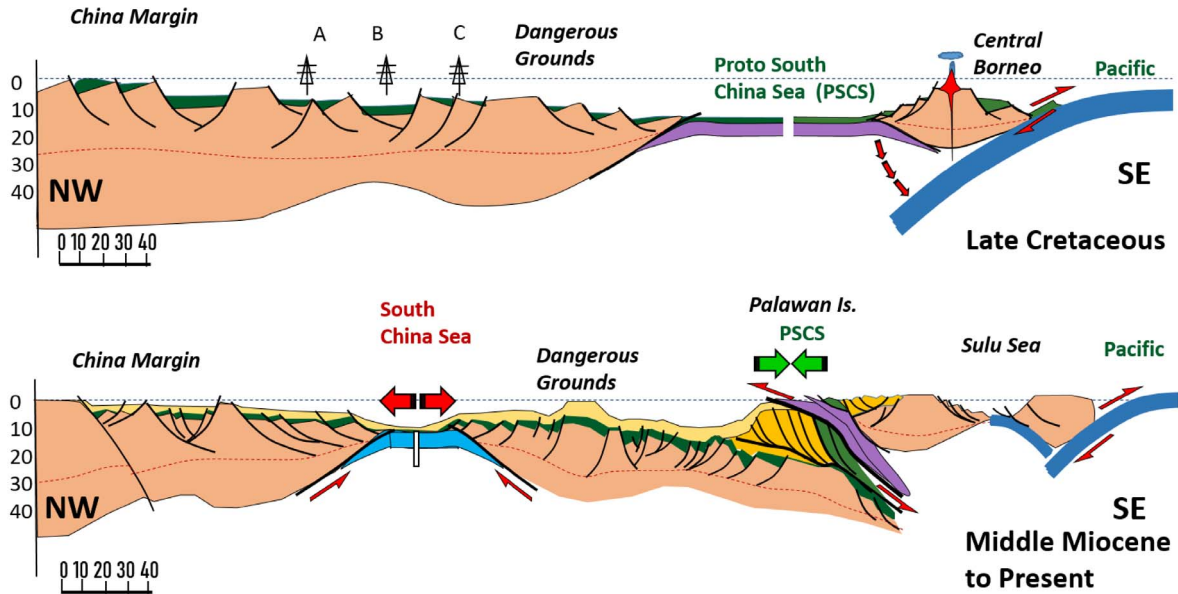


Figure 2. Cross-section lithosphere sections across the SCS and the PSCS. (A) Subduction of the Paleo-Pacific Plate went underneath the Eurasia Plate and forming the Proto-SCS as a back-arc setting in Cretaceous. Sampaguita, Kalamansi and Caolao wells are projected reference drill sites. (B) Same section during Late Neogene times.

2003, Morley, 2016]. Indeed, all these processes have somehow interacted; the global back-arc location of all the marginal basins of Southeast Asia [Rangin et al., 1990a, Pubellier et al., 2003], the existence of the large Red River and Wang Chau strike-slip faults, and the trench pull of the PSCS. The latter of these options was confronted to the observation that no active example exists on earth, although this configuration is admitted for the demise of the successive Tethysian basins, and that it was difficult to model, prior to the studies of Larvet et al. [2022].

In order to approach this issue, this study overviews the tectonic evolution of two marginal seas; the South China Sea (SCS) and the vanished Proto-South China Sea (PSCS), which have been studied extensively in the past decades [Taylor and Hayes, 1980, 1983, Holloway, 1982, Larsen et al., 2018]. In view of the complexity of the different extensional and contractional features of this paired configuration, the study attempts to establish tectono-stratigraphic correlations across the opposite margins of the SCS, and the PSCS. Various tectonic stages represented by the selected unconformities and integrating multi-disciplinary evidences are

combined to reconcile the different hypotheses for the tectonic evolution of this dual system.

2. Geological background

South China Sea is located at the junction between the Eurasia Plate, the Philippine Sea Plate, and the Indian–Australian Plate. Convergence around the Sunda Plate encompasses seismically active plate boundaries such as the Taiwan/Philippines Mobile Belt in the east, the Sumatra subduction zone in the south and east, up to the Himalaya collision in the west. Since Jurassic times, a northward subduction beneath the Eurasia Plate, initiated an extension and a SE migration of the subduction [Yan et al., 2014a, Pubellier and Morley, 2014, Li et al., 2018, 2020]. Several intra-plate marginal seas were formed (Figure 2) [Karig et al., 1978, Jolivet et al., 1989, Rangin et al., 1990b, Schellart et al., 2019], in a global setting which is within the upper plate of the Pacific/Indian Ocean subduction system.

The South China Sea is one of these marginal basins which opened along the SE China and the Vietnam continental margins. Its rifted margins developed along inherited structures, for instance, fold

limbs [Savva et al., 2014, Ye et al., 2020], or extensive granite massif [Kudrass et al., 1986, Yan et al., 2014b, Xiao et al., 2019, Miao et al., 2021]. Many syn-rift unconformities are described since the Paleogene, in response to the development of half-grabens marked by detachment faults while the continental crust extended over 600 km in both conjugated margins. A rapid breakup [Larsen et al., 2018], forming a significant V-shaped formed between 32 to 16 Ma [Figure 3, Briais et al., 1993, Le Pourhiet et al., 2018] with a narrow COT and localized magmatism [Nirrengarten et al., 2020]. A diachronous migration of the rifting and seafloor spreading has been proposed [Franke et al., 2014].

Another basin, known as the Proto South China Sea (PSCS), existed prior to the opening of the SCS, to its SE, but is presently totally subducted [Rangin et al., 1990b, Hall and Breitfeld, 2017], and only present as ophiolitic remnants [Omang and Barber, 1996, Dycoco et al., 2021]. The ocean-floored Proto-South China Sea (PSCS) was probably formed as a back-arc basin also referred to as the Rajang Sea [Rangin et al., 1990b] although a connection with the easternmost Tethys is possible. The existence of this ancient basin is based on the presence of ophiolite complexes and imbricated fold-and-thrust belt in both NW Borneo and Palawan (Figure 2). The ages of the ophiolites clustered in two main groups as Early Cretaceous and Middle Eocene [Rangin et al., 1990b, Omang and Barber, 1996, Graves et al., 2000, Keenan et al., 2016, Chien et al., 2019, Gibaga et al., 2020, Rahmat et al., 2020, Dycoco et al., 2021]. Many stratigraphic hiatuses and changes of sediment sources from the hinterlands reveal successive tectonic events since the Eocene [Cullen, 2010, Hennig-Breitfeld et al., 2019]. The termination of the last of these events (Sabah Orogeny) is dated from Late Miocene to Pleistocene [Tongkul, 2003, Lunt and Madon, 2017, Sapin et al., 2013, Hall and Breitfeld, 2017]. Few granite intrusions along Borneo and Palawan suggest the presence of a broken lithospheric slab in Late Miocene [Prouteau et al., 1996, Encarnacion and Mukasa, 1997, Hutchison et al., 2000, Cottam et al., 2010, Sapin et al., 2013, Forster et al., 2015].

3. Methodology

This paper reviews the unconformities which are indicators of tectonic instabilities of the margins, but also changes of seismic facies and subsidence history, in three different domains from East to Southwest (D1 to D3 on Figure 3) following Savva et al. [2014]. We extracted key published seismic profiles and wells (locations see Figure 3) to analyze the rift evolution on the grounds of seismic stratigraphy, biostratigraphy, and structures. Subsidence history is also examined. In a general, we identify Ro as a “stretching stage” in the sense of Péron-Pinvidic et al. [2007] which is characterized by numerous steeply dipping normal faults, R1 and R2 the thinning stages with an unconformity in the middle (IRU). These rifting stages are followed by the breakup.

In Section 4, the correlation of stratigraphic cuts related to the contraction is established through domains 1 to 3 in order to explore the timing of the collision. Observations in the field onshore and on seismic lines offshore is used to underline and date the crucial convergence-related unconformities. The facies changes in the deposits are also taken into account to evaluate fluctuations in the depositional environment and possible uplift periods. Ultimately, we try to evaluate chronological links between the two opposite margins (Section 6).

4. Tectono-stratigraphy of the rifting and spreading in the South China Sea

4.1. Rifting stratigraphy in Domain 1

On the China margin, the stratigraphy had been established confidently in the past decades according to the intense industrial research exploration.

Within the syn-rift sequence, some internal significant unconformities are found in the Pearl River Mouth Basin (PRMB) in front of Hong-Kong [Chan et al., 2010, Morley, 2016, Lunt, 2019], as well as in the Tainan Basin SW of Taiwan [Lin et al., 2003]. The timing of breakup and rifting has been interpreted as a diachronous event from east to southwest [Franke et al., 2014]. Although the onset of rifting has been long debated due to insufficient number of drillings [Morley, 2016], the age of the detachment fault during rifting, and the age of the breakup show a diachronous evolution as shown on Figure 4 [Franke

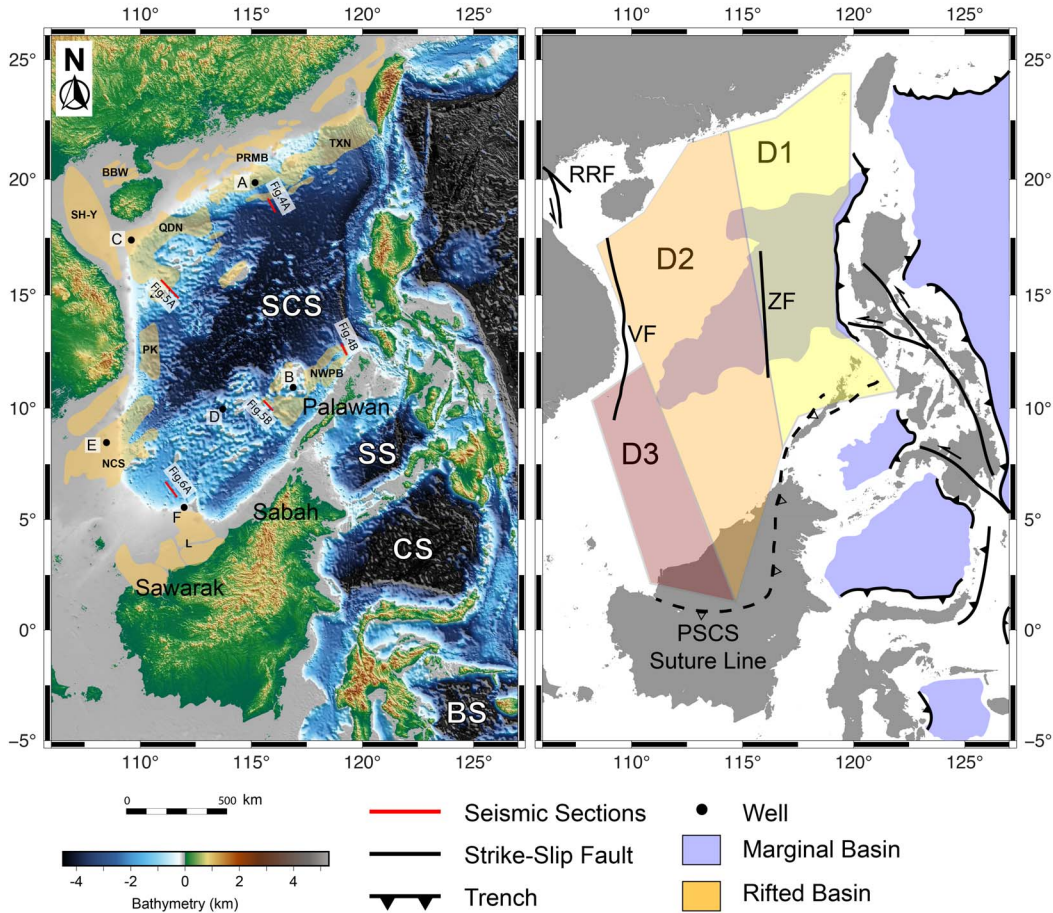


Figure 3. (A) Elevation in SE Asia illustrating oceanic basins including SCS: South China Sea, SS: Sulu Sea, CS: Celebes Sea, BS: Banda Sea, BBW: Beibuwan Basin, L: Luconia Basin, NCS: Nam Con Son Basin, NWPB: NW Palawan Basin, PK: Phu Khanh Basin, PRMB: Pearl River Mouth Basin, QDN: Qiongdongnan Basin, SH-Y: Song Hong-Yinggehai Basin, TXN: Taixinan Basin. The bathymetric map has a non-linear color bar to assist in highlighting certain features. Red lines represent the location of seismic profiles and black solid dots represent the locations of the wells. Reference to boreholes; A for Pearl River area, B for “Dangerous Grounds Area (e.g., Sampaguita-1 and Malampaya wells), C for Hainan shelf, E for Nam Con Son (NCS), D for Spratleys Shelf, F for Luconia Shelf. (B) The black dashed lines demonstrate the tentative location of the closure zone of the PSCS [modified from Zhou et al., 2008, Hall, 2012, Liu et al., 2014, Zhang et al., 2017].

et al., 2014, Savva et al., 2014]. An early phase of diffuse stretching R_0 begins possibly as early as Late Cretaceous [Chan et al., 2010], after the end of the compressional deformation [Nanni et al., 2017] and ended 45 Ma [Xie et al., 2019]. The syn-rift I (R_1) was deposited on a basement cut by high-angle normal faults (orange on Figure 4) and bracketed between 45 Ma and 37 Ma [Lin et al., 2003]. An Intra-

Rift Unconformity (IRU) separates a second rifting period (R_2) from 37 to 32 Ma. It is marked simultaneously on the SE China and Palawan margins by a significant hiatus, and a strong sagging period [Lin et al., 2003, Xie et al., 2019]. This period is characterized by thickly sedimented U-shaped seismic units in the lower part (green to pink horizon on Figure 4), typically expressed in the Liwan sag [Larsen et al.,

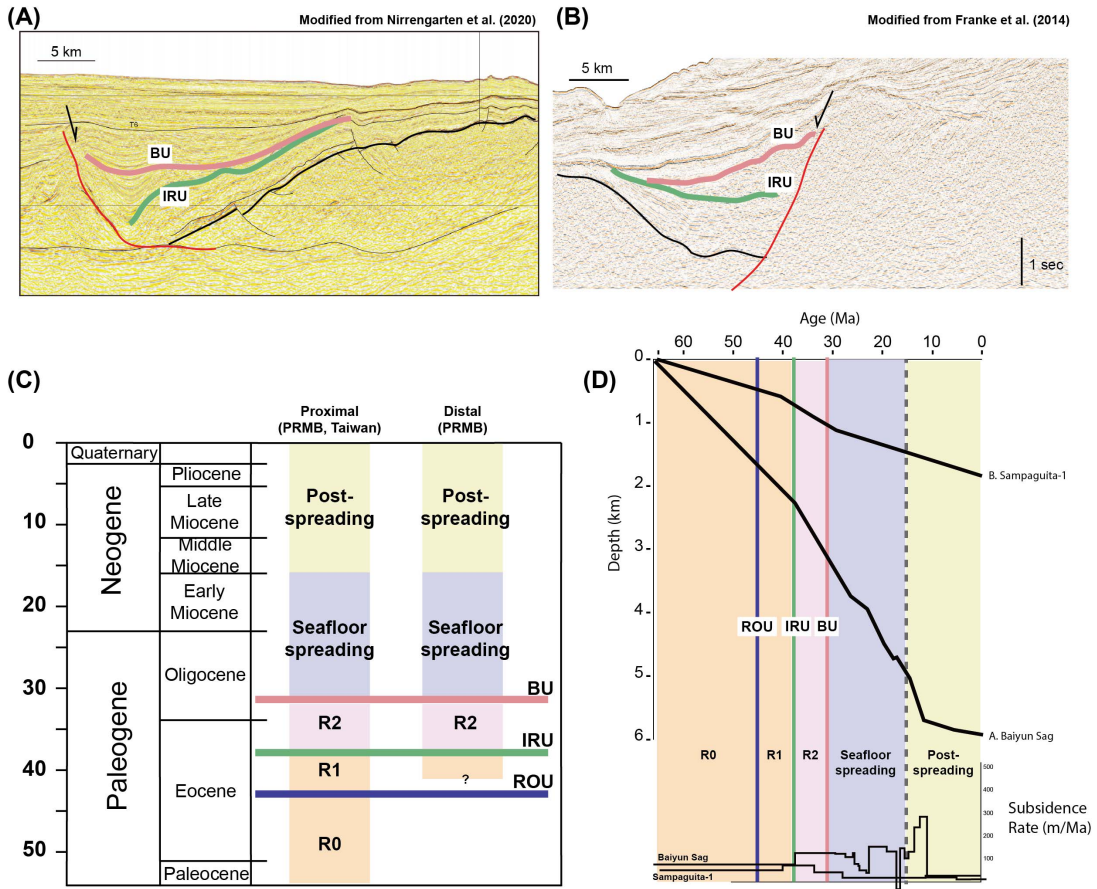


Figure 4. Selected portions of seismic lines and major horizons underlying the stratigraphic sequences R1, R2 and R3 discussed in text for Domain 1 (NE of the SCS). Location of the seismic profiles and wells see Figure 3. The intra-rift unconformity (green solid lines) separates the underlain R1 units and the overlying R2 units. The R2 characterizes detachment-related extension and onlapping onto the intra-rift unconformity, corresponding to the acceleration of rifting rate. The breakup unconformity (red solid lines) indicates the breakup time and the incipient seafloor spreading. Subsidence curve modified from Tang et al. [2014], Xie et al. [2014]; Clift et al. [2015]. ROU is the base of R1, IRU is between the 2 thinning events (between R1 and R2), and BU (Breakup Unconformity) marks the end of the rifting and the onset of the spreading at the domain location.

2018]. The thick R2 represents the last stage of the rifting prior to breakup. Spreading started around 32 Ma [Briais et al., 1993, Larsen et al., 2018, Chao et al., 2021], and ceased at ca. 16 Ma [Briais et al., 1993, Li et al., 2015]. If the extension alone can be invoked for the stretching and thinning of the SE China margin, the southern conjugate margin may in addition have suffered from a flexural fore-bulge effect induced by the subduction in Palawan [Steuer et al., 2014]. The most continuous record at Well

Sampaguita-1 documented a stratigraphic boundary formed around 49 Ma between the transition from the shelf to calcareous shale [Taylor and Hayes, 1980, Yao et al., 2012]. An extensive unconformity occurred in Sampaguita-1 and Malampaya at 37 Ma [T80; Fournier et al., 2005, Yao et al., 2012, Steuer et al., 2014], and this unconformity can be extended along the seismic profiles showing its distinct distribution in the Offshore Palawan Margin. There, to the south of Domain 1, the breakup unconformity is drawn

around 28–30 Ma, possibly indicating a small lag time, or at least an asymmetry for the start of spreading [Nirrengarten et al., 2020]. The age is witnessed by the drilling and seismic evidences [Holloway, 1982, Fournier et al., 2005, Franke et al., 2011, Yao et al., 2012, Steuer et al., 2013, 2014, Peng et al., 2020].

The tectonic subsidence and the subsidence rate are integrated from previous publications [Tang et al., 2014, Xie et al., 2014, Clift et al., 2015], and deduced from the seismic observation. The initial rifting corresponds to the minor subsidence (Figure 4), coinciding the R0 and R1 stratigraphy bounded by high-angle normal faults. The increase of the subsidence rate within the R2 is vigorously related to the detachment faults which thin the crust and generated a Late Eocene unconformity overlapped by the concave-up R2 units in SE China and NW Palawan Margins (Figure 4). This acceleration of extension rate is also suggested in the modelling prior to the rapid breakup in the SCS [Brune et al., 2016, Le Pourhiet et al., 2018].

4.2. Rifting stratigraphy in Domain 2

On the E Vietnam Margin, extension is localized both along sharp segments [Marquis et al., 1997, Roques et al., 1997, Fyhn et al., 2009], and along wide extremely stretched areas showing detachment features [Lei and Ren, 2016, Savva et al., 2014, Chang et al., 2022]. Similarly, the southwestern margin also developed extensive basins with detachment faults [Liang et al., 2019] resulting ultimately in an even thinner crust (Figure 5).

Likewise in Domain 1, the beginning of stretching is unclear (Late Cretaceous?) and ended up at 38 Ma [Lei and Ren, 2016]. The distinct ROU (regional onset unconformity) is reported mainly at 37 Ma (T80, bottom of Yacheng Fm.) or slightly older around 45 Ma (within Shixin Fm.), and documented locally around proximal domain such as the Beibuwan Basin or the Qiong Dong Nan Basin [Fyhn et al., 2009, Wu et al., 2009, Savva et al., 2013, Vu et al., 2017, Zhou et al., 2018, Wang et al., 2020, Figure 4]. The intra-rift unconformity (T70, bottom of Linshui Fm.) is an angular one around 28 Ma highlighting the development of detachment faults particularly in both proximal and distal margin such as in PK basin [Savva et al., 2013, Lei and Ren, 2016, Chang et al., 2022]. The breakup unconformity is

identified as 23 Ma (T60) marking a significant hiatus. In the Dangerous Ground Margin, the earliest unconformity is recorded around 37 Ma and observed within thick syn-rift sequences [Yan and Liu, 2004]. An intra-rift unconformity around 30 Ma is observed and dated by biostratigraphy data in the adjacent wells [T7, Hutchison, 2004, Yan and Liu, 2004, Hutchison and Vijayan, 2010, Ding et al., 2014, Zhang et al., 2020]. The breakup unconformity main consensus is around 23 Ma, namely the MMU in many studies [Steuer et al., 2014, Song and Li, 2015].

The main character of R2 is its homogeneous upper syn-rift thickness, which correlates well the northern and southern margins. The horizon of upper R2 flattens in several basins (Phu Khanh, Nam Con Son (NCS), and the COT of Nanshan Islands), and is offset slightly by normal faults. This stage illustrates the space accommodation which develops preferably horizontally rather than vertically. The possible age of R2 on the Northern margin is 28 to 23 Ma [Lei and Ren, 2016]. In the NW Borneo Margin, the same age of R2 is extracted from the Sampagita Well, although situated just N of the boundary with Domain 1, and its end correlates nicely to that of the incipient oceanic crust [Sibuet et al., 2016, Chang et al., 2022]. The breakup occurred at 23 Ma and the spreading lasted until 16 Ma. Likewise the Domain 1, the forebulge region resulted in a widespread area of shallow-water depositional environment, which developed a significant carbonate layer [Nido carbonates, Hatley, 1980, Williams, 1997, Steuer et al., 2014]. It is however deepening toward the Borneo-Palawan Trough, although a built-up reef exists along the crest of the horst in the Dangerous Ground area [Jamaludin et al., 2017].

Subsidence curves and subsidence rates from well logging and speculated from seismic lines show a mild subsidence until the middle of the Oligocene corresponding to the R0 and R1 units [Figure 5, Fang et al., 2016, Shi et al., 2017, Zhao et al., 2018]. A stronger subsidence began since 33 Ma and accelerated afterward. This sequence corresponds to R2, and onlaps on the seismic images prior to the breakup unconformity (Figure 5).

4.3. Rifting stratigraphy in Domain 3

In Domain 3, no oceanic crust was developed because the opening of the South China Sea aborted

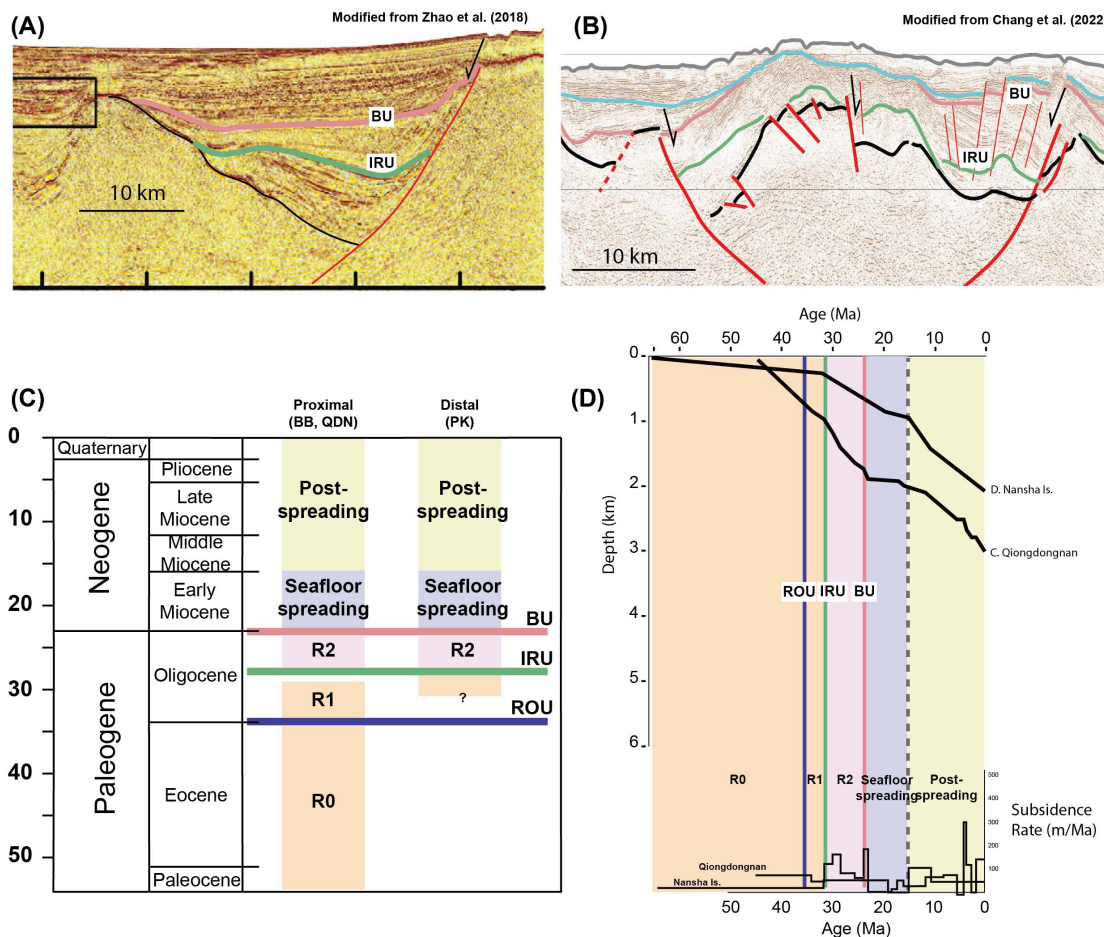


Figure 5. Selected portions of seismic lines and major horizons underlying the stratigraphic sequences R1, R2 and R3 discussed in text for Domain 2 (Central part of the SCS). Location of the seismic profiles and wells see Figure 3. ROU is the base of R1, IRU is between the 2 thinning events (between R1 and R2), and BU (Breakup Unconformity) marks the end of the rifting and the onset of the spreading at the domain location).

just before the breakup at 16 Ma. The continental crust recorded two stages of rifting and the extensional structures of the NCS and Luconia basins are influenced by the adjacent neighboring mid-ocean ridge [Xia and Zhou, 1993, Huchon et al., 2001, Hutchison, 2004, Ding et al., 2016, Luo et al., 2021, Madon and Jong, 2022]. Several unconformities predated apparently the mature syn-rift units by around 40 Ma and 32 Ma [Matthews et al., 1997, Madon et al., 2013], probably representing the rift onset in this region. One main unconformity suggested the major rifting period from 24 Ma until the extension terminated around 16 Ma as the

propagator ceased [Matthews et al., 1997, Madon et al., 2013, Li et al., 2014].

The early stage of rifting is obscured, and R0 and R1 (Cycle I; pre-24 Ma, in the Luconia province offshore Malaysia) cannot be undoubtedly discriminated. The Mesozoic basement was encountered at the bottom of the R0/R1 unit [Areshev et al., 1992, Wu and Yang, 1994]. Syn-rift units are separated into two groups (I and II), showing similarities in the NCS and Luconia basins [Franke et al., 2014, Madon et al., 2013, Clerc et al., 2018, Madon and Jong, 2022]. Until 23 Ma, The R2 (Cycle II and Cycle III for petroleum geologists of the S margin of the SCS) remains

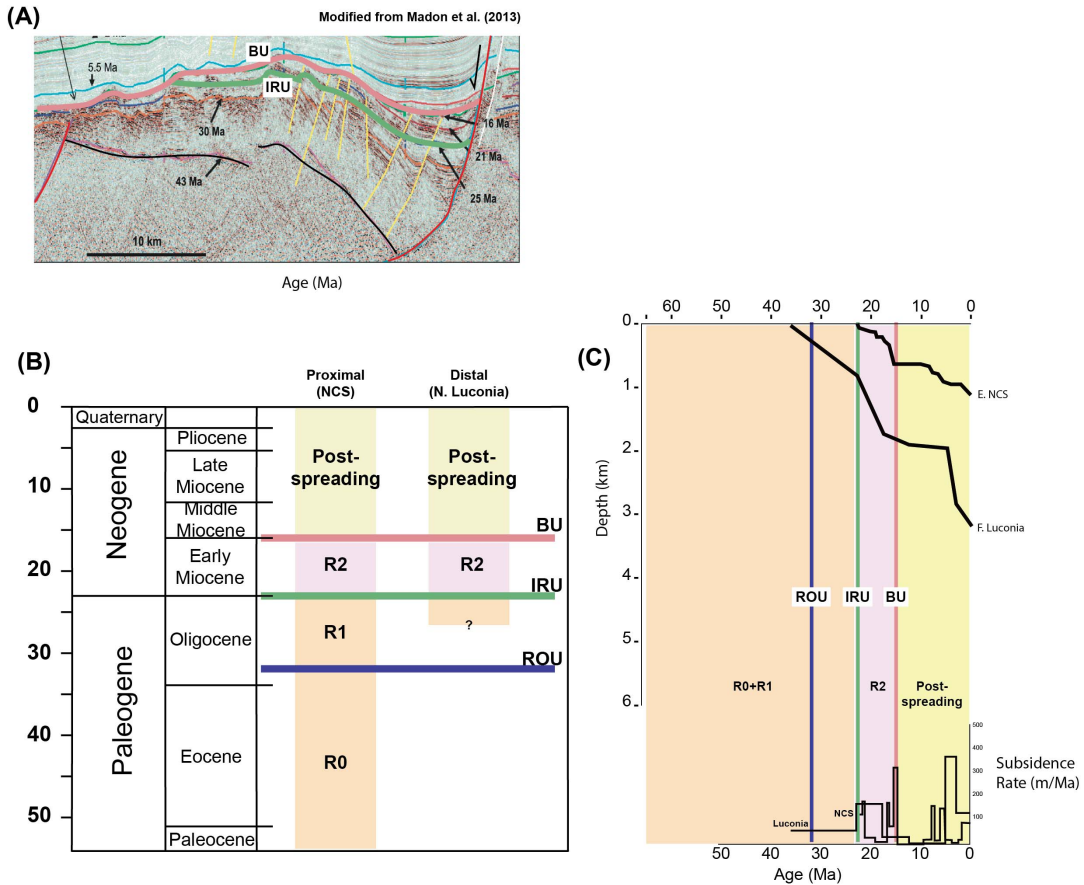


Figure 6. Selected portions of seismic lines and major horizons underlying the stratigraphic sequences R1, R2 and R3 discussed in text for Domain 3 (NE of the SCS). Location of the seismic profiles and wells see Figure 3. ROU is the base of R1, IRU is between the 2 thinning events (between R1 and R2), and BU (Breakup Unconformity) marks the end of the rifting and the onset of the spreading at the domain location.

characterized by horizontal to sub-horizontal seismic facies overlying the intra-rift unconformities, but without a breakup unconformity atop [Figure 6, Hutchison, 2004, Li et al., 2014, Clerc et al., 2018, Peng et al., 2018]. Most of the normal faults terminate at an horizon dated around 16 Ma [red horizon on Figure 6; Madon et al., 2013, Savva et al., 2014, Li et al., 2014, Lunt, 2019].

Paleo-water depth gradually deepened by the witness of the well logging and also the pseudo-well [Li et al., 2014, Madon et al., 2013]. Subsidence rate curves did not record the R0 and R1 subsidence curve in the published data. The distinct acceleration found in the previous sections began at 23 Ma, which corresponded to the detachment development, and

decreased after 16 Ma both in NCS and Luconia [Figure 6; Li et al., 2014, Jamaludin, 2022].

4.4. Diachronous rifting and seafloor spreading in the SCS Margin

According to the above mentioned temporal recording, most of the classical stages of evolution of a margin can be seen in the South China Sea, but appear at a time that varies from D1 to D3. A simple evolutionary age-table is compiled on Figure 7 to illustrate the diachronism of the extensional events. Although the end-members ages of the extension history of the SCS are not significantly different (Late Cretaceous for R0 to 16 Ma for the end of sea-floor

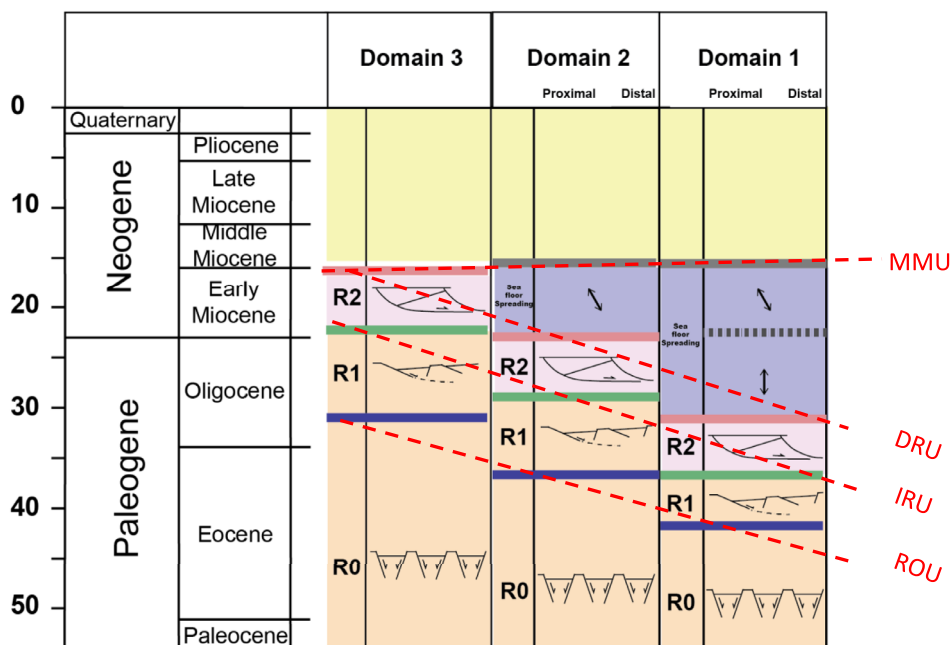


Figure 7. Rifting diachronism by juxtaposing D1 to D3. The diachronism appeared from R1 unit and goes on until the termination of seafloor spreading. ROU is the base of R1, IRU is between the 2 thinning events (between R1 and R2), and BU (Breakup Unconformity) marks the end of the rifting and the onset of the spreading at the domain location.

spreading), the different markers of the rifting vary from the East to the West. The bracket of ages for R1 to BU is younger toward the south; from 45–32 in D1, 38 to 23 in D2, and 45? to 16 in D3. Indeed, a ridge jump with a shift in spreading direction at 23 Ma [Sibuet et al., 2016] is known and constitutes an important point in time of the extension history. This event marks the end of a rifting style controlled by N–S wrench faults and pull-apart basins [Chang et al., 2022], which marks the early stage of the opening of the SCS, both for the rifting [Chan et al., 2010] and for the spreading [Briaies et al., 1993].

5. Convergent tectono-stratigraphy in Borneo and Palawan

The tectonic evolution of the convergent margin in Borneo and Palawan is also marked by key unconformities which represent different stages of subduction and subsequent collision, as the thinned continental margin of the south of the SCS progressively entered into the subduction zone of the PSCS.

In general, the core of the orogenic belt exposes older and metamorphosed rocks of the Cretaceous to Late Eocene Rajang Formation along the backbone in the central Borneo (grey shades in Figure 8). The ophiolitic complexes attributed to the relics of the PSCS are distributed in Palawan and Sabah (purple color in Figure 8) and show two juxtaposed clusters of ages [Eocene and Mesozoic, Burton-Johnson et al., 2020, Dycoco et al., 2021]. The metamorphism and ages of the sedimentary formations decrease outward in the case of the NW and SE Borneo edifices (Figure 8), in accordance to a normal wedge (actually a fold-and-thrust belt) proceeding toward the NW. On the NW side, the imbricated wedge gradually narrow toward Palawan [Aurelio et al., 2014]. This section reviews the stratigraphic unconformities and thermo-chronological data highlighting the initiation of uplift induced by subduction/collision in each domain (D1 to D3). The syn-tectonic and post-collision magmatism is also integrated to assess the closure history of the PSCS.

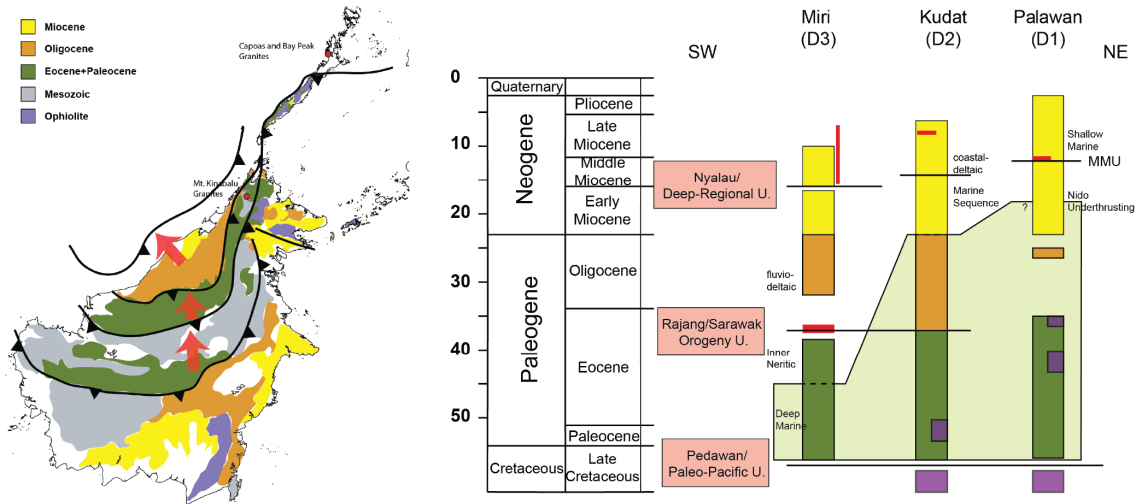


Figure 8. (Left) Simplified geological map of Borneo and Palawan and main stratigraphic elements for the convergence (Right) Tectono-stratigraphy of the closure of the PSCS from D3 to D1. The segment locations shown in Figure 3. Diachronism illustrated by the beginning of uplift in Sarawak (D3) migrating toward Palawan (D1). The termination of the orogenic event is around 16 Ma.

5.1. Tectonic-related stratigraphy in Domain 3

In the Sarawak region, each sedimentary formation has been analyzed in terms of biostratigraphy and detrital zircon [Galín et al., 2017, Hennig-Breitfeld et al., 2019]. The Sarawak Orogeny Unconformity (or Rajang Unconformity, Figure 8) is documented on the ground of a stratigraphic hiatus extensively distributed in central Borneo and along the Bukit Mersing Line separating the Sibiu and Miri Zone [Hutchison, 2005, Cullen, 2010, Hall, 2013, van Hattum et al., 2013, Hall and Breitfeld, 2017, Hennig-Breitfeld et al., 2019]. After a generally continuous deposition, another widespread unconformity, the Nyalau Unconformity dated around 16 Ma is found [Hennig-Breitfeld et al., 2019].

The Rajang Group mainly consists of deep-sea depositional environment in Sibiu Zone (SW Borneo) bearing sediments transported from Kuching hinterland toward the north [Haile, 1974, Tan, 1979, Bakar et al., 2007, Galín et al., 2017, Hennig-Breitfeld et al., 2019]. The water depth of the deposition appeared have shallowed since 45 Ma without a distinct stratigraphic hiatus in Sarawak [Figure 8, Haile, 1974, Tan, 1979, Hutchison, 1996, Bakar et al., 2007, Galín et al., 2017, Hall and Breitfeld, 2017]. The shallowing may suggest an uplift of sedimentary slices induced by

the embryonic subduction of the PSCS between 45 and 37 Ma. Acidic magmatism was produced within this period of time [Proureau et al., 1996]. Above the Late Eocene unconformity, the Nyalau Unconformity is underlain by Neogene strata, which is found in offshore stratigraphy [Hageman, 1987], and is characterized by gravity-driven deformation in the offshore fold-and-thrust belt of the Borneo-Palawan Trough.

5.2. Tectonic-related stratigraphy in Domain 2

In Sabah (NW Borneo), the Late Eocene unconformity dated around 37 Ma is similarly found [Cullen, 2010, Sapin et al., 2011, Hall, 2013], resting on the ophiolite exposed at the surface [Figure 8, Omang and Barber, 1996, Graves et al., 2000, Chien et al., 2019, Gibaga et al., 2020]. During latest Eocene to Mid-Miocene, the well-studied Rajang and Crocker groups, constitute the distal and proximal sediments of the PSCS, now thrust in the NW Borneo wedge. Then During the Miocene, a slight hiatus is recognized around 16 Ma and interpreted as the Deep-Regional Unconformity [DRU, Figure 8, Levell, 1987, Tan and Lamy, 1990, Hazebroek and Tan, 1993, Chang et al., 2019] or the Nyalau Unconformity in Hennig-Breitfeld et al. [2019]. It is followed by the

Shallow Regional Unconformity (SRU) dated at Late Miocene in most of Sabah area [Balaguru et al., 2003].

Abundant literature exist on these sediments of the central part of the NW Borneo wedge. The deep-sea sediments of the distal part of the PSCS (Rajang Group) exposed northernmost Borneo (Trusmadi, Kudat Peninsula area) are of early Paleogene. The sediments were transported from the Schwaner granitic province of Southern Borneo, as shown by paleo-current measurements and the prominent peak of detritus zircon [Jackson et al., 2009, Tongkul, 2003]. Later, the depositional environment changed from deep-sea to marginal marine or shallow marine in Croker Formation and Setap Shale in Sabah around Oligocene to Early Miocene [Jackson et al., 2009, Zakaria et al., 2013], suggesting a period of uplift in the neighboring land masses. Paleo-drainage reconstructions based on the age population of detrital zircon according to the sediment source suggest the NE–SW backbone in Borneo was extensively uplifted since Miocene, also resulting in the displacement of the paleo-coastline from NW–SE to NE–SW [Menier et al., 2017, Hennig-Breitfeld et al., 2019]. After DRU, horizontal to sub-horizontal strata appear to be restricted to close to the coastline or in the offshore above the Middle Miocene Unconformity (MMU) [Clennell, 1996, Cullen, 2010, Chang et al., 2019]. The deltaic and nearshore sedimentary input in the large Balingan and Baram deltas indicated thrusting activity by this time was replaced by gravity sliding [Sapin et al., 2012]. During the post-collision period, the gravity-driven deformation involves a late Neogene fold-and-thrust belt in offshore, surrounding circularly the Mount Kinabalu and accompanied with E–W transfer zones in tip of Borneo [Cullen, 2010, Franke et al., 2008, Steuer et al., 2014, Chang et al., 2019].

5.3. *Tectonic-related stratigraphy in Domain 1*

In Palawan, an early Cenozoic structural contact exists between the Cretaceous ophiolite and the Eocene formation, suggesting the absence of the original deep sea sediments overlying the Cretaceous crust of the PSCS [Aurelio et al., 2014, Ilao et al., 2018]. In the offshore Palawan, the ophiolite and its metamorphic sole have been dated at 35 Ma, suggesting that the subduction may have initiated at the PSCS mid-ocean ridge [Keenan et al., 2016, Dycoco

et al., 2021]. During the same period, and until the Early Miocene, a significant hiatus is observed onshore (although we have limited formation exposure) (Figure 8). A later extensively distributed unconformity, the (MMU), with a hiatus, seals the deformation around 15–20 Ma of the Nido Platform offshore and onshore. In the past decades, the timing of this MMU was debated due to the discrepancies in age from an area to another and because it may represent the end of the contraction of the wedge as well as the beginning of the gravity sliding period [Hutchison, 2004, Ilao et al., 2018].

In more detail, the Eocene stratigraphy (Panas Formation) consists of sandstone interbedded with shale and mudstone showing a deep-sea environment in the early history. With limited information on Oligocene formation, the Nido Carbonate shows the shallow water depth around Late Oligocene [Steuer et al., 2013]. The Isugod Formation commenced receiving the deposits derived from ophiolite while the Panas Formation characterizing deep-sea sediments [Suggate et al., 2014, Shao et al., 2017]. Meanwhile, the Nido Carbonate was thrust in offshore Palawan, suggesting the timing of uplifting in D1 region by the end of Early Miocene [Cullen et al., 2010, Steuer et al., 2014, Kessler and Jong, 2016]. In Palawan, the last stage of deformation is bracketed by the end of the Pagasa wedge post-dating the Nido Limestone (16 Ma) and before the deposition the Tabon Limestone [9 Ma, Taguibao et al., 2012, Ilao et al., 2018]. A gravity-driven structure affects a narrow belt induced by the shale tectonic in offshore in post-orogeny tectonic [Ilao et al., 2018].

6. **Integration SCS and PSCS: correlation of a paired extensional and contractional system**

The evolution of the paired system can be assessed by unconformities on the two margins. Although many unconformities are described during the Tertiary evolution of SE Asia, this study selects widespread events of the area encompassing the SCS and PSCS area. In the South China Sea, three main unconformities including the rift-onset unconformity (ROU), the intra-rift unconformity (IRU), and the breakup unconformity (BU) may illustrate in a simple way the diachronism of the rifting process from east to southwest (Figure 9). The extensional events

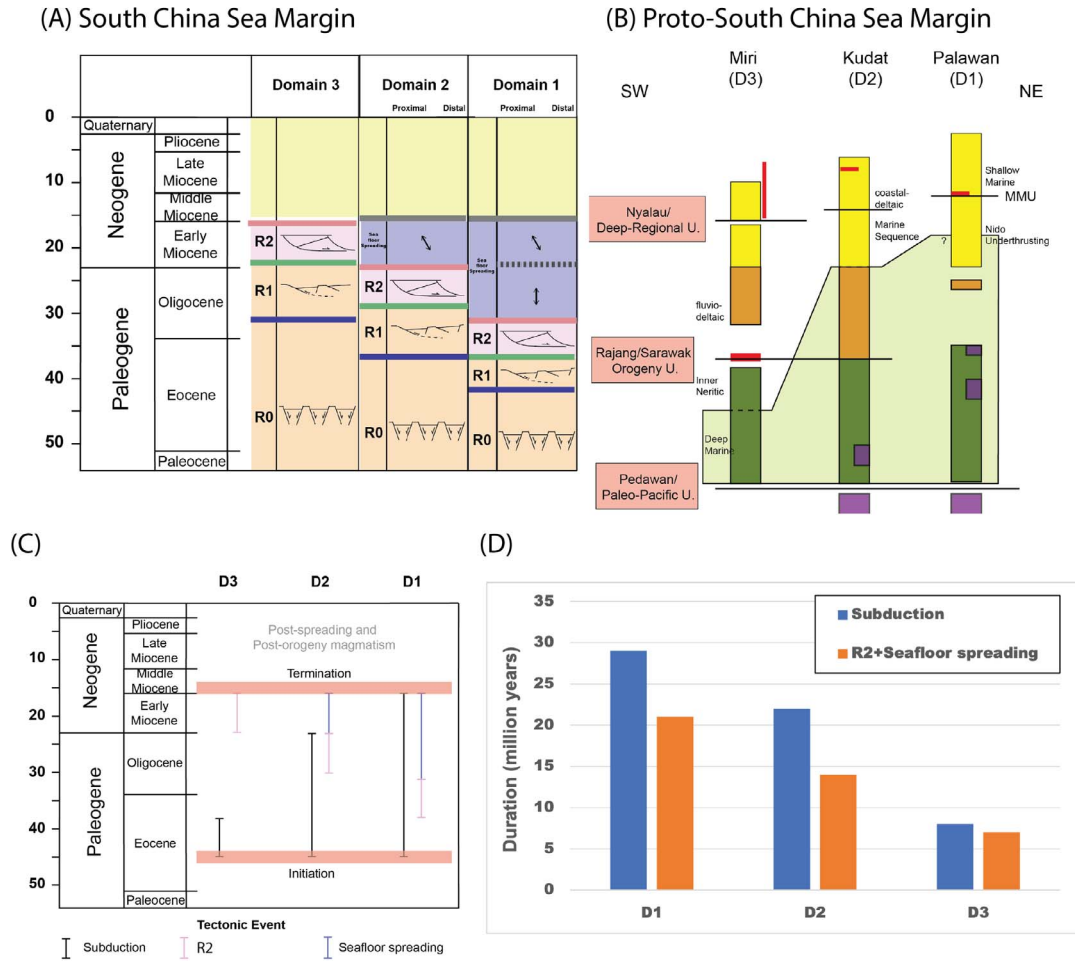


Figure 9. Correlation between the SCS passive margin and the closure of the PSCS. (A) Correlation of rifting events on the SCS margins. (B) Correlation of contractional events on the PSCS, based on unconformities and deformation in NW Borneo and Palawan Island. (C,D) Two representations of the correlation between the events in the neighboring basins between the Early Eocene and the Middle Miocene. Post Middle Miocene is mostly affected by post-tectonic vertical movements.

marked by the unconformities are found everywhere on the margins of the SCS but at a different time. In parallel, several main unconformities of the contractional realm of Borneo, illustrate the shortening of the PSCS. Although it is more difficult to pin point the ages of the different stages of the convergence, it is relevant to see if correlation between the opening of a basin and the closure of the other is relevant.

The IRU and the Sarawak Orogeny Unconformity where documented, are located within the Eocene (Figure 9). The latest Oligocene (23 Ma) highlights the initiation of shifting the extensional

direction in the SCS, and the related unconformity (Top Croker Unconformity—TCU) can be traced widespread c. 23 Ma [Briais et al., 1993, Sibuet et al., 2016, Lunt, 2019, and reference herein]. In the SCS, N–S rifting direction and seafloor spreading lasted until 23 Ma and changed progressively to a NW–SE direction. Precisions for the shift is recorded by a total of 30° between the final rifting in N–S direction and the oceanic formation in NW–SE direction (Figure 9), and is seen in the magnetic anomalies and the bathymetry on oceanic crust [Briais et al., 1993, Lee and Lawver,

1995, Sibuet et al., 2016]. It is also seen in the structural mapping of the Phu Khank Basin [Savva et al., 2013]. This modification was interpreted as a ridge jump in the oceanic formation. The counter-clockwise change is however relatively less obvious in the East Sub-Basin.

The next unconformity, known as the deep-regional unconformity (DRU) or Middle-Miocene Unconformity (MMU), has been documented and debated for decades. It marks the termination of orogeny in Borneo and Palawan [Ilao et al., 2018, Chang et al., 2019]. Chang et al. [2019] suggested that this unconformity is diachronous along the collision zone, which is dated at 16 Ma in Sarawak and appears northward around Palawan at c. 12 Ma [Steuer et al., 2014].

After the cessation of the opening, the SRU appeared extensively in Sabah and also the MMU in the offshore Palawan. Mobile shale was remobilized [Chang et al., 2019]. This period is also marked by several unconformities which are rather related to magmatism. They are for instance the Mount Kinabalu in Sabah, the Mount Capoas in the northern Palawan, and intra-plate Scarborough seamounts.

6.1. *Temporality of events on reconstructions*

The succession of events around the South China Sea shows striking indicators of correlation, but also of discrepancies. The global picture is that there is a general time-link between the subduction and closure of a basin, or a series of small basins, located south of the South China Sea (referred to as the Proto South China Sea), and the timing of rifting, spreading, change of spreading direction, and cessation of spreading followed by bathymetric collapse. The second order is that the precise review of the ages actually shows a migration of both the opening of the SCS and the subduction of the PSCS followed by the collision in NE Borneo. We illustrate this proposition in a series of simple sections and sketch maps (Figure 10).

6.1.1. *Before the Eocene times (Figure 10 top left)*

The first-stage rifting of the margins in the SCS is well documented with an early extension starting from the end of the Cretaceous to the Paleocene. The rifting occurred from SCS extending toward NE to the East China Sea [Teng and Lin, 2004, Guan et al., 2016, Cheng et al., 2021]. During this period, the

oceanic crust of PSCS was located to the south that juxtaposed with Dangerous Ground and the Borneo.

6.1.2. *During Eocene to Oligocene (45–23 Ma)*

The subduction initiated in Borneo and Palawan (Figure 10 top right), resulting in the beginning of developing detachment faults to accelerate thinning the continental crusts in the SCS. The crustal architectures suggest extensive development of the detachment faults associating the dramatic subsidence solely in the SCS while no similar impact on the East China Sea. While the collision occurred in Sarawak, the Sabah and Palawan areas continued subduction coincided the beginning of the rapid breakup in the East Sub-Basin in the SCS, following the hyperextension stages around 32 Ma. The first propagator migrating from East to West, stalling near the edge of the former granitic arc, with a slight E–W compression [Le Pourhiet et al., 2018]. The Southwest of the SCS continued the rifting, developing detachment faults in the main half grabens [Savva et al., 2013, Chang et al., 2022, Madon and Jong, 2022], mostly in N–S direction extension (Figure 10 top right).

6.1.3. *The latest Oligocene (23 Ma) and early Miocene (23–16 Ma)*

Highlight the shift of extensional direction in the SCS and the block rotation in Borneo. The spreading propagator continued operating southwestward and the spreading rate decreased from 25 to 15 mm·yr⁻¹ in half spreading rate until it stopped at 16 Ma [Briaies et al., 1993, Deng et al., 2018, Sibuet et al., 2016]. This may reflect a regional deceleration on both margins of the subduction-driven process. This rearrangement modified accordingly the extensional direction in the vicinity of Spratly Islands and also the Phu Khann Basin [Savva et al., 2013, Chang et al., 2022]. The mountain ranges progressively migrated northward to the Sabah region and modified the river drainages, suggesting the frontal wedge proceeding NW toward direction in Sabah and Palawan. The development of CCW rotation was accommodated by the trench which also proceeding northwestward. Back-arc extension started as a result in the Sulu Sea [Rangin, 1989].

6.1.4. *The middle Miocene to recent (after 16 Ma)*

Stage suggests that the end of orogeny is followed by the magmatism induced by slab breakoff,

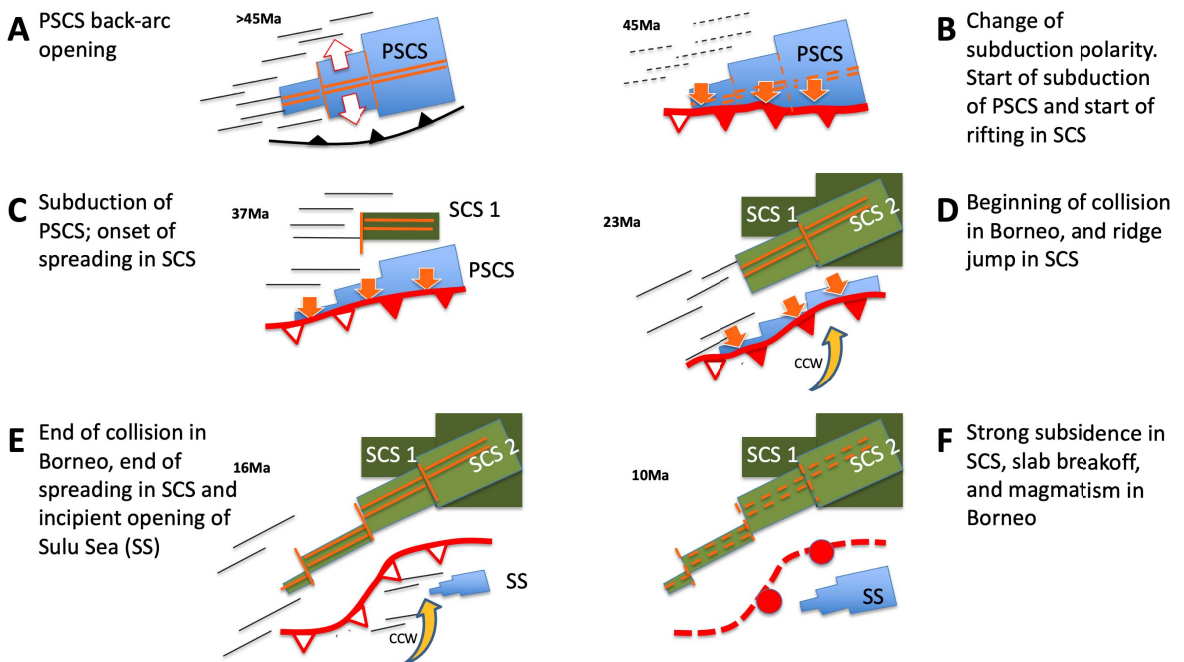


Figure 10. Schematic joint evolution of the PSCS/SCS; (A) opening of the PSCS as a back-arc basin. (B) Beginning of closure in N. Borneo and incipient rifting of the SCS. (C) Subduction of the PSCS. Right: beginning of rifting of the SCS and incipient sea floor spreading of the SCS in the Xisha Trough. (D) Shift in opening of the SCS (propagation of the SW sub-basin), following the subduction of the thinned continental margin of the SCS, beginning of the rotation of N. Borneo. (E) Suture of the PSCS basin and beginning of the opening of the Sulu Sea. (F) Post-collision setting in N. Borneo, with plutonic activity (Kinabalu Mt) and opening of the Sulu Sea propagating toward the SW. Arrow for the rotation of Borneo. Solid and open triangles for active and extinct subduction. Red dots for plutons.

for instance, the Mount Kinabalu in Sabah and the Mount Capoas in the northern Palawan [Encarnacion and Mukasa, 1997, Forster et al., 2015], and the ages clustering around 16–17 Ma of adakites found in Sarawak indicating asthenospheric upwelling after convergence [Prouteau et al., 1996, 2001, Breitfeld et al., 2019, Wu and Suppe, 2017]. A slab break-off magmatism followed this pattern and located the suture zones where the locations of the slabs detached underneath [Rangin et al., 1999, Sapin et al., 2011, Hall and Spakman, 2015, Wu and Suppe, 2017].

The collapse of post-collision sedimentary packages characterized diapiric mobile shale or remobilization of sedimentary mélangé [Morley and Guerin, 1996, Morley et al., 2003, Sapin et al., 2012, Ilao et al., 2018, Chang et al., 2019], induced by the magmatic intrusion and uplift. Without further mountain building, Late Neogene fold-and-thrust belt

developed in the offshore Borneo and Palawan. Several magmatism-related unconformities are also noticed during in the SCS, while no significant crustal thinning and seafloor spreading in this period [Jiang et al., 2018, Xia et al., 2018, Fan et al., 2019, Gao et al., 2019, Sun et al., 2020, Li et al., 2022].

7. Discussion

The correlation of the divergent and convergent margins provides a rare opportunity to evaluate the tectonic processes in the geodynamic perspective. The various timing of orogeny was often suggested resulting from arrival time of the thinned continental crust, derived from the South China, to the suture zone varying in time and space. The former PSCS margin geometry thus was implied a speculation of a V-shaped oceanic closure in the PSCS [Hall, 2002,

Pubellier et al., 2003], while coeval diachronism manifests the V-shaped oceanic opening in the SCS. This result strengthens the hypothesis that the SCS opening in response to the neighboring subduction.

The driving forces such as slab pull and retreat are acknowledged to be the main driving forces for opening and closure of marginal basins, although no active example of active opening in the lower plate exists on Earth. The mechanism of opening within the down-going (or lower plate) is however always invoked for the evolution of the Tethysides. In this setting, the subduction of the Tethys, is coeval with the rifting of belts on the northern margin of Gondwana. The process can nowadays be modelled [Larvet et al., 2022]. On the other hand, the down-going plate consists of heterogeneities of the crust such as lithologic variations, thickness and thermal conditions, and these parameters may vary along strike the collision. Additional forces have been proposed in the asthenospheric mantle, for the closure of a V-shaped marginal sea [Wallace et al., 2009], and may also account for the example of the SCS/PSCS dual system. The collision zone remains relatively immobile and the subduction front proceeds and moves toward to the trench, also suggested as a buoyant indenter. Examples of subduction varying sharply exist in many active places, such as the North arm of Sulawesi [Surmont et al., 1994]. Relevant production of igneous crust such as back-arc extension initiates behind or within the volcanic arc, as shown by the temporal and spatial variation in the Eastern Mediterranean Sea [Menant et al., 2016]. An additional driving force in the asthenosphere is invoked in some numerical simulations to propose that toroidal flows induced when the slab teared and triggers the rotation on the over-riding crust [Menant et al., 2016, Magni et al., 2017].

8. Conclusion

The rifting-to-drifting history of the South China Sea may at least be correlated in terms of stratigraphic cuts with the subduction-collision of the Proto South China Sea history observed in the NW Borneo wedge and Palawan Island. The initial rifting in the SCS is coeval with the beginning of the subduction in the south, and the seafloor spreading of the SCS started when the probably collision related classic sediments of the Crocker group were shed in the PSCS. The ridge jump in the SCS at 23 Ma may be connected with the

rotation in Borneo and Palawan during the Sarawak Orogeny. Both horizontal movements terminated at 16 Ma, when tectonics was marked by vertical movements illustrated by mass wasting on the Borneo-Palawan margins and abnormal subsidence in both margins. This interpretation is in line with a PSCS and a SCS linked in the Cenozoic. This rare example of the paired PSCS and SCS system may constitute an analogue to ancient orogenies in the world. Variations along the subduction of a marginal sea, including the rotation of the upper plate, may actually condition the rifting, the breakup, and the variation of spreading direction of another basin in the lower plate the lower plate.

Declaration of interests

The authors do not work for, advise, own shares in, or receive funds from any organization that could benefit from this article, and have declared no affiliations other than their research organizations.

Dedication

This paper is dedicated to Jean Dercourt, who taught MP (the 2nd author), stratigraphy and the meaning of unconformities.

Acknowledgements

MCS data processing had been performed at ENS-PSL/CNRS under the project “Mer de Chine T985”. We thank CGG for giving us access to the CGG Geovation 2013 software. The raw seismic data set can be found online (www.geologie.ens.fr/imagerie/). We are also grateful for the useful suggestions of anonymous reviewers.

References

- Areshev, E. G., Dong, T. L., San, N. T., and Shnip, O. A. (1992). Reservoirs in fractured basement on the continental shelf of Southern Vietnam. *J. Pet. Geol.*, 15(4), 451–464.
- Aurelio, M. A., Forbes, M. T., Taguibao, K. J. L., Savella, R. B., Bacud, J. A., Franke, D., Pubellier, M., Savva, D., Meresse, F., Steuer, S., and Carranza, C. D. (2014). Middle to Late Cenozoic tectonic events in

- south and central Palawan (Philippines) and their implications to the evolution of the south-eastern margin of South China Sea: Evidence from on-shore structural and offshore seismic data. *Mar. Pet. Geol.*, 58, 658–673.
- Bakar, Z. A. A., Madon, M., and Muhamad, A. J. (2007). Deep-marine sedimentary facies in the Belaga Formation (Cretaceous-Eocene), Sarawak: observations from new outcrops in the Sibu and Tatau areas. *Geol. Soc. Malaysia Bull.*, 53, 35–45.
- Balaguru, A., Nichols, G., and Hall, R. (2003). The origin of the “Circular Basins” of Sabah, Malaysia. *Bull. Geol. Soc. Malaysia*, 46, 335–351.
- Breitfeld, H. T., Macpherson, C., Hall, R., Thirlwall, M., Ottley, C. J., and Hennig-Breitfeld, J. (2019). Adakites without a slab: Remelting of hydrous basalt in the crust and shallow mantle of Borneo to produce the Miocene Sintang Suite and Bau Suite magmatism of West Sarawak. *Lithos*, 344–345, 100–121.
- Briais, A., Patriat, P., and Tapponnier, P. (1993). Updated interpretation of magnetic anomalies and seafloor spreading stages in the South China Sea: Implications for the Tertiary tectonics of Southeast Asia. *J. Geophys. Res.: Solid Earth*, 98(B4), 6299–6328.
- Brune, S., Williams, S. E., Butterworth, N. P., and Müller, R. D. (2016). Abrupt plate accelerations shape rifted continental margins. *Nature*, 536, 201–204.
- Burton-Johnson, A., Macpherson, C. G., Millar, I. L., Whitehouse, M. J., Ottley, C. J., and Nowell, G. M. (2020). A Triassic to Jurassic arc in north Borneo: Geochronology, geochemistry, and genesis of the Segama Valley Felsic Intrusions and the Sabah ophiolite. *Gondwana Res.*, 84, 229–244.
- Chan, L. S., Shen, W., and Pubellier, M. (2010). Polyphase rifting of greater Pearl River Delta region (South China): Evidence for possible rapid changes in regional stress configuration. *J. Struct. Geol.*, 32(6), 746–754.
- Chang, S.-P., Jamaludin, S. N. F., Pubellier, M., Zainuddin, N. M., and Choong, C. M. (2019). Collision, mélange and circular basins in north Borneo: A genetic link? *J. Asian Earth Sci.*, 181, article no. 103895.
- Chang, S.-P., Pubellier, M., Delescluse, M., Qiu, Y., Nirrengarten, M., Mohn, G., Chamot-Rooke, N., and Liang, Y. (2022). Crustal architecture and evolution of the southwestern South China Sea: Implications to continental breakup. *Mar. Pet. Geol.*, 136, article no. 105450.
- Chao, P., Manatschal, G., Chenin, P., Ren, J., Zhang, C., Pang, X., Zheng, J., Yang, L., and Kusznir, N. (2021). The tectono-stratigraphic and magmatic evolution of conjugate rifted margins: Insights from the NW South China Sea. *J. Geodyn.*, 148, article no. 101877.
- Cheng, Y., Wu, Z., Zhang, J., Liu, Y., Wang, Z., and Dai, Y. (2021). Cenozoic rifting and inversion of Beibuwan Basin and its linkage with the strike-slip movement along the Ailao Shan-Red River Shear Zone. *Int. Geol. Rev.*, 64(20), 2966–2983.
- Chenin, P., Manatschal, G., Picazo, S., Müntener, O., Karner, G., Johnson, C., and Ulrich, M. (2017). Influence of the architecture of magma-poor hyperextended rifted margins on orogens produced by the closure of narrow versus wide oceans. *Geosphere*, 13(2), 559–576.
- Chien, Y. H., Wang, K. L., Chung, S. L., Ghani, A. A., Iizuka, Y., Li, X. H., and Lee, H. Y. (2019). Age and genesis of Sabah Ophiolite complexes in NE Borneo. In *Goldschmidt Abstracts, 18–23 August 2019, Barcelona, Spain*, volume 598.
- Clennell, B. (1996). Far-field and gravity tectonics in Miocene basins of Sabah, Malaysia. *Geol. Soc. Lond. Spec. Publ.*, 106(1), 307–320.
- Clerc, C., Ringenbach, J.-C., Jolivet, L., and Ballard, J.-F. (2018). Rifted margins: Ductile deformation, boudinage, continentward-dipping normal faults and the role of the weak lower crust. *Gondwana Res.*, 53, 20–40.
- Clift, P. D., Brune, S., and Quinteros, J. (2015). Climate changes control offshore crustal structure at South China Sea continental margin. *Earth Planet. Sci. Lett.*, 420, 66–72.
- Cottam, M., Hall, R., Sperber, C., and Armstrong, R. (2010). Pulsed emplacement of the Mount Kinabalu granite, northern Borneo. *J. Geol. Soc.*, 167(1), 49–60.
- Cullen, A., Reemst, P., Henstra, G., Gozzard, S., and Ray, A. (2010). Rifting of the South China Sea: new perspectives. *Pet. Geosci.*, 16(3), 273–282.
- Cullen, A. B. (2010). Transverse segmentation of the Baram-Balabac Basin, NW Borneo: refining the model of Borneo’s tectonic evolution. *Pet. Geosci.*, 16(1), 3–29.
- Deng, P., Mei, L., Liu, J., Zheng, J., Liu, M., Cheng, Z.,

- and Guo, F. (2018). Episodic normal faulting and magmatism during the syn-spreading stage of the Baiyun sag in Pearl River Mouth Basin: response to the multi-phase seafloor spreading of the South China Sea. *Mar. Geophys. Res.*, 40(1), 33–50.
- Ding, W., Li, J., and Clift, P. D. (2016). Spreading dynamics and sedimentary process of the Southwest Sub-basin, South China Sea: Constraints from multi-channel seismic data and IODP Expedition 349. *J. Asian Earth Sci.*, 115, 97–113.
- Ding, W., Li, J., Dong, C., and Fang, Y. (2014). Oligocene–Miocene carbonates in the Reed Bank area, South China Sea, and their tectono-sedimentary evolution. *Mar. Geophys. Res.*, 36(2–3), 149–165.
- Dycoco, J. M. A., Payot, B. D., Valera, G. T. V., Labis, F. A. C., Pasco, J. A., Perez, A. D. C., and Tani, K. (2021). Juxtaposition of Cenozoic and Mesozoic ophiolites in Palawan island, Philippines: New insights on the evolution of the Proto-South China Sea. *Tectonophysics*, 819, article no. 229085.
- Encarnacion, J. and Mukasa, S. B. (1997). Age and geochemistry of an “anorogenic” crustal melt and implications for I-type granite petrogenesis. *Lithos*, 42(1–2), 1–13.
- Fan, C., Xia, S., Cao, J., Zhao, F., Sun, J., Wan, K., and Xu, H. (2019). Lateral crustal variation and post-rift magmatism in the northeastern South China Sea determined by wide-angle seismic data. *Mar. Geol.*, 410, 70–87.
- Fang, P., Ding, W., Fang, Y., Zhao, Z., and Feng, Z. (2016). Cenozoic tectonic subsidence in the southern continental margin, South China Sea. *Front. Earth Sci.*, 11(2), 427–441.
- Forster, M. A., Armstrong, R., Kohn, B., Lister, G. S., Cottam, M. A., and Suggate, S. (2015). Highly retentive core domains in K-feldspar and their implications for $^{40}\text{Ar}/^{39}\text{Ar}$ thermochronology illustrated by determining the cooling curve for the Capoas Granite, Palawan, The Philippines. *Aust. J. Earth Sci.*, 62(7), 883–902.
- Fournier, F., Borgomano, J., and Montaggioni, L. F. (2005). Development patterns and controlling factors of Tertiary carbonate buildups: Insights from high-resolution 3D seismic and well data in the Malampaya gas field (Offshore Palawan, Philippines). *Sediment. Geol.*, 175(1–4), 189–215.
- Franke, D., Barckhausen, U., Baristeads, N., Engels, M., Ladage, S., Lutz, R., Montano, J., Pellejera, N., Ramos, E. G., and Schnabel, M. (2011). The continent-ocean transition at the southeastern margin of the South China Sea. *Mar. Pet. Geol.*, 28(6), 1187–1204.
- Franke, D., Barckhausen, U., Heyde, I., Tingay, M., and Ramli, N. (2008). Seismic images of a collision zone offshore NW Sabah/Borneo. *Mar. Pet. Geol.*, 25(7), 606–624.
- Franke, D., Savva, D., Pubellier, M., Steuer, S., Mouly, B., Auxietre, J.-L., Meresse, F., and Chamot-Rooke, N. (2014). The final rifting evolution in the South China Sea. *Mar. Pet. Geol.*, 58, 704–720.
- Fyhn, M. B. W., Boldreel, L. O., and Nielsen, L. H. (2009). Geological development of the Central and South Vietnamese margin: Implications for the establishment of the South China Sea, Indochinese escape tectonics and Cenozoic volcanism. *Tectonophysics*, 478(3), 184–214.
- Galín, T., Breitfeld, H. T., Hall, R., and Sevastjanova, I. (2017). Provenance of the Cretaceous–Eocene Rajang Group submarine fan, Sarawak, Malaysia from light and heavy mineral assemblages and U–Pb zircon geochronology. *Gondwana Res.*, 51, 209–233.
- Gao, J., Bangs, N., Wu, S., Cai, G., Han, S., Ma, B., Wang, J., Xie, Y., Huang, W., Dong, D., and Wang, D. (2019). Post-seafloor spreading magmatism and associated magmatic hydrothermal systems in the Xisha uplift region, northwestern South China Sea. *Basin Res.*, 31(4), 688–708.
- Gibaga, C. R. L., Arcilla, C. A., and Hoang, N. (2020). Volcanic rocks from the central and southern Palawan Ophiolites, Philippines: Tectonic and mantle heterogeneity constraints. *J. Asian Earth Sci.*, X, 4, article no. 100038.
- Graves, J. E., Hutchison, C. S., Bergman, S. C., and Swauger, D. A. (2000). Age and MORB geochemistry of the Sabah ophiolite basement. *Bull. Geol. Soc. Malaysia*, 44, 151–158.
- Guan, D. L., Ke, X. P., and Wang, Y. (2016). Basement structures of East and South China Seas and adjacent regions from gravity inversion. *J. Asian Earth Sci.*, 117, 242–255.
- Hageman, H. (1987). Paleobathymetrical changes in NW Sarawak during Oligocene to Pliocene. *Geol. Soc. Malaysia Bull.*, 21, 91–102.
- Haile, N. S. (1974). Borneo. In Spencer, A. M., editor, *Mesozoic-Cenozoic Orogenic Belts: Data for Orogenic Studies*, Geological Society, London, Special

- Publications, 4, pages 333–347. Geological Society of London.
- Hall, R. (2002). Cenozoic geological and plate tectonic evolution of SE Asia and the SW Pacific: computer-based reconstructions, model and animations. *J. Asian Earth Sci.*, 20(4), 353–431.
- Hall, R. (2012). Late Jurassic–Cenozoic reconstructions of the Indonesian region and the Indian Ocean. *Tectonophysics*, 570–571, 1–41.
- Hall, R. (2013). Contraction and extension in northern Borneo driven by subduction rollback. *J. Asian Earth Sci.*, 76, 399–411.
- Hall, R. and Breiffeld, H. T. (2017). Nature and demise of the Proto-South China Sea. *Bull. Geol. Soc. Malaysia*, 63, 61–76.
- Hall, R. and Spakman, W. (2015). Mantle structure and tectonic history of SE Asia. *Tectonophysics*, 658, 14–45.
- Hatley, A. G. (1980). The Philippines Nido reef complex oil field, a case history of exploration and development of a small oilfield. In *Offshore Southeast Asia Conference, 26–29 February 1980*. Southeast Asia Petroleum Exploration Society (SEAPEX), Singapore, Singapore.
- Hazebroek, H. P. and Tan, D. N. K. (1993). Tertiary tectonic evolution of the NW Sabah continental margin. Tectonic framework and energy resources of the Western Margin of the Pacific Basin. *Geol. Soc. Malaysia Bull.*, 33, 195–210.
- Hennig-Breiffeld, J., Breiffeld, H. T., Hall, R., BouDagher-Fadel, M., and Thirlwall, M. (2019). A new upper Paleogene to Neogene stratigraphy for Sarawak and Labuan in northwestern Borneo: Paleogeography of the eastern Sundaland margin. *Earth-Sci. Rev.*, 190, 1–32.
- Holloway, N. H. (1982). North Palawan Block, Philippines—its relation to Asian mainland and role in evolution of South China Sea. *AAPG Bull.*, 66(9), 1355–1383.
- Huchon, P., Nguyen, T. N. H., and Chamot-Rooke, N. (2001). Propagation of continental break-up in the southwestern South China Sea. *Geol. Soc. Lond. Spec. Publ.*, 187(1), 31–50.
- Hutchison, C. S. (1996). The ‘Rajang accretionary prism’ and ‘Lupar Line’ problem of Borneo. *Geol. Soc. Lond. Spec. Publ.*, 106(1), 247–261.
- Hutchison, C. S. (2004). Marginal basin evolution: the southern South China Sea. *Mar. Pet. Geol.*, 21(9), 1129–1148.
- Hutchison, C. S. (2005). *Geology of North-West Borneo*. Elsevier, Sarawak, Brunei and Sabah.
- Hutchison, C. S., Bergman, S. C., Swauger, D. A., and Graves, J. E. (2000). A Miocene collisional belt in north Borneo: uplift mechanism and isostatic adjustment quantified by thermochronology. *J. Geol. Soc.*, 157(4), 783–794.
- Hutchison, C. S. and Vijayan, V. R. (2010). What are the spratly islands? *J. Asian Earth Sci.*, 39(5), 371–385.
- Ilaio, K. A., Morley, C. K., and Aurelio, M. A. (2018). 3D seismic investigation of the structural and stratigraphic characteristics of the Pagasa Wedge, Southwest Palawan Basin, Philippines, and their tectonic implications. *J. Asian Earth Sci.*, 154, 213–237.
- Jackson, C. A. L., Zakaria, A. A., Johnson, H. D., Tongkul, F., and Crevello, P. D. (2009). Sedimentology, stratigraphic occurrence and origin of linked debrites in the West Crocker Formation (Oligo-Miocene), Sabah, NW Borneo. *Mar. Pet. Geol.*, 26(10), 1957–1973.
- Jamaludin, S. N. F., Pubellier, M., and Menier, D. (2017). Structural restoration of carbonate platform in the southern part of Central Luconia, Malaysia. *J. Earth Sci.*, 29(1), 155–168.
- Jamaludin, S. N. F. B. (2022). *Cenozoic Tectonic Evolution and Succession of Carbonate Growth in Development of Luconia-Balingan Provinces, Sarawak, Malaysia*. Phd thesis, The Universiti Teknologi Petronas. 301 page.
- Jiang, T., Gao, H., He, J., and Tian, D. (2018). Post-spreading volcanism in the central South China Sea: insights from zircon U–Pb dating on volcaniclastic breccia and seismic features. *Mar. Geophys. Res.*, 40(2), 185–198.
- Jolivet, L., Huchon, P., and Rangin, C. (1989). Tectonic setting of Western Pacific marginal basins. *Tectonophysics*, 160(1–4), 23–47.
- Karig, D. (1974). Evolution of arc systems in the Western Pacific. *Annu. Rev. Earth Planet. Sci. Lett.*, 2, 51–75.
- Karig, D., Anderson, R., and Bibee, L. (1978). Characteristics of back-arc spreading in the Mariana Trough. *J. Geophys. Res.*, 83, 1213–1226.
- Keenan, T. E., Encarnacion, J., Buchwaldt, R., Fernandez, D., Mattinson, J., Rasoazanamparany, C., and Luetkemeyer, P. B. (2016). Rapid conversion of an oceanic spreading center to a subduction zone in-

- ferred from high-precision geochronology. *Proc. Natl. Acad. Sci. USA*, 47, E7359–E7366.
- Kessler, F. L. and Jong, J. (2016). The South China Sea: Sub-basins, regional unconformities and uplift of the peripheral mountain ranges since the eocene. *Berita Sedimentologi*, 35, 5–54.
- Kudrass, H. R., Wiedicke, M., Cepek, P., Kreuzer, H., and Müller, P. (1986). Mesozoic and Cainozoic rocks dredged from the South China Sea (Reed Bank area) and Sulu Sea and their significance for plate-tectonic reconstructions. *Mar. Pet. Geol.*, 3(1), 19–30.
- Larsen, H. C., Mohn, G., Nirrengarten, M., Sun, Z., Stock, J., Jian, Z., Klaus, A., Alvarez-Zarikian, C. A., Boaga, J., Bowden, S. A., Briais, A., Chen, Y., Cukur, D., Dadd, K., Ding, W., Dorais, M., Ferré, E. C., Ferreira, F., Furusawa, A., Gewecke, A., Hinojosa, J., Höfig, T. W., Hsiung, K. H., Huang, B., Huang, E., Huang, X. L., Jiang, S., Jin, H., Johnson, B. G., Kurzwski, R. M., Lei, C., Li, B., Li, L., Li, Y., Lin, J., Liu, C., Liu, C., Liu, Z., Luna, A. J., Lupi, C., McCarthy, A., Ningthoujam, L., Osono, N., Peate, D. W., Persaud, P., Qiu, N., Robinson, C., Satolli, S., Sauermilch, I., Schindlbeck, J. C., Skinner, S., Straub, S., Su, X., Su, C., Tian, L., van der Zwan, F. M., Wan, S., Wu, H., Xiang, R., Yadav, R., Yi, L., Yu, P. S., Zhang, C., Zhang, J., Zhang, Y., Zhao, N., Zhong, G., and Zhong, L. (2018). Rapid transition from continental breakup to igneous oceanic crust in the South China Sea. *Nat. Geosci.*, 11(10), 782–789.
- Larvet, T., Le Pourhiet, L., and Agard, P. (2022). Cimmerian block detachment from Gondwana: A slab pull origin? *Earth Planet. Sci. Lett.*, 596, article no. 117790.
- Le Pourhiet, L., Chamot-Rooke, N., Delescluse, M., May, D. A., Watremez, L., and Pubellier, M. (2018). Continental break-up of the South China Sea stalled by far-field compression. *Nat. Geosci.*, 11(8), 605–609.
- Lee, T.-Y. and Lawver, L. A. (1995). Cenozoic plate reconstruction of Southeast Asia. *Tectonophysics*, 251(1–4), 85–138.
- Lei, C. and Ren, J. (2016). Hyper-extended rift systems in the Xisha Trough, northwestern South China Sea: Implications for extreme crustal thinning ahead of a propagating ocean. *Mar. Pet. Geol.*, 77, 846–864.
- Leloup, P. H., Arnaud, N., Lacassin, R., Kienast, J. R., Harrison, T. M., Trong, T. T. P., Replumaz, A., and Tapponnier, P. (2001). New constraints on the structure, thermochronology, and timing of the Ailao Shan-Red River shear zone, SE Asia. *J. Geophys. Res.*, 106(B4), 6683–6732.
- Levell, B. K. (1987). The nature and significance of regional unconformities in the hydrocarbon-bearing Neogene sequences offshore West Sabah. *Bull. Geol. Soc. Malaysia*, 21, 55–90.
- Li, C.-F., Li, J., Ding, W., Franke, D., Yao, Y., Shi, H., Pang, X., Cao, Y., Lin, J., Kulhanek, D. K., Williams, T., Bao, R., Briais, A., Brown, E. A., Chen, Y., Clift, P. D., Colwell, F. S., Dadd, K. A., Hernández-Almeida, I., Huang, X.-L., Hyun, S., Jiang, T., Koppers, A. A. P., Li, Q., Liu, C., Liu, Q., Liu, Z., Nagai, R. H., Peleo-Alampay, A., Su, X., Sun, Z., Tejada, M. L. G., Trinh, H. S., Yeh, Y.-C., Zhang, C., Zhang, F., Zhang, G.-L., and Zhao, X. (2015). Seismic stratigraphy of the central South China Sea basin and implications for neotectonics. *J. Geophys. Res.: Solid Earth*, 120(3), 1377–1399.
- Li, F., Sun, Z., and Yang, H. (2018). Possible spatial distribution of the mesozoic volcanic arc in the present-day South China Sea continental margin and its tectonic implications. *J. Geophys. Res.: Solid Earth*, 123, 6215–6235.
- Li, F., Sun, Z., Yang, H., Lin, J., Stock, J. M., Zhao, Z., Xu, H., and Sun, L. (2020). Continental interior and edge breakup at convergent margins induced by subduction direction reversal: A numerical modeling study applied to the South China Sea margin. *Tectonics*, 39(11), article no. e2020TC006409.
- Li, G., Mei, L., Pang, X., Zheng, J., Ye, Q., and Hao, S. (2022). Magmatism within the northern margin of the South China Sea during the post-rift stage: An overview, and new insights into the geodynamics. *Earth-Sci. Rev.*, 225, article no. 103917.
- Li, L., Clift, P. D., Stephenson, R., and Nguyen, H. T. (2014). Non-uniform hyper-extension in advance of seafloor spreading on the vietnam continental margin and the SW South China Sea. *Basin Res.*, 26(1), 106–134.
- Liang, Y., Delescluse, M., Qiu, Y., Pubellier, M., Chamot-Rooke, N., Wang, J., Nie, X., Watremez, L., Chang, S. P., Pichot, T., Savva, D., and Meresse, F. (2019). Décollements, detachments, and rafts in the extended crust of dangerous ground, South China Sea: The role of inherited contacts. *Tectonics*, 38(6), 1863–1883.

- Lin, A. T., Watts, A. B., and Hesselbo, S. P. (2003). Cenozoic stratigraphy and subsidence history of the South China Sea margin in the Taiwan region. *Basin Res.*, 15(4), 453–478.
- Lin, Y. A., Colli, L., Wu, J., and Schuberth, B. S. A. (2020). Where are the Proto-South China Sea slabs? SE Asian plate tectonics and mantle flow history from global mantle convection modeling. *J. Geophys. Res.: Solid Earth*, 125(12), article no. e2020JB019758.
- Liu, W.-N., Li, C.-F., Li, J., Fairhead, D., and Zhou, Z. (2014). Deep structures of the Palawan and Sulu Sea and their implications for opening of the South China Sea. *Mar. Pet. Geol.*, 58, Part B, 721–735.
- Lunt, P. (2019). A new view of integrating stratigraphic and tectonic analysis in South China Sea and north Borneo basins. *J. Asian Earth Sci.*, 177, 220–239.
- Lunt, P. and Madon, M. (2017). Onshore to offshore correlation of northern Borneo; a regional perspective. *Bull. Geol. Soc. Malaysia*, 64, 101–122.
- Luo, P., Manatschal, G., Ren, J., Zhao, Z., Wang, H., and Tong, D. (2021). Tectono—Magmatic and stratigraphic evolution of final rifting and breakup: Evidence from the tip of the southwestern propagator in the South China Sea. *Mar. Pet. Geol.*, 129, article no. 105079.
- Madon, M. and Jong, J. (2022). The crustal structure and evolution of the Bunguran Trough, offshore Sarawak, Malaysia. *Mar. Pet. Geol.*, 139, article no. 105608.
- Madon, M., Kim, C. L., and Wong, R. (2013). The structure and stratigraphy of deepwater Sarawak, Malaysia: Implications for tectonic evolution. *J. Asian Earth Sci.*, 76, 312–333.
- Magni, V., Allen, M. B., van Hunen, J., and Bouilhol, P. (2017). Continental underplating after slab break-off. *Earth Planet. Sci. Lett.*, 474, 59–67.
- Marquis, G., Roques, D., Huchon, P., Coulon, O., Chamot-Rooke, N., Rangin, C., and Le Pichon, X. (1997). Amount and timing of extension along the continental margin off central Vietnam. *Bull. Soc. Géol. Fr.*, 168(6), 707–716.
- Matthews, S. J., Fraser, A. J., Lowe, S., Todd, S. P., and Peel, E. J. (1997). Structure, stratigraphy and petroleum geology of the south east Nam Con Son basin, offshore Vietnam. In Fraser, A. J., Matthews, S. J., and Murphy, R. W., editors, *Petroleum Geology of South East Asia*, Geological Society, London, Special Publications, 126, pages 89–106. Geological Society of London.
- Menant, A., Sternai, P., Jolivet, L., Guillou-Frottier, L., and Gerya, T. (2016). 3D numerical modeling of mantle flow, crustal dynamics and magma genesis associated with slab roll-back and tearing: The eastern Mediterranean case. *Earth Planet. Sci. Lett.*, 442, 93–107.
- Menier, D., Mathew, M., Pubellier, M., Sapin, F., Delcaillau, B., Siddiqui, N., Ramkumar, M., and Santosh, M. (2017). Landscape response to progressive tectonic and climatic forcing in NW Borneo: Implications for geological and geomorphic controls on flood hazard. *Sci. Rep.*, 7, article no. 457.
- Miao, X.-Q., Huang, X.-L., Yan, W., Yang, F., Zhang, W.-F., Yu, Y., Cai, Y.-X., and Zhu, S.-Z. (2021). Two episodes of Mesozoic mafic magmatism in the Nansha Block: Tectonic transition from continental arc to back-arc basin. *Lithos*, 404–405, article no. 106502.
- Morley, C. K. (2016). Major unconformities/termination of extension events and associated surfaces in the South China Seas: Review and implications for tectonic development. *J. Asian Earth Sci.*, 120, 62–86.
- Morley, C. K., Back, S., Van Rensbergen, P., Crevello, P., and Lambiase, J. J. (2003). Characteristics of repeated, detached, Miocene–Pliocene tectonic inversion events, in a large delta province on an active margin, Brunei Darussalam, Borneo. *J. Struct. Geol.*, 25(7), 1147–1169.
- Morley, C. K. and Guerin, G. (1996). Comparison of gravity-driven deformation styles and behavior associated with mobile shales and salt. *Tectonics*, 15(6), 1154–1170.
- Nanni, U., Pubellier, M., Chan, L. S., and Sewell, R. J. (2017). Rifting and reactivation of a Cretaceous structural belt at the northern margin of the South China Sea. *J. Asian Earth Sci.*, 136, 110–123.
- Nirrengarten, M., Mohn, G., Kuszniir, N. J., Sapin, F., Despinois, F., Pubellier, M., Chang, S. P., Larsen, H. C., and Ringenbach, J. C. (2020). Extension modes and breakup processes of the southeast China-Northwest Palawan conjugate rifted margins. *Mar. Pet. Geol.*, 113, article no. 104123.
- Omang, S. A. K. and Barber, A. J. (1996). Origin and tectonic significance of the metamorphic rocks associated with the Darvel Bay Ophiolite, Sabah, Malaysia. *Geol. Soc. Lond. Spec. Publ.*, 106(1), 263–

- 279.
- Peng, X., Li, C.-F., Shen, C., Li, K., Zhao, Z., and Xie, X. (2020). Anomalous lower crustal structure and origin of magmatism in the southeastern margin of the South China Sea. *Mar. Pet. Geol.*, 122, article no. 104711.
- Peng, X., Shen, C., Mei, L., Zhao, Z., and Xie, X. (2018). Rift–drift transition in the dangerous grounds, South China Sea. *Mar. Geophys. Res.*, 40(2), 163–183.
- Péron-Pinvidic, G., Manatschal, G., Minshul, T. A., and Sawyer, D. S. (2007). Tectonosedimentary evolution of the deep Iberia–Newfoundland margins: Evidence for a complex breakup history. *Tectonics*, 26(2), article no. TC2011.
- Prouteau, G., Maury, R. C., Pubellier, M., Cotten, J., and Bellon, H. (2001). Le magmatisme post-collisionnel du Nord-Ouest de Borneo, produit de la fusion d'un fragment de croûte océanique ancre dans le manteau supérieur. *Bull. Soc. Géol. Fr.*, 172(3), 319–332.
- Prouteau, G., Maury, R. C., Rangin, C., Suparka, E., Bellon, H., Pubellier, M., and Gotten, J. (1996). Miocene adakites from northwest Borneo and their relation to the subduction of the Proto South China Sea. *C. R. Acad. Sci.-Serie Ila: Sciences de la Terre et des Planetes*, 323(11), 925–932.
- Pubellier, M., Ego, F., Chamot-rooke, N., and Rangin, C. (2003). The building of pericratonic mountain ranges: structural and kinematic constraints applied to GIS-based reconstructions of SE Asia. *Bull. Soc. Géol. Fr.*, 174(6), 561–584.
- Pubellier, M. and Meresse, F. (2013). Phanerozoic growth of Asia; Geodynamic processes and evolution. *J. Asian Earth Sci.*, 72, 118–128.
- Pubellier, M. and Morley, C. K. (2014). The basins of Sundaland (SE Asia): Evolution and boundary conditions. *Mar. Pet. Geol.*, 58, 555–578. hal-03080821.
- Rahmat, R., Chung, S.-L., Chen, C.-T., Ghani, A., Lee, H.-Y., and Iizuka, Y. (2020). Zircon U–Pb ages and Geochemical characteristics of Eocene Ophiolitic Rocks from Banggi Island, Sabah (Northern Borneo), Malaysia. In *Conference Geosciences 2020: New Horizon and Beyond, Taiwan*.
- Rangin, C. (1989). The Sulu Sea, a back-arc basin setting within a Neogene collision zone. *Tectonophysics*, 161(1–2), 119–141.
- Rangin, C., Bellon, H., Benard, F., Letouzey, J., Muller, C., and Sanudin, T. (1990a). Neogene arc-continent collision in Sabah, Northern Borneo (Malaysia). *Tectonophysics*, 183(1–4), 305–319.
- Rangin, C., Jolivet, L., and Pubellier, M. (1990b). A simple model for the tectonic evolution of south-east Asia and Indonesian region for the past 43 My. *Bull. Géol. Soc. Fr.*, VI(6), 889–905.
- Rangin, C., Spakman, W., Pubellier, M., and Bijwaard, H. (1999). Tomographic and geological constraints on subduction along the eastern Sundaland continental margin (South-East Asia). *Bull. Soc. Géol. Fr.*, 170(6), 775–788.
- Roques, D., Ranero, C., and Huchon, P. (1997). Geometry and sense of motion along the Vietnam continental margin: onshore/offshore Da Nang area. *Bull. Soc. Géol. Fr.*, 168(4), 413–422.
- Sapin, F., Hermawan, I., Pubellier, M., Vigny, C., and Ringenbach, J.-C. (2013). The recent convergence on the NW Borneo Wedge—a crustal-scale gravity gliding evidenced from GPS. *Geophys. J. Int.*, 193(2), 549–556.
- Sapin, F., Pubellier, M., Lahfid, A., Janots, D., Aubourg, C., and Ringenbach, J. C. (2011). Onshore record of the subduction of a crustal salient: example of the NW Borneo Wedge. *Terra Nova*, 23(4), 232–240.
- Sapin, F., Ringenbach, J. C., Rives, T., and Pubellier, M. (2012). Counter-regional normal faults in shale-dominated deltas: Origin, mechanism and evolution. *Mar. Pet. Geol.*, 37(1), 121–128.
- Savva, D., Meresse, F., Pubellier, M., Chamot-Rooke, N., Lavier, L., Po, K. W., Franke, D., Steuer, S., Sapin, F., Auxietre, J. L., and Lamy, G. (2013). Seismic evidence of hyper-stretched crust and mantle exhumation offshore Vietnam. *Tectonophysics*, 608, 72–83.
- Savva, D., Pubellier, M., Franke, D., Chamot-Rooke, N., Meresse, F., Steuer, S., and Auxietre, J. L. (2014). Different expressions of rifting on the South China Sea margins. *Mar. Pet. Geol.*, 58, 579–598.
- Schellart, W. P., Chen, Z., Strak, V., Duarte, J. C., and Rosas, F. M. (2019). Pacific subduction control on Asian continental deformation including Tibetan extension and eastward extrusion tectonics. *Nat. Commun.*, 10(1), article no. 4480.
- Shao, L., Cao, L., Qiao, P., Zhang, X., Li, Q., and van Hinsbergen, D. J. J. (2017). Cretaceous–Eocene provenance connections between the Palawan Continental Terrane and the northern South China Sea margin. *Earth Planet. Sci. Lett.*, 477, 97–107.

- Shi, X., Jiang, H., Yang, J., Yang, X., and Xu, H. (2017). Models of the rapid post-rift subsidence in the eastern Qiongdongnan Basin, South China Sea: implications for the development of the deep thermal anomaly. *Basin Res.*, 29(3), 340–362.
- Sibuet, J.-C., Yeh, Y.-C., and Lee, C.-S. (2016). Geodynamics of the South China Sea. *Tectonophysics*, 692, 98–119.
- Song, T. and Li, C.-F. (2015). Rifting to drifting transition of the Southwest Subbasin of the South China Sea. *Mar. Geophys. Res.*, 36(2–3), 167–185.
- Steuer, S., Franke, D., Meresse, F., Savva, D., Pubellier, M., and Auxietre, J.-L. (2014). Oligocene–Miocene carbonates and their role for constraining the rifting and collision history of the Dangerous Grounds, South China Sea. *Mar. Pet. Geol.*, 58, 644–657.
- Steuer, S., Franke, D., Meresse, F., Savva, D., Pubellier, M., Auxietre, J.-L., and Aurelio, M. (2013). Time constraints on the evolution of southern Palawan Island, Philippines from onshore and offshore correlation of Miocene limestones. *J. Asian Earth Sci.*, 76, 412–427.
- Suggate, S. M., Cottam, M. A., Hall, R., Sevastjanova, I., Forster, M. A., White, L. T., Armstrong, R. A., Carter, A., and Mojares, E. (2014). South China continental margin signature for sandstones and granites from Palawan, Philippines. *Gondwana Res.*, 26(2), 699–718.
- Sun, Q., Magee, C., Jackson, C. A. L., Mitchell, S. J., and Xie, X. (2020). How do deep-water volcanoes grow? *Earth Planet. Sci. Lett.*, 542, article no. 116320.
- Surmont, J., Laj, C., Kissel, C., Rangin, C., Bellon, H., and Priadi, B. (1994). New paleomagnetic constraints on the Cenozoic tectonic evolution of the North Arm of Sulawesi, Indonesia. *Earth Planet. Sci. Lett.*, 3–4, 629–638.
- Taguibao, K. J., Aurelio, M. A., Savva, D., and Pubellier, M. (2012). Onshore Palawan structures: implications on the evolution of the South China Sea. In *Proceedings of the 34th International Geological Congress, Brisbane, Australia, 5–10 August 2012*.
- Tan, D. N. K. (1979). *Lupar Valley, West Sarawak, Malaysia: Explanation of Sheets 1-111-14, 1-111-15, and Part of 1-111-16*. National Printing Department.
- Tan, D. N. K. and Lamy, J. M. (1990). Tectonic evolution of the NW Sabah continental margin since the Late Eocene. *Bull. Geol. Soc. Malaysia*, 27, 241–260.
- Tang, X., Chen, L., Hu, S., Yang, S., Zhang, G., Shen, H., Rao, S., and Li, W. (2014). Tectono-thermal evolution of the Reed Bank Basin, Southern South China Sea. *J. Asian Earth Sci.*, 96, 344–352.
- Tapponnier, P., Peltzer, G., Le Dain, A. Y., Armijo, R., and Cobbold, P. (1982). Propagating extrusion tectonics in Asia: New insights from simple experiments with plasticine. *Geology*, 10(12), 611–616.
- Taylor, B. and Hayes, D. E. (1980). The tectonic evolution of the South China Basin. In Hayes, D. E., editor, *The Tectonic and Geologic Evolution of Southeast Asian Seas and Islands*. American Geophysical Union (AGU).
- Taylor, B. and Hayes, D. E. (1983). Origin and history of the South China Sea Basin. In Hayes, D. E., editor, *The Tectonic and Geologic Evolution of Southeast Asian Seas and Islands: Part 2*. American Geophysical Union (AGU).
- Teng, L. S. and Lin, A. T. (2004). Cenozoic tectonics of the China continental margin: insights from Taiwan. *Geol. Soc. Lond. Spec. Publ.*, 226(1), 313–332.
- Tongkul, F. (2003). The structural style of Lower Miocene sedimentary rocks, Kudat Peninsula, Sabah. *Bull. Geol. Soc. Malaysia*, 49, 119–124.
- van Hattum, M. W. A., Hall, R., Pickard, A. L., and Nichols, G. J. (2013). Provenance and geochronology of Cenozoic sandstones of northern Borneo. *J. Asian Earth Sci.*, 76, 266–282.
- Vu, A. T., Wessel Fyhn, M. B., Xuan, C. T., Nguyen, T. T., Hoang, D. N., Pham, L. T., and Van, H. N. (2017). Cenozoic tectonic and stratigraphic development of the Central Vietnamese continental margin. *Mar. Pet. Geol.*, 86, 386–401.
- Wallace, L. M., Ellis, S., and Mann, P. (2009). Collisional model for rapid fore-arc block rotations, arc curvature, and episodic back-arc rifting in subduction settings. *Geochem. Geophys. Geosyst.*, 10(5), article no. Q05001.
- Wang, P., Li, S., Suo, Y., Guo, L., Wang, G., Hui, G., Santosh, M., Somerville, I. D., Cao, X., and Li, Y. (2020). Plate tectonic control on the formation and tectonic migration of Cenozoic basins in northern margin of the South China Sea. *Geosci. Front.*, 11(4), 1231–1251.
- Williams, H. H. (1997). Play concepts-northwest Palawan, Philippines. *J. Asian Earth Sci.*, 15, 251–273.
- Wu, J. and Suppe, J. (2017). Proto-South China Sea


- plate tectonics using subducted slab constraints from tomography. *J. Earth Sci.*, 29, 1304–1318.
- Wu, J. M. and Yang, M. Z. (1994). Age analysis of seismic sequences in the southwestern South China Sea (in Chinese). *Geol. Res. South China Sea*, 6, 16–29.
- Wu, S. G., Yuan, S. Q., Zhang, G. C., Ma, Y. B., Mi, L. J., and Xu, N. (2009). Seismic characteristics of a reef carbonate reservoir and implications for hydrocarbon exploration in deepwater of the Qiongdongnan Basin, northern South China Sea. *Mar. Pet. Geol.*, 26(6), 817–823.
- Xia, K. Y. and Zhou, D. (1993). The geophysical characteristics and evolution of northern and southern margins of the South China Sea. *Geol. Soc. Malaysia Bull.*, 33, 223–240.
- Xia, S., Zhao, F., Zhao, D., Fan, C., Wu, S., Mi, L., Sun, J., Cao, J., and Wan, K. (2018). Crustal plumbing system of post-rift magmatism in the northern margin of South China Sea: New insights from integrated seismology. *Tectonophysics*, 744, 227–238.
- Xiao, M., Yao, Y.-J., Cai, Y., Qiu, H.-N., Xu, Y.-G., Xu, X., Jiang, Y.-D., Li, Y.-B., Xia, X.-P., and Yu, Y.-J. (2019). Evidence of early cretaceous lower arc crust delamination and its role in the opening of the South China Sea. *Gondwana Res.*, 76, 123–145.
- Xie, H., Zhou, D., Li, Y., Pang, X., Li, P., Chen, G., Li, F., and Cao, J. (2014). Cenozoic tectonic subsidence in deepwater sags in the Pearl River Mouth Basin, northern South China Sea. *Tectonophysics*, 615–616, 182–198.
- Xie, X., Ren, J., Pang, X., Lei, C., and Chen, H. (2019). Stratigraphic architectures and associated unconformities of Pearl River Mouth basin during rifting and lithospheric breakup of the South China Sea. *Mar. Geophys. Res.*, 40(2), 129–144.
- Yan, P. and Liu, H. L. (2004). Tectonic-stratigraphic division and blind fold structures in Nansha Waters, South China Sea. *J. Asian Earth Sci.*, 24(3), 337–348.
- Yan, P., Wang, L., and Wang, Y. (2014a). Late Mesozoic compressional folds in Dongsha Waters, the northern margin of the South China Sea. *Tectonophysics*, 615–616, 213–223.
- Yan, Q., Shi, X., and Castillo, P. R. (2014b). The late Mesozoic–Cenozoic tectonic evolution of the South China Sea: A petrologic perspective. *J. Asian Earth Sci.*, 85, 178–201.
- Yao, Y., Liu, H., Yang, C., Han, B., Tian, J., Yin, Z., Gong, J., and Xu, Q. (2012). Characteristics and evolution of Cenozoic sediments in the Liyue Basin, SE South China Sea. *J. Asian Earth Sci.*, 60, 114–129.
- Ye, Q., Mei, L., Shi, H., Du, J., Deng, P., Shu, Y., and Camanni, G. (2020). The influence of pre-existing basement faults on the Cenozoic structure and evolution of the proximal domain, northern South China Sea rifted margin. *Tectonics*, 39, article no. e2019TC005845.
- Zakaria, A. A., Johnson, H. D., Jackson, C. A. L., and Tongkul, F. (2013). Sedimentary facies analysis and depositional model of the Palaeogene West Crocker submarine fan system, NW Borneo. *J. Asian Earth Sci.*, 76, 283–300.
- Zhang, J., Wu, Z., Shen, Z., Dong, C., Wang, C., and Zhao, Y. (2020). Seismic evidence for the crustal deformation and kinematic evolution of the Nansha Block, South China Sea. *J. Asian Earth Sci.*, 203, article no. 104536.
- Zhang, Q., Guo, F., Zhao, L., and Wu, Y. (2017). Geodynamics of divergent double subduction: 3-D numerical modeling of a Cenozoic example in the Molucca Sea region, Indonesia. *J. Geophys. Res.: Solid Earth*, 122(5), 3977–3998.
- Zhao, Z., Sun, Z., Sun, L., Wang, Z., and Sun, Z. (2018). Cenozoic tectonic subsidence in the Qiongdongnan Basin, northern South China Sea. *Basin Res.*, 30, 269–288.
- Zhou, D. (2014). Marginal Seas. In Harff, J., Meschede, M., Petersen, S., and Thiede, J., editors, *Encyclopedia of Earth Sciences Series*, pages 1–7. Springer, Dordrecht.
- Zhou, D., Ru, K., and Chen, H.-Z. (1995). Kinematics of Cenozoic extension on the South China Sea continental margin and its implications for the tectonic evolution of the region. *Tectonophysics*, 251(1–4), 161–177.
- Zhou, D., Sun, Z., Chen, H.-Z., Xu, H.-H., Wang, W.-Y., Pang, X., Cai, D.-S., and Hu, D.-K. (2008). Mesozoic paleogeography and tectonic evolution of South China Sea and adjacent areas in the context of Tethyan and Paleo-Pacific interconnections. *Isl. Arc*, 17(2), 186–207.
- Zhou, Z., Mei, L., Liu, J., Zheng, J., Chen, L., and Hao, S. (2018). Continentward-dipping detachment fault system and asymmetric rift structure of the Baiyun Sag, northern South China Sea. *Tectonophysics*, 726, 121–136.



Research article

Tribute to Jean Dercourt

Synthesis of micropaleontological age constraints for the reconstruction of the Tethyan realm in the Lesser Caucasus (Armenia, Karabagh)

Taniel Danelian ^{*,a}, Maria Triantaphyllou ^b, Monique Seyler ^c, Ghazar Galoyan ^d, Arayik Grigoryan ^d and Marc Sosson ^e

^a Univ. Lille, CNRS, UMR 8198-Evo-Eco-Paleo, F-59000 Lille, France

^b National and Kapodistrian University of Athens, Faculty of Geology and Geoenvironment, Panepistimioupolis, 15784 Athens, Greece

^c Univ. Lille, CNRS, Univ. Littoral Côte d'Opale, UMR 8187, LOG, Laboratoire d'Océanologie et de Géosciences, F 59000 Lille, France

^d Institute of Geological Sciences of the National Academy of Sciences of the Republic of Armenia, 24A, Marshal Baghramyan Avenue, Yerevan 0019, Republic of Armenia

^e Université Côte d'Azur, CNRS, Observatoire de la Côte d'Azur, IRD, UMR Géoazur, 250 rue A. Einstein, 06560 Valbonne, France

E-mails: taniel.danelian@univ-lille.fr (T. Danelian), mtriant@geol.uoa.gr (M. Triantaphyllou), monique.seyler@univ-lille.fr (M. Seyler), ghazar.galoyan@gmail.com (G. Galoyan), aragrigroryan@yandex.ru (A. Grigoryan), marc.sosson@geoazur.unice.fr (M. Sosson)

Abstract. We present new biostratigraphic results from two ophiolite outcrops in Armenia. The discovery of upper Tithonian–lower Berriasian diagnostic radiolarian species (*Vallupus gracilis* Li and Sashida) in the lower radiolarites of the Dali section allows to date more accurately submarine lava eruptions of transitional to alkaline composition. The radiolarian results also indicate that blocks of shallow-water carbonates slid into the basin during this time interval. At Vedi, upper Coniacian–Santonian calcareous nannofossils identified in marls of the post-obduction sedimentary cover refine previous age data. Synthesis of the existing bio-chronostratigraphic constraints in Armenia and Karabagh sheds light to the depositional and magmatic history of Tethys in the Lesser Caucasus and highlights the age constraints of fossils on the timing of ophiolite obduction in the region.

Keywords. Micropaleontology, Radiolaria, Ophiolite, Tethys, Armenia, Lesser Caucasus.

Manuscript received 16 January 2023, revised and accepted 3 April 2023.

* Corresponding author.

1. Introduction

Micropaleontology is particularly helpful for the establishment of an accurate chronostratigraphic framework for the depositional and geodynamic history of Tethys. More particularly, radiolarians are extremely useful for dating radiolarites that are often stratigraphically associated with submarine lavas. Dating these past siliceous oozes, which accumulated presumably under mesotrophic waters and in a depositional environment starved of any carbonate or siliciclastic material [Baugmgartner, 2013], is of great significance for the geodynamic and paleoenvironmental reconstruction of the various Tethyan realms, often preserved in tectonically complex areas [e.g., Al-Riyami *et al.*, 2002, Avagyan *et al.*, 2017, Cordey, 2022, De Wever and Baudin, 1996, De Wever *et al.*, 1994, Danelian *et al.*, 2006, 2008a, Ferrière *et al.*, 2015, Goričan *et al.*, 2012, Robertson *et al.*, 2013, 2021, 2022, Vrielynck *et al.*, 2003]. Foraminifera and calcareous nannofossils are also useful in providing important biochronostratigraphic constraints for the timing of ophiolite obduction by dating the thrust sequences beneath the ophiolites and the post-obduction sedimentary cover [Danelian *et al.*, 2014, Okay *et al.*, 2022, Sosson *et al.*, 2010].

The Lesser Caucasus (Armenia and Karabagh) represents a key component of the Alpine-Himalayan mountain belt, as it preserves the remnants of a Neotethyan Mesozoic oceanic realm that continues westwards into northeastern Turkey [e.g., Zakariadze *et al.*, 1983, Galoyan, 2008, Galoyan *et al.*, 2007, 2009, Rolland *et al.*, 2009a, 2010, Sosson *et al.*, 2010, 2016], representing thus an over 700 km-long coherent Tethyan suture zone. The ophiolitic units preserved in the Lesser Caucasus are the relics of an oceanic domain that existed during the Mesozoic between the Somkheto-Karabagh volcanic arc, considered as part of the southern margin of Eurasia [Sosson *et al.*, 2010] and the South-Armenian Block (SAB), a Gondwana derived micro-continent that was detached from it during the Late Paleozoic–Early Mesozoic [Dercourt *et al.*, 1986, Barrier and Vrielynck, 2008].

Initial results on radiolarians extracted from the sedimentary cover of the ophiolites in the Lesser Caucasus were obtained at the time of the Soviet Union [Zakariadze *et al.*, 1983, Belov *et al.*, 1991, Knipper *et al.*, 1997, Vishnevskaya, 1995], but the bulk of existing radiolarian data was published dur-

ing the last 15 years following a number of French-Armenian joint projects. These results provided relatively accurate ages, generated from coherent successions of radiolarian cherts, which are either intercalated between successive lava flows or lie stratigraphically over them [Asatryan, 2009, Asatryan *et al.*, 2010, 2011, 2012, Danelian *et al.*, 2007, 2008b, 2010, 2012, 2014, 2016, 2017, Sosson *et al.*, 2010]. Special attention was paid in stating explicitly the provenance of studied samples with respect to their geological and stratigraphic setting, as well as in documenting with illustrations the identified fauna (or at least the age diagnostic species); the latter is important for communicating the species concept used during the process of identification.

We have recently undertaken additional micropaleontological studies in two sectors that are of key significance for the understanding of the evolution of the Tethyan realm in Armenia (Figure 1). In the Dali sector, north-east of lake Sevan, we have obtained more precise datings for the lower radiolarite interval that is intercalated between lavas of enriched tholeiitic (E-MORB) and alkaline affinities, as shown recently by Seyler *et al.* [2023]. In the Vedi sector, south-east of the capital city Yerevan, new datings using calcareous nanofossils confirm and further indicate the age of the marly sequence that is part of the transgressive post-obduction sedimentary cover, which helps to constrain the timing of obduction. Finally, a review of the currently available biochronological constraints in the context of their specific depositional and geodynamic settings allows us to illustrate the main contributions of micropaleontology in the reconstruction of the Tethyan realm preserved in the Lesser Caucasus. We thus attempt to address the following questions: (1) what is the age range of radiolarite accumulation that is stratigraphically related to volcanic events? (2) what are the age constraints for the obduction of ophiolites?

2. Geological outline and geodynamic significance

The ophiolites in the Lesser Caucasus are organized along two subparallel belts (Figure 1).

- The Sevan–Hakari (Akera) ophiolite extends in the east and south-east of lake Sevan; it is considered as representing the suture zone of the Tethys ocean in the region [Sosson *et al.*, 2010, and references

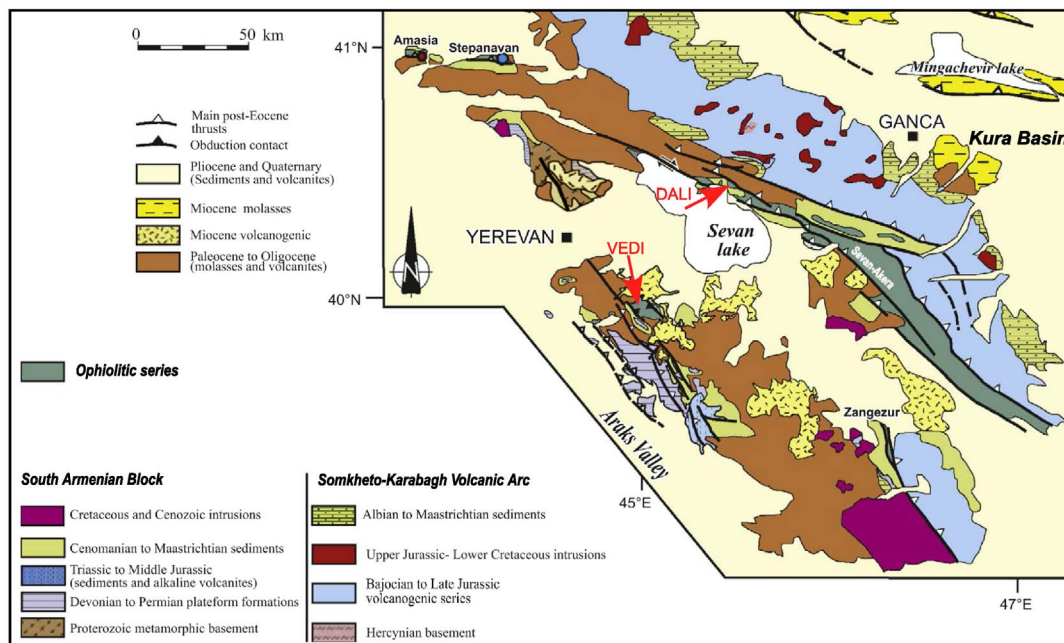


Figure 1. Schematic geological map of the Lesser Caucasus [modified after Sosson *et al.*, 2010 and Hässig *et al.*, 2015].

therein]. The Amasia and Stepanavan ophiolites, situated at the northwest of the country, are regarded as the northward extension of the Sevan-Hakari ophiolites, making the link to the Izmir-Ankara suture zone [e.g., Galoyan, 2008, Galoyan *et al.*, 2007, Hässig *et al.*, 2013a, 2016a,b].

- The Vedi ophiolite [Aslanyan and Satian, 1977, Knipper and Khain, 1980, Sokolov, 1977], located at the south-east of Yerevan, is a folded klippe unit that is transgressively overlain by Coniacian–Santonian sedimentary sequences following the obduction of ophiolites over Cenomanian carbonates and flysch of the SAB [Sosson *et al.*, 2010, Danelian *et al.*, 2014].

The Tethyan ophiolites preserved in the Lesser Caucasus are regarded as remnants of oceanic crust generated in an intra-oceanic supra-subduction [Seyler *et al.*, 2023] or back-arc basin setting [Galoyan, 2008, Galoyan *et al.*, 2009, Sosson *et al.*, 2010, Rolland *et al.*, 2020]. They are represented by lavas of different geochemistry (island-arc tholeiites, N-MORB, E-MORB and alkaline), oceanic sedimentary rocks (mainly radiolarites), covering in some places (i.e., the Dali sector) relics of a complex paleo-seafloor, composed essentially of serpentinites, hornblende-bearing gabbros and diorites [Galoyan,

2008, Sosson *et al.*, 2010], as well as mélangé units with metric blocks of igneous-ophiolitic and sedimentary lithologies.

The Dali sector east of lake Sevan was previously described in a number of publications [Galoyan, 2020, Galoyan *et al.*, 2009, Asatryan *et al.*, 2012, and references therein] and the reader is referred to them for a more detailed presentation. The petrology of the lavas have been recently studied by Seyler *et al.* [2023], who distinguished two main lithotectonic units. The lower unit is represented by a small dioritic massif intruded by trondjemites and unconformably overlain by an undated sequence of island-arc tholeiitic pillow lavas [group A lavas of Seyler *et al.*, 2023]. The upper unit is a ca. 100 m-thick volcano-sedimentary sequence of basaltic to trachybasaltic pillow lavas intercalated with radiolarites (Figure 2). Based on their Nb, Zr, Y and heavy REE contents and ratios, the volcanics range from low-K, enriched tholeiites (E-MORB; group B) to alkaline and OIB-like (group C). Despite high Nb concentrations, some of the lavas also exhibit Nb–Ta negative anomalies and enrichment of Th relative to Nb, which suggest a subduction influence. Moreover, alkaline amphiboles occur as phenocrysts in trachy-

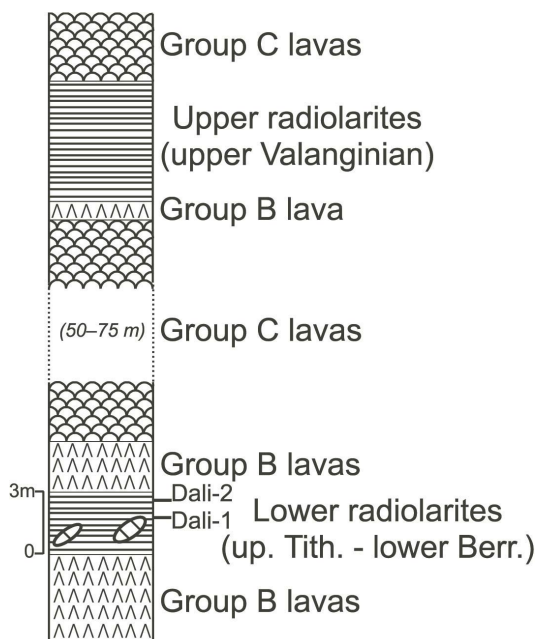


Figure 2. Synthetic lithostratigraphic column of the Tithonian–Valanginian volcano-sedimentary sequence at Dali [after Asatryan *et al.*, 2012 and Seyler *et al.*, 2023, modified]. Group B: enriched MORB-type. Group C: amphibole-phyric alkali trachybasalts and alkali basalts. Both groups of lavas may exhibit slight subduction-related signature.

basalts (group C1 lavas) or only in groundmass in alkalisalts (group C2 lavas), indicating crystallization from hydrous magmas. This double geochemical signature (e.g., within-plate and subduction-related) was interpreted by Seyler *et al.* [2023] as the result of the decompression melting of a heterogeneously enriched mantle during rifting of the previous intra-oceanic island-arc.

3. New biochronostratigraphic constraints

3.1. The Dali sector (northeast of lake Sevan)

Two prominent radiolarite intervals, each of them several metres thick, are intercalated in the upper volcano-sedimentary unit (Figure 2). The lower radiolarites are ca. 3 m-thick and located within a group B lava sequence. As reported by Seyler *et al.* [2023], the basaltic andesitic lava flow exposed just

above the sediments is partially intermingled with claystones of the underlying radiolaritic sequence. After digging a small trench, reddish shales were observed being intercalated in the upper levels of the group B lavas; this radiolarite interval has the particularity of containing in it metric and fairly rounded blocks of oolitic grainstones with crinoid fragments that have clearly slid into the deep basin (olistolithes) from the shallow water, wave-agitated environments, in which they were initially deposited. The lower radiolarites and group B lavas are in turn overlain by a ca. 50–75 m-thick lava sequence of alkaline lavas belonging to groups C1 and C2 (group C on Figure 2), themselves overlain by a thin basaltic flow of Group B lavas, then overlain by the upper interval of dark purple radiolarites, ca. 6 m-thick. Finally, the studied section is topped by Group C2 alkaline basalt. The contacts are not clearly visible on the field, but judging by the general arrangement of the rocks, they are inferred to be stratigraphic.

Based on the biozonation of Baumgartner *et al.* [1995], Asatryan *et al.* [2012] were able to assign the lower radiolarites to the Unitary Association Zones (UAZ) 13–17, correlated with the latest Tithonian–Valanginian interval and the upper radiolarites with the UAZ 17 only, correlated with the late Valanginian. Thus, in spite of the more numerous species identified in the two radiolarian assemblages obtained from the lower radiolarites, no age discrimination could be made with the more precise age obtained for the upper radiolarites.

In an attempt to better date the lower radiolarites we undertook additional laboratory work on the two previously studied radiolarian-bearing samples. Only the sample Dali 2 delivered radiolarians of additional biochronological significance, as compared to the age established by Asatryan *et al.* [2012]. More particularly, we were able to identify the species *Tethysetta mashitaensis* (Mizutani) (Figure 3a), which is known to occur in the UAZ 8–15 of Baumgartner *et al.* [1995], correlated with the Callovian/Oxfordian to late Berriasian/earliest Valanginian time interval. However, we also obtained a single specimen of *Vallupus gracilis* Li and Sashida, which is easily distinguished by the shape of its cortical collar that is gradually constricted to a small aperture (Figure 3b). To our knowledge, this species is only known from a tuffaceous radiolarian claystone sample (181-R003) recovered from the Mariana trench that contains

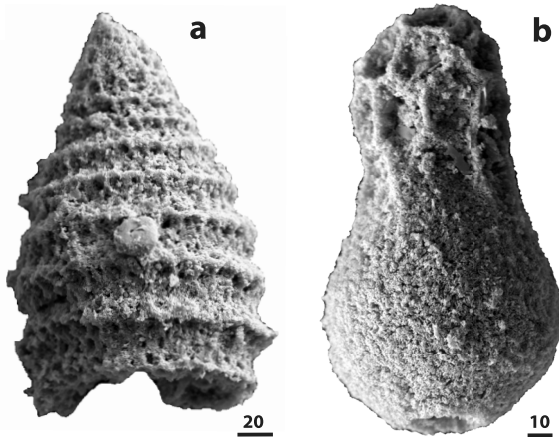


Figure 3. Age diagnostic radiolarians extracted from sample Dali-2; (a) *Tethysetta mashitaensis* and (b) *Vallupus gracilis*. The scale refers to microns.

an exceptionally well preserved and diverse (over 500 species) radiolarian assemblage [Li and Sashida, 2013]. The sample contains also calcareous nanofossils assigned to the CC1 zone and correlated with the early Berriasian. Therefore, the age of the lower radiolarites may be now restricted to the latest Tithonian–early Berriasian interval.

3.2. The Vedi sector

In the Vedi natural reserve exists the best outcrop to document the obduction of Tethyan ophiolites on the SAB, as well as the post-obduction sedimentary cover. Following Sokolov's [1977] detailed study, the general geological structure, lithological relationship and various contacts of the Vedi ophiolite are well described in Sosson *et al.* [2010] and reproduced here in Figure 4. Danelian *et al.* [2014] studied the 150 uppermost metres of the carbonate sequence of the SAB at the northern edge of the Spitakadjur anticlinal fold (south-western part of the section in Figure 4) and based on microfacies analysis and the frequent presence of rudist clasts they characterized them as back-reef limestones. They are stratigraphically overlain by a flysch-type sequence that contains, in its upper part, numerous blocks or olistoliths of various lithologies (limestones, lavas, etc.).

Eastwards, and just after the entry to the Mankouk valley (one of the right tributaries of the Vedi River),

one may observe over the ophiolitic lavas a thick transgressive sequence of red conglomerates. They are overlain by a ca. 50 m-thick sequence of marls and siltstones. The entire sequence is preserved in a synclinal form [Galoyan, 2008, Sosson *et al.*, 2010]. In the middle of this valley, at the base of the synclinal structure, a astounding rudist reef is developed between the transgressive sequence of conglomerates-marls and the lavas that are underneath.

We have recently sampled a ca. 30 m thick sequence of fragile marls that are located at the north-eastern part of the synclinal structure and deposited above the red-gray conglomerates. The two samples we collected come from the lower part (Vd22-03) and the middle/upper part (Vd22-02) of the marls (see Figure 4).

New observations confirm the presence of species *Zeughradotus diplogrammus*, *Z. embergeri*, *Tranolithus orionatus* and *Reinhardtites anthophorus* in sample Vd.22.02, while species *Eiffellithus turriseiffelii*, ? *Micula concava* and *Lithastrinus grillii* were identified in sample Vd.22.03 (Figure 5).

Hence, the combined biochronostratigraphic constraints of the species *Z. diplogrammus* and *L. grillii*, suggest a biostratigraphic assignment of the gray-greenish marls to biozones UC11a–UC12 of Burnett [1998] that correlates with the late Coniacian–Santonian time interval [86–84 Ma in the recent geological Time scale of Gradstein *et al.*, 2020].

4. Discussion

A synthesis of all biochronostratigraphic results available in the Lesser Caucasus allows to improve our understanding of the geological evolution of Tethys in the region (Figure 6). In this synthesis we thought it interesting to position also the absolute isotope ages known in the region and obtained from crustal magmatic rocks (i.e. gabbros and diorites) and the single lava flow dated by Rolland *et al.* [2010].

4.1. Reconstruction of the Tethyan oceanic realm

The oldest radiolarian assemblage reported from the Lesser Caucasus is late Carnian in age and comes from the Old Sotk Pass, in the Armenia–Karabagh border area [Knipper *et al.*, 1997]. The authors describe an over 200 m-thick volcano-sedimentary sequence displaying alternations of distal turbidites

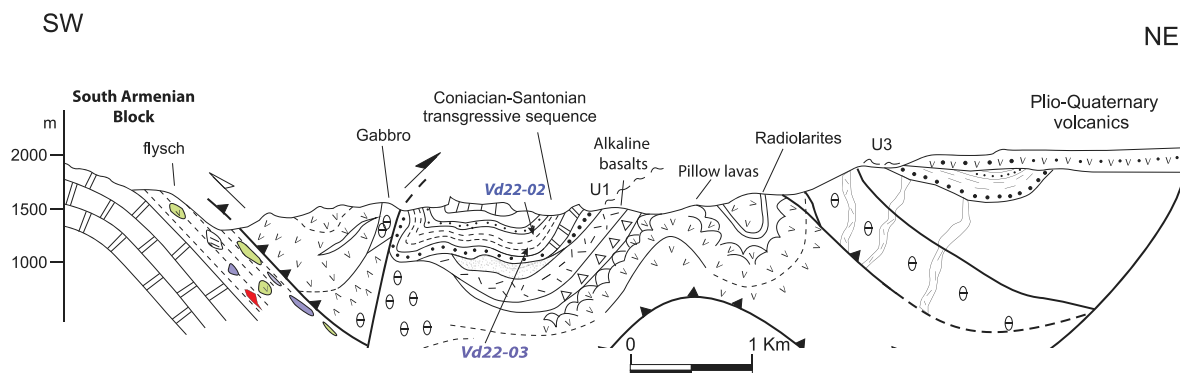


Figure 4. Geological section of the Vedi ophiolite obducted southwestwards onto the South Armenian Block and covered by the post-obduction conglomerates and marls [after Sosson *et al.*, 2010, modified].

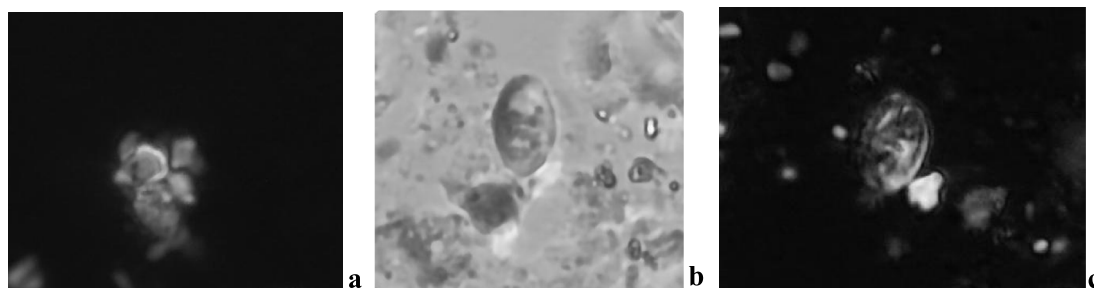


Figure 5. Age diagnostic coccoliths observed in the marls of the post-obduction sedimentary cover at Vedi (1000 \times). (a) *Lithastrinus grillii* identified in sample Vd.22.03. (b) *Tranolithus orionatus* identified in sample Vd.22.02. (c) *Zeugrabdodus diplogrammus* identified in sample Vd.22.02.

and greywackes and siliceous shales with basaltic lavas and breccias with gabbro-diabasic elements [see Figure 2 of Knipper *et al.*, 1997]. The upper Carnian radiolarians were recovered from a 20 m-thick interval of siliceous shales (pelites), while a younger assemblage of Toarcian affinity is reported from cherts situated at the middle part of their column, above which two levels of basaltic lavas are reported to include limestone blocks with Norian bivalves and conodonts. The study of Grigoryan [2005] showed that the Upper Triassic limestone olistoliths have a wide geographic distribution at the Old Sotk Pass, but they all have a short age range (early-middle Norian) and similar lithological composition. Vishnevskaya [1995] has also reported radiolarians from this section, stressing mainly on details concerning the Toarcian radiolarian assemblage. According to her, the sedimentary sequence at this locality displays three intervals: a lower 10 m-thick inter-

val, which yielded the upper Carnian radiolarians, is overlain by a 5 m-thick interval of “sediments with indistinct bedding and sorting, pelites and radiolarites” that yielded the Toarcian radiolarian assemblage; the sequence is finally overlain by a 100 m-thick “Jurassic volcano-sedimentary” interval that contains blocks of Norian limestone.

Having visited this locality ourselves, we prefer to consider this entire sequence at Old Sotk Pass as a highly tectonized mélangé zone. Nevertheless, the report of upper Carnian radiolarian shales and Toarcian radiolarian cherts is significant. In combination with the Upper Triassic gabbros dated by Bogdanovski *et al.* [1992] in Karabagh, they may be regarded as elements of a Tethyan oceanic crust that were accreted during the Late Cretaceous obduction of the ophiolites.

Based on their stratigraphic relation with dated radiolarites, lavas of Middle Jurassic age are

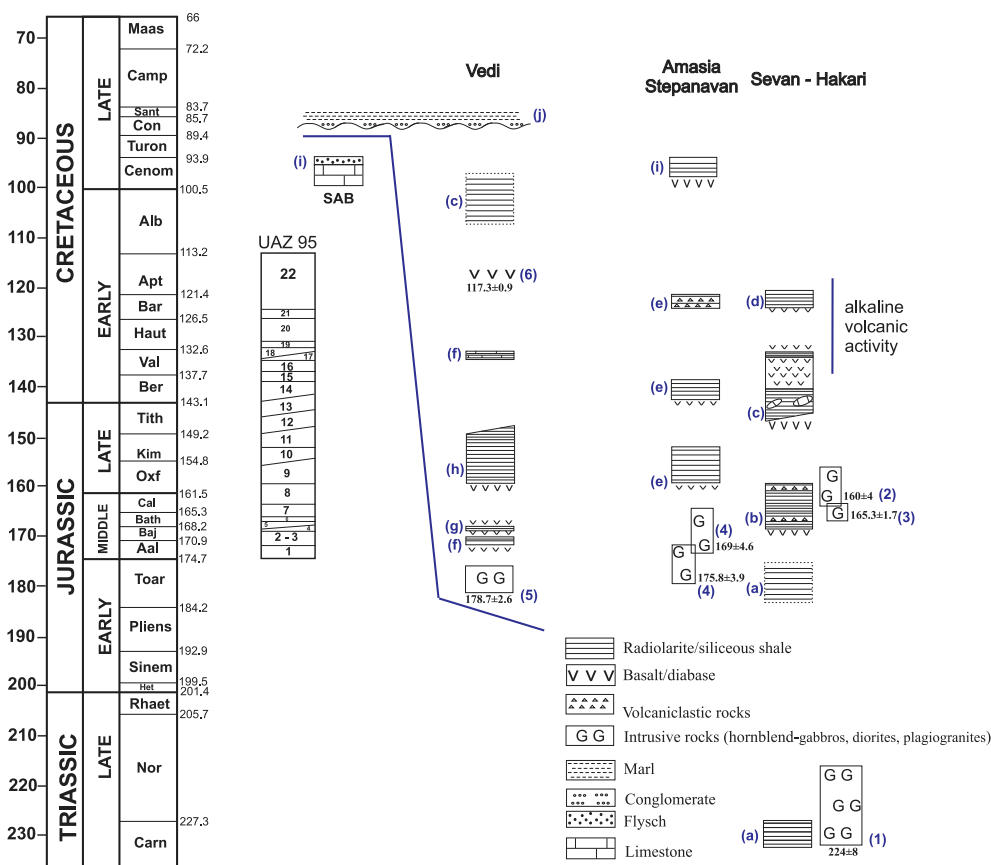


Figure 6. Synthesis of all dated radiolarites in the ophiolitic units of the Lesser Caucasus, the top of the sedimentary sequence of the South-Armenian Block on which they are obducted and the lower part of the post-obduction sedimentary cover. (a) Knipper *et al.* [1997], Vishnevskaya [1995]; (b) Asatryan *et al.* [2010]; (c) Asatryan *et al.* [2012], Danelian *et al.* [2012], this study; (d) Asatryan *et al.* [2011]; (e) Danelian *et al.* [2016]; (f) Danelian *et al.* [2017]; (g) Danelian *et al.* [2008b], Asatryan [2009]; (h) Danelian *et al.* [2010]; (i) Danelian *et al.* [2014]; (j) Sosson *et al.* [2010], this study. (1) Bogdanovski *et al.* [1992]; (2) Zakariadze *et al.* [1983]; (3) Galoyan *et al.* [2009]; (4) Hässig *et al.* [2013b]; (5) Rolland *et al.* [2010]; (6) Rolland *et al.* [2009b]. Time scale according to Gradstein *et al.* [2020].

well-established both in the Vedı and Sevan ophiolites. More specifically, in Vedı, radiolarites intercalated between pillow and massive variolitic lavas were dated initially as middle-late Bajocian [UAZ 3–4, Danelian *et al.*, 2008b], but it was later clarified that the radiolarian assemblage may be assigned to the single UAZ 4 and thus to be correlated only with the late Bajocian [Asatryan, 2009]. Older radiolarites, assigned to the UAZ 2–3 (late Aalenian–middle Bajocian) were recently revealed by Danelian *et al.* [2017] in a block preserved in the ophiolitic mélangé of the Erakh anticline, near Vedı. Here, the radio-

larians were extracted from cherts that are in stratigraphic contact with lavas, but it is unclear whether the radiolarites are younger or older than the lavas.

Within the Sevan-Hakari ophiolite zone, Vishnevskaya [1995] dated Bajocian to lower Bathonian radiolarian cherts at the Mt. Karawul of Karabagh, overlying basaltic lavas. In the same ophiolitic zone, Asatryan *et al.* [2010] studied at the valley of Sarinar (north-east of lake Sevan) a 40 m-thick sequence of radiolarites that is sandwiched between two lava flows; the lower lavas are stratigraphically overlain by radiolarites that are dated at their base (ca. 3 meters

above the contact with the lavas) as latest Bajocian–early Bathonian in age (UAZ 5). Several metric tuffite levels were observed in the lower 20 m of the radiolarite sequence and may be correlated with the Bathonian–Callovian, as one of the chert samples (Sar-10), situated close to the uppermost tuffite level, yielded well preserved radiolarians assigned to the UAZ 7–8 (late Bathonian–early Oxfordian).

All these radiolarian ages need to be examined in parallel with the radiometric ages obtained on diorites and hornblende-bearing gabbros from ophiolitic units at Sevan [Bathonian–early Callovian, Galoyan *et al.*, 2009], Vedi [Toarcian, Rolland *et al.*, 2010] and Amasia [late Toarcian–early Bajocian and Aalenian–Bathonian; Hässig *et al.*, 2013a,b], the petrographic and geochemical signature of which have all an oceanic arc component. All this evidence is consistent with the formation, at least since the Toarcian [Hässig *et al.*, 2017], of an intra-oceanic volcanic arc following the initiation of an intra-oceanic subduction in the interior of an oceanic realm, which was over 2000 km wide during the Middle Jurassic, between the SAB and the Eurasian margin [Bazhenov *et al.*, 1996, Meijers *et al.*, 2015]; the latter is represented by the Somketo-Karabagh continental arc [Sosson *et al.*, 2010] or island arc [Galoyan *et al.*, 2018], which is also considered to represent evidence for a northward Andean-type subduction under the Eurasian continent or a southward “Mariana-type” subduction in Paleotethys, respectively. The radiolarian age evidence discussed above and the important Bajocian volcanism known from the Somketo-Karabagh belt [Sosson *et al.*, 2010, Galoyan *et al.*, 2018, and references therein] argue for a Bajocian pulse in geodynamic activity. The latter correlates well with the Bajocian (170–168 Ma) onset of a convergence setting in the Neo-Tethyan realm preserved in the Hellenides [Jones and Robertson, 1991, Jones *et al.*, 1992, Ferrière *et al.*, 2016]. They may both be the result of a more general plate tectonic reorganization following the opening of the Central Atlantic Ocean since ~175–170 Ma [Smith and Spray, 1984, Maffione and van Hinsbergen, 2018, and references therein].

The evidence for Late Jurassic submarine volcanic activity in the Tethyan realm of the Lesser Caucasus is not conclusive. Upper Jurassic radiolarites are in stratigraphic relation with lavas in Stepanavan, Amasia and Vedi [Danelian *et al.*, 2007, 2010, 2016], but

the obtained ages are not accurate enough yet (i.e., UAZ 9–10 or 9–11).

The data of the Dali sector, discussed above and in Seyler *et al.* [2023], provide important chronostratigraphic constraints for submarine volcanic activity during the Jurassic/Cretaceous transitional interval generated by partial melting of a heterogeneous mantle source in the extensional regime of an intraoceanic arc-back-arc setting. Given the new, more precise age (latest Tithonian–early Berriasian) for the lower radiolarites, it can be now established for the first time that the enriched mantle-derived volcanism was initiated since at least the Berriasian. Therefore, given the early Aptian radiometric age (ca. 117 Ma) of alkaline lavas dated by Rolland *et al.* [2010], it may be now inferred that the E-MORB and alkaline, OIB-like volcanism lasted for at least 20–25 million years (ca. 143/138–117 Ma; early/late Berriasian to early Aptian) in the Tethyan realm of the Lesser Caucasus.

Seyler *et al.* [2023] consider that this enriched subalkaline–alkaline magmatic activity that took place during the Jurassic/Cretaceous transition may reflect a major change in the geodynamic regime of Tethys in the Lesser Caucasus, as they bear geochemical signatures of within-plate lavas, locally showing a subduction influence.

Finally, our new radiolarian results establish that it is during the latest Tithonian–early Berriasian time that blocks of oolitic limestones with clasts of echinoderms slid into the deep-sea basin of radiolarite accumulation. Although the age of these limestones is unknown, their facies attests to the presence of islands in the neighbourhood of the radiolarite basin, on which shallow water carbonate sedimentation accumulated. A second outcrop of radiolarites containing blocks of limestones is reported by Danelian *et al.* [2012] from a megablock in the Dzknaged mélange, north of the lake Sevan; the megablock displays a sequence of 6–7 m thick radiolarites with thin-bedded intercalations of lava flows and several small (20 cm-wide) rounded blocks of limestones with debris of echinoderms. The radiolarian assemblage extracted from a sample (Sevan-1) is correlated with the latest Tithonian–Valanginian (UAZ 13–17), but it may be reasonably assumed that it is of similar age as at Dali valley.

It is noteworthy, that the late Valanginian interval (UAZ 17) is dated both in the Vedi and Sevan

ophiolite zones. However, the block dated at the Erakh anticline [Danelian *et al.*, 2017], contains intercalations of bedded radiolarian cherts and pelagic limestones and therefore attests for an ocean floor situated above the Calcite Compensation Depth (CCD) of the time, in contrast with the upper radiolarites intercalated between alkaline lavas at Dali [Asatryan *et al.*, 2012, Seyler *et al.*, 2023].

Two volcanic events of late Barremian–earliest Aptian age are indirectly dated by radiolarians and may be correlated with the radiometrically dated lavas at Vedi [ca. 117 Ma; Rolland *et al.*, 2010]. The first comes from Karabagh, where middle upper Barremian to lowermost Aptian radiolarites overlying pillow lavas were dated by Asatryan *et al.* [2011], in a volcano-sedimentary sequence that is regarded as covering unconformably a complex paleo-seafloor of serpentinized peridotites. It is worth noting that in this case it is the discovery of the end member of the *Aurisaturnalis carinatus* evolutionary lineage that allowed a more accurate dating than the Zones (JAZ 18–22) of Baumgartner *et al.* [1995] to which the diverse and moderately well-preserved radiolarian assemblage was assigned. Indeed, the age range of species *Aurisaturnalis carinatus perforatus* Dumitrica and Dumitrica-Jud found in the Ar-10-16 sample coincides with the magnetozone M1 and is anterior of the OAE1a [Dumitrica and Dulitrcu-Jud, 1995]. The second volcanic event is dated in the Amasia ophiolite; here, Danelian *et al.* [2016] extracted upper Barremian–lowermost Aptian radiolarians from a volcanoclastic-chert sequence suggesting a subaerial volcanic activity more or less synchronous with submarine volcanism in the Sevan-Hakari ophiolite zone.

Finally, the youngest evidence for submarine volcanism comes also from the Amasia ophiolite, where Danelian *et al.* [2014] dated Cenomanian radiolarites overlying oceanic basaltic lavas. Here the assemblage is assigned to the *Dactyliosphaera silviae* Zone of O’Dogherty [1994].

4.2. Age constraints for the obduction of the ophiolites

The Vedi natural reserve and the Erakh anticline hold some key bio-chronostratigraphic elements to constrain the age of obduction of ophiolites in the Lesser Caucasus.

The first type of data comes from the uppermost carbonate sequences of the SAB. Hakobyan [1978] mentions the presence of upper Cenomanian layers with *Bicarinella bicarina* and *Pyrazopsis quinquecostatus* (both gastropods) and lower Turonian layers with *Radiolites peroni* (a rudist bivalve) and *Omphaloacteonella ovata* (a gastropod). In addition to these old data, which are difficult to be confirmed, Danelian *et al.* [2014] studied the 150 uppermost metres of the carbonate sequence of the SAB at Vedi and found benthic foraminifera suggesting a Cenomanian age, especially based on the presence of *Daxia cenomana*.

Regarding the age of the terrigenous sequences that are situated underneath the obducted ophiolites, Hakobyan [1978] considers the mélange unit at Erakh as early Coniacian in age; he mentions the presence of ammonites (*Barrosiceras onilahyense*) and several gastropod species found in siltstones and quartz-feldspar sandstones of the mélange unit.

Sosson *et al.* [2010] presented some calcareous nannofossil biostratigraphic results from the Vedi sector based on identifications by Carla Müller (see their Table 1). Here, we attempt to discuss their results based on the biostratigraphic scheme of Burnett [1998] and biostratigraphic information available in the Nannotax online database (https://www.mikrotax.org/Nannotax3/index.php?dir=ntax_mesozoic).

At the Vedi valley, the ARS16 sample was collected from the base of the flysch capping the SAB carbonate sequence. The species *Podorhabdus albanus* (now *Axopodorhabdus albanus*), mentioned in the assemblage, is known between the Albian and the Cenomanian (biozones BC25-UC5a); however, the contemporaneous presence of *Corollithion exiguum* (Turonian–Maastrichtian) in the assemblage points to a Cenomanian–Turonian age, therefore diverging from the Cenomanian age assignment provided in Sosson *et al.* [2010].

Similarly, the samples AR63 05, AR64-65 05 and AR67 05, coming from the upper part of the flysch sequence at Vedi are featured by the presence of *Reinhardtites anthophorus* (Turonian–UC15d to Campanian) and *Lucianorhabdus cayeuxii* (UC11c in latest Coniacian to Maastrichtian), pointing to a latest Coniacian to Campanian time interval.

The second type comes from the age of the lowermost sedimentary levels of the transgressive

sequence. Sosson *et al.* [2010] presented results of calcareous nannofossils from the marls overlying the red conglomerates and found a Coniacian–Santonian age. Samples AR72-73 05, coming from the upper part of the flysch sequence at Vedi, are featured by the presence of *R. anthophorus* (Turonian–UC15d to Campanian) and *L. cayeuxii* (UC11c in latest Coniacian to Maastrichtian), pointing to a latest Coniacian to Campanian time interval. Our results confirm and slightly improve this age assignment.

5. Conclusions

In the Tethyan realm preserved in the Lesser Caucasus radiolarian biochronology suggests episodic or continuous submarine volcanic activity for over 70–75 million years (Bajocian to Cenomanian) in relation to an intra-oceanic supra-subduction geodynamic regime. The significant volcanic activity recorded during the Bajocian in both the oceanic realm and the Somkheto-Karabagh volcanic arc may reflect a Bajocian pulse in geodynamic activity due to a plate re-organisation in the western Tethys in response to the opening of the Central Atlantic Ocean.

In addition, the new radiolarian ages from the Dali sector of the Sevan ophiolite establish that the onset of enriched subalkaline–alkaline volcanism dates back to the Berriasian, reflecting also a major change in the geodynamic regime of Tethys in the Lesser Caucasus. The geochemical affinity of lavas at Dali confirms that ophiolites were formed in the context of an intra-oceanic subduction. The shallow water carbonate olistoliths that slid into the deep water radiolarite basin from a nearby island arc may be also interpreted as the echo of such a tectonic event. E-MORB and alkaline volcanic activity lasted for at least 20 million years (Valanginian to early Aptian).

Radiolarian biochronology establishes also episodic or continuous subaerial volcanic input to the radiolarite basin for at least 45 millions years (Bathonian to Barremian), with the oldest tuffite deposits dated in the Sevan ophiolite [Asatryan *et al.*, 2010] and the youngest in the Amasia ophiolite [Danelian *et al.*, 2016]. This evidence is in good agreement with the presence of a volcanic island arc in the neighborhood of the oceanic basin in which the lava-radiolarite sequences were formed.

Our new results on calcareous nanofossils confirm and provide more accurate ages for the

post-obduction sedimentary cover; the marls overlying the red transgressive conglomerates may be safely assigned to the late Coniacian–Santonian interval, UC 11a–UC 12 zones, which is correlated with the 86–84 Ma interval [Gradstein *et al.*, 2020]. It is also clear that the carbonate sequence of the SAB accumulated at least up to the Cenomanian. Therefore, the ophiolite obduction took place some time during the Turonian–Coniacian interval. However, further work is needed in the future to better constrain the obduction by clarifying the age of the flysch deposited on the SAB and of the mélange sequence that accumulated in the trench formed in front of the advancing ophiolite thrust belt.

Conflicts of interest

Authors have no conflict of interest to declare.

Acknowledgments

Funding from the DARIUS program and the GDRI-CNRS « South Caucasus » is gratefully acknowledged. Fieldwork was also facilitated by the logistic support of the Institute of Geological Sciences and the Project 21T-1E119, supported by the Committee of Science of the Ministry of ESCS of RA. The Erasmus + ICM allowed TD to do additional fieldwork during one of his educational visits. The University of Lille is thanked for funding MT as an invited Professor to Lille. Sylvie Regnier and Valentin De Wulf are thanked for help with radiolarian chert sample processing, radiolarian picking, and SEM photography. Constructive remarks by A. H. F. Robertson (Edinburgh) and S. Goričan (Ljubljana) helped improve the initial manuscript.

References

- Al-Riyami, K., Danelian, T., and Robertson, A. H. F. (2002). Radiolarian biochronology of Mesozoic deep-water successions in NW Syria and Cyprus: implications for south-Tethyan evolution. *Terra Nova*, 14, 271–280.
- Asatryan, G. (2009). New data about the age of ophiolites in the Vedi zone on the basis of radiolarian assemblages. *Proc. Natl. Acad. Sci. Armenia*, 62, 16–28.

- Asatryan, G., Danelian, T., Seyler, M., Sahakyan, L., Galoyan, G., Seyler, M., Sosson, M., Avagyan, A., Hubert, B. L. M., and Ventalon, S. (2012). Latest Jurassic–early Cretaceous radiolarian assemblages constrain episodes of submarine volcanic activity in the Tethyan oceanic realm of the Sevan ophiolites (Armenia). *Bull. Soc. Géol. France*, 183, 319–330.
- Asatryan, G., Danelian, T., Sosson, M., Sahakyan, L., and Galoyan, G. (2011). Radiolarian evidence for early Cretaceous (late Barremian–early Aptian) submarine volcanic activity in the Tethyan oceanic realm preserved in Karabagh (Lesser Caucasus). *Ofioliti*, 36, 117–123.
- Asatryan, G., Danelian, T., Sosson, M., Sahakyan, L., Person, A., Avagyan, A., and Galoyan, G. (2010). Radiolarian ages of the sedimentary cover of Sevan ophiolite (Armenia, Lesser Caucasus). *Ofioliti*, 35, 91–101.
- Aslanyan, A. T. and Satian, M. A. (1977). On the geological features of Transcaucasian ophiolitic zones. *Izv. Akad. Nauk Armenian SSR, Nauki o Zemle* 4–5, 13–26. (in Russian).
- Avagyan, A., Shahidi, A., Sosson, M., Sahakyan, L., Galoyan, G., Muller, C., Vardanyan, S., Firouzi, K. B., Bosch, D., Danelian, T., Asatryan, G., Mkrtychyan, M., and Shokri, M. A. (2017). New data on the tectonic evolution of the Khoy region, NW Iran. In Sosson, M., Stephenson, R. A., and Adamia, S. A., editors, *Tectonic Evolution of the Eastern Black Sea and Caucasus*, volume 428 of *Geological Society, London, Special Publications*, pages 99–116. Geological Society of London.
- Barrier, E. and Vrielynck, B. (2008). *Palaeotectonic Map of the Middle East, Atlas of 14 Maps, Tectonosedimentary-Palinspastic Maps from Late Norian to Pliocene*. Commission for the Geologic Map of the World (CCMW, CCGM), Paris.
- Baumgartner, P. O. (2013). Mesozoic radiolarites – accumulation as a function of sea surface fertility on Tethyan margins and in ocean basins. *Sedimentology*, 60, 292–318.
- Baumgartner, P. O., Bartolini, A., Carter, E. S., Conti, M., Cortese, G., Danelian, T., De Wever, P., Dumitrica, P., Dumitrica-Jud, R., Gorican, S., Guex, J., Hull, D. M., Kito, N., Marcucci, M., Matsuoka, A., Murchey, B., O’Dogherty, L., Savary, J., Vishnevskaya, V., Widz, D., Yao, A., et al. (1995). Middle Jurassic to early Cretaceous radiolarian biochronology of tethys based on unitary associations. In Baumgartner, P. O. et al., editors, *Middle Jurassic to Lower Cretaceous Radiolaria of Tethys: Occurrences, Systematics, Biochronology*, volume 23 of *Mémoires de Géologie (Lausanne)*, pages 1013–1048. Université de Lausanne, Lausanne.
- Bazhenov, M., Burtman, V. S., and Levashova, N. M. (1996). Lower and middle Jurassic paleomagnetic results from the south Lesser Caucasus and the evolution of the Mesozoic Tethys ocean. *Earth Planet. Sci. Lett.*, 141, 79–89.
- Belov, A., Bragin, N., Vishnevskaya, V., Satian, M., and Sokolov, S. (1991). New data on the age of Vedi ophiolite (Armenia). *Proc. Acad. USSR*, 321, 784–787. (in Russian).
- Bogdanovski, O. G., Zakariadze, G. S., Karpenko, S. F., Zlobin, S. K., Pukhovskaya, V. M., and Amelin, Yu. V. (1992). Sm–Nd age of the gabbroids of a tholeiitic series of the ophiolites of the Sevan-Akera zone of the Lesser Caucasus. *Acad. Sci. Russia*, 327, 566–569. (in Russian).
- Burnett, J. A. (1998). Upper Cretaceous. In Bown, P. R., editor, *Calcareous Nannofossil Biostratigraphy*, British Micropalaeontological Society Publications Series, pages 132–199. Chapman and Kluwer Academic Publishers, London.
- Cordey, F. (2022). Looking for sources of an ophiolitic mélange: the case of Rhodes (Dodecanese, Greece) and its ties with eastern Mediterranean units. *Ofioliti*, 47, 51–64.
- Danelian, T., Asatryan, G., Galoyan, G., Sahakyan, L., and Stepanyan, J. (2016). Late Jurassic–early Cretaceous radiolarian age constraints from the sedimentary cover of the Amasia ophiolite (NW Armenia), at the junction between the Izmir–Ankara–Erzincan and Sevan–Hakari suture zones. *Int. J. Earth Sci.*, 105, 67–80.
- Danelian, T., Asatryan, G., Galoyan, G., Sosson, M., Sahakyan, L., Caridroit, M., and Avagyan, A. (2012). Geological history of ophiolites in the Lesser Caucasus and correlation with the Izmir–Ankara–Erzincan suture zone: insights from radiolarian biochronology. *Bull. Soc. Géol. France*, 183, 331–342.
- Danelian, T., Asatryan, G., Sahakyan, L., Avagyan, A., and Galoyan, G. (2017). Radiolarian evidence for the age of chert blocks from the upper Cretaceous ophiolitic mélange unit of the Erakh area. In *Geological Society, London, Special Publications*,

- volume 428, pages 62–72. Geological Society of London.
- Danelian, T., Asatryan, G., Sahakyan, L., Galoyan, G., Sosson, M., and Avagyan, A. (2010). New and revised radiolarian biochronology for the sedimentary cover of ophiolites in the Lesser Caucasus (Armenia). In *Geological Society, London, Special Publications*, volume 340, pages 383–391. Geological Society of London.
- Danelian, T., Asatryan, G., Sosson, M., Person, A., Sahakyan, L., and Galoyan, G. (2008b). Discovery of middle Jurassic (Bajocian) Radiolaria from the sedimentary cover of the Vedi ophiolite (Lesser Caucasus, Armenia). *C. R. Palevol.*, 7, 327–334.
- Danelian, T., De Wever, P., and Durand Delga, M. (2008a). Revised Radiolarian ages for the sedimentary cover of the Balagne ophiolite (Corsica, France). Implications for the palaeoenvironmental evolution of the Balano-Ligurian margin. *Bull. Soc. Géol. France*, 179, 169–177.
- Danelian, T., Galoyan, G., Rolland, Y., and Sosson, M. (2007). Palaeontological (radiolarian) late Jurassic age constraint for the Stepanavan ophiolite (Lesser Caucasus, Armenia). *Bull. Geol. Soc. Greece*, 40, 31–38.
- Danelian, T., Robertson, A. H. F., Collins, A., and Poisson, A. (2006). Biochronology of Jurassic and Early Cretaceous radiolarites from the Lycian Mélange (SW Turkey) and implications for the evolution of the Northern Neotethyan ocean. In Robertson, A. H. F. and Mountrakis, D., editors, *Tectonic Development of the Eastern Mediterranean Region*, volume 260 of *Geological Society, London, Special Publications*, pages 229–236. Geological Society of London.
- Danelian, T., Zambetakis-Lekkas, A., Galoyan, G., Sosson, M., Asatryan, G., Hubert, B., and Grigoryan, A. (2014). Reconstructing upper Cretaceous (Cenomanian) paleo environments in Armenia based on radiolarian and benthic foraminifera; implications for the geodynamic evolution of the Tethyan realm in the Lesser Caucasus. *Palaeogeogr. Palaeoclimatol. Palaeoecol.*, 413, 123–132.
- De Wever, P., Azéma, J., and Fourcade, E. (1994). Radiolarians and radiolarites: primary production, diagenesis and paleogeography. *Bull. Cent. Rech. Explor. Prod. Elf-Aquitaine*, 18, 315–379.
- De Wever, P. and Baudin, F. (1996). Palaeogeography of radiolarite and organic-rich deposits in Mesozoic Tethys. *Geol. Rundsch.*, 85, 310–326.
- Dercourt, J., Zonenshain, L. P., Ricou, L. E., Kazmin, V. G., Le Pichon, X., Knipper, A. L., Grandjacquet, C., Perchersky, D. H., Boulin, J., Sibuet, J. C., Savostin, L. A., Sorokhtin, O., Westphal, M., Bashrov, M. L., Lauer, J. P., and Biju-Duval, B. (1986). Geological evolution of the Tethys belt from the Atlantic to the Pamirs since the Lias. *Tectonophysics*, 123, 241–315.
- Dumitrica, P. and Dulitrcă-Jud, R. (1995). *Aurisaturnalis carinatus* (Foreman), an example of phyletic gradualism among saturnalid-type radiolarians. *Rev. Micropaleontol.*, 38, 195–216.
- Ferrière, J., Baumgartner, P. O., and Chanier, F. (2016). The Maliac Ocean: the origin of the Tethyan Hellenic ophiolites. *Int. J. Earth Sci.*, 105, 1941–1963.
- Ferrière, J., Chanier, F., Baumgartner, P. O., Dumitrica, P., Caridroit, M., Bout-Roumazeilles, V., Graveleau, F., Danelian, T., and Ventalon, S. (2015). The evolution of the Triassic-Jurassic Maliac oceanic lithosphere: insights from the supra-ophiolitic series of Othris (continental Greece). *Bull. Soc. Géol. France*, 186, 399–411.
- Galoyan, G. (2008). *Etude Pétrologiques, Géochimiques et Géochronologiques des Ophiolites du Petit Caucase (Arménie)*. PhD thesis, University of Nice-Sophia Antipolis. 287 p. (in French).
- Galoyan, G. (2020). Oceanic crust or Island arc: manifestations of magmatism in the ophiolite section of the Dali river valley on the shore of Lake Sevan. *Sci. J. NAS RA "Katchar"*, 1, 16–29. (in Armenian).
- Galoyan, G., Rolland, Y., Sosson, M., Corsini, M., Billo, S., Verati, C., and Melkonian, R. (2009). Geology, geochemistry and $^{40}\text{Ar}/^{39}\text{Ar}$ dating of sevan ophiolites (lesser Caucasus, Armenia): evidence for Jurassic back-arc opening and hot spot event between the south Armenian block and Eurasia. *J. Asian Earth Sci.*, 34, 135–153.
- Galoyan, G., Rolland, Y., Sosson, M., Corsini, M., and Melkonyan, R. (2007). Evidence for superposed MORB, oceanic plateau and volcanic arc series in the Lesser Caucasus (Stepanavan, Armenia). *C. R. Geosci.*, 339, 482–492.
- Galoyan, G. L., Melkonyan, R. L., Atayan, L. S., Chung, S.-L., Khorenyan, R. H., Lee, Y.-H., and Amiraghyan, S. V. (2018). On the petrology and geochemistry of Jurassic magmatics of the Somkhethi segment of Somkhetho–Karabagh tectonic zone

- (Northern Armenia). *Proc. NAS RA, Earth Sci.*, 71(1), 3–27.
- Goričan, Š., Pavšič, J., and Rožič, B. (2012). Bajocian to Tithonian age of radiolarian the Tolmin basin (NW Slovenia). *Bull. Soc. Géol. France*, 183, 369–382.
- Gradstein, F. M., Ogg, J. G., Schmitz, M. D., and Ogg, G. M. (2020). *Geologic Time Scale 2020*, volume 1. Elsevier, Amsterdam.
- Grigoryan, A. G. (2005). Upper Triassic Conodonts from the Sevan ophiolitic zone of Armenia. *Proc. NAS RA, Earth Sci.*, 58, 16–18. (in Russian).
- Hakobyan, V. T. (1978). *Biostratigraphy of the Upper Cretaceous Deposits of the Armenian SSR*. Publ. House Acad. Sci. Armenian SSR, Yerevan. (in Russian).
- Hässig, M., Duretz, T., Rolland, Y., and Sosson, M. (2016b). Obduction of old oceanic lithosphere due to reheating and plate reorganization: insights from numerical modelling and the NE Anatolia–Lesser Caucasus case example. *J. Geodyn.*, 96, 35–49.
- Hässig, M., Rolland, Y., Duretz, T., and Sosson, M. (2016a). Obduction triggered by regional heating during plate reorganization. *Terra Nova*, 28, 76–82.
- Hässig, M., Rolland, Y., Sahakyan, L., Sosson, M., Galoyan, G., Avagyan, A., Bosch, D., and Müller, C. (2015). Multi-stage metamorphism in the South Armenian block during the Late Jurassic to early Cretaceous: tectonics over south-dipping subduction of Northern branch of Neotethys. *J. Asian Earth Sci.*, 102, 4–23.
- Hässig, M., Rolland, Y., and Sosson, M. (2017). From seafloor spreading to obduction: Jurassic–Cretaceous evolution of the northern branch of the Neotethys in the Northeastern Anatolian and Lesser Caucasus regions. In *Geological Society, London, Special Publications*, volume 428. Geological Society of London.
- Hässig, M., Rolland, Y., Sosson, M., Galoyan, G., Müller, C., Avagyan, A., and Sahakyan, L. (2013b). New structural and petrological data on the Amasia ophiolites (NW Sevan-Akera suture zone, Lesser Caucasus): insights for a large-scale obduction in Armenia and NE Turkey. *Tectonophysics*, 588, 135–153.
- Hässig, M., Rolland, Y., Sosson, M., Galoyan, G., Sahakyan, L., Topuz, G., Çelik, Ö. F., Avagyan, A., and Müller, C. (2013a). Linking the NE Anatolian and Lesser Caucasus ophiolites: evidence for large scale obduction of oceanic crust and implications for the formation of the Lesser Caucasus-Pontides Arc. *Geodin. Acta*, 26, 311–330.
- Jones, G., De Wever, P., and Robertson, A. H. F. (1992). Significance of radiolarian age data to the Mesozoic tectonic and sedimentary evolution of the northern Pindos Mountains, Greece. *Geol. Mag.*, 129, 385–400.
- Jones, G. and Robertson, A. H. F. (1991). Tectono-stratigraphy and evolution of the Mesozoic Pindos Ophiolite and related units, northwestern Greece: an integrated supra-subduction zone spreading and subduction-accretion model. *J. Geol. Soc. Lond.*, 148, 267–288.
- Knipper, A. L., Bragin, N. Y., and Satian, M. A. (1997). Upper Triassic–lower Jurassic volcanogenic and sedimentary deposits of the Old Zod pass (Transcaucasia). *Stratigr. Geol. Correl.*, 5, 58–65. (in Russian).
- Knipper, A. L. and Khain, E. V. (1980). The structural position of ophiolites of the Caucasus. *Ofoliti*, 2, 29–314.
- Li, R. Q. and Sashida, K. (2013). Morphological variability and phylogeny of the Upper Tithonian–Berriasian Vallupinae (Radiolaria) from the Mariana Trench. *J. Paleontol.*, 87, 1186–1194.
- Maffione, M. and van Hinsbergen, D. J. J. (2018). Reconstructing plate boundaries in the Jurassic Neotethys from the east and west Vardar Ophiolites (Greece and Serbia). *Tectonics*, 37, 858–887.
- Meijers, M. J. M., Smith, B., Kirscher, U., Mensink, M., Sosson, M., Rolland, Y., Grigoryan, A., Sahakyan, L., Avagyan, A., Langereis, C., and Müller, C. (2015). A paleolatitude reconstruction of the south Armenian block (Lesser Caucasus) for the late Cretaceous: constraints on the Tethyan realm. *Tectonophysics*, 644–645, 197–219.
- O’Dogherty, L. (1994). *Biochronology and Paleontology of Mid-Cretaceous Radiolarians from Northern Apennines (Italy) and Betic Cordillera (Spain)*, volume 21 of *Mémoires de Géologie (Lausanne)*. Université de Lausanne, Lausanne.
- Okay, A. I., Altiner, D., Danelian, T., Topuz, G., Özcan, E., and Kylander-Clark, A. R. C. (2022). Subduction-accretion complex with boninitic ophiolite slices and Triassic limestone seamounts: Ankara Mélange, central Anatolia. *Geol. Mag.*, 159, 1699–1726.

- Robertson, A., Parlak, O., Ustaömer, T., Taslý, K., and Dumitrica, P. (2021). Late Palaeozoic-Neogene sedimentary and tectonic development of the Tauride continent and adjacent Tethyan ocean basins in eastern Turkey: new data and integrated interpretation. *J. Asian Earth Sci.*, 220, article no. 104859.
- Robertson, A. H. F., Parlak, O., and Dumitrica, P. (2022). Role of Late Cretaceous volcanosedimentary melanges, specifically the Aladağ melange, E Turkey, in the rift-drift-subduction-accretion-emplacement history of the Tethyan Inner Tauride ocean. *Int. Geol. Rev.*, 64, 1139–1190.
- Robertson, A. H. F., Parlak, O., Ustaömer, T., Taslý, K., Ýnan, N., Dumitrica, P., and Karaođlan, F. (2013). Subduction, ophiolite genesis and collision history of Tethys adjacent to the Eurasian continental margin: new evidence from the Eastern Pontides, Turkey. *Geodin. Acta*, 26, 230–293.
- Rolland, Y., Billo, S., Corsini, M., Sosson, M., and Galoyan, G. (2009a). Blueschists of the Amassia-Stepanavan suture zone (Armenia): linking Tethys subduction history from E-Turkey to W-Iran. *Int. J. Earth Sci.*, 98, 533–550.
- Rolland, Y., Galoyan, G., Bosch, D., Sosson, M., Corsini, M., Fornari, M., and Verati, C. (2009b). Jurassic back-arc and Cretaceous hot-spot series in the Armenian ophiolites — implications for the obduction process. *Lithos*, 112, 163–187.
- Rolland, Y., Galoyan, G., Sosson, M., Melkonian, R., and Avagyan, A. (2010). The Armenian ophiolite: insights for Jurassic back-arc formation, lower Cretaceous hot spot magmatism and upper Cretaceous obduction over the South Armenian block. In *Geological Society, London, Special Publications*, volume 340, pages 353–382. Geological Society of London.
- Rolland, Y., Hässig, M., Bosch, D., Bruguier, O., Melis, R., Galoyan, G., Topuz, G., Sahakyan, L., Avagyan, A., and Sosson, M. (2020). The East Anatolia–Lesser Caucasus ophiolite: an exceptional case of large-scale obduction, synthesis of data and numerical modelling. *Geosci. Front.*, 11, 83–108.
- Seyler, M., Galoyan, G., Witt, C., and Danelian, T. (2023). Tholeiitic to calc-alkaline and alkaline volcanisms in an extensional arc setting of a Tethyan ophiolite. Insights from small-scale compositional and temporal transitions from the Dali sector (Armenia). *J. Asian Earth Sci.*, 241, article no. 105478.
- Smith, A. G. and Spray, J. G. (1984). A half-ridge transform model for the Hellenic-Dinaric ophiolites. In Dixon, J. E. and Robertson, A. H. F., editors, *The Geological Evolution of the Eastern Mediterranean*, volume 17 of *Geological Society, London, Special Publications*, pages 629–644. Geological Society of London.
- Sokolov, S. D. (1977). *The Olistostroms and Ophiolitic Nappes of the Lesser Caucasus*. Izdatelstvo Nauka, Moscow. (in Russian).
- Sosson, M., Rolland, Y., Danelian, T., Muller, C., Melkonian, R., Adamia, S., Babazadeh, V., Kangarli, T., Avagyan, A., Galoyan, G., and Mosar, J. (2010). Subductions, obduction and collision in the Lesser Caucasus (Armenia, Azerbaijan, Georgia), new insights. In *Geological Society, London, Special Publications*, volume 340, pages 329–352. Geological Society of London.
- Sosson, M., Stephenson, R., Sheremet, Y., Rolland, Y., Adamia, S., Melkonian, R., Kangarli, T., Yegorova, T., Avagyan, A., Galoyan, G., Danelian, T., Hässig, M., Meijers, M., Müller, C., Sahakyan, L., Sadradze, N., Alania, V., Erukidze, O., and Mosar, J. (2016). The eastern Black Sea-Caucasus region during the Cretaceous: new evidence to constrain its tectonic evolution. *C. R. Geosci.*, 348, 23–32.
- Vishnevskaya, V. (1995). Jurassic and Cretaceous Radiolarians from the Lesser Caucasus (Zod Pass, Mount Karawul and Site 22 in the Koshuni River Basin). In Baumgartner, P. O. et al., editors, *Middle Jurassic to Lower Cretaceous Radiolaria of Tethys: Occurrences, Systematics, Biochronology*, volume 23 of *Mémoires de Géologie (Lausanne)*, pages 701–708. Université de Lausanne, Lausanne.
- Vrielynck, B., Bonneau, M., Danelian, T., Cadet, J. P., and Poisson, A. (2003). New insights on the Antalya Nappes in the apex of the Isparta angle: the Isparta Cay unit revisited. *Geol. J.*, 38, 283–293.
- Zakariadze, G. S., Knipper, A. L., Sobolev, A. V., Tsamerian, O. P., Dimitriev, L. V., Vishnevskaya, V. S., and Kolesov, G. M. (1983). The ophiolite volcanic series of the Lesser Caucasus. *Ofoliti*, 8, 439–466.



Research article

Tribute to Jean Dercourt

The Middle to Late Triassic of Central Saudi Arabia with emphasis on the Jilh Formation. Part I: lithostratigraphy, facies and paleoenvironments, palaeontology and biostratigraphic age calibration from outcrop studies

Yves-Michel Le Nindre ^{*,a}, Denis Vaslet ^b, Bruno Vrielynck ^c, Leopold Krystyn ^d, Jacques Manivit ^{†,e}, Abdullah Memesh ^f and Roger Brett Davies ^g

^a Geo-consultant (BRGM retired), 58 Rue Gustave Flaubert 45100, Orléans, France

^b Geo-consultant (BRGM retired), 275 Route Royale, 33240 La Lande de Pomerol, France

^c Institut des Sciences de la Terre de Paris (UMR 7193), Université Pierre et Marie Curie (UPMC) (retired), France

^d Department of Palaeontology (Geozentrum), University of Vienna, Althanstrasse 14, Josef-Holaubek-Platz 2 (UZA II), 1090 Vienna (retired), Austria

^e (BRGM, retired), Orléans, France

^f Saudi Geological Survey, 54141, Ahmed bin Mohammed Al Ashab St., Jeddah 21514, Saudi Arabia

^g Davies Geoconsulting (retired), Wintergreen House, Queen's Road, Harrogate, North Yorkshire, HG2 0HB, UK

E-mails: yc.lenindre@wanadoo.fr (Y.-M. Le Nindre), d-d.vaslet@wanadoo.fr (D. Vaslet), bruno.vrielynck@orange.fr, bjm.vrielynck@orange.fr (B. Vrielynck), leopold.krystyn@univie.ac.at (L. Krystyn), Memesh.AM@sgs.gov.sa (A. Memesh), davies.geoconsulting@btinternet.com (R. B. Davies)

Abstract. The Middle to Late Triassic (Anisian–Carnian) Jilh Formation crops out along an approximately 880 km belt in Central Saudi Arabia to the east of the Proterozoic Arabian Shield. This outcrop belt has been mapped, described and analysed in detail, first by geologists of the BRGM (1990–1991) and more recently by the present authors. The current synthesis, which includes the results of previous comprehensive analyses of the overlying Norian to Early Jurassic Minjur Sandstone/Formation in outcrop and subsurface locations, is being published in two parts. The first part (Part I) consolidates previous sedimentological and biostratigraphic analyses, and introduces new stratigraphic results provided by conodonts and ammonoid studies. Part II “Sequence stratigraphy, depositional and structural evolution, and regional correlations” exploits the results of Part I, providing a dynamic reconstruction and a renewed vision of the Middle to Late Triassic at the regional scale.

* Corresponding author.

† Deceased.

The Jilh Formation at outcrop consists of a multilayer system of thinly bedded, mixed siliciclastics with subordinate carbonates and evaporites, representing non-marine to offshore settings. Individual beds are difficult to correlate at regional scale. A pre-existing outcrop-based, three-fold, sub-division of the Jilh Formation into lithological units is shown to cross timelines and cannot be used as the basis for regional correlation. Instead, new identifications of Middle and Late Triassic conodonts in the formation and at the base of the overlying Minjur Sandstone/Formation, allied to re-interpretation of previously described ammonoids, provide new paleogeographic and chronostratigraphic data, which improve our understanding of transgressive–regressive (T–R) sequences at the outcrop and platform scales and demonstrate that the lithostratigraphic units of the Jilh Formation were inconsistently recognized at outcrop north of 25°30′N due to erosion by a fourth unit of early Alaunian (Middle Norian) age; this raises the issue of the Jilh–Minjur boundary addressed in Part II. Marine flooding events are indicated by tidal flat sediments during the Anisian, and thin carbonate beds during the Ladinian, late Julian (Early Carnian), associated with Fe-oolite beds, and Tuvalian (Late Carnian). We recognise a regional Carnian–Norian hiatus and an early Middle Norian transgression, as well as marine and continental erosional discontinuities affecting the stacking pattern of the T–R wedges. These observations and analyses provide a sound foundation for sequence stratigraphic analysis and regional correlation, which are the subjects of Part II.

Keywords. Saudi Arabia, Triassic, Jilh Formation, Paleoenvironments, Biostratigraphy, Conodonts, Ammonoids.

Manuscript received 23 March 2023, revised 29 April 2023, accepted 2 May 2023.

1. Introduction

Studies of the Triassic stratigraphy across the Arabian Plate have a long history. Early work was by staff belonging to international oil companies but remained proprietary. The first formal, widely available definitions of Triassic lithostratigraphy were published between the late 1950s and the 1970s in the series *Lexique Stratigraphique International*, including volumes on Saudi Arabia, Qatar, Iraq, Iran, Lebanon, Syria and Jordan, Yemen and adjacent areas of southern Oman. The United States Geological Survey published a series of Professional Papers on the Geology of the Arabian Peninsula, with volumes on Saudi Arabia, south-western Iraq and Yemen, also in the 1960s. Together these volumes from the *Lexique Stratigraphique International* and the USGS Professional Papers provide the original definitions of the Jilh and Minjur Formations and their equivalents.

Most of the Arabian Plate suffers from poor biostratigraphic age control during the Triassic. It is only in a few sections near the margins of the Arabian Plate or outcrops such as those described in Part I, that have yielded good faunal or floral evidence. This emphasises the importance of new biostratigraphic data from the Central Saudi Arabian outcrops, for better understanding of the regional picture. Work by the BRGM [Le Nindre *et al.*, 1990a] had identified thin marine units within dominantly siliciclastic, continental to paralic Sudair, Jilh and Minjur formations. These marine incursions are ob-

vious candidates for Maximum Flooding Surfaces (MFS) addressed in Part II. Extensive documentation of their sedimentology, fauna, flora and stratigraphic architecture is provided in Part I.

The Triassic Jilh Formation and the Minjur Sandstone of Saudi Arabia crop out in a 50 km-wide belt between latitudes 28°N and 21°N, along the eastern margin of the Arabian Shield (Figure 1). Together with the Permian–Early Triassic Khuff Formation and the Early Triassic Sudair Shale, these formations form an unconformable cover over the Pre-Permian rocks, and are in turn unconformably overlain by Jurassic and younger formations [Figure 2, Vaslet *et al.*, 1983]. During the USGS-supported mapping of Saudi Arabia in the 1960s [Powers *et al.*, 1966, Powers, 1968], initial analysis of the lithology of the Jilh and Minjur formations led to their interpretation as alternating marine or and paralic-continental units. Powers [1968] suggested a “Late Permian (?Kungurian–Kazanian)” age for the Khuff Formation, a “Permian–Triassic (Tatarian–Buntsandstein)” age for the Sudair Shale, a “Buntsandstein–Muschelkalk” age for the Jilh Formation, and a “Keuper to Liassic” age for the Minjur Sandstone. The available data also suggested that the intra-formational boundaries were isochronous [Powers, 1968]. Subsequently, Le Nindre *et al.* [1987, 1990a] gave a revised description of the lithostratigraphy, biostratigraphy and sedimentology of the Permian–Triassic at outcrop, based on the results of the cover rock geological mapping program at 1:250,000 scale by the Directorate Min-

eral Resources of Saudi Arabia (DMMR) and France's Geological Survey (BRGM). More recent publications give a detailed description and interpretation of the underlying Khuff Formation [e.g., Vachard *et al.*, 2005, Vaslet *et al.*, 2005] and overlying Minjur Sandstone [Issautier *et al.*, 2012a,b, 2019]. The objective of Part I is not to re-analyse and re-interpret the lithostratigraphy and the sedimentology already comprehensively documented by Le Nindre *et al.* [1987]. This information has also been published in the Explanatory Notes to the Geological Map Quadrangles (Figure 1), and in Le Nindre *et al.* [1990a,b], from which the results are briefly synthesized and summarised herein. Part I is specifically oriented to identification and biostratigraphic age calibration of the main T–R events in view of establishing an MFS-based sequence stratigraphy, reconstructing the depositional and structural evolution, and making regional correlations in Part II.

The present paper describes the sedimentary evolution within the Jilh Formation, using precise biostratigraphic calibration, and the internal organization of the T–R depositional sequences. The biostratigraphic analysis, essentially based on conodonts collected from outcrops of the Jilh Formation and from the base of the Minjur Sandstone, and on ammonoids, makes it possible to define the age of the units at different latitudes, to establish the chronostratigraphic boundaries, and to demonstrate that successive Middle to Late Triassic transgressions had a strong northerly component. Part of the biostratigraphic data comes from samples collected in the 1980s and was synthesized in Le Nindre *et al.* [1990a]. New key results come from samples collected in 1991–1992 within the Qibah Quadrangle and were not studied previously. Conodont taxonomy has been updated. In addition, a revision of ammonoids from previous identifications, and a new specimen collected in 2016 has reinforced the conodont-based calibration. Inclusion of new data on Minjur Sandstone stratigraphy [Issautier *et al.*, 2019] also provides a correlation tool within the Jilh–Minjur systems, in the subsurface and at the platform scale, regardless of lithologic variations.

Results, discussions, and conclusions are presented in two parts: Part I, the present paper, is dedicated to lithostratigraphy, paleoenvironments, ages, and subsequent stratigraphic geometry; a subsequent paper, Part II, will discuss sequence stratigraphy,

structural evolution, subsurface correlations, and Triassic paleogeography.

2. Previous definitions

2.1. *Jilh Formation*

Initially defined by Bramkamp [1945, *in* Powers *et al.*, 1966] as the “Jilh limestone member”, this unit was raised to the rank of formation (the Jilh Formation) by Steineke and Bramkamp [1952]. The type section was taken at Jilh al 'Ishar from 24°03'48"N, 45°46'00"E to 24°11'06"N, 45°51'30"E. In the type region (Wadi Ar Rayn Quadrangle, Figure 1), the formation, with a total thickness of 326 m, is generally consists of cross-bedded sandstone with clayey interbeds, incorporating several limestone and dolomite bands. However, the formation displays marked lateral variations across its outcrop area, essentially comprising continental sandstone in the southeast, and predominantly marine carbonate sediments in the northwest.

In the type region, Bramkamp and Steineke [*in* Arkell, 1952] distinguished two units based on lithological analysis of the formation. From base to top, the “Lower Jilh” (142 m) comprises 81 m of quartzose sandstone alternating with clay, 25 m of gypsumiferous clay, and 36 m of limestone containing interbeds of marl and fine-grained sandstone. From base to top, the “Upper Jilh” (184 m) displays 118 m of quartzose sandstone, the lower part of which contains interbeds of fine-grained sandstone with two thin beds of limestone at the midpoint, overlain by 66 m of sandstone and clay incorporating several beds of sandy limestone, in turn overlain by a bed of hard oolitic sandstone.

A fauna comprising the bivalve *Myophoria* sp. and fragments of ammonoid nuclei is recorded 45–55 m from the top of the formation [Powers, 1968]. According to Arkell [1952], these cephalopods typify the Mid-Triassic, although Siberling [personal communication to Powers, 1968] held the view that most of the specimens can be assigned to a Late Triassic genus. Based on data from the study of spores and pollen grains in formations intersected by drill holes, Powers [1968] nonetheless assigned an Early and Middle-Triassic age (Buntsandstein–Muschelkalk) to the Jilh Formation.

Sedimentologic data were subsequently provided by Sharief [1977, 1981], who described nine sedimentary facies in the Jilh Formation, including fluvialite,

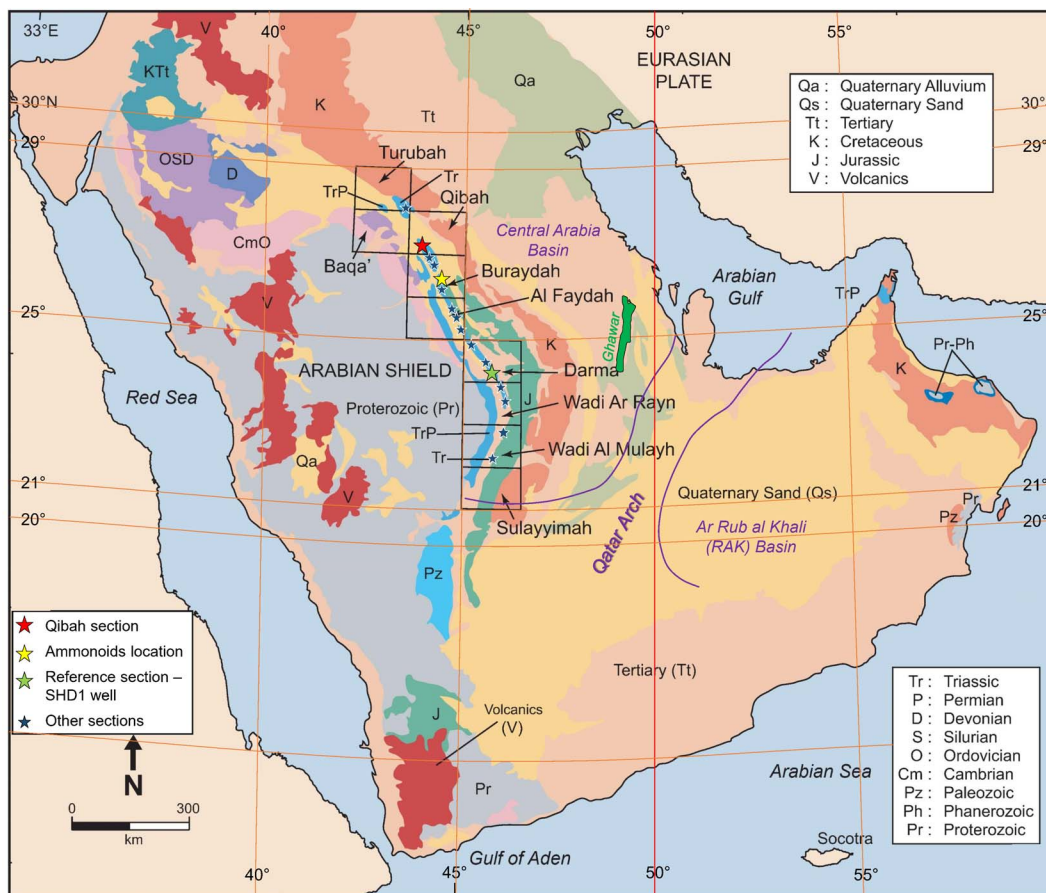


Figure 1. Simplified geological map of the Arabian Peninsula showing the quadrangles in which the Jilh Formation crops out. These quadrangles in Central Saudi Arabia were mapped by the DMMR (now Saudi Geological Survey) and France's BRGM [Hawasina nappes in Oman not shown, Qatar Arch from Stewart *et al.*, 2016].

supratidal, coastal, and shallow-marine sediments deposited in cyclic units (“cyclothems”); the overall succession comprises interfingering regressive and transgressive intervals [Sharief, 1981]. Sharief [1977] also mentioned the development of carbonate facies north of 25°30'N and of abundant evaporitic facies in the upper part of the formation around 26°30'N. Vaslet *et al.* [1983], Manivit *et al.* [1985a] and Vaslet *et al.* [1985a] assigned the Jilh Formation to the Anisian–Norian, ages principally based on conodonts and ammonoid faunas; mapping and sedimentologic analyses by these authors led to the definition of three units (lower, J1; middle, J2; and upper, J3), each corresponding to a sedimentary cycle. Manivit *et al.* [1985a] described a reference section at Khashm Dolqan near the original

type section (24°13'N, 45°37'E to 24°12'N, 46°05'E). Northward and southward lateral variations along the outcrop were described by Le Nindre *et al.* [1990a].

2.2. Minjur Sandstone

Originally named the Upper Es Sirr Sandstone by Bramkamp [1950, *in* Powers *et al.*, 1966], and subsequently recorded and defined as the Minjur Sandstone by Steineke and Bramkamp [1952] and Steinecke [*in* Arkell, 1952], this formation was described by Powers [1968] as essentially composed of continental sandstones incorporating conglomerate lenses and clay intercalations.

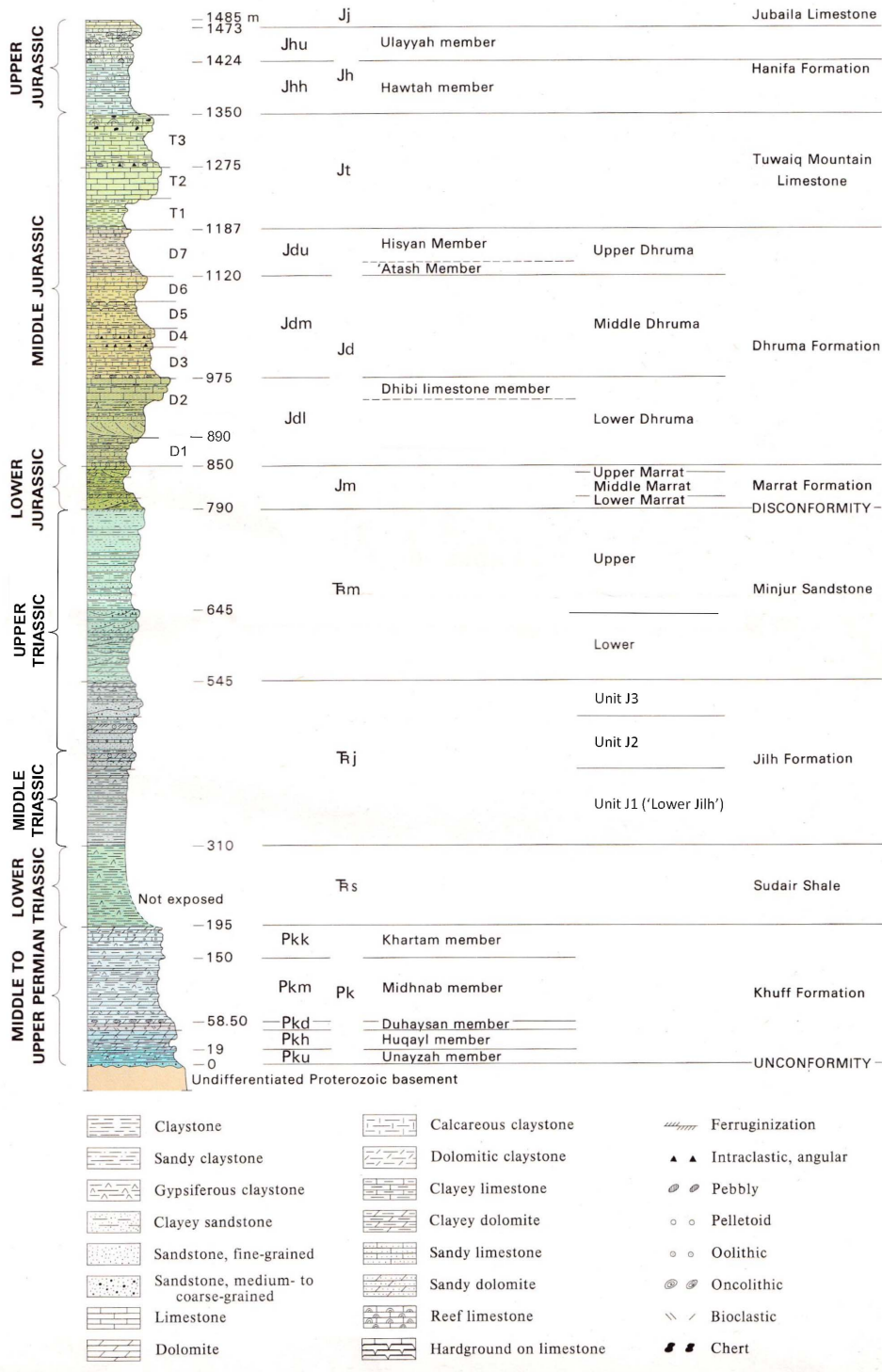


Figure 2. Lithostratigraphic column of the Ar Rayn quadrangle (23°–24°N, 45–46°30'E), slightly updated from Vaslet *et al.* [1983].

The formation is 315 m thick in the type locality, “Khashm al Mānjur” (=Khashm al Khalta, 23°35′24″N, 46°10′36″E), but varies in thickness from 185 to 362 m. It contains plant debris and silicified wood remains. Powers [1968] assigned a Late Triassic age (Carnian, Middle Keuper) to the lower part of the formation from correlation with dated subsurface sequences, based on palynologic data. The upper part was said to contain unspecified Lower Jurassic microflora. Vaslet *et al.* [1985a] assumed a ?Norian to Rhaetian age based on previous work (Late Triassic) and on interpreted ages of the underlying Jilh Formation (Anisian–Norian). As mentioned above, this formation was further described in outcrop by Le Nindre *et al.* [1987, 1990a] and Issautier *et al.* [2012a,b]. Le Nindre *et al.* [1990a] confirmed a Norian age based on the conodont *Epigondolella abneptis* (Huckriede), recovered from carbonates near the base of the formation (26°50′N and northward).

In 2019, Issautier *et al.* [2019] proposed an updated stratigraphy for the Minjur Sandstone in outcrop and shallow subsurface. In the subsurface, palynology has established a fourfold biostratigraphic subdivision (partly illustrated here in Figure 12) extending from latest Carnian–early Norian to latest Rhaetian–Pliensbachian (Triassic–Early Jurassic). Subsequent to a period of subaerial exposure in the west, transgression in the early middle Norian was marked by marginal marine environments, with peak marine influence in the Middle Norian. Its significance in terms of MFS is discussed in Part II. This was followed by the development of a gently inclined alluvial or coastal plain. Palynology has also demonstrated an intra-Rhaetian hiatus which separates the Lower Minjur Formation from the Upper Minjur Formation. A variety of depositional environments are represented, including alluvial fans proximally, grading to fluvial, then to coastal plain and shallow marine environments distally. Regional evidence (chronostratigraphic chart in Part II) indicates that this hiatus appears comparable in importance to the Toarcian to Aalenian unconformity separating Sharland *et al.*'s [2001] Tectonic Mega-Sequences (TMS) AP6 and AP7.

An important aspect of the present study is the definition of the base of the Minjur Sandstone in outcrop, and the nature of the contact with the underlying Jilh Formation. The overall definition of the base of the Minjur Sandstone adopted in the different

measured sections from the BRGM/DMMR mapping program is the following: generally, the base of the Minjur Sandstone in most of the sections was taken from beds of black, ferruginous, microconglomeratic sandstone with plant remains, debris of silicified wood, and sometimes the accumulation of silicified tree trunks. Lag deposits with quartz grains up to 2 cm in diameter and trough cross-stratification may also characterize this horizon. Thus, the basal Minjur beds contrast sharply with the underlying marginal marine deposits of the Jilh Formation although mixed facies of dolomite pebbles, reworked in thinly bedded sandstone, often marks the transition in the uppermost beds of the Jilh Formation.

3. Lithostratigraphy of the Jilh Formation

In the 1980s, the mapping program at 1:250,000 by the DMMR and BRGM surveyed the outcrops of the Jilh Formation over 880 km from latitude 21°07′N at Khashm Mishlah up to 28°10′N near Shamat al Akbad in nine quadrangles (Figure 1) from south to north: Sulayyimah [Vaslet *et al.*, 1985b], Al Mula'yh [Manivit *et al.*, 1985b], Wadi Ar Rayn [Vaslet *et al.*, 1983], Ad Darma' [Manivit *et al.*, 1985a], Al Faydah [Vaslet *et al.*, 1985a], Buraydah [Manivit *et al.*, 1986], Qibah (Robelin *et al.*, surveyed in 1992–1993 and published in 1994), Baqa' [Vaslet *et al.*, 1987], and Turubah [Lebret *et al.*, 1999]. Lithostratigraphy, biostratigraphy and sedimentology of the formation were first published in the explanatory notes of the maps and then synthesized by Le Nindre *et al.* [1987, 1990a,b] from field and laboratory studies.

The three lithostratigraphic units (J1, J2, J3, or lower, middle, upper unit, respectively) originate from a sedimentological and sequential approach to overcome lithological variability, although fine-grained sediments dominate in J1, sandstone in J2, and carbonate in J3 [Le Nindre *et al.*, 1987, 1990a, p. 198; Vaslet *et al.*, 1983]. The three units are particularly well demonstrated in the vicinity of the of the Khashm Dolqan reference section (24°13′21″N, 45°37′34″E, Figure 3) and by the Khabra Halwah section—23°59′N—(see Section 4.2.4, Figure 8).

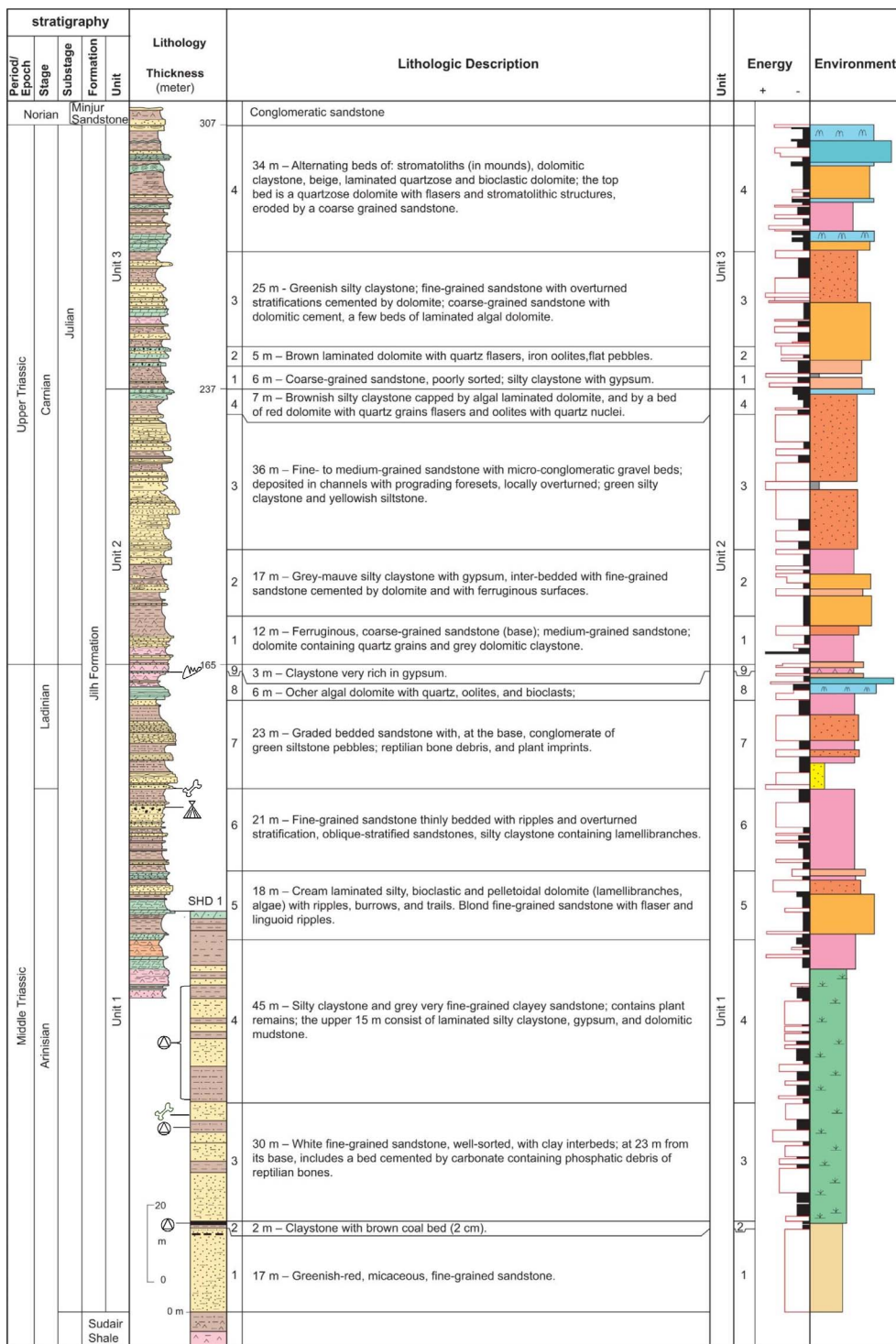


Figure 3. Continued on next page.

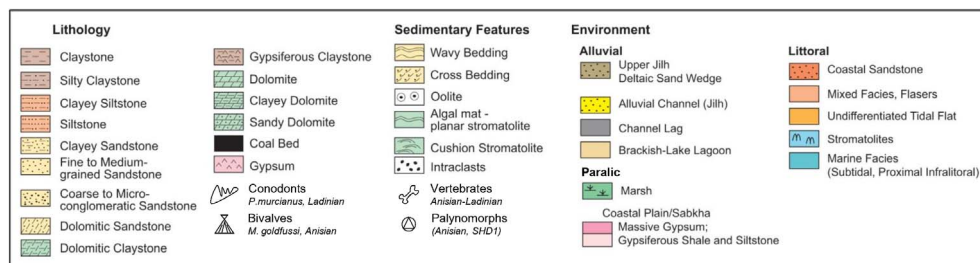


Figure 3 (cont.). Reference section of the Jilh Formation at Khashm Dolqan, modified from 1:500 description of December 1981 by Y. M. Le Nindre, C. Cavelier, D. Vaslet, J. M. Brosse and J. Manivit.

Typically, the Jilh Formation between latitudes 23°N and 25°N consists of three transgressive sequences of clay-siltstone, sandstone, and carbonate, in which the sandstone occupies a variable position depending on the type of sedimentary bodies it represents, and where the carbonates, marking the most offshore marine settings, cap each sequence. The latter thus are essential markers for correlations. A cuesta morphology is commonly associated with these cycles, facilitating lateral mapping between the sections.

- On the geological maps, between 1979 (first map surveyed) and 1999 (last map published), this three-fold nomenclature was variably applied depending principally on outcrop conditions. North of Lat. 25°30'N, three sequences were also recognized, but in fact four are stacked, the fourth (i.e., youngest) eroding the third. This stratigraphic geometry was interpreted as a transgressive erosional wedge by Le Nindre *et al.* [1987, 1990a]. Already, Vaslet *et al.* [1985a] within the Al Faydah quadrangle, and Manivit *et al.* [1986] within the Buraydah quadrangle (i.e., north of 25°N) had mentioned Late Carnian and Norian in respect of Unit J3 and Manivit [1987 in Le Nindre *et al.*, 1987, Livre 2] had demonstrated an apparent south–north diachroneity of the lithostratigraphy, but, looking more carefully, uncertainties over ages and geometries remained. From these uncertainties was born the need for a revised stratigraphy using new biostratigraphic results coupled with modern Sequence Stratigraphy principles.

Historically, and where the three-fold subdivision was not fully applicable, “Lower Unit” and “Upper

Unit” were used. The “Lower Unit”, represented on the maps with a clay or sandstone pattern, simply corresponds to the J1 Unit, dominantly clastic and unconsolidated, whose basal contact with the underlying Sudair Shale is commonly obscured beneath recent sediments (Figure 2).

3.1. Reference section

The reference section at Khashm Dolqan, (24°13'21"N, 45°37'34"E to 24°12'N, 46°05'E, Figure 1) near the original type section, has a total thickness of 307 m. The outcropping portion is supplemented by 79 m of section from the cored SHD-1 well (23°13'40"N, 45°37'30"E), drilled from the first dolomitic cuesta of the formation, representing the lower portion hidden under the Nafud Desert sands (Figures 3 and 4).

3.1.1. Lower boundary

In the SHD-1 well, the transition from the Sudair Shale below, to the Jilh Formation above, is gradual and marked by an upward increase of sandstone content, from red-brick claystone with gypsum, characteristic of the Sudair Shale, to greenish-red clayey sandstone and to white fine-grained micaceous sandstone. The base of the Jilh Formation is placed at the base of the first horizon of greenish-red, micaceous, fine-grained sandstone.

3.1.2. Upper boundary

The contact between the Jilh Formation and overlying Minjur Sandstone is placed on an erosional surface between a dolomitic mudstone with quartz-sand flasers, representing the last bed of the Jilh Formation, and a ferruginous sandstone with reworked clasts of dolomite, the first bed of the Minjur Sandstone.

3.1.3. *Lithostratigraphic units and paleoenvironments*

The formation in the reference section is subdivided into three units, named J1 (165 m), J2 (72 m) and J3 (70 m), from bottom to top. The section is described in detail in Figure 3. The column “Environments” depicts a seaward evolution of the sedimentation with time and two major flooding events, one at the top of Unit J1, and one at the top of Unit J3, in accord with our sequential units definitions. Ladinian and Julian (Lower Carnian) ages respectively are based on fossils content of this and of adjacent sections (see Section 5, and Supplementary Section A, Plate A.3).

3.2. *Lithostratigraphy northward and southward from the reference section*

3.2.1. *Measured sections*

The lithostratigraphic sections measured in the Jilh–Minjur systems from Lat. 22°11′N to Lat. 28°05′N, are shown at a reduced scale in Supplementary Section A with 5 plates and tables which provide locations of the key fossils and their age interpretation. They mention the original lithologic subdivisions of Le Nindre *et al.* [1990a], units and subunits.

Three sections measured after 1990, of which the lithostratigraphy was tentatively based on the adjacent Buraydah quadrangle, complement the description:

- The Jabal Mudarraj–Didah reference section for the Qibah Quadrangle (27°10′N) measured by BRGM in December 1991 (Supplementary Section B, Plate B.1).
- Two sections within the Buraydah Quadrangle: Ar Rubay’iyah (26°23′N)—Supplementary Section B, Plate B.2—and Ibn al Fuhayd (26°42′N—not published herein but used in Figure 4) measured in March 2016 by the SGS in a dedicated survey.

All these sections are represented on the north-south (N–S) transect of the facies and paleoenvironments (Figure 4).

3.2.2. *Mapped units*

The variations northwards and southwards of the reference section were described section by section by Vaslet in Le Nindre *et al.* [1987, 1990a] on the basis of the three units, J1, J2 and J3, despite discontinuous outcrop in places. Note that the Units J1 to J3 of the reference section were originally defined southward within the Wadi A Rayn quadrangle [Vaslet *et al.*, 1983] at Khabrah Halwah (23°58′N, 44°49′E) as three informal lithologic assemblages named lower, middle and upper Jilh (see the Section 4.2.4 dedicated to this particular case with Figure 8). These three units and their subunits, are still in use in the individual descriptions of the lithostratigraphic sections, which are included herein (Supplementary Section A), especially for purpose of sample and key fossil’s location with the related biostratigraphic results.

Laterally, in the field, Units J1 to J3 were correlated on facies and on lithomorphology by using the presence of cuestas with soft material at the foot and hard benches of dolomite or sandstone, on their top (Figure 5). This method is reliable at quadrangle scale provided a laterally constant lithology is present. However, the new biostratigraphic studies have assigned ages to these lithological units which have proved facies diachroneity [Bruno Vrielynck, Edward T. Tozer, and Jacques Manivit in Le Nindre *et al.*, 1987, 1990a] and the presence of disconformities. Complex and changing lithologies make the use of this lithomorphology uncertain over long distances.

Therefore, at the outcrop scale, the three lithostratigraphic units are not differentiated and the formation is indistinctly mapped as TrJ (Triassic, Jilh) or TrJl (“lower Jilh”) and TrJu (“upper Jilh”) e.g., Vaslet *et al.* [1983]. Additional patterns are used where notable sandstone bodies or shales occur.

The Figure 4, shows the facies distribution along a N–S transect. Updated from previous work, it now indicates the location of the three new sections and the age calibrations obtained by biostratigraphy. This new approach, based on analysis of T–R depositional units and on biostratigraphy will be used for building a new Sequence and chronostratigraphy in the subsequent Part II paper.

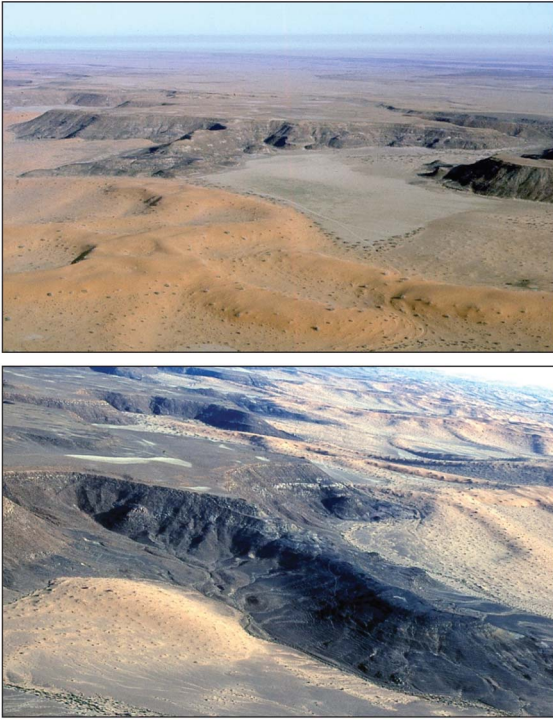


Figure 5. Aerial views of the first cuestas of the Jilh Formation, near the location of the lithostratigraphic section “Safra ar Ruwaykibah”, Al Faydah Quadrangle. (Photos by Jacques Manivit.)

3.3. Upper contact with the Minjur Sandstone

The upper contact with the Minjur Sandstone was recognized in most of the sections. It is defined in outcrop by lag deposits resting on a paleosol and by evidence of subaerial exposure, notably with plants and tree remains.

At Khashm Munayyifiyah (22°11'N, Al Mulayh Quadrangle), the base of the Minjur Sandstone is a channelised sandstone with mud pebbles and an erosional contact on the underlying paleosol. At Khashm Mawan (22°50'N, Al Mulayh Quadrangle), the base Minjur is a conglomeratic lag of rounded quartz, 2 cm in diameter, above a ferruginous surface, overlain by trough cross-bedded sandstone.

At Khashm al Khalta (23°38'N, Ar Rayn Quadrangle), the base Minjur, as recognized by Issautier *et al.* [2012a], is an incised high-energy paleo-river valley filled with black ferruginous, coarse-grained sandstone with planar (upper flow regime quartz lags) and

trough cross-stratification. It contains debris of silicified tree branches, and plant imprints. Two tributaries of this type were observed within a 10 km radius. At Khabra Halwah (23°58'N, Ar Rayn Quadrangle), above a brecciated bed of dolomite in fine-grained sandstone, the basal Minjur is a conglomeratic coarse-grained sandstone overlain by a fine-grained sandstone with black hematite.

At al Gullah (24°19'N, Ad Darma' Quadrangle), above the Khashm Dolqan section of the Jilh Formation, the basal Minjur is characterized by soil with gravel and poorly sorted coarse-grained sandstone with plant debris; it rests on supratidal fine-grained deposits with a reworked bed of dolomite in sandstone, and a ferruginous surface; below in the Khashm Dolqan section, transitional flasers of sandstone are present in the dolomite bearing bed.

In the south of the Al Faydah Quadrangle (25°08'N), the basal Minjur is a conglomeratic sandstone with ferruginous cement resting on a red-violet algal dolomite. At Safra ar Ruwaykibah (25°32'N, Al Faydah Quadrangle) the basal Minjur is a conglomeratic sandstone with iron cement containing plants or wood, and channeling in paleosols. At Safra al Mustawi (25°40'N, Al Faydah Quadrangle), the basal Minjur is a trough cross-bedded, coarse-grained sandstone with silicified wood debris and gypsiferous paleosol, resting on a pink-red sandy dolomite.

At Safra ar Ruwaydah (~26°05'N–26°25'N, Buraydah Quadrangle) it is a micro-conglomeratic brown ferruginous sandstone resting on dolomitic sandstone and laminated sandy dolomite. At Khashm al Garrah—Al Barud (26°50', Buraydah Quadrangle) it is a micro-conglomeratic sandstone with quartz gravel resting on a laminated dolomite and followed by quartzitic thinly bedded sandstone containing a remarkable accumulation of silicified tree trunks.

These descriptions show an apparent homogeneity with wood accumulation and lag deposits. Some uncertainty appears north of 26°N; basal channels with coarse-grained quartz in trough cross-stratification become rare and localized and are replaced at the boundary by sandy-dolomitic deposits. Wood debris are found in coastal-plain sabkhas as well. Therefore, distinction between the Jilh and Minjur formations is not so clear in some places. Nevertheless, at the map scale, the boundary is clearly marked by a low cuesta and a reddish colour of the sandstone reflecting exposure.

4. Facies and paleoenvironments

Paleoenvironments interpretation from facies refers to ancient and modern examples commonly illustrated in the literature [e.g., Ginsburg, 1975, Scholle and Spearing, 1982, Scholle *et al.*, 1983], to oceanographic definitions and personal field work on modern littoral sediments, specifically on Arcahon Bay tidal systems [e.g., Le Nindre, 1971, Le Nindre and Dutartre, 1993, Le Nindre *et al.*, 2000, 2004, 2006] as well as the Aquitaine Coast dynamics—Bay of Biscay [Le Nindre *et al.*, 1998, 1999, 2001]. The facies observed in the lithostratigraphic sections of the Jilh Formation and along the entire outcrop belt, can be classified by their lithology, sedimentary structures, and paleontological content. They reflect paleoenvironments ranging from infralittoral, brackish lagoonal, and fluvio-deltaic within a coastal fringe. Continental clastic influx is alternated with thin, but significant, marine transgressions. The rest of the time, paralic brackish-lagoonal to evaporitic environments represent equilibrium conditions. The position of sandstones in the sequence reflects their depositional environment and the dominant mechanism. This is discussed at the end of the facies description.

4.1. Mapping facies and paleoenvironments along a N–S transect

The facies described in outcrop in the Jilh Formation can be grouped and subdivided into three main categories: marine, paralic, and fluvio-deltaic. They were mapped from 22°N up to 27°N (Figure 4). The paralic facies form the background of the sedimentation. Depending on cyclicity and local tectonics, they may contain evaporite—mainly in lower part, being incised by continental discharge—mainly in middle part, or flooded by marine shallow deposits—mainly in upper part of the formation.

4.1.1. Marine facies

These facies are the most diversified.

- (A) *Sandstone with hummocky cross stratification*; this facies, typical of the lower shoreface [McCubbin, 1982], is rare (Figure 6a).
- (B) *Sandstones, with well-sorted quartz grains, small-scale cross stratification, and a wide range of current directions*; their distribution

is well controlled, vertically transitional between the brackish claystone–siltstone and the sandy dolomites of the Unit J2, and horizontally from 24°N to 26°N. These characters reflect tidal sand flats particularly well represented in the Khashm al Midiya'ah section (Jabal Math'abah, c. 24°31'N).

The A and B facies are mapped as “Coastal Sandstone” on the transect, Figure 4.

- (C) *Mixed sandstone-dolomite facies*, consisting of sandstone with lenticular and flaser bedding of carbonate mud, and sandy dolomite (Figures 6b,d; 7a) has the same distribution as the tidal sandstone below. The presence of lenticular structures, flasers, oolites, stromatolites, and traces of biologic activity such as trails and burrows, and ichthyoliths, makes it possible to infer a tidal context of the depositional environment, whereas the presence of organisms such as bryozoans, ophiuroids, and conodonts, shows the discrete, but effective, influence of a more open-sea environment.

The close association of quartzose deposits and carbonate sedimentation illustrates the dynamics: the sand carried by rivers was taken up in the littoral domain and finally redeposited by the sea as sheets in the dolomites; therefore, resulting lithologic types may range from pure dolomite to pure sandstone. Also, related to the same process, quartz grains form the nuclei of limonitic ooids. These phenomena clearly show the competition between the two influences.

This C facies is mapped as “Mixed Facies, Flasers”, specifically, or with the “Undifferentiated Tidal Flat” when described as a thin bedded complex assemblage of laminated sand, mud, evaporite, and sedimentary structures.

- (D) *Laminated dolomite* with algal mats and pseudomorphs (Figure 7a,b), of intertidal mudflat, are widely distributed at the top of each unit. This D facies is mapped with the “Undifferentiated Tidal Flat” on the transect, Figure 4.
- (E) *Stromatolites* (Figure 6c), especially large size (1 m) cushion like stromatolites, are mainly

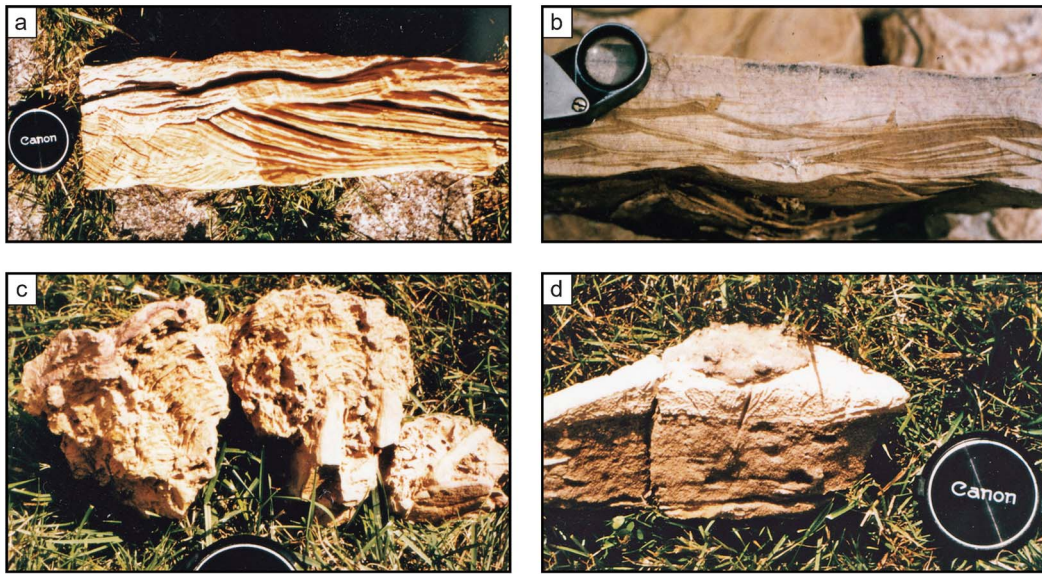


Figure 6. Selection of typical macrofacies. (a) Sandstone with hummocky cross stratification. (b) Current ripples: alternating sandy and muddy beds due to tidal currents periodicity (mixed quartz-carbonate sedimentation). (c) Convex stromatolite encrusting lithoclasts (flat pebbles of dolomite, early lithified, on top of a more clayey series; Sample JMA82-157, Unit J3, Khashm Dolqan). (d) Mixed quartz-dolomitic sedimentation, alternating quartzose dolomite (in brown, at the base), dolomitic mudstone (cream in the middle), and coarser-grained sandstone with small dolomitic pebbles (grey on top; Sample JMA82-160, Unit J3, Khashm Dolqan). (a), (c), (d), photos by Y. M. Le Nindre; (b) photo by D. Vaslet.

represented in the Tuvalian interval of the Unit J3 and associated with the most marine facies, north of 25°N.

- (F) *Carbonate (limestone–dolomite) deposits containing a marine fauna:* echinoderms (particularly ophiuroids), conodonts, bryozoans, and involutinid foraminifers. They develop preferentially north of 25°N and are mapped as “Shallow Marine Facies (subtidal, proximal infralittoral)”.

In detail, major recurrences of D, E, F facies are visible, but the tops of sequences are marked by better development of tidal plain facies.

4.1.2. *Paralic facies*

The paralic facies are most dominant near the base of the formation (Anisian, Ladinian) and reflect more-or-less saline conditions of coastal plain settings: varicolored claystone and siltstone with gypsum, and sometimes massive gypsum, likely pass to anhydrite in the subsurface (Early Ladinian near

24°N and Early Norian near 27°N); this setting is more similar to sabkha conditions. This facies includes bone debris (Figure 7e, JMA81-25) as described by Vickers-Rich *et al.* [1999]. It is mapped as “Coastal Plain-Sabkha” in the transect, Figure 4.

4.1.3. *Fluvio-deltaic facies*

These facies are of two types. The first are wedges of amalgamated bars organized into a deltaic system, with fairly well-sorted quartz grains, graded bedded foresets and overturned cross stratification. This type of facies corresponds to the main clastic influx localized in Central Saudi Arabia (23°N to 24°N, Jabal Al Arid, 23°38'N and 23°32'N). It prefigures the main channel of the Minjur Sandstone, almost superimposed on it in the same area (Khashm al Khalta, 23°35'N). This feature, mapped within the Ar Rayn Quadrangle [Vaslet *et al.*, 1983], is clearly observed by the satellite imagery.

The second type consists of a more erratic complex of small fluvial channels, with coarser grained

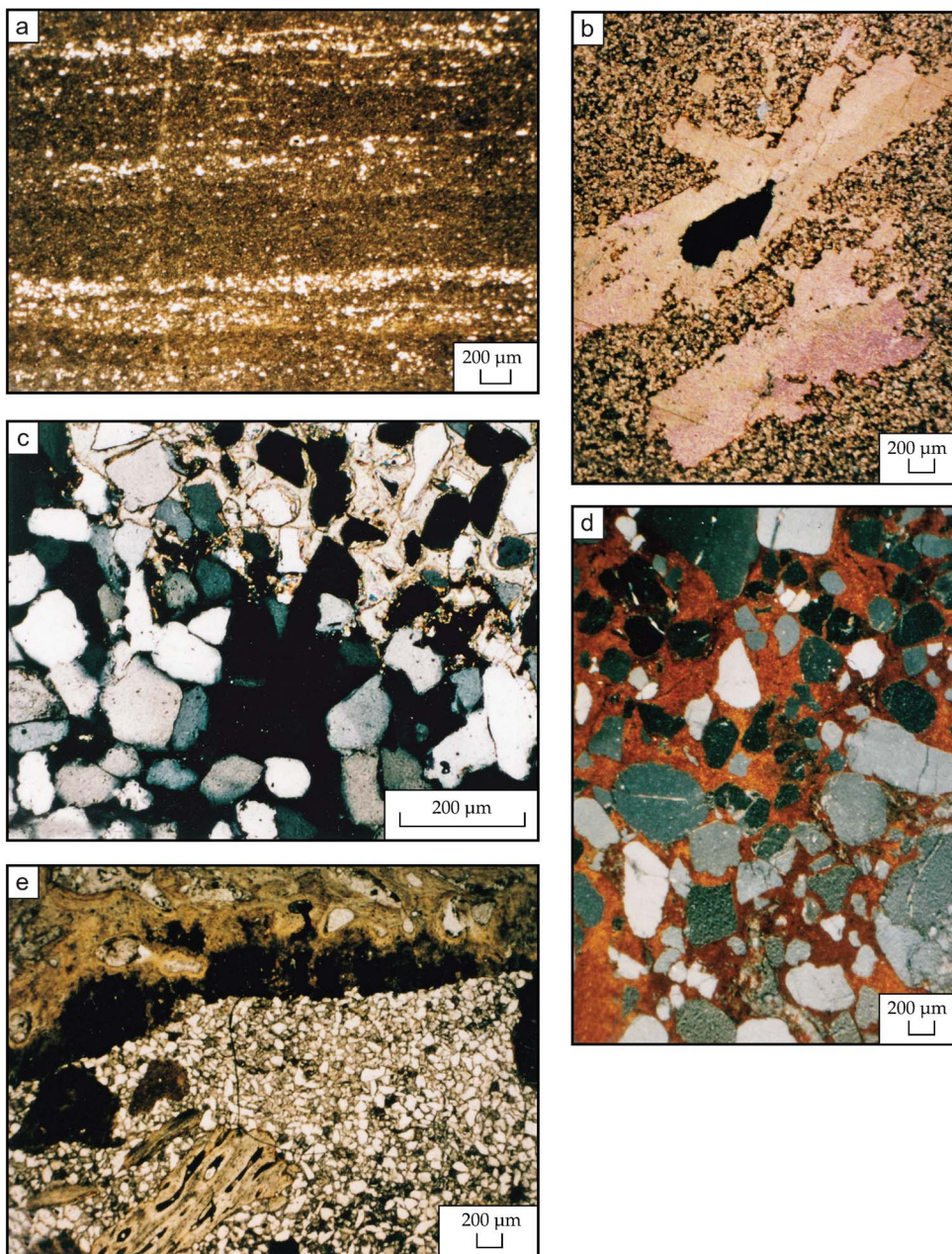


Figure 7. Selection of typical microfacies. (a) JMA81-7—B40669 Natural light—Dolomitic mudstone with silty laminae. (b) JMA82-135—B40338 Polarized light—Dolomitic mudstone with anhydrite pseudomorphs. (c) JMA82-132—B40338 Polarized light—Siltstone with cement of poikilitic calcite in the upper part and of authigenic quartz in the lower part. (d) JMA82-149—B40355 Polarized light—Sandstone with mature grains and ferruginous cement. (e) JMA81-25—B38670 Natural light—Wackestone-packstone with bone debris and lithoclastes of siltstone, themselves containing smaller debris. Photos by Y. M. Le Nindre.

and poorly sorted quartz grains, sometimes cemented by iron oxides (Figure 7d). The sand bodies are analysed and interpreted in details in Le Nindre *et al.* [1990a, p. 198–210] and in the Section 3.3. The channels are inserted in pedogenic siltstones of coastal/flood plain environments in the immediate vicinity of the river (depicted as “Alluvial Channels (Jilh)” and “Fluvio-deltaic coastal plain” on Figure 4).

4.2. Vertical evolution of depositional environments

4.2.1. Anisian–Ladinian

Within Unit J1, three lithofacies—gypsiferous siltstones, sandstone, and carbonates—correspond to different parts of a littoral complex comprising: coastal plain, estuaries, tidal flats and lagoons with a restricted fauna. The vertebrate faunas collected by Vickers-Rich *et al.* [1999] and Kear *et al.* [2010a,b], from Unit J1 illustrate climate—alternating dry and humid seasons—and these paleoenvironments. Their contribution to age calibration is presented further in Section 5.3. Vickers-Rich *et al.* [1999] have studied a fauna from the Ar Rubayiyah–Ash Shimasiyah area (26°25'N, 44°14'E)–(26°22'N, 44°16'E) mainly composed of sharks and osteichthyans. Most of these vertebrates seem to have been free-swimming forms, although a few isolated teeth may also indicate bottom-feeders. Subsequently Kear *et al.* [2010b] discovered the first lungfish *Ceratodus* sp. found in the Arabian Peninsula. This particular fish demonstrates, by its adaptation to both aquatic and aerial breath, periods of dryness alternating with flooding characteristic of this transitional environment.

4.2.2. Early Carnian

The Early Carnian marks the start of a transgressive phase typified by an initial influx of abundant siliciclastics originating from the Arabian Shield. These terrigenous detrital sediments were deposited in a marine environment consisting of intertidal carbonate flats, and variably reworked in a littoral environment, passing through lagoons characterized by clayey silty sedimentation. This type of evolution is thus very similar to that encountered in estuarine sequences [Clifton, 1982] and are observed in modern environments such as the Bassin d’Arcachon

[Aquitaine, France, YML, pers. observ. e.g., Le Nindre and Dutartre, 1993]. So, as shown by Figures 4 and 10, there may be several separate or stacked estuarine environments along the coast.

4.2.3. Late Carnian to Norian

The reconstruction of Late Carnian to Norian environments shows a predominantly mid-littoral influence, although temporarily more seaward, infralittoral domain may have prevailed.

The presence of cushion-like stromatolites is reminiscent of some present-day settings in the Arabian Gulf. We observe a relative decrease in terrigenous detrital input, and a concomitant expansion of the carbonate deposits at the edge of the marine platform. Some hardgrounds occurred, and the setting was less confined, although the water depth remained shallow.

4.2.4. Exemplary case of the Khabra Halwah Section

Located farther south, near the reference section (23°58'N, 44°49'E), the Khabra Halwah Section (Figure 8) adds an improved understanding of the sequential arrangement of the Jilh Formation and particularly demonstrates the sedimentation of the intertidal flats. Each sequence is transgressive and capped by tidal carbonate. The succession of facies used to define the three lithostratigraphic units comprises: (1) silty and gypsiferous claystone typical of lagoons and the littoral plain, (2) intertidal flat dolomites, and (3) sandy bodies located at various positions in the sequence depending on the environment to which they are related, as follows.

- *Fluvial sandstone* is at the base of the sequence, followed by brackish claystone–siltstone and capped by the tidal carbonate;
- *Deltaic-estuarine sandstone* is deposited partly in place of the brackish claystone–siltstone and develops southward as a wedge in the Unit J3 at Jabal al Arid (23°38'N) centred on an alluvial valley while bays and algal mats dominate northward at Khashm Dolqan (24°15'N);

Tidal sandstone overlies the brackish claystone–siltstone, and is capped by the tidal carbonate. It is particularly present in the Unit J2, and well illustrated by the section at Khashm al Midiya'ah (24°27'N). The tidal

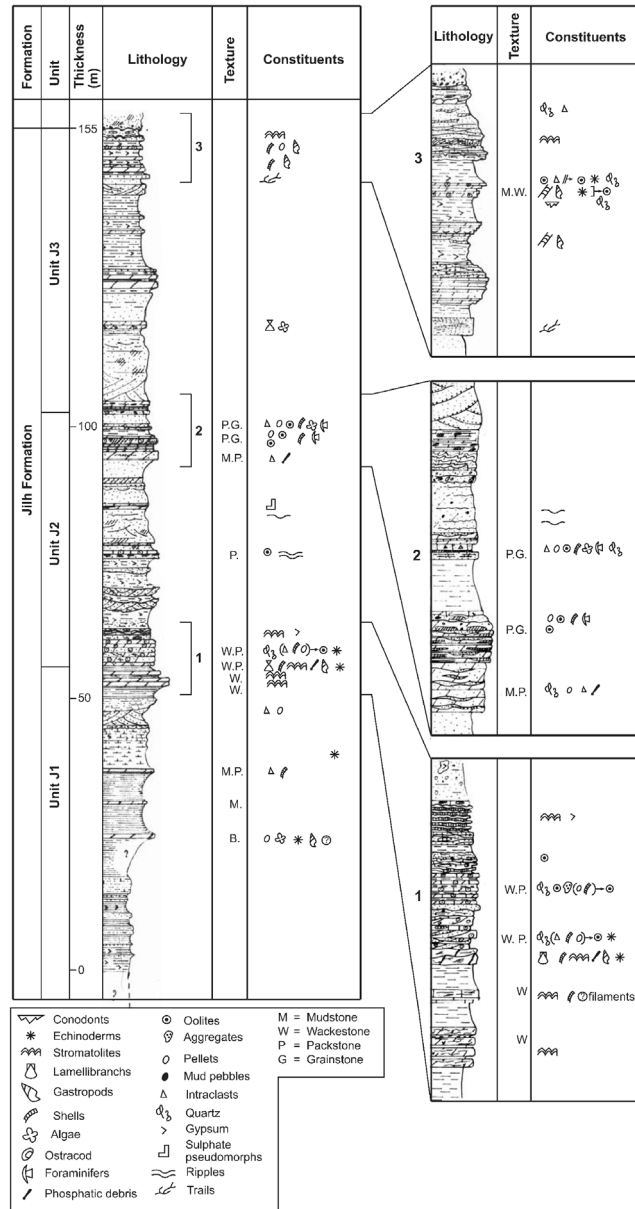


Figure 8. Stratigraphy and sedimentology of the Jilh Formation in the Khabra Halwah section [23°58'N, 44°49'E, measured October 1980, modified after Le Nindre *et al.*, 1987, 1990a].

flat deposits generally end with salt marsh or laminated sabkha sediments, which form the cap to the depositional sequence.

of such deposits by the sea (Figure 8).

The Khabra Halwah Section thus particularly well illustrates the alternation between phases favouring alluvial deposits and phases leading to the reworking

4.3. Interpretation of transgression–regression (system tracts geometry)

On the basis of the analysis summarized above, we depict at larger scale the T–R sequences that characterise this formation. The ages of these sequences are discussed in Section 5. A fairly clear understanding of the processes is given by mapping several key features along a N–S transect, as follows.

Ferruginous (Fe) oolites generally have a quartz nucleus, and are likely to be chloritic oolites diagenetically altered by weathering in outcrop (Figure 4). They are equivalent to, or associated with, the formation of glauconite when chemical processes dominate the sedimentation processes, and delineate condensed intervals. Also, a thin ledge of coarse-grained quartz-rich sandstone (sometimes with gravel) may predate the Fe-oolite horizon. The thin ledge horizon is usually very continuous, as generally observed for this type of surface, and forms *cuestas* that can be easily correlated. The Fe-oolite horizons are significant as they typically mark the maximum rates of transgression and are associated with carbonate beds which contain age-diagnostic faunas. One in particular marks the top of the second major transgressive sequence taken as J2–J3 boundary above the main clastic event.

The distribution of carbonates in the Jilh Formation along a N–S transect (Figure 9) is represented according to two environments: most of them correspond to intertidal flats; coming from the north (as viewed in outcrop), more marine influences identify the maximum flooding intervals. This transect demonstrates a more carbonate-rich and more marine sedimentation north of 25°N, and five marine pulses, which can be grouped into three major flooding intervals, the main one reaching as far south as at least 23°N. The sedimentary wedges depict a progradation-like geometry, particularly visible near the upper boundary of the formation with the Minjur Sandstone.

The distribution of sandstones in the formation in outcrop (Figure 10) is represented according to two environments: (1) fluvial or fluvio-deltaic sandstones which reflect the continental, prograding clastic influx; and (2) marine littoral sandstones, in general, intertidal, which reflects marine reworking of the clastics brought by the rivers and thus transgres-

sive processes. This transects (Figure 10) demonstrates the following patterns. The coarse-grained sandstones of the Minjur Sandstone overlie the top of the Jilh Formation with the most typical facies including a basal lag with plants, silicified wood or pieces of silicified tree trunks.

Sandstone becomes more abundant between 23°N and 26°N, and especially between 23°N and 25°N. Fluvial-deltaic sandstones are distributed either in small coastal river channels or as the deltaic wedge observed at Jabal al Arid near 23°30'N. Correlations show that this body appears abruptly in lateral correspondence with thinner tidal flat deposits; the same corridor was later used by the main stream of the Minjur Sandstone. This observation is interpreted as due to a subsiding area, likely related to a NE-trending fault bounding the northern bank of the valley and superimposed on a Permian paleohigh [Le Nindre *et al.*, 2003, Issautier *et al.*, 2012a].

The tidal sandstones accompanying the transgressive trends concluded by the carbonates, occur particularly in the sandstones of Unit J2 between 24°N and 26°N. In detail, the sandstones of this unit show that within the overall transgressive process, higher frequency prograding and retrograding stages of the coastal domain are manifested [Le Nindre *et al.*, 1990a, p. 206–210].

To summarize this aspect of the sedimentation, sandstones represent various trends, more generally fining-upward transgressive, and intertidal tracts, although some coarsening-upward prograding bodies were described in Unit J2. Carbonates represent the most transgressive intervals; they can be capped by short pre-evaporitic and algal supratidal sediments, as well as by salt marshes and paleosols representing reduced regressive tracts.

5. Paleontology, and age interpretation

Systematic sampling along the outcrops was performed during the BRGM/DMMR mapping program for petrographic and biostratigraphic analysis. Samples have provided a fairly varied fauna, and locally, palynoflora. In particular, ten sections (A to J) in the Jilh Formation and base of the Minjur Sandstone measured between latitudes 23°33'N and 28°01'N (Table 1; Figure 11) have yielded rich conodont faunas. These faunas, studied by Vrielynck

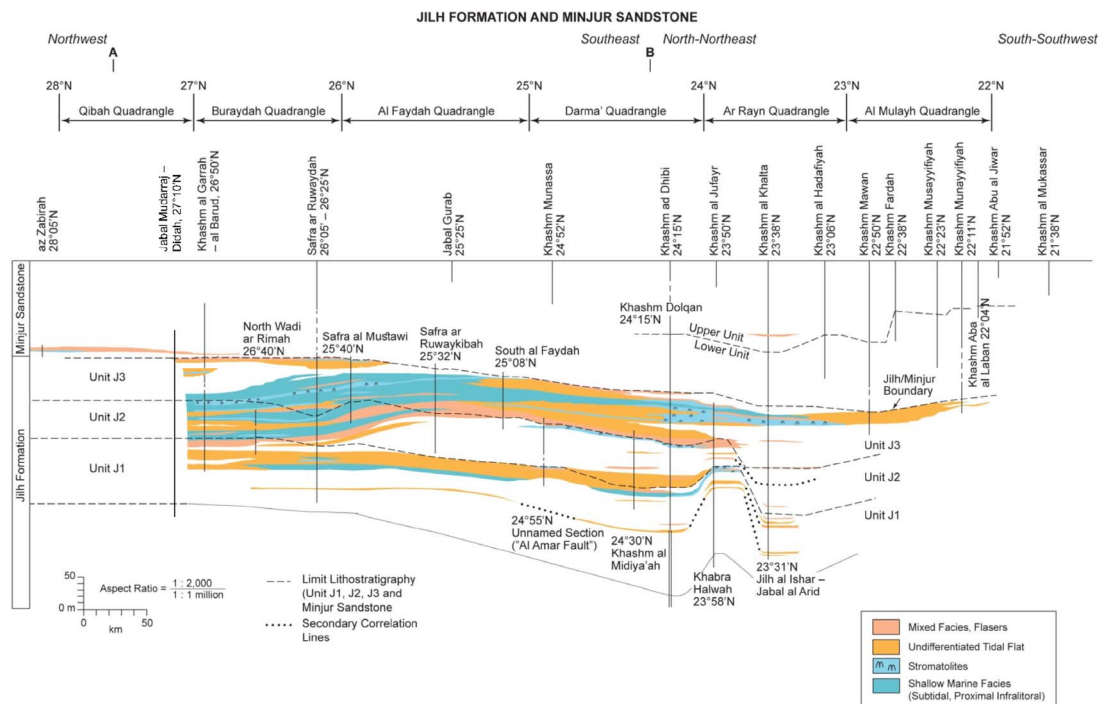


Figure 9. Distribution of marine carbonates and clastics-carbonates facies of the Jilh Formation along the N-S strike of the outcrops [modified after Le Nindre et al., 1987, 1990a]. See Figure 1 for location of quadrangles.

[Vrielynck et al., 1986] and Krystyn (this study) are specifically described here for the precise results that they are roughly of age identical to this. The study follows Chen et al. [2015] for the Ladinian, Orchard [2014] for the Carnian, and Orchard [2018], for the Norian. Here specifically, *Paragondolella polygnathiformis* (Budurov and Stefanov), was replaced by *Quadralella polygnathiformis*, *Metapolygnatus* aff. *auriformis* (Kovacs) by *Quadralella* aff. *auriformis* and *Carnepigondolella carpathica* (Mock) by *Quadralella carpathica*. The conodonts age calibrations are from the authors cited (e.g., Chen et al., Kilic et al., Orchard, Vrielynck, Mazza et al., Krystyn), principally in Section 5.3. Two ammonoid faunas were also described in the J3 upper unit near Ash Shimasiyah–Ar Rubaiyah (~26°22'N) which corroborate conodont age assignments. Compared to Le Nindre et al. [1987, 1990a], new insight is provided in this study by the conodont fauna from the Qibah Quadrangle, and by the examination of other specimens of the ammonoid fauna from the Buraydah Quadrangle. The samples are located referring to units and subunits (e.g., J1(2)) of the concerned sec-

formation. Other intermediate locations have yielded biostratigraphic results that complement this under the same nomenclature as on the logs (Supplementary Section A, and Figure 11).

5.1. Data from the reference section

As already mentioned in section “Lithostratigraphy”, the reference section for the Jilh Formation is located at Khashm Dolqan (Figure 1 and Section C, 24°15'N Figure 10) near the original type section, and is composed of the outcropping portion completed by 79 m of series from the SHD-1 well stratigraphic core drill for the lower portion (Figure 3). The portion from J1(2) to J1(4) in the SHD-1 well has yielded a palyonoflora which characterizes the Anisian, especially in J1(4) with *Densoisporites nejburgii* (Schulze) Balme, *Alisporites* cf. *opii* Daguerty, *Camerosporites* cf. *pseudoverrucatus* Scheuring, and more specifically *Platysaccus* cf. *queenslandii* De Jersey. The fossils in the reference section occur in the upper part of Unit J1 (J1(5–6) and J1(8)) (Figure 11 and Supplementary Section A, Plate A.3) and comprise bivalves,

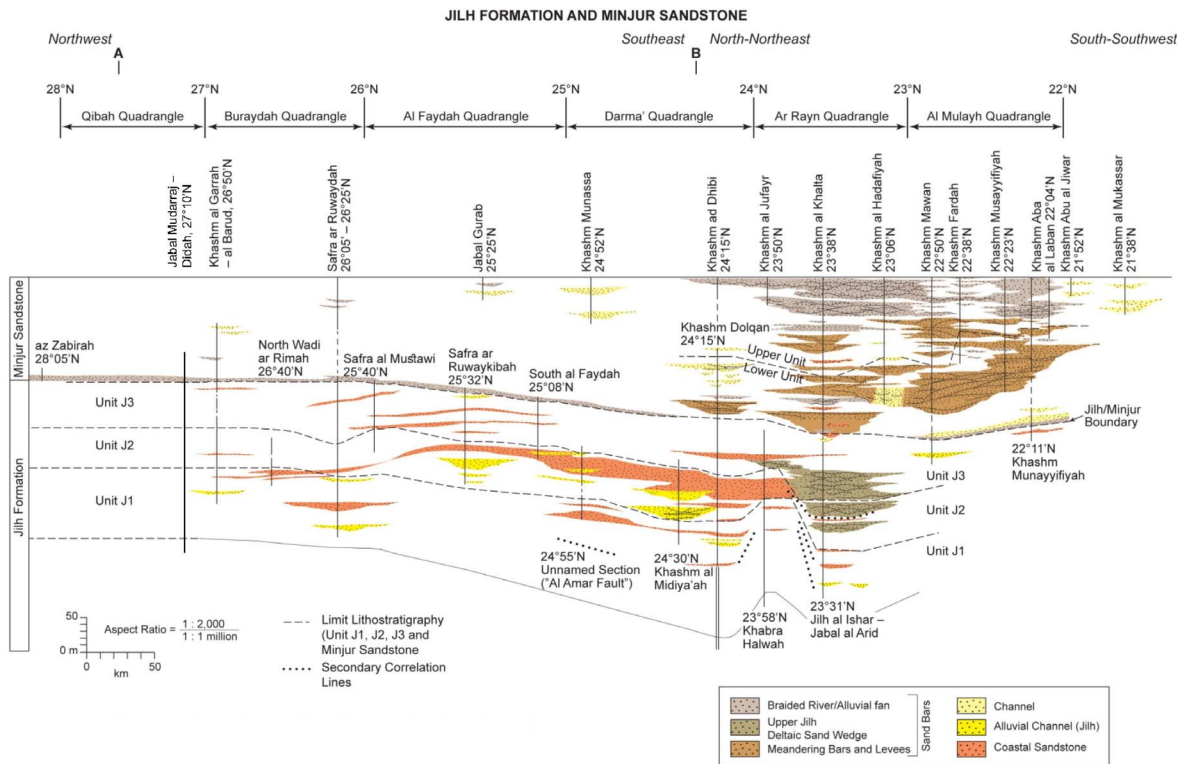


Figure 10. Distribution of sandy facies of the Jilh Formation along the N-S strike of the outcrops [modified after Le Nindre et al., 1987, 1990a]. See Figure 1 for location of quadrangles.

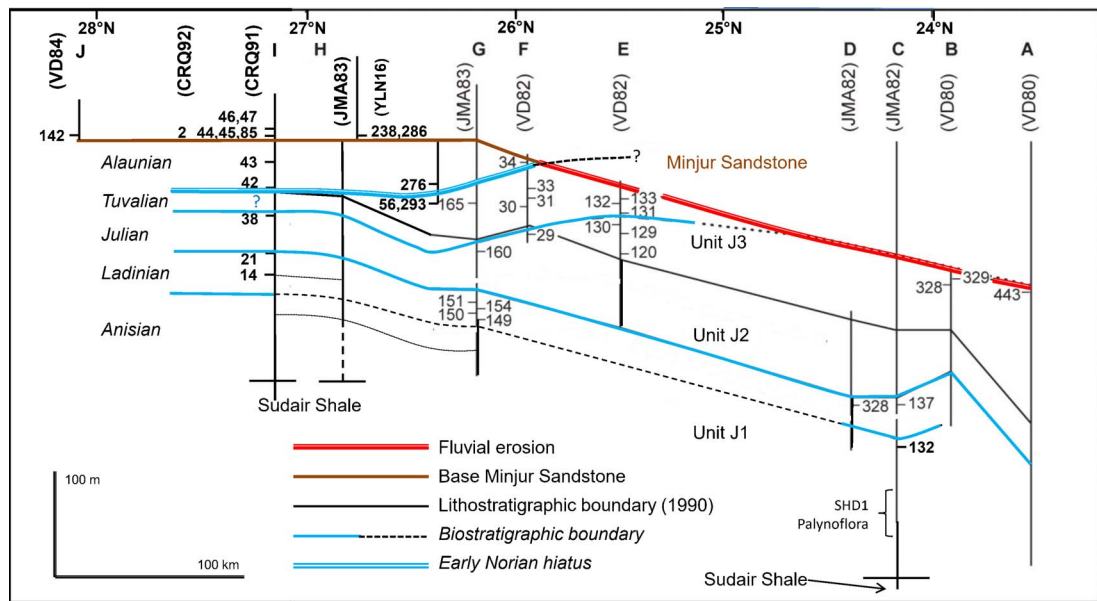


Figure 11. Location of the sections and samples having yielded age-decisive fossils along a N-S transect. Base Tuvalian, is subject to vertical adjustment. For name and location see Table 1 above. The apparent diachroneity of the J2–J3 boundaries is discussed below in Section 5.4.

Table 1. List of lithostratigraphic sections having yielded age-decisive fossils

Section name	Quadrangle	Scale	Coordinates bottom	Coordinates top	Survey date	Authors	Letter
Az Zabirah	Turubah—28F	1:499	28°05'N—43°27'E	28°05'—43°28'E	02/82	D. Vaslet, A. Berthiaux	J
Jabal Mudarrāj—Didah	Qibah—27G	1:500	27°10'N—43°44'E	27°09'N—44°02'E	11/91	Y. M. Le Nindre, C. Robelin, D. Janjou, J. Gouyet	I
Khashm al Garrāh—Al Barud	Buraydah—26G	1:500	26°47'N—43°58'E	26°57'N—44°13'E	12/82–02/83	P. Le Strat, D. Vaslet, J. Manivit, A. Berthiaux	H
Safra ar Ruwaydah	Buraydah—26G	1:500	26°05'N—44°20'E	26°25'N—44°23'E	02/83	P. Le Strat, J. Manivit, D. Vaslet, A. Berthiaux	G
Safra al Mustawi	Al Faydah—25G	1:500	25°40'N—44°32'E	25°50'N—44°40'E	03/82–11/82	Y. M. Le Nindre, P. Le Strat, D. Vaslet, J. Manivit, A. Berthiaux	F
Safra ar Ruwaykibah—Jabal Ghurab	Al Faydah—25G	1:500	25°32'N—44°43'E	25°25'N—45°00'E	03/82–11/82	Y. M. Le Nindre, P. Le Strat, D. Vaslet, J. Manivit, A. Berthiaux	E
Khashm Midiya ah	Darmā—24H	1:500	24°27'N—45°28'E	24°43'N—45°29'E	02/82	Y. M. Le Nindre, D. Giot, J. Manivit, J. M. Brosse	D
Khashm Dolqan*	Darmā—24H	1:500	24°13'N—45°37'E	24°12'N—46°05'E	12/81	Y. M. Le Nindre, J. Manivit, D. Vaslet, J. M. Brosse, C. Cavelier	C
SHD1 stratigraphic borehole	Darmā—24H	1:500	24°13'40"N—45°37'30"E		08/81	J. Manivit, D. Vaslet	C
Khabra Halwah	Wādī Ar Rayn—23H	1:500	23°58'N—44°49'E	23°59'N—46°10'E	10/80	Y. M. Le Nindre, D. Vaslet, J. M. Brosse, J. Manivit	B
Jilh al Ishar—Jabal al Arid	Wādī Ar Rayn—23H	1:500	23°31'N—46°00'E	23°36'N—46°13'E	10/80	Y. M. Le Nindre, D. Vaslet, J. Manivit, J. M. Brosse	A

* Reference section.

conodonts, bryozoans, foraminifers and ichthyoliths. The bivalves identified as *Myophoria goldfussi*, (JMA82-132) are indicative of the Anisian. The Ladinian conodont *Pseudofurnishius murcianus* Van Den Boogaard is also recognized (sample JMA82-137, J1(8), Supplementary Section C, Plate C.7). The boundary between the Anisian and the Ladinian is thus located between the two faunal beds in the upper fifth of Unit J1 (c. J1(6)–(7) boundary) at the latitude of the reference section.

5.2. Data from other sections

The results are summarized in Figure 11 and Supplementary Section A. Units and subunits refer to Figure 11 and to the lithostratigraphic sections, in Supplementary Section A.

In Section A (Jilh al “Ishar—Jabal al Arid, 23°31’N, Supplementary Section A, Plate A.4), only sample VD80-443 could be dated. It was collected from the uppermost part of Unit J3, and contains conodonts belonging to the species *Quadralella polygnathiformis* (Budurov and Stefanov), present throughout the Carnian (Julian and Tuvalian).

In Section B (Khabra Halwah, 23°58’N, Supplementary Section A, Plate A.3), the top of Unit J3 contains conodonts, echinoderm debris, bryozoans, and ichthyoliths. Sample VD80-328 contains *Paragondolella inclinata* Kovacs, and *Q. polygnathiformis*, an association typical of the Julian (Early Carnian). Sample VD80-329 contains *Q. polygnathiformis*, indicative of the Carnian without further precision.

In Section D (Khashm Midiya’ah, 24°27’N, Supplementary Section A, Plate A.3) where the top of Unit J1 and all of Unit J2 are exposed, only Sample JMA82-328 collected at the top of the Unit J1 is fossiliferous. It contains the conodonts *Budurovignathus truempyi* (Hirsch) and *B. cf. mungoensis* (Diebel), an association indicative of the Late Ladinian.

In relation to the evolution of paleoenvironments described above, the outcrops located northwest of 25°N contain more fossils than those to the southeast.

In Section E (Safra ar Ruwaykibah—Jabal Gurab, 25°32’N, Supplementary Section A, Plate A.2) where the totality of Units J2 and J3 is exposed, Unit J2 proved to be barren, whereas many conodonts associated with foraminifers and ichthyoliths are encountered in Unit J3. Sample VD82-120 collected

at the base of Unit J3 contains *Mazzaella carnica* (Krystyn), characteristic of the Julian. Sample VD82-129 collected from the middle of the unit contains *Quadralella* aff. *auriformis* (Kovacs) and *Q. polygnathiformis*. This is a Carnian association, and the presence of *Q. aff. auriformis* indicates the Julian. The samples collected from the upper part of Unit J3 (samples VD82-130-133) are monospecific, containing only *Q. polygnathiformis*, which persists throughout the Carnian, with the exception of the very uppermost part.

In Section F (Safra al Mustawi, 25°40’N, Supplementary Section A, Plate A.2), where the top of Unit J2, all of Unit J3, and the base of the Minjur Sandstone are exposed, the sample collected from J2 (VD82-29) contains *M. carnica*, typical of the Julian. The samples collected from the middle part of Unit J3 contain foraminifers, ostracods, bryozoans, and conodonts. The conodonts belong to the Carnian species *Q. polygnathiformis*, associated in sample VD82-33 with *Q. carpathica* (Mock), known exclusively from the Tuvalian (Late Carnian). A Tuvalian age can thus be assigned to the middle part of Unit J3. The uppermost beds of Unit J3 (sample VD82-34) contain *Epigondolella abneptis* (Huckriede), known in the Norian, together with some ichthyoliths.

In Section G (Safra ar Ruwaydah, 26°05’N, Supplementary Section A, Plate A.2) where the whole of the Jilh Formation, except for the very bottom, and the Minjur Sandstone are exposed, the upper part of Unit J1 contains echinoderm debris, ostracods, and conodonts. Samples JMA83-149 and JMA83-150 contain *B. truempyi*, and samples JMA83-151 and JMA83-154 contain *P. murcianus* (Supplementary Section C, Plate C.7). Both these species are indicative of the Ladinian. Sample JMA83-160 from the upper third of Unit J2 contains *Q. polygnathiformis* and *M. carnica*, an association typical of the Julian. The middle part of Unit J3 (sample JMA83-165) contains *Q. polygnathiformis* associated with echinoderms debris and bryozoans indicating a Carnian age.

About 30 km northward, near Rubay’iyah (26°28’N) the formation has yielded two faunas of ammonoids (Supplementary Section C, Plates C.1 to C.6):

- The top of the lithological Unit J3(3) is marked by a weathered dolomite containing a fauna of Tropitids (JMA83-293) with a “*Clydonites*-like” form (E. T. Tozer written

communication, 1985), similar to the species cited by Powers *et al.* [1966]. E. T. Tozer suggested a Carnian age for this fauna. Similarly, in November 2016 in the same area (Ash Shimasiyah, 26°21'37.00"N, 44°20'10.00"E), D. Vaslet and Y. M. Le Nindre collected a Tropitid ammonoid (YLN16-056) identified as *?Discotropites* of Late Carnian age by H. Bucher (written communication, 2017) which is reinterpreted here as *?Pleurotropites* sp. by LK.

- 18 m above this horizon, within the unit J3(4), a yellow carbonate horizon, continuous and well exposed in outcrop, yielded another monospecific fauna; several tens of specimens were collected (JMA83-276), identified as "*Neotibetites* sp." by E. T. Tozer who assigned them to a Mid-Norian and rather late Mid-Norian age (written communication, 1985). This concentration reflects a local thanatocoenosis.
- Other specimens of the same samples as above were examined by LK and J. Marcoux, and reported with the following taxa and ages (new unpublished results):
 - JMA 83-293: *Pleurotropites* sp.ind., *Sirenites* sp., *Shastites* sp.; age: Tuvalian Tuvalian 1, *Tropites dilleri* zone, eventually Tuvalian 2/I)
 - JMA 83-276: *Anatibetites kelvini* Mojs., *Paratibetites* cf. *geikiei* Mojs., *?Metacarnites* sp.; age: Middle Norian (Alaunian); if the questionable *Metacarnites* is true, then Alaunian 1.

In Section H (Khashm al Garrah—al Barud 26°47'–26°57'N,—also named Safra al Agyah, (Supplementary Section A, Plate A.1) ranging from the middle part of Unit J1 up to the lower layers of the Minjur Sandstone, numerous conodonts belonging to the species *E. abneptis* and some ichthyoliths are found in sample JMA83-286 just above a remarkable accumulation of tree trunks (JMA83-238) taken as the base of the Minjur Sandstone; the conodont indicates a Norian age. In the same section, marker foraminifera were identified by D. Vachard (written communication, 1984) at the top of Unit J1, the sample JMA83-60 contains among the bioclasts a few foraminifera: *Globivalvulina* sp., "*Nodosaria*" sp.,

and *Glomospira* sp. ("cf. *Meandrospira*") assigned to a Permian association. In fact, the petrographic study by Le Nindre shows that they are reworked constituents related to a transgressive surface (mid-Julian marker bed, see "Depositional History and Sequence Analysis"), and that this fauna originates from the Khuff Formation. Near the top of Unit J3, just underneath the base of the Minjur Sandstone dated Norian by conodonts, the sample JMA83-75 yielded *Involutina eomesozoica* (Oberhauser), which is a marker of the Ladinian–Carnian. Due to the fact that the petrographic study reveals, here again, a bed of quartzarenite containing obviously reworked carbonate constituents, and that a Norian age was retained for the coeval lateral beds, it is very likely that the foraminifer was reworked from the substratum into the Norian sandstone, supporting interpretation of a Carnian–Norian unconformity.

In Section I (Jabal Mudarra—Didah, 27°10'N, Supplementary Section A, Plate A.1, and Supplementary Section B, Plate B.1 and Supplementary Section C, Plates C.8 to C.10), newly studied conodonts were found throughout the Jilh Formation. In the upper part of the Unit J1, samples from the dolomite forming the first main cuesta provided a (Late?) Ladinian age: CRQ91-14 with *Pseudofurnishius shagami* (Benjamin and Cheepstow-Lusti), containing also vertebrae, and CRQ91-21 with *P. shagami* and *P. cf. shagami* transitional to *Budurovignathus truempyi* (Hirsch). In the Middle part of the Unit J2, the sample CRQ91-38 yielded interesting though poor material of *Mazzaella carnica*, indicating late Early Carnian. Various horizons of the J3 Unit provided conodonts. Of six studied samples, four (CRQ91-42, 43, 44, 45) yielded platform conodonts (*Ancyrogondolella*) of basal Middle Norian age (Alaunian 1) and the other 2 were barren (CQR 91-81, 92-3). All of the productive samples yielded the same 2 species: *Ancyrogondolella praeslovakensis* (Kozur, Masset and Moix) and a new *Ancyrogondolella*, here called as *A. ex gr. uniformis* (Orchard). *Epigodolella abneptis* is comparably rare and restricted to the highest sample CRQ91-45. *A. praeslovakensis* has been described by Moix *et al.* [2007] from Middle Norian limestones within the Mersin melange, Turkey, where it co-occurs with Alaunian 1 ammonoids (*Cyrtopleurites*, collected and determined by LK). Also, the new species, *Ancyrogondolella ex gr. uniformis*, is found in many Alaunian 1

ammonoid dated Hallstatt sections between Austria and Timor (unpubl. data, LK).

The exact position of CR91-42 in section (between samples 41 and 43) is not recorded in the field book. But, from sample description, and by comparison with a similar horizon in Section H, it very likely originates from a bioclastic–oolitic grainstone beneath the khaki shale interval, just on top of sample 41, at the base of Unit J3. True *Epigondolella abneptis* occurs in sample CRQ91-45. Samples CRQ91-46 and 47 were taken from holes in black silty claystone of sabkha deposits, about 6–7 m above the samples 44 and 45 and 2 m above silicified wood occurrence. Palynology indicates a Norian age based on association of Circumpolles, *Camerosporites tenuis*, *Ovalipollis pseudoalatus*, and *Spiritisporites spirabilis* (internal technical note Danielle Fauconnier 92-GEO-GSM 040, 1992). This silicified wood is coeval with the tree trunks found in Al Barud, a few kilometers southward [Manivit *et al.*, 1986] and with the flora from Hunaydhel (Hunayzil on the Buraydah Geological Map) recently studied by El-Atfy *et al.* [2022].

The Alaunian age of the Jilh–Minjur boundary was confirmed in two other locations: from another similar section in Unit J3, the sample CRQ91-85, in a situation comparable to CRQ91-44, indicates again Middle Norian (Alaunian 1). From a portion of section in Aba ad Dud, the sample CRQ92-2 taken from a Fe-oolite grainstone with oncolites in a transgressive horizon yielded the same conodont fauna of Alaunian 1 age.

In Section J (Az Zabirah, 28°05'N, Supplementary Section A, Plate A.1) at the base of the Minjur Sandstone, many conodonts of the species *E. abneptis* of Norian age were found in Sample VD84-142.

5.3. Discussion of age interpretations

5.3.1. Anisian

The Anisian was dated by *Myophoria goldfussi*—although the age range of this bivalve may be disputed—and by palynology in the reference section.

Vickers-Rich *et al.* [1999] have studied a rich fauna of vertebrates from the Ar Rubaiyah–Ash Shimasayah area (26°25'N, 44°14'E)–(26°22'N, 44°16'E) already cited above in section “Vertical Evolution of

Depositional Environments”. It includes hybodontiform sharks, actinopterygians, and sauropterygian reptiles such as a pachypleurosaur, *Simosaurus*, nothosaurs and cyamodontoid placodonts. This fauna compares well with other Middle Triassic faunas from the Germanic and Alpine Triassic, and from the northern Gondwanan shelf, in particular with the fauna from Makhtesh Ramon, Negev.

Similar horizons were described in several sections by BRGM, in particular those that we mentioned at Khashm Dolqan (Figure 2, Darma quadrangle) and Al Mudarra–Didah (Supplementary Section B, Plate B.1, Qibah quadrangle), and by SGS at Ar Rubay'iyah within the Unit J1 and in particular near the top of this unit (Plate B.2). By comparison of the fossils with those from other localities, the age best estimated by Vickers-Rich would range from Late Anisian to Ladinian, close to the Anisian–Ladinian boundary. This estimate matches well the stratigraphy established herein by the other indicators (palynomorphs, bivalves, conodonts).

Kear *et al.* [2010a,b] conducted a new field survey near Ar Rubay'iyah, but also on the Reference Section of Khashm Dolqan which yielded large quantities of vertebrate fossils ranging from Upper Anisian to lowermost Carnian in age. These finds prompt a revision of the existing faunal list of sharks, fishes and marine reptiles, in particular the discovery of the lungfish, *Ceratodus* sp., [Kear *et al.*, 2010b]. The remains thus comprise sauropterygian marine reptiles (*Psephosaurus* sp., *Nothosaurus* cf. *tchernovi*, *Nothosaurus* cf. *giganteus*, *Simosaurus* sp.), a lungfish (*Ceratodus* sp.), hybodontiform sharks (*Hybodus* sp.) and saurichthyiform actinopterygians (*Saurichthys* sp.). For Kear *et al.* [2010b, p. 1]: “palaeobiogeographical assessment reinforces Tethyan affinities for the assemblage and reflects the close proximity of the Arabian region to the “Sephardic Realm”, a compositionally distinct circum-Mediterranean faunal province characterized by hypersaline “Muschelkalk facies”. This paleobiogeographic interpretation matches a similar conclusion by Vrielynck based on Ladinian conodonts (see in Part II, Section “paleogeography”).

5.3.2. Ladinian

The Ladinian is well constrained from south to north by the conodonts *Pseudofurnishius murcianus* Van Den Boogaard (Supplementary Section C,

Plate C.7), and *Budurovignathus truempyi* (Hirsch) at Khashm Dolqan (24°15'N), Khashm Midiya'ah (24°27'N) and Safra ar Ruwaydah (26°05'N). In the section at Khashm Midiya'ah the association *B. truempyi* and *B. cf. mungoensis* (Diebel) is indicative of the Late Ladinian [Hornung, 2006, Vrielynck, 1984, Vrielynck *et al.*, 1986], former *Protrachyceras archelaus* zone, Longobardian 2. In the south of the Qibah Quadrangle, the laterally correlated horizon (first main cuesta) is also of Ladinian age as confirmed by the recovery of *Pseudofurnishius shagami* [Benjamini and Chepstow-Lusty, 1986], and *P. cf. shagami* transitional to *Budurovignathus truempyi* (CRQ91-14 and 21). Note that this conodont association is slightly different in this northern area than more south, in other sections. This point could be explained in two different ways:

- **Age-based difference:** from Plasencia *et al.* [2015], *P. shagami* would be restricted to Fassanian (Early Ladinian), whereas southward, in coeval beds *P. murcianus*, although known possibly since Fassanian, proliferates in the uppermost Ladinian horizons in our sections and thus very likely in the Longobardian, in agreement with Plasencia *et al.* [2015, their Figure 8]. In this option, a satisfactory correlation with ammonoid zonation would appear for *P. shagami*, *B. truempyi* and *B. mungoensis* with Curionii, Gredleri, and former “Archelaus” zones (*cf.* Longobardicus), respectively. This hypothesis would imply a diachronic sheet-transgression on a ramp (coastal onlap), based on the occurrence of older (Fassanian) species in the north, and of younger (Longobardian) species only, south of Lat. 26°30'N (Fassanian hiatus). However, one remaining question is why the Longobardian would not be recognized in the north?
- **Environment-based difference:** one of the authors (LK) prefers an effect of the paleoenvironment on species distribution, with *Budurovignathus* associated to flooding events, or deeper settings, and *Pseudofurnishius* associated to the regressive phase, or shallower setting. This hypothesis is supported by the vertical distribution of the conodonts where the two are present, and by restriction of *Budurovignathus* to a more

marine area (lat. 24°27'N–26°21'N).

Fish debris are common in two separate horizons that can be identified at various locations along the full extent of the outcrop. As we have seen above in the previous paragraphs [Vickers-Rich *et al.*, 1999], the age of the upper beds of fish and reptiles remains found in several sections is compatible with the Ladinian age provided by conodonts.

5.3.3. Julian

A reasonable correlation is found at the base of the Julian carbonates with *M. carnica* (JMA83-160, VD82-29, VD82-120), in the condensed horizon with Fe-oolites, supporting its use for further correlations. A late Early Carnian age was confirmed in the south of the Qibah quadrangle by *M. carnica/baloghi* (CRQ91-38). Its presence is very likely related to a significant flooding event on the Arabian shallow shelf. In Hornung *et al.* [2007], the “auriformis” abundance zone (AZ) and “carnicus” interval zone are shown after Gallet *et al.* [1994, their Figure 2] within the late early Julian (Julian 1/II and base Julian 2). According to Kovacs [1977] and to the most recent paper by Kiliç *et al.* [2015], the *Mazzaella* lineage derives from *Quadralella auriformis* (Kovacs). *Q. aff. auriformis* (Kovacs) is present in sample VD82-129, just adjacent to VD82-120.

The Julian age on top of the formation at Khabra Halwah (23°58'N) is provided by *Paragondolella inclinata* (VD80-328). This species, which can be present in association with *B. mungoensis* since the Late Ladinian/Longobardian [Hornung, 2006], is found here as a Ladinian relict species which survives up to the extinction event at the Early/Late Carnian boundary [Rigo *et al.*, 2005].

5.3.4. Tuvalian

The populations of *Q. polygnathiformis*, though of large age range, are more frequent in the upper Jilh, where they would indicate either Julian or Tuvalian when in association with specific markers (*e.g.*, *P. inclinata* for the Julian and *Q. carpathica* for the Tuvalian). Its abundance zone is shown in Tuvalian 1 and Tuvalian 2/1 by Hornung *et al.* [2007, after Gallet *et al.*, 1994].

Q. carpathica (VD82-33) indicates an early to middle Tuvalian age. Similar to *M. carnica*, derived from *Quadralella* through a late Julian lineage, *Q. carpathica* derives from *Q. polygnathiformis* through a

Tuvalian lineage [Orchard, 2014]. Following Gallet *et al.* [1994, *in* Hornung *et al.*, 2007] the “carpathicus” abundance zone (AZ) is shown in the Tuvalian 2/II though the species may appear already in the early Tuvalian according to Mazza *et al.* [2012]. The specimens of trochitids ammonoids (JMA83-293) observed by J. Marcoux and L. Krystyn would be rather Tuvalian 1, eventually up to 2/I. In any case, this Tuvalian age is consistent with the specimens submitted to E. T. Tozer and with the last sample recently submitted to H. Bucher (YLN16-056) from the same horizon within the Buraydah Quadrangle. The reference section of the Qibah Quadrangle did not provide evidence of Tuvalian sediments, and thus, Tuvalian may have been partially absent or eroded and may be part of the Early Norian hiatus.

5.3.5. Norian

The Norian was first recognized in the Unit J3 of the Jilh Formation and in the Lower Minjur by *Epigondolella abneptis* (Huckriede), originally identified in the samples by Vrielynck [1984]. This species was regarded by previous authors as ranging throughout most of the Norian as well as the late Carnian.

The older forms assigned to this species were later subdivided into several subspecies by Orchard [1983], all ranging in the Laciian (Early Norian, his Figure 10); but this age conflicts with the age given by the co-occurring Middle Norian Tibetitidae.

Recently, Orchard [2018] assigned the Lower Norian “Epigondolellas” to the genus *Ancyrogondolella*, whereas Krystyn [2008] identified *Epigondolella abneptis* at its type locality as a distinct Middle Norian form.

This uncertainty was resolved by the new study on the Qibah conodonts. Five samples, from the reference section (CRQ 91-42, 43, 44, 45), and from coeval outcrops (CRQ 91-85 and CRQ92-2) yielded the same species of basal Middle Norian age (Alaunian 1): *Ancyrogondolella praeslovakensis* (Kozur, Masset and Moix) and another *Ancyrogondolella* of the *A. uniformis* group. *A. praeslovakensis* and the new *Ancyrogondolella* are found in many Alaunian 1 ammonoid-dated sections cited above (see Section 5.2, Section I).

Thus, both conodonts and ammonoids converge towards an early Alaunian age which implies a hiatus of more than 10 Ma, and likely greater (11–14 Ma) in the case of erosion of the Tuvalian, as in Qibah

area, where it has not been found. North of 25°30'N, continuity of facies and of environment, and lack of coarse-grained clastics which would reflect an obvious discontinuity or a sequence boundary, make causes and mechanisms of this hiatus hypothetical. In this case we would assume a transgressive erosional wedge (marine onlap). We have already formulated this hypothesis [Le Nindre *et al.*, 1987, 1990a], but on a different age basis.

At the upper contact with or at the base of the Minjur Sandstone, a good correlation is found by *E. abneptis* in several sections, from north to south: Az Zabirah (VD84-142), Jabal Mudarradj-Didah (CRQ91-45), Al Barud (JMA83-286), and Safra al Mustawi (VD82-34). One of the authors (LK), does not exclude that this horizon might be a bit younger in the Alaunian [according to the age range of *E. abneptis*, up to Alaunian 3 in Krystyn *et al.*, 2009].

5.4. Diachronous lithostratigraphic boundaries: erosional hiatuses

Previous studies of the conodonts and ammonoids (Jacques Manivit, Bruno Vrielynck and Eward T. Tozer in Le Nindre *et al.* [1987, 1990a]) had demonstrated that the historical Units J2 and especially J3 as defined in the south and in the north are diachronous (Figure 11). Increasingly, various publications document this diachroneity at a plate-wide scale. In particular, Davies and Simmons [2018], Davies *et al.* [2019] attempted to demonstrate this for the Sudair Shale in their Figure 5 while also showing the lower part of the Jilh Formation.

For explaining this diachroneity north of Lat. 25°30'N, Y. M. Le Nindre had invoked an erosional wedge, tentatively related to a transgressive Tuvalian surface. In fact, this new study, providing complementary and more accurate ages within this area demonstrates (Figure 12) that the main causes of this apparent diachroneity is a Carnian–Alaunian hiatus with a time gap greater than 10 Ma due to:

- A fluvial erosion by the Minjur sandstone; south of Lat 25°30'N, which incised the Jilh tidal deposits [see also Issautier *et al.*, 2019].
- A marine Tuvalian-Early Norian hiatus of more than 10 Ma (11–14 Ma?), north of Lat. 25°30', which can be still interpreted as a Norian transgressive erosional wedge.

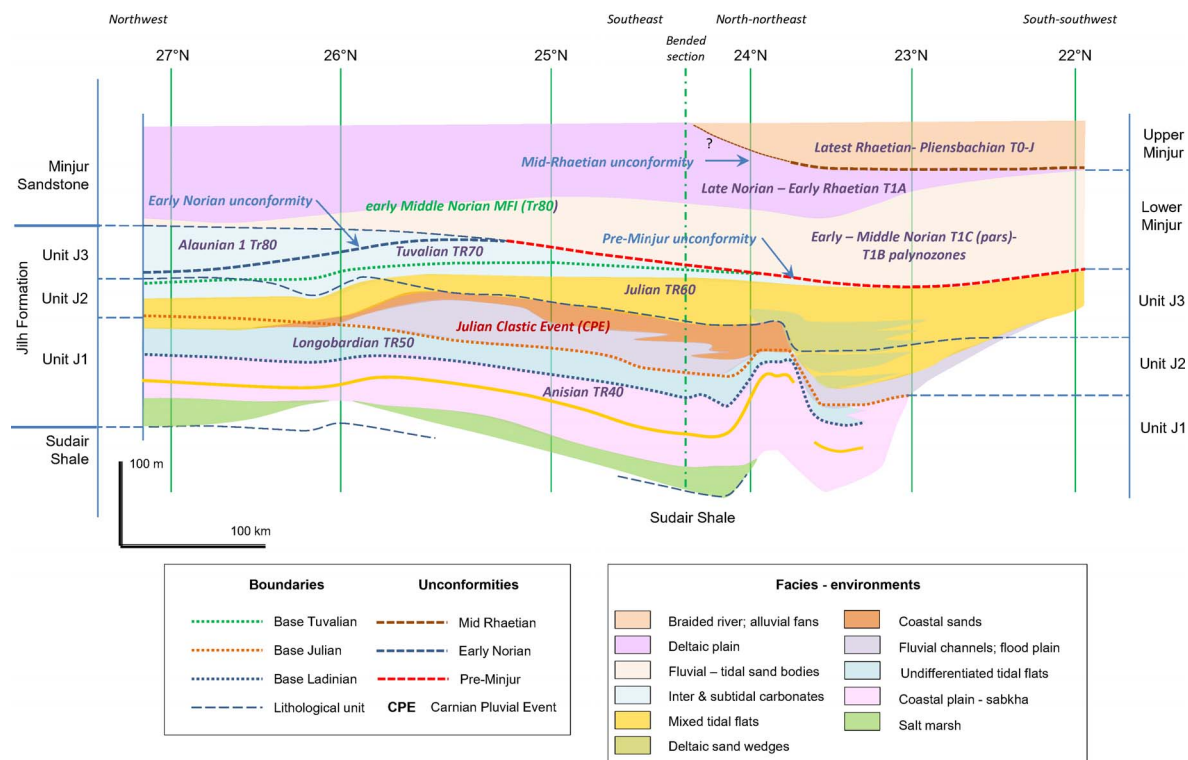


Figure 12. Conceptual sketch of the Jilh–Minjur systems in outcrop. Summary of lithological units, paleo-environments, ages, unconformities and flooding sequences including update from Issautier *et al.* [2019]. The Early Ladinian was not recognized south of Lat. 27°N. Correlations with regional maximum floodings (Tr), and CPE, are discussed in Part II.

The Early Norian disconformity or unconformity is thus more than a simple obliquity of time lines on stratigraphy. A dynamic reconstruction of the depositional structures by time slices in Part II better demonstrates all geometric relationships.

6. Conclusion on Part I: Jilh formation chronostratigraphy of the depositional units

(1) The Anisian to Carnian Jilh Formation crops out extensively in Central Saudi Arabia (latitudes 22°N to 28°N). It was previously mapped and analysed in 1990–1991 by BRGM geologists, who described predominantly mixed siliciclastic lithologies with subordinate carbonates and evaporites representing non-marine to offshore environments. The current study builds on this previous work.

- (2) Stratigraphic understanding of the Jilh Formation has been improved by analyses of new conodont finds and a re-evaluation of existing ammonoid data.
- (3) There is a pre-existing three-fold scheme of lithostratigraphic units for the Jilh Formation based on the field mapping of cuestas but the new biostratigraphic data confirms that these landforms are discontinuous and the units diachronous along the full length of the outcrop and should not be used as the basis for regional correlation. This raises the issue of the Jilh–Minjur boundary, addressed in Part II.
- (4) Four large scale transgressive–regressive cycles can be identified in the Jilh Formation. An Anisian flooding event is defined by tidal flat deposits. Ladinian, Julian (Early Carnian) and Tuvalian (Late Carnian) flooding events all culminated in fossiliferous

marine carbonates. The age of these marine carbonates are closely defined by the new conodont and re-evaluated ammonoid data. Of these flooding events, the Julian transgression was the most regionally extensive. The Tuvallian flooding event is missing by erosion in outcrops south of latitude 24°N.

- (5) The current study identifies a major influx of continental clastics at the end of the Ladinian, and in the early Julian, likely related to late Ladinian regression. It may have laterally equivalent evaporitic deposits. Subsequent marine transgressions reworked the deltaic sands brought by the rivers to long-shore coastal sand bodies.
- (6) Further subdivisions that are candidates for sequence boundaries in the Jilh Formation can be proposed at the base of the Julian clastics and at the base of the Late Julian transgression marked by iron oolites overlying paleosols.
- (7) At the Khashm al Khalta section, transitional facies previously assigned to the Minjur Sandstone are now included in the Jilh Formation and cap the Julian Jilh dolomite equivalent. They are overlain by erosional channel sandstones.
- (8) South of latitude 25°30'N, an erosional unconformity marks the boundary between the Jilh Formation and the overlying Early Norian (pars) to Early Jurassic, continental to marginal marine Minjur Sandstone, previously described by Issautier *et al.* [2019]. The unconformity is readily identified in southern outcrops where fluvial sandstones erosively overlie mixed marginal marine deposits of the Jilh Formation (Figure 12). It accounts for the southward erosion of the Tuvallian flooding event beneath Norian fluvial sandstones.
- (9) North of latitude 25°30'N, ammonoids and conodont finds are reported from the upper part of the Jilh Formation and the basal part of the Minjur Sandstone. Together with previously documented dinoflagellate cyst data, these new finds identify a ≥ 10 Ma hiatus covering part of the Tuvallian and the Early Norian. These observations unequivocally demonstrate that the

lithostratigraphic boundary between the Jilh Formation and the Minjur Sandstone lies above the Carnian–Norian hiatus in outcrops north of 25°30'N but marks the hiatus itself in outcrops further south. The finds also confirm the presence of a Middle Norian (Alaunian) transgression that corresponds to the *Rhaetogonyaulax wigginsii* flooding event identified by Issautier *et al.* [2019] (Figure 12). The latter authors identified a second, younger flooding event associated with the dinoflagellate cyst *Rhaetogonyaulax rhaetica*.

- (10) The identification of probable 3rd order transgressive–regressive cycles and a major hiatus provides a strong foundation for sequence stratigraphic analysis and regional correlations. Correlations within the outcrops of the Jilh Formation and overlying Minjur Sandstone and into the near subsurface [Issautier *et al.*, 2019] highlight geometric and chronostratigraphic aspects of the stratigraphy (Figure 12). This discussion is continued in Part II.

Conflicts of interest

Authors have no conflict of interest to declare.

Acknowledgments

The authors thank the Deputy Ministry for Mineral Resources, Kingdom of Saudi Arabia, for his support to the Phanerozoic Cover Rock Mapping Program during which most of the field works were performed and for permission to publish (BRGM-OF-06-31). The publication of this Synthesis on the Triassic of Saudi Arabia was made possible through this Special Publication as a Tribute to Jean Dercourt under the auspices of the French Académie des Sciences. Authors are especially grateful to the editors François Baudin, Sorbonne Université, François Chabaux, Strasbourg University and Eric Calais, Ecole Normale Supérieure for their invitation, encouragement, and support. The authors have special thanks to Augustus Wilson and to Moujahed I. Al-Husseini, former Editor in Chief of GeoArabia, for their constructive comments while writing this paper. The new decisive results on conodonts from the

Qibah area by Leopold Krystyn were made possible thanks to the support provided by Benoit Issautier and Olivier Serrano, BRGM. Thanks to James W. Haggart from the Geological Survey of Canada who very kindly spared his time for providing photos of the original Tozer's collection of ammonoids in Vancouver, and to Raymond Enay, for specimens stored in the University Lyon I, we have now illustration of this key fauna. The authors are also very grateful to Nino Buhay, former graphic team of GeoArabia. We thank Mike Simmons and an anonymous reviewer whose insightful comments greatly improved the paper.

Supplementary data

Supporting information for this article is available on the journal's website under <https://doi.org/10.5802/crgeos.217> or from the author.

References

- Arkell, W. J. (1952). Jurassic ammonoids from Jebel Tuwaiq, central Arabia, with Stratigraphical introduction by R. A. Bramkamp and M. Steineke. *Philos. Trans. Royal Soc. Lond. B*, 236, 241–313.
- Benjamini, C. and Chepstow-Lusty, A. (1986). Neospathodus and other conodonts from the Saharonim formation (Anisian-Ladinian) at Makhtesh Ramon, Negev, southern Israel. *J. Micropalaeontol.*, 5, 67–75.
- Chen, Y., Krystyn, L., Orchard, M. J., Lai, X.-L., and Richoz, S. (2015). A review of the evolution, biostratigraphy, provincialism and diversity of Middle and Early Late Triassic conodonts. *Pap. Palaeontol.*, 2(2), 235–263.
- Clifton, H. E. (1982). Estuarine deposits. In Scholle, A. and Spearing, D., editors, *Sandstone Depositional Environments*, volume 31 of *AAPG Memoir*, pages 179–189. American Association of Petroleum Geologists, Tulsa. ISBN: 0-89181-307-1.
- Davies, R. B. and Simmons, M. D. (2018). Triassic sequence stratigraphy of the Arabian plate. In Pöppelreiter, M. C., editor, *Lower Triassic to Middle Jurassic Sequence of the Arabian Plate*, pages 101–162. EAGE Publications bv, The Netherlands.
- Davies, R. B., Simmons, M. D., Jewell, T. O., and Collins, J. (2019). Regional controls on siliciclastic input into Mesozoic depositional systems of the Arabian Plate and their petroleum significance. In AlAnzi, H. R., Rahmani, R. A., Steel, R. J., and Soliman, O. M., editors, *Siliciclastic Reservoirs of the Arabian Plate*, volume 116 of *AAPG Memoir*, pages 103–140. American Association of Petroleum Geologists, Tulsa.
- El-Atfy, H., Aba Alkhayl, S. S., and Uhl, D. (2022). Zambites (Bennettitales) from the Minjur Formation (Norian) of Saudi Arabia—a unique record from the Late Triassic palaeotropics of Gondwana. *Bot. Lett.*, 169(4), 588–597.
- Gallet, Y., Besse, J., Krystyn, L., Theveniaut, H., and Marcoux, J. (1994). Magnetostratigraphy of the Mayerling section (Austria) and Erenkolu Mezarlik (Turkey) section: improvement of the Carnian (late Triassic) magnetic polarity time scale and the Carnian origin of calcareous nannoplankton and dinosaurs. *Geology*, 34(12), 1009–1012.
- Ginsburg, R. N., editor (1975). *Tidal Deposits. A Casebook of Recent Examples and Fossils Counterparts*. Springer Verlag, Berlin, Heidelberg, New-York. 6 sections. 428 p. ISBN 3-540-06823-6, 0-387-06823-6 (New-York).
- Hornung, T. (2006). Conodonts biostratigraphy of the Lercheck/Königsleiten section near Berchtesgaden, (Late Ladinian, Hallstatt Limestone). *Geo. Alp.*, 3, 23–31.
- Hornung, T., Bradner, R., Krystner, L., Joachimski, M. M., and Keim, L. (2007). Multistratigraphic constraints on the New Tethyan “Carnian Crisis”. In Lucas, S. G. and Spielmann, J. A., editors, *The Global Triassic*, New Mexico Museum of Natural History and Science Bulletin 41, pages 59–67. The New Mexico Museum of Natural History & Science, New Mexico.
- Issautier, B., Le Nindre, Y. M., Hooker, N., Reid, C., Memesh, A., and Dini, S. (2019). Depositional environments, age, and sequence stratigraphy of the Minjur Formation in outcrop and near subsurface—Central Saudi Arabia. In Al-Anzi, H. R., Rahmani, R. A., Steel, R. J., and Soliman, O. M., editors, *Siliciclastic Reservoirs of the Arabian Plate*, volume 116 of *AAPG Memoir*, pages 141–184. American Association of Petroleum Geologists, Tulsa.
- Issautier, B., Le Nindre, Y. M., Memesh, A., Dini, S., and Viseur, S. (2012a). Managing clastic reservoir heterogeneity I: Sedimentology and sequence stratigraphy of the Late Triassic Minjur Sandstone at the Khashm al Khalta type locality, Central Saudi

- Arabia. *GeoArabia*, 17(2), 17–56.
- Issautier, B., Le Nindre, Y. M., Viseur, S., Memesh, A., and Dini, S. (2012b). Managing clastic reservoir heterogeneity II: Geological modeling and reservoir characterisation of the Minjur Sandstone at the Khashm al Khalta type locality (Central Saudi Arabia). *GeoArabia*, 17(3), 61–80.
- Kear, B. P., Rich, T. H., Vickers-Rich, P., Ali, M. A., Al-Mufarrih, Y. A., Matari, A. H., Masary, A. M., and Halawani, M. A. (2010a). A review of aquatic vertebrate remains from the Middle–Upper Triassic Jilh Formation of Saudi Arabia. *Proc. R. Soc. Victoria*, 122(1), 1–8. ISSN 0035-9211.
- Kear, B. P., Rich, T. H., Vickers-Rich, P., Ali, M. A., Al-Mufarrih, Y. A., Matiri, A. H., Masary, A. M., and Halawani, M. A. (2010b). First Triassic lungfish from the Arabian Peninsula. *J. Paleontol.*, 84, 137–140.
- Kiliç, A. M., Plasencia, P., Ishida, K., and Hirsch, F. (2015). The case of the Carnian (Triassic) Conodont Genus *Metapolygnatus* Hayashi. *J. Earth Sci.*, 26(2), 219–223.
- Kovacs, S. (1977). New conodonts from the North Hungarian Triassic. *Acta Miner. Petr. Szeged*, 23, 77–90.
- Krystyn, L. (2008). An ammonoid-calibrated Tethyan conodont time scale of the late upper Triassic. *Berichte Geol. B.-A.*, 76, 9–11. ISSN 1017-8880—Upper Triassic ... Bad Goisern (28.09–02/10/2008).
- Krystyn, L., Mandl, G., and Schauer, M. (2009). Growth and termination of the upper Triassic platform margin of the Dachstein area (Northern Calcareous Alps, Austria). *Aust. J. Earth Sci.*, 102, 23–33.
- Le Nindre, Y. M. (1971). Étude des traces laissées par des invertébrés marins dans les sédiments meubles de la zone intertidale. Thèse Docteur en Sciences Biologiques Université Bordeaux I. Décembre 1971. 2 volumes. I. Texte, 101 p., II, Illustrations, 55 pl.
- Le Nindre, Y. M., Benhammouda, S., Rouzeau, O., Haas, H., and Quessette, J. A. (2001). Elaboration d'un outil de gestion de la Côte Aquitaine. Phase 3: diagnostic d'évolution et recommandations. Contribution du BRGM. Rapport BRGM RP-50822-FR, 115 p., 55 fig., 5 tabl., 2 ann. <http://infoterre.brgm.fr/rapports//RP-50822-FR.pdf>.
- Le Nindre, Y. M., Bodéré, G., Izac, J. L., Putot, E., Levasseur, J., and Rossignol, B. (2006). Etude pour le maintien de l'équilibre bio-sédimentaire des estrans de la côte sud du bassin d'Arcachon. Rapport BRGM RP-54814-FR, 129 p., 24 tabl., 93 fig., 4 ann. <http://infoterre.brgm.fr/rapports//RP-54814-FR.pdf>.
- Le Nindre, Y. M. and Dutartre, Ph. (1993). Découverte spatiale du bassin d'Arcachon. In *With collaboration of J.M. Bouchet, P.J. Labourg, A. Berthiaux, L. Minoux, F. Giraud, and support of Association Française des Sédimentologistes (A.S.F.)*, Document du BRGM, n° 215. Editions BRGM, Orléans, France. 105 p., 27 fig. 1 tabl., 27 photo-plates. Bib. References. 1993. ISBN 2-7159-0680-3. <http://infoterre.brgm.fr/rapports//89-SGN-410-GEO-TED.pdf>.
- Le Nindre, Y. M., Fauconnier, D., Rouzeau, O., Chassignol, A. L., Le Pochat, G., Dutartre, Ph., Manaud, E., L'yavanc, J., Loarer, R., Trut, G., and Tougeron, C. (1999). Elaboration d'un outil de gestion de la Côte Aquitaine. Phase 2: image actuelle. Rapport de synthèse. Rapport BRGM RR-40178-FR-IFREMER R.INT.DEL/99/00, 51 p., 18 fig., 6 tabl., 5 ann. <http://infoterre.brgm.fr/rapports//RR-40178-FR.pdf>.
- Le Nindre, Y. M., Le Pochat, G., Dutartre, Ph., Chassignol, A. L., Manaud, E., Dreno, J. P., L'yavane, J., and Guchamp, A. (1998). Elaboration d'un outil de gestion prévisionnelle de la côte Aquitaine. Phase 1: reconnaissance, évolution historique. Rapport de synthèse. Rapport BRGM RR-39882-FR-IFREMER R.INT.DEL/97.12, 78 p., 21 fig., 7 tabl., 17 ph., 1 pl., 5 ann. <http://infoterre.brgm.fr/rapports//RR-39882-FR.pdf>.
- Le Nindre, Y. M., Levasseur, J. E., Benhammouda, S., Cottet, M., and Lafon, T. (2004). Etude pour le maintien de l'équilibre bio-sédimentaire des plages du Nord-Est dans le Bassin d'Arcachon. Rapport BRGM RP-53282-FR, 101 p., 60 fig., 15 tabl., 6 ann. <http://infoterre.brgm.fr/rapports//RP-53282-FR.pdf>.
- Le Nindre, Y. M., Manivit, J., and Vaslet, D. (1987). Histoire géologique de la bordure occidentale de la plate-forme arabe du Paléozoïque inférieur au Jurassique supérieur (en 4 livres). Thèses de Doctorat ès Sciences Naturelles, Université Pierre et Marie Curie, Paris VI, 3 juin 1987.
- Le Nindre, Y. M., Manivit, J., and Vaslet, D. (1990a). Le Permo-Trias d'Arabie centrale. In *Histoire géologique de la bordure occidentale de la plate-forme arabe*, Vol. 3, Documents du BRGM, n° 193.

- Editions du BRGM, Orléans. ISSN: 0221-2536, ISBN: 2-7159-0507-6. 290 p., 51 fig., 4 tabl., 11 pl., 3 annexes.
- Le Nindre, Y. M., Manivit, J., and Vaslet, D. (1990b). Géodynamique et Paléogéographie de la Plate-Forme Arabe du Permien au Jurassique. In *Histoire Géologique de la Bordure Occidentale de la Plate-Forme Arabe, Vol. 2*, Documents du BRGM, n° 192. Editions du BRGM, Orléans. ISSN: 0221-2536, ISBN: 2-7159-0497-5. 273 p. 54 fig., 4 tab., 4 annexes.
- Le Nindre, Y. M., Thom, C., Souchon, J. Ph., Benhammouda, S., Siguié, C., and Rouzeau, O. (2000). Terra Symphonie—Aménagement intégré du Bassin d'Arcachon. Etude n°5: Mise au point d'un outil de surveillance et d'aide à la décision en matière d'exhaussement des fonds du Bassin d'Arcachon. Rapport BRGM RP-50578-FR. 67 p., 22 fig., 3 tabl., 1 ann. <http://infoterre.brgm.fr/rapports//RP-50578-FR.pdf>.
- Le Nindre, Y. M., Vaslet, D., Le Metour, J., Bertrand, J., and Halawani, M. (2003). Subsidence modelling of the Arabian platform from Permian to Paleogene outcrops. *Sediment. Geol.*, 156(1–4), 263–285.
- Lebret, P., Halawani, M. A., Memesh, A., Bourdillon, C., Janjou, D., Le Nindre, Y. M., Roger, J., Shorbaji, H., and Kurdi, H. (1999). *Geologic map of the Turubah quadrangle, Kingdom of Saudi Arabia. Geoscience Map GM-63C, scale 1:250,000, sheet 28F*. Deputy Ministry for Mineral Resources, Ministry of Petroleum and Mineral Resources, Kingdom of Saudi Arabia. Explanatory notes, 46 p.
- Manivit, J., Pellaton, C., Vaslet, D., Le Nindre, Y. M., Brosse, J. M., Breton, J. P., and Fourniguet, J. (1985a). *Geologic map of the Darma' Quadrangle, Kingdom of Saudi Arabia. Geoscience map GM-101C, scale 1:250,000, sheet 24H*. Deputy Ministry for Mineral Resources, Ministry of Petroleum and Mineral Resources, Kingdom of Saudi Arabia. Explanatory notes, 33 p.
- Manivit, J., Pellaton, C., Vaslet, D., Le Nindre, Y. M., Brosse, J. M., and Fourniguet, J. (1985b). *Geologic map of the Wadi Al Mulayh Quadrangle, Kingdom of Saudi Arabia. Geoscience Map GM-92C, scale 1:250,000, sheet 22H*. Deputy Ministry for Mineral Resources, Ministry of Petroleum and Mineral Resources, Kingdom of Saudi Arabia. Explanatory notes, 32 p.
- Manivit, J., Vaslet, D., Berthiaux, A., Le Strat, P., and Fourniguet, J. (1986). *Explanatory notes to the geologic map of the Buraydah Quadrangle, Kingdom of Saudi Arabia. Geoscience Map GM-114 C, scale 1:250,000, sheet 26G*. Deputy Ministry for Mineral Resources, Ministry of Petroleum and Mineral Resources, Kingdom of Saudi Arabia. Explanatory notes, 32 p.
- Mazza, M., Rigo, M., and Gullo, M. (2012). Taxonomy and stratigraphic record of the Upper Triassic conodonts of the Pizzo Mondello section (Western Sicily, Italy), GSSP candidate for the base of the Norian. *Riv. Ital. Pale. Stratigr.*, 118, 85–130.
- McCubbin, D. G. (1982). Barrier island and strand plain facies. In Scholle, A. and Spearing, D., editors, *Sandstone Depositional Environments*, volume 31 of *AAPG Memoir*, pages 247–279. American Association of Petroleum Geologists, Tulsa. ISBN: 0-89181-307-1.
- Moix, P., Kozur, H. W., Stampfli, G. M., and Mostler, H. (2007). New paleontological, biostratigraphic and paleogeographic results from the Triassic of the Mersin Mélange, SE Turkey. *New Mexico Mus. Nat. Hist. Sci. Bull.*, 41, 282–311.
- Orchard, M. J. (1983). *Epigondolella* populations and their phylogeny and zonation in the Upper Triassic. *Foss. Strata.*, 15, 177–192.
- Orchard, M. J. (2014). Conodonts from the Carnian-Norian Boundary (Upper Triassic) of Black Bear Ridge, southeastern British Columbia, Canada. *New Mexico Mus. Nat. Hist. Sci. Bull.*, 64, 1–139.
- Orchard, M. J. (2018). The Lower-Middle Norian (Upper Triassic) boundary: New conodont taxa and a refined biozonation. *Bull. Am. Paleontol.*, 395–396, 165–193.
- Plasencia, P., Hirsch, F., Sha, J., and Márquez-Aliaga, A. (2015). Taxonomy and evolution of the Triassic conodont *Pseudofurnishi*. *Acta Palaeontol. Pol.*, 60(2), 385–394.
- Powers, R. W. (1968). *Lexique Stratigraphique International*, volume III of *Asie, Fas. 10 b1, Arabie Saoudite*. Centre National de la Recherche Scientifique, Paris.
- Powers, R. W., Ramirez, L. F., Redmond, C. D., and Elberg Jr., E. L. (1966). Geology of the Arabian Peninsula: Sedimentary geology of Saudi Arabia. United States Geological Survey Professional Paper 560-D, 147 p.
- Rigo, M., Preto, N., Roghi, G., and Stanley, S. M. (2005). Upper Triassic conodont extinction events.

- Geophys. Res. Abstr.*, 7, article no. 02339. SRef-ID: 1607-7962/gra/EGU05-A-02339. © European Geosciences Union 200.
- Robelin, C., Al-Muallem, M. S., Brosse, J. M., Fourniguet, J., Garcin, M., Gouyet, J.-F., Halawani, M. A., Janjou, D., and Le Nindre, Y. M. (1994). *Geologic map of the Qibah Quadrangle, Kingdom of Saudi Arabia. Geoscience Map GM-136, scale 1:250,000, sheet 27G.* Deputy Ministry for Mineral Resources, Ministry of Petroleum and Mineral Resources, Kingdom of Saudi Arabia. Explanatory notes, 33 p.
- Scholle, P. A., Bebout, D. G., and Moore, C. H., editors (1983). *Carbonate Depositional Environments*, volume 33 of *AAPG Memoir*. American Association of Petroleum Geologists, Tulsa. ISBN: 0-89181-310-1.
- Scholle, P. A. and Spearing, D., editors (1982). *Sandstone Depositional Environments*, volume 31 of *AAPG Memoir*. American Association of Petroleum Geologists, Tulsa. ISBN: 0-89181-307-1.
- Sharief, F. A. M. (1977). *Sedimentary facies of the Jilh Formation, Saudi Arabia. A regional paleostratigraphy and tectonic evolution of the Middle East during the Middle Triassic period.* PhD thesis, Rice University, Houston, Texas. 117 p.
- Sharief, F. A. M. (1981). Transgressive-regressive intervals of the Tethys sea in the Middle Triassic Jilh Formation, Saudi Arabia. *Stratigr. Newlett., Berlin*, 10(3), 127–139. 9 fig., 1 tabl.
- Sharland, P. R., Archer, R., Casey, D. M., Davies, R. B., Hall, S. H., Heward, A. P., Horbury, A. D., and Simmons, M. D. (2001). *Arabian Plate Sequence Stratigraphy*, volume 2 of *GeoArabia Special Publication*. Gulf PetroLink, Bahrain.
- Steineke, M. and Bramkamp, A. (1952). Mesozoic rocks of eastern Saudi Arabia. *Am. Assoc. Pet. Geol. Bull. Abstr.*, 36(5), 909.
- Stewart, S. A., Reid, C. T., Hooker, N. P., and Kharouf, O. W. (2016). Mesozoic siliciclastic reservoirs and petroleum system in the Rub' Al-Khali basin, Saudi Arabia. *Am. Assoc. Pet. Geol. Bull.*, 100(5), 819–841.
- Vachard, D., Gaillot, J., Vaslet, D., and Le Nindre, Y. M. (2005). Foraminifers and algae from the Khuff Formation (late Middle Permian-Early Triassic) of central Saudi Arabia. *GeoArabia*, 10(4), 137–186.
- Vaslet, D., Beurrier, M., Villey, M., Manivit, J., Le Strat, P., Le Nindre, Y. M., Berthiaux, A., Brosse, J. M., and Fourniguet, J. (1985a). *Geological map of the Al Faydah Quadrangle, sheet 25G.* Saudi Arabian Deputy Ministry for Mineral Resources, Kingdom of Saudi Arabia. Geosciences Maps GM-102A, scale 1:250,000. Explanatory notes, 28 p.
- Vaslet, D., Kellogg, K. S., Berthiaux, A., Le Strat, P., and Vincent, P. L. (1987). *Geologic map of the Baq'a Quadrangle, Kingdom of Saudi Arabia. Geoscience Map GM-116 C, scale 1:250,000, sheet 27F.* Deputy Ministry for Mineral Resources, Ministry of Petroleum and Mineral Resources, Kingdom of Saudi Arabia. Explanatory notes, 45 p.
- Vaslet, D., Le Nindre, Y. M., Vachard, D., Broutin, J., Crasquin-Soleau, S., Berthelin, M., Gaillot, J., Halawani, M., and Al-Husseini, M. I. (2005). The Permian-Triassic Khuff Formation of central Saudi Arabia. *GeoArabia*, 10(4), 77–134.
- Vaslet, D., Manivit, J., Le Nindre, Y. M., Brosse, J. M., Fourniguet, J., and Delfour, J. (1983). *Geologic map of the Wadi Ar Rayn Quadrangle, Kingdom of Saudi Arabia. Geoscience Map GM-63C, scale 1:250,000, sheet 23H.* Deputy Ministry for Mineral Resources, Ministry of Petroleum and Mineral Resources, Kingdom of Saudi Arabia. Explanatory notes, 46 p.
- Vaslet, D., Pellaton, C., Manivit, J., Le Nindre, Y. M., Brosse, J. M., and Fourniguet, J. (1985b). *Geologic map of the Sulayyimah Quadrangle, Kingdom of Saudi Arabia. Geoscience Map GM-100C, scale 1:250,000, sheet 21H.* Deputy Ministry for Mineral Resources, Ministry of Petroleum and Mineral Resources, Kingdom of Saudi Arabia. Explanatory notes, 31 p.
- Vickers-Rich, P., Rich, T. H., Rieppel, O., Thulborn, R. A., and McClure, H. A. (1999). A Middle Triassic vertebrate fauna from the Jilh Formation, Saudi Arabia. *Neues Jahrb. Geol. Paläontol. Abh.*, 213, 201–232.
- Vrielynck, B. (1984). Révision des gisements à conodontes de l'Anisien supérieur et du Ladinien des Alpes carniques occidentales et des Dolomites (Italie du Nord). *Geobios, Lyon*, 17(2), 177–199.
- Vrielynck, B., Manivit, J., Vaslet, D., and Le Nindre, Y. M. (1986). Conodont stratigraphy of the Jilh Formation and the base of the Minjur Sandstone. Middle and Late Triassic (Central Saudi Arabia). Identification of depositional diachronism. Saudi Arabia Deputy ministry for Mineral Resources. Open File Report BRGM-OF-06-31, 13 p., 5 fig.



Research article

Tribute to Jean Dercourt

The Middle to Late Triassic of Central Saudi Arabia with emphasis on the Jilh Formation. Part II: sequence stratigraphy, depositional and structural history, correlations and paleogeography

Yves-Michel Le Nindre ^{*a}, Roger Brett Davies ^b, Benoit Issautier ^c, Leopold Krystyn ^d, Denis Vaslet ^e, Bruno Vrielynck ^f and Abdullah Memesh ^g

^a Geo-consultant (BRGM retired), 58 Rue Gustave Flaubert 45100, Orléans, France

^b Davies Geoconsulting (retired), Wintergreen House, Queen's Road, Harrogate, North Yorkshire, HG2 0HB, UK

^c BRGM, 3, Avenue Claude Guillemin, B.P. 36009, 45060, Orléans Cedex 2, France

^d Dept. of Palaeontology (Geozentrum), University of Vienna, Althanstrasse 14, Josef-Holaubek-Platz 2 (UZA II) 1090 Vienna (retired), Austria

^e Geo-consultant (BRGM retired), 275 Route Royale, 33240 La Lande de Pomerol, France

^f Institut des Sciences de la Terre de Paris (UMR 7193), Université Pierre et Marie Curie (UPMC) (retired), France

^g Saudi Geological Survey, 54141, Ahmed bin Mohammed Al Ashab St., Jeddah 21514, Saudi Arabia

E-mails: yc.lenindre@wanadoo.fr (Y.-M. Le Nindre),

davies.geoconsulting@btinternet.com (R. B. Davies), b.issautier@brgm.fr

(B. Issautier), leopold.krystyn@univie.ac.at (L. Krystyn), d-d.vaslet@wanadoo.fr

(D. Vaslet), bruno.vrielynck@orange.fr, bjm.vrielynck@orange.fr (B. Vrielynck),

Memesh.AM@sgs.gov.sa (A. Memesh)

Abstract. New biostratigraphic data reported by Le Nindre et al. (2023 – this volume) improve the sequence stratigraphic understanding of the Middle–Late Triassic mixed carbonate-siliciclastic Jilh Formation and overlying siliciclastic Minjur Formation at outcrop in Central Saudi Arabia. The Anisian Tr40, Ladinian Tr50, Julian Tr60, Tuvanian Tr70 and Alauanian Tr80 MFS are all identified and their ages discussed. A major Carnian–Norian hiatus (Tr80 SB) approximates to but notably cuts across the mapped Jilh–Minjur Formation boundary. A younger Late Norian–Rhaetian transgression (Tr90 MFS?) is also identified. All of these major transgressive–regressive sequences and hiatuses can be identified with confidence and correlated at the regional scale with time-equivalent carbonates. The ages of subsurface lithostratigraphic units identified elsewhere across the Arabian Plate, notably the “Jilh, Sefidar and Marker Dolomites”, “Jilh Evaporite” (sometimes “Carnian Salinity Crisis”) and the *incertae sedis* Baluti Formation, and their equivalence in the Saudi Arabian outcrops, are assessed in the light

* Corresponding author.

of these results. The presence of significant siliciclastics at the base of the Carnian stratigraphy (“Julian Clastic Event”) is also discussed.

Ladinian conodont faunas belonging to the Sephardic Province (Iberia, North Africa) and associated vertebrate faunas confirm transgression from the north. Similar conclusions are drawn for the Carnian and Norian transgressions.

The improved geochronologic understanding enabled a reconstruction of the structural phases of the Jilh geohistory in four steps from Anisian to Norian, showing the relationships of retrogradation–progradation processes and tectonic pulses to hiatuses and periods of erosion. A synthetic sequence stratigraphy is proposed.

Keywords. Saudi Arabia, Triassic, Jilh Formation, Minjur Sandstone, Sequence stratigraphy, Correlations, Paleogeography.

Manuscript received 2 March 2023, revised 24 June 2023, accepted 26 June 2023.

1. Introduction

This study is the second part of an updated reconstruction of the sedimentary complex formed by the Jilh Formation and the overlying Minjur Sandstone (Middle and Late Triassic) in Saudi Arabia and adjacent countries, principally, but not exclusively, from outcrop data. It builds on a factual litho- and biostratigraphic base set up in Part I [Le Nindre *et al.*, 2023], which the reader should refer to, in a first stage.

Part I of this study (this volume), provided updated and detailed descriptions of the litho- and biostratigraphy of the Middle to Late Triassic Jilh Formation and Minjur Sandstone along a 50 km-wide outcrop belt extending between latitudes 28° N and 21° N, along the eastern margin of the Arabian Shield (Figure 1). Together with the Permian–Early Triassic Khuff Formation and the Early Triassic Sudair Shale, these formations form an unconformable cover over the Pre-Permian rocks, and are in turn unconformably overlain by Jurassic and younger formations [Powers *et al.*, 1966, Powers, 1968]. Le Nindre *et al.* [1987, 1990b] published a revised description of the lithostratigraphy, biostratigraphy and sedimentology of the Permian–Triassic at outcrop, based on the results of the cover rock geological mapping program at 1:250,000 scale by the Directorate Mineral Resources of Saudi Arabia (DMMR) and France’s Geological Survey (BRGM). More recent publications provide a detailed description and interpretation of the underlying Khuff Formation [e.g. Vachard *et al.*, 2005, Vaslet *et al.*, 2005] and overlying Minjur Sandstone [Issautier *et al.*, 2012a,b, 2019, Figure 2].

Key results of Part I were provided by new analyses of conodonts, and a revision of previous ammonoids identifications, including a new specimen collected in 2016. In particular Part I identified an Early Norian hiatus of more than 10 Ma within the upper Jilh For-

mation accompanied by marine and fluvial erosion.

Most of the Arabian Plate suffers from poor biostratigraphic age control during the Triassic. It is only in a few sections near the margins of the Arabian Plate or outcrops such as those described in Part I that have yielded good faunal or floral evidence. This emphasises the importance of new biostratigraphic data from the Central Saudi Arabian outcrops (documented in Part I, this volume) to understanding the more regional picture.

This Part II describes the internal organization of the transgressive–regressive (T–R) depositional sequences in the Jilh Formation and Minjur Sandstone based on precise dating by conodonts and ammonoids. Comparisons are made to regional maximum flooding events. From this point, reference to stages and substages, palynozones, sequences and maximum floodings is preferred to lithological units. Building on this, it is possible to reconstruct the tectonic and depositional history of the Jilh Formation and provide an overall sequence stratigraphic framework for the Middle to Late Triassic outcrops. Applying this knowledge to published sections of the Jilh Formation in the Central Ghawar area and eastwards into the eastern Rub al Khali Bains [Deville de Periere *et al.*, 2022] demonstrates the applicability of the scheme at a regional scale. By including new data on Minjur Sandstone stratigraphy [Issautier *et al.*, 2019], this analysis provides a correlation tool for the entire Middle to Late Triassic stratigraphy, extending from the outcrops to subsurface sections at the platform scale regardless of lateral facies changes.

Biogeographic and paleogeographic considerations demonstrate the northerly provenance of transgressions in the Middle to Late Triassic setting. An updated chronostratigraphic chart of the Permian to Mid Toarcian sedimentation includes these new results and summarizes the overall time evolution of

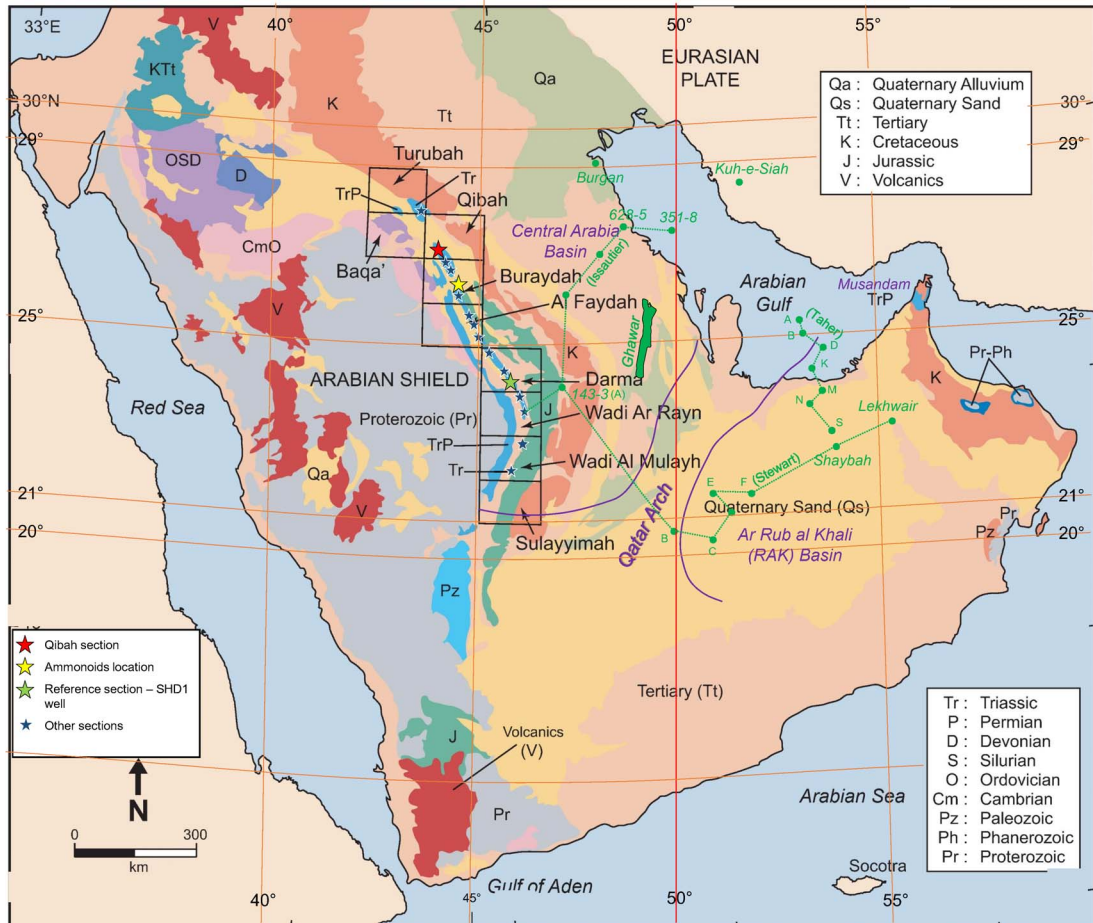


Figure 1. Simplified geological map of the Arabian Peninsula showing the quadrangles in which the Jilh Formation crops out. These quadrangles in Central Saudi Arabia were mapped by the DMMR (now Saudi Geological Survey) and France's BRGM (Hawasina nappes in Oman not shown, Qatar Arch from Stewart *et al.*, 2016; in green, wells and transects cited in the text).

the depositional systems.

2. Geometry and ages of the depositional sequences

Accounting for both the system tracts geometry, obtained by mapping lithology and paleoenvironments, and the ages of the main marine intervals obtained from conodont and ammonite biostratigraphy in Part I, it is now possible to combine the two in order to reconstruct isochronous depositional sequences (Figure 5). This exercise demonstrates the importance of combining age and sequence stratigraphy to reconstruct a correct and

reliable geometry, based on genetic criteria. It faithfully reflects the depositional mechanisms, beyond the apparent lithostratigraphy, as seen section after section over more than 880 km. The results highlight structural processes, erosional surfaces and unconformities, as discussed below (Figures 6a–d and 7).

2.1. Maximum flooding intervals and surfaces

There is limited consensus on sequence stratigraphic schemes for the Triassic of the Arabian Plate, mainly due to the sparsity of biostratigraphic control. The most widely cited scheme, Sharland *et al.*'s [2001] sequence stratigraphic model for the

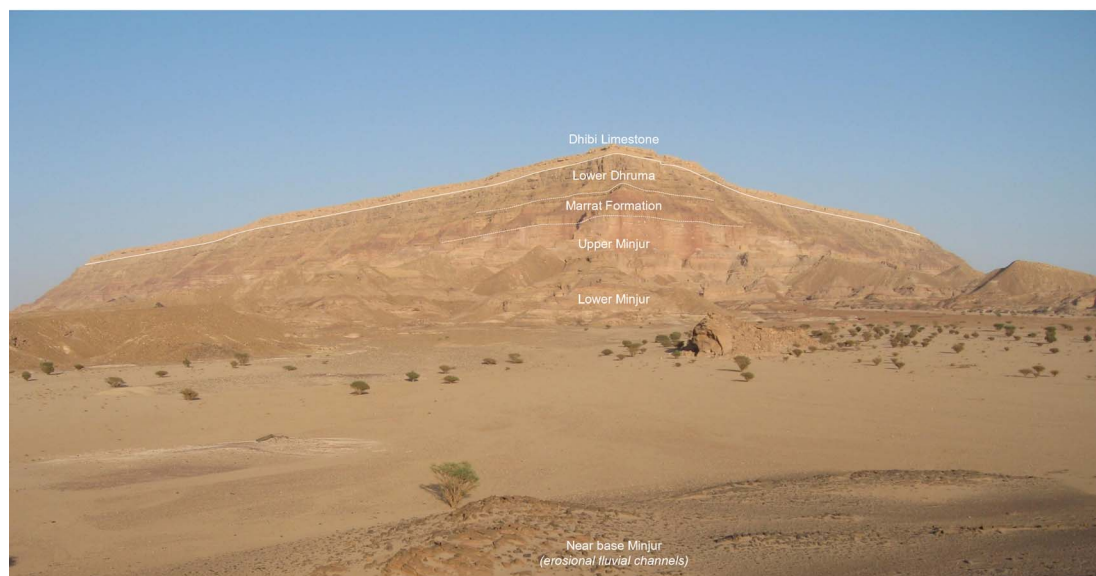


Figure 2. The Khashm al Khalta (K. al Minjur) promontory, type locality of the Minjur Sandstone, capped by the Marrat Formation, and the Lower Dhurma Formation; (c. 23°35' N, 46°09' E, Ar Rayn quadrangle). The foreground corresponds to the base of the Formation. The isolated hill of sandstone was interpreted as a flow tidal sand ridge [Sequence 2, Issautier *et al.*, 2012a]. See Figure 3 for sequences and MFS interpretation in relation with the Jilh Formation. Photo Y. M. Le Nindre, Nov. 2008.

Middle to Late Triassic was based to a large degree on the succession in Iraq but subsequent publications demonstrate that it was misapplied over the southern half of the Arabian Plate including Saudi Arabia, particularly in their interpretation that the Anisian is missing. This led to a re-evaluation of Triassic sequence stratigraphy by a number of authors.

In this study, the maximum flooding surface nomenclature (MFS, Table 1) is adapted from Sharland *et al.* [2001, 2004] as revised by Davies and Simmons [2018], as their scheme has the best match with the new age data and stratigraphic organisation identified in the current study. Davies and Simmons [2018] proposed new reference sections for both MFS and SB on the Arabian Plate that had the best published biostratigraphic control. These tended to be in outcrops either towards the margins of the Arabian Plate, or along the Saudi Arabian outcrop where a fuller range of faunas and floras had been investigated and thus dating was better defined [e.g., Le Nindre *et al.*, 1990b, 2023].

These MFS are positioned in our marine intervals (MFI) in outcrop (Figure 5) on the basis of the most commonly accepted ages of the surfaces, ir-

respective of the original sections taken for definition, which mostly suffer from poor or negligible biostratigraphic control (Table 1). The main marine surfaces/intervals containing fauna dated in Part I [Le Nindre *et al.*, 2023] are MFS/MFI Tr40 (Anisian), Tr50 (Ladinian), Tr60 (Early Carnian), Tr70 (Late Carnian), and Tr80 (Norian). Then, the biostratigraphic ages of the surfaces have been refined according to the accuracy of the latest biostratigraphic results from outcrop. It is noteworthy that Deville de Periere *et al.* [2022], using palynology, also identify four sequences with comparable ages in the Jilh Formation of the eastern Rub al Khali Basin.

Numerical ages in the Triassic are poorly constrained with most stage boundaries only provisionally dated with few formal Global Boundary Stratotype Section and Points [GSSPs, nine for the Triassic in Ogg and Chen, 2020]. Thanks to the contribution of Moujahed Al-Husseini, we have tentatively assigned numerical ages to the successive MFS on the Arabian shelf by using the International Chronostratigraphic Chart v2015/01 [Cohen *et al.*, 2013, updated; Ogg, 2012, 2015], and the software TimeScale Creator, version 6.4, February 2015. The age model for Version 6.4 is from “The Geologic Time Scale

Table 1. Tentative numerical ages (Ma) Triassic MFS on the Arabian shelf

Surface (this study)	Sharland et al. [2001] and GTS 96	Haq and Al-Qahtani [2005] and GTS 2004	Davies and Simmons [2018] GTS 2020	This study GTS 2020-03	Sequence [Ogg and Chen, 2020]	Sequence [Haq, 2018]	Age (Ma)	Max sea level (Ma)
Triassic/Jurassic				201.4			201.36	
Mid Norian MFS Tr80	215	211.0	Late Norian <i>c.</i> 213	217.0	TNo3?	TNo3?	222.5–217.3	?
Tuvalian MFS Tr70	222	220.0	Tuvalian <i>c.</i> 230	230.0	TCar2	TCa2	233.5–229.0	230
Latest Julian MFS Tr60	226	226.0	Julian <i>c.</i> 234.7	234.0	TCar1	TCa1	236.2–233.5	234.5
Late Ladinian MFS Tr50	233	234.0	E. Ladinian <i>c.</i> 241	239.0	TLad2	TLa2	239.5–238.0	238.5
Anisian MFS Tr40	238	241.0	Pelsonian <i>c.</i> 243.8	242.5	TAn3	TAn3	243.5–242.1	242.5
Olenekian MFS Tr30	245	249.8	Smithian <i>c.</i> 249	248.5	TIn3	TIn3	250.0–247.9	248.5

2012” [Gradstein *et al.*, 2012], and the Triassic scale is by Ogg [2012].

The latest International Chronostratigraphic Chart 2022/10 [Cohen *et al.*, 2013, updated] shows only very minor changes (on base Induan and top Rhaetian) from the 2015-01 version. Those changes do not materially affect our interpretations. The ages are the following: Base Induan: 251.9 Ma (252.17 in version 2015-01); Induan–Olenekian: 251.2; Olenekian–Anisian: 247.2; Anisian–Ladinian: 242; Ladinian–Carnian: 237; Carnian–Norian: 227; Norian–Rhaetian: 208.5; Rhaetian–Hettangian: 201.4 ± 0.2.

2.1.1. *Maximum flooding surface MFS Tr30 and MFS Tr40*

MFS Tr30. In this study we do not address the Early Triassic (mid-Scythian) MFS Tr30 of Sharland *et al.* [2001, 2004] but for the sake of completeness, we briefly mention it here. They picked MFS Tr30 within the upper Sudair Formation [Sharief, 1986], and dated it 245 Ma in GTS 1996. Haq and Al-Qahtani [2005] followed Sharland *et al.* by also picking MFS Tr30 in the Sudair Shale and revised its age to 249.75 Ma in the Olenekian (upper Scythian) in GTS 2004. More recently, Davies and Simmons [2018] have updated the plate-wide correlation of the Triassic T–R sequences in coordination with this study. In Saudi Arabia, MFS Tr30 was picked in the Sudair Shale in a bioclastic arenitic dolomite with marine

fauna at 187 m in the SHD-1 Well [Manivit *et al.*, 1985a, Darmā quadrangle] and suggested to be of probable Early Olenekian (Smithian) age. The best candidate in the Haq [2018] and Ogg and Chen [2020] schemes would be in their sequence TIn3. Davies *et al.* [2019] identified strong diachroneity between siliciclastics of the Sudair and lower Jilh Formations and the carbonates and evaporites of the Dashtak Formation on opposite sides of the Arabian Gulf.

MFS Tr40. Sharland *et al.* [2001] interpreted Anisian MFS Tr40 in the Arabian Plate and dated it 238 Ma according to GTS 1996, but had not identified it in Saudi Arabia or neighbouring countries. Haq and Al-Qahtani [2005] revised the numerical age to 241 Ma in GTS 2004 and followed Sharland *et al.* in assuming it is missing due to a hiatus in the Anisian. While the Anisian age for MFS Tr40 remains valid, the numerical age assignments are clearly outmoded due to updates to the time scale. In Davies and Simmons [2018], a Mid-Anisian (Pelsonian) age of the MFS Tr40 is demonstrated by the presence of ammonoids of the *Balatonicus* zone in the Tethyan domain, and supported by the presence of the conodont *Nicoraella kockeli*, in carbonate beds of the Ra’af Formation (Negev southern Israel) taken as reference section.

Here we assign MFS Tr40 to the tidal and infralittoral bioclastic dolomite slab forming the first cuesta of the Jilh Formation at the outcrop from which the

SHD-1 Well was drilled. An equivalent horizon can be followed at the outcrop scale. This interpretation matches that of Davies and Simmons [2018] which was undertaken in concert with one of the authors (YML).

Given this biostratigraphic age, the MFS Tr40 best corresponds to sequence TAn2, from 244.24 (SB) to 243.33 Ma (TAn3 SB) and maximum sea level at 244 Ma in Haq [2018] and Ogg and Chen [2020], GSSP, adopted here.

2.1.2. *Maximum flooding surface MFS Tr50*

Sharland *et al.* [2001] dated MFS Tr50 at 233 Ma in the Ladinian and tentatively positioned it in the Jilh Formation in Saudi Arabia [Sharief, 1986, Vickers-Rich *et al.*, 1999]. Haq and Al-Qahtani [2005] revised the numerical age to 234 Ma in GTS 2004, and picked it in the Ladinian part of the lower Jilh Formation. The Ladinian age remains valid but the numerical age has changed due to timescale updates. Davies and Simmons [2018] assigned it to “thin dolomite beds containing the conodont *Pseudofurnishius murcianus* immediately below the J1/J2 boundary in the Jilh Formation reference section at outcrop [Le Nindre *et al.*, 1990b]”.

In our study two marine episodes appear during the Ladinian, the first one characterised by *Budurovignathus truempyi*, and the second one by *B. mungoensis*. They both occur in the upper part of Unit J1. The first marine event is characterized by the association *P. shagami*, *P. murcianus* and *B. truempyi*. In one hypothesis, it thus would correspond to the mid-late Fassanian transgressive cycle TLad1 of GSSP 2020 [Ogg and Chen, 2020].

However, we interpret that the major MFS is defined instead by the southward extent of the *P. murcianus*–*B. mungoensis*, association of Late Ladinian (Longobardian) age, as explained in Part I. In fact, *Budurovignathus* appears associated with flooding events, and is recovered from the dolomitic benches, representing more offshore (deeper?) settings, whereas *Pseudofurnishius* is associated with the clastic regressive phase above, or more proximal (shallower?) settings. This hypothesis is supported by the vertical distribution of the conodonts where the two are present, and by restriction of *Budurovignathus* to a more marine area (lat. 24°27' N–26°21' N).

In the chart of Haq [2018], this time interval corresponds to a transgressive cycle TLa2 from 239.5

(SB) to 238 Ma (TLa3 SB), spanning the Longobardicum and Neumayri ammonite zones—early-mid Longobardian—with the maximum sea level at 238.5 Ma. The same is recorded in Ogg and Chen [2020]. This major carbonate marine event is recognized and dated all along the outcrop from Khashm Dolqan (24°15' N) northward.

2.1.3. *Maximum flooding surface MFS Tr60*

Sharland *et al.* [2001] picked MFS Tr60 in the Jilh Formation in Saudi Arabia [Sharief, 1986, Vickers-Rich *et al.*, 1999] and dated it at 226 Ma in the Carnian. Haq and Al-Qahtani [2005] also estimated its age as 226 Ma, and similarly picked it in the Carnian part of the lower Jilh Formation. Referring to Haq [2018], it best corresponds to the sequence TCa1 from 236.2 (SB) to 233.5 Ma (TCa2 SB), with the maximum eustatic sea level at 234.5 Ma.

In our study, Late Triassic, latest Julian (Early Carnian) MFS Tr60 occurs in mapped Unit J2, or mapped Unit J3 respectively north and south of 25° N. It is the major maximum flooding interval (MFI) of the Jilh Formation, as shown by the more transgressive facies, while the major clastic influx at the base of this sequence occurred in early Julian. This transgressive event reached up to Jabal al Arid (23°31' N) where the dolomite on top of the Unit J3 contains *Quadralella polygnathiformis* (Carnian) with the southernmost marker of Julian, *P. inclinata*, at Khabra Halwah (23°55' N) just beneath the pre-Minjur unconformity.

Davies and Simmons [2018], placed Tr60 in dolomitic beds bearing *Quadralella polygnathiformis* on top of the Unit J3 of the Khashm Dolqan reference section. Although these beds correctly represent the MFI, in fact the key markers (*P. inclinata*—Julian—and *Q. polygnathiformis*—Carnian *s.l.*) were provided by the neighbouring section of Khabra Halwah (VD80-328, 329) as explained above, and not by the reference section.

The numerical age of the Julian/Tuvalian boundary is not adequately constrained in GTS 2015 and may be about 233.6 Ma [Ogg, 2015, Ogg and Chen, 2020]. Furin *et al.* [2006] reported a $^{206}\text{Pb}/^{238}\text{U}$ age of 230.91 Ma \pm 0.33 Ma for zircons from an ash bed within the range of the conodont *Metapolygnathus nodosus* in the middle-upper Tuvalian. These age estimates imply latest Julian MFS Tr60 is no younger than 230.9 Ma and probably older than 233.5 Ma, or

about 8 Ma older than previous estimates. We attribute an approximate age of about 234.0 Ma for latest Julian MFS Tr60.

2.1.4. *Maximum flooding surface MFS Tr70*

Sharland *et al.* [2001] did not identify MFS Tr70 in Saudi Arabia. Based on undated outcrop data from Iraq they estimated its age as 222 Ma, while Haq and Al-Qahtani [2005] estimated its numerical age as 220 Ma, both in the Late Carnian, and showed it in the Carnian part of the upper Jilh Formation. Davies and Simmons [2018] had identified it, based of work by one of the authors (YML), interpreting its age as Late Carnian on the ammonoid “*Clydonites sp.*,” identification of which was reinterpreted in Part I. They also noted the presence of the conodont *P. inclinata* in the reference section. In fact, *P. inclinata* was found on top of a neighbouring section (VD80-328, 329, Khabra Halwah), and is a fossil marker of the Julian.

In our study, Tuvalian (Late Carnian) is identified in Unit J3, principally north of 25° N. The development of marine carbonates in the north with Tropitids and conodonts identifies this flooding event. The presence of the conodont *Quadralella carpathica* points to the early to middle Tuvalian, while Tuvalian 1 up to Tuvalian 2/I is indicated by the Tropitid ammonoids. A common associate is *Q. polygnathiformis*.

With a Carnian–Norian boundary at 227 Ma (ICC 2020/03 and 2022/10) and the base of Tuvalian at 233.6 Ma, an age of 230.91 ± 0.33 Ma in middle–upper Tuvalian is correct. Thus, we estimate the numerical age of MFS Tr70 around 230 Ma. This MFS best corresponds to sequence TCar2 in Ogg and Chen [2020] from 233.6 Ma (SB) to 228 Ma (TCar3 SB), with a maximum sea level at 230 Ma.

2.1.5. *Maximum flooding surface MFS Tr80*

In the literature, definitions and assignments of MFS Tr80 are uncertain and multiple, principally due to lack of reliable biostratigraphic or numerical ages. Furthermore, the Norian period was characterised by the broad extent of continental areas and sedimentary hiatuses [Davies and Simmons, 2018, Maurer *et al.*, 2008, 2015]. This situation engendered subsequent confusing and conflicting interpretations.

Sharland *et al.* [2001] assigned a Norian age to MFS Tr80 (215 Ma, *i.e.*, mid Norian in the time scale

of 1996) but age diagnostic fossils were lacking at the time of writing (apart from potentially Norian pollens in Kuwait). They did not identify Tr80 in Saudi Arabia although the surface was tentatively picked in neighbouring Kuwait and Abu Dhabi. Sharland *et al.* proposed a reference section near the base of the Sarki Formation in Iraq, although they acknowledged the absence of biostratigraphic age control. If the age of the Lower Sarki Formation is Norian [Hanna, 2007, Lunn *et al.*, 2019], Sharland *et al.*’s interpretation that the “Marker Dolomite” of Lunn *et al.* near the top of the Kurra Chine Formation, equivalent to the Sefidar Dolomite, near the top of the Dashtak Formation in Iran, also contains MFS Tr80 cannot be correct. The Baluti Formation separates the underlying “Marker Dolomite” from the overlying Sarki Formation [Lunn *et al.*, 2019]. Palynological data confirms that at least part (but not necessarily all) of the Baluti Formation is Late Carnian [only composite samples were analysed—Lunn *et al.*, 2019], thereby confirming that the “Marker Dolomite” is also of Carnian age. The Sefidar Dolomite corresponds, by the underlying lithologic succession (dolomite–evaporite–dolomite) and by its wire line characteristic response to the “Marker Dolomite”, elsewhere named “Jilh Dolomite” in Saudi Arabia. This equivalence is best demonstrated by the presence of the distinctive Jilh Dolomite in offshore gas fields, notably Karan, that lie adjacent to the median line with Iran [Sodagar, 2015]. This unit is assigned herein to the Early Carnian MFS Tr60 [see further paragraph 4.2 on “Jilh Dolomite” and Davies and Simmons, 2018].

As noted previously, Sharland *et al.* [2004] placed the MFS Tr80 in the early Middle Norian: from this point of view, it would correspond to our Alauanian 1 transgression dated in Part I. Haq and Al-Qahtani [2005, see their Enclosure 2] estimated its age as 211 Ma, and showed it in the Norian Minjur Formation.

Davies and Simmons [2018], revising Sharland *et al.* [2001], selected a new reference location for the MFS Tr80, in Musandam UAE. They picked the MFS within the Milaha Formation in the first limestone beds with megalodonts and crinoids, above the marker foraminifer *Triasina hantkeni* of late Middle Norian to Rhaetian age [Leopold Krystyn, Urban *et al.*, 2023], and below the latest Norian beds of the Asfal Member (lower part of the Ghalilah Formation) dated by the ammonoid *Neotibetites* and by

the conodont *Epigondolella bidentata* [Maurer *et al.*, 2008, 2015, location on Figure 1].

In accord with the present study, the sequence boundary (Tr80 SB) was picked in the Early Norian hiatus.

Additional graphical evidence presented by Urban *et al.* [2023] reveals that the boundary of the Milaha Formation and the overlying Asfal Member of the Ghalilah Formation is an erosional discontinuity marked by a reworked limestone conglomerate. This erosional discontinuity is an obvious candidate for an additional sequence boundary, which might be designated as Tr90 SB.

Issautier *et al.* [2019] have demonstrated that there are three maximum flooding intervals (MFI) in the Minjur Sandstone through a southwest–northeast transect from outcrop to the Gulf (location on Figure 1):

- **Early to Middle Norian:** in subsurface, beds containing the marine dinocyst *Rhaetogonyaulax wigginsii*. In Well 143-3, the closest to the outcrop (location on Figure 1), a thick sandstone interval was deposited between 1050 ft and 1150 ft (320–350 m), capped by a 50 ft (15 m) thick mudstone interval in which *R. wigginsii* was found at 1042 ft (318 m) (FDO and LDO). The palynology study revealed that this shallow marine bio-marker is the most widespread and could date the peak transgression within the Triassic portion of the Minjur Formation. The FDO of *R. wigginsii*, within the paly-nosubzone T1B, suggests a position close to the middle–early Norian boundary, following the work of Nicoll and Foster [1994, 1998] who correlated conodont zones with the ranges of selected dinoflagellate cysts, including *R. wigginsii*. In outcrop these beds are correlated with Minjur Sequence 4 [Issautier *et al.*, 2012a, 2019] which is characterized, by a basal braided sand sheet overlain by cross-bedded sandstones representing tidal channels, bioturbated sandstones, and dolomitic siltstones representing associated mudflats.
- **Latest Norian–Early Rhaetian:** in subsurface locations, beds containing the dinocyst *Rhaetogonyaulax rhaetica*. In the SW–NE traverse studied by Issautier *et al.* [2019],

R. rhaetica occurrence is restricted to coastal well 628-5. In outcrop, Issautier *et al.* formulated three hypotheses: either the *R. rhaetica* transgression never reached the outcrop or was eroded by the intra-Minjur unconformity, or the *R. rhaetica* transgression might be partly equivalent to the transgressive systems tract of upper Sequence 5, represented by tidal flat and channel facies. Issautier *et al.* [2019] also correlated these beds with the Malihah and the lower Ghalilah formations (Asfal Member) of comparable age in the UAE section [Maurer *et al.*, 2008, 2015].

- **Latest Rhaetian to Early Pliensbachian:** in subsurface, beds containing the dinocysts *Dapcodinium priscus*, for which no MFS *sensu* Sharland *et al.* [2001] has been identified. In outcrop, they are likely coeval with the transgressive intervals of the Minjur Sequences 6, 7, and 8 including marginal marine or tidal deposits. The upper one is underlined by marine carbonate in the upper part of the formation and would correspond to the uppermost tidal channel of Sequence 8. It seems probable that the as yet unidentified MFS is located in the overlying Early Jurassic (Hettangian–Sinemurian?) section. A comparable Rhaetian to Early Jurassic transgression can be identified in Kuwait [Kadar *et al.*, 2015].

Issautier *et al.* [2012a, 2019] explain the different extents of the *R. wigginsii* and *R. rhaetica* transgressions by modified paleogeographic settings. A flatter landscape with tidal flats during Early–Mid Norian enabled retrogradation of *R. wigginsii* marine facies to more proximal settings. A more contrasted landscape during Late Norian and Rhaetian, with an upstream part supplying abundant clastics deterred landward retrogradation of *R. rhaetica* facies.

Fine-grained fluvial-lagoonal and littoral deposits containing echinoderms debris, were used for subdividing a lower from an upper unit in the Minjur Sandstone within the Ar Rayn quadrangle by Vaslet *et al.* [1983], and within the Al Mulayh quadrangle by Manivit *et al.* [1985b]. Due to lack of biostratigraphic constraints, it is not clear with which of the two Norian MFS's it is associated. However, the EarthVision® 3D model (by B. Issautier and Y.

M. Le Nindre, 2011, unpublished) shows a strict correspondence between Sequence 4 and the 90–130 m marker of the Khashm al Khalta section of Vaslet *et al.* [1983], which is taken as the base of the “Upper Unit” (Figure 3a). The ophiurid vertebrae were observed from the uppermost dolomitic siltstone beds (sample VD80-122, Figure 4).

The base of Sequence 4 truncates Sequence 3 and partially Sequence 2 of the Minjur Sandstone as a north-dipping surface observed in the field and modelled (EathVision® 3D, Figure 3b) by B. Issautier and Y. M. Le Nindre in 2011 [annex work to Issautier, 2011].

Issautier *et al.* [2019] thus assigned the MFS Tr80 to the early Middle Norian *R. wigginsii* beds, widespread on both sides of the Qatar Arch as shown by their figure 16 after Stewart *et al.* [2016]. It matches the Alaunian 1 ages obtained in Part I of our study, on top of the Jilh Formation and at the base of the Minjur Sandstone northwards of 25°30' N, from ammonoids and from the conodonts *Ancyrogondolella praeslovakensis*, and *Epigondolella abneptis* in several sections.

Within this given context, for matter of simplification, and following Issautier *et al.* [2019], in the next pages we keep using Tr80 for the Alaunian 1 regional transgression separated from the Tualian Tr70 by a disconformity of more than 10 Ma. The renaming of Tr80 is out of the scope of this study. Nevertheless Tr80, Tr90, and either Tr100 or more likely J05, could be proposed for Alaunian (T1B), Sevatian (T1A), and latest Rhaetian–Early Pliensbachian (T0-J) transgressions, respectively. J10 is still in the overlying Marrat Formation.

The Emirates-Musandam section [Maurer *et al.*, 2008, 2015, Urban *et al.*, 2023] contains two transgressive events separated by an erosional discontinuity, the lower one at the base of the Milaha Formation, the upper one at the base of the Asfal member of the Ghalilah Formation. The only marker fossil recorded in the Milaha Formation is the foraminifer *Triasina hantkeni* which was recovered 21 m above its base and 50 m below the contact with the overlying Asfal Member [Maurer *et al.*, 2008, 2015, Urban *et al.*, 2023]. Davies and Simmons [2018] followed other workers in interpreting that the range of *T. hantkeni* was Late Norian (Sevatian) to Rhaetian, which accounts for their assignment of the MFS in the Milaha Formation to the Late Norian. However Urban

et al. argue that a Middle Norian age for *T. hantkeni* cannot be ruled out. This remains the opinion of one of the authors (LK) We note that *T. hantkeni* is commonly reported in lagoonal sediments also containing megalodonts, as is the case of the Milaha Formation, and therefore wonder if it may have been, at least partially, facies controlled. Consequently, the lower transgressive event could be (partly) contemporaneous of the Alaunian transgression in central Arabia, and the erosional surface capped by a conglomerate that separates the Milaha and Ghalilah Formations likely represents the same event that marks the base of Sequence 5 (scour surface SB5) of Issautier *et al.* [2019]. It would set up the interesting possibility that the upper transgression in the Asfal Member is (partly) equivalent to the *R. rhaetica* flooding as suggested by Issautier *et al.* [2019]. This would be consistent with the nomenclature suggested above, namely that the Alaunian transgression was associated with MFS Tr80, and that the younger Late Norian–Rhaetian event could represent a newly identified MFS Tr90.

Note that Lunn *et al.* [2019] and Lunn [2020] use “Tr80” (previously “Tr80 v1”) in place of MFS Tr60 within the Jilh Dolomite unit (see Section 4: “Particular events and their regional correlations”). Lunn assigned a “Tr 100” (previously “Tr80 v3”) to the *R. rhaetica* MFS in Wells 143-3 and 628-5, T1A palynosubzone, referring to Issautier *et al.* [2019]. Readers should note that Lunn misidentified the Jilh Dolomite equivalent in well 143-3.

In our study MFS Tr80 is interpreted as early Middle Norian and the base of the Alaunian is at 217.49 Ma [Ogg and Chen, 2020]. It could therefore correlate to MFS Nor1 in Time Scale Creator at c. 217 Ma, the best guess for the age of Tr80 so far (Table 1). However, in the Haq [2018] chart, as well as in the Ogg and Chen chart, this age corresponds to a sea level lowstand; subsequently, this transgression could eventually match the top of the TNo3 sequence in the Late Lacin, revealing that broad uncertainties exist on the Norian sea-level and coastal onlap curves.

In conclusion, at the regional scale (Iran, Iraq, Kuwait, UAE, Oman, Saudi Arabia), we have not yet in hand all the elements for establishing a hierarchy of the major flooding events of the Late Triassic at plate scale. Disagreements between the authors in a broader spectrum of papers on ages and correla-

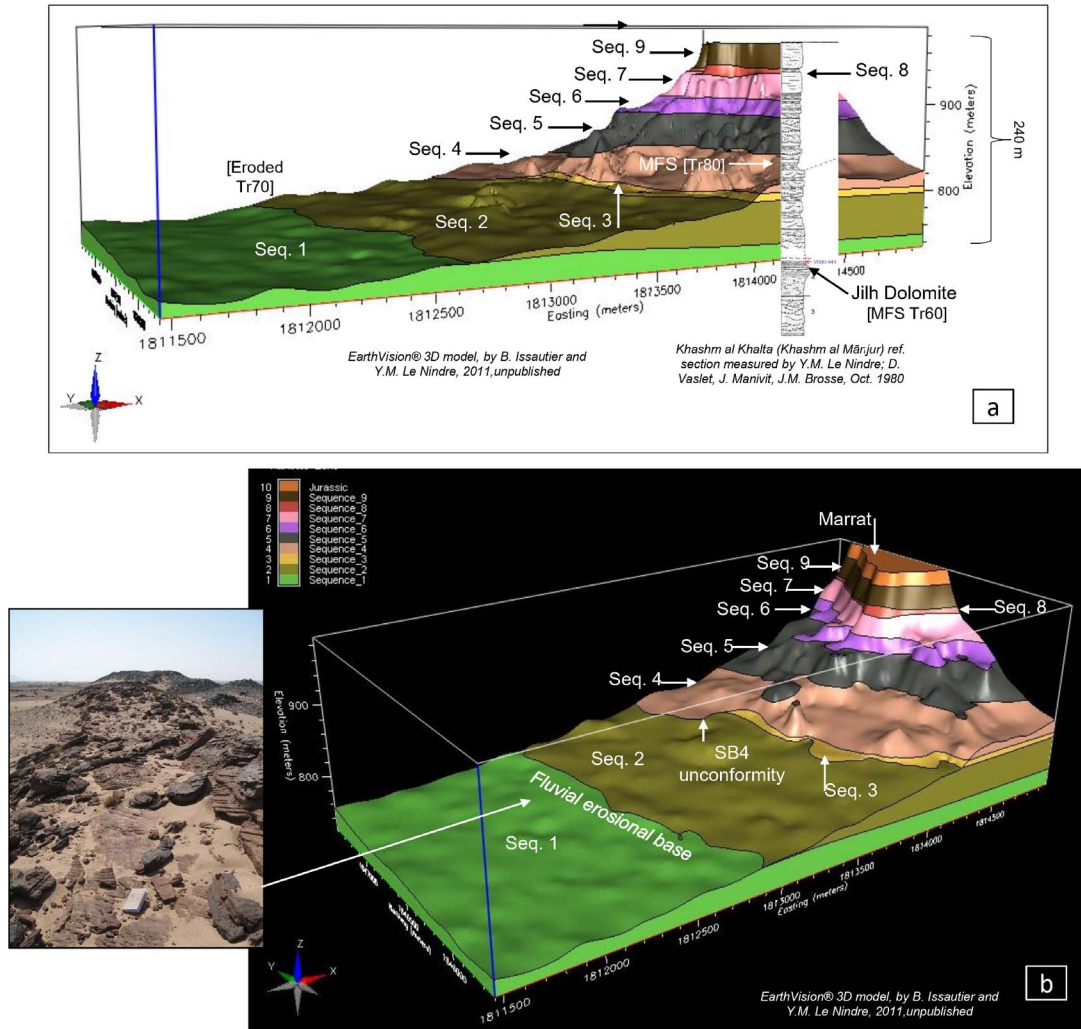


Figure 3. Learning from the Minjur 3D model at Khashm Al Khalta (Khashm al Mānjur) type locality. (a) Correspondence between the model and the section measured by Le Nindre and others in Oct. 1980—see Part I, Le Nindre *et al.* [2023]—with indication of the MFS [Tr80] horizon, and Jilh Dolomite Tr60. Tr70 is eroded from the North at this latitude—view from South; (b) Other view—from west-southwest—emphasizing the SB4 unconformity (early–mid Norian) and the pre-Minjur fluvial erosion (Carnian–Norian boundary). Minjur sequences nomenclature of Issautier *et al.* [2012a].

tions within this period persist due to an obvious lack in biostratigraphic data and in numerical ages for making reliable correlations regardless of the lithologies as we present now for Saudi Arabia. In particular outcrop paleontological studies using both ammonoids and conodonts are not developed sufficiently to confirm correlations in the subsurface using only well logs or facies associations and need further investigation.

2.2. Depositional and structural evolution from Ladinian to Norian

Using the available time markers (datums or assumed), we have split the geohistory of the Jilh Formation into four stages (Figures 6a to 9d). This exercise demonstrates the evolution of the structural setting, and the vertical and horizontal relationships between the successive depositional units.

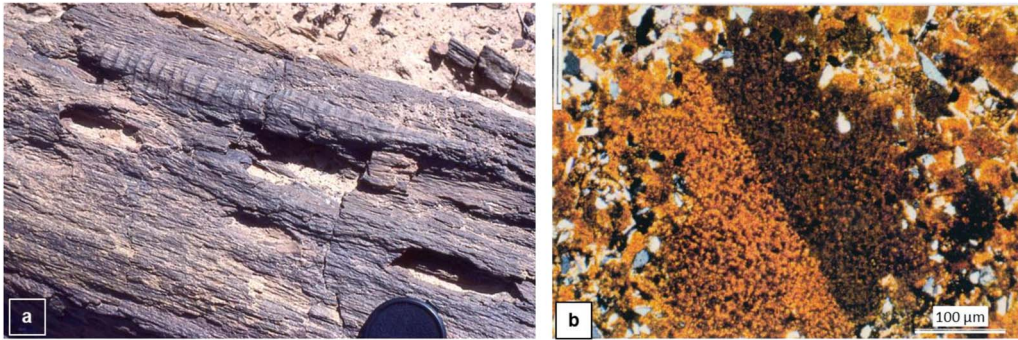


Figure 4. Two remarkable fossils of the Minjur Sandstone: silicified tree trunk (a), and skeletal piece of Ophiuridea (b). (a) Tree trunk (length ≤ 5 m, diameter ≤ 50 cm) of a Mid Norian petrified forest near Al Barud (c. $24^{\circ}50'$ N, $44^{\circ}11'$ E) Sample JMA83-238, Buraydah quadrangle. Photo J. Manivit. (b) Siltstone with angular and splinter quartz, cemented by dolomicrosparite, detail: typical section of ophiuroid vertebra reflecting temporary marine incursion into a dominantly fluvio-deltaic setting (MFS Tr80?). sample VD80-122, B28450, polarized light, Khashm al Khalta section (c. $23^{\circ}35'$ N, $46^{\circ}10'$ N), Ar Rayn quadrangle. Photo Y. M. Le Nindre.

In Figure 6, we have intentionally abandoned the use of the lithological units J1 to J3 since Part I established diachroneity in these units. Instead, we introduce letters A to J to denote “horizons”; i.e., layers with relatively uniform facies and thicknesses. Several horizons contain individual “bodies” that represent lateral changes in facies or thickness, such as those that represent the Julian Clastic Event. The numbers 1 to 11 are “surfaces”, time lines or events (e.g., MFS, SB) and they separate horizons that can be interpreted as subaerial sequence boundary (SB), transgressive (TST) and highstand (HST) systems tracts.

2.2.1. Top Ladinian datum

In Figure 6a the top Ladinian (surface 5) is chosen as the datum to illustrate that the Anisian and Ladinian facies and structure are fairly monotonous and relatively uniform in thickness. The top of the Sudair Shale is generally covered by the Nafud Desert and not marked by a cuesta, and so it is only known at three points (Khashm Dolqan by SHD-1 Well, Khabra Halwah, and Al Mudarra). In the top Ladinian datum cross-section, the top Sudair is most likely represented by surface 1, but it could be surface 2 in the south.

The upper part of the Sudair Shale represents the continental early TST of a sequence that passes

to an Anisian late TST (horizon A) culminating in MFS Tr40 (surface 3), above which horizon B represents the Anisian HST. Horizons A and B are well dated by pollens and by *Myophoria goldfussi*, a lamellibranch that commonly inhabited this kind of brackish environment. Horizon C represents a younger shallow-marine cycle that includes MFI Tr50 and is dated as Ladinian by conodonts. A hiatus may occur between Anisian horizon B and Ladinian horizon C and is a candidate for the Tr50 SB.

The upper part of horizon C is marked by a thin Ladinian sequence and capped by a gypsum deposit at Khashm Dolqan. The contrast between the gypsum below and clastics above suggests a hiatus (corresponding to surface 5—candidate for Tr60 SB). The clastics above surface 5 are not dated; they could be latest Ladinian or more likely early Julian. They correspond to a change in clastic influx and climate conditions from arid (gypsum in upper Ladinian) to humid which from Haq [2018], would correspond to the sea level lowstand 237.5 Ma, TLa3 sequence, at the Ladinian-Carnian boundary. When compared with the Alps and the Germanic basin, hiatuses are very likely between the Ladinian evaporite and the Julian clastics [Hornung *et al.*, 2007]. We tentatively assign these clastics to the “Julian Clastic Event”.

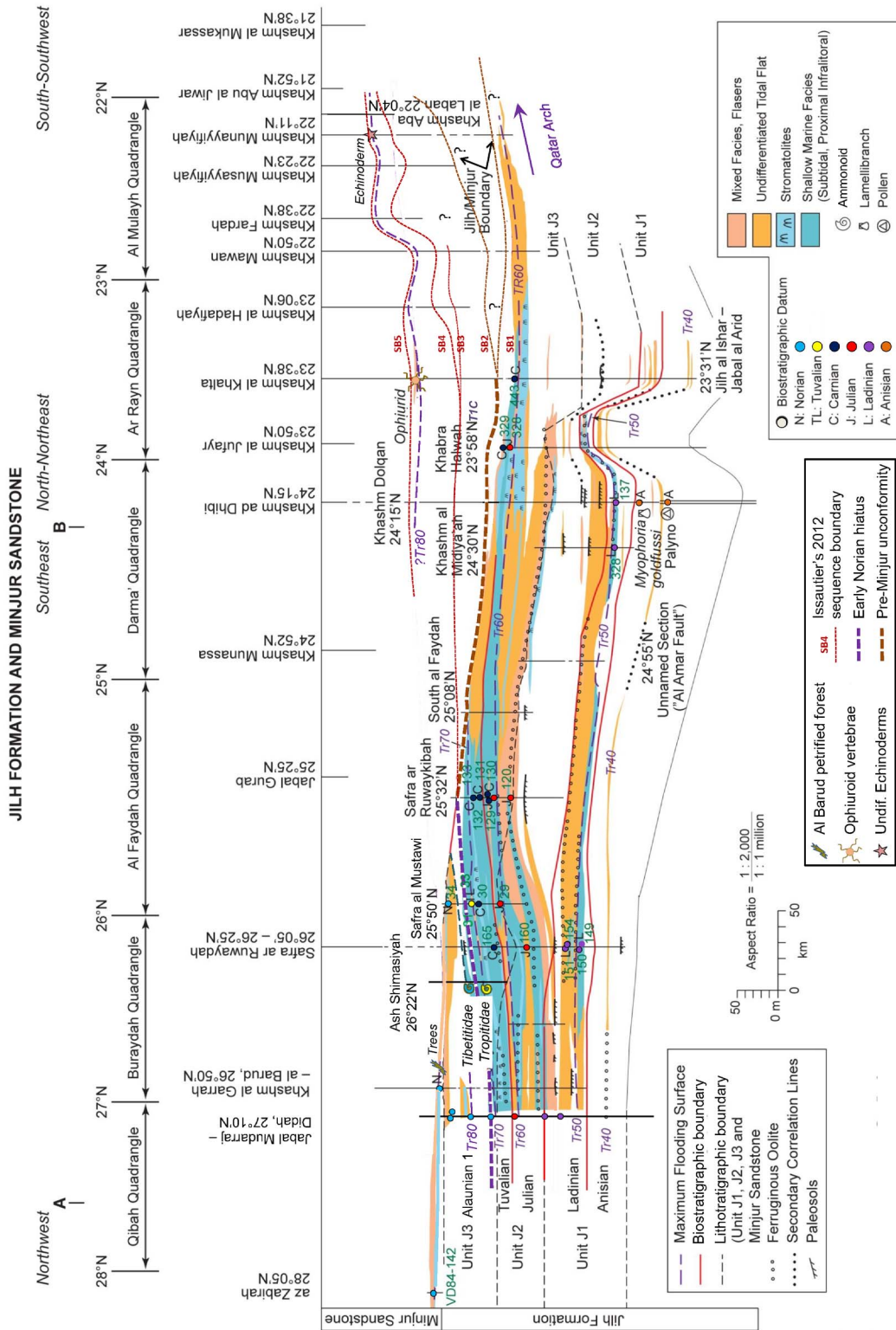


Figure 5. Ages and maximum flooding events of the Jilh–Minjur systems based on marine carbonates stratigraphy.

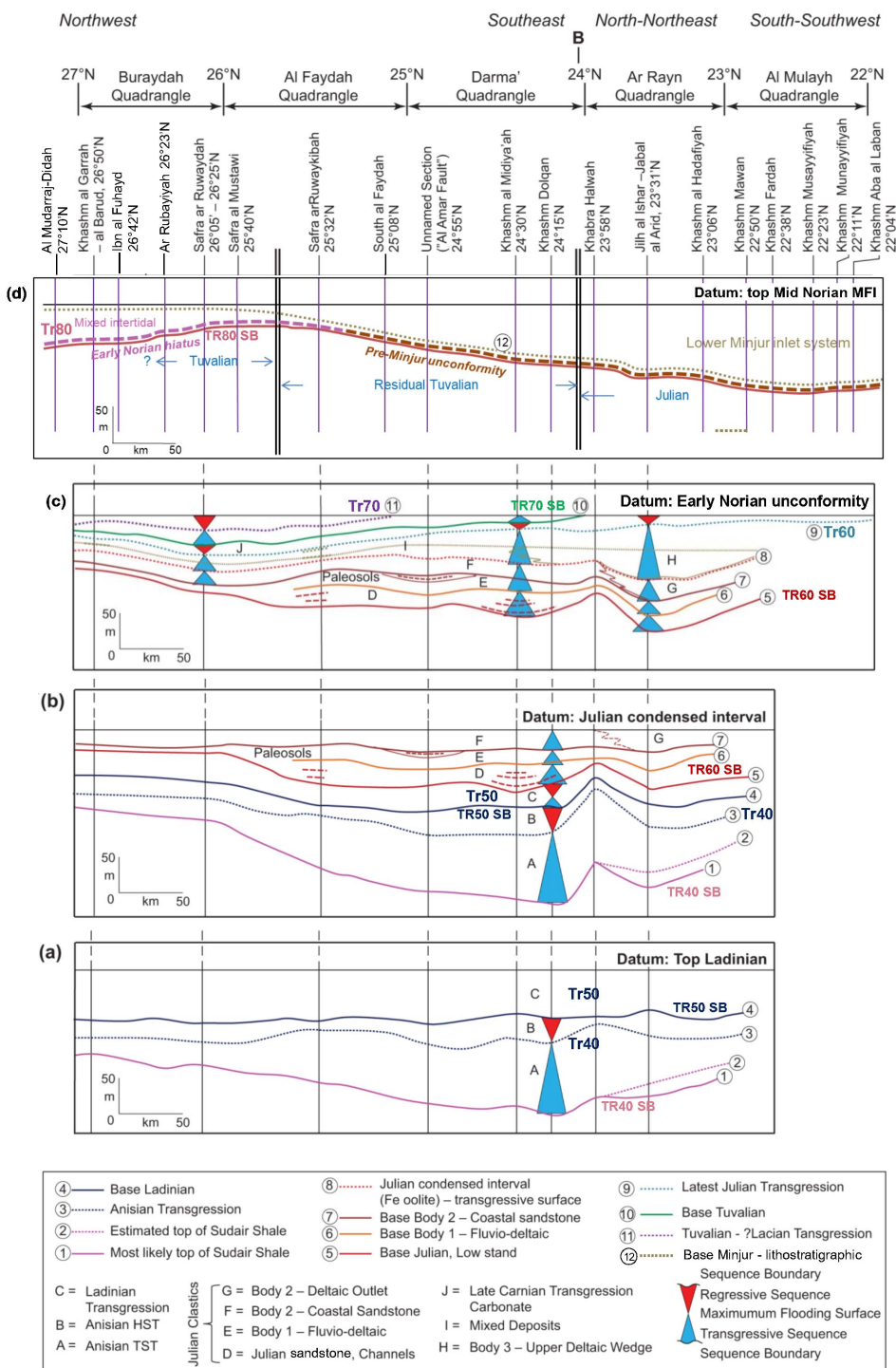


Figure 6. (a)–(d) Stratigraphy of the depositional sequences at four stages of the Jilh Formation sedimentary history.

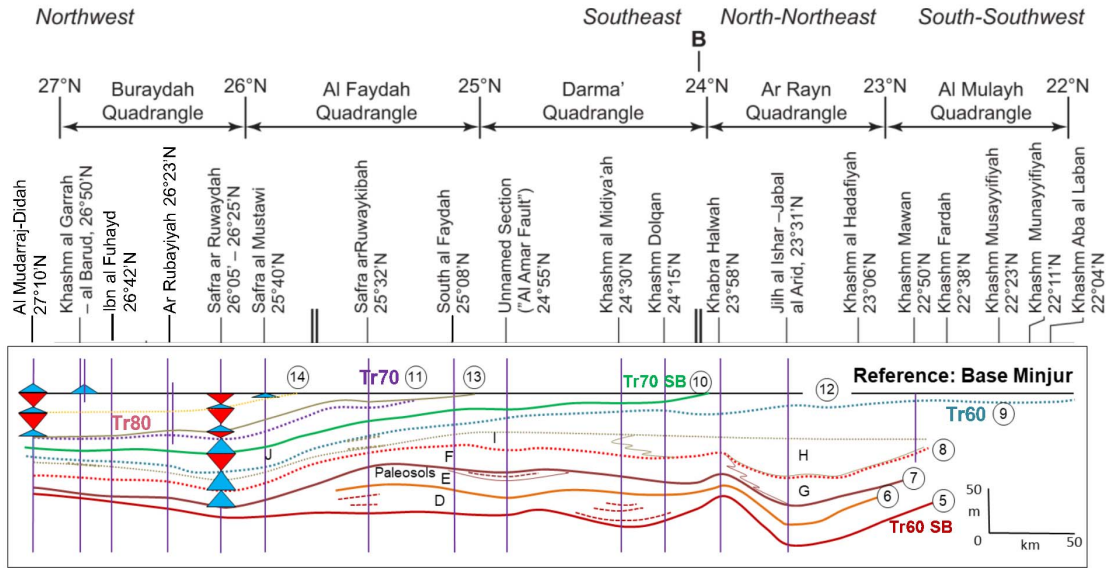


Figure 7. Stratigraphy of the depositional sequences of the Jilh Formation from the late Ladinian-basal Carnian low-stand, horizontalized at the base of Minjur clastics (lithostratigraphic). Letters and numbers refer to the legend of Figure 6(a)–(d). In addition, (13): Early Norian hiatus unconformity surface; (14): intermediate Alaunian tidal sequence boundary.

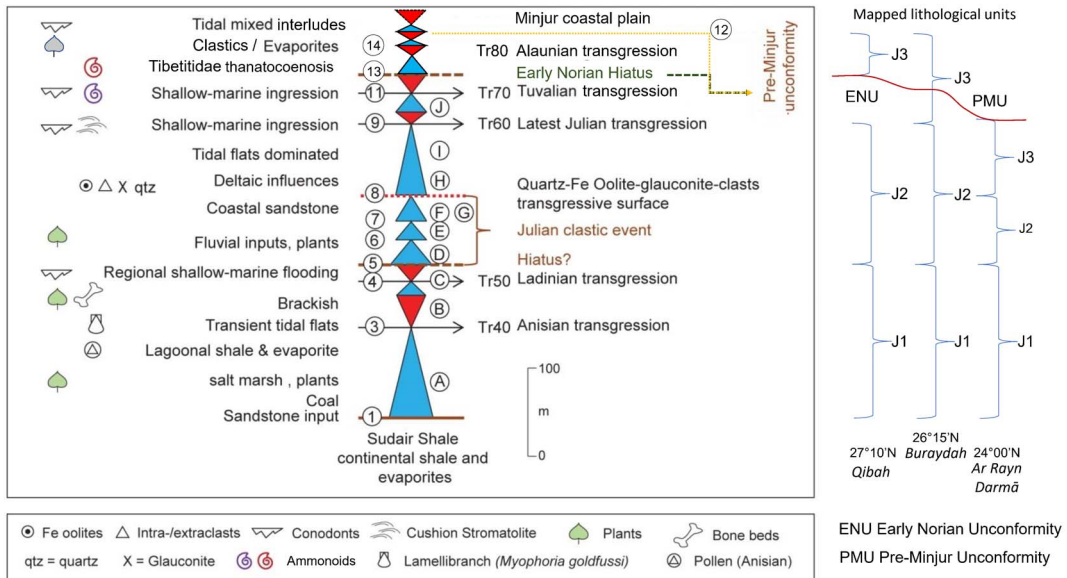


Figure 8. Synthetic sequence stratigraphy of the Jilh Formation in outcrop between latitudes 22° N and 27° N. Surface (12): base of the Minjur Sandstone (lithostratigraphic). Early Norian (pars) present in the Lower Minjur in Central Arabia.

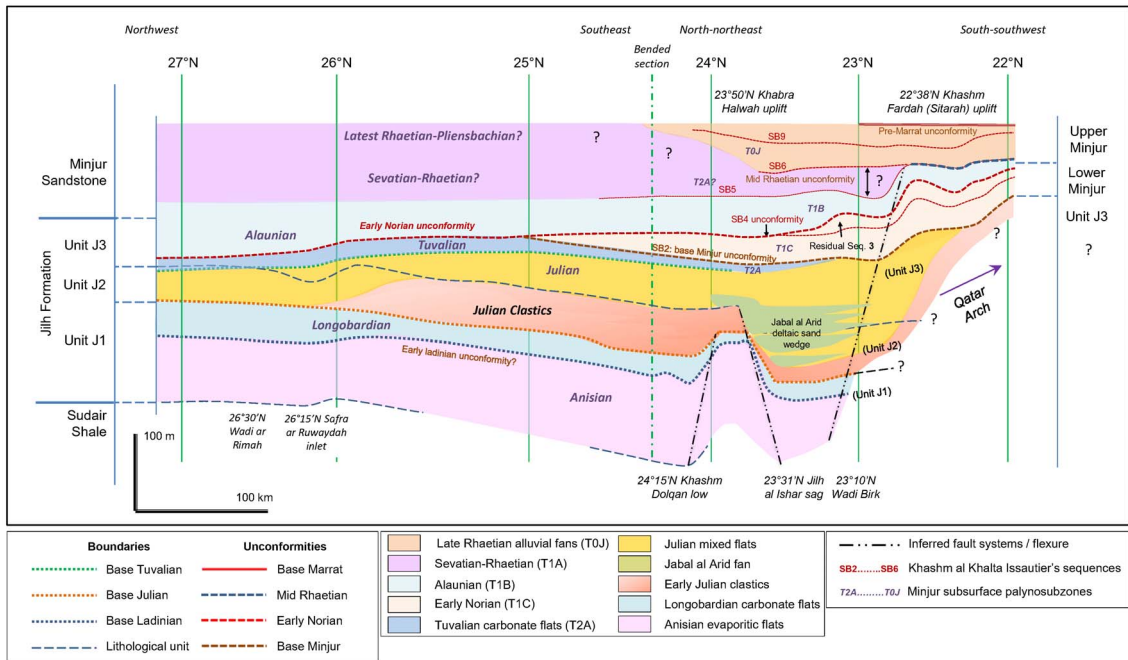


Figure 9. Synthetic conceptual sketch of the Jilh–Minjur systems in outcrop summarising the main structural features, the geometric relationships of the depositional sequences, especially the unconformable Alaunian transgressive wedge.

2.2.2. *During Julian (Time reference: ?mid Julian condensed interval)*

This datum, which we name “Julian condensed interval” (*sensu* Vail’s school), is characterized by Fe-oolite (formerly chlorite?), glauconite, quartz and intraclasts with reworked Permian fauna (surface 8, Figure 6b) and estimated by *M. carnica* as ?mid–late Julian. The first observation is the structural change of the previous deposits, related to a tectonic phase predating and/or accompanying the deposition of the clastics (horizons D, E and F), but principally of the two depositional horizons D and E, generally capped by paleosols.

Horizon D is assigned to the Julian and characterized by a landscape of supralittoral shales and creeks with channels of heterometric fluvial sandstone. Sandstone bodies, in channels in horizon D, become aggregated in Julian horizon E. Laterally at Jabal al Arid, horizon E corresponds to the deposition of the first deltaic sandstones [Le Nindre et al., 2023].

Sandstone bodies D and E evolved to Julian sandstone body F by transgression and reworking of

the fluvial sandstone to coastal and tidal sandstone, which are extensive, relatively sheet-like and uniform in thickness. Laterally, at Jabal al Arid, a deltaic outlet incises the coastal sandstone (body G). So, this time interval is characterized simultaneously by tectonic structuration and clastic influx, filling lowlands between the structures. At this stage it is difficult to determine if the basal sandstone and change of regime were driven by a sea-level low stand, or principally by a change in clastic influx related to tectonics and climate, or even a combination of these. Therefore, the base of the Julian Clastic Event (surface 5) can be considered as a sequence boundary (presumably Tr60 SB) with a possible hiatus following the Ladinian transgression. A tectonic setting with sandstone bodies infilling the grabens (and carbonates on the flat tops) is also common elsewhere during the Triassic. East of the outcrops, Faqira et al. [2009] interpreted the presence of north–south trending horsts and grabens that developed in response to regional extension during the Triassic. In this study, structures such as Qatar high (south of 21°30’ N), “Khashm Fardah (Sitarah) uplift” [22°38’ N, Le Nindre et al., 1983],

“Jilh al Ishar sag” (23°31′ N) and “Khabrah Halwah uplift” (23°50′ N) control the sedimentation. Lineaments in the basement (N135) or major present valleys as the Wadi Birk (23°10′ N) and the Wadi Ar Rimah (26°30′ N) may reveal syn-sedimentary fault systems, active during the Triassic, and, later on, during the Jurassic [Wadi Birk, Al-Mojel, 2017].

2.2.3. Carnian–Norian boundary: Early Norian unconformity

At outcrop, the flat reference taken as base Norian is the disconformity surface (Tr80 SB) dated by the first Norian occurrence within the Jilh Formation (Alaunian 1, early Middle Norian) in the north, or by base Minjur, dated Early to Middle Norian in the centre where part of the Early Norian is demonstrably absent [Issautier *et al.*, 2019] (Figure 6c). The main features raised by this choice of levelling reference are the structure of the deltaic wedge at Jabal al Arid in the south (upper deltaic wedge, body H), and a smooth subsident trough in the north (horizon J) through which the marine transgressions of the latest Julian (surface 9 = MFI Tr60) and Tuvalian (surface 11 = MFI Tr70) progressed from the NNE. Clastic inputs persisted laterally (horizon I) during the deposition of a broad deltaic wedge, clearly visible on DTM and satellite imagery [see Issautier *et al.*, 2012a]. This feature enhances the clastic trough of Jabal al Arid.

In contrast, the central area of Khabra Halwah remained dominated by tidal flats and must have been a very low relief setting. The broader transgression is latest Julian (surface 9) and is detected up to 22° N (tidal flat), with more marine conditions (fossils) northward up to 23°30′. With time, the next transgressions are less and less extensive upwards. The orientation of the outcrop, and consequently of the cross section, shows in fact an oblique view of the transgressive wedges. They appear in a transversal section with a south–north progressive regression of the successive pulses that continued during the Norian (Figure 13). So, this cycle reflects a transgressive system up to the latest Julian transgression (MFS Tr60) followed by a progressive retrogradation of the successive marine pulses via the Late Carnian MFS Tr70 until the Mid-Norian (MFS Tr80) later on, although there is clear southwards truncation of the Tr70 flooding event, indicating regional tectonism (and possibly a concurrent eustatic

sea-level low) associated with the base Minjur Formation unconformity identified in Part I (Figure 6c). The evaporites of the northern area mentioned by Sharief [1977, 1986] that overlie surface 11 represent the post-Tr70 Tuvalian–Lacian regression [Sharland *et al.*, 2001].

2.2.4. During Norian (early Mid Norian Transgressive Interval Tr80)

Descriptions of the Jilh/Minjur boundary from south to north show a major event generally characterized by lag deposits at outcrop scale. The deposits are most likely related to a peneplain over the previous deposits after uplift (in the south) and subsidence (in the north) of the Jilh Formation. In this interpretation, an erosional unconformity separates the Jilh Formation from the Minjur Sandstone (Figure 6d). Flattening the cross section on top of the Alaunian 1 MFI as interpreted in this study (early Mid Norian Tr80), emphasises that south of 25°35′ N, and especially south of 24° N, the major subsident trough of the Lower Minjur gave way to the main streams and deltaic wedge of the stacked Jilh and Minjur reservoirs of central Arabia. As pointed out by Issautier *et al.* [2012a], this area was likely a persistently weak tectonic zone. North of 25°35′ N, a shallow-marine trough developed during the subsequent regression within the previously more marine area.

Away from the main upstream source of clastic supply, the unconformity separating the Minjur and Jilh formations is difficult to identify in the more fines-dominated succession to the north, although simple stratigraphic relationships indicate that a cryptic time gap must be present in that area.

From the Al Faydah quadrangle to the north of the Buraydah quadrangle both geological maps [Manivit *et al.*, 1986, Vaslet *et al.*, 1985] and satellite images show an evolution of the Jilh outcrops which spread out in relation with facies changes.

From the base, during the Ladinian, deposition of sandstone and dolomite around 26°13′ N are not observed further south. Near the top, a cuesta, mapped as the uppermost Jilh lithological assemblage on the Buraydah geological map [Manivit *et al.*, 1986] is developed, seemingly conformably overlain by the cover of fine-grained sandstone and shale of the Minjur Sandstone, although a significant time gap is probable. Its facies of grey/yellow argillaceous rocks,

with associated dolomite and evaporites, is similar to the one defined as the Baluti Shale Formation in Iraq [van Bellen *et al.*, 1959–2005] mapped by Ziegler [2001] within the “Carnian to Norian paleogeography, together with the Lower Minjur in a narrow zone of “marginal-marine to shallow-marine clastics” (Figure 13). The presence of this marginal-littoral to shallow marine facies, with the *Tropitidae* fauna, below, and the *Tibetitidae* fauna above, reflects a smooth trough that was penetrated from the north by successive marine incursions (26°15' N, “Safra ar Ruwaydah inlet”).

The lithological assemblage dated Norian by the conodonts and the ammonoids is thus part of the Lower Minjur, and confirms more marine conditions. The present-day morphological character of Wadi Ar Rimah area is probably related to an ancient deep structural feature that was active from Ladinian to Norian. From MFS Tr60, although interrupted by the Early to Middle Norian unconformity, the depositional system was overall regressive with a culmination during the Rhaetian, associated with a reactivation of the hinterland erosion and creation of alluvial fan and of hyperpycnitic bodies.

2.3. Carnian–Norian back-stepping, progradation, and diachronism

Coming back to the interpretation of a diachronism of the depositional lithostratigraphic units by J. Manivit and B. Vrielynck [in Le Nindre *et al.*, 1987, DrSc theses, and Le Nindre *et al.*, 1990b, p. 187, Figure 38, and this study, above] it is now possible to decipher this conclusion more clearly. By using the method of the Figure 6a–d, we have flattened the Carnian–Norian deposits at the time of the Minjur “petrified forest”—coarse grained clastics, trunks and wood debris—which reflect a change in climate and tectonics and was taken as lithostratigraphic base of the formation (Figure 7). This event erodes the previous marginal marine deposits.

This representation depicts, besides a diachronic lithostratigraphy, principally the mechanisms it originates from. Following the sea level lowstand at 237.5 Ma, during the Early Carnian, the sequences are essentially transgressive and landward backstepping until the latest Julian Tr60 maximum flooding, reaching up to Lat. 22° N southward. Younger sequences are dominantly regressive and accompanied

by a northward seaward progradation. Thus, MFS Tr60 represents the most prominent transgression, which accords well with the plate-wide correlation of the Jilh, Sefidar and Marker Dolomites.

A similar hypothesis was formulated for the Gulailah Formation in Abu Dhabi by Hu *et al.* [2015] who divided the Jilh-equivalent Gulailah Formation into Lower and Upper Units, with the lower unit being more layer cake and the upper more regressive. They do not appear to have considered differential erosion beneath a base Minjur Formation unconformity.

The picture is complicated by two superimposed unconformities: the Early Norian hiatus in the marginal marine area (north), and the pre-Minjur erosion, in the fluvial-deltaic domain (south), and principally in the axis of the Minjur inlet [see Issautier *et al.*, 2012a, 2019]. Consequently, it is not possible to determine how far the Tuvalian transgression had reached before truncation by the clastic channels. This configuration is likely due to an uplift of the hinterland during the Early–Mid Norian causing its erosion and thus an increased clastic influx.

Southeastward, in the Rub al Khali Basin of central to eastern Saudi Arabia, Deville de Periere *et al.* [2022] interpreted that the Late Carnian to Early Norian tectonic pulse that generated the unconformity was responsible for the uplift of paleostructures such as the Qatar Arch and the widespread differential erosion of the Jilh Formation.

3. Synthesis of sequence stratigraphy

The stratigraphic evolution of the Jilh and Minjur Formations along the outcrop belt is summarized in Figure 8, which compiles the elementary sequences described along the steps (a) to (d) on the cross sections. This evolution is summarised below:

Anisian transgression (horizon A): Starting from the continental shales and evaporites of the Sudair Shale, the sequence boundary (surface 1) at the bottom is marked by sand input and coal seams. Then, the Anisian shows a period of transgression through salt marshes, with plants and pollens, lagoonal shales and evaporites, ending with transient tidal flats (MFS Tr40, surface 3).

Anisian regression (horizon B): A more confined, possibly lagoonal, setting represented by brackish

shale and sandstone and the lamellibranch *Myophoria goldfussi* completes the HST of the Anisian cycle.

Ladinian cycle (horizon C): A coarse-grained reworked horizon with plants and vertebrate (reptilian and fishes) bone debris marks the sequence boundary (surface 4 = Tr50 SB). It is followed by a rapid regional shallow-marine flooding with a diversified fauna and algae, well dated by conodonts along the outcrop belt (MFS Tr50). It is followed by a regression leading to gypsum deposits in the reference section. In the Ladinian paleogeography, this event likely corresponds to generalized evaporite deposits and to the end of the first arid period. It may be correlated to the sea level low stand from 238 to 237.5 Ma, TLa3 SB of Haq [2018] and Ogg and Chen [2020].

Julian Clastic Event (horizons D to F, and body G): A sharp change occurs in sedimentary conditions with the beginning of a period of major clastic influx marking the Julian sequence boundary (surface 5 = Tr60 SB). Erosional hiatuses may separate the Julian from the Ladinian as explained above. In a landscape of a littoral plain, several fluvial sequences are stacked: horizons D and E, with coarse-grained sandstone and overturned stratifications, capped by thin lagoonal deposits. With progression of the transgression, the sand brought by the river was reworked into coastal/tidal sandstone (horizon F), interrupted by some distal fluvial/estuarine outlets (body G).

Julian Transgression (body H and horizon I): Following the Julian Clastic Event, the transition from clastic to carbonate is underlined by the “TSF” [Time Specific Facies, Brett *et al.*, 2012, Pavia and Martire, 2015], which marks the ongoing transgression with quartz Fe-oolites, glauconites, and intra/extraclasts (surface 8), and some fauna. Deltaic influences persisted in the Jabal al Arid area (body H), but the overall trend is the generalized expansion of tidal flats and an increasing marine influence (horizon I). During the late Julian, the shallow-marine ingressions, dated by conodonts and accompanied by marine fauna and cushion stromatolites, reached its maximum (MFS Tr60, surface 9). It was followed by a brief return to more lagoonal conditions representing the succeeding HST.

Tuvalian transgression (horizon J): Several high-frequency cycles of transgression-regression are recorded in the carbonates of the northern area. They can be considered as part of a new shallow-

marine transgression accompanied by a rich marine fauna including ammonoids, and recorded north of 25° N (MFS Tr70, surface 11). The cycle is completed by a return to restricted conditions during the subsequent HST, though this is variably preserved because of erosion beneath the Early to Middle Norian unconformity (Tr80 SB).

Norian transgressive–regressive cycles: A new short-lived transgressive pulse of limited lateral extent is recorded during the Norian north of 26° N as shown by thin carbonate layers and the presence of Norian marker conodonts. The sequence boundary corresponds to a hiatus, owing to the presence of marker conodonts and of *Tibetitidae* of Alaunian 1 age found in a transgressive horizon not far from the Carnian/Norian boundary. Transient returns to evaporite deposits reflect temporary, higher frequency regressions.

One result of this study is the concept of an early Alaunian wedge, corresponding to the Sequence 4 of Issautier *et al.* [2019] tentatively correlated in outcrop from latitudes 22° N up to 27° N on the basis of similar ages and of a regional flooding event, assigned herein to MFS Tr80, and which truncates the underlying Minjur Sequences 2 and 3 (SB4 unconformity) (Figure 9). However continuous correlation between north and south remains uncertain between latitudes 25° N and 26° N (Al Faydah quadrangle) where the Minjur Sandstone is covered by aeolian sand.

This chronology is comparable with the one proposed by Korngreen and Benjamini [2010] for the northern Arabian Plate. The Mohilla Formation cited in the paper contains abundant interbedded volcanics which complicates interpretation but even so five low-order (LO) cycles were identified and integrated into a sequence-stratigraphic model with eustatic, tectonic, and differential subsidence components: LO Cycle 1 is Late Anisian (Pelsonian), Cycle 2 is Late Anisian to Longobardian, Cycle 3 is Early Carnian, Cycle 4 is Late Carnian, and Cycle 5 is at the Carnian–Norian transition. However, Cycle 5 is likely missing by erosion in Saudi Arabia and over most of the Arabian Plate, being replaced by the early Norian hiatus, but probably preserved in the Israeli boreholes because of their locations towards the western margin of the Arabian Plate. There is no equivalent to the Minjur Sandstone in Israel because of Late Triassic rift-related uplift, thus the pre-

Minjur unconformity is almost certainly merged with the younger Latest Triassic–Early Jurassic unconformity [End Triassic unconformity of Lunn *et al.*, 2019]. Jurassic volcanics or sediments overlie the incomplete Cycle 5.

As mentioned by Issautier *et al.* [2012a] the Minjur clastics may originate from a regional uplift of the hinterland related to a thermic dome as modelled by Le Nindre *et al.* [2003].

4. Particular events and their regional correlations

Jilh sedimentation is marked by important clastic influx, especially during the early Julian alternating with biogenic and chemical deposits such as carbonates and evaporites, following tectonic or global changes. It displays marked lateral facies change into shales, dolomites and anhydrites in the Ghawar area subsurface [Zhou *et al.*, 2009, location on Figures 1 and 12]. Carnian clastics events are well documented in the literature (“Carnian pluvial event”). In contrast, the precise timings of evaporite in the sequence are less well constrained even though Carnian evaporites are common across the Arabian Plate (“Carnian Salinity Crisis”). These alternations are controlled by a combination of tectonic phases, such as the Late Ladinian–Early Carnian rifting, and climate changes which have regional consequences recorded in the sedimentation. Hence, carbonate and evaporite marker horizons can be followed at a plate scale. Thus, the MFS identified in this study (Tr40, Tr50, Tr60, Tr70 and Tr80) should all be readily correlated, except, where eroded beneath regional unconformities. Therefore, in this section we set the early Norian unconformity demonstrated herein in the context of more regional Carnian–Norian hiatuses.

4.1. Age and cause of the Julian Clastic Event

Based on structural considerations and on ages of the events described at the Ladinian/Julian boundary in section “Depositional and structural evolution...”, above, it seems likely that the Julian Clastic Event and its lateral variations, and probable hiatus between Ladinian and Carnian are related to a second phase of Neo-Tethyan extensional tectonics—first phase at the Permian-Triassic boundary—which occurred during this period in the eastern part of the

Arabian Platform [Le Métour *et al.*, 1995, *in* Ziegler, 2001]. Le Nindre *et al.* [2003], also invoked a thermal doming causing erosion of the hinterland during the Late Triassic time. Ziegler [2001] also mentions that: “early in the Carnian a very pronounced relative drop in sea level was recorded throughout the circum-Mediterranean region”.

Following this rifting phase, a contrast between Late Ladinian marine carbonate below and locally coarse clastic deposits above is observed in the studied area as well as for instance, in the Tarasci section (Taurus autochthon) in Turkey [Assereto and Monod, 1974]. At the scale of the Arabian platform, these Early Julian Clastics likely represent the time gap separating the Ghail Formation, dated Olenekian to Ladinian (-Carnian?), from the overlying Milaha Formation, dated Mid to-Late Norian in the Emirates Musandam [Maurer *et al.*, 2008, Urban *et al.*, 2023].

Later on, field and well descriptions of the Jilh Formation and of the Minjur Sandstone show interfingering of clastics, dolomite, and evaporite. So, both the Julian Clastic Event and Jilh evaporites (see next section “Jilh evaporites”) could be partly related to these tectonic events. This interpretation is favoured over one due solely to climate change, as invoked with the Carnian Pluvial Event (CPE) recorded in the Alps and the German Basin for the late Julian or the Julian/Tuvalian boundary [Claudel, 1999, Gaetani, 2010, Somma *et al.*, 2008]. In the Jilh, this interpretation might explain the latest deltaic event (body H of J3), but it does not match the main clastic event which predates *Mazzaella carnica*, and it is contradictory to carbonate dominance during the latest Julian.

However, according to Arche and López-Gómez [2014] the “Carnian Pluvial Event” occurred over large tracts of Central Pangea. It was a short-lived event (>1 Ma), coeval with a marked sea-level fall and active rifting. These authors have identified the CPE in the Iberian Peninsula as a continental clastic wedge forming the Manuel Formation and coeval sediments, in between marine evaporite formations during a marked sea-level drop event; its age is considered to be Julian by palynological and paleogeographic considerations. They propose, for this period, a new correlation of the sediments of the Iberian Peninsula with coeval sediments of Western Europe, NW Africa and Eastern North America, demonstrat-

ing that the geographical extent of the siliciclastic sediments related to the CPE was much larger than accepted before.

4.2. *Jilh Dolomite*

The Jilh Dolomite is a term used to denote a distinctive interval of clean dolomites widely identified from Kuwait to Abu Dhabi, the eastern Rub al Khali Basin and Oman [Deville de Periere *et al.*, 2022, Obermaier *et al.*, 2012]. Davies and Simmons [2018] interpreted it as of Early Carnian age containing their Tr60 MFS, whereas Lunn *et al.* [2019] correlated it with their “Marker Dolomite” which they consider a plate-wide marker, also identified in Iran, Iraq, Syria and Jordan. Lunn *et al.* [2019] assigned a Latest Carnian age to the Jilh Dolomite and picked their Tr80 MFS initially at its base, although Lunn [2020] shifted the pick higher to within the unit. Given these published disagreements, we propose to use our new data to provide a more definitive interpretation.

4.2.1. *Definition*

The subsurface “Jilh Dolomite” is characterized as a tight interval of approximately 30 m thick and c. 25 to 75 m beneath the Minjur Sandstone. It has very distinctive wireline responses, sharp, cylindrical, with a low gamma ray, a low porosity, a high sonic velocity, and the grain density of dolomite, facilitating recognition as the regional “Dolomite Marker” in wells (see Section 2, Triassic Stratigraphy of the Arabian Plate).

4.2.2. *Ar Rub al Khali Basin (Saudi Arabia)*

In the central Rub al Khali Basin, Stewart *et al.* [2016, location on Figure 1] show this tight dolomite interval with an average thickness of c. 30 m. at the boundary with the Minjur sandstones near the Qatar Arch, (although its identification in their well B appears to be in a limestone and may be an older unit), and up to c. 300 feet (91 m) deeper eastward in the basin at the well Lekhwair-70 in Oman (location on Figures 1 and 12). It is eroded on top of the Qatar Arch. The Minjur Sandstone is similarly eroded. Both are unconformably overlain by the Jurassic. Note that the well denoted “A” in central Arabia is Well 143-3 of Issautier *et al.* [2019].

In the north Rub al Khali Basin, Deville de Periere *et al.* [2022] show the same horizon, which includes

a marine median limestone band, with an average thickness of c. 32 m, and lying c. 115 m beneath the Minjur Sandstone. While they do not present sampling information, Deville de Periere *et al.* display age interpretations based on palynology that indicate that the Jilh Dolomite is of Carnian, and almost certainly Early Carnian age given the proximity of the underlying Ladinian beds. Along the eastern flank of the Qatar Arch, it is considerably reduced and probably missing by truncation over the Arch itself. The preserved Jilh Formation is immediately overlain by a residual Minjur Sandstone or directly by Jurassic limestone. The most complete section is in their Well L. Comparison with Well G of Stewart *et al.* identifies this as the same well and therefore located in the Shaybah Field (location on Figure 1).

4.2.3. *Abu Dhabi*

In Abu Dhabi, Taher *et al.* [2012] in connection with tight gas exploration, present a cross section of the Gulailah (Jilh)–Minjur succession (Location on Figure 1). The Gulailah Formation was deposited in similar environments than the Jilh Formation, and, with marked thickening towards the east-northeast that Taher *et al.* interpreted as due to progradation into an intrashelf basin rather than differential truncation beneath the base Minjur unconformity. The “Jilh Dolomite” is easily recognized through its typical wireline response with an average thickness of c. 30 m, with a low permeability. The MFS Tr40 50, and 60 can tentatively be identified through the wireline response and by comparison with the Ghawar section of Zhou *et al.* [2009], respectively at c. 90, 220, and 370 m above the base of the formation. The upper part of the formation is truncated towards the north by the pre-Minjur and pre-Marrat unconformities in relation with the Qatar Arch. In the south, in the wells N and S, the lithological unit above the Tr60 “Jilh Dolomite” and beneath the Minjur (c. 195 m) could be assigned to the Tuvalian (MFS Tr70 at c. 515 m, in part or in totality, by analogy with the northern outcrops of the Jilh Formation. This would be consistent with the interpretations of Davies and Simmons [2018] concerning the equivalent stratigraphy in neighbouring parts of Oman [Obermaier *et al.*, 2012]. Thicknesses are estimated from the isopach map, figure 5 of Taher *et al.* [2012].

4.2.4. Central Arabian Basin

According to Khan *et al.* [2015], in the Central Arabian Basin, in eastern Saudi Arabia, the “Jilh Dolomite” member forms a 90–100 ft. (27–30 m) thick blocky and laterally persistent unit in the upper part of the Jilh succession, with generally low log porosities of 5–10%, although some higher measured core porosities (up to c. 30%) are recorded. From a Sequence Stratigraphy point of view, using palynological data, they assigned it to the Early Carnian MFS Tr60, which is in accord with the conclusions of the current study.

In the Ghawar good examples are provided by the wells A2 and B3 in the Ghawar area, east-central Saudi Arabia [Zhou *et al.*, 2009]. Here, the “Jilh Dolomite” is easily recognized through a complete set of wirelines. It matches an interval of c. 45 m thick between the horizons JLDM (top Jilh Dolomite) and BJDM (base Jilh Dolomite) and c. 45 m below the Minjur Sandstone.

In the central Arabian Basin, Lunn [2020, his figures 4 and 6], incorrectly interpreted the correlations of the “Jilh Dolomite” in the Minjur cross-section from Issautier *et al.* [2019, their figure 14].

- First of all, the “Jilh Dolomite” (12 m) was picked in a layered shale–dolomite interval, c. 25 m below the base Minjur whereas the “dolomite marker” appears 50 m deeper, with a sharp contrast in wireline response between shale, above, and dolomite, below.
- This clayey–dolomitic interval was correlated with a dolomitic bed at the base of the Khashm al Khalta section in outcrop. The latter, in fact on top of the Jilh al Ishar–Jabal al Arid Jilh section [23°36' N, Vaslet *et al.*, 1983] is the “Jilh Dolomite” dated by Le Nindre *et al.* [1987, 1990b] as Carnian age by the conodont *Quadralella polygnathiformis* [see Part I, Le Nindre *et al.*, 2023 and its Appendix A4], the most landward faunal indicator of the MFS Tr60 in outcrop (see Figure 5).

4.2.5. Correlations

The “Jilh Dolomite” or “Dolomite Marker” is identifiable at the scale of the platform, as shown by the “Triassic regional stratigraphic correlation panel Jordan–Syria–Iraq–Lurestan–Kuwait–Saudi Arabia. (Datum: base Marker Dolomite)” of Lunn [2020],

his figure 6. This correlation plate demonstrates that, starting from the outcrop sequence through the Ghawar [Zhou *et al.*, 2009, see above], two major transgressive dolomitic horizons are always present: the (late) Ladinian containing the MFS Tr50, and the late Early Carnian Tr60. Through all these sections, it is interesting to observe that:

- The uppermost dolomite of the section Jilh al Ishar–Jabal al Arid Jilh section (Section A, Part I, 23°36' N), is the “Jilh Dolomite” in outcrop and is dated of Carnian age by the conodont *Q. polygnathiformis* (see Part I), and the most landward faunal indicator of the MFS Tr60.
- Sequence 1 of Issautier *et al.* [2012a, 2019] “Transition Jilh–Minjur”, above the “Jilh Dolomite” of the Jilh al Ishar–Jabal al Arid section and below the first fluvial beds of the Minjur Sandstone in Khashm al Khalta, may correspond, by its evaporite and clastic content, and by the correlation done, to the intermediate sequence observed in wells [e.g., Sequence 4 of Deville de Periere *et al.*, 2022]. So, it would correspond to a residual, evaporitic, undated Tuvallian, on the basis of a Late Carnian age of this intermediate lithological unit in other wells (T2A palynosubzone).

4.3. Jilh Evaporites

In the Middle East, thick Triassic evaporites occur in several formations that are coeval with the Jilh Formation. They are sometimes grouped together as the “Carnian Salt Crisis” [Al-Husseini, 2008, Haq and Al-Qahtani, 2005, Lunn *et al.*, 2019, Sharland *et al.*, 2001, 2004]. These evaporites are referred to as the “Jilh Salt” in subsurface Saudi Arabia, “Middle Salt” in Kuwait, Kurra Chine Salt or Lower Kurra Chine Evaporite in Syria, the Zerqa (Zarqa) Gypsum or Halite in Jordan, and Evaporite members of the Dashtak Formation in Iran. This “salinity crisis” [Hirsch, 1992] expressed itself in the epicontinental regions as a typical lowstand evaporite sequence dominated by halite and sulphate deposition, continental sands, marls and shales. Evidence from the Palmyride Trough in Syria is of very shallow water deposition throughout the thick Triassic section [Lucic *et al.*, 2010], indicating that sedimentation generally maintained pace

with the creation of accommodation space even in areas prone to greater subsidence.

4.3.1. *Surface Saudi Arabia*

Our study indicates that the Jilh Formation in outcrop contains disseminated evaporitic beds rather than a major evaporitic interval clearly differentiated in the stratigraphy as Haq and Al-Qahtani [2005] had suggested in their chart. This is likely due to the proximal outcrop setting which corresponds to a marginal location where siltstone–claystone deposition dominated over evaporites (Figure 3, Part I) which are more concentrated in central or eastern depressions [Glantzboeckel, 1981, Ziegler, 2001]. However horizons with evaporitic or pre-evaporitic facies are observed: (1) in the Anisian of Unit J1; (2), in the Ladinian–early Julian Unit J1, essentially in the reference section (24°15' N); (3) in the latest-Julian–Tuvalian Unit J3 between 24°30' N and 23°30' N (Khabra Halwah, Khashm al Khalta), and (4) in the Norian Unit J3, north of 26° N. Elsewhere, evaporites occur as thin intercalations within the dolomitic tidal flats and algal mats of sabkha deposits of the formation. In this discussion we review the age interpretations of various evaporitic units in other regions and their relationship to the Jilh outcrop in Central Arabia.

4.3.2. *Subsurface Saudi Arabia*

In subsurface Saudi Arabia, Haq and Al-Qahtani [2005, see their enclosure 2] show the Jilh evaporite in mid-Carnian, immediately pre-dating Tr70, and above the “Lower Jilh”, although we would caution that their model was based on the flawed Sharland *et al.* [2001] interpretation. Comparison with the original definitions in the reference section of the “Lower Jilh” and “Upper Jilh” indicates that the former corresponds to Anisian–Ladinian Unit J1 (Figure 2, Part I). The position of the Jilh evaporite in lowermost Unit J2 strongly implies an early Julian rather than a mid-Carnian age. An early Julian age is in agreement with the age of the “Carnian Salt Crisis” of Ziegler [2001], who related the evaporites to the sea-level lowstand of the early Carnian “Saharan Salinity Crisis”. It is also consistent with the Julian age for the “Carnian Salt Crisis” in the Middle East, based on ostracods and palynomorphs determined by Gerry *et al.* [1990].

The regional vertical distribution of the Jilh Evaporite into four stages is shown by Issautier *et al.* [2019, their figure 16, p. 166]:

- The Anisian evaporite, predates the dolomite and tidal flats of the transgression Tr40.
- The Mid Ladinian evaporite, corresponds to the coastal plain and sabkha deposits (gypsum silts and clays) underlying Ladinian MFS Tr50 in outcrop (Figure 3, Part I).
- The Late Ladinian–early Julian evaporite corresponds to the gypsum above MFS Tr50 in the reference section at Khashm Dolqan and to the relative lowstand near the base of the Julian clastics. These two episodes are coeval with the coastal plain/sabkha deposits shown in Figure 3, Part I. They occur above and below the Ladinian tidal flats and, together with the Julian clastics, match the Early Carnian Salt Crisis of Ziegler [2001, his figure 5].
- The Tuvalian evaporite is locally observed above the dolomite Tr60, as for instance in Minjur Sequence 1 of Issautier *et al.* [2012a] which Issautier *et al.* [2019] correlated with the T2A palynozone in the nearest Well 143-3 [Well A of Stewart *et al.* [2016], location on Figure 1].

In summary, compiling well logs [e.g., Deville de Periere *et al.*, 2022, Lunn, 2020, Zhou *et al.*, 2009] shows that the Jilh evaporites in subsurface Saudi Arabia are commonly interstratified as anhydrite stringers within dolomitic beds between the two major flooding intervals Tr50, Ladinian, and Tr60, Julian (“Jilh Dolomite”), thus time equivalent with the “Julian Clastics”, as well as preceding the Ladinian flooding Tr50 and in the Anisian. Anhydrite stringers may also be observed in the Norian portion in equivalence with the Alaunian 1 evaporite described in the field, north of the Wadi ar Rimah (Lat. 26° N, North Wadi ar Rimah and Ibn al Fuhayd sections).

4.3.3. *Northern Arabian Plate*

In the northern Arabian Plate, Sadooni and Al-sharhan [2004] described an Anisian–Ladinian “Keuper type” evaporite and an early Carnian “Raibl type” (“Pan-Mediterranean salt crisis”). These evaporites correlate to the Anisian and Ladinian–early Julian

evaporites in the Saudi Arabian outcrops. In the Minagish and Burgan fields in Kuwait (location on Figures 1 and 12), Lunn [2020] mentioned it as “Jilh Salt” in between two major dolomitic intervals which, similarly, corresponds to the same Ladinian and Julian MFI’s, referring to current study, Davies and Simmons [2018], and to larger scale correlations.

Equivalences of the Norian evaporite mentioned in the Jilh Formation and at the base of the Minjur Sandstone north of the Wadi ar Rimah (26°30′ N, see Part I, Appendix A1) are not well documented at the regional scale. A likely coeval evaporite restricted to the northern Arabian Basin is mapped by Ziegler [2001, his figure 6]. It is uncertain whether the ?Lacian–Alaunian evaporites represented by Sharland *et al.* [2004] associated with hiatuses in Jordan (Abu Ruweis Formation) and Syria (Mulussa Formation or in Iraq (Upper Kurra Chine Formation) may be time equivalent.

4.3.4. *Iran*

In the Iranian Zagros, the Dashtak Formation represents the Middle to Late Triassic [James and Wynd, 1965]. Biostratigraphic control is limited. Szabo and Kheradpir [1978] recognised four carbonate–evaporite cycles in the Dashtak Formation that could be correlated the length of the Zagros (e.g., Dashtak-1 and Kuh-e-Siah-1 wells, location on Figures 1 and 12). This four-fold stratigraphic layering continues to be identified in multiple recent publications including Hajian Barzi *et al.* [2015], Davies and Simmons [2018], Esrafil-Dizaji and Dalvand [2018] and Horbury [2018], demonstrating the utility of these subdivisions.

The sequence stratigraphy of the Dashtak Formation by Sharland *et al.* [2001, p. 190–191 and their figure 3.22] was revised by Davies and Simmons [2018] and may be correlated with the Jilh Formation at outcrop: the Dashtak Evaporite A corresponds to the Sudair Shale, Evaporite B matches the top of the Anisian sequence. Evaporite C occurs between MFS Tr50 and Tr60 (the Sefidar Dolomite Member, (alias “Jilh Dolomite”) and would match the late Ladinian–Early Carnian Julian Clastics and evaporites in Saudi Arabia [Davies and Simmons, 2020, their figure 3]. Anhydrite stringers interstratified in the limestone above Tr70 and below J10SB (Neyriz Formation) are differentially preserved beneath the unconformity truncating the Dashtak Formation, where

the two unconformities identified in this study are superimposed. Hence these stringers are much more likely equivalent to the highstand overlying MFS Tr70 than the Alaunian evaporite present north of the 25°30′ N in outcrop in Saudi Arabia (see Figure 3, Part I).

4.4. *Baluti formation and Carnian–Norian unconformity*

For a better understanding of this Early to Middle Norian time gap, it is worth briefly considering stratigraphic data from the northern Arabian Plate. The Baluti Formation, is mentioned by Ziegler in its paleogeographic map of the Late Triassic (Tr60–J10) as a narrow southward incursion of “shallow marine to marginal marine clastics”. Although lying in the Ladinian–Liassic interval, the Baluti Formation was originally accepted as of Rhaetian age, by regional correlation in the Stratigraphic Lexicon of Iraq [van Bellen *et al.*, 1959–2005] and thus not synchronous with the early Mid Norian transgression. However, uncertainty continues with respect to the age of the Baluti shales and recent publications present contradictory interpretations of its regional correlations at the scale of the Arabian Plate. For example, Sharland *et al.* [2004] positioned the Baluti clastics above an early Norian unconformity, between the Upper Kurra Chine Formation (dolomite) and the Butmah Formation, in the late Lacian. In their model, the Baluti Formation predates the Tr80 MFS positioned in the Early Alaunian. This interpretation is not far from the schema proposed for the Jilh–Minjur in our present study but in detail cannot represent the true Baluti Formation as defined by Lunn *et al.* [2019].

Lunn *et al.* [2019] commented on the confusion concerning the Baluti shales, noting that the term was not used consistently in outcrop and subsurface sections in northern Iraq. In detail they stated that Sharland *et al.* [2001] misapplied the term to three separate shales (“Shales 1–3”), According to Lunn [2020], only “Shale 2” corresponds to the true Baluti shales. Palynological data for this “Shale 2” in Well Atrush-1—location on Figure 12—[figure 6 of Lunn *et al.*, 2019], provides a general Carnian age, and show a palynoflora discontinuity in the Lower Sarki Formation between 2155 m (LDO of *Classopollis*, Late Norian) and 2170 m (FDO of *Partitissporites*, Carnian).

Lunn *et al.* [2019] mentioned a Tuvallian (late Carnian) age based on proprietary data from Jebel Gara in northernmost Iraq, although another palynological study by Hanna [2007], stated a Julian (Early Carnian) age for the basal Baluti at the same locality with a possible Norian age for the uppermost beds of the formation. Azo [2020] also interprets the Baluti shales as being partially of Julian age. Thus, the biostratigraphic data available to date remains equivocal and does not refute our interpretation that the “Marker Dolomite” that underlies the Baluti Formation is older than previously interpreted and of Julian (Early Carnian) age, and therefore equivalent to the Jilh Dolomite of Saudi Arabia and neighbouring countries, as proposed by Lunn *et al.* [2019]. A further consequence of this interpretation is that the thick carbonate–evaporite cycles that form Kurra Chine B and C, as observed in Jebel Kand-1, are most likely of Ladinian to Julian age, and therefore represent higher frequency events that are only easily recognised in areas of increased sedimentation where rapid subsidence generated significant accommodation space. This has important implications for the regional extent of the source–reservoir–seal combination identified in Kurra Chine B in northern Iraq [Lunn, 2020].

From the figures 1 and 3 of Lunn [2020], the shale portion of the Baluti Formation in subsurface (e.g., wells Jebel Kand-1 and Sheikh Adi-1 near Atrush-1—location on Figure 12) is clearly above the Kurra Chine A Dolomite Marker and evaporite sequence, with a sharp contrast above and below suggesting discontinuities. We have explained above in section “Jilh Dolomite” how this marker corresponds to the Late Julian MFS Tr60. Davies and Simmons [2020] in a discussion of Lunn *et al.* [2019] suggest the Baluti Formation (Shale 2) may comprise two distinct units: a lower main portion of Carnian (possibly Tuvallian) age—overlying the Kurrachine Formation and representing the highstand above MFS Tr60—and a minor upper portion, of Late Norian (Sevatian age)—underlying the Sarki (= Butmah *sensu lato*) Formation—separated by a major time hiatus. This disconformity—although not pointed out in these papers—appears implicitly above BS.25 as “CRN or NOR” (i.e., “Carnian or Norian”, BS.34-35) in the palynological chart of Lunn *et al.*, 2019, their figure 4 [after Hanna, 2007], Jebel Gara section. In this chart, the shale portion of the Baluti Formation strictly cor-

responds to the Baluti shales of the well logs, while the upper limestone portion corresponds with the Lower Sarki/Butmah of the well logs. Erosional relief on this unconformity, comparable to that identified in Saudi Arabia (this study) means that a more complete Tuvallian section, including beds containing MFS Tr70, is almost certainly differentially preserved across northern Iraq. Further biostratigraphic analysis of the Kurra Chine, Baluti and Sarki Formations, particularly focused on conodonts, in multiple sections is recommended.

5. Paleogeography

From Ladinian to Norian times, the paleogeography of the Arabian shelf was dominated by transitional environments (coastal plain to shallow-marine shelf) and mixed carbonate–clastic–evaporite sediments [Glantzboeckel, 1981, Le Nindre *et al.*, 1990a, Murris, 1981, Ziegler, 2001]. In the western area of the shelf, fine-grained clastics were deposited (“shale”: siltstone and claystone with some anhydrite), while mixed carbonates and evaporites dominated in the Gulf area. The main events in proximal areas were: deposition of marginal marine deposits with evaporites during the Anisian, influx of continental clastic to the shelf during the Julian and during the Norian (Lower Minjur Sandstone). Marine transgressions occurred during the Ladinian (Tr50), Late Julian (Tr60) and Tuvallian (Tr70), and to a less extent, during the early Alaunian (Tr80) resulting in deposition of marine carbonates. When compared to sections located in the south, the relative abundance of fauna collected from sections now located further north bears witness to the fact that marine conditions persisted for longer in the north than in the south, and this argues in favour of connections with an open-sea environment to the north (outcrop belt is oblique on the general paleogeographic trends).

5.1. Connection with the Sephardic Province during the Ladinian

The Early Triassic global paleogeographic setting [Figure 10, modified after Scotese, 2001, and Blakey, 2003] shows the location of the Arabian Plate on the margin of the Neo-Tethys Ocean. A configuration of barred platform (Zagros, Qatar Arch) with stronger

marine connectivity from the north had already appeared at this time.

The paleobiogeography of the Ladinian conodonts (Figure 11) demonstrates the existence of four different associations [Dercourt *et al.*, 2000a,b, Vrielynck and Cros, 1992, Vrielynck *et al.*, 1994].

A major one—Tethyan type—is restricted to open-marine areas in which the sequences of the northern (Alpine), western (Dinarids, Hellenids), and southern (Taurids) margin were deposited; this pelagic association is also encountered in the facies of the eastern Neo-Tethys as far and beyond as Japan.

The other three associations are encountered in relatively shallow-water facies in (1) Germany, (2) the Sephardic Province, and (3) the Balkans. Geographic separation may account for the differences between conodont associations in the Germanic and Sephardic provinces. The specificity of the Balkan shelf is seen as due to its isolation from the Laurasian Plate. An oceanic buffer (the Paleo-Tethys Ocean) may be invoked, having been more substantial during the Ladinian than during the Pliensbachian [Kazmin *et al.*, 1986, Ricou *et al.*, 1985, 1986].

For the Ladinian, among the species collected in this study, forms belonging to the genus *Pseudofurnishius* are characteristic of the Sephardic Province defined by Hirsch [1972], whereas pelagic Tethyan type conodonts [Bender, 1967, Gedik, 1975, Krystyn, 1983, 2008, Vrielynck, 1980, 1987] are missing. The observed Sephardic biofacies thus appears to be associated with sedimentary conditions such as salinity, water depth (shallow platforms surrounding the Neo-Tethys), and temperature or—as envisaged by Tollmann [1984], and Tollmann and Kristan-Tollmann [1985]—the presence of anti-clockwise currents bounding emergent sectors of the African Plate and hampering colonization of the Arabian shelf by open-sea fauna.

During the Carnian and Norian, the Sephardic and Tethyan conodont provincialism either disappears or has yet to be identified.

Kear *et al.* [2010a,b] come to a similar conclusion given by the vertebrate assemblages collected from the lower Jilh Unit 1 of which affinities reflect the close proximity of the Arabian region to the Sephardic Province, characterized by a distinct faunal composition. This thesis was developed above in the section “Discussion of Ages” with more emphasis on genera and species present.

5.2. *Jilh time-evolution in the paleogeography of the Arabian Plate*

Glantzboeckel [1981, BRGM internal report] drew a series of palaeogeographic maps of Saudi Arabia that included the Middle to Late Triassic stratigraphy described herein. Ziegler [2001] drew, with the input of two of the present authors (YML and DV), two palaeogeographic maps corresponding to the Middle to Late Triassic, although still without the full benefit of our current stratigraphic understanding, in particular the importance of the Late Carnian to Early Norian hiatus. In detail Ziegler’s two maps depicted composite representations of:

- the paleofacies of the Middle Triassic spanning the deposition of the Jilh Formation and of its regional equivalents from MFS Tr40 to intra- Tr60 (his figure 5);
- the paleofacies of the Late Triassic spanning the deposition of the Upper Jilh and of the Minjur Sandstone from MFS Tr60 to intra-MFS J10 (his figure 6). It can be argued that this latter map is more representative of the Carnian sediments preceding the hiatus in the northern half of the Arabian Plate (e.g., Carnian evaporites in the Palmyride Trough), but of the Norian sediments postdating the hiatus in the southern half, including the outcrops that are the main subject of the present study.

Transposing the facies limits from a N–S section (see Figure 6) to these maps highlight the horizontal dynamics and illustrates the evolution of the transgressions from Ladinian to Norian as visible in the Jilh Formation outcrops, and thus after truncation by the pre-Minjur unconformity (Figure 12).

During the Ladinian and the Lower Carnian (Figure 12), it illustrates the difference of trends between the clastic inputs (towards the northeast) and the marine incursions (from the north), consistent with the migration of Ladinian conodonts from the Sephardic Province. (See Section 5.1. “Connection with the Sephardic Province during the Ladinian” above). Evaporitic pans are concentrated in the Central Arabian Basin. The first stage of transgression corresponds to the southward extent of the Ladinian tidal flats (1) associated with MFS Tr50. Then, during the Early Carnian, clastic wedges prograded from the

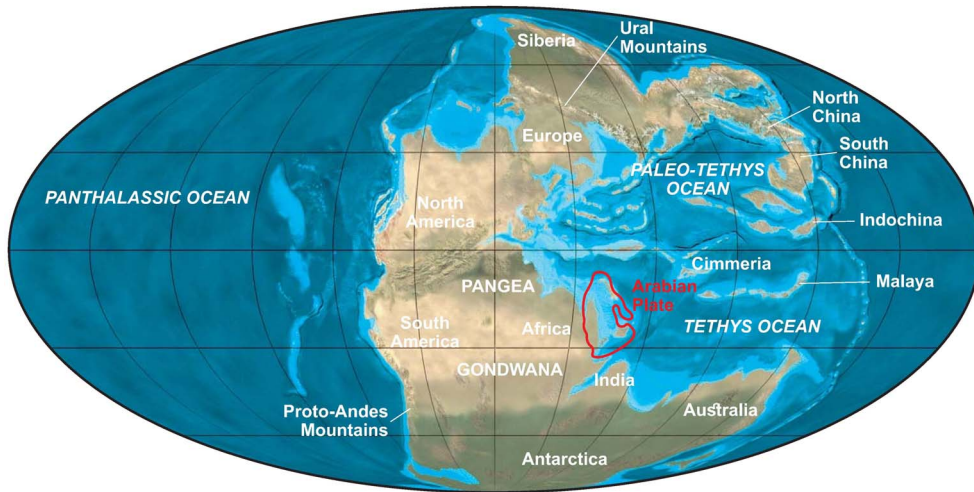


Figure 10. Early Triassic plate-tectonic setting showing the position of the Arabian Plate (in red) with northward opening of the Central Arabia Basin [modified from Scotese, 2001; Blakey, 2003].

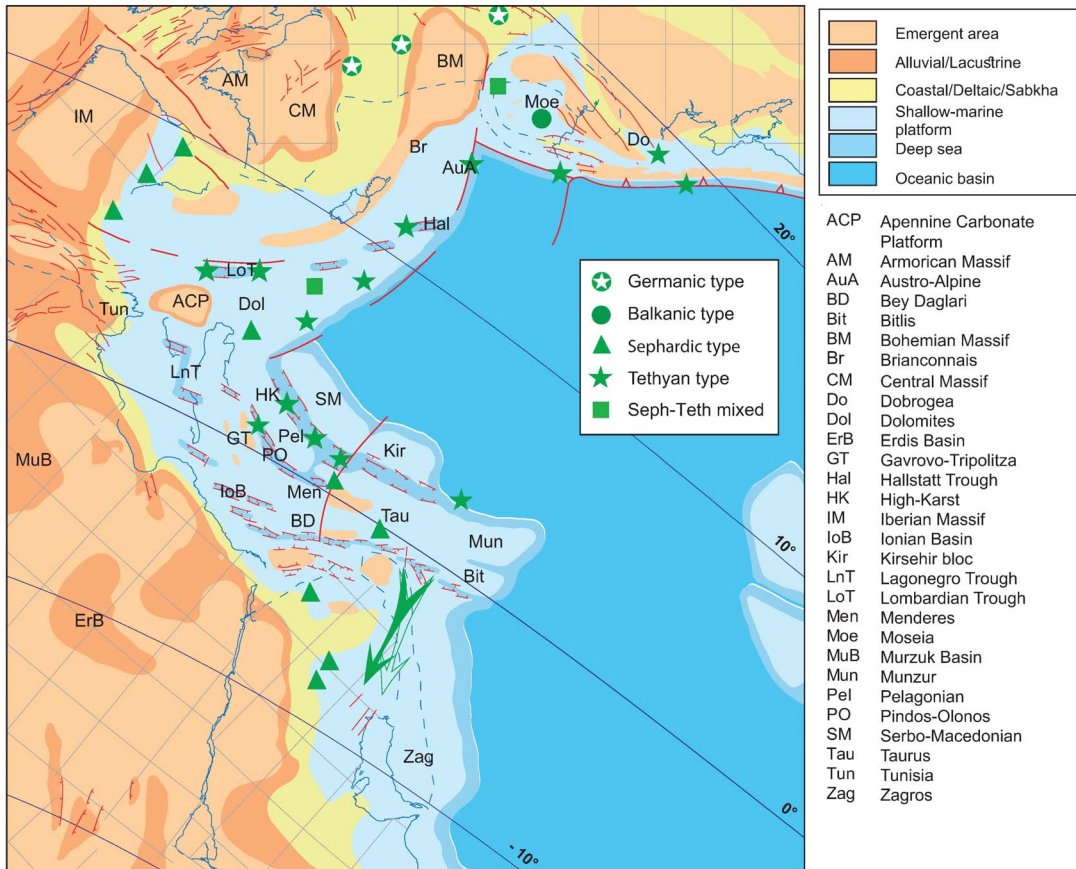


Figure 11. Distribution of Ladinian conodonts throughout the Mediterranean Tethyan domain [palaeogeographical base-map modified from Dercourt *et al.*, 2000a,b, Barrier and Vrielynck, 2008].

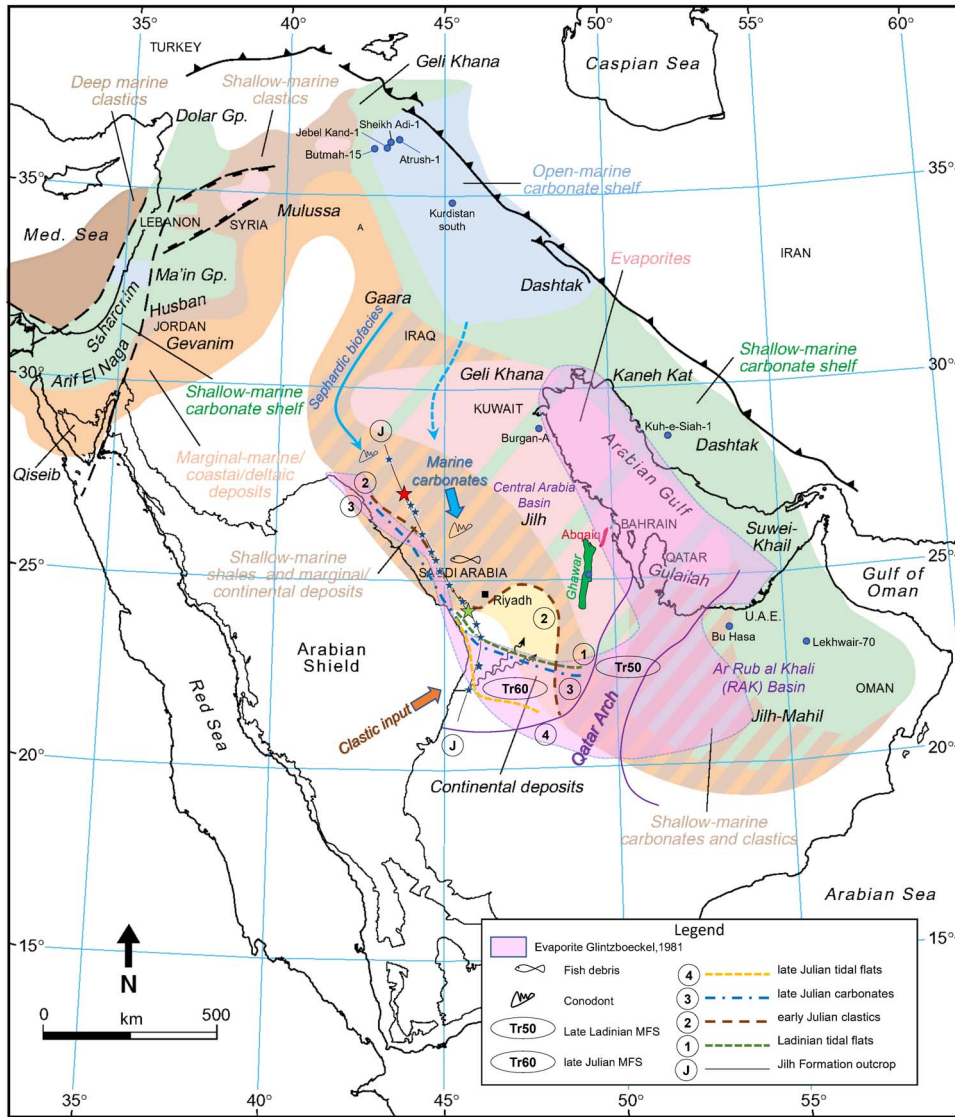


Figure 12. Extent of the main sedimentary events of the Jilh Formation, from Ladinian to late Julian in chronologic order, as in outcrop, and inferred under the early Norian–pre-Minjur unconformity. Base map modified after Ziegler [2001] by permission of GeoArabia, with contribution of Le Nindre et al. [1990a] for the outcrop. Legend for outcrop, see Figure 1.

shelf (2 in Figure 12). During the Julian, the shallow-marine facies (3) achieved their maximum extent southward (23°30' N) since the Ladinian; meanwhile generalized tidal flats (mixed or carbonated) capped the clastics further south up to 22° N (4, MFS Tr60, Figure 12). Glintzboeckel [1981] depicted more common evaporites in the Gulf, while marine carbonates occupied a broader surface in the north central area,

whereas Ziegler [2001] maps a mixed evaporites and shallow marine carbonate shelf which is more consistent with our present knowledge. In a further difference between the two accounts, Ziegler maps shallow marine carbonates and clastics in the Rub al Khali Basin, while Glintzboeckel extended evaporites into this basin, which is principally true during the Anisian, and partially true during the Carnian [Dev-

ille de Periere *et al.*, 2022].

During the Tuvalian and the Norian (Figure 13), the general shape we give to the transgressive wedges is inspired from the tongue of “Marginal-marine to shallow-marine clastics” (Baluti Formation facies) which penetrates the “continental deposits” during the Norian.

The Tuvalian transgression (5), likely truncated, reached up to 25° N, a little more with tidal flats, and likely up to 23°30' N: Issautier *et al.* [2012a] and Issautier *et al.* [2019] have supposed that the Tuvalian (Tr70) may have a more southern extension at the base of the “Minjur Sandstone” *sensu* Vaslet *et al.* [1983] at least up to 23°30' N with sabkha facies (Sequence 1), and in the near subsurface upper Jilh of the well 143-3 (Palynozone T2-A,) but any more southerly extent was truncated by the Carnian–Early Norian unconformity (SB2, Figure 9). The Norian marine deposits (Tr80) reached more or less 25°30' N southward in the Jilh Formation while tidal flats and local tidal inlet are identified up to 23°30' in the Minjur Formation. The Ladinian to Norian transgressive pulses appear with the marine influences progressively regressing northwards in relative to the central evaporitic basin. This Norian paleogeography is consistent with the global Neo-Tethys reconstruction for this period of Berra and Angiolini [2014].

6. Conclusions

- (1) New correlations within the Jilh Formation and the Minjur Sandstone in outcrop and subsurface highlight geometric and chronostratigraphic aspects of the Middle–Late Triassic in Saudi Arabia.
- (2) Five main marine flooding intervals characterizing the late Mid–Late Triassic Epochs were demonstrated from outcrops on the western margin of the Arabian shelf. It is likely that the Anisian tidal flats deposits represent the MFS Tr40. The other marine flooding events are well constrained by marker faunas: Ladinian MFS Tr50, late Julian (Early Carnian) MFS Tr60, Tuvalian (Late Carnian) MFS Tr70, and early Alaunian (Mid Norian). Different populations of Ladinian conodonts in stratigraphically equivalent horizons are explained by environmental factors, instead of age differences. La-

cian rocks are probably absent owing to erosion beneath the combined Late Carnian to Early Norian and Early to Middle Norian unconformities [SB2 and SB4 respectively, of Issautier *et al.*, 2012a, 2019]. The Alaunian MFS (S4 MFS) is, dated by *Tibetitidae* and the *Ancyrogondolella praeslovakensis* faunas, north of Lat. 25° N, in correspondence with the *Rhaetogonyaulax wigginsii* palynosubzone of the middle Minjur. It is tentatively assigned to “Tr80” in Central Arabia. An alternative definition of “Tr80” exists in Musandam in the Milaha Formation [Davies and Simmons, 2018], but the most recent results from that section [Urban *et al.*, 2023] appear to favour a similar Middle Norian age for this MFS, with a Late Norian age for the overlying sequence in the Ghalilah Formation (MFS Tr90?).

- (3) Truncations separating the packages could be invoked at the base of the Julian clastics (base Unit J2), at the base of the Late Julian transgression (TSF, Time Specific Facies—Brett *et al.*, 2012, Pavia and Martire, 2015—with Fe oolites) on top of paleosols, and between the Carnian and the Norian. These are candidates for plate-wide sequence boundaries (Tr60 SB, Tr70 SB and Tr80 SB). The nature of the boundary between the Anisian and the Ladinian is not definitively resolved at the regional scale.
- (4) The boundary between the Jilh Formation and the Minjur Sandstone [SB2 of Issautier *et al.*, 2012a, 2019] is sharp, with an erosional contact in the fluvial portion of the system in central Arabia near the reference sections. Towards the south, a valley fill containing tidal inlet, sabkha, and fluvial deposits is identified. An undated sequence [Minjur Sequence 1 of Issautier *et al.*, 2012a,b] with sabkha facies previously assigned to the Minjur Sandstone caps the Julian Jilh Dolomite and underlies these erosional channels. By lateral correlation we have interpreted these horizons as residual Tuvalian (T2A palynosubzone). An important finding of this study is reconstruction of an early Alaunian transgressive wedge, with an erosive base taken on the sequence boundary (SB4) which

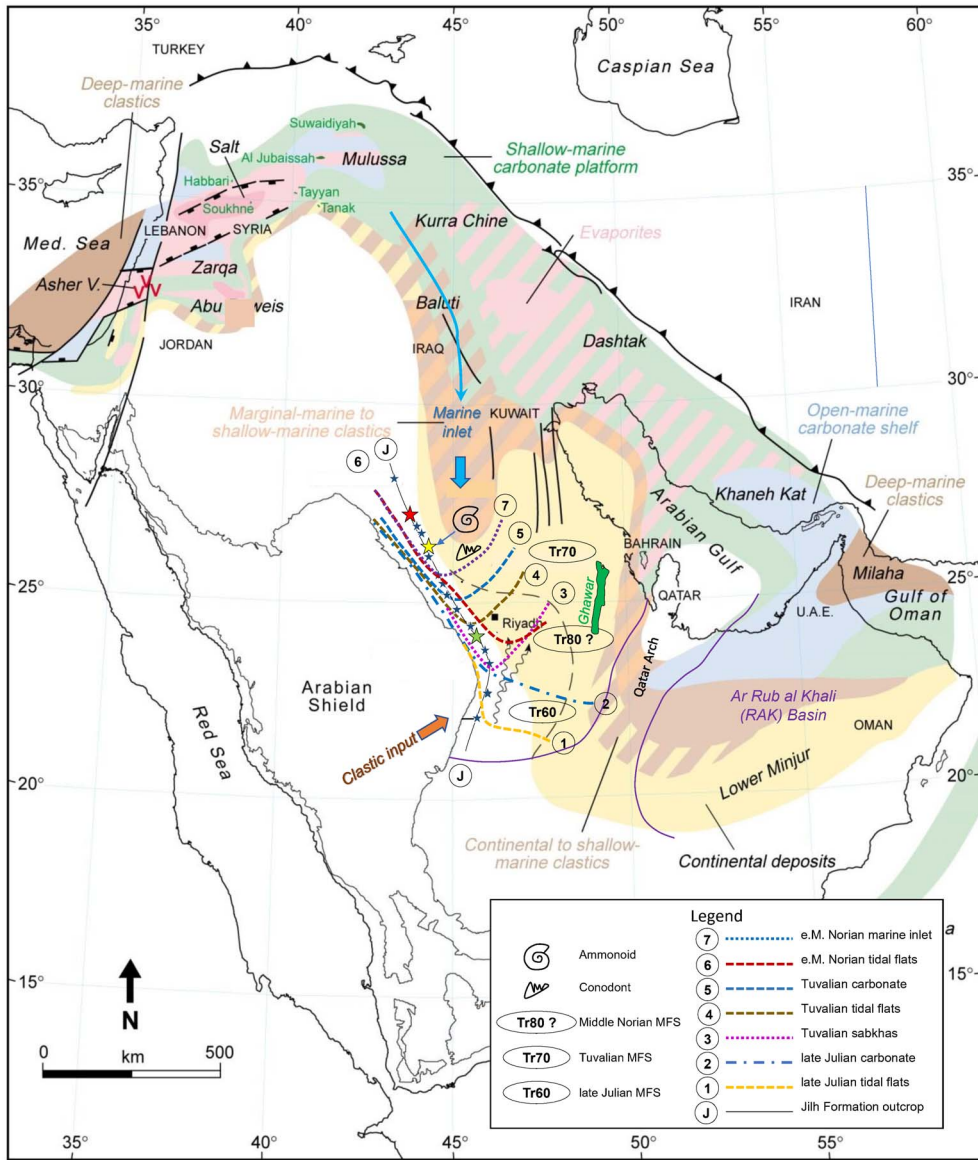


Figure 13. Extent of the main sedimentary events of the Jilh Formation, from late Julian to Middle Norian in chronologic order, as in outcrop, and inferred under the early Norian–pre-Minjur unconformity. Base map modified after Ziegler [2001] by permission of GeoArabia, with contribution of Le Nindre et al. [1990a] for the outcrop. For legend of the Jilh outcrop, see Figure 1.

had been correlated from central to north Arabia.

- (5) Interfingering of various sediment types, and abrupt changes in lithology, as at the Ladinian Carnian boundary, are not explained by sea level changes alone. The deconstruction done, employing multiple datums, il-

lustrates the role of tectonics, by identifying several structures active during the sedimentation. This does not exclude a probable, though possibly minor, role of the climate, including the Carnian Pluvial Event. This study enables a better understanding of the complex relationships between carbon-

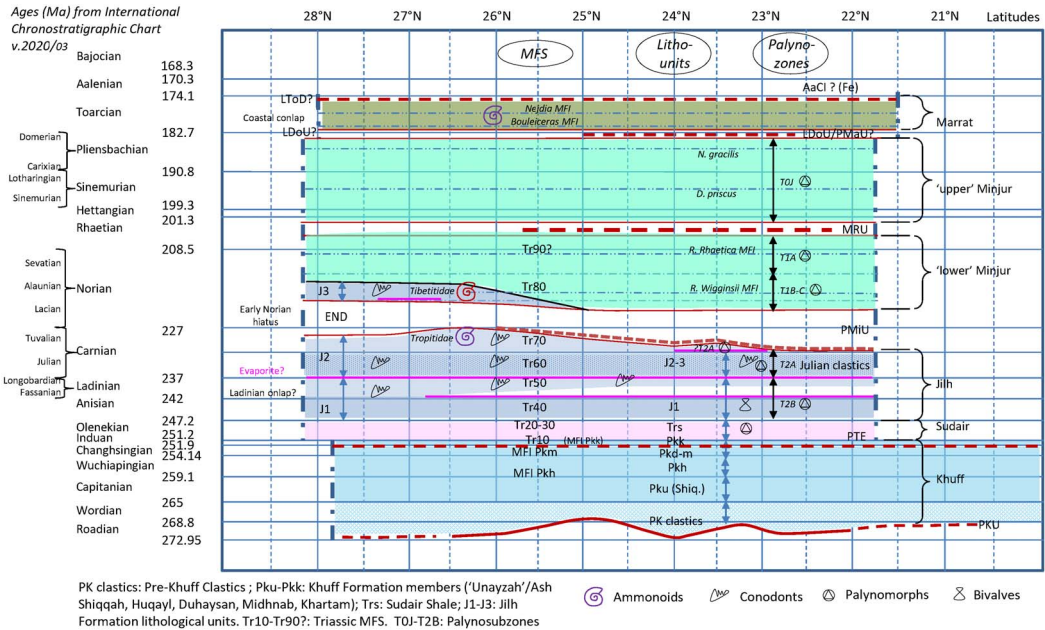


Figure 14. Overall chronostratigraphic chart of the Late Permian to Mid Toarcian time interval. MFS modified after Davies and Simmons [2018]; Permian and Triassic depositional units after Le Nindre *et al.* [1990b] and Vaslet *et al.* [2005]; palynozones after Issautier *et al.* [2019] and Deville de Periere *et al.* [2022]. (PKU: Pre-Khuff unconformity; END: Early Norian disconformity; PMiU: Pre Minjur unconformity; MRU: Mid Rhaetian unconformity; LDou?/PMaU: Domerian/Pre-Murrat unconformity; LTod: Late Toarcian disconformity; AaCi (Fe): Aalenian condensed interval.)

ate, evaporites and siliciclastic detrital rocks which are the major characteristic of these Mid–Late Triassic Epochs. Through a stratigraphic analysis based, not just on well logs facies correlation but on reliable biostratigraphic studies in outcrop (to be continued), better regional correlations are made possible.

- (6) The paleogeographic reconstruction first inserts the faunas collected for the study in a Tethyan paleo-biogeography. Understanding their migration is a precious aid to reconstruction of the processes of transgression and regression at large scale. The lessons learned from outcrop are now integrated in the Middle East paleogeography of the Mid–Late Triassic, showing the dynamic keys of the different periods.
- (7) From the results obtained in Parts I and II of this study, complemented by previous publications [e.g., Davies and Simmons, 2018, Deville de Periere *et al.*, 2022, Haq, 2018, Is-

sautier *et al.*, 2019, Le Nindre *et al.*, 1990b, 2022, 2023, Manivit *et al.*, 1990, Vaslet *et al.*, 2005], we have derived an overall chronostratigraphic chart spanning this time interval and expanded to include the Late Permian to Early Triassic Khuff Formation and Sudair Shale, and the Early Jurassic Murrat Formation (Figure 14). The absolute ages are from GTS 2020/03 [Cohen *et al.*, 2013, updated 2020]. These results facilitate correlation throughout the platform, especially where reliable biostratigraphic markers are present.

Conflicts of interest

Authors have no conflict of interest to declare.

Acknowledgments

The authors thank the Deputy Ministry for Mineral Resources, Kingdom of Saudi Arabia, for his sup-

port to the Phanerozoic Cover Rock Mapping Program during which most of the field works were performed and for permission of publishing (BRGM-OF-06-31). The publication of this Synthesis on the Triassic of Saudi Arabia was made possible through this Special Publication as a Tribute to Jean Der-court under the auspices of the French Académie des Sciences. Authors are especially grateful to the editors François Baudin, Sorbonne Université, François Chabaux, Strasbourg University and Eric Calais, Ecole Normale Supérieure for their invitation, encouragement, and support. The authors have special thanks to Augustus Wilson and Moujahed I. Al-Husseini, former GeoArabia Editor in Chief, for their constructive comments while writing this paper. The new decisive results on conodonts from the Qibah area by Leopold Krystyn were made possible thanks to the support provided by Olivier Serrano, BRGM. Thanks to James W. Haggart from the Geological Survey of Canada who very kindly took from his time for providing photos of the original Tozer's collection of ammonoids in Vancouver, and to Raymond Enay, for specimens stored in the University Lyon I, we have now illustration of this key fauna. The authors are also very grateful to Nino Buhay, former graphic team of GeoArabia. We thank the anonymous reviewers whose insightful comments greatly improved the paper.

References

- Al-Husseini, M. I. (2008). Launch of the middle east geologic time scale. *GeoArabia*, 13(4), 185–188. p. 11.
- Al-Mojel, A. S. (2017). *Sedimentology and Sequence Stratigraphy of the Jurassic, Jabal Tuwaiq, Central Saudi Arabia*. Thesis 2017 bor30037, Doctorate Sciences and Technology, Université Bordeaux Montaigne. 01/12/2017, 368 p., 87 figures.
- Arche, A. and López-Gómez, J. (2014). The Carnian Pluvial event in Western Europe: new data from Iberia and correlation with the Western Neotethys and Eastern North America–NW Africa regions. *Earth-Sci. Rev.*, 128, 196–231.
- Assereto, R. and Monod, O. (1974). Les formations triassiques du Taurus occidental à Seydischir (Turquie méridionale). Stratigraphie et interprétation sédimentologique. *Memorie Riv. Ital. Paleontol. Stratigr.*, 14, 159–191. Milano Italy. ISSN 0035-6833, online ISSN 2039-4992.
- Azo, N. M. (2020). *Palytology of the Baluti Formation (Upper Triassic) in two selected sections at Amediya District, Kurdistan Region, Iraq*. Unpublished msc thesis, Soran University, Iraq. 147 p., 16 Plates.
- Barrier, E. and Vrielynck, B. (2008). Palaeotectonic maps of the Middle East. In *Tectono-sedimentary-palinspastic Maps from Late Norian to Pliocene*, Commission for the Geological Map of the World (CGMW/CCGM). Commission de la Carte Géologique du Monde, Paris. ISBN 9782917310007, 14 maps.
- Bender, H. (1967). Zur Gliederung der mediterranen Trias. II; Die Conodontchronologie der mediterranen Trias. *Ann. Géol. Pays Helléniques*, 19, 465–540.
- Berra, F. and Angiolini, L. (2014). The evolution of the Tethys region throughout the Phanerozoic: A brief tectonic reconstruction. In Marlow, L., Kendall, C., and Yose, L., editors, *Petroleum Systems of the Tethyan Region*, AAPG Memoir 106, pages 1–27. AAPG, Tulsa, Oklahoma.
- Blakey, R. C. (2003). Carboniferous–Permian paleogeography of the assembly of Pangaea. In Wong, T. E., editor, *Proceedings of the XVth International Congress on Carboniferous and Permian Stratigraphy, Utrecht, the Netherlands, 10–16 August 2003*, pages 443–456. Royal Netherlands Academy of Arts and Sciences.
- Brett, C. E., McLaughlin, P. I., Histon, K., Schindler, E., and Ferretti, A. (2012). Time-specific aspects of facies: State of the art, examples, and possible causes. *Palaeogeogr. Palaeoclimatol. Palaeoecol.*, 367–368, 6–18.
- Claudel, M.-E. (1999). *Reconstitution paléogéographique du domaine briançonnais au Mésozoïque. Ouvertures océaniques et raccourcissements croisés*. PhD thesis, Université Joseph-Fourier – Grenoble, France.
- Cohen, K. M., Finney, S. C., Gibbard, P. L., and Fan, J. X. (2013). The ICS International Chronostratigraphic chart. *Episodes*, 36, 199–204. <http://www.stratigraphy.org/ICSchart/Chronostratchart2020-03.pdf>.
- Davies, R. B. and Simmons, M. D. (2018). Triassic sequence stratigraphy of the Arabian Plate. In Pöppelreiter, M. C., editor, *Lower Triassic to Middle Jurassic Sequence of the Arabian Plate*, pages 101–162. EAGE Publications B.V., The Netherlands.

- Davies, R. B. and Simmons, M. D. (2020). Dating and correlation of the Baluti Formation, Kurdistan, Iraq: implications for the regional recognition of a Carnian “marker dolomite” and a review of the Triassic to Early Jurassic sequence stratigraphy of the Arabian Plate by G. A. Lunn, S. Miller and A. Samarrai. Discussion. *J. Pet. Geol.*, 43(I), 95–108.
- Davies, R. B., Simmons, M. D., Jewell, T. O., and Collins, J. (2019). Regional controls on siliciclastic input into Mesozoic depositional systems of the Arabian Plate and their petroleum significance. In AlAnzi, H. R., Rahmani, R. A., Steel, R. J., and Soliman, O. M., editors, *Siliciclastic Reservoirs of the Arabian Plate*, AAPG Memoir 116, pages 103–140. AAPG, Tulsa, Oklahoma.
- Dercourt, J., Gaetani, M., and Vrielynck, B. (2000a). General features of the atlas. In Crasquin, S., editor, *Atlas Peri-Tethys, Palaeogeographical Maps*, pages XI–XX. CCGM/CGMW, Paris. Explanatory notes.
- Dercourt, J., Gaetani, M., Vrielynck, B., Barrier, E., Biju-Duval, B., Brunet, M. F., Cadet, J. P., Crasquin, S., and Sandulescu, M., editors (2000b). *Atlas Peri-Tethys, Palaeogeographical Maps*. CCGM/CGMW, Paris. 24 maps, 269 p.
- Deville de Periere, M., Breuer, P., Alsinan, F., and Lu, F. (2022). Sedimentology, sequence stratigraphy, palynology, and diagenetic evaluation of the Triassic Jilh Formation. New insights from Saudi Arabia. *J. Afr. Earth Sci.*, 196, article no. 104714.
- Esfafili-Dizaji, B. and Dalvand, M. (2018). Early–middle triassic dashtak formation in the zagros domain. In Pöppelreiter, M. C., editor, *Iran: Controls of Eustasy, Tectonic, and Palaeoclimate*, Lower Triassic to Middle Jurassic Sequence of the Arabian Plate, pages 163–178. EAGE Publications B.V., The Netherlands.
- Faqira, M., Rademakers, M., and Afifi, A. M. (2009). New insights into the Hercynian Orogeny, and their implications for the Paleozoic Hydrocarbon System in the Arabian Plate. *GeoArabia*, 14(3), 199–228.
- Furin, S., Preto, N., Rigo, M., Roghi, G., Gianolla, P., Crowley, J. L., and Bowering, S. A. (2006). High-precision U-Pb zircon age from the Triassic of Italy: Implications for the Triassic time scale and the Carnian origin of calcareous nannoplankton and dinosaurs. *Geology*, 12, 1009–1012.
- Gaetani, M. (2010). From Permian to Cretaceous: Adria as pivotal between extensions and rotations of Tethys and Atlantic Oceans. *J. Virtual Explor.*, 36, article no. 6. (Electronic Edition). In (Eds.) M. Beltrando, A. Peccerillo, M. Mattei, S. Conticelli, C. Doglioni, *The Geology of Italy: tectonics and life along plate margins*.
- Gedik, I. (1975). Die Conodonten der Trias auf der Kocaeli-Halbinsel (Türkei). *Paleontogr. Abt. A.*, 150, 99–160.
- Gerry, E., Honigstein, A., Rosenfeld, A., Hirsch, F., and Eshet, Y. (1990). The Carnian Salinity Crisis, Ostracods and Palynomorphs as Indicators of Palaeoenvironment. In Whatley, R. C. and Maybury, C., editors, *Ostracoda and Global Events (Conference Paper, International Symposium on Ostracoda 10; 1988)*, British Micropalaeontological Society, Publication Series, pages 87–97. Chapman and Hall, New York. Chapter 6, 5 fig.
- Glantzboeckel, C. (1981). A tentative synopsis of the Geology of the Saudi Arabian sedimentary basin in relation to phosphate prospecting. D.M.M.R. Jeddah, Open File Report BRGM OF-01- 23, 145 p, 59 fig., 3 tabl.
- Gradstein, F. M., Ogg, J. G., Schmitz, M., and Ogg, G. (2012). The Geologic Time Scale. *Newsl. Stratigr.*, 45(2), 171–188.
- Hajian Barzi, M., Aleali, M., Jahini, D., and Falahkheyrkhah, M. (2015). Microfacies, sedimentary environment, sequence stratigraphy and strontium dating of the dashtak formation in the Persian Gulf, Fars and Izeh Regions. *Geosciences*, 24, 185–198.
- Hanna, M. T. (2007). *Palynology of the upper part of the Baluti Formation (Upper Triassic) and the nature of its contact with the Sarki formation at Amadiya district, northern Iraq*. PhD thesis, University of Mosul, Iraq. 219 p.
- Haq, B. U. (2018). Triassic eustatic variations reexamined. *GSA Today*, 28(12), 9. with supplement online at www.geosociety.org/datarepository/2018/.
- Haq, B. U. and Al-Qahtani, A. M. (2005). Phanerozoic cycles of sea-level change on the Arabian Platform. *GeoArabia*, 10(2), 127–160.
- Hirsch, F. (1972). Middle Triassic conodonts from Palestine, southern France, and Spain. *Mitt. Gesellschaft Geologie Berganstudien*, 21, 811–828.
- Hirsch, F. (1992). Circummediterranean Triassic eustatic cycles. *Israeli J. Earth Sci.*, 40, 29–33.
- Horbury, A. (2018). Petroleum Geology and its relation to Stratigraphic Architecture of the Triassic

- to Middle Jurassic (Induan to Aalenian) Interval on the Arabian Plate. In Pöppelreiter, M. C., editor, *Lower Triassic to Middle Jurassic Sequence of the Arabian Plate*, pages 49–100. EAGE Publications B.V., The Netherlands.
- Hornung, T., Bradner, R., Krystner, L., Joachimski, M. M., and Keim, L. (2007). Multistratigraphic constraints on the New Tethyan “Carnian Crisis”. In Lucas, S. G. and Spielmann, J. A., editors, *The Global Triassic*, New Mexico Museum of Natural History and Science Bulletin 41, pages 59–67. New Mexico Museum of Natural History and Science, New Mexico.
- Hu, J., Witte, J., and Neves, F. (2015). Evolution of the Middle-Triassic Gulailah intra-shelf basin in Abu Dhabi, Abu Dhabi National Oil Company (ADNOC). In *Abu Dhabi International Petroleum Exhibition and Conference, Abu Dhabi, UAE, 9–12 November 2015*, Society of Petroleum Engineers SPE-177586-MS. SPE, Texas. 6 p. 19 figures.
- Issautier, B. (2011). *Estimation de l'impact des hétérogénéités sédimentaires fluviatiles sur le stockage géologique du CO₂*. Thesis, Université de Provence, Aix-Marseille I. 2011AIX10136 Geosciences de l'Environnement. Geology of carbonate systems and reservoirs, E.A. 4234. 20 December 2011, 152 p.
- Issautier, B., Le Nindre, Y. M., Hooker, N., Reid, C., Memesh, A., and Dini, S. (2019). Depositional environments, age, and sequence stratigraphy of the Minjur Formation in outcrop and near subsurface–Central Saudi Arabia. In Al-Anzi, H. R., Rahmani, R. A., Steel, R. J., and Soliman, O. M., editors, *Siliciclastic Reservoirs of the Arabian Plate*, AAPG Memoir 116, pages 141–184. AAPG, Tulsa, Oklahoma. Chapter 5.
- Issautier, B., Le Nindre, Y. M., Memesh, A., Dini, S., and Viseur, S. (2012a). Managing clastic reservoir heterogeneity, I: Sedimentology and sequence stratigraphy of the Late Triassic Minjur Sandstone at the Khashm al Khalta type locality, Central Saudi Arabia. *GeoArabia*, 17(2), 17–56.
- Issautier, B., Le Nindre, Y. M., Viseur, S., Memesh, A., and Dini, S. (2012b). Managing clastic reservoir heterogeneity II: Geological modeling and reservoir characterisation of the Minjur Sandstone at the Khashm al Khalta type locality (Central Saudi Arabia). *GeoArabia*, 17(3), 61–80.
- James, G. A. and Wynd, J. G. (1965). Stratigraphic nomenclature of the Iranian Oil Consortium Agreement Area. *Am. Assoc. Pet. Geol. Bull.*, 49, 2182–2245.
- Kadar, A. P., De Keyser, T., Neog, N., Karam, K. A., Le Nindre, Y.-M., and Davies, R. B. (2015). Calcareous nannofossil zonation and sequence stratigraphy of the Jurassic System, onshore Kuwait. *GeoArabia*, 20(4), 125–180.
- Kazmin, V., Ricou, L. E., and Sborshchikov, I. M. (1986). Structure and evolution of the passive margin of the eastern Tethys. *Tectonophysics*, 123, 153–179.
- Kear, B. P., Rich, T. H., Vickers-Rich, P., Ali, M. A., Al-Mufarrih, Y. A., Matiri, A. H., Masary, A. M., and Halawani, M. A. (2010a). A review of aquatic vertebrate remains from the Middle–Upper Triassic Jilh Formation of Saudi Arabia. *Proc. R. Soc. Victoria*, 122(1), 1–8. ISSN 0035-9211.
- Kear, B. P., Rich, T. H., Vickers-Rich, P., Ali, M. A., Al-Mufarrih, Y. A., Matiri, A. H., Masary, A. M., and Halawani, M. A. (2010b). First Triassic lungfish from the Arabian Peninsula. *J. Paleontol.*, 84, 137–140.
- Khan, S., Al-Eid, G., Reid, C., Hooker, N., Ertug, K., and Tang, D. (2015). *EAGE 5th Arabian Plate Geology Workshop, Lower Triassic to Middle Jurassic Evaporite–Carbonate–Siliciclastic Systems of the Arabian Plate (Sudair to Dhurma and Time Equivalent), 8–11 February 2015, Kuwait*.
- Korngreen, D. and Benjamini, C. (2010). The epicontinental subsiding margin of the Triassic in Northern Israel, North Arabian Plate. *Sediment. Geol.*, 228(1–2), 14–45.
- Krystyn, L. (1983). Das Epidaurus-Profil (Griechenland). Ein Beitrag zur Conodonten-Standardzonierung des thethyalen Ladin und Unterkarn. *Oesterr. Akad. Wiss. Schriftenreihe Erdwissenschaften*, 5, 231–258.
- Krystyn, L. (2008). An ammonoid-calibrated Tethyan conodont time scale of the late upper Triassic. *Berichte Geol. B.-A.*, 76, 9–11. ISSN 1017-8880 — Upper Triassic... Bad Goisern (28.09–02/10/2008).
- Le Métour, J., Michel, J. C., Béchenec, F., Platel, J. P., and Roger, J. (1995). *Geology and Mineral Wealth of the Sultanate of Oman*. M.P.M. Geological Documents. Ministry of Petroleum and Minerals, Directorate General of Minerals, Oman. 285 p.
- Le Nindre, Y. M., Manivit, J., and Vaslet, D. (1987). *Histoire géologique de la bordure occidentale de*

- la plate-forme arabe du Paléozoïque inférieur au Jurassique supérieur (en 4 livres)*. PhD thesis, University of P. et Marie Curie, Paris VI. 3 juin 1987.
- Le Nindre, Y.-M., Manivit, J., and Vaslet, D. (1990a). Géodynamique et Paléogéographie de la Plateforme Arabe du Permien au Jurassique. In *Histoire Géologique de la Bordure Occidentale de la Plate-Forme Arabe, Volume 2*, Documents du BRGM no. 192. Editions du BRGM, Orléans. 273 p., 54 fig., 4 tabl., 4 annexes. ISSN 0211-2536, ISBN 2-7159-0947-5.
- Le Nindre, Y. M., Manivit, J., and Vaslet, D. (1990b). Le Permo-Trias d'Arabie centrale. In *Histoire géologique de la bordure occidentale de la plate-forme arabe, Vol. 3*, Documents du BRGM n° 193. Editions du BRGM, Orléans. ISSN: 0221-2536, ISBN: 2-7159-0507-6, 290 p, 51 fig., 4 tabl., 11 pl., 3 annexes.
- Le Nindre, Y. M., Vaslet, D., Énay, R., Manivit, J., and Al-Husseini, M. I. (2022). Sequence architecture of the Toarcian Marrat Formation: The Khashm adh Dhibi reference section. ResearchGate, 35 p.
- Le Nindre, Y. M., Vaslet, D., Le Métour, J., Bertrand, J., and Halawani, M. (2003). Subsidence modelling of the Arabian platform from Permian to Paleogene outcrops. *Sediment. Geol.*, 156(1–4), 263–285.
- Le Nindre, Y. M., Vaslet, D., and Manivit, J. (1983). Sedimentary evolution of Saudi Arabian Jurassic (Toarcian–Upper Oxfordian) deposits in outcrop between latitudes 24° N and 22° N. BRGM Open File Report BRGM-OF-03-05. 34 p, 3 fig., 4 tables, 7 appendixes. Ministry of Petroleum and Mineral Resources. Deputy Ministry for Mineral Resources. Jiddah, Kingdom of Saudi Arabia. 1403 A.H., 1983 A.D.
- Le Nindre, Y. M., Vaslet, D., Vrielynck, B., Krystyn, L., Manivit, J., Memesh, A., Abdullah, M. S., and Davies, R. B. (2023). The Middle to Late Triassic of Central Saudi Arabia with emphasis on the Jilh Formation. Part I: lithostratigraphy, facies and paleoenvironment, palaeontology and biostratigraphic age calibration from outcrop studies. *C. R. Géosci.*, 355(S2), 1–31. (in this issue). Volume Spécial, Hommage à Jean Dercourt.
- Lucic, D., Ivkovic, Z., Takec, D., Bubnic, J., and Koch, G. (2010). Depositional sequences and palynology of Triassic carbonate-evaporite platform deposits in the Palmyrides, Syria. In van Buchem, F. S. P., Gerdes, K. D., and Esteban, M., editors, *Mesozoic and Cenozoic Carbonate Systems of the Mediterranean and the Middle East: Stratigraphic and Diagenetic Reference Models*, Geological Society, London, Special Publications, 329, pages 43–63. Geological Society of London.
- Lunn, G. A. (2020). Dating and correlation of the Baluti Formation, Kurdistan, Iraq: Implications for the regional recognition of a Carnian “Marker Dolomite”, and a review of the Triassic to Early Jurassic sequence stratigraphy of the Arabian Plate by G. A. Lunn G. A., S. Miller, and A. Samarrai. Reply to discussion by R. B. Davies and M. D. Simmons. *J. Pet. Geol.*, 43(1), 109–126.
- Lunn, G. A., Miller, S., and Samarrai, A. (2019). Dating and correlation of the Baluti Formation, Kurdistan, Iraq: implications for the regional recognition of a Carnian “marker dolomite” and a review of the Triassic to Early Jurassic sequence stratigraphy of the Arabian Plate. *J. Pet. Geol.*, 42(1), 5–36.
- Manivit, J., Le Nindre, Y. M., and Vaslet, D. (1990). Le Jurassique d'Arabie Centrale. In *Histoire Géologique de la Bordure Occidentale de la Plate-forme Arabe, Volume 4*, Document du BRGM n° 194. Editions du BRGM, Orléans. 559 p, 74 fig., 1 tabl., 12 pl. photo, 3 ann. (ann. 1: 12 pl.). ISSN: 0221-2536, ISBN: 2-7159-0508-4.
- Manivit, J., Pellaton, C., Vaslet, D., Le Nindre, Y. M., Brosse, J. M., Breton, J. P., and Fourniguet, J. (1985a). *Geologic map of the Darma' quadrangle, Kingdom of Saudi Arabia. Geoscience map GM-101C, scale 1:250,000, sheet 24H*. Deputy Ministry for Mineral Resources, Ministry of Petroleum and Mineral Resources, Kingdom of Saudi Arabia. Explanatory notes, 33 p.
- Manivit, J., Pellaton, C., Vaslet, D., Le Nindre, Y. M., Brosse, J. M., and Fourniguet, J. (1985b). *Geologic map of the Wadi Al Mulayh quadrangle, Kingdom of Saudi Arabia. Geoscience Map GM-92C, scale 1:250,000, sheet 22H*. Deputy Ministry for Mineral Resources, Ministry of Petroleum and Mineral Resources, Kingdom of Saudi Arabia. Explanatory notes, 32 p.
- Manivit, J., Vaslet, D., Berthiaux, A., Le Strat, P., and Fourniguet, J. (1986). *Geologic map of the Buraydah quadrangle, Kingdom of Saudi Arabia. Geoscience Map GM-114 C, scale 1:250,000, sheet 26G*. Deputy Ministry for Mineral Resources, Ministry of Petroleum and Mineral Resources, Kingdom of Saudi Arabia. Explanatory notes, 32 p.

- Maurer, F., Krystyn, L., Martini, R., Mcroberts, C., Rettori, R., and Hofmann, P. (2015). Towards a refined Arabian Plate Triassic stratigraphy: insights from the Musandam Peninsula (UAE & Oman). In *5th Arabian Plate Geology Workshop, Lower Triassic to Middle Jurassic Evaporite–Carbonate–Siliciclastic Systems of the Arabian Plate (Sudair to Dhurma and Time Equivalent), 8–11 February 2015, Kuwait*.
- Maurer, F., Rettori, R., and Martini, R. (2008). Triassic stratigraphy, facies and evolution of the Arabian shelf in the northern United Arab Emirates. *Int. J. Earth Sci. (Geol. Rundsch.)*, 97, 765–784. First online: 22 May 2007.
- Murris, R. J. (1981). Middle East: stratigraphic evolution and oil habitat. *Geol. Mijnbouw*, 60, 467–486.
- Nicoll, R. S. and Foster, C. B. (1994). Late Triassic conodont and palynomorph biostratigraphy and conodont thermal maturation, North West Shelf, Australia. *AGSO J. Australian Geol. Geophys.*, 15(1), 101–118.
- Nicoll, R. S. and Foster, C. B. (1998). Revised conodont-palynomorph biostratigraphic zonation and the stratigraphy of the Triassic of the western and northwestern margins of Australia and Timor. In Purcell, P. G. and Purcell, R. R., editors, *Sedimentary basins of Western Australia 2: Proceedings of Petroleum Exploration Society Australia Symposium, Perth, 1998*, pages 129–139.
- Obermaier, M., Aigner, T., and Forke, H. C. (2012). Facies, sequence stratigraphy and reservoir/seal potential of a Jilh Formation outcrop equivalent (Wadi Sahtan, Triassic, Upper Mahil Member, Sultanate of Oman). *GeoArabia*, 17(3), 85–128.
- Ogg, J. G. (2012). The triassic period. In Gradstein, F. M., Ogg, J. G., Schmitz, M., and Ogg, G., editors, *The Geological Time Scale*, pages 681–730. Elsevier, Amsterdam. Chapter 25.
- Ogg, J. G. (2015). The mysterious Mid-Carnian “Wet Intermezzo” global event. *J. Earth Sci.*, 26(2), 181–191.
- Ogg, J. G. and Chen, Z. Q. (2020). Chapter 25—The triassic period. In Gradstein, F. M., Ogg, J. G., Schmitz, M. D., and Ogg, G. M., editors, *The Geologic Time Scale 2020*, volume 2, pages 903–953. Elsevier, Amsterdam.
- Pavia, G. and Martire, L. (2015). Indirect biostratigraphy in condensed successions: a case history from the Bajocian of Normandy (NW France). *Volumina Jurassica*, VII, 67–76.
- Powers, R. W. (1968). *Lexique Stratigraphique International. Volume III, Asie, Fas. 10 b1, Arabia Saoudite*. Centre National de la Recherche Scientifique, Paris.
- Powers, R. W., Ramirez, L. F., Redmond, C. D., and Elberg Jr., E. L. (1966). Geology of the Arabian Peninsula: Sedimentary geology of Saudi Arabia. United States Geological Survey Professional Paper 560-D, 147 p. 10 plates. US Department of Interior.
- Ricou, L. E., Dercourt, J., Geysant, J., Grandjacquet, C., Lepvrier, C., and Biju-Duval, B. (1986). Geological constraints on the Alpine evolution of the Mediterranean Tethys. *Tectonophysics*, 123, 83–122.
- Ricou, L. E., Zonenshain, L. P., Dercourt, J., Kazmin, V. G., Le Pichon, X., Knipper, A. L., Grandjacquet, C., Sborshchikov, I. M., Lepvrier, C., Pechersky, D. M., Boulin, J., Sibuet, J. C., Savostin, L. A., Sorokhtin, O., Westphal, M., Lauer, J. P., and Biju-Duval, B. (1985). Méthodes pour l'établissement de neuf cartes paléogéographiques au 1:20 million s'étendant de l'Atlantique au Pamir pour la période du Lias à l'Actuel. *Bull. Soci. Géol. France*, 1(5), 625–635.
- Sadooni, F. N. and Alsharhan, A. S. (2004). Stratigraphy, lithofacies, and petroleum potential of the Triassic strata of the northern Arabian plate. *Am. Assoc. Pet. Geol. Bull.*, 88(4), 515–538.
- Scotese, C. R. (2001). *Atlas of Earth History, Volume 1. Paleogeography*. PALEOMAP Project, Arlington, Texas.
- Sharief, F. A. M. (1977). *Sedimentary facies of the Jilh Formation, Saudi Arabia. A regional paleostratigraphy and tectonic evolution of the Middle East during the Middle Triassic period*. PhD thesis, Rice University, Houston, Texas. 117 p.
- Sharief, F. A. M. (1986). Depositional environments of the Triassic system in central Saudi Arabia. *Geol. J.*, 21, 403–420.
- Sharland, P. R., Archer, R., Casey, D. M., Davies, R. B., Hall, S. H., Heward, A. P., Horbury, A. D., and Simmons, M. D. (2001). *Arabian Plate Sequence Stratigraphy*. GeoArabia Special Publication 2. Gulf PetroLink, Bahrain.
- Sharland, P. R., Casey, D. M., Davies, R. B., Simmons, M. D., and Sutcliffe, O. E. (2004). Arabian plate sequence stratigraphy. *GeoArabia*, 9(1), 199–214.
- Sodagar, T. M. (2015). Revelation of the Triassic Gas

- Potential with Insight of Iso Frequency Spectral Decomposition in Saudi Arabia's Offshore. In *Proceedings of the SPE Middle East Oil & Gas Show and Conference, 8–11 March 2015, Manama, Bahrain*, SPE Paper 172625. 16 p.
- Somma, R., Martín-Rojas, I., Estévez, A., Perrone, V., Zamparelli, V., and Delgado, F. (2008). The Ladinian to Carnian rifting stage recorded by the peritidal carbonate platform of the Betic Cordillera. In *STT-02 Structure and Formation of Rift Basins and Passive Margins from Surface to Depth: Observations and Modelling, International Geological Congress, Oslo 6–14th 2008*. Abstract.
- Stewart, S. A., Reid, C. T., Hooker, N. P., and Kharouf, O. W. (2016). Mesozoic siliciclastic reservoirs and petroleum system in the Rub' Al-Khali basin, Saudi Arabia. *AAPG Bull.*, 100(5), 819–841.
- Szabo, F. and Kheradpir, A. (1978). Permian and Triassic stratigraphy, Zagros Basin, southwest Iran. *J. Pet. Geol.*, 1, 57–82.
- Taher, A., Al-Shateri, A., Al-Mehsin, K., Witte, J., Al-Zaabi, M., and Obaid, K. (2012). Tight gas exploration potential of Middle Triassic to Early Jurassic successions in Abu Dhabi. In *Abu Dhabi International Petroleum Exhibition and Conference, Abu Dhabi, UAE, 11–14 November 2012*, Society of Petroleum Engineers, SPE-162355. 16 p, 20 figures, 1 table.
- Tollmann, A. (1984). Entstehung und früherer Werdegang der Tethys mit besonderer Berücksichtigung des mediterranen Raumes. *Mitt. Oesterreichischer Geologischen Ges.*, 77, 93–113.
- Tollmann, A. and Kristan-Tollmann, E. (1985). Paleogeography of the European Tethys from Palaeozoic to Mesozoic, and in the Triassic relations of the eastern part of the Tethys and Pa, thalassa. In Nakazawa, K. and Dickins, J. M., editors, *The Tethys: Her Paleogeography and Paleobiogeography from Palaeozoic to Mesozoic*, pages 3–22. Tokai University Press, Tokyo.
- Urban, I., Demangel, I., Krystyn, L., Calner, M., Kovács, Z., Gradwohl, G., Lernpeiss, S., Maurer, F., and Richoz, S. (2023). Mid-Norian to Hettangian record and time-specific oolites during the end-Triassic Mass Extinction at Wadi Milaha, Musandam Peninsula, United Arab Emirates. *J. Asian Earth Sci.* X, 9, article no. 100138.
- Vachard, D., Gaillot, J., Vaslet, D., and Le Nindre, Y. M. (2005). Foraminifers and algae from the Khuff Formation (late Middle Permian-Early Triassic) of central Saudi Arabia. *GeoArabia*, 10(4), 137–186.
- van Bellen, R. C., Dunnington, H. V., Wetzell, R., and Morton, D. M. (1959–2005). Lexique Stratigraphique International. 03 10 Asie, (Iraq), 333 pages. Reprinted by permission of CNRS by Gulf PetroLink, Bahrain.
- Vaslet, D., Beurrier, M., Villey, M., Manivit, J., Le Strat, P., Le Nindre, Y. M., Berthiaux, A., Brosse, J. M., and Fourniguet, J. (1985). *Geologic map of the Al Faydah quadrangle, sheet 25G, Kingdom of Saudi Arabia, Geosciences Maps GM-102A, scale 1:250,000*. Saudi Arabian Deputy Ministry for Mineral Resources, Kingdom of Saudi Arabia. Explanatory notes, 28 p.
- Vaslet, D., Le Nindre, Y. M., Vachard, D., Broutin, J., Crasquin-Soleau, S., Berthelin, M., Gaillot, J., Halawani, M., and Al-Husseini, M. I. (2005). The Permian-Triassic Khuff formation of central Saudi Arabia. *GeoArabia*, 10(4), 77–134.
- Vaslet, D., Manivit, J., Le Nindre, Y.-M., Brosse, J.-M., Fourniguet, J., and Delfour, J. (1983). *Geologic map of the Wadi Ar Rayn quadrangle, Kingdom of Saudi Arabia. Geoscience Map GM-63C, scale 1:250,000, sheet 23H*. Deputy Ministry for Mineral Resources, Ministry of Petroleum and Mineral Resources, Kingdom of Saudi Arabia. Explanatory notes, 46 p.
- Vickers-Rich, P., Rich, T. H., Rieppel, O., Thulborn, R. A., and McClure, H. A. (1999). A Middle Triassic vertebrate fauna from the Jilh Formation, Saudi Arabia. *Neues Jahrb. Geol. Paläontol. Abh.*, 213, 201–232.
- Vrielynck, B. (1980). Précisions sur la stratigraphie du Trias d'Argolide (Péloponèse, Grèce), et conséquences structurales. *Bull. Soc. Géol. France* (7), XXII(3), 345–352.
- Vrielynck, B. (1987). *Conodontes du Trias périméditerranéen : Systématique, stratigraphie*. PhD thesis, Université Claude-Bernard, France. Book, 300 p.
- Vrielynck, B. and Cros, P. (1992). Les conodontes du Ladinien des faciès de transition bassin/plateforme dans les Dolomites (Latemar, Italie). Evolution sédimentaire et tectonique d'un massif caractéristique de la marge sud-téthysienne. *C. R. Acad. Sci., Paris*, II, 1223–1229.
- Vrielynck, B., Dercourt, J., and Cottureau, N. (1994). Des seuils lithosphériques dans la Téthys. *C. R. Acad. Sci. Paris*, II, 1677–1685.

- Zhou, S., Al-Hajhog, J., Simpson, M. A., Luo, M., Mohiuddin, M., and Tan, C. (2009). Study of Jilh formation. Overpressure and its prediction. In *Proceedings of the SPE/IADC Middle East Drilling Technology Conference and Exhibition, Manama, Bahrain 26–28 October 2009*, SPE Paper 125657. 17 p.
- Ziegler, M. A. (2001). Late Permian to Holocene paleofacies evolution of the Arabian Plate and its hydrocarbon occurrences. *GeoArabia*, 6(3), 445–504.



Research article

Tribute to Jean Dercourt

Insights on the Permian tuff beds from the Saint-Affrique Basin (Massif Central, France): an integrated geochemical and geochronological study

Marc Poujol^{Ⓜ,*,a}, Mathilde Mercuzot^{Ⓜ,a}, Michel Lopez^{Ⓜ,b}, Sylvie Bourquin^{Ⓜ,a}, Olivier Bruguier^{Ⓜ,b}, Erwan Hallot^{Ⓜ,a} and Laurent Beccalotto^{Ⓜ,c}

^a Univ. Rennes, CNRS, Géosciences Rennes, UMR6118, F-35000 Rennes, France

^b Géosciences Montpellier, Université de Montpellier, CNRS, F-34000 Montpellier, France

^c BRGM, F-45060 Orléans, France

E-mails: marc.poujol@univ-rennes1.fr (M. Poujol), mathilde.mercuzot@outlook.com (M. Mercuzot), michel.lopez@umontpellier.fr (M. Lopez), sylvie.bourquin@univ-rennes1.fr (S. Bourquin), Olivier.Bruguier@gm.univ-montp2.fr (O. Bruguier), erwan.hallot@univ-rennes1.fr (E. Hallot), l.beccalotto@brgm.fr (L. Beccalotto)

Abstract. The Permian marks the transition between the end of the accretion of the supercontinent Pangea and the beginning of its dislocation. In the Eastern Pangea intertropical domain (i.e. the present-day Western Europe), the late-Paleozoic (i.e. uppermost Carboniferous–Permian) history remains poorly constrained due to the lack of precise radiometric data. This is particularly true for Permian basins from the southern part of the French Massif Central, making it difficult to determine correlations between basins and therefore robust timings and constraints on the environmental and climate events described in these basins, and to compare them with the larger-scale settings. This article focuses on the Saint-Affrique Basin, via an integrated petrological, geochemical and geochronological study of eight of the volcanic-ash levels interbedded in the sedimentary succession. It highlights the existence of two different groups of felsic volcanoclastic rocks. The first group, located at the base of the basin and attributed to the Stephanian continental stage, is related to a late-orogenic volcanic setting and corresponds to calc-alkaline trachy-andesitic tuffites that could not be dated due to the lack of volcanic zircon. The second group, located towards the top of the succession, is composed of calc-alkaline dacitic ash beds and tuffites yielding Kungurian ages, i.e. late early Permian (Cisuralian, 283.5 ± 0.6 to 273.01 ± 0.14 Ma), and are attributed to a post-orogenic deposition setting. These ages show that the sedimentary filling of the basin is younger than hitherto expected (i.e. Artinskian, 290.1 ± 0.26 to 283.5 ± 0.6 Ma). The elemental geochemistry, the presence of inherited detrital zircons and the Hf signatures of the volcanic ones indicate the involvement of an

* Corresponding author.

old (Proterozoic and older) basement in the magma genesis; this crustal contribution becomes more prominent towards the top of the sedimentary succession.

Keywords. Continental Permian basin, Zircon, LA-ICP-MS dating, Volcanism, French Massif Central.

Manuscript received 23 July 2022, revised 31 October 2022, accepted 15 November 2022.

1. Introduction

The Permian marks the transition between the end of the accretion of the supercontinent Pangea and the beginning of its dislocation [e.g. Scotese and Langford, 1995, Stampfli and Kozur, 2006, Stampfli *et al.*, 2013, Domeier and Torsvik, 2014]. From the end of the Carboniferous onwards, the Variscan belt, still in erosion, experienced a gravitational collapse [Ménard and Molnar, 1988, Malavieille *et al.*, 1990, Van Den Driessche and Brun, 1992, Burg *et al.*, 1994, Faure, 1995]. The eastern Pangea intra-mountain domain then underwent a generalized extension that resulted in the formation of extensive structures and rifts forming narrow continental basins at the end of the Carboniferous, which widened during the Permian [Ménard and Molnar, 1988, Vallé *et al.*, 1988, Van Den Driessche and Brun, 1989, 1992, Burg *et al.*, 1990, Malavieille *et al.*, 1990, Faure and Becq-Giraudon, 1993, Faure, 1995, Becq-Giraudon *et al.*, 1996, Genna *et al.*, 1998, Choulet *et al.*, 2012, Beccaletto *et al.*, 2015]. This late-to-post-Variscan transition was widely accompanied by aerial volcanism which has been well recorded in numerous continental siliciclastic sedimentary basins, either as a volcanogenic fraction in the sediments, or as inter-layered volcanic ash beds that are still mostly undated [Odin and Conrad, 1987, Châteauneuf and Farjanel, 1989, Nmila, 1995, Timmerman, 2004, Pellenard *et al.*, 2017, Ducassou *et al.*, 2019].

Due to the lack of precise radiometric data and marine biostratigraphic markers, the timings of the late Paleozoic (i.e. uppermost Carboniferous–Permian) history remains poorly constrained in the Eastern Pangea intertropical domain (i.e. the present-day western European basins). This is therefore problematic to accurately reconstruct the paleogeography and the evolution of the depositional environments. The current stratigraphic framework implies a nomenclature specific to European continental basins, with a terminology based on lithology as well as on the floristic and ichnological content [Izart *et al.*, 1998, Lucas and Shen, 2018, Schneider *et al.*, 2020]. Thus, the most recent late-Paleozoic paleogeographic reconstructions incorporate the

Middle to Upper Permian series without distinction. In addition, it is not currently possible to provide a paleogeographic outline of the Lower Permian basins for the terrestrial domain [e.g. Bourquin *et al.*, 2011]. Moreover, new age constraints on the sedimentary successions will allow to accurately link the observed environmental and climate perturbations recorded in the sedimentary successions [e.g. Mercuzot *et al.*, 2021] to the global climate dynamics.

Significant advances have been recently obtained in terms of temporal calibration (dating of volcanogenic levels) and depositional environments of the Carboniferous–Permian finite age series of the northern Massif Central [Pellenard *et al.*, 2017, Ducassou *et al.*, 2019, Mercuzot. *et al.*, 2021, Mercuzot *et al.*, 2021, 2022].

In contrast, little is known about the age and nature of the volcanism in the Carboniferous–Permian basins from south of the Massif Central (Saint-Affrique, Lodève-Graissessac and Gabian-Neffiès basins), where only a few volcanogenic layers in the Lodève-Graissessac Basin have been dated so far [e.g. Bruguier *et al.*, 2003, Michel *et al.*, 2015]. However, numerous volcanic ash beds have been described [Goloubinoff, 1979, Rolando, 1988], in particular thanks to the discovery of uranium mineralization in 1957 in the Lodève Basin during a radio-prospecting campaign performed by the French atomic energy commission (i.e. CEA, Commissariat à l’Energie Atomique). Nearly 240 wells were then drilled and twenty-four different ash beds were identified and numbered using Roman numerals (I to XXIV), following the order of discovery and consequently not the stratigraphic order. Once these benchmark levels had been described and identified in the Lodève Basin, uranium prospectors then mapped the Saint-Affrique Basin (Figure 1A) in order to look for potential sister uranium deposits. There, they also identified several volcanic ash beds and established correlations with those described in the Lodève Basin based on their facies architecture [e.g. Hübner *et al.*, 2011]. These volcanic ash beds have not been dated yet, nor characterized geochemically. Therefore, the aim of this study is to provide new information on

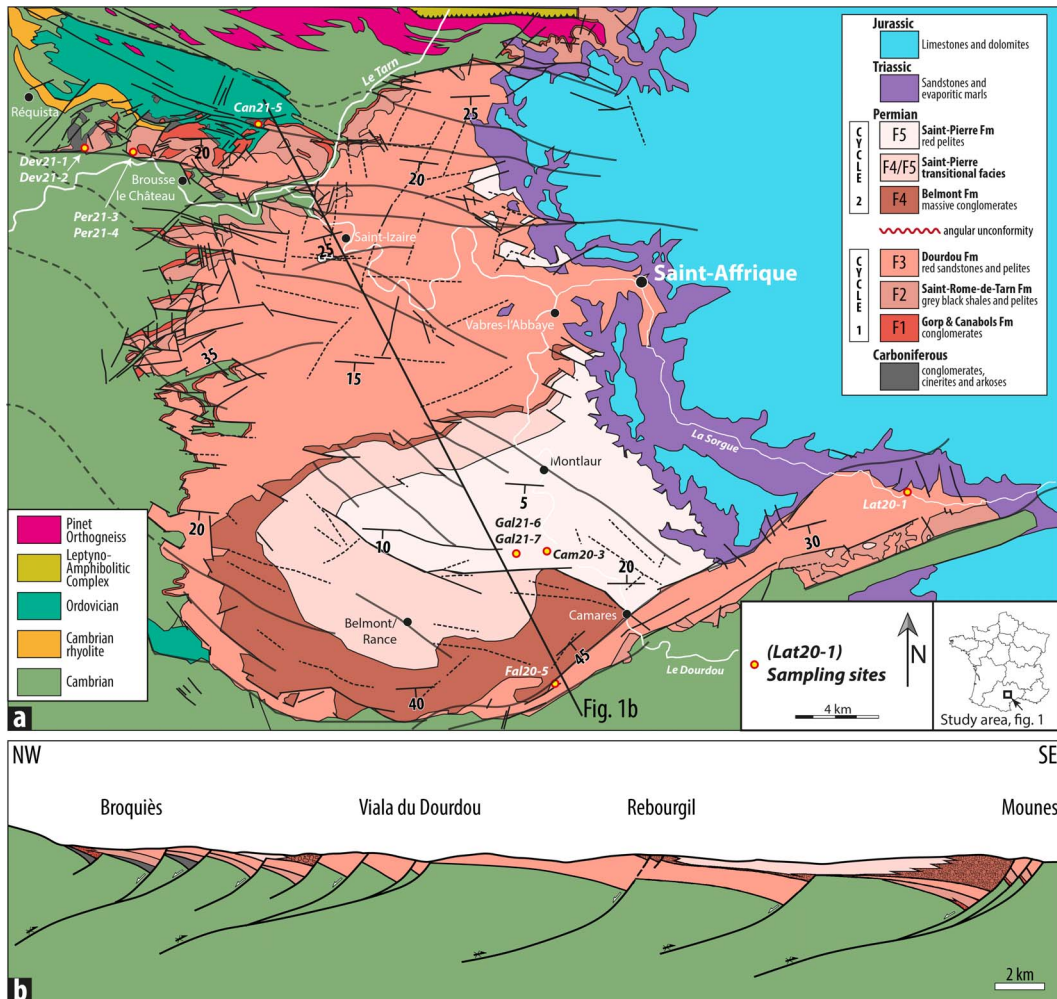


Figure 1. (A) Simplified geological map of the Saint-Affrique Basin [modified after Guérangé-Lozes and Guérangé, 1991, Guérangé-Lozes et al., 1995 and Guérangé-Lozes and Alabouvette, 1999]; and (B) NWSE cross section of the Saint-Affrique Basin showing the successive back-faulting and southward migrating depocenter controlled by the rejuvenation and inversion of major Variscan thrusts [modified after Legrand, 1990].

the age and origin of these volcanic ash beds in order to shed light on the chronology of the Saint-Affrique Basin development and on the geodynamical setting prevailing south of the Massif Central at the end of the Variscan orogeny.

2. Geological setting

The Saint-Affrique Basin (Figure 1A) is one of the major intramountain Carboniferous–Permian continental basin from southwestern France [e.g. Rolando,

1988, Rolando et al., 1988]. It is considered as an overall southward-dipping half-graben basin, controlled by repeated back faulting along major Variscan thrusts that were successively inverted during the late Carboniferous to Permian crustal thinning and collapse of the Variscan-related Montagne Noire thrust belt [Figure 1B; Legrand, 1990]. Most of the late Carboniferous to Permian deposits unconformably onlap onto the Precambrian to Cambro-Ordovician feldspathic sandstones and black schists of the Saint-Sernin-sur-Rance nappe, with a ma-

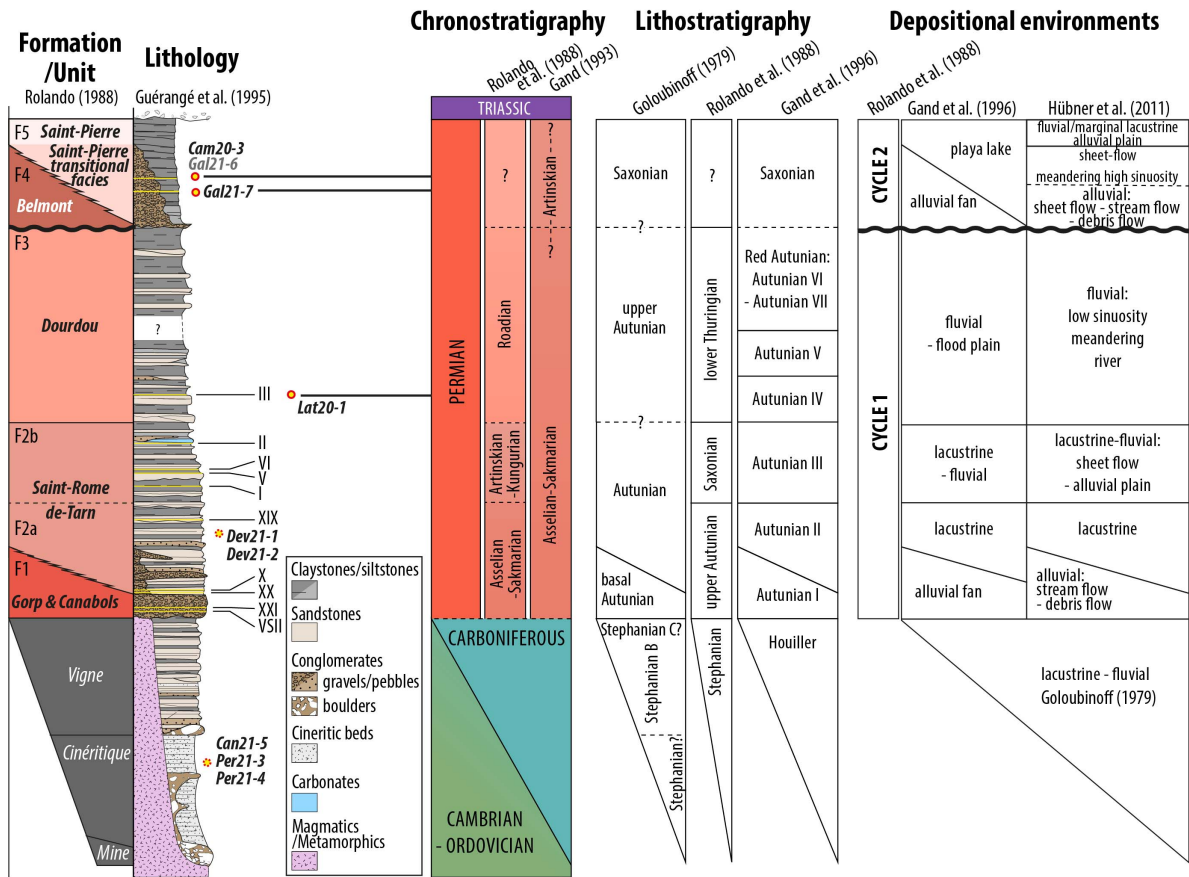


Figure 2. General description of the Saint-Affrique Basin sedimentary succession [based on Guérangé-Lozes et al., 1995] with the stratigraphic location of the selected volcanic ash bed samples, chronostratigraphic and lithostratigraphic subdivisions [after Goloubinoff, 1979, Rolando et al., 1988, Gand, 1993, Gand et al., 1996], and depositional environment evolution [after Goloubinoff, 1979, Rolando et al., 1988, Gand et al., 1996 and Hübner et al., 2011].

norward detrital input coming from the erosion of the uplifted northern limb of the Montagne Noire Massif. The latter includes Cambrian to Ordovician sandstone, shale and carbonate deposits of the metasedimentary cover, as well as gneisses, migmatites and biotite and garnet granites of the axial core complex. The tilted northern border of the basin is in turn fed by calc-alkaline metamonzogranites and metasyenogranites fringing the leptyno-amphibolite group of the Lézéou.

Syn-rift faulting controlled the asymmetric geometry, depositional partitioning and architecture of an overall alluvial to lacustrine sedimentation [Rolando, 1988, Legrand et al., 1994]. The stratigraphic range of the basin infill is assumed to cover the late

Carboniferous, with a low angular unconformity in the northern part of the basin, to the middle Permian [Figure 2; Rolando et al., 1988, Gand, 1993].

It has been reported that the late Carboniferous corresponds to the Stephanian continental subdivision and includes three main formations (fms): at the base, the *Mine* Formation (Fm) is composed of a coarse conglomerate and breccia package and is overlapped unconformably by volcanoclastic deposits, including fine-grained ash layers and volcanic breccias belonging to the *Cinérétique* Fm (Figure 2). The latter passes transitionally to the *Vigne* Fm, mainly composed of volcanic breccias alternating with coarse arkosic sandstones [David, 1967, Goloubinoff, 1979, Rolando, 1988; Figure 2].

The Permian deposits correspond to five formations accumulated during two sedimentary cycles. Cycle 1 corresponds to the F1, F2 and F3 fms and Cycle 2 to the F4 and F5 fms [Figure 2; Rolando *et al.*, 1988]. At the base, the F1 Fm, named the *Gorb and Canabols* Fm (Figure 1A and B), is mainly composed of stacked conglomerates considered as streamflow and debris flow deposits [Hübner *et al.*, 2011], passing laterally to fluvio-lacustrine deposits [Rolando, 1988]. The F2 Fm, named the *Saint-Rome-de-Tarn* Fm [Rolando, 1988], conformably overlays the F1 Fm and is divided into two lithologic units: the F2a Unit, described as lacustrine [Rolando, 1988, Hübner *et al.*, 2011], and the F2b Unit, considered as fluvio-lacustrine to lacustrine [Rolando, 1988], evolving upward into sheetflood to alluvial plain deposits [Hübner *et al.*, 2011]. This formation is overlain by the fluvial F3 Fm, named the *Dourdou* Fm [Rolando, 1988], interpreted as a low sinuosity meandering river system [Hübner *et al.*, 2011]. After a regional erosive event marked by a low angular unconformity, the F4 Fm, named the *Belmont* Fm, is attributed to the emplacement of alluvial-fan deposits during a major tectonic rejuvenation event from the southern border of the basin. The thick massive conglomerate package passes upwards and laterally to playa-lake deposits identified as the F5 Fm, named the *Saint-Pierre* Fm [Rolando, 1988; Figure 1A and B]. Hübner *et al.* [2011] consider that part of the F4 and F5 fms, denoted as F4/F5, i.e. the *Saint-Pierre transitional facies* Fm, is transitional and marks the lateral and vertical evolution from alluvial fan to meandering and alluvial plain deposits (Figure 2).

The stratigraphic setting of this sedimentary succession was firstly based on palynological analyses, i.e. defining continental floristic stages (Figure 2). Based on the microflora composition, i.e. spores and pollens, sediments of Cycle 1 were attributed to late Autunian to early Thuringian subdivisions [Rolando *et al.*, 1988]. However, using fauna biostratigraphy and in particular freshwater jellyfish, in comparison with German basins, Gand *et al.* [1996] proposed an early Asselian age for the F2b Unit, in which the species *Medusina atava* was identified, but they did not exclude that a simple paleoenvironment control could explain this fossil distribution in the stratigraphy. In turn, the upper part of the F3 Fm provided the *Medusina limnica* species which unfortunately

straddles a large stratigraphical repartition from the Sakmarian to the late Permian. By using climate-relevant geochemical, petrological and sedimentological proxies, Hübner *et al.* [2011] correlated the climate cycles from the Saint-Affrique and Lodève basins and proposed an Asselian to Artinskian age for Cycle 1 (F1, F2 and F3 fms), and an Artinskian age for the base of Cycle 2 (F4 and the base of F5 fms, Figure 2). As these stratigraphic interpretations based on fauna and flora depend on environmental and climate conditions, they lead to large age uncertainties thereby highlighting the need for absolute dating.

Several volcanic ash layers, named under the general term of cinerites, were described throughout the Carboniferous to Permian sedimentary succession [Goloubinoff, 1979, Rolando, 1988]. Some of these layers are reported as equivalent to those found in the Lodève Basin [Laversanne, 1976, Odin and Conrad, 1987]. Given their instantaneous deposition, these tuff beds are the best candidates to provide accurate absolute dating. In outcrops, they are easily identifiable by their pale-light colour (from white to salmon), their regular thickness and their hardness contrasting with the surrounding rocks. The major key tuff beds were identified in the *Cinéritique* Fm at the base of F1 Fm and in the F2 and F3 fms [Figure 2; e.g. Rolando, 1988]. In order to constrain the age of the sedimentary successions, six different volcanic ash and tuffitic beds have been collected throughout the stratigraphic column of the Saint-Affrique Basin (see Figure 1A).

3. Samples and methods

3.1. Sampling

Eight samples have been collected in the entire basin (Figures 1A and 2 and Table 1). Three of them (Per21-3, Per21-4 and Can21-5) have been sampled in the so-called *Cinéritique* Fm belonging to the Stephanian subdivision, but due to lack of continuous outcrops, their precise stratigraphic location in this Fm is not known (Figures 1A and 2). One sample (Dev21-1) was collected in the *Saint-Rome-de-Tarn* Fm (F2), in the Grey Autunian subdivision (Figures 1A, B and 2). Another one (Lat20-1) is located within the *Dourdou* Fm (F3; Figures 1A, B, 2 and 3A) and corresponds to Rolando's cinerite III (1988). The remaining three samples (Gal21-6, Gal21-7 and Cam20-3) were collected within the *Saint-Pierre transitional facies* Fm

Table 1. GPS coordinates of the selected samples

Samples	Locations	Lat/long coordinates
Per21-4	Along the road between the farm of Le Cluzel and the hamlet of Peret	44° 0' 58.76" N 2° 34' 59.44" E
Per21-3	Near the hamlet of Peret	44° 1' 08" N 2° 35' 13" E
Can21-5	Along the road to the north-east of the Cansac hamlet	44° 1' 23" N 2° 40' 11" E
Dev21-1	Left bank of the Jauret creek	44° 00' 41" N 2° 35' 55" E
Lat20-1	Just outside the village of Latour-sur-Sorgues along the D7 road	43° 47' 39" N 2° 50' 26" E
Gal21-7	Near the farm of Galamans along the road to the hamlet of Verrières, above the Riaudou creek	43° 50' 50.36" N 2° 49' 12.88" E
Cam20-3	Along the D999 road	43° 50' 47" N 2° 50' 5" E
Gal21-6	Same layer as sample Cam 20-3	43° 50' 47" N 2° 49' 02" E

(F4/F5), close to the top of the red Autunian subdivision (Figures 1A, B, 2 and 3B for sample Cam20-3).

3.2. Whole-rock geochemical analyses

Samples were crushed at Thin Section Lab (TSL, Toul, France) following a standard protocol to obtain adequate powder fractions using agate mortars. Chemical analyses (Supplementary Table 1) were performed by the Service d'Analyse des Roches et des Minéraux (SARM; CRPG-CNRS, Nancy, France) using an ICP-AES (inductively coupled plasma-atomic emission spectroscopy) for major-elements and an ICP-MS (inductively coupled plasma-mass spectrometry) for trace-elements, following the techniques described in Carignan *et al.* [2001]. All geochemical classification and tectonic discrimination diagrams used in this study were drawn using the GCDkit software [Janousek *et al.*, 2006].

3.3. Zircon U–Pb dating

A classic mineral separation procedure has been applied to concentrate zircon grains suitable for U–Pb dating using the facilities available at TSL. Zircon grains were imaged by cathode luminescence (CL)

using a Reliotron CL system equipped with a digital colour camera available at the GeOHeLiS platform (University of Rennes 1, France).

U–Pb geochronology of zircon was conducted by in-situ LA-ICP-MS (laser ablation-inductively coupled plasma-mass spectrometry) at the GeOHeLiS analytical platform using an ESI NWR193UC Excimer laser (193 nm wavelength), coupled to a quadrupole Agilent 7700x ICP-MS equipped with a dual pumping system to enhance sensitivity [Paquette *et al.*, 2014]. The methodology used to perform the analyses can be found in Nosenzo *et al.* [2022] as well as in Supplementary Table 2. Concordia diagrams have been generated using IsoplotR [Vermeesch, 2018].

3.4. Zircon Hf analyses

Lu–Hf isotopes were measured at the Géosciences Montpellier Laboratory, University of Montpellier (AETE-ISO regional facility of the OSU OREME) using a ThermoFinnigan Neptune+ MC-ICP-MS (multicollector-inductively coupled plasma-mass spectrometer) coupled with a Photon-Machine Analyte G2 Excimer laser (193 nm wavelength). Ablation was performed using a 50 µm spot size. The laser frequency was 5 Hz and the energy density of the

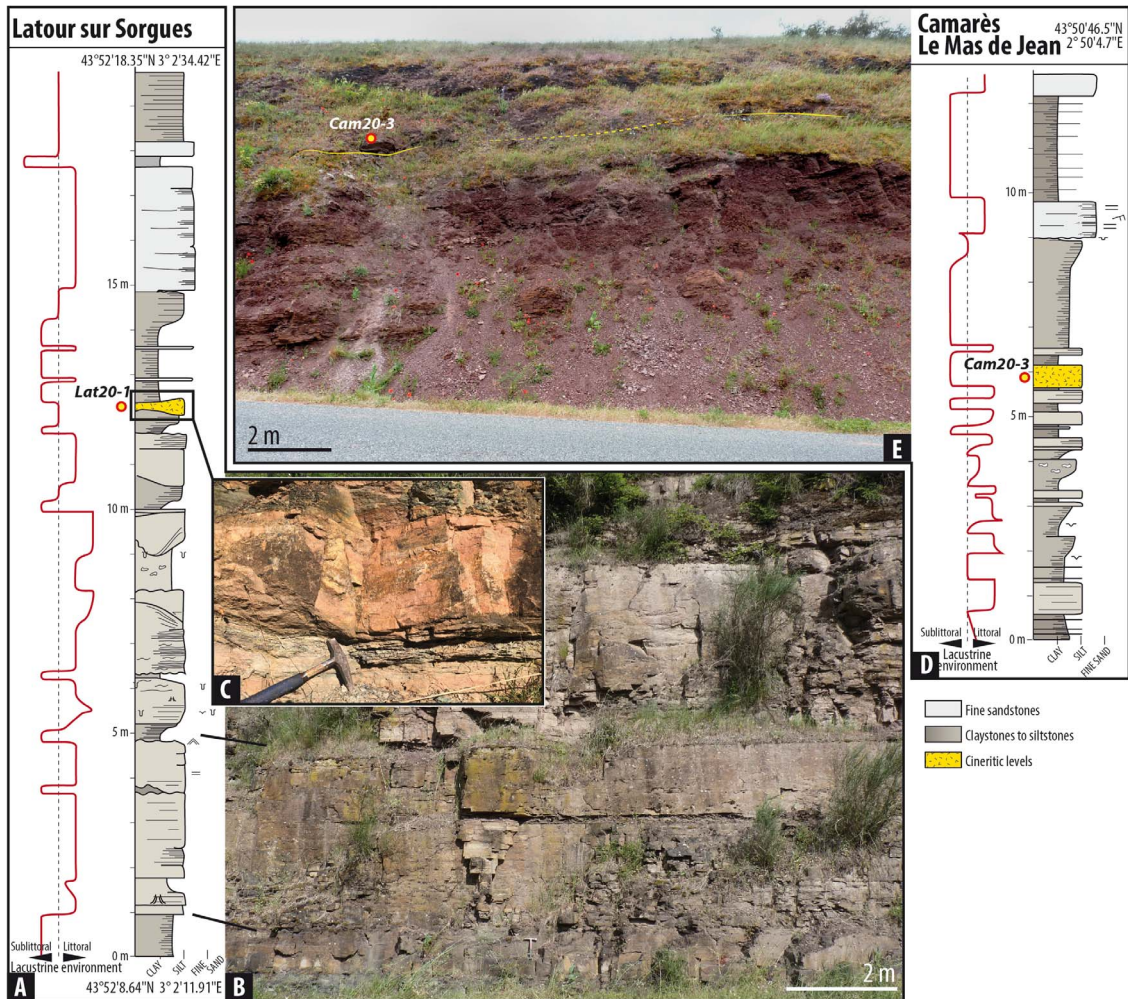


Figure 3. (A) Detailed sedimentary section of the outcrop of Latour-sur-Sorgues located along the D7 road, where sample Lat20-1 was collected; (B) Photography of the base of the section; (C) Photography of the cineritic bed providing the Lat20-1 sample; (D) Detailed sedimentary section of the outcrop of Le Mas de Jean located near the Camarès village along the D999 road, where sample Cam20-3 was collected; (E) Photography of the outcrop with the stratigraphic location of the cinerite providing the Cam20-3 sample.

laser beam was $c. 6 \text{ J/cm}^2$. A typical analysis was 80 s, including a 40 s background measurement and a 40 s ablation period. The correction for the interferences and mass bias followed the procedure outlined in previous reports [e.g. Bruguier *et al.*, 2020]. The correction for the isobaric interference of Yb and Lu on ^{176}Hf was made following a method detailed in Fisher *et al.* [2011]. For Yb, the interference-free ^{171}Yb was corrected for mass bias effects using an exponential

law and $^{173}\text{Yb}/^{171}\text{Yb} = 1.130172$ [Segal *et al.*, 2003]. The mass bias-corrected ^{171}Yb was monitored during the run and the magnitude of the ^{176}Yb interference on ^{176}Hf was calculated using $^{176}\text{Yb}/^{171}\text{Yb} = 0.897145$ [Segal *et al.*, 2003]. For Lu, the interference-free ^{175}Lu was corrected for mass bias effects assuming $\beta\text{Lu} = \beta\text{Yb}$ and using an exponential law. The mass bias-corrected ^{175}Lu was monitored during the run and the magnitude of the ^{176}Lu interference on ^{176}Hf

was calculated using $^{176}\text{Lu}/^{175}\text{Lu} = 0.02655$ [Vervoort *et al.*, 2004]. Interference-corrected $^{176}\text{Hf}/^{177}\text{Hf}$ were corrected for mass bias using an exponential law and $^{179}\text{Hf}/^{177}\text{Hf} = 0.7325$ [Patchett *et al.*, 1981]. Initial Hf isotope ratios and ϵHf values were calculated using the decay constant for ^{176}Lu of $1.867 \times 10^{-11} \text{ yr}^{-1}$ [Söderlund *et al.*, 2004] and the CHUR values of 0.282785 and 0.0336 for $^{176}\text{Hf}/^{177}\text{Hf}$ and $^{176}\text{Lu}/^{177}\text{Hf}$ [Bouvier *et al.*, 2008]. The accuracy and long-term reproducibility of the measurements were gauged by analysing three zircon reference standards [91,500, GJ1 and Plešovice with reference values taken from Blichert-Toft, 2008, Morel *et al.*, 2008, Sláma *et al.*, 2008, respectively] and all values were found to be in agreement with the reference values: 91,500 ($^{176}\text{Hf}/^{177}\text{Hf} = 0.282298 \pm 24$, $n = 30$), Plešovice ($^{176}\text{Hf}/^{177}\text{Hf} = 0.282473 \pm 19$, $n = 13$) and GJ1 ($^{176}\text{Hf}/^{177}\text{Hf} = 0.282007 \pm 32$, $n = 15$) (all errors at 2 s.d. level).

4. Results

4.1. Petrology

Sample Per21-4, from the *Cinéritique* Fm (Figures 1A and 2), is a tuffite characterized by a centimetric-scale layering related to grain size alternation. In thin section, it is dominated by a very fine-grained matrix including floating flat parallel unsorted silt to rare coarse sand-size clasts responsible for the laminated fabric. The clast fraction is mainly composed of large elongated quartz grains including micro bubble-like cavities compatible with ancient glass shards, K-feldspars and abundant muscovite flakes (Figure 4A). Secondary carbonates can also be observed.

Also from the *Cinéritique* Fm (Figure 2), the matrix of sample Can21-5 was collected in a 20 cm thick light-beige layer containing numerous plant remnants. It is extremely fine-grained and contains a dispersed very-fine silt-size fraction, including resorbed quartz crystal clasts (Figure 4B) and K-feldspar clasts, consistent with a pyroclastic origin, as well as terrigenous muscovite flakes.

Sample Dev21-1 corresponds to a 5 cm thick very fine-grained light-grey layer belonging to the *Saint-Rome-de-Tarn* Fm (Figures 1A and 2). In thin section (Figure 4C), it is composed of an extremely fine-grained matrix-supported silt- to sand-size unsorted clastic fraction, including larger angular to subangular quartz fragments of possible altered glass shards,

K-feldspar clasts, as well as rare tiny terrigenous muscovite flakes, indicating the lack of hydrodynamical sorting (Figure 4C).

Sample Lat20-1 belongs to the *Dourdou* Fm (F3 Unit, Figures 1A, 2 and 3A). It is a pinkish to light-beige fine-grained tuff with an eutaxitic-like fabric marked by black flame-like structures, suggesting a pyroclastic flow deposit, rather than a fall deposit. In thin section (Figure 4D), the sample is highly recrystallized and displays an anhedral quartz-rich mosaic invading the residual cryptocrystalline matrix with large dispersed carbonate patches and remaining K-feldspar and plagioclase clasts. A striking feature is the strong late carbonatation and recrystallization that this tuff suffered, possibly during the diagenetic processes.

Sample Gal21-7 belongs to the *Saint-Pierre* Fm (F5 Fm, Figure 2). In thin section, it is characterized by a dominant cryptocrystalline matrix, probably at least partly vitreous, containing millimetre thick bands enriched with fine sand-size to silt-size quartz and K-feldspar debris, together with smaller biotite and detrital muscovite grains. As shown on Figure 4E, some of the quartz clasts show resorption gulfs, which is consistent with their interpretation as rhyolitic quartz that underwent fast decompression in volcanic conduits. Lithic fragments, among which angular polycrystalline quartz clasts, can also be found.

Samples Cam20-3 and Gal21-6 were sampled in the same 20 cm thick tuffitic layer of the *Saint-Pierre* Fm (F5, Figures 1A, 2 and 3B). Sample Cam20-3 is a light-grey tuffite with a centimetric scale layering. In thin section, it contains a fair number of lithic fragments and angular quartz clasts (Figure 4F) compatible with a pyroclastic origin, as well as K-feldspar and plagioclase clasts together with chlorite after biotite, muscovite, accessory tourmaline and opaque minerals into a cryptocrystalline matrix. Muscovite and tourmaline indicate a mixing of the pyroclastic content with a terrigenous input. As shown on Figure 4F, this sample also reveals the presence of secondary carbonate minerals. Sample Gal21-6 is a very fine-grained tuffite similar to sample Gal21-7, but with a much smaller grain size with a clear planar microfabric marked by the alignment of the quartz clasts and muscovite microdebris (Figure 4G). Some late goethite veins can be found in this sample (Figure 4G).

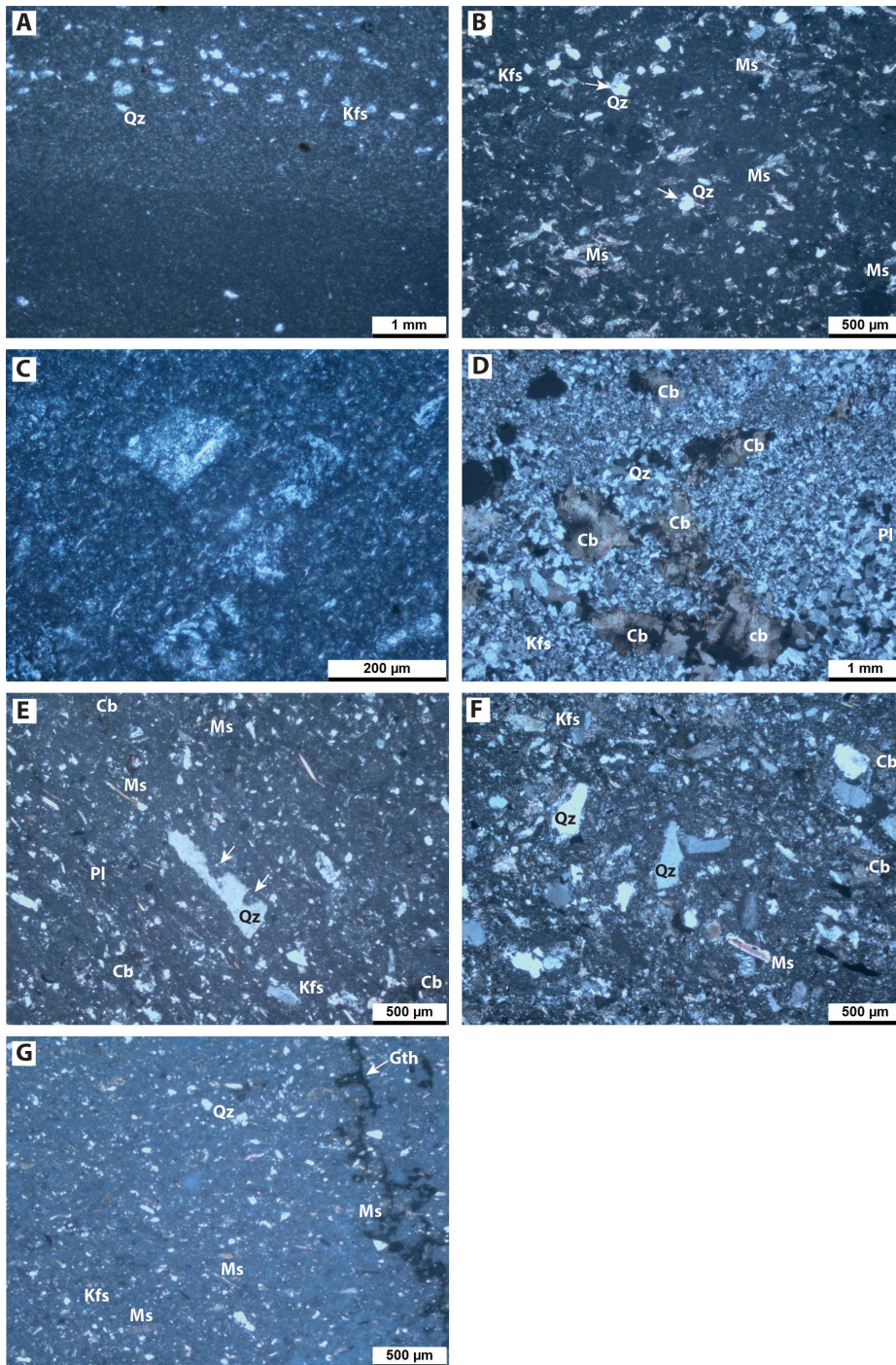


Figure 4. Optical cross-polarized light microphotographs for the samples from the Saint-Affrique Basin. (A) Sample Per21-4; note the layering marked by the variations of granulometry. (B) Sample Can21-5; white arrows show resorbed quartz grains. (C) Sample Dev21-1. (D) Sample Lat20-1; note the strong carbonatation. (E) Sample Gal21-7; white arrows show a decompression-related resorbed quartz crystal. (F) Sample Cam20-3; note the presence of angular quartz fragments. (G) Sample Gal21-6; note the presence of late goethite veins. Mineral abbreviations: Cb carbonate minerals; Gth goethite; Kfs K-feldspar; Ms muscovite; Pl plagioclase; Qz; quartz.

4.2. Whole-Rock geochemistry

Eight samples have been selected for major and trace element analyses (Supplementary Table 1). As illustrated in the previous section, all samples consist of ash tuffs and tuffites in which the terrigenous input is variable but obviously difficult to accurately quantify for each of the samples, a feature that may disturb their volcanic geochemical signatures. In addition, some samples underwent late (i.e. post-deposition) diagenetic modifications, such as carbonatation, sometimes fairly important, as for sample Lat20-1 that contains more than 10 wt% CaO. This increase in CaO (and Sr) content consequently dilutes the other elements. These characteristics can limit the usefulness of geochemical diagrams, which therefore need to be used with caution, especially those based on major element concentrations. In the conventional total alkali-silica (TAS) diagram (Figure 5A), sample Lat20-1 plots in the field of basaltic trachy-andesite, while all the others plot in the rhyolite field.

Whole-rock immobile trace and REE elements are often used in the case of volcanic ashes studies as they are usually less sensitive to post deposition processes (such as diagenesis). In the Zr/TiO₂ versus Nb/Y diagram of Winchester and Floyd [1977], two distinct groups appear (Figure 5B). A first group, comprising Per21-4, Per21-3, Can21-5 and Dev21-1 plots in the field of trachyte/trachy-andesite whereas a second group (Gal21-6, Gal21-7, Cam20-3 and Lat20-1) plots in the rhyodacite/dacite field. It should be noticed that yttrium can be lost during the alteration of volcanic rocks [Hill *et al.*, 2000] and therefore the alkalinity attributed to the samples should be considered as a maximum estimate.

In a Primitive Mantle normalized multi-elements diagram [McDonough and Sun, 1995, Figure 6a], all the studied samples yield trends that are comparable with the Upper Continental Crust [UCC, Taylor and McLennan, 1985]. Overall, the samples show a strong enrichment in LREE (Figure 5B), and, with the exception of sample Dev21-1, a negative Eu/Eu* anomaly, often found in felsic volcanic rocks [Wray, 1999]. In further detail, it is noteworthy that samples belonging to the two groups defined above present two distinct trends overall (Supplementary Table 1 and Figure 6B). Samples from the first group (Per21-4, Per21-3, Can21-5 and Dev21-1) display a low REE content

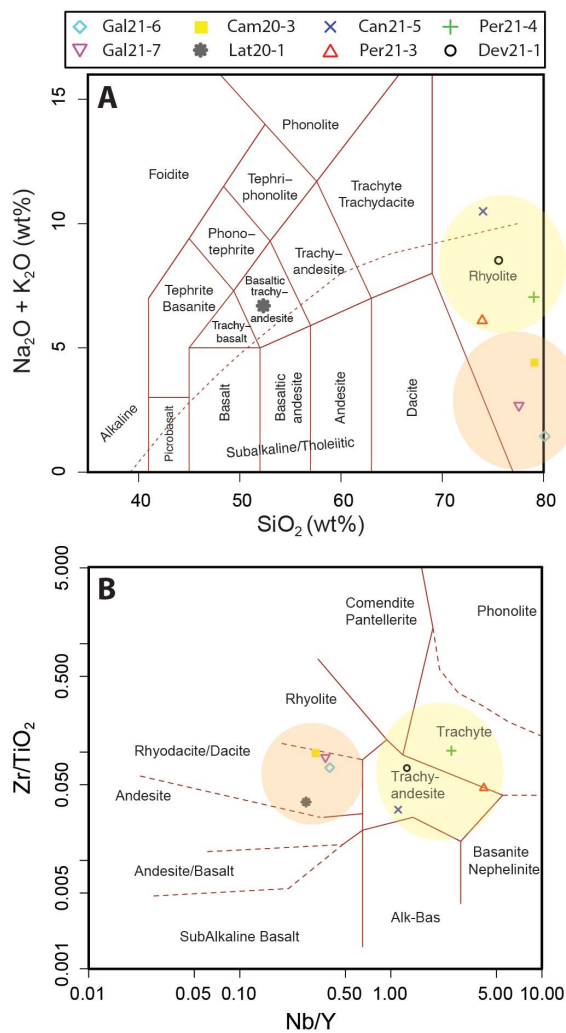


Figure 5. Geochemical classification diagrams for the samples collected within the Saint-Affrique Basin. (A) Total alkali-silica diagram [TAS, Le Maitre *et al.*, 1989]; (B) Zr/TiO₂ versus Nb/Y diagram [Winchester and Floyd, 1977]. The yellow ellipse corresponds to the first group of samples; the orange one to the second group of samples.

(22 to 98 ppm), a less pronounced negative Eu/Eu* anomaly (0.65 to 0.98) and strong HREE depletions. In contrast, samples from the second group (Gal21-6, Gal21-7, Cam20-3 and Lat20-1) present a higher REE content (143 to 158 ppm), a more pronounced Eu/Eu* anomaly (between 0.17 to 0.69) and flat HREE patterns. If the REE contents are normalized to that

of the Cody shale [Figure 6C; Jarvis and Jarvis, 1985], most samples show a negative Eu anomaly, are depleted in LREE and are either flat (second group) or depleted (first group) in HREE, which are all typical features for volcanic ashes [Wray and Wood, 1998, Ducassou *et al.*, 2019]. The fact that trend for Dev21-1 is fairly flat (Figure 6C) is often characteristic of a non-negligible detrital input [Wray and Wood, 1998, Ducassou *et al.*, 2019].

In the tectonic discrimination diagram (Figure 7A) presented by Schandl and Gorton [2002], the first group of previously defined (see above) samples plots in the “Within Plate Volcanic Zones” field while the second group plots in the “Active Continental Margin” field. In the tectonic diagram of Wood [1980], based on Hf/3–Th–Ta (Figure 7B), the second group of samples is characterized by a calc-alkaline chemistry, while the first group displays a higher Ta content relative to Th and Hf.

4.3. U–Pb dating of zircon

Unfortunately, it was not possible to find any minerals suitable for U–Pb dating in samples Per21-3 and Dev21-1.

Very few zircon grains were present in sample Per21-4 (*Cinéritique* Fm). Nine grains with various sizes were analyzed (Supplementary Table 3). They yielded variable U and Pb contents and fairly consistent Th/U ratios. With the exception of three discordant analyses (Figure 8A), three age groups can be defined: a first one around 2.0 Ga, a second one around 1.0 Ga and the last one around 0.6 Ga.

Again, very few zircon grains were found in sample Can21-5 (*Cinéritique* Fm). Thirteen grains with variable sizes were analyzed. They yield very high U (up to 3220 ppm) and Pb (up to 7648 ppm) contents (Supplementary Table 3) together with very high common Pb contents (f206c up to 39%). Their Th/U ratios are also highly variable (from 0.03 up to 0.53). Reported in a Concordia diagram (Figure 8B) they plot mostly in a discordant position with the exception of two grains (Zr12 and 13) which are concordant around 2.0 Ga.

Twenty-four analyses out of sixteen different zircon grains were acquired for sample Lat20-1 (Figure 3A; Supplementary Table 3). All zircon grains were prismatic, ranging in size between 70 and 200 μm and with simple concentric zoning (Figure 9).

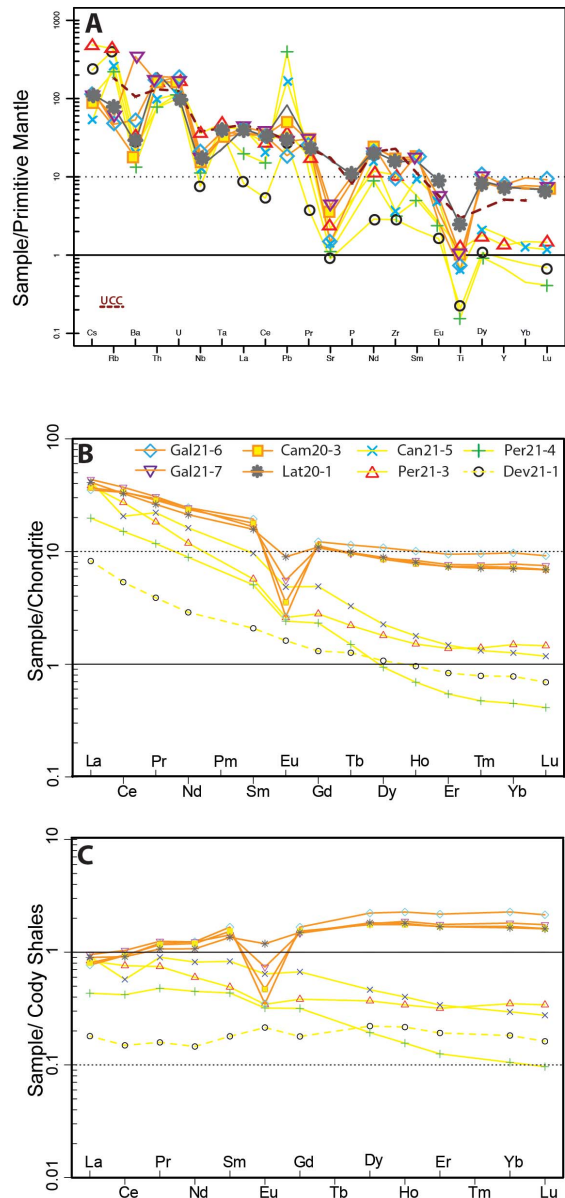


Figure 6. (A) Multi-element diagram normalized to Primitive Mantle [Sun and McDonough, 1989]. UCC = upper continental crust [Taylor and McLennan, 1985]; (B,C) Rare earth element plots for the tuff samples collected within the Saint-Affrique Basin. REE data are normalized (B) to the CI-chondrite [McDonough and Sun, 1995] and (C) to the Cody Shale [Jarvis and Jarvis, 1985]. Yellow lines correspond to the first group of samples; the orange line to the second group of samples.

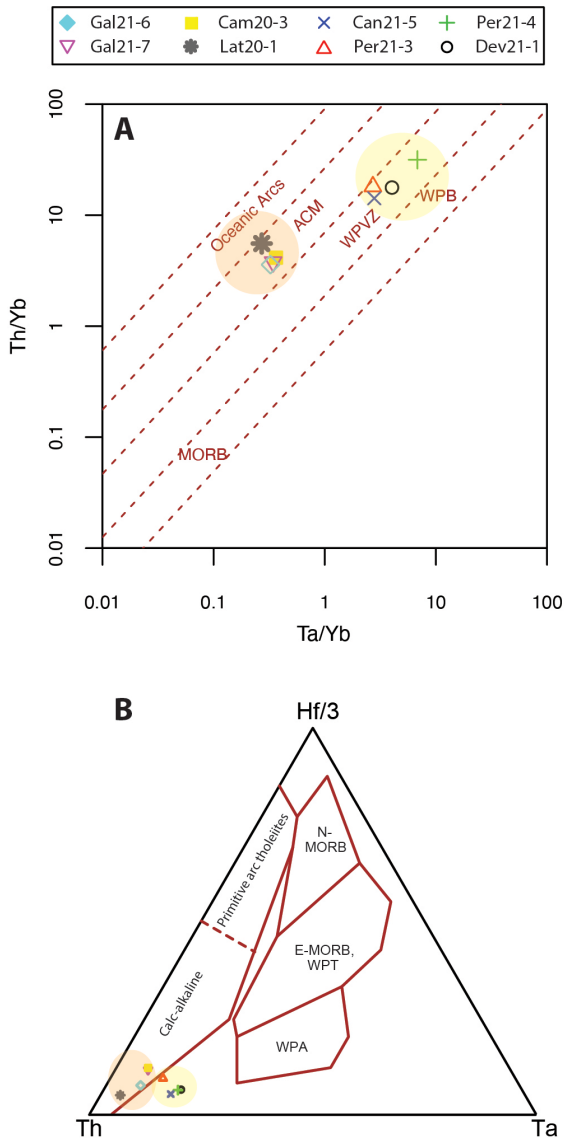


Figure 7. (A) Th/Yb versus Ta/Yb tectonic discrimination diagrams [after Schandl and Gorton, 2002]. ACM = active continental margin, MORB = mid-ocean ridge basalts, WPB = within plate basalts, WPVZ = within plate volcanic zones; (B) Hf/3–Th–Ta triangular diagram [after Wood, 1980]. WPA = within plate alkaline basalts and differentiates, WPT = within plate tholeiitic basalts and differentiates. The yellow ellipse corresponds to the first group of samples; the orange one to the second group of samples.

They yield variable U (236 to 9651 ppm) and Pb (50 to 908 ppm) contents with Th/U ratios consistent with a magmatic origin [0.1 to 0.26; see Witt *et al.*, 2017 and references therein]. Eighteen analyses plot in a concordant position (Figure 8C) and yield a concordia date of 280.3 ± 2.6 Ma (MSWD = 1.2). Two analyses (Zr 1.1 and Zr 11.2, Supplementary Figure 1) were acquired on grains that contain a non-negligible common Pb content (f206c of 1.56 and 6.38% respectively) and that probably belong to the same age group. Two analyses acquired on the same grain (Zr2) plot in a concordant position with apparent $^{206}\text{Pb}/^{238}\text{U}$ ages of around 320 Ma (Supplementary Figure 1), whereas a last analysis (Zr12, containing a non-negligible amount of common Pb; f206c% = 6.4), is highly discordant (52%; Supplementary Figure 1).

Thirty-one analyses (Supplementary Table 3) out of thirty-one different zircon crystals were acquired for sample Gal21-7 (Figures 1A and 2). Most crystals are rather elongated (up to 250 μm) and most of them display simple concentric magmatic zoning (Figure 9). Here again, the U (108 to 1886 ppm) and Pb (35 to 875 ppm) contents are highly variable. All the Th/U ratios, however, are compatible with a magmatic origin (0.13 to 0.48). A group of twenty-nine analyses (Figure 8D) define a concordia date of 278.4 ± 2.3 Ma (MSWD = 1.6). One grain (Zr5), characterized by a non-negligible common Pb content (f206c = 1.1%), plots to the right of the main batch of analyses and probably belongs to the same age group. The last analysis (Zr15) yields a concordant date around 470 Ma.

Thirty-two analyses (Supplementary Table 3) were acquired out of thirty-one zircon grains for sample Cam20-3 (Figure 3B). Zircon grains are generally prismatic with sizes ranging from 50 to 200 μm and display a magmatic zoning when imaged by cathode luminescence (Figure 9). They present variable U (212 to 1757 ppm) and Pb (41 to 1162 ppm) contents, with Th/U ratios ranging from “typical” metamorphic (0.03 to 0.09) to magmatic (0.16 to 0.62). Four age groups can be identified (Figure 8E and Supplementary Figure 1). The oldest zircon (Zr 27) yields an apparent $^{207}\text{Pb}/^{206}\text{Pb}$ age of ca. 2646 Ma (Supplementary Figure 1). One grain (Zr 25) yields a concordant date of ca. 940 Ma (Supplementary Figure 1). A third group of six zircon grains (Zr 1, 7, 8, 11, 17 and 20) returns apparent ages around 450–460 Ma

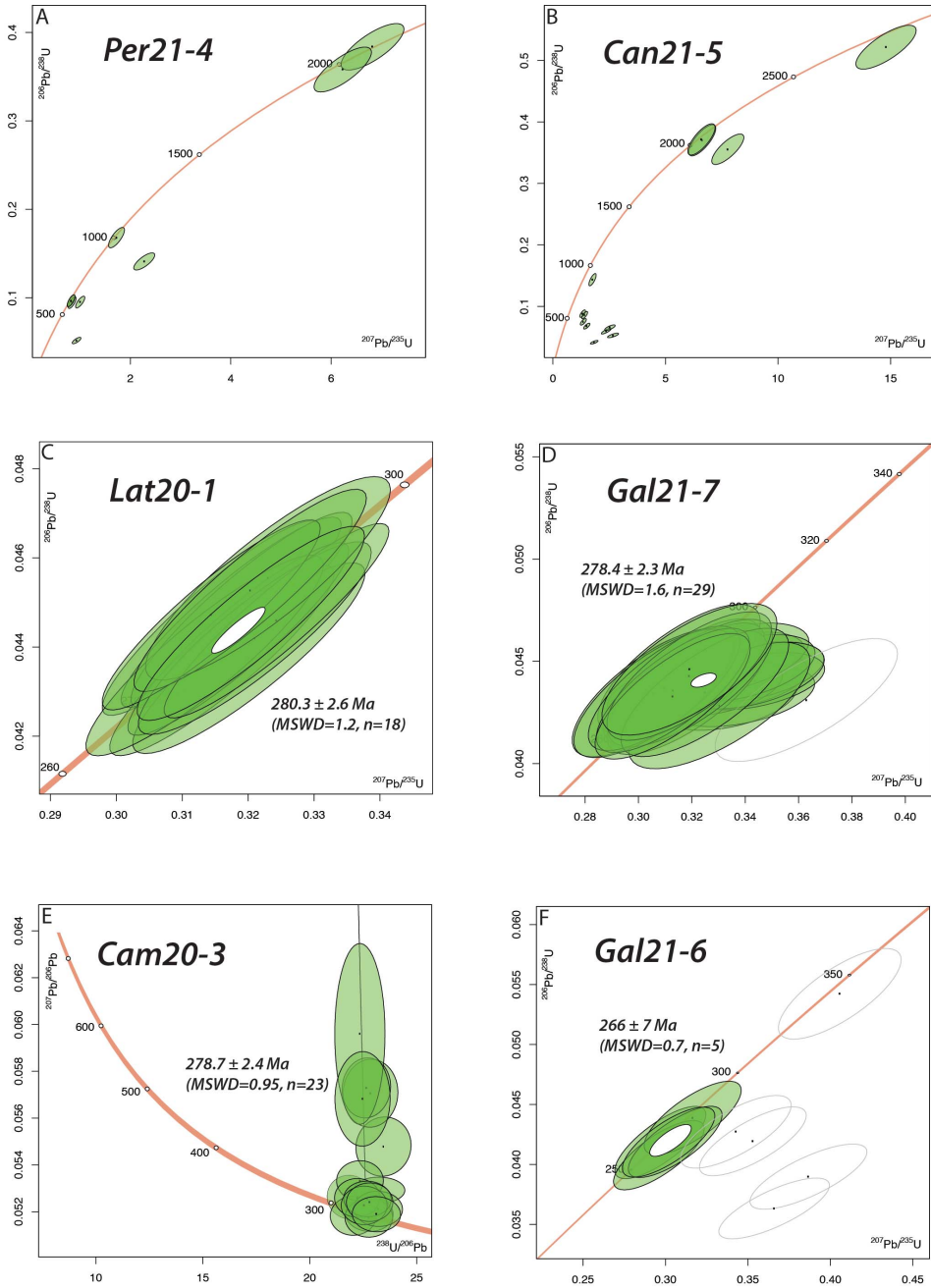


Figure 8. (A) Wetherill concordia diagram for sample Per21-4; (B) Wetherill concordia diagram for sample Can21-5; (C) Wetherill concordia diagram for sample Lat20-1; (D) Wetherill concordia diagram for sample Gal21-7; (E) Tera-Wasserburg concordia diagram for sample Cam20-3; (F) Wetherill concordia diagram for sample Gal21-6. MSWD = Mean Square Weighted Deviation. n = number of analyses used to calculate the U–Pb dates. All MSWD are calculated for concordance + equivalence. Grey ellipses were not used for age calculation.

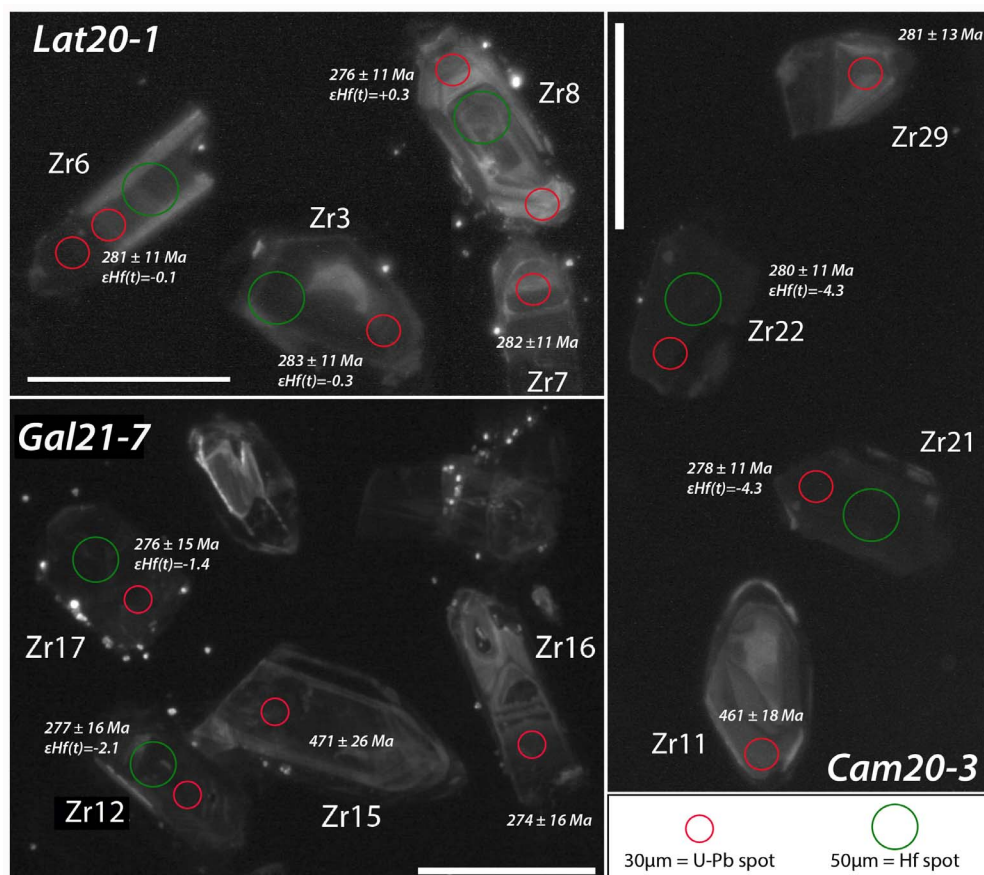


Figure 9. Cathode-luminescence imaging of some of the analyzed zircon grains. The white bar represents 200 μm .

(Supplementary Figure 1), yielding the lowest (metamorphic?) Th/U ratios. The youngest group composed of twenty-three different zircon grains (Figure 8E) yields a lower intercept date of $278.7 \pm 2.4 \text{ Ma}$ (MSWD = 0.95).

Ten zircon grains were found in sample Gal21-6 (Figure 1A and 2; Supplementary Table 3). All the grains were prismatic with concentric magmatic zoning (not shown). They are rich in U (up to 2558 ppm) and Pb (up to 1393 ppm), with fairly consistent Th/U ratios characteristic of magmatic sources (0.21 to 0.66). With the exception of one grain (Zr1) with a concordant date around 340 Ma (Figure 8F), the remaining five concordant analyses yield a concordia date of $266 \pm 7 \text{ Ma}$ (MSWD = 0.7, $n = 5$), whereas the oldest concordant zircon from this group has a $^{206}\text{Pb}/^{238}\text{U}$ apparent age of $277 \pm 15 \text{ Ma}$. The four

other analyses are discordant with variable amount of common Pb ($f_{206\text{c}}$ up to 2.78%).

4.4. Zircon Hf isotope composition

Three samples were selected for zircon Hf isotope measurements (Lat20-1, Cam20-3 and Gal21-7, Supplementary Table 3).

For each sample, ten zircon grains (eleven for sample Cam20-3), previously analysed for U–Pb, were targeted for Hf isotopes. Hf analyses were done as close as possible to the U–Pb ablation pits. The results are reported in Figure 10.

For sample Lat20-1, the analyzed zircon grains display very low $^{176}\text{Lu}/^{177}\text{Hf}$ (0.0009 ± 1) and initial (calculated at 280 Ma) $^{176}\text{Hf}/^{177}\text{Hf}$ ranging from 0.282600 to 0.282630, with nearly chondritic $\epsilon_{\text{Hf}}(t)$

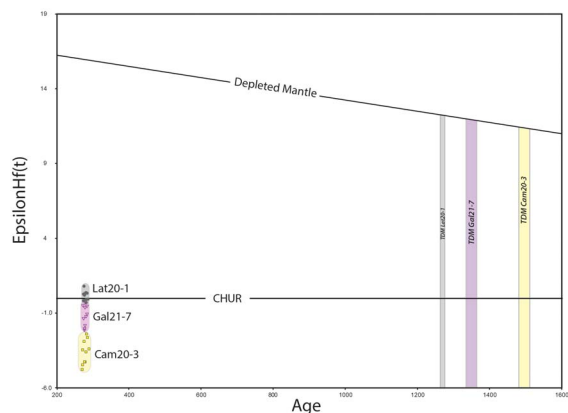


Figure 10. $\epsilon\text{Hf}(t)$ versus $^{206}\text{Pb}/^{238}\text{U}$ age of some selected zircon grains from samples Lat201, Gal21-7 and Cam20-3. Depleted Mantle and New Crust evolutions after Dhuime *et al.* [2011].

values (Figure 10) ranging from 0.8 to -0.3 (mean 0.1 ± 0.2). T_{DM} model ages are broadly similar to those measured from the two other samples and display a mean value of 1269 ± 13 Ma.

Zircons from sample Gal21-7 (Supplementary Table 3) yield low $^{176}\text{Lu}/^{177}\text{Hf}$ (0.0019 ± 3) and a mean $^{176}\text{Hf}/^{177}\text{Hf}_i$ of 0.282576 ± 12 (calculated at 278 Ma). $\epsilon\text{Hf}(t)$ are slightly sub-chondritic (Figure 10), ranging from -0.3 to -2.1 (mean = -1.2 ± 0.4). The T_{DM} mean value is 1352 ± 27 Ma.

For sample Cam20-3, the analyzed zircon grains present low $^{176}\text{Lu}/^{177}\text{Hf}$ ratios (0.0024 ± 6) and homogeneous $^{176}\text{Hf}/^{177}\text{Hf}_i$ ratios (0.282507 ± 15) calculated at 279 Ma. The corresponding initial ϵHf are subchondritic, with values ranging from -4.8 to -2.4 , and a mean $\epsilon\text{Hf}(t)$ of -3.6 ± 0.5 (Figure 10). Their T_{DM} yield a mean value of 1507 ± 33 Ma. One xenocryst, dated at 454 Ma, was also analyzed and provides a distinct, slightly supra-chondritic $\epsilon\text{Hf}(t)$ of 1.0.

5. Discussion

5.1. Age and nature of the volcanism in the Saint-Affrique Basin

Two groups of samples can be distinguished among the studied samples.

The first group of volcanoclastic beds (Can21-5, Per21-3, Per21-4 and Dev21-1) belonging to the

Cin ritique Fm (Figures 1A and 2), with a proposed Stephanian age (i.e. late Carboniferous), contains clasts (quartz and K-feldspars) that are consistent with a volcanic origin, and a fairly large detrital component. In the Zr/TiO_2 versus Nb/Y diagram (Figure 5B, yellow ellipse) they plot in the field of trachyte/trachy-andesite, and they yield trace-element contents compatible with a felsic composition. They all have a calc-alkaline chemistry and exhibit “Within Plate Volcanic Zone”-like characteristics in the volcano-tectonic diagram of Wood [1980]; these features are compatible with a late to post-collisional volcanism. Sample Dev21-1, belonging to the *Saint-Rome-de-Tarn* Fm (i.e. proposed lower Cisuralian in age), exhibits a flat REE pattern when normalized to shale (Figure 6C), but also displays a “Within Plate Volcanic Zone” geochemical composition (Figure 7B). Unfortunately, it was not possible to date these samples because of the absence of volcanic zircon grains. The detrital zircon grains found in two of these samples demonstrates however the existence of a complex basement underneath and/or aside the Saint-Affrique Basin with ages ranging from the Paleo- to the Neo-Proterozoic (Figure 8A and B).

The second group of samples belong either to the *Dourdou* Fm (Lat20-1) or to the *Saint-Pierre* Fm (Gal21-6 and 21-7 and Cam20-3). These formations were so far attributed to the Sakmarian and Artinskian, respectively [Gand, 1993]. Although these samples have a fair amount of muscovite indicating a terrigenous contribution, and can be sometime affected by a strong carbonation (Lat20-1), they all contain clasts of feldspars and quartz demonstrating the presence of a rather important volcanic content. These samples can be classified as dacites/rhyodacites, have a strong negative Eu/Eu^* anomaly, a significant LREE enrichment and a fairly flat HREE spectrum; these features are all in a good agreement with their felsic nature, and can be defined as calc-alkaline rocks. All of these features are in a good agreement with a post-orogenic deposition setting. All of these samples provided volcanic zircon grains. The stratigraphically oldest sample from this group (Lat20-1) records a volcanic episode during the Kungurian. The obtained date of 280 ± 2.6 Ma for this sample is interpreted as the age of the deposition of the bed, assuming that the dated zircon grains were not reworked after the volcanic eruption [e.g. Rossignol *et al.*, 2019]. Applying the same assump-

tion, the samples at the top of the sedimentary succession were then deposited at 278.4 ± 2.3 Ma (Gal21-7) and 278.7 ± 2.4 Ma (Cam20-3) respectively, i.e. also during the Kungurian. The date of 266 ± 7 Ma found for sample Gal21-6 may be related to slight Pb losses enhanced by the zircon's high U content (>1500 ppm) and has to be considered as a minimum age of deposition, as this sample belongs to the same ash bed as Cam20-3. Therefore, we propose that the date of 277 ± 15 Ma found for the oldest concordant zircon from this sample is the best estimate for the deposition age of this volcanic ash bed.

The mean $\varepsilon\text{Hf}(t)$ calculated for the zircon grains from the three dated volcanic ash beds Lat20-1, Gal21-7 and Cam20-3 provides chondritic to subchondritic values of 0.1 ± 0.2 ; -1.2 ± 0.4 and -3.6 ± 0.5 , respectively. The corresponding Hf model ages of 1.3–1.5 Ga represent an average of the sources involved in magma genesis or assimilated during the travel path upward to the surface of the magmas. In any case, this indicates a significant degree of recycling of Proterozoic or older material, which is also consistent with the occurrence (in the three volcanic levels) of zircon grains with apparent ages ranging from the Archean to the Neoproterozoic. It is however difficult to evaluate whether the Hf isotope signature of the analysed zircon grains reflects either a source signature or an open system evolution, such as assimilation of an older crust by juvenile, mantle-derived, magmas. Clarification of this point is key to the interpretation of the geochemical data, as it could indicate crustal reworking processes, or new crustal growth by addition of material issued from the mantle during the post-collisional Variscan period. Although sampled at different stratigraphical levels, samples Gal21-7 and Cam20-3 belong to the same F4/F5 formation and display remarkably similar U–Pb ages (278.4 and 278.7 Ma, respectively) and trace- and major-element chemistry. Both samples display subchondritic, but substantially different, Hf isotope signatures ($\varepsilon\text{Hf} = -1.2 \pm 0.4$ and -3.6 ± 0.5 respectively). This difference indicates that magma genesis involved partial melting of a compositionally heterogeneous crustal section. The mean age for this crustal section is estimated between 1.3–1.6 Ga, assuming felsic precursors (with a $^{176}\text{Lu}/^{177}\text{Hf}$ ratio of 0.015), or 1.6–2.0 Ga, assuming mafic precursors (with a $^{176}\text{Lu}/^{177}\text{Hf}$ ratio of 0.021). Sample Lat20-1 yields a chondritic value that can be explained

in two ways. The first is a mixing (at *c.* 280 Ma) between a suprachondritic mantle-derived magma and subchondritic Paleoproterozoic or older crustal sources in proportions that coincidentally produced a εHf chondritic value. An alternative possibility is a remelting (at *c.* 280 Ma) of a 1.3 Ga old or 1.6 Ga old Paleoproterozoic source, which would have evolved with a calculated $^{176}\text{Lu}/^{177}\text{Hf}$ ratio of, respectively, 0.015 assuming a felsic precursor, or a ratio of 0.021, typical of the time-integrated evolution of a mafic (lower) crust (Figure 9). It is worth noting that the vertical scattering observed for all analyses in Figure 9 (from 0.8 to -4.8) may reflect such a mixing trend between mantle- and crustally-derived components. Whichever hypothesis is retained, it requires a heat source that can be found in mantle-derived magmas present at the base of the continental crust, as mentioned in many previously published studies [e.g. Breiterkruz and Kennedy, 1999]. Therefore, although our results indicate intra-crustal remelting and recycling of an old Paleoproterozoic to Archean basement, the addition of juvenile magmas triggering partial melting of the lower crust or mixed with crustally-derived magmas cannot be ruled out.

Although this needs further investigation, the Hf analyses tend to indicate an increase of crustal input in the production of the magmas, with εHf chondritic values for the oldest sample (Lat20-1) becoming increasingly negative towards the top of the basin. Interestingly, there is also a correlation between $\varepsilon\text{Hf}(t)$ and Eu/Eu^* , which may indicate that the magmas producing the stratigraphically most elevated volcanic ash beds Gal21-7 and Cam20-3 underwent fractional crystallization processes involving plagioclase, more pronounced than the other samples, and that they possibly had more time to interact with, and assimilate crustal material.

The first group of samples consists of trachyandesitic lavas, which are characterized by a greater HREE depletion and smaller Eu/Eu^* anomalies than the rhyodacitic samples of group 2 (including the dated samples Lat20-1, Gal21-7 and Cam21-3). The greater HREE depletion of group 1 samples may indicate that the magmas were generated at a greater depth than samples from group 2. Lastly, the identification of Neoproterozoic to Archean zircon grains in the volcanic ashes substantiates the occurrence of a complex and old basement both underneath and alongside the basin.

The different geochemical signatures of the two groups mark a significant change in the petrological processes producing the magmas, especially an evolution of the main magmatic sources involved, as the geodynamical conditions evolved from a late- to a post-orogenic setting with time. The “Within Plate”- versus “Active Margin”-like signatures, coupled with our Hf data interpretations in the younger group, reflect that the crustal contribution increased as time proceeded. In any late- to post-orogenic setting, this has to be controlled by substantial modifications of the geothermal gradient, and a significant increase of the heat flux, which can hardly be conceived without a simultaneous increase of the production of mantle melts triggering crustal melting. Because the production of mantle magmas at high rates may induce significant crustal melting, it is likely that from the base to the top of the sedimentary succession, the Saint-Affrique pyroclastic layers recorded the transition from a late-orogenic extension to a post-orogenic extension at much higher rates as the basin enlarged.

Our new constraints on the age and nature of the volcanism recorded in the sedimentary succession also questions the location of the emission centres of the volcanic ashes, in the absence of known volcanic edifices near the Saint-Affrique Basin, feature which is a recurrent issue in Western Europe Carboniferous and Permian continental basins [e.g. Koniger and Stollhofen, 2001, Pellenard *et al.*, 2017]. Explosive subaerial calc-alkaline volcanic activity with Permian ages is known in the Central Pyrenees (about 200 km from the Saint-Affrique Basin), where it is associated with high-intensity explosive magmatic eruptions of rhyodacitic to rhyolitic lavas and associated widespread pyroclastic flows and overriding ash clouds [Marti, 1996, Pereira *et al.*, 2014], and transported several hundreds of kilometres under the dominant wind. On the other side, Permian subaerial calc-alkaline volcanic episodes, including andesitic, dacitic and rhyolitic ignimbrite lavas are known in northwestern Corsica and Sardinia [Cabanis *et al.*, 1990, Timmerman, 2004, and references therein], and in the Esterel Massif [Zheng *et al.*, 1992, Nmila, 1995], and could also represent good candidates for the volcanic ash input. Nonetheless, the possible pyroclastic flow nature of the sampled layer from the *Dourdou* Fm (sample Lat20-1) suggests that edifices that were more proximal to the basin still

have to be identified.

5.2. Implications for the deposition of the Saint-Affrique Basin

The new radiochronological ages presented in this study refine the chronological setting of the Saint-Affrique Basin (Figure 11), the sedimentary successions of which were considered as deposited from the early to the middle Permian [Rolando *et al.*, 1988, Figures 2 and 11], and then during the early Permian only [Gand, 1993, Figures 2 and 11]. Our new ages encompass the Kungurian Stage (uppermost Cisuralian, Figure 11). The oldest age (Lat20-1, 280.3 ± 2.6 Ma), i.e. in the lower part of the *Dourdou* Fm, is, within errors, very close to the lower limit of the Kungurian, given that the Artinskian–Kungurian boundary is set at 283.5 ± 0.6 Ma [Cohen *et al.*, 2013, updated; Figure 11]. No age could be determined at the base of the sedimentary succession, but it is likely that Asselian to Sakmarian (lower Cisuralian) deposits are preserved.

The top of the sedimentary succession of the Saint-Affrique Basin is not dated, but considering the youngest age found in this study (Cam20-3, 278.7 ± 2.4 Ma), located less than 100 m below the youngest preserved deposits, as well as the absence of significant erosional surfaces or discontinuity in the sedimentation above this volcanic level, it is highly probable that the top of the sedimentary succession was also deposited during the Kungurian, the upper limit of which is set at 273.01 ± 0.14 Ma [Cohen *et al.*, 2013, updated].

The maximum duration of the sedimentary deposition between the stratigraphically lowest and highest dated volcanic ash beds levels, i.e. Lat20-1 (280.3 ± 2.6 Ma) and Cam20-3 (278.7 ± 2.4 Ma), is 6.6 Ma. During this timeframe, the sediment thickness estimated by coupling borehole data and spatial correlations [based on the 1/50,000 geological map of Guérangé-Lozes *et al.*, 1995] is about 1100 to 1500 m. Considering this maximum duration, the sedimentation rates (compacted sedimentary succession), appear to be low, ranging from 0.160 mm/yr to 0.230 mm/yr. It is worth noting the mean sedimentation rate estimated for other late-Carboniferous–early Permian basins presenting

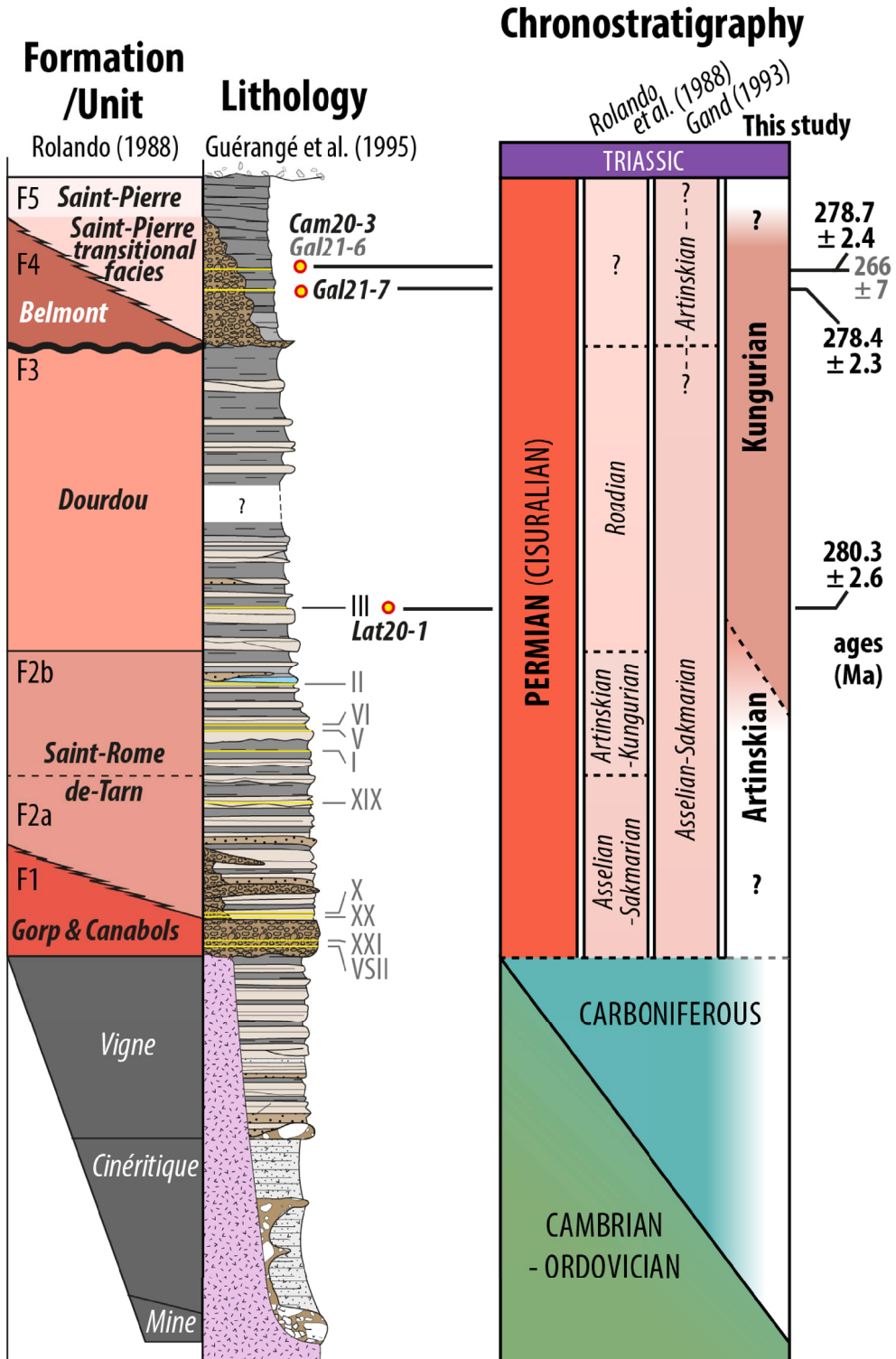


Figure 11. Refined chronostratigraphic setting for the Saint-Affrique Basin sedimentary succession based on the new ages obtained in this study.

a similar geological setting: in the northeastern Massif Central Autun Basin [Mercuzot, 2020], sedimentation rates based on precise radiometric ages were estimated at 0.45 mm/yr, taking the compacted sedimentary succession into account, and at 1.1 mm/yr when estimating a decompacted succession thickness. In the Saar-Nahe Basin (western Germany) the sedimentation rate is also higher, i.e. 0.3 mm/yr (compacted sedimentary succession). Some modern lacustrine systems, e.g. the Lake Titicaca (Altiplano, late-orogenic setting) and the North-American Great Lakes (Superior, Erie and Huron, glacial lakes) exhibit sedimentation rates between 0.1 and 7.4 mm/yr [Kemp and Harper, 1976, Kemp *et al.*, 1977, 1978, Durham and Joshi, 1980, Lojka *et al.*, 2009] that are consistent with our calculated rates. It also demonstrates that the sedimentation rates calculated in this study might be underestimated because of the lack of precise petrophysical and burial condition data. Consequently, the discontinuity between F3 and F4 fms (Figures 2 and 11) should not represent a substantial hiatus.

These new chronostratigraphical data clearly indicate the lack of the Middle (Guadalupian) and Upper (Lopingian) Permian deposits in the present-day sedimentary succession. Moreover, if we consider a middle-Anisian age for the basal Triassic sandstone deposits, as in the Lodève Basin [Lopez and Mader, 1985], the angular unconformity between the youngest Permian and the Triassic deposits represents a major hiatus of about 23 Myrs, during which the residual Variscan reliefs and the upper part of the Permian sedimentary succession of the Lodève and Saint-Affrique basins were eroded and peneplaned. In the Lodève Basin, the overall thickness of the eroded sedimentary succession between the top of the Permian deposits and the middle-Anisian unconformity is estimated at 1000 to 1500 m [Lopez *et al.*, 2008, Figure 2].

In Europe, increasing correlations are tentatively made between Carboniferous–Permian basins, based on both radiometric ages and biostratigraphic data [e.g. Schneider and Scholze, 2018, Pellenard *et al.*, 2017, Ducassou *et al.*, 2019, Schneider *et al.*, 2020]. The Lodève Basin is one of the most used basin to establish correlations in Western Europe, mostly because of its almost complete sedimentary succession from the late Carboniferous to the late Guadalupian [i.e. late middle Permian; Schneider

et al., 2020]. However, the present re-evaluation of the ages of the Saint-Affrique Basin, located in the direct vicinity and formed in the same geodynamic setting, calls for new radiometric age constraints in the Lodève Basin.

6. Conclusion

Our study focuses on several volcanic ash beds encountered within the sedimentary successions of the Saint-Affrique Basin. Two different groups of volcanoclastic rocks are defined: (i) the first group, located at the base of the sedimentary succession and considered as Carboniferous in age, could not be dated due to a lack of volcanic zircon grains in the studied samples, and hence requires further analyses to refine the age of these ante-Artinskian deposits. These volcanoclastic beds include a significant terrigenous input and yield mostly trachytic to trachy-andesitic felsic compositions. They can be defined as calc-alkaline rocks that reproduce, in a late orogenic setting, a “Within Plate Volcanic Zone” signature; (ii) the second group consists of dacitic to rhyodacitic ash beds with a calc-alkaline affinity, and a geochemical signature resembling to that of “Active Continental Margin” rocks. Their deposition ages are younger than previously estimated, i.e. Kungurian instead of Artinskian.

The geochemical analyses (elemental and isotopic) of samples from both groups attest to a crustal recycling of older material (Proterozoic and older). This crustal component becomes more prominent toward the top of the Permian successions, possibly due to an increase of a mantle contribution triggering crustal melting. Overall, their petrological and geochemical features are compatible with volcanic activities that took place during late- to post-collisional regional extension. These types of volcanic centres are known during the late Carboniferous and Permian, both in the Central Pyrenees and in the Provence–Corsica–Esterel domain. The presence of these different volcanoclastic ash beds within the basin demonstrates the persistence and recurrence of the volcanic activity in the region during the Permian. Lastly, although preliminary, these new ages allow to calculate rather low minimum sedimentation rates (around 0.2 mm/yr) during the Kungurian in the Saint-Affrique Basin.

The dating the volcanic ash bed from the outcrop of Latour-sur-Sorgues (Lat20-1 sample, evidenced as a key-bed in 70's mining reports in drilled wells located along the southeastern border of the basin) would constitute a new robust anchor point to precisely correlate the sedimentary successions at basin-scale. Furthermore, several other volcanic ash beds, which unfortunately were not recognized in the field during this work, were also identified during the 70's at the same stratigraphical position on the different logs in the *Saint-Rome-de-Tarn* Fm (F2). Identifying these discrete volcanic levels in the *Saint-Rome-de-Tarn* Fm cropping out in the hanging wall of the southern bordering fault would make it easier to date the oldest Permian deposits of the basin.

While contributing to the refinement of the stratigraphic setting of the Saint-Affrique Basin, this study also demonstrates the need for additional precise dating in the neighbouring basins (e.g. Lodève Basin), as well as in other late Paleozoic basins from Western Europe related to the late Variscan dynamics. This would provide some important contributions for the recalibration of the Western Europe continental biostratigraphic scales. In addition, establishing correlations between these basins is paramount to better constrain the precise and accurate timing of their filling history, the relationships between sedimentation and tectonic and geodynamic processes, and to assess the various climate events that prevailed during the Permian in the Eastern Pangea intertropical domain.

Conflicts of interest

Authors have no conflict of interest to declare.

Acknowledgements

This study is dedicated to the memory of Jean-Louis Paquette who greatly contributed, among other things, to our understanding of the French Massif Central. Xavier Le Coz (Géosciences Rennes) is thanked for the making of the thin sections, and Cindy Maliverney (TSL) for sample preparations. Jean Poujol is thanked for his hospitality during the two sampling fieldtrips and Sara Mullin for correcting the English content. Finally, the authors want to thank J. Barbarand, V. Bosse and S. Duchêne for their insightful comments on the previous version of this manuscript.

Supplementary data

Supporting information for this article is available on the journal's website under <https://doi.org/10.5802/crgeos.184> or from the author.

References

- Beccaletto, L., Capar, L., Serrano, O., and Marc, S. (2015). Structural evolution and sedimentary record of the Stephano–Permian basins occurring beneath the Mesozoic sedimentary cover in the southwestern Paris basin (France). *Bull. Soc. Géol. Fr.*, 186, 429–450.
- Becq-Giraudon, J. F., Montenat, C., and Van Den Driessche, J. (1996). Hercynian high-altitude phenomena in the French Massif Central: tectonic implications. *Palaeogeogr. Palaeoclimatol. Palaeoecol.*, 122, 227–241.
- Blichert-Toft, J. (2008). The Hf composition of zircon reference material 91500. *Chem. Geol.*, 253(3/4), 252–257.
- Bourquin, S., Bercovici, A., López-Gómez, J., Diez, J. B., Broutin, J., Ronchi, A., Durand, M., Arche, A., Linol, B., and Amour, F. (2011). The Permian–Triassic transition and the beginning of the Mesozoic sedimentation at the Western peri-Tethyan domain scale: palaeogeographic maps and geodynamic implications. *Palaeogeogr. Palaeoclimatol. Palaeoecol.*, 299, 265–280.
- Bouvier, A., Vervoort, J. D., and Patchett, P. J. (2008). The Lu–Hf and Sm–Nd isotopic composition of CHUR: Constraints from unequilibrated chondrites and implications for the bulk composition of terrestrial planets. *Earth Planet. Sci. Lett.*, 273, 48–57.
- Breitkreuz, C. and Kennedy, A. (1999). Magmatic flare-up at the Carboniferous/Permian boundary in the NE German Basin revealed by SHRIMP Zircon Ages. *Tectonophysics*, 302, 307–326.
- Bruguier, O., Becq-Giraudon, J.-F., Champenois, M., Deloule, E., Ludden, J., and Mangin, D. (2003). Application of in situ zircon geochronology and accessory phase chemistry to constraining basin development during post-collisional extension: a case study from the French Massif Central. *Chem. Geol.*, 201, 319–336.
- Bruguier, O., Caby, R., Bosch, D., Ouzegane, K., Deloule, E., Dhuime, B., Bendaoud, A., and Kienast,

- J. R. (2020). A case study of in situ analyses (major and trace elements, U-Pb geochronology and Hf-O isotopes) of a zircon megacryst: implication for the evolution of the Egéré terrane (Central Hoggar, Tuareg Shield, Algeria). *Precambrian Res.*, 351, article no. 105966.
- Burg, J. P., Brun, J. P., and Van Den Driessche, J. (1990). Le sillon houiller du Massif Central français : faille de transfert pendant l'aminicissement crustal de la chaîne. *C. R. Acad. Sci. Paris*, 311, 147–152.
- Burg, J. P., Van Den Driessche, J., and Brun, J. P. (1994). Syn-to post-thickening extension: mode and consequences. *C. R. Acad. Sci. Paris*, 319, 1019–1032.
- Cabanis, B., Cochemé, J. J., Vellutini, P. J., Joron, J. L., and Treuil, M. (1990). Post-collisional Permian volcanism in northwestern Corsica: an asseement based on mineralogy and trace-element geochemistry. *J. Volcanol. Geotherm. Res.*, 44, 51–67.
- Carignan, J., Hild, P., Mevelle, G., Morel, J., and Yeghicheyann, D. (2001). Routine analyses of trace elements in geological samples using flow injection and low pressure on-line liquid chromatography coupled to ICP-MS: A study of geochemical reference materials BR, DR-N, UB-N, AN-G and GH. *Geostand. Newsl.*, 25, 187–198.
- Châteauneuf, J.-J. and Farjanel, G. (1989). Synthèse géologique des bassins permien français. In *Mémoires du Bureau de Recherches Géologiques et Minières*, volume 128, page 288. BRGM, Paris.
- Choulet, F., Faure, M., Fabbri, O., and Monié, P. (2012). Relationships between magmatism and extension along the Autun–La Serre fault system in the Variscan Belt of the eastern French Massif Central. *Int. J. Earth Sci.*, 101, 393–413.
- Cohen, K. M., Finney, S. C., Gibbard, P. L., and Fan, J.-X. (2013). The ICS International Chronostratigraphic Chart. *Episodes*, 36, 199–204. (updated).
- David, A. (1967). *Etude géologique du bassin permien de Belmont-sur-Rance (Aveyron) et ses minéralisations uranifères et cuprifères*. Thèse 3ème cycle, Université de Clermont-Ferrand. 96 pages.
- Dhuime, B., Hawkesworth, C., and Cawood, P. (2011). When continents formed. *Science*, 331, 154–155.
- Domeier, M. and Torsvik, T. H. (2014). Plate tectonics in the late Paleozoic. *Geosci. Front.*, 5(3), 303–350.
- Ducassou, C., Mercuzot, M., Bourquin, S., Rossignol, C., Beccaletto, L., Pierson-Wickmann, A. C., Pellenard, P., Poujol, M., and Hue, C. (2019). Sedimentology and U-Pb dating of Carboniferous to Permian continental series of the northern Massif Central (France): local palaeogeographic evolution and larger scale correlations. *Palaeogeogr. Palaeoclimatol. Palaeoecol.*, 533, article no. 109228.
- Durham, R. and Joshi, S. (1980). Recent sedimentation rates, 210Pb fluxes, and particle settling velocities in Lake Huron, Laurentian Great Lakes. *Chem. Geol.*, 31, 53–66.
- Faure, M. (1995). Late orogenic carboniferous extensions in the Variscan French Massif Central. *Tectonics*, 14, 132–153.
- Faure, M. and Becq-Giraudon, J. F. (1993). Sur la succession des épisodes extensifs au cours du désépaissement carbonifère du Massif Central français. *C. R. Acad. Sci. Paris*, 316, 967–973.
- Fisher, C. M., Hanchar, J. M., Samson, S. D., Dhuime, B., Blichert-Toft, J., Vervoort, J. D., and Lam, R. (2011). Synthetic zircon doped with hafnium and rare earth elements: A reference material for in situ hafnium isotope analysis. *Chem. Geol.*, 286, 32–47.
- Gand, G. (1993). La palichnofaune de vertébrés tétrapodes du bassin permien de Saint-Affrique (Aveyron) : comparaisons et conséquences stratigraphiques. *Géol. de la France*, 1, 41–56.
- Gand, G., Garric, J., Schneider, J., Sciau, J., and Walter, H. (1996). Biocénoses à méduses du permien français (bassin de Saint-Affrique, Massif Central). *Geobios*, 29/4, 379–400.
- Genna, A., Roig, J. Y., Debriette, P. J., and Bouchot, V. (1998). Le bassin houiller d'Argentat (Massif Central français), conséquence topographique d'un plissement de son substratum varisque. *C. R. Acad. Sci. Paris*, 327, 279–284.
- Goloubinoff, C. (1979). *Le permo-houiller du nord du bassin de St Affrique (Aveyron)*. Thèse de 3ème cycle, Université Paris-Sud. 143 pages.
- Guérangé-Lozes, J. and Alabouvette, B. (1999). *Carte Géologique de la France au 1/50 000 — feuille de Saint-Sernin-sur-Rance*. Bureau de Recherches Géologiques et Minières (BRGM), Orléans.
- Guérangé-Lozes, J., Burg, J. P., Vinchon, C., Alabouvette, B., Defaut, B., Astruc, J. G., Galharague, J., Leyreloup, A., Michard, A. G., Perrin, C., and Servelle, C. (1995). *Carte Géologique de la France au 1/50 000 — feuille de Réquista*. Bureau de Recherches Géologiques et Minières (BRGM), Orléans.
- Guérangé-Lozes, J. and Guérangé, B. (1991). *Carte Géologique de la France au 1/50 000 — feuille de*

- Camarès. Bureau de Recherches Géologiques et Minières (BRGM), Orléans.
- Hill, I. G., Worden, R. H., and Meighan, I. G. (2000). Yttrium: The immobility-mobility transition during basaltic weathering. *Geology*, 28, 923–926.
- Hübner, N., Körner, F., and Schneider, J. (2011). Tectonics, climate and facies of the Saint Affrique Basin and correlation with the Lodève Basin (Permian, Southern France). *Z. Dtsch. Ges. fur Geowiss.*, 162(2), 157–170.
- Izart, A., Vaslet, D., Briand, C., Broutin, J., Coquel, R., Davydov, V., Donsimoni, M., Wartiti, M. E., Ensebaev, T., Geluk, M., Goreva, N., Gôrür, N., Iqbal, N., Joltaev, G., Kossovaya, O., Krainer, K., Laveine, J.-P., Makhlina, M., Maslo, A., Nemirovskaya, T., Kora, M., Kozitskaya, R., Massa, D., Mercier, D., Monod, O., Oplustil, S., Schneider, J., Schönlaub, H., Stschegolev, A., Süss, P., Vachard, D., Vai, G. B., Vozarova, A., Weissbrod, T., and Zdanowski, A. (1998). Stratigraphic correlations between the continental and marine Tethyan and Peri-Tethyan basins during the Late Carboniferous and the Early Permian. In Crasquin-Soleau, S., Izart, A., Vaslet, D., and De Wever, P., editors, *Peri-Tethys: Stratigraphic Correlations 2, Geodiversitas*, volume 20(4), pages 521–595. MNHN, Paris.
- Janousek, V., Farrow, C. M., and Erban, V. (2006). Interpretation of whole-rock geochemical data in igneous geochemistry: introducing Geochemical Data Toolkit (GCDkit). *J. Petrol.*, 47, 1255–1259.
- Jarvis, I. and Jarvis, K. E. (1985). Rare-earth element geochemistry of standard sediments: A study using inductively coupled plasma spectrometry. *Chem. Geol.*, 53, 335–344.
- Kemp, A., Dell, C., and Harper, N. (1978). Sedimentation rates and a sediment budget for Lake Superior. *J. Great Lakes Res.*, 4, 276–287.
- Kemp, A. and Harper, N. (1976). Sedimentation rates and a sediment budget for Lake Ontario. *J. Great Lakes Res.*, 2, 324–339.
- Kemp, A., MacInnis, G., and Harper, N. (1977). Sedimentation rates and a revised sediment budget for Lake Erie. *J. Great Lakes Res.*, 3, 221–233.
- Koniger, S. and Stollhofen, H. (2001). Environmental and tectonic controls on preservation potential of distal fallout ashes in fluvio-lacustrine settings: the Carboniferous-Permian Saar-Nahe Basin, south-western Germany. volume 30 of *Special Publication—International Association of Sedimentologists*, pages 263–284.
- Laversanne, J. (1976). *Sédimentation et minéralisation du Permien de Lodève*. Thèse doc/ing, Université d'Orsay. 300 pages.
- Le Maitre, R. W., Streckeisen, A., Zanettin, B., Le Bas, M. J., Bonin, B., and Bateman, P. (1989). Igneous rocks: a classification and glossary of terms. In *Recommendations of the International Union of Geological Sciences, Subcommittee on the Systematics of Igneous Rocks*, page 193. Blackwell, Oxford.
- Legrand, X. (1990). *Effets de la tectonique extensive en milieu continental. Le Bassin Permien de Saint Affrique*.
- Legrand, X., Soula, J.-C., and Rolando, J.-P. (1994). The Saint-Affrique Permian basin (southern France): an example of a roll-over controlled alluvial sedimentation during regional extensional tectonics. *Geodin. Acta*, 7(2), 103–120.
- Lojka, R., Drábková, J., Zajíc, J., Sykorová, I., Franc, J., Bláhová, A., and Grygar, T. (2009). Climate variability in the Stephanian B based on environmental record of the Mšec Lake deposits (Kladno-Rakovník Basin, Czech Republic). *Palaeogeogr. Palaeoclimatol. Palaeoecol.*, 280, 78–93.
- Lopez, M., Gand, G., Garric, J., and Körner, F. (2008). The playa environments of the Lodève Permian Basin (Languedoc, France). *J. Iber. Geol.*, 34, 29–56.
- Lopez, M. and Mader, D. (1985). Gravelly and sandy braidplain, evolving into floodplain and playa-lake deposition and vice versa, in the Bundsanstein facies sediments and marine incursions. In Mader, D., editor, *Triassic of the Lodève Region (Southern France)*, volume 4 of *Lecture Note in Earth Sciences*, pages 509–518. Heidelberg, Berlin.
- Lucas, S. G. and Shen, S.-Z. (2018). The Permian chronostratigraphic scale: history, status and prospectus. volume 450 of *Geol. Soc. Lond., Special Publications*, pages 21–50.
- Malavieille, J., Guihot, P., Costa, S., Lardeaux, J. M., and Gardien, V. (1990). Collapse of the thickened Variscan crust in the French Massif Central: Mont Pilat extensional shear zone and St. Etienne Late Carboniferous basin. *Tectonophysics*, 177, 139–149.
- Marti, J. (1996). Genesis of crystal-rich volcanoclastic facies in the Permian red beds of the Central Pyrenees (NE Spain). *Sediment. Geol.*, 106, 1–19.
- McDonough, W. F. and Sun, S. S. (1995). The composition of the Earth. *Chem. Geol.*, 120, 223–253.
- Ménard, G. and Molnar, P. (1988). Collapse of a Her-

- cynian Tibetan plateau into a late Palaeozoic European Basin and Range province. *Nature*, 334, 235–237.
- Mercuzot, M. (2020). *Reconstitutions paléoenvironnementales et paléoclimatiques en contexte tardi-orogénique : cas des bassins fini-carbonifères à permien du nord-est du Massif Central, France*. Thèse de 3ème cycle, Université de Rennes 1, France.
- Mercuzot, M., Bourquin, S., Beccaletto, L., Ducassou, C., Rubi, R., and Pellenard, P. (2021). Palaeoenvironmental reconstitutions at the Carboniferous–Permian transition south of the Paris Basin, France: implications on the stratigraphic evolution and basin geometry. *Int. J. Earth Sci.*, 110(1), 9–33.
- Mercuzot, M., Bourquin, S., Pellenard, P., Beccaletto, L., Schnyder, J., Baudin, F., Ducassou, C., Garel, S., and Gand, G. (2022). Reconsidering Carboniferous–Permian continental palaeoenvironments in eastern equatorial Pangea: facies and sequence stratigraphy investigations in the Autun Basin (France). *Int. J. Earth Sci.*, 111, 1663–1696.
- Mercuzot, M., Thomazo, T., Schnyder, J., Pellenard, P., Baudin, F., Pierson-Wickmann, A.-C., Sans-Jofre, P., Bourquin, S., Beccaletto, L., Santoni, A.-L., Gand, G., Buisson, M., Glé, L., Munier, T., Saloume, A., Boussaid, M., and Boucher, T. (2021). Carbon and nitrogen cycle dynamic in continental late-Carboniferous to early Permian basins of eastern Pangea (northeastern Massif Central, France). *Front. Earth Sci.*, 9, 1–24.
- Michel, L. A., Tabor, N. J., Montanez, I. P., Schmitz, M. D., and Davydov, V. I. (2015). Chronostratigraphy and paleoclimatology of the lodeve basin, France; evidence for a pantropical aridification event across the Carboniferous–Permian boundary. *Palaeogeogr. Palaeoclimatol. Palaeoecol.*, 430, 118–131.
- Morel, M. L. A., Nebel, O., Nebel-Jacobsen, Y. J., Miller, J. S., and Vroon, P. Z. (2008). Hafnium isotope characterization of the GJ-1 zircon reference material by solution and laser-ablation MC-ICPMS. *Chem. Geol.*, 255, 231–235.
- Nmila, A. (1995). *L’empreinte du volcanisme dans le remplissage permien du bassin de Lodève, étude pétrographique et géochimique, implication métallogénique*. Thèse de 3ème cycle, Université Pierre et Marie Curie, France.
- Nosenzo, F., Manzotti, P., Poujol, M., Ballèvre, M., and Langlade, J. (2022). A window into an older orogenic cycle: P–T conditions and timing of the pre-Alpine history of the Dora-Maira Massif (Western Alps). *J. Metamorph. Geol.*, 40/4, 789–821.
- Odin, B. and Conrad, G. (1987). Les cinérites, marqueurs aséquentiels au sein de la sédimentation permienne, continentale et rythmique, du bassin de Lodève (Hérault, France). *Ann. Soc. Géol. Belg.*, 110, 271–278.
- Paquette, J.-L., Piro, J.-L., Devidal, J.-L., Bosse, V., Didier, A., Sanac, S., and Abdelnous, Y. (2014). Sensitivity enhancement in LA-ICP-MS by N₂ addition to carrier gas: Application to radiometric dating of U-Th-bearing minerals. *Agilent ICP-MS J.*, pages 1–5.
- Patchett, J. P., Kouvo, O., Hedge, C. E., and Tatsumoto, M. (1981). Evolution of continental crust and mantle heterogeneity: evidence from Hf isotopes. *Contrib. Mineral. Petrol.*, 78, 279–297.
- Pellenard, P., Gand, G., Schmitz, M., Galtier, J., Broutin, J., and Stéyer, J. S. (2017). High-precision U-Pb zircon ages for explosive volcanism calibrating the NW European continental Autunian strato-type. *Gondwana Res.*, 51, 118–136.
- Pereira, M. F., Castro, A., Chichorro, M., Fernández, C., Díaz-Alvarado, J., Martí, J., and Rodríguez, C. (2014). Chronological link between deep-seated processes in magma chambers and eruptions: Permo-Carboniferous magmatism in the core of Pangaea (Southern Pyrenees). *Gondwana Res.*, 25, 290–308.
- Rolando, J.-P. (1988). *Sédimentologie et stratigraphie du bassin Permien de Saint-Affrique (Aveyron)*. Thèse de 3ème cycle, Université Paul Sabatier, Toulouse. 226 pages.
- Rolando, J.-P., Doubinger, J., Bourges, P., and Legrand, X. (1988). Identification de l’Autunien supérieur, du Saxonien et du Thuringien inférieur dans le bassin de Saint-Affrique (Aveyron, France). Corrélations séquentielles et chronostratigraphiques avec les bassins de Lodève (Hérault) et de Rodez (Aveyron). *C. R. Acad. Sci. Paris*, 307, 1459–1464.
- Rosignol, C., Hallot, E., Bourquin, S., Poujol, M., Jolivet, M., Pellenard, P., and Dabard, M. P. (2019). Using volcanoclastic rocks to constrain sedimentation ages: To what extent are volcanism and sedimentation synchronous? *Sedim. Geol.*, 381, 46–64.
- Schandl, E. S. and Gorton, M. P. (2002). Application of high field strength elements to discriminate tec-

- tonic settings in VMS environments. *Econ. Geol.*, 97, 629–642.
- Schneider, J. W., Lucas, S. G., Scholze, F., Voigt, S., Marchetti, L., Klein, H., Opluštil, S., Werneburg, R., Golubev, V. K., Barrick, J. E., Nemyrovska, T., Ronchi, A., Day, M. O., Silantiev, V. V., Rößler, R., Saber, H., Linnemann, U., Zharinova, V., and Shen, S. (2020). Late Paleozoic—early Mesozoic continental biostratigraphy—links to the Standard Global Chronostratigraphic Scale. *Palaeoworld*, 29, 186–238.
- Schneider, J. W. and Scholze, F. (2018). Late Pennsylvanian–Early triassic conchostracan biostratigraphy: a preliminary approach. volume 450 of *Geol. Soc. Lond., Special Publications*, pages 365–386.
- Scotese, C. R. and Langford, R. P. (1995). Pangea and the paleogeography of the Permian. In *The Permian of Northern Pangea*, pages 3–19. Springer, Berlin.
- Segal, I., Halicz, L., and Platzner, I. T. (2003). Accurate isotope ratio measurements of ytterbium by multiple collection inductively coupled plasma mass spectrometry applying erbium and hafnium in an improved double external normalization procedure. *J. Anal. Atom. Spectr.*, 18, 1217–1223.
- Sláma, J., Košler, J., Condon, D. J., Crowley, J. L., Gerdes, A., Hanchar, J. M., Horstwood, M. S. A., Morrish, G. A., Nasdalai, L., Norberg, N., Schaltegger, U., Schoene, B., Tubrett, M. N., and Whitehouse, M. J. (2008). Plesovice zircon – A new natural reference material for U–Pb and Hf isotopic microanalysis. *Chem. Geol.*, 249(1–2), 1–35.
- Söderlund, U., Patchett, P. J., Vervoort, J. D., and Isachsen, C. (2004). The ^{176}Lu decay constant determined by Lu–Hf and U–Pb isotope systematics of Precambrian mafic intrusions. *Earth Planet. Sci. Lett.*, 219, 311–324.
- Stampfli, G. M., Hochard, C., Vérard, C., and Wilhem, C. (2013). The formation of Pangea. *Tectonophysics*, 593, 1–19.
- Stampfli, G. M. and Kozur, H. W. (2006). Europe from the Variscan to the Alpine cycles. *Mem.-Geol. Soc. Lond.*, 32, 57–82.
- Sun, S. S. and McDonough, W. F. (1989). Chemical and isotopic systematics of oceanic basalts: implications for mantle composition and processes. volume 42 of *Geol. Soc. Lond. Special Publications*, pages 313–345.
- Taylor, S. R. and McLennan, S. M. (1985). *The Continental Crust: its Composition and Evolution*. Blackwell, Oxford.
- Timmerman, M. J. (2004). Timing, geodynamic setting and character of Permo–Carboniferous magmatism in the foreland of the Variscan Orogen, NW Europe. In Wilson, M., Neumann, E.-R., Davies, G. R., Timmerman, M. J., Heeremans, M., and Larsen, B. T., editors, *Permo–Carboniferous Magmatism and Rifting in Europe*, volume 223 of *Geol. Soc. Lond., Special Publications*, pages 41–74.
- Vallé, B., Courel, L., and Gelard, J. P. (1988). Les marqueurs de la tectonique synsédimentaire et syndiagenétique dans le bassin stéphanien à régime cisailant de Blanzly-Montceau (Massif Central, France). *Bull. Soc. Géol. Fr.*, 4, 529–540.
- Van Den Driessche, J. and Brun, J. (1992). Structure and evolution of late Variscan extensional gneiss dome (Montagne Noire, southern Massif Central, France). *Geodin. Acta*, 5, 85–99.
- Van Den Driessche, J. and Brun, J. P. (1989). Un modèle cinématique de l’extension paléozoïque supérieur dans le Sud du Massif Central. *C. R. Acad. Sci. Paris*, 309, 1607–1613.
- Vermeesch, P. (2018). IsoplotR: A free and open toolbox for geochronology. *Geosci. Front.*, 9, 1479–1493.
- Vervoort, J. D., Patchett, P. J., Soderlund, U., and Baker, M. (2004). Isotopic composition of Yb and the determination of Lu concentrations and Lu/Hf by isotope dilution using MC-ICPMS. *Geochem. Geophys. Geosys.*, 5, 1–15.
- Winchester, J. A. and Floyd, P. A. (1977). Geochemical discrimination of different magma series and their differentiation products using immobile elements. *Chem. Geol.*, 20, 325–343.
- Witt, C., Rivadeneira, M., Poujol, M., Barba, D., Beida, D., Beseme, G., and Montenegro, G. (2017). Tracking ancient magmatism and Cenozoic topographic growth within the Northern Andes forearc: Constraints from detrital U–Pb zircon ages. *Geol. Soc. Am. Bull.*, 129(3–4), 415–428.
- Wood, D. A. (1980). The application of a ThHfTa diagram to problems of tectonomagmatic classification and to establishing the nature of crustal contamination of basaltic lavas of the British Tertiary Volcanic Province. *Earth Planet. Sci. Lett.*, 50, 11–30.
- Wray, D. S. (1999). Identification and long-range cor-

- relation of bentonites in Turonian-Coniacian (Upper Cretaceous) chalks of northwest Europe. *Geol. Mag.*, 136, 361–371.
- Wray, D. S. and Wood, C. J. (1998). Distinction between detrital and volcanogenic clay-rich beds in Turonian-Coniacian chalks of eastern England. *Proc. Yorkshire Geol. Soc.*, 52, 95–105.
- Zheng, J. S., Mermet, J.-F., Toutin-Morin, N., Hanes, J., Gondolo, A., Morin, R., and Féraud, G. (1992). Datation ^{40}Ar - ^{39}Ar du magmatisme et de filons minéralisés permien en Provence orientale (France). *Geodin. Acta*, 5(3), 203–215.



Research article

Tribute to Jean Dercourt

The Brécy depocenter as part of a new northern Massif Central Carboniferous–Permian Basin (France)

Laurent Beccaletto ^{Ⓜ,*,a} and Sylvie Bourquin ^{Ⓜ,b}

^a BRGM, 45060 Orléans, France

^b Univ Rennes, CNRS, Géosciences Rennes - UMR 6118, 35000 Rennes, France

E-mails: l.beccaletto@brgm.fr (L. Beccaletto), sylvie.bourquin@univ-rennes1.fr (S. Bourquin)

Abstract. The reinterpretation of deep wells and the reprocessing and interpretation of 115 km of industrial seismic lines can be used to update the geometry, depositional environments and tectonic evolution of the Carboniferous–Permian Brécy depocenter (southwest Paris Basin). The present-day geometry of the Brécy depocenter is controlled by several eastward dipping normal faults, some of which possibly connected to deep detachments that were active during the late Carboniferous–Permian history. It is estimated that the maximum thickness of the Brécy depocenter is 3900 m. The filling provides evidence for a thick late Carboniferous–lower Permian syn-rift stage overlain by a thin post-rift stage, probably similar to the tectonic evolution of the northeastward basins in the Lorraine region of France and Germany and thus attributed to the lower-middle Permian. The facies generally characterize lake environments, with occurrences of sediment supply attributed to fluvial, alluvial fan and delta fan deposits. They mainly display a retrogradational–progradational pattern during the syn-rift stage, and a retrogradational pattern during the post-rift stage. The Brécy area was part of a larger late Variscan basin during the latest Carboniferous–early Permian times in the northern Massif Central region.

Keywords. Late Carboniferous, Permian, Paris Basin, Deep well, Seismic interpretation, Regional correlation.

Manuscript received 25 August 2023, revised and accepted 21 November 2023.

1. Introduction

The late Carboniferous–Permian is a period of large-scale geodynamic reorganization, (i) with the final accretion of Pangea (Variscides/Mauretanicides/Alleghenides orogeneses) and the beginning of its breakup (NeoTethys opening) [e.g., Domeier and Torsvik, 2014, Scotese and Langford, 1995, Stampfli et al., 2013], coeval with (ii) the acme of the Late Paleozoic Ice Age (LPIA), constituting a turning point in

the climate regimes of the Paleozoic [e.g., Gastaldo et al., 1996, Montañez et al., 2007].

From the end of the Carboniferous onwards, the over-thickened and hot Variscan crust collapsed [late-orogenic collapse; Burg et al., 1994, Faure, 1995, Malavieille et al., 1990, Ménard and Molnar, 1988, Van Den Driessche and Brun, 1992], triggering the rise of high-grade metamorphic domes along low-angle detachment faults, and the development of half-graben or pull-apart multi-directional intramountain coal basins [Costa and Rey, 1995, Gardien et al., 2022, Malavieille, 1993, McCann et al.,

* Corresponding author.

2008a,b, Ménard and Molnar, 1988, Van Den Driessche and Brun, 1989].

These late orogenic Carboniferous–Permian basins (hereafter LOCPB) therefore widely developed around 300 Ma in the internal parts of the belt south of the northern Variscan Front. They crop out in several limited locations in and around the Variscan basement of western Europe (Pyrenees, Massif Central, Brittany, Vosges–Black Forest, Alps, Harz), in close genetic relationships with major Variscan tectonic structures (e.g., Sillon Houiller, South-Hunsrück Fault; Figure 1 and related references).

They were filled with siliciclastic volcanoclastic continental material—from alluvial to lacustrine through fluvial environments—at intertropical latitudes [Donsimoni, 1990, Gand, 2003, Mercuzot et al., 2021, 2022, Schäfer, 2011, Schneider and Romer, 2010, Soreghan et al., 2020]. LOCPB were also accompanied by widespread intrusive and extrusive magmatic activity with a crustal or mantle origin with mostly felsic and rare mafic signatures [Neumann et al., 2004, Timmerman, 2004, McCann et al., 2006]. Apart from scientific research, LOCPB were extensively studied for their resources such as oil, gas, coal, uranium or other ore deposits [Bouchot et al., 1997, 2005, Courel et al., 1986, Delmas et al., 2002, Dill et al., 1991, Mascle, 1990], and more recently for geothermal [Aretz et al., 2016] or natural helium [Hauville et al., 2021] purposes.

In map view, they occur as small isolated and disconnected “basins” with incomplete sedimentary successions and numerous sedimentation and erosional gaps [e.g., Schneider et al., 2020]. Their present-day area does not reflect their initial extent and thickness, which can be explored by studying their subsurface prolongation beneath the Meso-Cenozoic sedimentary covers [Beccaletto et al., 2015, Mercuzot et al., 2021, Schneider and Scholze, 2018, Ziegler, 1990]. These basins usually reach thicknesses of several kilometers like, for instance, in the southern French Massif Central [e.g., Lodève, Carmaux—La Grésine; BRGM, 1989] or central Europe [e.g., Saar-Nahe and Thuringian Forest basins; Schneider and Romer, 2010]. Generally speaking, the ages of the LOCPB broadly range from Gzhelian to Guadalupian encompassing the Stephanian, Autunian, lower Rotliegend and part of the upper Rotliegend western European stages [ca. 303 Ma to ca. 270 Ma; e.g., Ducassou et al., 2019, Michel et al., 2015, Lützner

et al., 2020, Opluštil et al., 2016, Pellenard et al., 2017, Poujol et al., 2023, Voigt et al., 2022].

One recurrent question that arises from the study of the LOCPB is based on sedimentological, structural and temporal criteria: what are their regional correlations and extents? The answer to this question calls for the recognition of reference basins with enough useful data to make correlations. On one hand, recent advances in their age calibration using radiochronological methods have led to improved inter-basin comparisons [e.g., Ducassou et al., 2019, Mercuzot et al., 2023, Opluštil et al., 2016, Pellenard et al., 2017, Schneider et al., 2020, Voigt et al., 2022]. On the other hand, fewer significant works have been carried out recently on their structural pattern and tectonic evolution [Beccaletto et al., 2015, and references therein], and therefore the poor understanding of their tectonic framework limits their comparison at local or regional scales.

One good way to discuss the tectono-sedimentary history of hidden subsurface LOCPB is to use seismic data to look for them under their Meso-Cenozoic sedimentary cover given that they may be considered as fossil basins with preserved pre-Triassic depositional and structural patterns. We present new results from the interpretation of industrial seismic lines spanning 115 kilometers, while targeting the Brécyc depocenter in the southwest Paris Basin, which has recently been reprocessed within the framework of an International Continental Scientific Drilling Program proposal [ICDP Deepdust project; Soreghan et al., 2020]. First, we aim to discuss the structural features, thickness and tectonic evolution of the Brécyc depocenter and the related sedimentary filling using seismic and well data. Last, we compare and propose correlations between the Brécyc depocenter and other Carboniferous–Permian deposits in the northern Massif Central, as well as other places in France and Germany.

2. Geological setting of the Brécyc depocenter

The Brécyc depocenter is one of the three several-kilometer-thick depocenters recently revealed by the interpretation of reprocessed vintage seismic lines in the southwestern part of the Paris Basin [together with the Contres and Arpheuilles depocenters; Figures 1, 2; Beccaletto et al., 2015]. It has a roughly

elongated shape striking N30 parallel to the northern trend of the Sillon-Houiller fault zone. The opening of the basin was thought to be controlled by the activity of several N030-trending normal faults accommodating the deposition of the Stephanian-Permian deposits which have estimated thicknesses up to 3000 m.

The age of the Carboniferous–Permian series in the Brécy area comes from the description of the Bertray-1, Brécy-1 and Saint-Georges-sur-Moulon-1 well cuttings (from drilling reports; hereafter called the BTY1, BRC1 and SGS1 wells, respectively; Figure 2), and from palynological data from the core of the scientific Couy-1 well [Orszag-Sperber et al., 1992; hereafter COU1; Figure 2].

In the COU1 well, the sedimentary succession, attributed to the Permian based on the presence of several Darwinulacea ostracods [Orszag-Sperber et al., 1992], is composed of approximately 250 m of mainly red silty-clay sediments with sandstones and few conglomerates at the base. This succession describes a general trend from alluvial fan to shallow lake deposits; neither tonstein (volcanic ashes transformed into clay minerals) nor palynological data exist to shorten the age range [Juncal et al., 2018]. In this area, the Permian deposits end with the Triassic unconformity, overlain by middle Anisian deposits [Early and early-Middle Triassic gap; Bourquin et al., 2006, Juncal et al., 2018].

In BTY1, from 2963 m to 2842 m, the sedimentary succession is mainly composed of black-gray silty-clay interbedded with detrital coal, sandstones and conglomerates. The age is attributed to the late Carboniferous based on: gastropods and ostracods from the *Carbonita* genus found in the calcareous level at the base, bisaccate pollens at 2963 m and the presence of *Lycospora pellucida* and *Florinites junior* pollen at 2850 m [Bertray1, 1987].

In BRC1, below 1806 m, the facies are more carbonated with argillaceous-dolomitic limestones interbedded in fine-grained gray-green argillaceous sandstones. Between 1802 m and 1806 m, plant fragments suggesting a Carboniferous age [Brécy1, 1966] have been found in micaceous silty-claystone.

The drilling of the SGS1 well has reached a Paleozoic succession from 1639 to 1878.3 m attributed to the Cambro-Silurian by comparison with known facies in outcrops in the Massif Central [St. Georges-

sur-Moulon1, 1964].

In COU1, the basement, composed of metamorphic rocks, starts at a depth of 941.65 m. It is overlain by a highly tectonized Paleozoic sedimentary series [Lorenz et al., 1987] until 925.35 m. The Paleozoic upper part is composed of volcanoclastic deposits attributed to the Stephanian [Chantraine et al., 1992]; trachy-andesites sampled at the bottom of the Stephanian unit (925.35 m and 941.65 m) yielded an Ar–Ar plateau age of 301.6 ± 6.3 Ma [Costa and Maluski, 1988]. The Stephanian volcanoclastic unit is overlain by Permian fluvio-lacustrine deposits above an angular unconformity [Lorenz et al., 1987].

3. Material and methods

3.1. Seismic data reprocessing

The present study is based on the reprocessing of five seismic lines representing approximately 115 km, acquired by the ESSOREP oil company in 1984 and 1985 (CHER survey, denoted as CH; Figure 2). This new dataset completes the ca. 200 km of vintage industrial seismic reflection profiles that were reprocessed and interpreted in the Brécy area in the initial study of Beccaletto et al. [2015].

Given the acquisition parameters used in these exploration surveys, mainly the frequency bandwidth of the seismic source and the recording length (up to 4 s TWT—Two-Way-Time), the estimated depth of investigation is roughly 7–8 km, with a vertical resolution of approximately 25 m and 30–35 m respectively in the shallow and deepest part of the lines. These vintage seismic data have been reprocessed using modern Pre-Stack time migration (PSTM) methods and algorithms, thereby significantly improving the quality of the resulting seismic section and providing enhanced descriptions of the geological structures [Beccaletto et al., 2011, 2015]. Efforts were focused on three key steps that were repeated several times throughout the processing unit: (a) computing primary and residual static corrections in order to remove the topographic and velocity effects of the superficial rock layer, strongly affecting the seismic signal; (b) detailed velocity analysis; and (c) various methods of organized and random noise attenuation. Pre-stack time migration enhanced the details of the structural features and completed this reprocessing unit before stacking the data [cf. Laurent

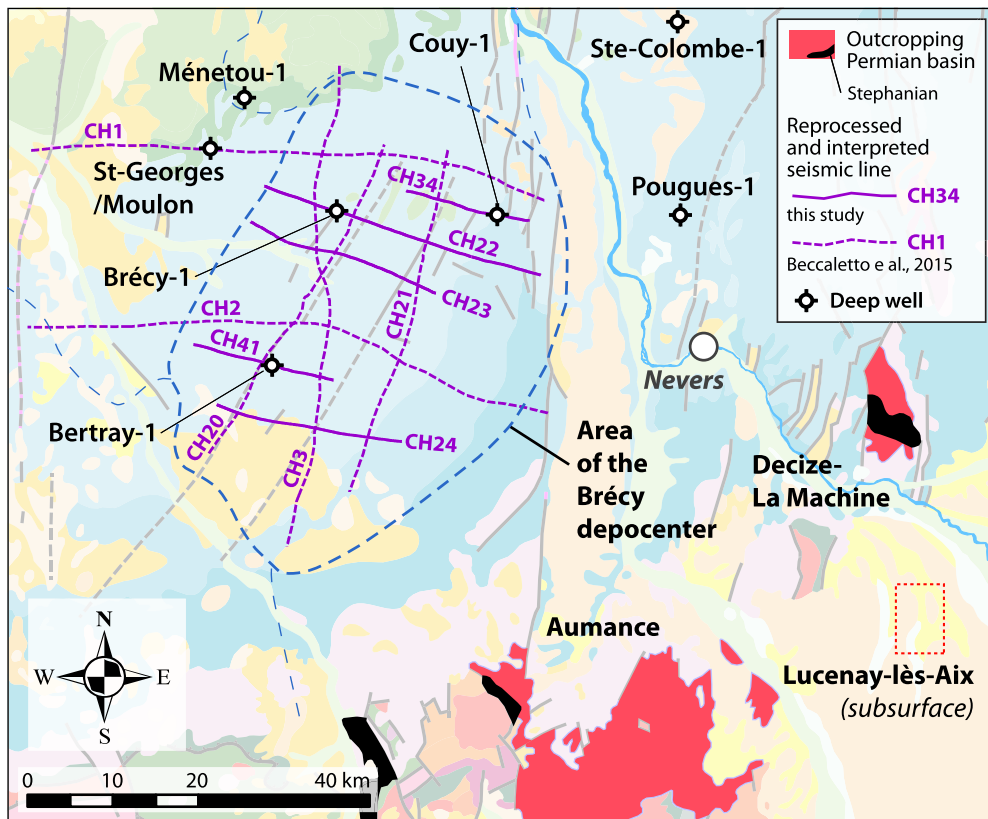


Figure 2. Geological map of the study area depicting the Brécly depocenter and adjacent LOCPB, the location of the reprocessed seismic lines, and deep wells. The geological background is from the 1:1,000,000 geological map of France [BRGM, 2003].

et al., 2021 for another example of seismic reprocessing and interpretation in Carboniferous basins].

3.2. Seismic interpretation and well-data

In a first step, the seismic facies and reflector geometries were interpreted by using nearby wells to calibrate and tie the seismic lines for the main horizons. Unlike the previous regional study of Beccaletto et al. [2015], the BTY1, BRC1 and COU1 wells are located directly on some of the newly reprocessed seismic lines (resp. CH41, CH22 and CH34; Figure 2), thereby preventing any lateral projection bias. Once the targeted horizons were identified near the BTY1 and BRC1 wells (deepest wells), they were correlated step by step, from line to line, by comparing the seismic facies using the Gverse Geophysics module of the Gverse suite (© Landmark), and by

checking their 3D structural consistency (using the 3D viewer of the interpretation software). Steps two and three correspond to the building of the structural scheme and the thickness map of the Brécly depocenter, respectively. In a fourth step, the electrofacies and depositional environments are described within the framework of the seismic interpretation by using subsurface well data such as: (i) the description of the cuttings from reports and well data (gamma Ray (GR), sonic or neutron, and resistivity) for the BRC1, BTY1, and SGS1 wells; and (ii) core description and complete well log data (GR, sonic, resistivity, density, photo electric factor (Pef), and neutron) for the COU1 well [Juncal et al., 2018]. In a last step, these four wells were correlated to give a lithostratigraphic and sequential framework to the Brécly area.

4. Results

4.1. Seismic interpretation, targeted horizons and seismic facies

Figures 3 and 4 display four examples of investigated seismic profiles in an uninterpreted and interpreted form. The main seismic features and units are discussed below from bottom to top.

The base of the late Carboniferous–Permian sedimentary fill (Base Basin Unconformity—BBU) corresponds to the top of the pre-Stephanian substratum. The four wells in the Brécý area do not reach the substratum, however it is cut across by fifteen wells in the westward Contres and Arpheuilles depocenters. There, the substratum could be sedimentary, metamorphic or plutonic [Beccaletto et al., 2015]. In most places, the top of the pre-Stephanian substratum matches the top of the acoustic basement, where the seismic signal becomes chaotic. However, some sets of reflectors, belonging to pre-Stephanian units, still appear locally below the BBU (line CH3, Figure 4).

The end-Carboniferous–Permian deposits s.s. correspond to the seismic facies observed between the Top Paleozoic Unit (TPU) and the BBU. In general, they are stratified with an overall wedge-shape geometry slightly thinning eastward, and continuous reflectors varying from low to high amplitudes and medium to high frequencies; chaotic or semi-transparent facies are also possible. The topmost preserved Permian beds display toplap geometries below the TPU (Figures 3 and 4). However, in closer detail, it is possible to distinguish three seismic sequences:

- (1) A *lower seismic sequence* with thicknesses less than 0.5 s TWT made of low-frequency/(very) high-amplitude, continuous to discontinuous reflectors; in the BTY1 well, these reflectors are correlated with Stephanian conglomeratic and coal beds, as seen in the Arpheuilles-1 well [Beccaletto et al., 2015];
- (2) a much thicker *intermediate seismic sequence* (up to 2 s TWT) with lateral thickness variations in units A, B and C; in particular, note the thickening of unit A toward the center of the basin. These three units were deposited during normal fault activity and, as a whole,

represent the syn-rift stage of the Brécý depocenter (cf. Section 5.1);

- (3) a thinner *upper seismic sequence*, (less than 0.25 s TWT), made up of unit D, located just below the TPU; this unit does not display any thickness variations related to fault activity. The seismic facies are more transparent here than in the lower and intermediate units, certainly due to less contrasting lithologies (cf. Section 4.1). The horizons of the *intermediate seismic sequence* display a toplap geometry beneath the base of the *upper seismic sequence*, indicating an erosional phase in between. This *upper seismic sequence* represents the post-rift stage of the Brécý depocenter (cf. Section 5.1).

The Mesozoic sedimentary cover of the Paris Basin unconformably overlies the Permian Brécý deposits and consists of parallel to sub-parallel continuous reflectors with medium- to high-frequencies and alternating medium- to high-amplitudes related to lithological variations within the Triassic and Jurassic deposits. The reflectors gently dip northward towards the center of the Paris Basin.

4.2. Fault patterns and structural schemes

All seismic lines display normal faults, which are the norm in the Brécý depocenter; the vast majority of the faults developed during the Meso-Cenozoic, as suggested by the equal down-throw all along the fault plane both across the Carboniferous–Permian and Mesozoic strata (blue arrows in Figures 3 and 4). Some faults characterized by different thicknesses of Carboniferous–Permian deposits on both sides are expected to have controlled the late Carboniferous–Permian filling. The seismic lines do not clearly image the prolongation of these normal faults through the base of the basin downward to the acoustic basement (Figures 3, 4). Deeply seated reflectors located in the prolongation of eastward dipping normal faults may correspond to low angle normal faults (detachments; Figures 3, 4; cf. Section 5.1). These initial Carboniferous–Permian faults also display Meso-Cenozoic activity, as shown by the down-throw of the TPU and overlying Mesozoic strata (black arrows in Figures 3, 4).

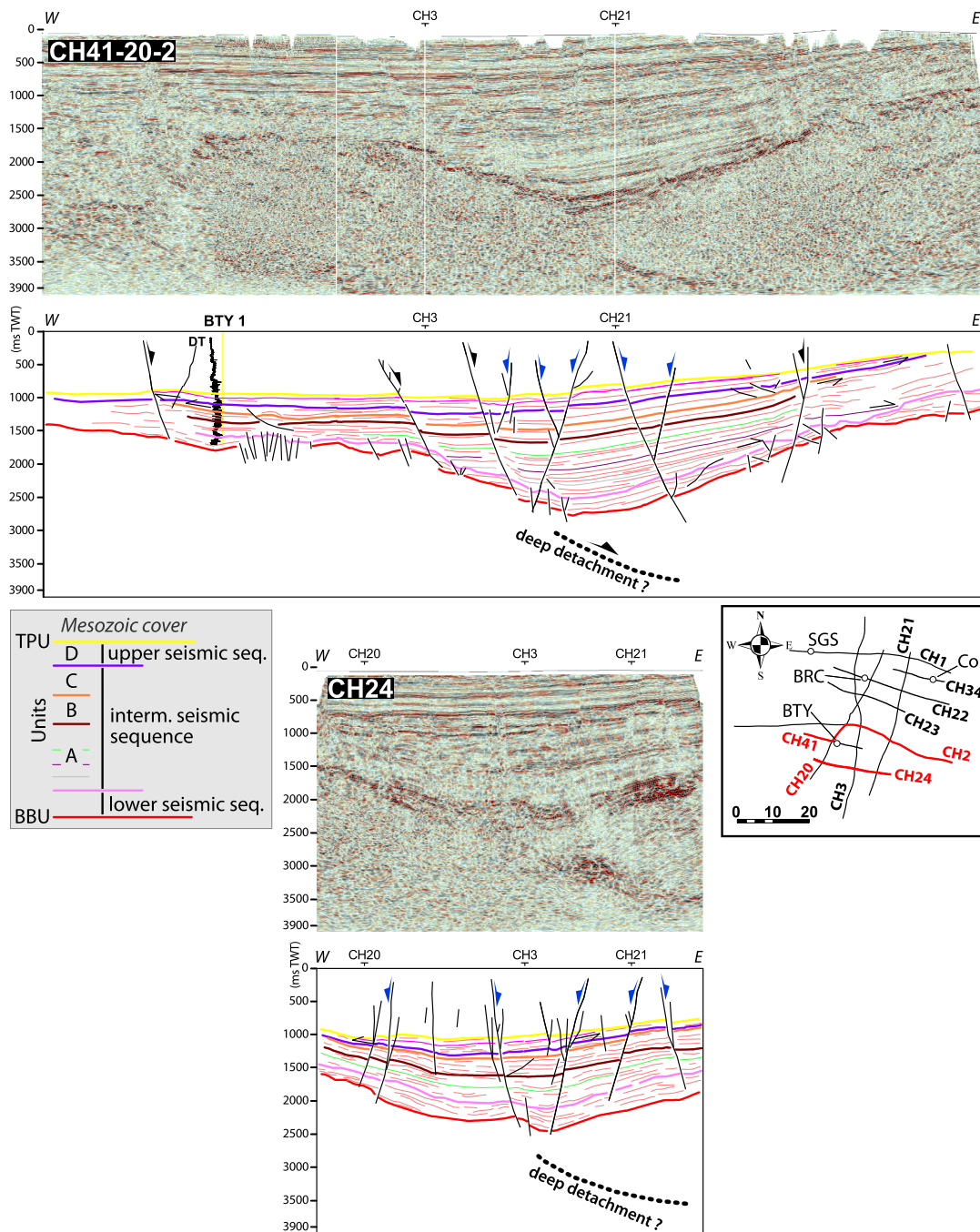


Figure 3. W-E composite line CH41-20-2 and line CH24, interpreted and uninterpreted, depicting the main structural features of the Brécý depocenter; blue arrows: Meso-Cenozoic faults, black arrows Carboniferous–Permian and Meso-Cenozoic faults; see text for details.

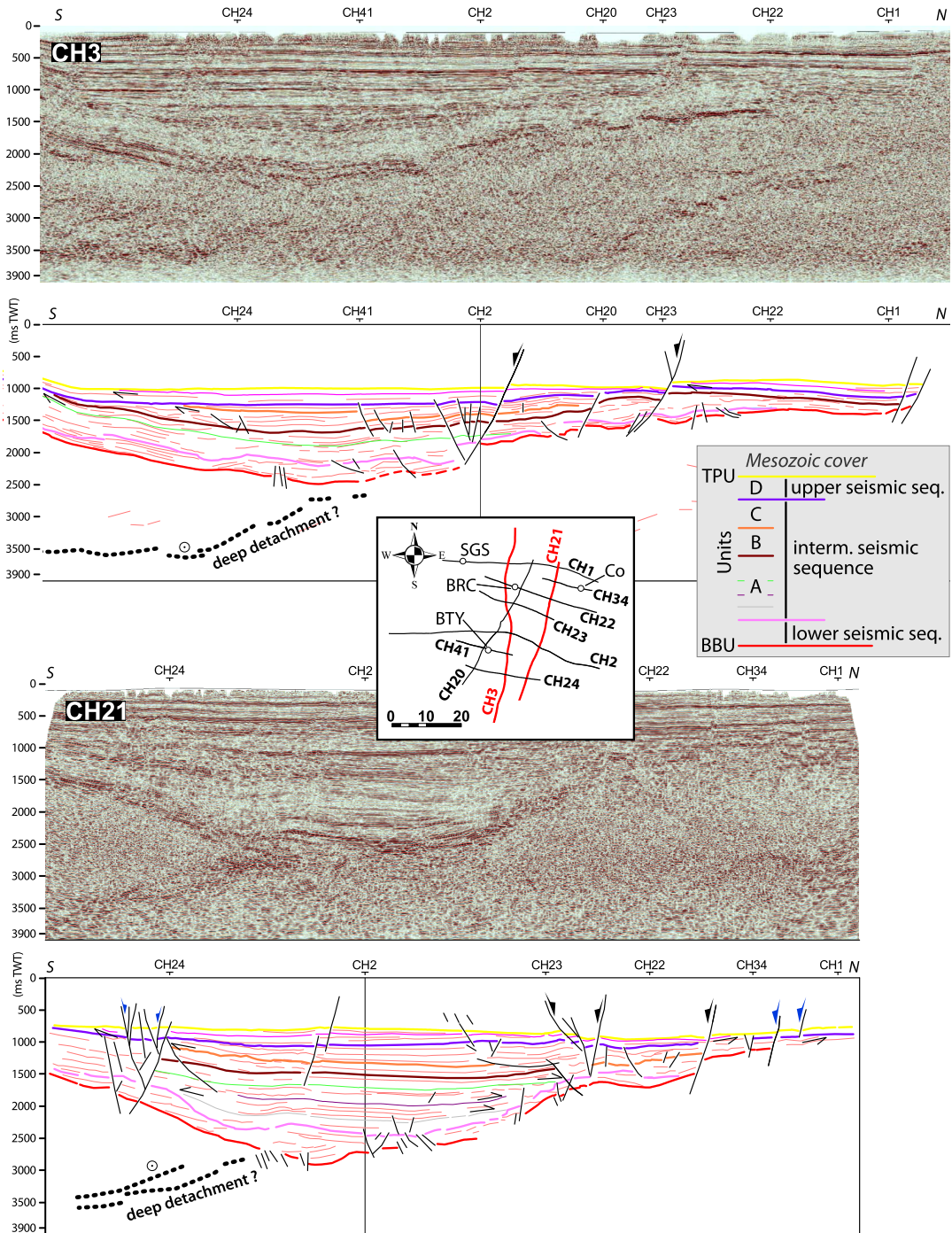


Figure 4. N-S line CH3 and line CH21, interpreted and uninterpreted, depicting the main structural features of the Brécy depocentre; blue arrows: Meso-Cenozoic faults, black arrows Carboniferous-Permian and Meso-Cenozoic faults; see text for details.

The reprocessing and interpretation of the additional seismic lines make it possible to build a detailed structural scheme for the Brécý depocenter, greatly improving the spatial resolution of the structural pattern drawn by Beccaletto et al. [2015]. The present study leads to the recognition of seven “major” faults (i.e., with a large cartographic extent and usually cutting through several seismic lines), and eleven secondary faults (i.e., cutting through one or two seismic lines to a lower extent; Figure 5). Most of these faults display an eastward dip, and only the antithetic fault has a westward dip. Their orientation varies between 20 and 40°N with an average value of approximately 30°N. As mentioned above, the structural pattern is actually a Meso-Cenozoic scheme, as all the faults—including those active during the Carboniferous–Permian—were active during the Mesozoic. We do not exclude the occurrence of smaller scale transverse faults (e.g., with N80 to N180 trends), but the numerous N30-trending faults may mask them and/or the density of the seismic dataset does not allow to discern them.

4.3. Thickness maps of the Brécý depocenter

The new seismic dataset is used to accurately estimate the thickness of the Brécý depocenter (Figure 6). Thickness maps in TWT (then in meters) of the Brécý depocenter have been computed based on the interpreted horizons according to the following four steps methodology, by using the Gverse GeoAtlas module of the Gverse suite (© Landmark):

- Computation of grids in TWT for both the TPU and BBU horizons (these grids were calculated by interpolating the corresponding seismic horizons and faults).
- Computation of a thickness map in TWT of the Carboniferous–Permian sedimentary succession by subtracting the two previous grids.
- Calculation of an average interval velocity for the Carboniferous–Permian deposits from the BTY1, SGS1 and COU1 wells, all of which have identified Permian deposits. The velocity for each well is calculated from the thickness of the Permian in meters and in TWT from the seismic data, giving a value of 3778 m/s. We apply this “Permian” velocity to the whole filling, including (i) the intermediate

seismic sequence not fully reached by the three reference wells, because the seismic facies are similar suggesting similar lithologies, and (ii) the basal low-frequency/high-amplitude facies, because (a) they represent much lower thicknesses than the Permian deposits and are sometimes even missing, and (b) this velocity is very close to the one estimated in the Arpheuilles well [3615 m/s, Beccaletto et al., 2015; location in Figure 1].

- Computation of a thickness grid in meters by multiplying the thickness grid in TWT by the constant velocity of 3778 m/s.

As the thickness map is based only on the seismic data (there are no close outcropping geological contours to be used as hanging points), the map is hypothetical outside the zones where subsurface data are present. The resulting map displays the Brécý depocenter and its surroundings with an unprecedented resolution. The maximum thickness of the Carboniferous–Permian deposits reaches ca. 3900 m along the CH21 seismic line just south of the CH2 line; it is ca. 900 m thicker than originally expected [Beccaletto et al., 2015] due to a larger velocity value and better interpolation controls (because of the availability of more seismic lines). The minimum thicknesses—about 0 m—are located northeast of the main depocenter.

At the main depocenter, the maximum thicknesses of the *lower*, *intermediate* and *upper seismic sequences* are roughly 900 m, 2500 m, and 500 m respectively. The maximum thicknesses of the syn-rift deposits (*lower* and *intermediate seismic sequences*, A, B and C units) and post-rift deposits (*upper seismic sequence*, D unit) are ca. 3400 m and 500, respectively. In more detail, the maximum thicknesses of the A, B, C and D units are approximately 1600 m, 400 m, 500 m and 500 m, respectively.

The main depocenter has an elongated shape trending N60, which is slightly different to the average N30 trend of the scarce Carboniferous–Permian faults; in greater detail, it appears that the successive depocenters represented by the contour lines 3300 m, 3000 m, 2700 m and 2400 m display a clockwise rotation of their longest axis (inset in Figure 6). This could be the result of a dextral strike-slip component during the activity of the normal faults and the opening of the Brécý depocenter, either related or not to the activity of roughly W–E

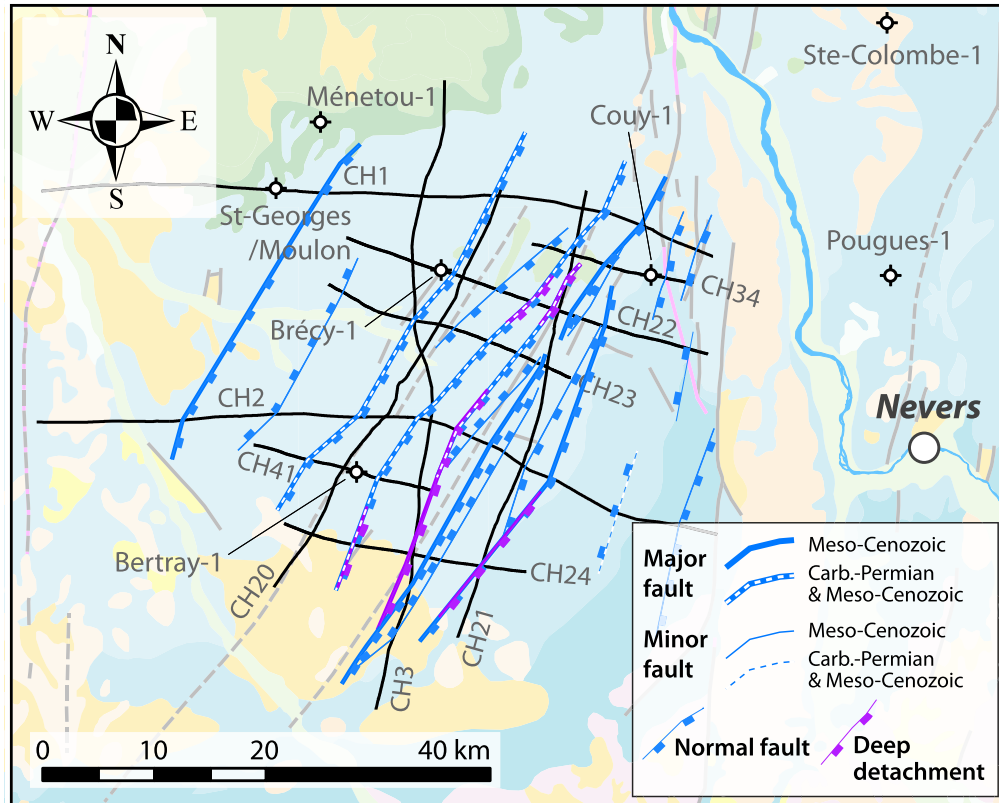


Figure 5. Structural scheme of the Brécly depocenter, depicting the major/minor faults, those with a Meso-Cenozoic tectonic activity or a Permo-Carboniferous and Meso-Cenozoic tectonic activity, and deep detachments; the geological background is from the 1:1,000,000 geological map of France [BRGM, 2003].

oriented normal faults (not depicted on the seismic lines as mentioned previously). Broadly speaking, the area displays a roughly SW-NE and then a W-E “thick” axis, located south of a roughly W-E oriented “thin” axis. These features suggest the combination of two deformational trends—N30 vs. W-E—the N30 trend is the only one expressed by normal faults. One hypothesis for this could be that the W-E trend is evidence of similar deeper trends that have already been identified in the basement [Baptiste et al., 2016].

4.4. Depositional environment of the four reference wells

4.4.1. Electrofacies description

The lithological evolution can be defined from each studied well using well-log data and the description of the cuttings.

Based on biostratigraphy data [Bertray1, 1987], the boundary between the Carboniferous and Permian is located at 2842 m. The lower Permian sedimentary succession is characterized by the Autunian facies [Bertray1, 1987], which is composed of, from base to top (Figure 7):

- from 2842 to 2260 m, by conglomerates (only until 2778 m) and coarse-grained sandstones characterized by low to medium GR (15 to 80 API) and Sonic (50 to 70 $\mu\text{s}/\text{ft}$) values, thereby evidencing low-porosity facies, alternating with clayey sandstones with GR from 80 to 120 API and Sonic below 60 $\mu\text{s}/\text{ft}$, and brown silty-clay facies characterized by GR from 120 to 200 API and Sonic from 55 to 110 $\mu\text{s}/\text{ft}$;
- from 2260 to 1881 m, by brick-red micaceous silty-clay with traces of anhydrite and dolomite, (GR from 120 to 140 API and Sonic

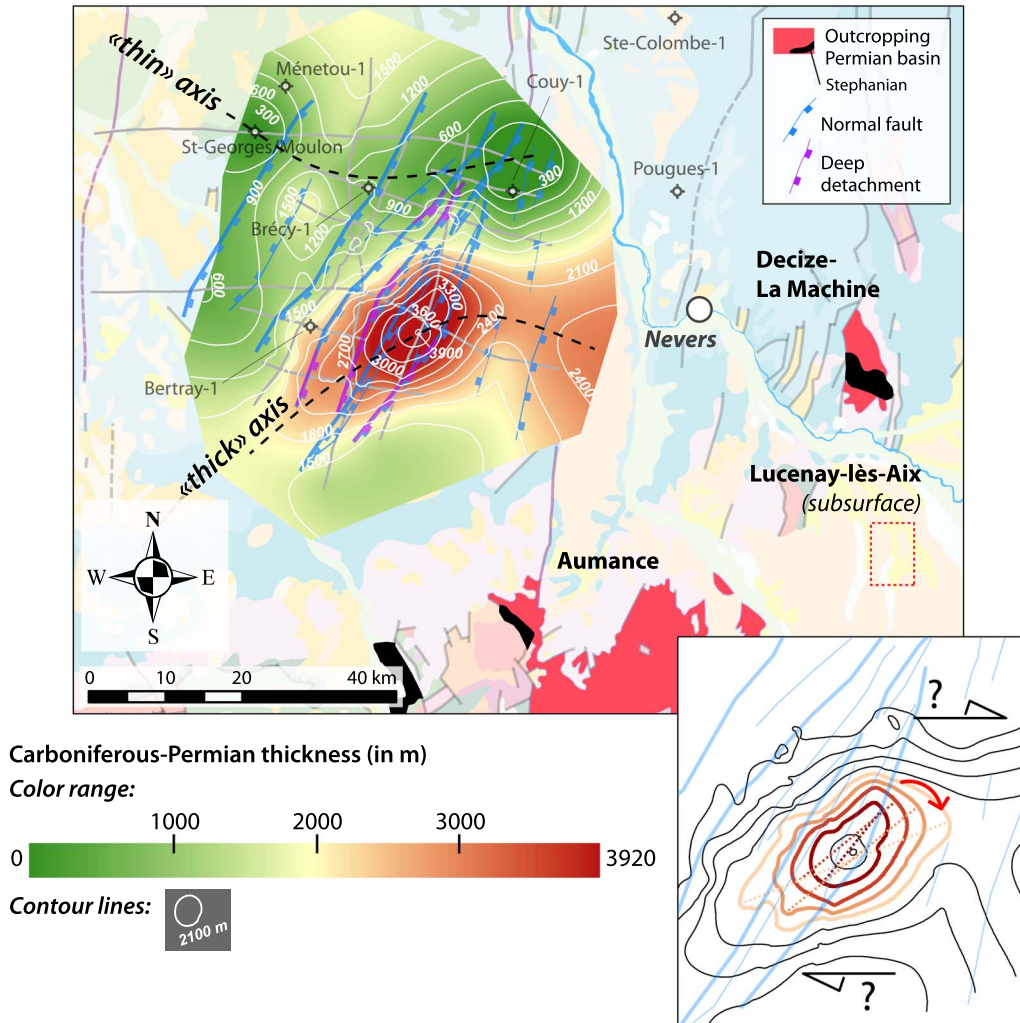


Figure 6. Thickness map (color range and contour lines) of the Brécly depocenter overlain by the structural map; the geological background is from the 1:1,000,000 geological map of France [BRGM, 2003]. Inset: clockwise rotation of the depocenters.

from 55 to 70 $\mu\text{s}/\text{ft}$), alternating with fine- to very fine-grained clayey micaceous sandstones (GR from 90 to 120 API and Sonic from 50 to 60 $\mu\text{s}/\text{ft}$), and white quartzite sandstones (GR from 45–90 API and Sonic from 40–50 $\mu\text{s}/\text{ft}$).

The upper part of the BTY1 well is composed of two distinct facies from base to top, the name of these formations is found in Bertrayl [1987]:

- the Upper Permian Sandstones Formation, from 1881 m to 1652 m, is characterized by

pink fine- to coarse-grained unconsolidated well-rounded sandstones (GR from 45–75 API and Sonic from 55–65 $\mu\text{s}/\text{ft}$), with few beds of conglomerates described from cuttings around 1800 m, and alternating with brick-red clay (GR from 90 to 130 API and Sonic from 75–90 $\mu\text{s}/\text{ft}$) or micaceous silty-clay (GR from 75 to 150 API and Sonic from 60 to 75 $\mu\text{s}/\text{ft}$);

- the Upper Clay Formation, from 1652 to 1314 m, is composed of brick-red micaceous silty-clay with few beds of green clay in its upper

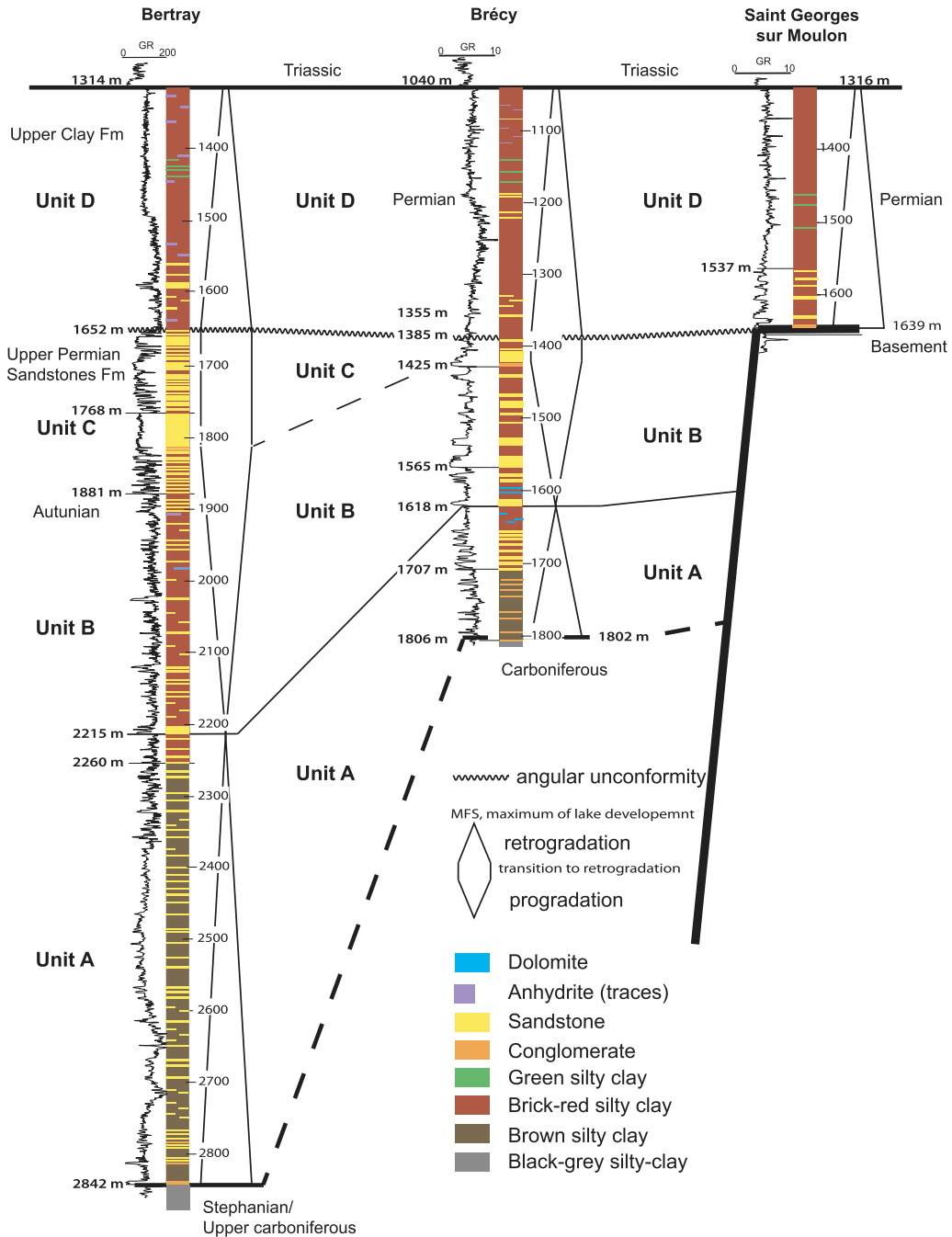


Figure 7. Correlations between the BTY1, BCY1 and SGS1 wells based on stratigraphic cycles.

part (GR from 90 to 150 API and Sonic from 40–80 $\mu\text{s}/\text{ft}$), and traces of anhydrite; this formation is sandier at the base.

The BRC1 well, drilled in [1966], is older than the BTY1 well [1987] and therefore has only GR in c/s, Neutron (c/s) and resistivity well-logs, and thus can

only be used to provide a qualitative comparison of the GR signal with the other wells (Figure 7). In Brécy1 [1966], the Carboniferous is reached below 1802 m, and the sedimentary succession up to 1707 m has been considered as transitional facies from the Carboniferous to Permian based on conglomerates interbedded within brown-red micaceous silty-clay. Based on a previous seismic interpretation (cf. chapter 4.1) and well-log data, these facies are considered as Permian. Above 1707 m, BCY1 is considered as undifferentiated Permian Brécy1 [1966] and has the following composition, from base to top:

- from 1707 m to 1565 m: coarse-grained sandstones to conglomerates interbedded with brown-red micaceous clay with carbonaceous clay around 1676 m, clayey sandstones and dolomitic nodules (highest resistivity and lower GR values between 1580 and 1651 m);
- from 1565 m to 1425 m, the sandstones, with sometime dolomitic cement, are interbedded in micaceous brick-red silty-clay;
- from 1425 m to 1355 m, the sandstones, interbedded with brick-red micaceous silty-clay, are pink, sometimes clayey, with a thin conglomeratic bed at the base of the sandstone level (lowest GR value and highest resistivity);
- from 1355 m to 1040 m, the succession is composed of brick-red micaceous silty-clay, sometimes green and interbedded with a rare and thin bed of fine-grained clayey sandstones (lowest GR value and highest resistivity) or traces of anhydrite and gypsum [Brécy1, 1966].

The SGS1, dated 1964, has only GR (c/s) and resistivity, and is considered as an undifferentiated Permian succession [St. Georges-sur-Moulon1, 1964] that is characterized from the base to top by (Figure 7):

- from 1639 m to 1537 m, conglomerates and fine- to medium-grained micaceous white to pink sandstones, sometimes dolomitic, interbedded with brick-red-brown micaceous and dolomitic silty-clay;
- from 1537 m to 1316 m, brick-red micaceous silty-clay with sometimes green

clay, rare sandstone levels and traces of anhydrite.

4.4.2. Interpretation of depositional environment

An interpretation of the depositional environment evolution can be proposed by performing a comparison with adjacent areas. The wells with thicker and deeper deposits, i.e., BTY1 and BCY1, display different facies at the base of the succession with coarse-grained and conglomerate facies interbedded with brown silty clay facies, with scarce carbonaceous clays. These facies could attest to a sediment supply attributed to an alluvial fan or delta fan within deeper lake deposits as described southward in the Lucenay-lès-Aix area [Ducassou et al., 2019, Mercuzot et al., 2021].

Compared with the core description of COUY1 [Juncal et al., 2018], the mainly red silty-clay facies observed in the upper part of these wells (unit D, Figure 8), with some dolomitic beds, can be considered as a shallow lake. The sandstone and very few conglomerates, attesting to a sediment supply from a continental area, are attributed to an alluvial fan sediment supply within the lake [Juncal et al., 2018], the sediment supply is higher in COUY1 than in the three other wells (Figures 7, 8). This upper part of the sedimentary succession shows traces of anhydrite and gypsum from the description of the cuttings that could reflect an environment with more evaporation. However, given that only traces were observed and that no anhydrite has been observed in the shallow lake deposits of the COUY1 well [Juncal et al., 2018], we cannot exclude that these evaporites originate from the aforementioned Triassic deposits. Furthermore, the presence of paleosol developments may be indicated by dolomitic nodules and green clay facies, which could characterize either dolocretes or hydro-morphic paleosols [Retallack, 1988, Tabor and Montañez, 2004], such as those observed in the COUY1 well [Juncal et al., 2018].

The depositional environment of unit B (Figures 7, 8), compared with the lithology defined in units A and D, could be considered as fluvial or an alluvial fan in a lake environment, but with predominantly coarse-grained sediment from the continental area. The unconsolidated well-rounded pink sandstones described only at BTY1 (unit C) could be attributed to aeolian deposits, but due to the lack of core data, this is difficult to confirm.

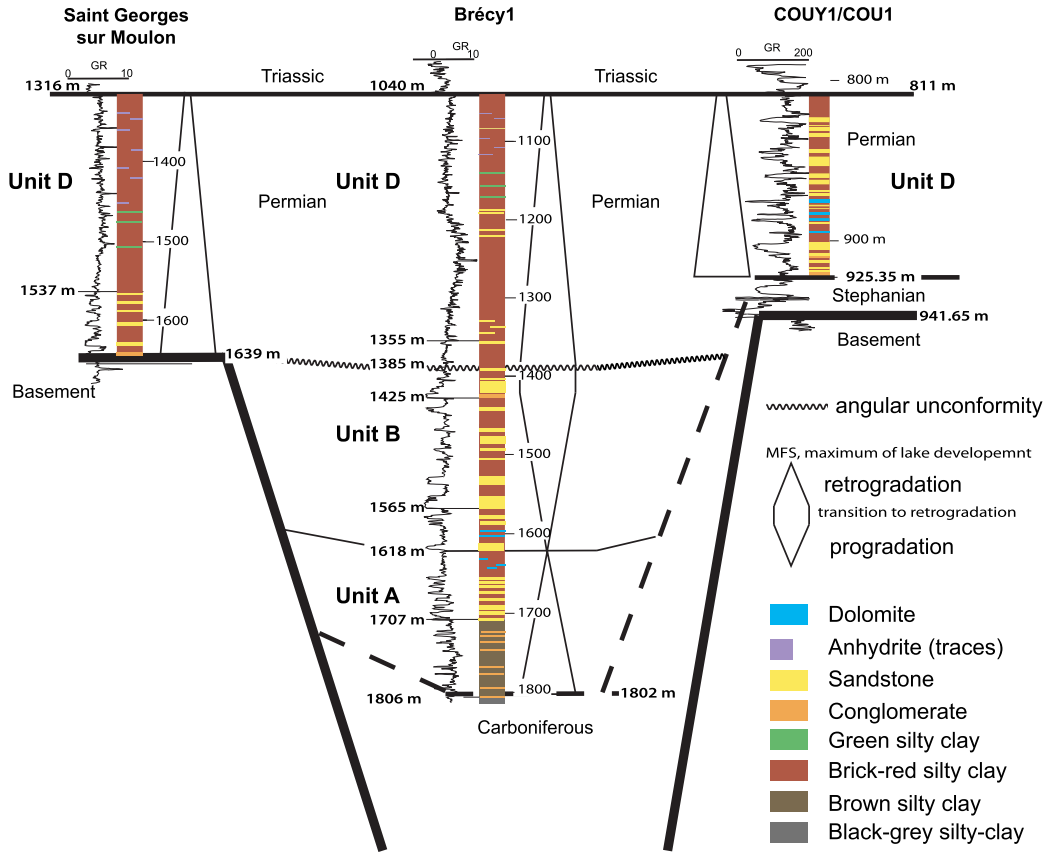


Figure 8. Correlations between the SGS1, BCY1 and COUY1 wells based on stratigraphic cycles.

4.5. *Sequence stratigraphy correlations*

The correlations have been cross-checked with the seismic lines to maintain coherency between the well and seismic interpretations. We propose correlations between the four wells based on the electrofacies description and the vertical evolution of the depositional environment (Figures 7, 8). The most complete Permian sedimentary succession is observed in the BTY1 well. From 2842 m to around 2215 m, the vertical evolution from a predominance of conglomerates and sandstones to a predominance of silty-clay corresponds to unit A on the seismic lines (Figures 3, 4) and attests to a general trend towards an open lake (Figure 7). The sandstones and conglomerates can be attributed to alluvial or delta fan deposits in comparison with adjacent areas [e.g., Ducassou et al., 2019, Mercuzot et al., 2021, 2022]. After this maximum of lake development (Figure 7),

the clay facies become micaceous, sandier, and display some level dolomites indicating a shallower lake environment that corresponds to unit B on the seismic lines (Figures 3, 4). They vertically evolve to well-developed sandstone facies reached at 1652 m and correspond to unit C (Figure 7). This evolution from the maximum of lake deposits to the top of the sandstones attests to a general coarsening upward trend with more sediment supply around 1768 m (Figure 3). These sandstones are usually characterized by a clayey matrix and some conglomerate beds and could be attributed to fluvial or alluvial fan deposits; their upward evolution until 1652 m to unconsolidated well-rounded sandstones could suggest aeolian deposits interbedded within some red-silty clay facies. The general evolution, which corresponds to the *intermediate seismic sequence* (Figures 3, 4), allows to characterize a retrogradation and progradational trend from unit A to unit B

(Figure 7). Unit C may characterize the transition to a next retrogradational trend. However, it is difficult to define without core data, i.e., the sandstone recorded the transition from a progradational to retrogradational trend, and particularly if aeolian deposits are preserved [Bourquin et al., 2009, Olivier et al., 2023]. Moreover, based on seismic data, a well-defined angular unconformity has been defined at the top of unit C (i.e., in between the intermediate and upper seismic sequences; Figures 3, 4). As a result, unit D is not in continuity with the previous sedimentary succession. Above 1652 m, the sedimentary succession shows shallow lake deposits made of clay with some traces of evaporites, green clay and dolomitic nodules; the latter most probably represents some paleosol developments. This evolution characterizes a retrogradational trend (Figures 7, 8) ended by the Triassic unconformity and corresponds to the *upper seismic sequence* (Figures 3, 4).

For the BCY1 well, the whole sedimentary succession overlying probable Carboniferous deposits (top at 1802 m) is thinner than in the BTY1 well. A first trend is observed from conglomerates and sandstones until a maximum of lake deposits around 1618 m is reached (unit A; Figures 7, 8), correlated with the basal retrogradational trend of BTY1. A progradational trend, with well-developed sandstones and conglomerates evolving to fine-grained micaceous sandstones is observed until 1425 m (unit B; Figures 7, 8). Unit C is less developed in this borehole. Above the angular unconformity (1385 m), the same retrogradational trend as in BTY1 is observed, but with more sandstone and conglomerate deposits attesting to an area with more sediment supply (unit D; Figures 7, 8).

In the SGS1 and COU1 wells, the Permian sedimentary succession has a reduced thickness corresponding to a general retrogradational trend from conglomerates and sandstones to silty-clay facies. The latter corresponds to the same facies belonging to the upper retrogradational trend of the three other wells (unit D; Figures 7, 8), with the occurrence of more sandy beds in COU1 (Figure 8). In this well, eight retrogradational–progradational cycles were described based on core analyses within this retrogradational trend [Juncal et al., 2018], but in the absence of core data it is impossible to propose correlations at this high-resolution scale with the BTY1, BCY1 and SGS1 wells.

5. Discussion

5.1. *Tectonic evolution of the Brécý depocenter—regional comparisons*

The new seismic reprocessing greatly improves the understanding of the structural style of the Brécý depocenter, leading us to discuss the modality of its syn- and post-rift tectonic evolution (Figure 9), and to look for similar patterns in other LOCPB.

5.1.1. *Syn-rift stage*

The new interpretation confirms and refines the multi-step widening scenario for the Brécý depocenter, controlled by the westward migration of a few successive active normal faults and their related depocenters, thinning and onlapping each other eastward (Figure 9). Some of the normal faults may be connected to deep detachments located in the pre-Stephanian basement, giving them a listric geometry at the time of the deposition (Figure 9). In fact, upper crustal extensional detachments in the footwall of LOCPB are a common structural feature around the Massif Central [Echtler and Malavieille, 1990, Burg et al., 1994, Faure, 1995, Gardien et al., 2022], and such detachments have been described close to the study area in the Autun and La Serre regions 150 km east of the Brécý depocenter [Choulet et al., 2012].

This induced the creation of an accommodation space that recorded a retrogradational trend characterized by well extended lacustrine deposits (unit A), followed by a progradational trend (unit B), due to increasing sediment supply in this subsiding context, before a probably new retrogradational trend (unit C) was abruptly ended by the angular unconformity (Figures 7, 8).

The intersecting N20-trending CH3 and CH21 lines are parallel to the main structural trend (Figure 6). There, the eastward facing normal faults are sub-parallel to the lines, so that they appear as flat lens-shape features subparallel to the BBU, disturbing the geometry of its reflectors. Deeply seated highly energetic reflectors in the basement below the BBU also occur and are similarly interpreted as potential extensional detachments planes.

All the above observations point to a syn-tectonic filling of the basin in an overall extensive tectonic regime during the latest Carboniferous–early

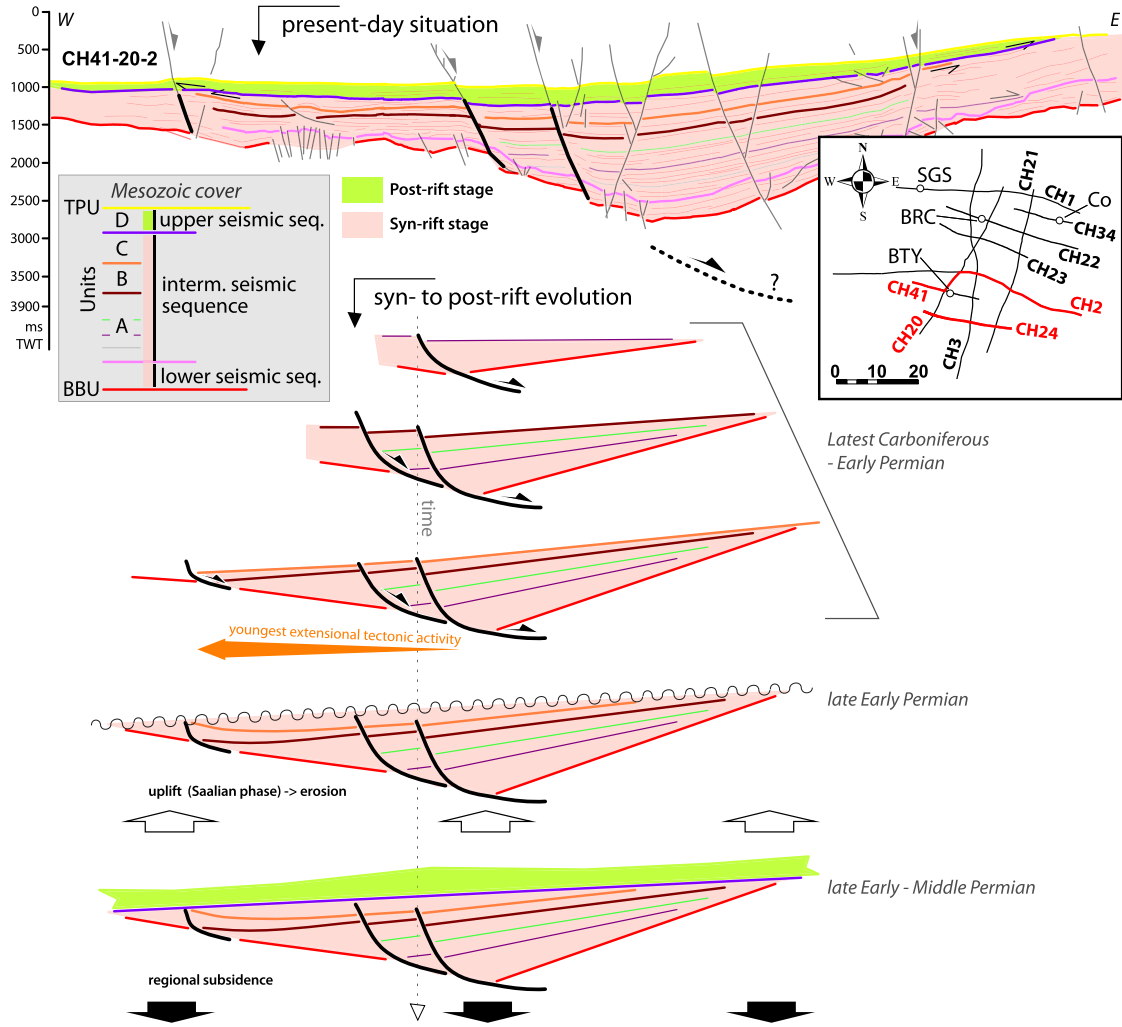


Figure 9. Present-day situation and tectonic evolution of the Brécý depocenter, using the representative composite CH41-20-2 seismic line. The syn-rift, uplift and post-rifts phases are successively depicted; the ages come from comparison with the Lorraine-Saar-Nahe Basin; see text for explanations.

Permian, characterizing the syn-rift stage of the Brécý depocenter. The maximum thickness of the syn-rift stage is ca. 3400 m.

5.1.2. *Post-rift stage*

The syn-rift activity is followed by a post-rift stage, whose occurrence is documented by the toplap geometry of the horizons of the syn-rift stage (mainly belonging to units B and C) below the first deposits of the overlying unit D (*upper seismic sequence*,

that corresponds to a new stratigraphic cycle where only its retrogradational phase is recorded due to an unconformity before Triassic sediment preservation) (Figures 5, 6, 9). The toplap geometries, observed in the whole area, provide evidence for the uplift and subsequent erosion of the syn-rift sediments before the deposition of the post-rift stage s.s. The latter is roughly isopach throughout the Brécý depocenter (ca. 0.25 s TWT, corresponding to ca. 500 m), and extends laterally beyond the

syn-rift stage. Another typical feature characterizing the post-rift stage is the absence of faults controlling the sedimentation. When considered together, these features suggest that the post-rift stage developed under a regional subsidence regime, which is certainly related to the late orogenic thermal relaxation of the hot Variscan crust [e.g., Averbuch and Piromallo, 2012, Vanderhaeghe et al., 2020, and references therein]. Toplaps of horizons belonging to the post-rift stage below the Triassic deposits suggest that the whole Brécý depocenter (i.e., syn-rift and post-rift stage) was then slightly tilted and subsequently eroded before the arrival of the first Triassic sediments. This erosional event may explain the relative low thickness of the post-rift stage (well depicted in the CH21, CH3 and CH41-20-2 seismic lines, Figures 5, 6). Beccaletto et al. [2015] checked and found similar geometrical and structural patterns in the adjacent Contres and Arpheuilles depocenters (thick syn-rift record beneath a thin isopach post-rift record).

The transition from a tectonic subsidence regime accommodated by discrete faults (syn-rift stage) to a regional subsidence regime (post-rift stage) through an uplift phase has not been documented yet in other French LOCPB, except in the Lorraine region (location in Figure 1). There, the latest Carboniferous–lower Permian syn-rift deposits are also controlled by listric normal faults rooting downward in deep decollement levels [Hemelsdaël et al., 2023]. They are then eroded following their uplift and tilting, before the arrival of the early to middle Permian post-rift sediments [Henk, 1993, Stollhofen, 1998]. The latter are then themselves eroded (toplap geometries below the Triassic deposits) before the deposition of the first Triassic sediments, as in the Brécý area [Hemelsdaël et al., 2023]. Further east in Germany, the Upper Rotliegend units of the Saar-Nahe (eastward prolongation of the Lorraine Basin), Thuringian Forest and Saale basins may also record these post-rift events [Hertle and Littke, 2000, Schäfer, 2011, Schneider and Romer, 2010]. In the literature, the tectonic phase responsible for the uplift is attributed to the end of early Permian Saalian phase [e.g., McCann et al., 2008a, Pharaoh et al., 2010, Stille, 1924, Ziegler, 1990], originally described in Central Germany, where folding and local tectonic inversion occur [Hertle and Littke, 2000, Kneuper, 1976]. In addition to the observations made in the Brécý depocen-

ter, the shortening phases recognized in some French LOCPB may also be related to this poorly known Saalian phase [Blès et al., 1989, Bonijoly and Castaing, 1983, Gélard et al., 1986, Genna and Debriette, 1994, Mattauer and Matte, 1998]. Going back to the Brécý area and according to this scenario, the base of the post-rift stage (unit D) would correspond to the superposition of two regional unconformities, i.e., the post-rift unconformity and the post-Saalian unconformity.

Lastly, it is unsurprising to not find explicit evidence of such a post-rift event in the French outcropping LOCPB, as the related deposits have certainly been partly removed by subsequent Meso-Cenozoic erosion [Barbarand et al., 2013, Guillocheau et al., 2000]. They are best fully described in subsurface settings beneath their Mesozoic cover, where the Permian deposits (including post-rift sediments) are still preserved and therefore accessible to seismic observations; in other words, the subsurface prolongation of other LOCPB around the Massif Central (e.g., Brive, Rodez, Saint-Affrique) may indeed preserve such post-rift deposits, even though they have not yet been identified. The recognition of a syn-rift stage followed by a regional uplift and a post-rift stage in the late Carboniferous–Permian Brécý depocenter is of great importance, as it allows to make a geodynamic connection with known LOCPB in eastern France and Germany. It confirms that the development of late Variscan basins is controlled by a large-scale (western Europe) underlying geodynamic event [e.g., the lithospheric delamination and removal of the Variscan mantle roots, e.g., Arnold et al., 2001, Averbuch and Piromallo, 2012]. Later, the arrival of the first Triassic sediments attests to the subsequent long-term Mesozoic thermal subsidence of the lithosphere, which led to the formation of the Paris Basin as a post-Variscan sag basin [Averbuch and Piromallo, 2012, Prijac et al., 2000, Robin et al., 2000].

5.2. *The Brécý depocenter was belonging to a much larger basin—local vs. regional correlations*

In addition to structural and tectonic aspects, which are difficult to understand without seismic data, another way to look for lateral correlations of the Brécý depocenter with neighboring basins is to track

the thicknesses of preserved end-Carboniferous–Permian deposits, their facies and paleoenvironments, and age similarities. In this section, we aim to connect the Brécy depocenter to the LOCPB of the northern Massif Central, before looking for wider-scale regional correlations.

First, as already demonstrated, the Brécy depocenter is undoubtedly connected westward to the Contres depocenter (which itself is connected to the Arpheuilles depocenter), as shown by the continuity of the Permian reflectors on the seismic lines between the three depositional areas [Beccaletto et al., 2015]. It is difficult to assess the occurrence of end-Carboniferous–Permian deposits north to northeast of the Brécy depocenter as there are no available seismic lines; this is also the case for its southwest prolongation. The few available spatially dispersed wells in these areas indicate that the Triassic deposits rest directly on basement rocks without intervening Carboniferous–Permian deposits (weathered granite in the Pougues-1 and Sainte-Colombes-1 wells, micaschists in the Ménetou-1 wells; location in Figure 2). It is however impossible to definitively conclude on the complete absence of Carboniferous–Permian rocks to the north of the Brécy depocenter based on such scarce data, as they may occur in between the wells. It could for instance be the case along the roughly N–S Loire-Sancerre fault zone and its northward prolongation as suggested by Delmas et al. [2002] (Figure 10). In addition, recent work done by the 45-8 Energy Company and BRGM leads to the recognition of new small subsurface Permian deposits southwest of the La Machine area [Hauville et al., 2021, Jacob et al., 2021]. This very local Permian occurrence may be connected to the Brécy depocenter, but their connection is not yet known.

Further south, it is strongly tempting to extend the Brécy depocenter to the outcropping Aumance Basin, although there is no direct evidence for this (no seismic line or well data). Extensive research has been carried out in the Aumance area for the purpose of uranium exploration, resulting in detailed sedimentological and structural descriptions based on numerous borehole and scarce seismic data [Mathis and Brulhet, 1990]. There, the Buxières Formation with gray Autunian facies has been dated close to the Carboniferous–Permian transition [298.59 ± 0.35 Ma, CA-ID-TIMS method, Mercuzot

et al., 2023; Figure 11]. This formation is overlain by red Autunian alluvial to lacustrine facies (Renière Fm.). Both facies are similar to those belonging to the intermediate seismic sequences (units A and B) of the Brécy depocenter. When considered together, these facies provide evidence for a syn-rift stage [Mathis and Brulhet, 1990, Paquette, 1980]. Note that the Aumance is not located along strike of the N30-trending Brécy depocenter, but instead is shifted to the east, such that the former should not be seen as the southward prolongation of the latter but as a parallel basin (Figure 10).

Eastward, recent works from Mercuzot et al. [2021, 2022] suggest the connection of the Decize-La-Machine (including the Lucenay-lès-Aix depocenter), Aumance, Autun and Blanzay-Le Creusot Stephano-Autunian basins: their lacustrine environments (from alluvial fan/fan delta to deep lake) and depositional ages are similar [latest Carboniferous to early Permian; Ducassou et al., 2019, Pellenard et al., 2017]. Here again, the Permian facies are similar to the intermediate (units A) seismic sequences of the Brécy depocenter, and they display seven retrogradational–progradational cycles within a general retrogradational trend ended by an unconformity overlain by Triassic deposits [Mercuzot et al., 2021]. Even though we observed the same general retrogradational evolution in the Brécy area (unit A), it is not possible to make a detailed comparison between these two areas because no age is available at the top of the Permian in the Decize-La-Machine area. Consequently, the absence of sandstones in units B and C (i.e., mainly a progradational trend) in Decize-La-Machine is either due to the erosion of these units or to a local sediment supply in the Brécy area, which is not recorded in Decize-La-Machine. However, a significant difference lies in the cumulative thickness of the deposits, which are unsurprisingly much lower in the outcropping basins (ca. 1 to 1.2 km) compared to the Brécy depocenter (2.5 km; Figure 11). Such large cumulative thicknesses are only reported from the Blanzay-Le Creusot composite basin, where more than two kilometers of Stephano-Autunian deposits are described from coal exploration boreholes [Figure 11, BRGM, 1989, Gand, 2003]. Further east, structural connections between the Autun, La Serre, Burgundy and southern Vosges basins have also been proposed [Choulet et al., 2012].

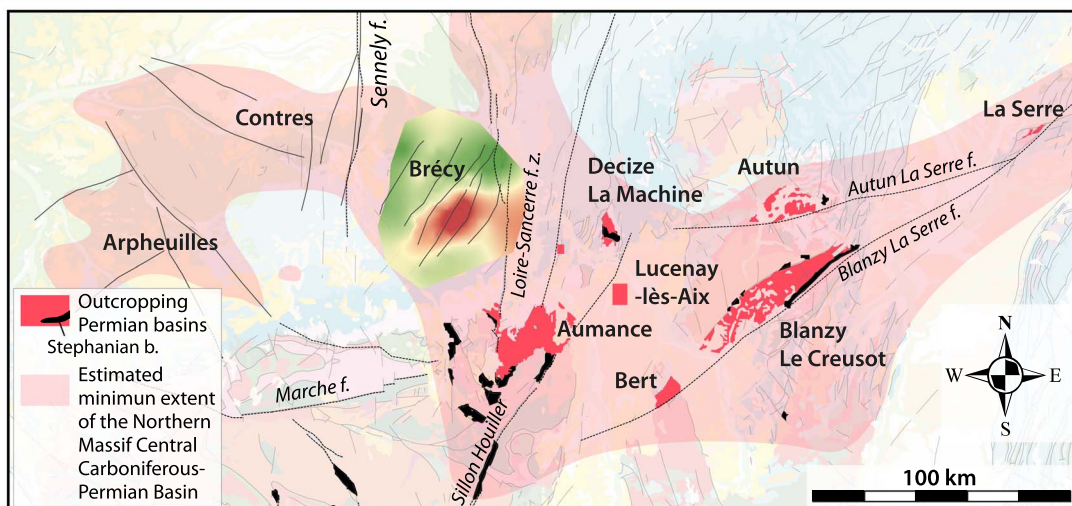


Figure 10. Estimated extent of the “northern Massif Central Carboniferous–Permian Basin” on a present-day geological map; the geological background is from the 1:1,000,000 geological map of France [BRGM, 2003].

All these observations and interpretations, correlating neighboring basins to each other, imply that these present-day isolated outcropping and subsurface basins, represented by the Stephano-Autunian facies, were part of a larger basin during the latest Carboniferous–early Permian. This larger basin encompassed the subsurface Arpheuilles, Contres and Brécly depocenters and the eastward smaller outcropping basins, spanning more than four hundred kilometers in length, with a roughly W–E trend (“northern Massif Central Carboniferous–Permian Basin”, Figure 10). These regional connections are also confirmed by paleobiogeography data from freshwater shark remains found in the Stephano-Autunian sediments, suggesting connections between all the French LOCPB of the northern Massif Central [including the Aumance, Autun and Blanzly-Le Creusot basins as well as on a much larger scale as far away as Germany; Luccisano et al., 2021, Fischer et al., 2013, Schneider et al., 2020].

It is important to note that the area depicted in Figure 10 (pale blue color) may represent a *minimum* extent of this wide basin. Indeed, some upper Carboniferous and lower Permian deposits have certainly been removed through time and are therefore lacking, due to (i) the erosion phases known before the arrival of the Triassic sediments [as discussed above and in Beccaletto et al., 2015], and

(ii) the Meso-Cenozoic uplift of the Massif Central area and subsequent erosion [Barbarand et al., 2013, Guillocheau et al., 2000].

On a wider scale, unlike the northern Massif Central, several-km-thick Stephano-Autunian deposits are encountered in several LOCPB of the southern Massif Central. These basins, such as Brive, Decazeville-Rodez, Carmaux-La Grésine, Saint-Affrique or Graissessac-Lodève, display similar Stephano-Autunian facies and ages to those observed in the Brécly depocenter and connected smaller basins, and reach thicknesses of up to four kilometers [Figure 11; BRGM, 1989, Pochat and Van Den Driessche, 2011, Poujol et al., 2023]. Due to the lack of subsurface seismic data, their extensional structural control is rarely imaged [Serrano et al., 2006 for a counterexample in the Aquitaine Basin] and is inferred from indirect observations [Chen et al., 2006, Pochat and Van Den Driessche, 2011].

Such thick series are also known in the LOCPB of Germany, for example in the Saar-Nahe and Thuringian Forest basins [Schneider and Romer, 2010, Schneider et al., 2020]. There, studies benefit both from favorable outcrop conditions and a large range of subsurface dataset including seismic lines. Consequently, the sedimentary facies and paleoenvironments are well constrained, the lithostratigraphic and extensional structural features are

well described, and recent absolute depositional ages are available [Henk, 1993, Stollhofen, 1998, Schäfer, 2011, Lützner et al., 2020, Voigt et al., 2022; Figure 11]. Based on all of these characteristics, they can be considered as other robust reference basins for large-scale LOCPB correlations.

All other LOCPB occurrences in western Europe generally occur in deformed areas as small, isolated patches with low preserved thicknesses, like in the Pyrenees (French and Spanish sides), Cantabria, Sardinia and the Alps and surrounding areas (France, Italy, Switzerland) [Barnolas and Chiron, 1996, BRGM, 1989, Capuzzo et al., 2003, Cassinis et al., 2012, Knight and Álvarez-Vázquez, 2021, Lloret et al., 2018, Pittau et al., 2002, Toutin, 1980]. We should also mention the supposedly wider basins with uncertain boundaries, thickness and age attributions that are also known offshore based on seismic data [e.g., Bay of Biscay, Western Approaches; Bois et al., 1991, Ziegler, 1990]. These characteristics make all these basins unsuitable for reliable wide-scale comparisons, and cannot be considered as reference basins.

Lastly, arguments in favor of the Brécý depocenter being part of a new wider-scale reference basin (which would be useful for further large-scale correlations, and located in between the two poles represented by the LOCPB of the southern Massif Central and Germany) include: its large preserved thickness (up to 3.9 kilometers), structural record (syn- and then post-rift stages) and age calibration (paleontological and absolute ages from deep wells and comparison with close connected basins with absolute temporal calibrations).

6. Summary and conclusion

The structural pattern, thickness, tectonic evolution and depositional environments of the late Carboniferous–Permian Brécý depocenter are revealed based on the reprocessing and interpretation of 115 km of vintage seismic lines combined with deep well data.

The present-day geometry of the Brécý depocenter is controlled by seven major and eleven minor eastward dipping normal faults; all these faults were active during the Meso-Cenozoic period, and some of them were possibly connected to deep detachments active during the late Carboniferous–Permian

history. The maximum thickness of the Brécý depocenter is reevaluated and estimated to be 3900 m.

The filling indicates a thick late Carboniferous–early Permian syn-rift stage overlain by a thin early to middle post-rift stage, similar to the tectonic evolution of the northeastward basins in Lorraine and Germany. The facies generally characterize lake environments, with occurrences of fluvial, alluvial and delta fan deposits. They mainly display a retrogradational–progradational pattern during the syn-rift stage, and a retrogradational pattern during the post-rift stage. The Brécý area is therefore the thickest depocenter known in the northern Massif Central by far. We propose that it was part of a larger basin during the latest Carboniferous–early Permian times, with a roughly W–E trend spanning more than four hundred kilometers in length in the northern Massif Central region. Strictly speaking, all the other so-called outcropping basins (Aumance, Decize-La-Machine, etc.) should be considered as depocenters, as they belong to a wider scale basin.

Because of the above features, this “northern Massif Central Carboniferous–Permian Basin” may be seen as a reference LOCPB, comparable to the basins known in the southern Massif Central, eastern France and Germany. Lastly, our work emphasizes the need for a further multi-method approach to explore LOCPB, especially their subsurface occurrences, as it is crucial to have a full view of these basins that contain information that is inaccessible to their outcropping remnants. It definitely highlights that LOCPB were obviously much wider and thicker than previously expected, with potential effective impacts on the understanding of the late Variscan tectonic and climatic evolution in France and western Europe.

Declaration of interests

The authors do not work for, advise, own shares in, or receive funds from any organization that could benefit from this article, and have declared no affiliations other than their research organizations.

Acknowledgements

This publication was initiated within the framework of the ICDP Deepdust project and was supported by the BRGM’s Research Division. The authors gratefully acknowledge François Baudin, coordinator of

this special issue dedicated to Jean Dercourt, for his patience and perseverance. They thank the two anonymous reviewers for their constructive comments, which have greatly improved the manuscript. The authors also thank Sara Mullin for proofreading the English content.

References

- Aretz, A., Bär, K., Götz, A. E., and Sass, I. (2016). Outcrop analogue study of Permocarboniferous geothermal sandstone reservoir formations (northern Upper Rhine Graben, Germany): impact of mineral content, depositional environment and diagenesis on petrophysical properties. *Int. J. Earth Sci.*, 105, 1431–1452.
- Arnold, J., Jacoby, W. R., Schmeling, H., and Schott, B. (2001). Continental collision and the dynamic and thermal evolution of the Variscan orogenic crustal root—numerical models. *J. Geodyn.*, 31, 273–291.
- Averbuch, O. and Piromallo, C. (2012). Is there a remnant Variscan subducted slab in the mantle beneath the Paris basin? Implications for the late Variscan lithospheric delamination process and the Paris basin formation. *Tectonophysics*, 558–559, 70–83.
- Baptiste, J., Martelet, G., Faure, M., Beccaletto, L., Reninger, P.-A., Perrin, J., and Chen, Y. (2016). Mapping of a buried basement combining aeromagnetic, gravity and petrophysical data: The substratum of southwest Paris Basin, France. *Tectonophysics*, 683, 333–348.
- Barbarand, J., Quesnel, F., and Pagel, M. (2013). Lower Paleogene denudation of Upper Cretaceous cover of the Morvan massif and southeastern Paris basin (France) revealed by AFT thermochronology and constrained by stratigraphy and paléosurfaces. *Tectonophysics*, 608, 1310–1327.
- Barnolas, A. and Chiron, J.-C. (1996). *Synthèse géologique et géophysique des Pyrénées. Volume 1: Introduction. Géophysique. Cycle hercynien*. Edition BRGM, Orléans, ITGE, Madrid.
- Beccaletto, L., Capar, L., Serrano, O., and Marc, S. (2015). Structural evolution and sedimentary record of the Stephano-Permian basins occurring beneath the Mesozoic sedimentary cover in the southwestern Paris basin (France). *Bull. Soc. Géol. Fr.*, 186, 429–450.
- Beccaletto, L., Hanot, F., Serrano, O., and Marc, S. (2011). Overview of the subsurface structural pattern of the Paris Basin (France): Insights from the reprocessing and interpretation of regional seismic lines. *Mar. Pet. Geol.*, 28, 861–879.
- Bertrayl (1987). Rapport de fin de sondage. Esso Rep, 24 p.
- Blès, J.-L., Bonijoly, D., Castaing, C., and Gros, Y. (1989). Successive post-Variscan stress fields in the French Massif Central and its borders (western European plate); comparison with geodynamic data. *Tectonophysics*, 169, 79–111.
- Bois, C., Gabriel, O., and Pinet, B. (1991). Les campagnes sismiques SWAT et WAM, leur réalisation et leur interprétation par une équipe du programme ECORS. *Mém. Soc. Géol. Fr.*, 159, 9–24.
- Bonijoly, D. and Castaing, C. (1983). Fracturation et genèse des bassins stéphaniens du Massif central français en régime compressif. *Ann. Soc. Géol. Nord*, CIII, 187–199.
- Bouchot, V., Ledru, P., Lerouge, C., Lescuyer, J. L., and Milesi, J. P. (2005). Late Variscan mineralizing systems related to orogenic processes: The French Massif Central. *Ore Geol. Rev.*, 27(1–4), 169–197.
- Bouchot, V., Milesi, J.-P., Lescuyer, J.-L., and Ledru, P. (1997). Les minéralisations aurifères de la France dans leur cadre géologique autour de 300 Ma. *Chron. de la Rech. Minière*, 528, 13–62. (with map at 1/1,000,000).
- Bourquin, S., Guillocheau, F., and Péron, S. (2009). Braided river within an arid alluvial plain (example from the early Triassic, western German Basin): criteria of recognition and expression of stratigraphic cycles. *Sedimentology*, 56, 2235–2264.
- Bourquin, S., Peron, S., and Durand, M. (2006). Lower Triassic sequence stratigraphy of the western part of the Germanic basin (west of Black Forest): fluvial system evolution through time and space. *Sediment. Geol.*, 186, 187–211.
- Brécyl (1966). Rapport de fin de sondage. IDEHCO H 40, Compagnie d'exploration pétrolière, 15 p.
- Breitkreuz, C., Ehling, B.-C., and Sergeev, S. (2009). Chronological evolution of an intrusive/extrusive system: the Late Paleozoic Halle Volcanic Complex in the northeastern Saale Basin (Germany). *Z. Dtsch. Ges. Geowiss.*, 160(2), 173–190.
- BRGM (1970). *Notice de la carte géologique au 1/50000 de Saint-Etienne*. Edition BRGM, Orléans. feuille 745.

- BRGM (1976). *Notice de la carte géologique au 1/50000 de Montceau-les-Mines*. Edition BRGM, Orléans. feuille 578.
- BRGM (1984). *Synthèse géologique du Sud-Est de la France*, volume 126 of *Mém. du Bureau de Rech. Géol. Minières*. Edition BRGM, Orléans.
- BRGM (1989). *Synthèse géologique des bassins permien français*, volume 128 of *Mém. du Bureau de Rech. Géol. Minières*. Edition BRGM, Orléans.
- BRGM (2003). *Carte géologique de la France au 1/1000000ème*. 6ème édition révisée. Edition BRGM, Orléans.
- Bruguier, O., Becq-Giraudon, J. F., Champenois, M., Deloule, E., Ludden, J., and Mangin, D. (2003). Application of *in situ* zircon geochronology and accessory phase chemistry to constraining basin development during post-collisional extension: a case study from the French Massif Central. *Chem. Geol.*, 201, 319–336.
- Burg, J. P., Van Den Driessche, J., and Brun, J. P. (1994). Syn- to post-thickening extension: mode and consequences. *C. R. Acad. Sci. Ser. IIA*, 319(2), 1019–1032.
- Capuzzo, N., Handler, R., Neubauer, F., and Wetzel, A. (2003). Post-collisional rapid exhumation and erosion during continental sedimentation: the example of the late Variscan Salvain-Doré naz basin (Western Alps). *Int. J. Earth Sci.*, 92, 364–379.
- Cassinis, G., Perotti, C. R., and Ronchi, A. (2012). Permian continental basins in the Southern Alps (Italy) and peri-mediterranean correlations. *Int. J. Earth Sci.*, 101, 129–157.
- Chantraine, J., Lorenz, C., Mégnien, C., Million, R., and Lienhardt, M.-J. (1992). Forage scientifique de Sancerre-Couy (Cher): Synthèse d'études 1986–1992. *Mém. du Bureau de Rech. Géol. Minières, Géol. Profonde de la Fr.*, 3, 1–230.
- Chen, Y., Henry, B., Faure, M., Becq-Giraudon, J. F., Talbot, J. Y., Daly, L., and Goff, M. L. (2006). New Early Permian paleomagnetic results from the Brive basin (French Massif Central) and their implications for Late Variscan tectonics. *Int. J. Earth Sci.*, 95, 306–317.
- Choulet, F., Faure, M., Fabbri, O., and Monié, P. (2012). Relationships between magmatism and extension along the Autun-La Serre fault system in the Variscan Belt of the eastern French Massif Central. *Int. J. Earth Sci. (Geol. Rundsch)*, 101, 393–413.
- Costa, S. and Maluski, H. (1988). Datations par la méthode ^{39}Ar - ^{40}Ar de matériel magmatique et métamorphique paléozoïque provenant du forage de Couy-Sancerre (Cher, France). Programme G.P.F. *C. R. Acad. Sci. Paris*, 306(II), 351–356.
- Costa, S. and Rey, P. (1995). Lower crustal rejuvenation and growth during post-thickening collapse: Insights from a crustal cross section through a Variscan metamorphic core complex. *Geology*, 23(10), 905–908.
- Courel, L., Donsimoni, M., and Mercier, D. (1986). La place du charbon dans la dynamique des systèmes houillers intramontagneux. *Mém. Soc. Géol. Fr.*, 149, 37–50.
- Delmas, J., Houël, P., and Vially, R. (2002). Paris Basin, Petroleum potential. IFP regional report.
- Dill, H., Teschner, M., and Wehner, H. (1991). Geochemistry and lithofacies of Permo-Carboniferous rocks from the southwestern edge of the Bohemian massif (Germany). A contribution to facies analysis of continental anoxic environments. *Int. J. Coal Geol.*, 18, 251–291.
- Domeier, M. and Torsvik, T. H. (2014). Plate tectonics in the late Paleozoic. *Geosci. Front.*, 5, 303–350.
- Donsimoni, M. (1990). Le gisement de charbon de Lucenay-lès-Aix (Nièvre). Documents du BRGM 179.
- Ducassou, C., Mercuzot, M., Bourquin, S., Rossignol, C., Pellenard, P., Beccaletto, L., Poujol, M., Hallot, E., Pierson-Wickmann, A. C., Hue, C., and Ravier, E. (2019). Sedimentology and U-Pb dating of Carboniferous to Permian continental series of the northern Massif Central (France): Local palaeogeographic evolution and larger scale correlations. *Palaeogeogr. Palaeoclimatol. Palaeoecol.*, 533, article no. 109228.
- Durand, M. (2014). Le bassin permien de saint-Dié-Villé (lorraine- alsace) et sa couverture gréseuse triasique. *Bull. Inf. Géol. du Bassin Paris*, 51(3), 3–24.
- Echtler, H. and Malavieille, J. (1990). Extensional tectonics, basement uplift and Stephano-Permian collapse basin in a late Variscan metamorphic core complex (Montagne Noire, Southern Massif Central). *Tectonophysics*, 177, 125–138.
- Faure, M. (1995). Late orogenic carboniferous extensions in the Variscan French Massif Central. *Tectonics*, 14, 132–153.
- Fischer, J., Schneider, J. W., Voigt, S., Joachimski, M. M., Tichomirowa, M., Tütken, T., Götze, J., and

- Berner, U. (2013). Oxygen and strontium isotopes from fossil shark teeth: Environmental and ecological implications for Late Palaeozoic European basins. *Chem. Geol.*, 342, 44–62.
- Gand, G. (2003). Le bassin permien de Blanzly-Le Creusot et ses bordures carbonifères. *Bull. Inf. Géol. du Bassin Paris*, 40(3), 4–19.
- Gand, G., Garric, J., Schneider, J., Sciau, J., and Walter, H. (1996). Biocénoses à méduses du permien français (bassin de Saint-Affrique, Massif Central). *Geobios*, 29(4), 379–400.
- Gardien, V., Martelat, J.-E., Leloup, P.-H., Mahéo, G., Bevilard, B., Allemand, P., Monié, P., Paquette, J.-L., Grosjean, A.-S., Faure, M., Chelle-Michou, C., and Fellah, C. (2022). Fast exhumation rate during late orogenic extension: The new timing of the Pilat detachment fault (French Massif Central, Variscan belt). *Gondwana Res.*, 103, 260–275.
- Gast, R. E., Dusar, M., Breitzkreuz, C., Gaupp, R., Schneider, J. W., Stemmerik, L., Geluk, M. C., Geisler, M., Kiersnowski, H., Glennie, K. W., Kabel, S., and Jones, N. S. (2010). Rotliegend. In Doornenbal, J. C. and Stevenson, A. G., editors, *Petroleum Geological Atlas of the Southern Permian Basin Area*, pages 101–121. EAGE Publications b.v., Houten.
- Gastaldo, R. A., DiMichele, W., and Pfefferkorn, H. (1996). Out of the icehouse into the greenhouse: a late paleozoic analog for modern global vegetational change. *GSA Today*, 6(10), 1–7.
- Gélard, J.-P., Castaing, C., Bonijoly, D., and Grolier, J. (1986). Structure et dynamique de quelques houillers limniques du Massif central. *Mém. Soc. Géol. Fr. Nouvelle Série*, 149, 57–72.
- Genna, A. and Debriette, P. J. (1994). Structures en fleur dans le bassin houiller d'Alès. Implications structurales. *C. R. Acad. Sci. Sér. 2 Sci. de La Terre et Des Planètes*, 318(7), 977–984.
- Goloubinoff, C. (1979). *Le permo-houiller du nord du bassin de St Affrique (Aveyron)*. Thèse de 3ème cycle, Université Paris-Sud. 143 p.
- Guillocheau, F., Robin, C., Allemand, P., Bourquin, S., Brault, N., Dromart, G., Friedenberg, R., Garcia, J.-P., Gaulier, J.-M., Gaumet, F., Grosdoy, B., Hanot, F., Le Strat, P., Mettraux, M., Nalpas, T., Prijac, C., Rigoltet, C., Serrano, O., and Grandjean, G. (2000). Meso-Cenozoic geodynamic evolution of the Paris Basin: 3D stratigraphic constraints. *Geodinam. Acta*, 13, 189–245.
- Hauville, B., Laine, C., Pélissier, N., Boka Mene, M., Jacob, Th., and Coppo, N. (2021). Exploration d'hélium en France : avancées du projet Fonts-Bouillants dans la Nièvre et résultats apportés par de multiples acquisitions géophysiques et géochimiques. RST2021 Lyon.
- Hemelsdaël, R., Averbuch, O., Beccaletto, L., Izart, A., Marc, S., Capar, L., and Michels, R. (2023). A deformed wedge-top basin inverted during the collapse of the Variscan belt: The Permo-Carboniferous Lorraine Basin (NE France). *Tectonics*, 42, article no. e2022TC007668.
- Henk, A. (1993). Late orogenic Basin evolution in the Variscan internides: the Saar-Nahe Basin, south-west Germany. *Tectonophysics*, 223, 273–290.
- Hertle, M. and Littke, R. (2000). Coalification pattern and thermal modelling of the Permo-Carboniferous Saar Basin, SW-Germany. *Int. J. Coal Geol.*, 42, 273–296.
- Hübner, N., Körner, F., and Schneider, J. (2011). Tectonics, climate and facies of the Saint Affrique Basin and correlation with the Lodève Basin (Permian, Southern France). *Z. Dtsch. Ges. Geowiss.*, 162(2), 157–170.
- Jacob, Th., Coppo, N., Dubois, F., Wawrzyniak, P., Portal, A., Bitri, A., Gaudot, I., Beccaletto, L., Le Maire, P., Laine, Ch., Hauville, B., and Pellissier, N. (2021). Exploration géophysique au sein du PER “Fonts-Bouillants” : apport des méthodes gravimétriques, audiomagnétotelluriques et électromagnétiques à source contrôlée. RST2021 Lyon.
- Juncal, M. A., Bourquin, S., Beccaletto, L., and Diez, J. B. (2018). New sedimentological and palynological data from the Permian and Triassic series of the Sancerre-Couy core, Paris Basin, France. *Geobios*, 51, 517–535.
- Kneuper, G. (1976). Regional geologische folgerungen aus der bohrung saar-1. *Geol. Jahrb.*, 27, 417–428.
- Knight, J. A. and Álvarez-Vázquez, C. (2021). A summary of upper Pennsylvanian regional substages defined in NW Spain—the chronostratigraphic legacy of Robert H. Wagner. *News. Stratigr.*, 54(3), 275–300.
- Laurent, A., Averbuch, O., Beccaletto, L., Graveleau, F., Lacquement, F., Capar, L., and Marc, S. (2021). 3-D structure of the variscan thrust front in Northern France: new insights from seismic reflection profiles. *Tectonics*, 40(7), 1–33.

- Lloret, J., Ronchi, A., López-Gómez, J., Gretter, N., De la Horra, R., Barrenechea, J. F., and Arche, A. (2018). Syn-tectonic sedimentary evolution of the continental late Palaeozoic-early Mesozoic Erill Castell-Estac Basin and its significance in the development of the central Pyrenees Basin. *Sediment. Geol.*, 374, 134–157.
- Lorenz, C., Mégnien, C., Delavenna, M., Galbrun, B., Gallet, Y., and Giot, D. (1987). Premiers résultats du sondage implanté sur l'anomalie magnétique du bassin de Paris, au Sud de Sancerre (Cher). Programme géologie profonde de la France. *C. R. Acad. Sci. Sér. 2, Méc. Phys. Chim. Sci. de l'univers, Sci. de la Terre*, 305(12), 1099–1104.
- Luccisano, V., Pradel, A., Amiot, R., Gand, G., Steyer, J.-S., and Cuny, G. (2021). A new Triodus shark species (Xenacanthidae, Xenacanthiformes) from the lowermost Permian of France and its paleobiogeographic implications. *J. Vertebr. Paleontol.*, 41(2), article no. e1926470.
- Lützner, H., Tichomirowa, M., Käßner, A., and Gaupp, R. (2020). Latest Carboniferous to early Permian volcano-stratigraphic evolution in Central Europe: U-Pb CA-ID-TIMS ages of volcanic rocks in the Thuringian Forest Basin (Germany). *Int. J. Earth Sci.*, 110, 377–398.
- Malavieille, J. (1993). Late Orogenic extension in mountain belts: Insights from the basin and range and the Late Paleozoic Variscan Belt. *Tectonics*, 12, 1115–1130.
- Malavieille, J., Guihot, P., Costa, S., Lardeaux, J. M., and Gardien, V. (1990). Collapse of the thickened Variscan crust in the French Massif Central: Mont Pilat extensional shear zone and St. Etienne Late Carboniferous basin. *Tectonophysics*, 177, 139–149.
- Masclé, A. (1990). Géologie pétrolière des bassins permien français; Comparaison avec les bassins permien du Nord de l'Europe. Petroleum geology of French Permian basins; comparison with the Permian basins of northern Europe; Potentiel économique des bassins permien français. Economic potential of French Permian basins. *Chron. Rech. Minière*, 499, 69–86.
- Mathis, V. and Brulhet, J. (1990). Les gisements uranifères du bassin permien de Bourbon-l'Archambault (nord du Massif central français). *Chron. Rech. Minière*, 499, 19–30.
- Mattauer, M. and Matte, P. (1998). Le bassin Stéphanien de St-Etienne ne résulte pas d'une extension tardi-hercynienne généralisée : c'est un bassin pull-apart en relation avec un décrochement dextre. *Geodinam. Acta*, 11(1), 23–31.
- McCann, T., Kiersnowski, H., Krainer, K., Vozarova, A., Peryt, T. M., Oplustil, S., Stollhofen, H., Schneider, J., Wetzel, A., Boulvain, F., Dusar, M., Torok, A., Haas, J., Tait, J., and Koerner, F. (2008a). Permian. In McCann, T., editor, *The Geology of Central Europe; Precambrian and Palaeozoic 1*, pages 531–597. Geological Society of London, London, UK.
- McCann, T., Pascal, C., Timmerman, M. J., Krzywiec, P., López-Gómez, J., Wetzel, L., Krawczyk, C. M., Rieke, H., and Lamarche, J. (2006). Post-Variscan (end Carboniferous-Early Permian) basin evolution in western and central Europe. *Geol. Soc. Lond. Mem.*, 32(1), 355–388.
- McCann, T., Skompski, S., Poty, E., Dusar, M., Vozarova, A., Schneider, J., Wetzel, A., Krainer, K., Kornpihl, K., Schaefer, A., Krings, M., Oplustil, S., and Tait, J. (2008b). Carboniferous. In McCann, T., editor, *The Geology of Central Europe; Precambrian and Palaeozoic 1*, pages 411–529. Geological Society of London, London, UK.
- Ménard, G. and Molnar, P. (1988). Collapse of a Hercynian Tibetan plateau into a late Palaeozoic European Basin and Range province. *Nature*, 334, 235–237.
- Mercuzot, M., Bourquin, S., Beccaletto, L., Ducassou, C., Rubi, R., and Pellenard, P. (2021). Palaeoenvironmental reconstitutions at the Carboniferous-Permian transition south of the Paris Basin, France: implications on the stratigraphic evolution and basin geometry. *Int. J. Earth Sci. (Geol. Rundsch)*, 110, 9–33.
- Mercuzot, M., Bourquin, S., Pellenard, P., Beccaletto, L., Schnyder, J., Baudin, F., Ducassou, C., Garel, S., and Gand, G. (2022). Reconsidering Carboniferous-Permian continental paleoenvironments in eastern equatorial Pangea: facies and sequence stratigraphy investigations in the Autun Basin (France). *Int. J. Earth Sci.*, 111, 1663–1696.
- Mercuzot, M., Rossignol, C., Bourquin, S., Ramezani, J., Ducassou, C., Poujol, M., Beccaletto, L., and Pellenard, P. (2023). U-Pb age constraints on the Carboniferous-Permian transition in continental basins of eastern equatorial Pangaea (France): implications for the depositional history and correlations across the late Variscan Belt. *J. Geol. Soc.*, 180(6), article no. jgs2023-075.

- Michel, L. A., Tabor, N. J., Montañez, I. P., Schmitz, M. D., and Davydov, V. I. (2015). Chronostratigraphy and paleoclimatology of the Lodève Basin, France : evidence for a pan-tropical aridification event across the Carboniferous-Permian boundary. *Palaeogeogr. Palaeoclimatol. Palaeoecol.*, 430, 118–131.
- Montañez, I. P., Tabor, N. J., Niemeier, D., DiMichele, W. A., Frank, T. D., Fielding, C. R., Isbell, J. L., Birgenheier, L. P., and Rygel, M. C. (2007). CO₂-forced climate and vegetation instability during Late Paleozoic deglaciation. *Science*, 315(5808), 87–91.
- Neumann, E.-R., Wilson, M., Heeremans, M., Spencer, E. A., Obst, K., Timmerman, M. J., and Kirstein, L. (2004). Carboniferous-Permian rifting and magmatism in southern Scandinavia, the North Sea and northern Germany: a review. In *Permo-Carboniferous Magmatism and Rifting in Europe*, Geological Society, London, Special Publications, 223, pages 11–40. Geological Society of London.
- Olivier, M., Bourquin, S., Desaubliaux, G., Ducassou, C., Rossignol, C., Daniau, G., and Chaney, D. (2023). The Late Paleozoic Ice Age in western equatorial Pangea: Context for complex interactions among aeolian, alluvial, and shoreface sedimentary environments during the Late Pennsylvanian early Permian. *Gondwana Res.*, 124, 305–338.
- Opluštil, S., Schmitz, M., Cleal, C. J., and Martínek, K. (2016). A review of the Middle-Late Pennsylvanian west European regional substages and local biozones, and their correlation to the Geological Time Scale based on new U-Pb ages. *Earth Sci. Rev.*, 154, 301–335.
- Orszag-Sperber, F., Freytet, P., and Lebreton, M. L. (1992). Le Permien du forage de Sancerre-Couy: depots de plaine d'inondation. *Géol. Fr.*, 3–4, 43–49.
- Paquette, Y. (1980). *Le Bassin autunien de l'Aumance (Allier): sédimentologie (charbon, cinérites...), tectonique syndiagénétique*. Thèse de doctorat. 278 p.
- Pellenard, P., Gand, G., Schmitz, M., Galtier, J., Broutin, J., and Stéyer, J.-S. (2017). High-precision U-Pb zircon ages for explosive volcanism calibrating the NW European continental Autunian stratotype. *Gondwana Res.*, 51, 118–136.
- Pharaoh, T. C., Duser, M., Geluk, M. C., Kockel, F., Krawczyk, C. M., Krzywiec, P., Scheck-Wenderoth, M., Thybo, H., Vejbæk, O. V., and Van Wees, J. D. (2010). Tectonic evolution. In Doornenbal, J. C. and Stevenson, A. G., editors, *Petroleum Geological Atlas of the Southern Permian Basin Area*, pages 25–57. EAGE Publications b.v., Houten.
- Pittau, P., Barca, S., Cocherie, A., Del Rio, M., Fanning, M., and Rossi, P. (2002). Le bassin permien de Guardia Pisano (Sud-Ouest de la Sardaigne, Italie): palynostratigraphie, paléophytogéographie, corrélations et âge radiométrique des produits volcaniques associés. *Geobios*, 35(5), 561–580.
- Pochat, S. and Van Den Driessche, J. (2011). Filling sequence in Late Paleozoic continental basins: A chimera of climate change? A new light shed given by the Graissessac-Lodève basin (SE France). *Palaeogeogr. Palaeoclimatol. Palaeoecol.*, 302, 170–186.
- Poujol, M., Mercuzot, M., Lopez, M., Bourquin, S., Bruguier, O., Hallot, E., and Beccaletto, L. (2023). Insights on the Permian tuff beds from the Saint-Affrique Basin (Massif Central, France): an integrated geochemical and geochronological study. *C. R. Géosci.*, 355, 1–25.
- Prijac, C., Doin, M. P., Gaulier, J. M., and Guillocheau, F. (2000). Subsidence of the Paris Basin and its bearing on the late Variscan lithosphere evolution: a comparison between Plate and Chablis models. *Tectonophysics*, 323, 1–38.
- Retallack, G. J. (1988). Field recognition of paleosols. In Reinhardt, J. and Sigleo, W. R., editors, *Paleosols and Weathering Through Geologic Time: Principles and Applications*, Geological Society of America, Special Paper, 216, pages 1–20. Geological Society of America.
- Robin, C., Guillocheau, F., Allemand, P., Bourquin, S., Dromart, G., Gaulier, J.-M., and Prijac, C. (2000). Echelles de temps et d'espace du contrôle tectonique d'un bassin flexural intracratonique; le bassin de Paris. *Bull. Soc. Géol. Fr.*, 171, 181–196.
- Roig, J. Y., Alabouvette, B., Collomb, P., Bogdanoff, S., Guérangé-Lozes, J., Genna, A., Couturié, J. P., Monchoux, P., and Ciszak, R. (2001). *Notice explicative, Carte géol. France (1/50,000), feuille Decazeville (859)*. BRGM, Orléans. 94 p. Carte géologique par J. Y. Roig et al. (2001).
- Rolando, J.-P. (1988). *Sédimentologie et stratigraphie du bassin Permien de Saint-Affrique (Aveyron)*. Thèse de 3ème cycle, Université Paul Sabatier, Toulouse. 226 p.

- Schäfer, A. (2011). Tectonics and sedimentation in the continental strike-slip Saar-Nahe Basin (Carboniferous-Permian, West Germany). *Z. Dtsch. Ges. Geowiss.*, 162, 127–155.
- Schäfer, A. and Korsch, R. J. (1998). Formation and sediment fill of the Saar-Nahe basin (Permo-Carboniferous, Germany). *Z. Deutsch. Geol. Ges.*, 149(2), 233–269.
- Schneider, J. and Romer, R. L. (2010). The Late Variscan Molasses (Late Carboniferous to Late Permian) of the Saxo-Thuringian Zone. In Linnemann, U. and Romer, R. L., editors, *Pre-Mesozoic Geology of Saxo-Thuringia—From the Cadomian Active Margin to the Variscan Orogen*, pages 323–346. Schweizerbart, Stuttgart.
- Schneider, J. W., Körner, F., Roscher, M., and Kroner, U. (2006). Permian climate development in the northern peri-Tethys area—The Lodève basin, French Massif Central, compared in a European and global context. *Palaeogeogr. Palaeoclimatol. Palaeoecol.*, 240, 161–183.
- Schneider, J. W., Lucas, S. G., Scholze, F., Voigt, S., Marchetti, L., Klein, H., Opluštil, S., Werneburg, R., Golubev, V. K., Barrick, J. E., Nemyrovska, T., Ronchi, A., Day, M. O., Silantiev, V. V., Rößler, R., Saber, H., Linnemann, U., Zharinova, V., and Shen, S.-Z. (2020). Late Paleozoic-early Mesozoic continental biostratigraphy—Links to the Standard Global Chronostratigraphic Scale. *Palaeoworld*, 29, 186–238.
- Schneider, J. W. and Scholze, F. (2018). Late Pennsylvanian-Early Triassic conchostracan biostratigraphy: a preliminary approach. In *The Permian Timescale*, Geological Society, London, Special Publications, 450, pages 365–386. Geological Society of London.
- Scotese, C. R. and Langford, R. (1995). *Pangea and the paleogeography of the Permian, The Permian of northern Pangea; Volume I, Paleogeography, paleoclimates, stratigraphy*. Springer-Verlag, Germany.
- Serrano, O., Delmas, J., Hanot, F., Vially, R., Herbin, J. P., Houel, P., and Tourlière, B. (2006). Le bassin d'Aquitaine : Valorisation des données sismiques, cartographie structurale et potentiel pétrolier. Rapport Régional d'Évaluation Pétrolière, Ed. BRGM, 245 p.
- Soreghan, G. S., Beccaletto, L., Benison, K. C., Bourquin, S., Feulner, G., Hamamura, N., Hamilton, M., Heavens, N. G., Hinnov, L., Huttenlocker, A., Looy, C., Pfeifer, L. S., Pochat, S., Sardar Abadi, M., Zambito, J., and the Deep Dust workshop participants (2020). Report on ICDP Deep Dust workshops: probing continental climate of the late Paleozoic icehouse-greenhouse transition and beyond. *Sci. Drill.*, 28, 93–112.
- St. Georges-sur-Moulon1 (1964). Rapport de fin de sondage, EMESCO 250, Compagnie d'exploration pétrolière. 20 p.
- Stampfli, G. M., Hochard, C., Vérard, C., Wilhem, C., and vonRaumer, J. (2013). The formation of Pangea. *Tectonophysics*, 593, 1–19.
- Stille, H. (1924). *Grundfragen vergleichender Tektonik*. Borntraeger, Berlin.
- Stollhofen, H. (1998). Facies architecture variations and seismogenic structures in the Carboniferous-Permian Saar-Nahe Basin (SW Germany): evidence for extension-related transfer fault activity. *Sediment. Geol.*, 119, 47–83.
- Tabor, N. J. and Montañez, I. P. (2004). Morphology and distribution of fossil soils in the Permian-Pennsylvanian Wichita and Bowie Groups, north-central Texas, USA: implications for western equatorial Pangean palaeoclimate during icehouse-greenhouse transition. *Sedimentology*, 51(4), 851–884.
- Timmerman, M. J. (2004). Timing, geodynamic setting and character of Permo-Carboniferous magmatism in the foreland of the Variscan Orogen, NW Europe. In *Permo-Carboniferous Magmatism and Rifting in Europe*, Geological Society, London, Special Publications, 223, pages 41–74. Geological Society of London.
- Toutin, N. (1980). *Le Permien continental de la Provence orientale (France)*. Thèse de doctorat. vol. 2, 594 p.
- Van Den Driessche, J. and Brun, J. P. (1989). Un modèle cinématique de l'extension paléozoïque supérieur dans le Sud du Massif Central. *C. R. Acad. Sci. Sér. 2 Mécanique, Physique, Chimie, Sciences de l'univers, Sciences de la Terre*, 309, 1607–1613.
- Van Den Driessche, J. and Brun, J. P. (1992). Tectonic evolution of the Montagne Noire (French Massif Central): a model of extensional gneiss dome. *Geodynam. Acta*, 5, 85–97.
- Vanderhaeghe, O., Laurent, O., Gardien, V., Moyen, J.-F., Gébelin, A., Chelle-Michou, C., Couzinié, S., Villaros, A., and Bellanger, M. (2020). Flow of partially molten crust controlling construction, growth and

- collapse of the Variscan orogenic belt: the geologic record of the French Massif Central. *Bull. Soc. Géol. Fr. Earth Sci. Bull.*, 191, article no. 25.
- Voigt, S., Schindler, T., Tichomirowa, M., Käßner, A., Schneider, J. W., and Linnemann, U. (2022). First high-precision U-Pb age from the Pennsylvanian-Permian of the continental Saar-Nahe Basin, SW Germany. *Int. J. Earth Sci. (Geol. Rundsch)*, 111, 2129–2147.
- Ziegler, P. A. (1990). *Geological Atlas of Western and Central Europe*. Shell Internationale Petroleum Maatschappij B.V. Geological Society Publishing House (Bath), The Hague, Netherlands.



Research article

Tribute to Jean Dercourt

Molecular fossils of Aptian–Albian blue marls of the Vocontian Basin (France), depositional conditions and connections to the Tethys Ocean

Armelle Riboulleau^{*,a}, Melesio Quijada^{*,a}, Alexis Caillaud^a, François Baudin^{*,b}, Jean-Noël Ferry^c and Nicolas Tribouvillard^{*,a}

^a Laboratoire d'Océanologie & Géosciences, Université de Lille, UMR LOG 8187 Univ Lille-CNRS-ULCO-IRD, 59000, Lille, France

^b Sorbonne Université, CNRS, IStEP, 75005, Paris, France

^c TOTAL S.A., CSTJE, 64000 Pau, France

E-mails: armelle.riboulleau@univ-lille.fr (A. Riboulleau), melesioquijada@gmail.com

(M. Quijada), caillaud.alexis@gmail.com (A. Caillaud),

francois.baudin@sorbonne-universite.fr (F. Baudin), jean-noel.ferry@total.com

(J.-N. Ferry), nicolas.tribouvillard@univ-lille.fr (N. Tribouvillard)

Abstract. The Mesozoic witnessed some episodes of marked accumulation and burial of organic matter (OM) in the Tethys Ocean and satellite basins, such as the Vocontian Basin (SE-France). These famous episodes, termed Oceanic Anoxic Events (OAEs), resulted from various factors, acting in complex synergies; the consensus about the key factors has not been reached yet. The Aptian–Albian Blue Marls Formation (Fm.) of the Vocontian Basin recorded the various substages of OAE1, plus additional organic-rich levels of regional extension. The semi-pelagic marlstones of the Blue Marls Fm. allow to carry out a detailed examination of the molecular fossils, to assess the respective weights of the factors involved in the OM storage process. In this work, we examined the lipid biomarkers of six organic-rich levels ranging from the Goguel Level to the Paquier Level in stratigraphic order. Biomarkers reputed to be characteristic of some OAEs are observed here: 2-methylhopanoids in the Goguel Level (OAE1a) and archaeal lipids in the Jacob, Kilian and Paquier Levels (OAE1b). This study shows that, in the Vocontian Basin, OM deposition resulted mostly from local factors and that each level has its own peculiarities; however, overarching connections with the Tethys Ocean were critical for the recording of global anoxic events.

Keywords. Vocontian basin, Organic matter, Lower Cretaceous, OAE1a, OAE1b, Biomarkers.

Manuscript received 16 January 2023, revised 23 August 2023, accepted 6 September 2023.

1. Introduction

The mid-Cretaceous Blue Marls Formation of the Vocontian Basin (SE-France) is a thick sequence (650–800 m cumulated thickness) dominated by grey-colored pelagic to hemipelagic marls that were

deposited in a fast subsiding basin [Bréhéret, 1995, Friès, 1986]. These deposits very well recorded both local and global environmental changes [Bréhéret, 1995, Friès, 1986]. Consequently, two Global Boundary Stratotype Sections and Points (GSSPs), namely the Col de Pré-Guittard section for the base of the Albian Stage [Kennedy et al., 2017] and the Mont Risou section for the base of the Cenomanian stage [Kennedy et al., 2004] are located in the Blue

* Corresponding author.

Marls Formation. One of the most remarkable features of the Blue Marls Formation is the recurrence of pluridecimeteric dark colored layers, which have been collectively termed “organic levels” (OL), though the organic matter (OM) enrichment in these levels is highly variable [Br  h  ret, 1995, Caillaud *et al.*, 2022]. All Cretaceous oceanic anoxic events (OAEs) were recorded in the Vocontian Basin [Leckie *et al.*, 2002, F  llmi, 2012], but in particular OAEs 1a to 1d and OAE2 are characterized by organic-rich deposits within the Blue Marls Formation. Nevertheless, additional OLs not related to global events are also observed.

Using sedimentation rate, grain size analysis, Rock-Eval analysis, trace metal content, and preliminary biomarker data, Caillaud *et al.* [2022] compared six of these OLs, namely the Goguel Level, Niveau Noir, Fallot Interval, Jacob Level, Kilian Level, and Paquier Level (Supplementary Figure 1). They concluded that the OLs were formed under variable conditions, but that in the absence of high primary productivity and bottom water anoxia, the supposedly “favorable” factors (e.g. rapid burial, sediment condensation, dominance of refractory terrestrial OM, ...), only caused modest OM enrichments in the sediment [Caillaud *et al.*, 2022]. We here present the continuation of the work by Caillaud *et al.* [2022] with detailed molecular fossil results of the same six OLs. These data complement the previous dataset and allow to reconsider the depositional model of some of these OLs.

2. Materials and methods

2.1. Sampling and bulk analysis

For bulk analysis, more than 130 samples were collected from 8 sections located in the Vocontian Basin (Figure 1, Supplementary Figure 2). Detailed information on the different sampled OLs and sections can be found in Supplementary text 1 and in Caillaud *et al.* [2022]. For each sample, 500 g–1 kg of rock were sampled. The surface sediment was removed on a thickness of 30–50 cm, in order to sample material not affected by weathering. The rock samples were kept in aluminum foils to avoid contamination. All samples were characterized by Rock-Eval analysis at Sorbonne University (ISTeP) using a RE6 device and the bulk rock method [Caillaud *et al.*, 2022].

2.2. Biomarker analysis

64 samples, corresponding to black shales, dark-colored marls and bioturbated marls (Supplementary Figure 2), were selected for molecular fossil analysis. The procedure for lipid biomarker analysis is detailed in Supplementary text 2. Briefly, between 50 and 70 g of sediments were extracted using a mixture of dichloromethane and methanol 2:1 v/v with an accelerated solvent extractor. Maltenes-like fractions were recovered after reducing the total extracts to dryness by rotary evaporation and solubilisation in cyclohexane. The maltenes-like were separated in three fractions over an activated silica column using solvents of increasing polarity. The aliphatic and aromatic fractions were analyzed by gas chromatography–mass spectrometry (Supplementary text 2).

3. Results

3.1. Bulk OM

The total organic carbon (TOC) and results of Rock-Eval analysis of the total sample set were previously described [Caillaud *et al.*, 2022]. Only the most important features of the samples selected for the present study are briefly recalled here. The highest TOC contents are observed in the samples from the Goguel Level at les Sauzeries section (av. 3.3%), followed by the Paquier Level (av. 2.7%). The Goguel Level at Saint Jaume and Notre Dame sections, part of the Fallot Interval, the Jacob Level, and the Kilian Level show TOC contents between 1 and 2%. The Goguel Level at Glaise section, the upper part of the Fallot Interval, and the Niveau Noir show TOC contents lower than 1%, which are comparable to the TOC content of the surrounding marls. Generally, the Hydrogen Indices (HI) are positively correlated with the TOC contents (Figure 2; Supplementary Figure 3). The highest HI are observed in the Goguel Level at les Sauzeries (387 mgHC/gTOC on average) and Paquier Level (290 mgHC/gTOC), indicating type II kerogen. The other sections are characterized by low to very low HI (67–202 mgHC/gTOC), reflecting type III to type II–III kerogen. The majority of samples bears T_{\max} values below 435 °C suggesting thermal immaturity. However, the T_{\max} values from Glaise and les Sauzeries sections are generally higher (435

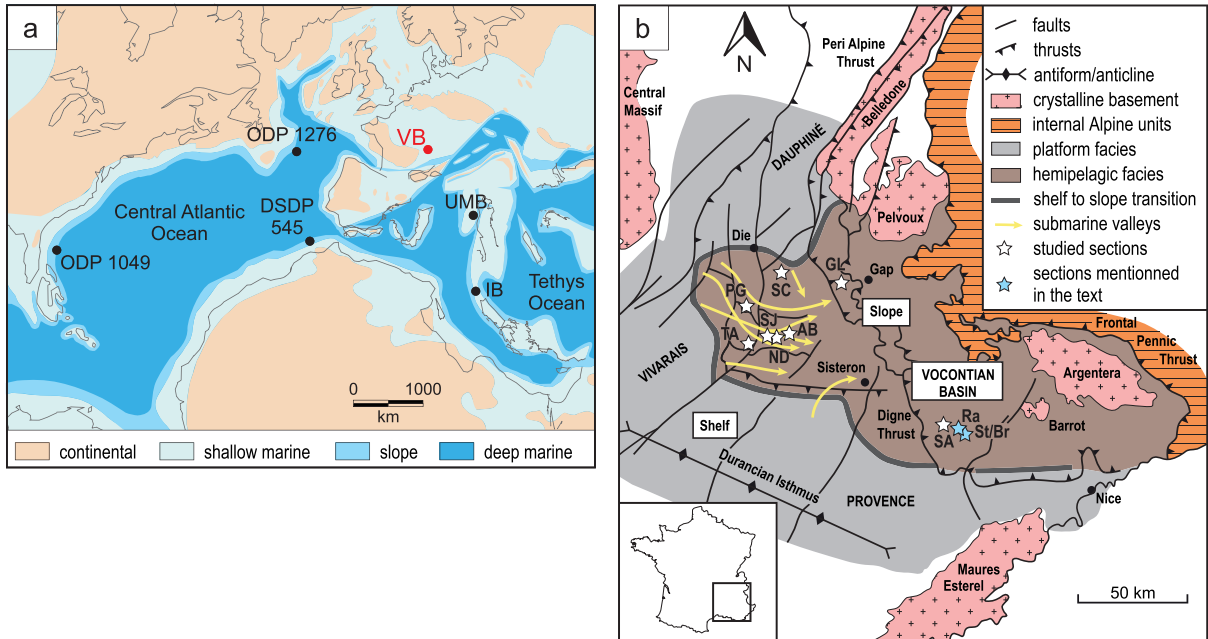


Figure 1. (a) Paleogeographic map of Late Aptian [simplified from Golonka, 2007] showing the location of the Vocontian Basin (VB) and the main other areas cited in the text. Central Atlantic Ocean: ODP Sites 1049 and 1276, DSDP Site 545; UMB: Umbria-Marche Basin; IB: Ionian Basin. (b) Map of the geological context of the Vocontian Basin during the Aptian times. Modified from Friès and Parize [2003]. AB: l’Arboudeysse; Br: les Briers; GL: Glaise; ND: Notre Dame; PG: Pré-Guittard; Ra: Ravel; SA: les Sauzeries; SC: Serre Chaitieu; SJ: Saint Jaume; St: Saint-André-les-Alpes; TA: Tarendol.

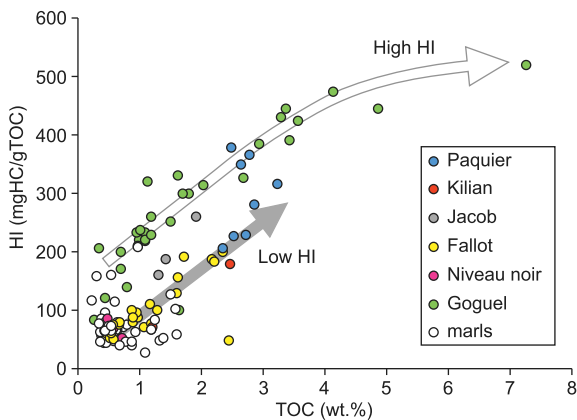


Figure 2. Cross plot of the total organic carbon (TOC) content and Hydrogen Index (HI) for the rock samples of the Blue Marls Formation. The two trends depicted by the arrows are discussed in the text. See electronic version for colors.

and 439 °C, respectively), indicating that the OM has reached early oil-generating window.

Two parallel trends are observed for the positive correlation between TOC content and HI (Figure 2; Supplementary Figure 3). They are termed as “high HI” and “low HI” for the sake of simplicity. The high HI trend includes samples from the Goguel Level at all sections plus a few samples from the Paquier Level. The low HI trend includes samples from the Kilian Level, Fallot Interval, Niveau Noir, part of the Paquier Level, and some samples from the Goguel Level at Saint Jaume section. The few samples from the Jacob Level are located in between these two trends. These two trends are also visible when Rock-Eval data from other studies of the Blue Marls Formation [Bréhéret, 1994, Giraud *et al.*, 2018, Westermann *et al.*, 2013] are included.

3.2. Molecular fossils

A large variety of lipid biomarkers was found in the saturated and aromatic fractions of the studied samples. The molecular fossil content is similar in all samples. However, a few samples contain additional compounds, as will be described below. A detailed description of compounds distributions is presented in Supplementary text 3.

3.2.1. Linear and branched alkanes

Linear alkanes (*n*-alkanes) generally dominate the saturated fractions. *n*-Alkanes comprise short chain compounds from C₁₃ to C₂₂, with a maximum in C₁₆ or C₁₇ (Figure 3), which are generally ascribed to phytoplanktic sources [Blumer *et al.*, 1971, Giger *et al.*, 1980], and long chain compounds from C₂₃ to C₃₃, presenting a predominance of odd-carbon-numbered compounds. Though odd-carbon-numbered long-chain *n*-alkanes may originate from micro- or macroalgae [e.g. Aichner *et al.*, 2010, Allard and Templier, 2000], these compounds mainly derive from the epicuticular waxes of terrestrial plants [Eglinton and Hamilton, 1967]. The terrestrial vs. aquatic ratio [TAR; Bourbonniere and Meyers, 1996] is generally lower than 0.4, reflecting a low contribution of long chain *n*-alkanes (Supplementary Table 1). Marl samples at Pré-Guittard have an average TAR of 5, and TAR > 0.4 are observed in the Fallot Interval and Paquier Level. The lowest TAR values are observed in the Goguel Level at les Sauzeries and Saint Jaume. The predominance of odd-carbon-numbered long *n*-alkanes, as indicated by OEP₂₇ [Scalan and Smith, 1970], is present in the majority of samples (Supplementary Table 1). The highest OEP₂₇ are observed in the Fallot Interval (av. 1.9) and Paquier Level (av. 1.8). In the samples of the Goguel Level at les Sauzeries and Glaise, the OEP₂₇ ~ 1 is ascribed to the high thermal maturity of the OM in these sections.

Series of 2-methyl- and 3-methyl-alkanes, ranging from C₁₅ to C₂₁, maximizing around C₁₇, are observed in most of the samples. These compounds generally derive from branched *iso*- and *anteiso*- fatty acids of gram positive bacteria [Goossens *et al.*, 1986, Kaneda, 1991]. The highest relative abundances of branched alkanes are observed in the Niveau Noir while low abundances are observed in the Fallot Interval (Supplementary Table 1).

3.2.2. Acyclic and monocyclic isoprenoids

Acyclic isoprenoids mainly consist of a series of head-to-tail linked (regular) compounds ranging from C₁₄ to C₂₁ and are dominated by pristane (Pr) and phytane (Ph). Regular isoprenoids are generally less abundant than short *n*-alkanes (Supplementary Table 1; Figure 3a). In the Paquier and Jacob Levels, however, the relative abundance of regular isoprenoids is higher (Figure 3, Supplementary Table 1) and 2,6,10-trimethyltetradecane (C₁₆) is the dominant regular isoprenoid in the samples of the Jacob Level. The samples from the Paquier Level also contain a series of tail-to-tail linked C₂₄–C₂₆ irregular isoprenoids (TMI, PMI and ETMI) which were previously described by Vink *et al.* [1998, Figure 3] in the same interval. An additional compound belonging to this series, pentamethylhenicosane (PMH), is also tentatively identified (Supplementary Figure 4). Three isoprenoid compounds with a cyclohexyl ring ranging from C₁₇ to C₁₉ previously described by Vink *et al.* [1998] are also present with significant contents in the samples of the Paquier Level. Numerous other compounds showing comparable structures were tentatively identified based on their mass spectra (Supplementary Figure 5). The latter compounds, ranging from C₁₄ to C₂₀, are also present in one sample of the Jacob Level.

Pristane and phytane are often related to chlorophyll [Didyk *et al.*, 1978], which is present in many photosynthetic organisms, but can also originate from the degradation of tocopherols, carotenoids or biphytane structures [Goossens *et al.*, 1984, Li *et al.*, 1995, ten Haven *et al.*, 1987], so they are not source-specific. PMI derives from the membrane lipids of archaea [Holzer *et al.*, 1979, Brassell *et al.*, 1981]. PMI and other archaea-derived isoprenoids, such as biphytanes, presenting a highly depleted carbon isotopic signature point to methanotrophic archaea as the source of these compounds [e.g. Elvert *et al.*, 1999, Birgel *et al.*, 2006]. Nevertheless, in deposits coeval to the Paquier Level, phytane, PMI and biphytanes have a heavy carbon isotopic signature [Kuypers *et al.*, 2002]. Isotopically heavy PMI is present in the deep part of the chemocline of the Black Sea and Cariaco Basin, and is related to chemoautotrophic archaea [Wakeham *et al.*, 2007, 2012]. Vink *et al.* [1998] suggested that

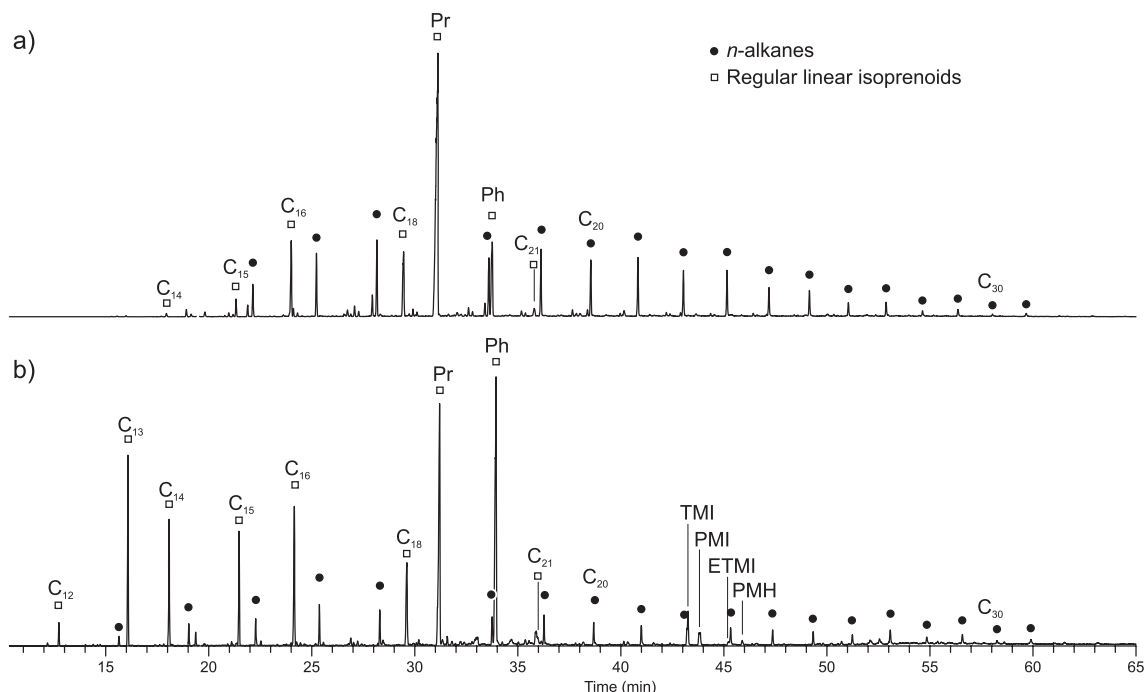


Figure 3. Mass chromatogram m/z 57 of selected aliphatic fractions showing the distribution of acyclic compounds. (a) Sample TAFE2OG003—Kilian Level; (b) sample ARBOG002A—Paquier Level. Pr: pristane; Ph: pyhtane; TMI: 2,6,15,19-tetramethylicosane; PMI: 2,6,10,15,19-pentamethylicosane; ETMI: 10-ethyl-2,6,15,19-tetramethylicosane; PMH: pentamethylhenicosane, C_x = number of carbon atoms.

TMI and ETMI originated from the same source as PMI. Similarly, we consider likely that the other isoprenoids, including monocyclic compounds, present in abundance in the samples of the Paquier and Jacob Levels, also originate from chemoautotrophic archaea.

Most of the samples have a Pr/Ph ratio higher than 1 (Figure 4, Supplementary Table 1). The highest values of Pr/Ph, up to 8.6, are observed in the marl samples at Pré-Guittard, followed by the Fallot Interval. Only some samples from the Jacob and Paquier Levels have Pr/Ph close to or lower than 1 (Figure 4, Supplementary Table 1).

3.2.3. Steroids

A wide variety of steroids is observed in most of the samples. The compounds include diaster-13(17)-enes, diasteranes, regular steranes, ring-C monoaromatic steroids and triaromatic steroids, as well as methylated counterparts. The highest relative abundances of steroids are observed in the Paquier Level and the Goguel Level at Notre Dame. Low relative

abundances of steroids are generally observed in the marls.

Regular steranes are generally dominated by C₂₉ compounds (Figure 5, Supplementary Figure 6). In the Paquier Level, however, C₂₇ isomers are dominating regular steranes. The relative abundance of C₂₇, C₂₈ and C₂₉ regular steranes [Huang and Meinschein, 1979] suggests a mixed contribution of algal and terrestrial OM for all samples (Figure 5). Nevertheless, 24-*n*-propylcholestanes are observed in significant proportion in most of the samples (Supplementary Table 1). Precursors of 24-*n*-propylcholestane have been observed in marine algae [Raederstorff and Rohmer, 1984], desmosponges [Zumberge, 2019] and a foraminifer [Grabenstatter *et al.*, 2013]. 24-*n*-Propylcholestane could also result from diagenetic methylation of C₂₉ sterols [Bobrovskiy *et al.*, 2021]. Nevertheless, 24-*n*-propylcholestanes are generally considered as indicative of deposition under marine conditions [Moldowan *et al.*, 1985]. The highest abundances of 24-*n*-propylcholestanes are observed in the Paquier Level (Supplementary Table 1).

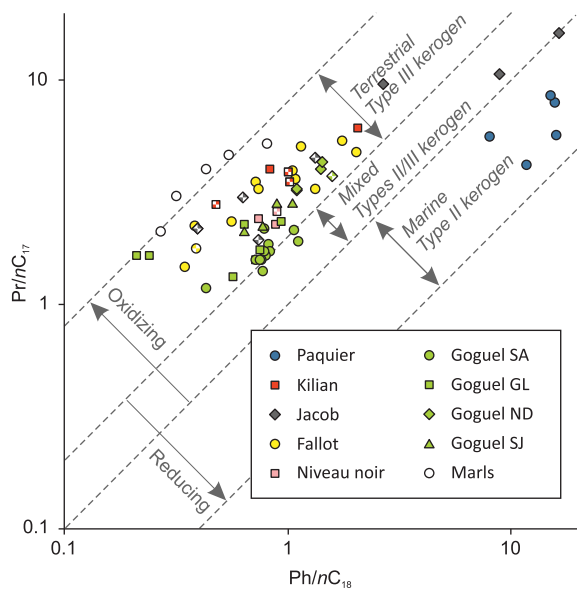


Figure 4. Pristane/ nC_{17} vs. phytane/ nC_{18} cross plot of samples from the Vocontian Basin. Partially filled symbols correspond to marls collected close to the organic levels.

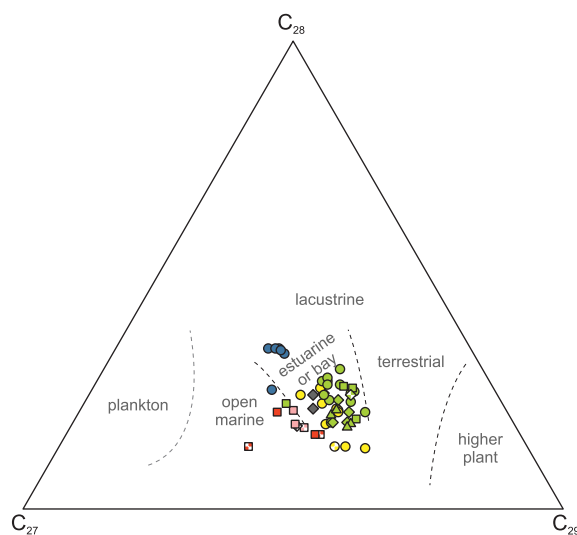


Figure 5. Ternary plot showing the distribution of C_{27} , C_{28} , and C_{29} regular steranes in the aliphatic fractions. Legend of symbols as in Figure 4.

Methylsteroids comprise saturated and aromatic compounds methylated at position 2-, 3-, and 4-, as well as dinosteroids (based on the 4,23,24-

trimethylcholestane skeleton; Supplementary Figures 6, 10). 2-Methyl- and 3-methyl-steroids originate from diagenetic rearrangements in the sediment [Summons and Capon, 1988, 1991] and seem present in relatively stable proportion in the samples. Conversely, 4-methylsteroids and dinosteroids mainly originate from dinoflagellates [Summons *et al.*, 1987], and are present in variable proportion in the samples. The highest proportions of 4α -methylsteranes, dinosteranes and triaromatic dinosteroids are observed in the Paquier and Goguel Levels at Notre Dame and Saint Jaume.

3.2.4. Hopanoids

A wide variety of hopanoids is observed in the samples (Supplementary text 3). The dominant hopanoids are saturated $\alpha\beta$ -hopanes ranging from C_{27} to C_{35} (C_{28} absent) with a maximum in C_{30} and a progressive decrease of the abundance of homohopanoids with increasing chain length (Figure 6). The low abundance of C_{34} and C_{35} hopanes is indicative of a deposition in non-hypersaline conditions [ten Haven *et al.*, 1985]. The distribution of hopanoids isomers is comparable in most of the samples and reflects the thermal immaturity of the OM; however, the distribution differs at les Sauzeries and Glaise sections, reflecting the higher thermal maturity at these locations (Supplementary Table 1).

2-Methyl hopanes ranging from C_{28} to C_{35} , with a maximum in C_{31} , are present in significant proportion in most of the studied samples from the Goguel Level, with 2-methyl hopane index [2-MHI; Ando *et al.*, 2022] ranging between 6 and 23 (Figure 6; Supplementary Table 1). If present in the other OLs, the abundance of 2-methyl hopanes is very low. 2-Methyl hopanes are absent from the extract of marl samples (Supplementary Table 1). Traces of 3-methyl-hopanes are detected in many samples (Figure 6).

Desmethyl hopanoids mostly originate from bi-hopanoids present in the cell walls of many bacteria, including cyanobacteria [Ourisson and Rohmer, 1992, Talbot *et al.*, 2008, Kusch and Rush, 2022], so desmethyl hopanes are poorly specific bacterial markers. In contrast, methyl-hopanes are more specific: though their origin is still discussed, 2-methyl-hopanes mainly originate from cyanobacteria and alphaproteobacteria [Summons *et al.*,

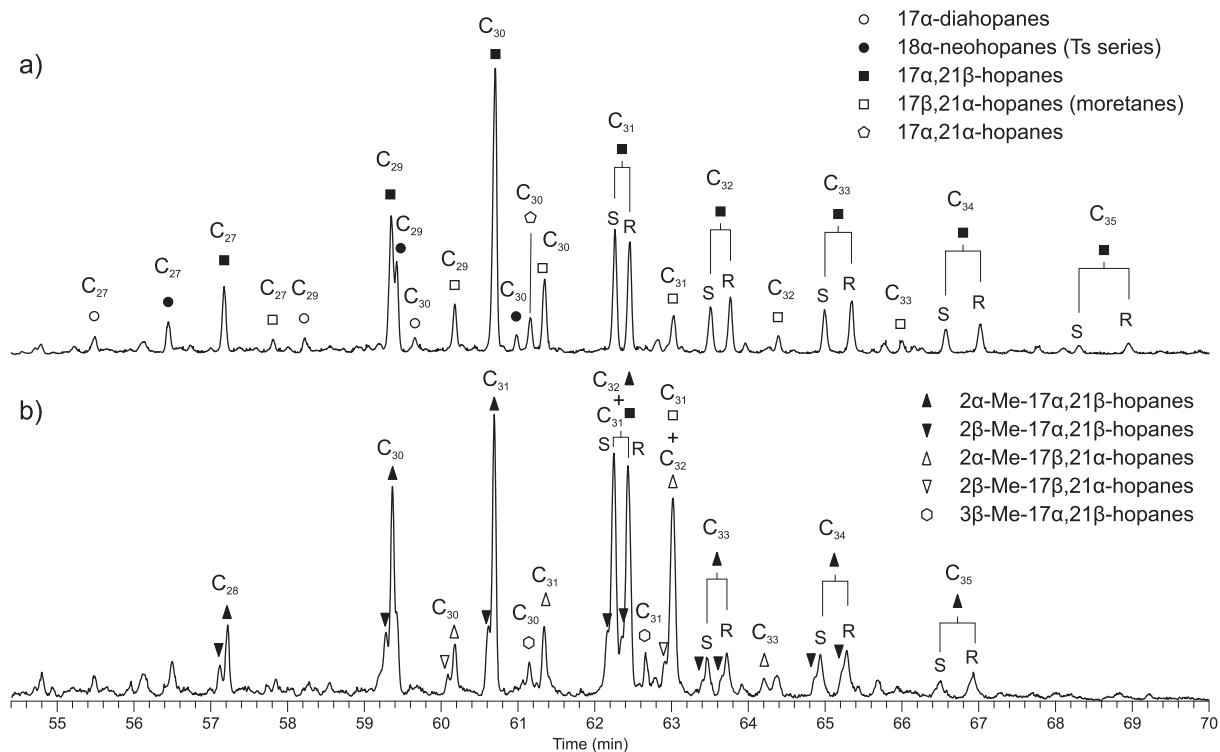


Figure 6. Partial mass chromatograms showing the distribution of (a) hopanes and moretanes (m/z 191) and (b) methylhopanes (m/z 205). Sample NDOG003—Goguel Level.

1999, Naafs *et al.*, 2022, Kusch and Rush, 2022], while 3-methylhopanes originate from aerobic methanotrophs [Neunlist and Rohmer, 1985, Cordova-Gonzalez *et al.*, 2020].

3.2.5. Aryl isoprenoids

Aryl isoprenoids are detected in most of the OLS, though generally in low abundance. This series ranges from C₁₃ to C₂₀, with the C₂₄ and C₂₉ compounds also often present in low proportion. Values of the aryl isoprenoid ratio [AIR; Schwark and Frimmel, 2004] are generally higher than 1, reflecting the dominance of short aryl isoprenoids (C₁₃–C₁₅); nevertheless, AIR are lower than 1 in the Paquier Level (Supplementary Table 1). The highest proportions of arylisoprenoids are observed in the Paquier Level, as well as the Goguel Level at Glaise and Notre Dame.

Aryl isoprenoids are often considered to derive from carotenoids of anoxygenic photosynthetic bacteria [Summons and Powell, 1987, Brocks and Schaefer,

2008]. Nevertheless, other sources, in particular the aromatisation of carotene, are also likely when these compounds are observed in rocks deposited in well oxygenated environments [Koopmans *et al.*, 1996b]. From the very low abundance of aryl isoprenoids longer than C₂₀, the absence of C₄₀ aryl isoprenoids as well as of commonly observed isorenieratene derivatives [Koopmans *et al.*, 1996a], the arylisoprenoids observed in the sediments of the Vocontian Basin likely do not originate from anoxygenic photosynthetic bacteria. In particular, the abundant aryl isoprenoids and substituted alkylbenzenes (Supplementary text 3) observed in the samples from the Paquier Level could originate from the degradation and aromatisation of archaea-derived biphytanyl compounds.

3.2.6. Other terpenoids

Terpenoids of microbial origin, namely dammar-13(17)-enes and 13 β ,17 α (H)-dammaranes [Meunier-Christmann *et al.*, 1991] are observed

in the samples of the Paquier Level only, while cheilanthanes [Peters *et al.*, 2005] are widespread in the samples from the Goguel Level, Niveau Noir, and the Paquier Level.

The aromatic terpenoids retene, cadalene, and 6-isopropyl-1-isoheptyl-2-methylnaphthalene are detected in most of the samples. These three compounds mainly derive from higher plant terpenoids and are thus generally related to a terrestrial source [van Aarssen *et al.*, 2000]. Their relative abundance is maximum in the marl samples from Pré-Guittard and minimum in the Goguel Level at Glaise and les Sauzeries. High relative abundances are also observed in the Paquier Level (Supplementary Table 1). Cadalene, a non-specific terrestrial plant biomarker [van Aarssen *et al.*, 2000] is largely dominant in all the samples, though its relative abundance is slightly lower in the Goguel Level at les Sauzeries section.

Series of methylated 2-methyl-(trimethyltridecyl)-chromans (MTTC) are present in most of the samples, except those from Pré-Guittard, les Sauzeries and Glaise sections. These compounds likely originate from the rearrangement of the phytol side chain of chlorophyll [Li *et al.*, 1995] but are widely used as paleosalinity indicators. The dominance of the 5,7,8-trimethyl-isomer in the samples from the Vcontian Basin indicates normal salinity conditions [Sinninghe Damsté *et al.*, 1993].

3.2.7. Polycyclic aromatic hydrocarbons

Condensed polycyclic aromatic hydrocarbons ranging from triaromatic (phenanthrene and anthracene) to heptaaromatic (coronene) are detected in most of the samples (Supplementary Table 1, Supplementary Figure 13). These compounds generally have a pyrogenic origin [Wakeham *et al.*, 1980, bin Abas *et al.*, 1995] and can be used as tracers of terrigenous inputs. The highest relative abundances of PAHs are associated to a predominance of benzo[ghi]perylene and coronene, and are observed in the marl samples from Pré-Guittard section, Tarandol (Kilian and Jacob Levels), and Serre Chaitieu sections (Fallot Interval). Low relative abundances of PAHs are observed in the samples of the Goguel Level, Niveau Noir and Paquier Level.

Dibenzofuran is detected in most of the samples, except the marls from Pré-Guittard. Its highest

abundance is observed in the Niveau Noir. Dibenzofuran and its alkylated counterparts have been related to lichens and can be used as tracers of terrigenous inputs [Radke *et al.*, 2000]. Nevertheless, our data suggest that dibenzofuran here results from the degradation of an algal or microbial biomass (see Section 4).

3.2.8. Sulfur containing compounds

Organo-sulfur compounds (OSCs) are present in all the samples from the Paquier Level. They correspond to a C₂₀ isoprenoid thiophene and several isomers of C₂₀ isoprenoid benzothiophenes. OSCs are not observed in the other samples.

4. Discussion

4.1. Thermal maturity

Based on Rock-Eval analysis and molecular indicators (Supplementary Table 1), the majority of the studied outcrops are thermally immature, allowing to compare the biomarker content with each other in these different settings. Nevertheless, consistent with previous studies [Bréhéret, 1995], our data indicate that the oil-generating window was reached at les Sauzeries and Glaise sections (Supplementary Table 1). The biomarker content of the Goguel Level at these two outcrops must therefore be considered in the light of this higher thermal maturity.

4.2. Comparison of the different OLS

Previous characterisations of the OM in the Blue Marls Formation based on palynofacies, palynology or organic geochemistry, showed that the OM was mainly of marine origin, with variable contributions of terrestrial plant debris [Bodin *et al.*, 2023, Bréhéret, 1994, Friedrich *et al.*, 2003, Heimhofer *et al.*, 2006, Herrle *et al.*, 2010, 2003b, Kuypers *et al.*, 2002, Okano *et al.*, 2008b, Tribovillard and Gorin, 1991]. The biomarkers identified in the present study confirm the mainly autochthonous origin of the OM, while the contributions from higher plants are present, but are low in most of the samples. According to previous studies (*op. cit.*), the variations of the organic content reflect several factors: sea-level evolution during the Aptian to Albian interval, variations of primary productivity, orbitally induced climate fluctuations,

and oceanic anoxic events. In addition, turbiditic corridors are well documented in the western part of the Vocontian Basin [Bréhéret, 1995, Friès, 1986, Friès and Parize, 2003], so that the location within the basin might also influence the organic content.

The Blue Marls Formation is characterized by alternations of light and dark levels related to orbitally induced climate oscillations [Ait-Itto *et al.*, 2023, Charbonnier *et al.*, 2023, Gale *et al.*, 2011]. These orbitally induced oscillations are also visible in the OLS, as the latter frequently present alternations of black shales or dark-colored laminated marls and bioturbated marls (Supplementary Figure 2). Since the sampling for molecular fossil analyses was mainly focussed on the darkest sub-levels, the discussion below concentrates on the conditions most prone to OM deposition.

4.2.1. *Hemipelagic marls*

Though located in the west part of the Vocontian Basin, the Pré-Guittard section does not show major turbidites in the sampled interval (Supplementary Figure 2) and can therefore be considered as representative of the hemipelagic sedimentation. The very low TOC content and HI, as well as high OI [Caillaud *et al.*, 2022, Ait-Itto *et al.*, 2023], are typical for highly degraded OM (type IV). Such observation is consistent with the high Pr/Ph ratio and the absence of C₃₅ homohopanes, indicative of well oxygenated conditions in the sediment [Didyk *et al.*, 1978, Peters and Moldowan, 1991]. The very low abundance of steroids, the notable contribution of resistant compounds, such as long *n*-alkanes from terrestrial plant waxes and fire-derived PAHs, and the CPI of *n*-alkanes close to 1, are also consistent with extensive biodegradation [Hoefs *et al.*, 2002, Peters *et al.*, 2005]. Dibenzofuran is hardly observed at Pré-Guittard, while other land-sourced compounds, e.g. long-chain *n*-alkanes, cadalene and PAHs are relatively abundant. The latter compounds are mainly delivered to the marine environment as aerosols [Simoneit and Mazurek, 1982, Simoneit, 1984], while dibenzofuran could be delivered by rivers, thus explaining this discrepancy. Nevertheless, an alternative source for dibenzofuran is suggested by our data (see below). It should be noted that in the marl samples from the Pré-Guittard section, the terrestrial signature is higher than in the marl

samples from the other sections (Supplementary Table 1).

4.2.2. *Goguel Level*

The Goguel Level is recording the Oceanic Anoxic Event (OAE) 1a in the Vocontian Basin. The OAE1a is a global event characterized by a carbonate crisis, deposition of organic-rich sediments in marine settings and a marked negative carbon isotope excursion in both carbonates and OM [see Föllmi, 2012, for a review].

The Goguel Level was sampled at four different outcrops (Figure 1, Supplementary Figure 2). Les Sauzeries was in a distal setting, far from detrital influences [Bréhéret, 1995]. Nevertheless, the OM is thermally mature. Glaise section is as well supposed as a distal setting, but was influenced by detrital inputs, as indicated by the fine turbidites. The OM is thermally mature, as for les Sauzeries. Saint Jaume and Notre Dame sections were located in a more proximal setting and contain more detrital deposits, as indicated by the numerous turbidites, though the turbidites are thin at Saint Jaume and relatively thick à Notre Dame. As a result of the detrital influence, lower TOC and HI are observed at Glaise, Notre Dame and Saint Jaume compared to les Sauzeries (Supplementary Figure 3); still, the four outcrops all belong to the “High HI” trend, the same trend as observed in the coeval Selli Level, in the Umbria-Marche Basin [Baudin *et al.*, 1998].

Consistent with previous molecular fossil studies [Heimhofer *et al.*, 2004, Okano *et al.*, 2008a,b, Ando *et al.*, 2022, 2017], the molecular signature of the Goguel Level is marked by the predominance of autochthonous algal and microbial OM, without marked difference in the four studied sections (Supplementary Table 1). In particular, all four sections show a similar low abundance of land-derived inputs. The moderate amounts of dibenzofurans in these sections suggest that this compound is not land-derived. The high sterane/hopane ratio in the least thermally mature sections reflects an important contribution of eukaryotes and in particular a significant contribution of dinoflagellates, which can be related to the observation of dinocysts and acritarchs in the palynofacies [Heimhofer *et al.*, 2006, Ando *et al.*, 2022]. A high abundance of dinosteroids was similarly observed in the coeval mid-Pacific organic-rich de-

posits of Shatsky Rise [Dumitrescu and Brassell, 2005].

Though indicators of severe water column anoxia were described in the coeval deposits from northern Tethys [Pancost *et al.*, 2004, van Breugel *et al.*, 2007], and sediment anoxia at Shatsky Rise [Dumitrescu and Brassell, 2005], molecular fossils of euxinia or anoxia, like aryl isoprenoids are not observed in the Vocontian Basin. The Goguel Level presents a “paper shale” texture, and the benthic fauna is overall rare [Friès, 1986, Bréhéret, 1995, Giraud *et al.*, 2018]. Moreover, the dominance of fluorescing amorphous OM in the palynofacies and the high HI indicate a good degree of OM preservation [Heimhofer *et al.*, 2004, 2006, Ando *et al.*, 2022]. These data point to anoxic conditions at the sediment water interface (Figure 7a), consistent with the high values of the C₃₅ homohopane ratio [Peters and Moldowan, 1991]. Episodic oxygenation is indicated by the intermittent presence of benthic foraminifera or bioturbation in the Goguel Level [Friès, 1986, Bréhéret, 1995, Giraud *et al.*, 2018], but the low enrichments of redox-sensitive trace elements [Westermann *et al.*, 2013, Caillaud *et al.*, 2020] could reflect a basin reservoir effect [Caillaud *et al.*, 2020]. Despite the dominance of anoxia in the sediment, high Pr/Ph are observed in the Goguel Level [this study; Okano *et al.*, 2008b, Ando *et al.*, 2017]; it thus appears that the Pr/Ph ratio is not a good indicator of oxygenation conditions in this level. The high Pr/Ph ratio could be related to an abundance of pristane precursors, such as tocopherols, in the organic flux to the sediment [Goossens *et al.*, 1984], or to peculiar diagenetic conditions, as also suggested by the abundance of MTTC [Li *et al.*, 1995].

The abundance of 2-methylhopanoids at the four studied sections is distinctive of the Goguel Level compared to the other OLs of the Vocontian Basin. The abundance of 2-methylhopanoids has been previously described in different organic-rich deposits of OAE1a [Kuypers *et al.*, 2004b, Dumitrescu and Brassell, 2005, 2006, Karakitsios *et al.*, 2018, Castro *et al.*, 2019], but also in the deposits of the Toarcian OAE [Farrimond *et al.*, 1994, Blumenberg and Wiese, 2012, Ruebsam *et al.*, 2018, Ajuaba *et al.*, 2022], and OAE2 [Farrimond *et al.*, 1990, Kuypers *et al.*, 2004a, Forster *et al.*, 2008]. The significance of elevated concentrations of 2-methyl hopanoids is still highly discussed [Kusch and Rush, 2022]. Neverthe-

less, a recent review suggests that the abundance of 2-methylhopanoids during these events reflects an expansion of marine anoxygenic photoautotrophic α -proteobacteria as a response to water column deoxygenation [Naafs *et al.*, 2022]. A high contribution of α -proteobacteria during deposition of the Goguel Level is consistent with the oligotrophic conditions indicated by the nannofossil content [Herrle and Mutterlose, 2003, Giraud *et al.*, 2018]. Oligotrophic conditions are generally not prone to favor deoxygenation of the water column or sediment. Conversely, high productivity is documented at the beginning of OAE1a in the Tethys Ocean [Aguado *et al.*, 2014, Sabatino *et al.*, 2015]. For this reason, it appears more likely that the deoxygenation in the Vocontian Basin resulted from the spreading of oxygen-poor waters originating from the Tethys Ocean (Figure 7a). The Goguel Level was deposited during a transgressive period [Supplementary Figure 14; Rubino, 1989, Friès and Parize, 2003, Ferry *et al.*, 2022], which favored communications between the Tethys Ocean and the Vocontian Basin. The gradient of the phosphorus content in the sediment [Westermann *et al.*, 2013], and the observation of maximum 2-MHI in the most basinal section at les Sauzeries, are consistent with this scenario. Sedimentary condensation likely also favored OM enrichment [Supplementary Figure 14; Caillaud *et al.*, 2022, 2020].

4.2.3. *Niveau noir*

The Niveau Noir has not been correlated with other organic-rich levels outside the Vocontian Basin and is considered a local event. In the present study, only the two upper sub-levels of the Niveau Noir were analyzed (NN3 and NN4, Supplementary Figure 2). The biomarker content of these two samples indicate that the OM is mainly of algal to bacterial origin. The low abundances of continent-derived long-chain *n*-alkanes and cadalene, as well as fire-derived PAHs, are consistent with the absence of turbidites from the Niveau Noir, though turbidites are present in other parts of Saint Jaume section. Molecular indicators of the redox state of the water column and sediment (homohopane ratio, AIR, ...) indicate oxygenated conditions, consistent with the absence of redox-sensitive trace metal enrichment [Caillaud *et al.*, 2022]. The abundance of branched alkanes suggests efficient bacterial activity under aerobic conditions. Nevertheless, the sterane/hopane ra-

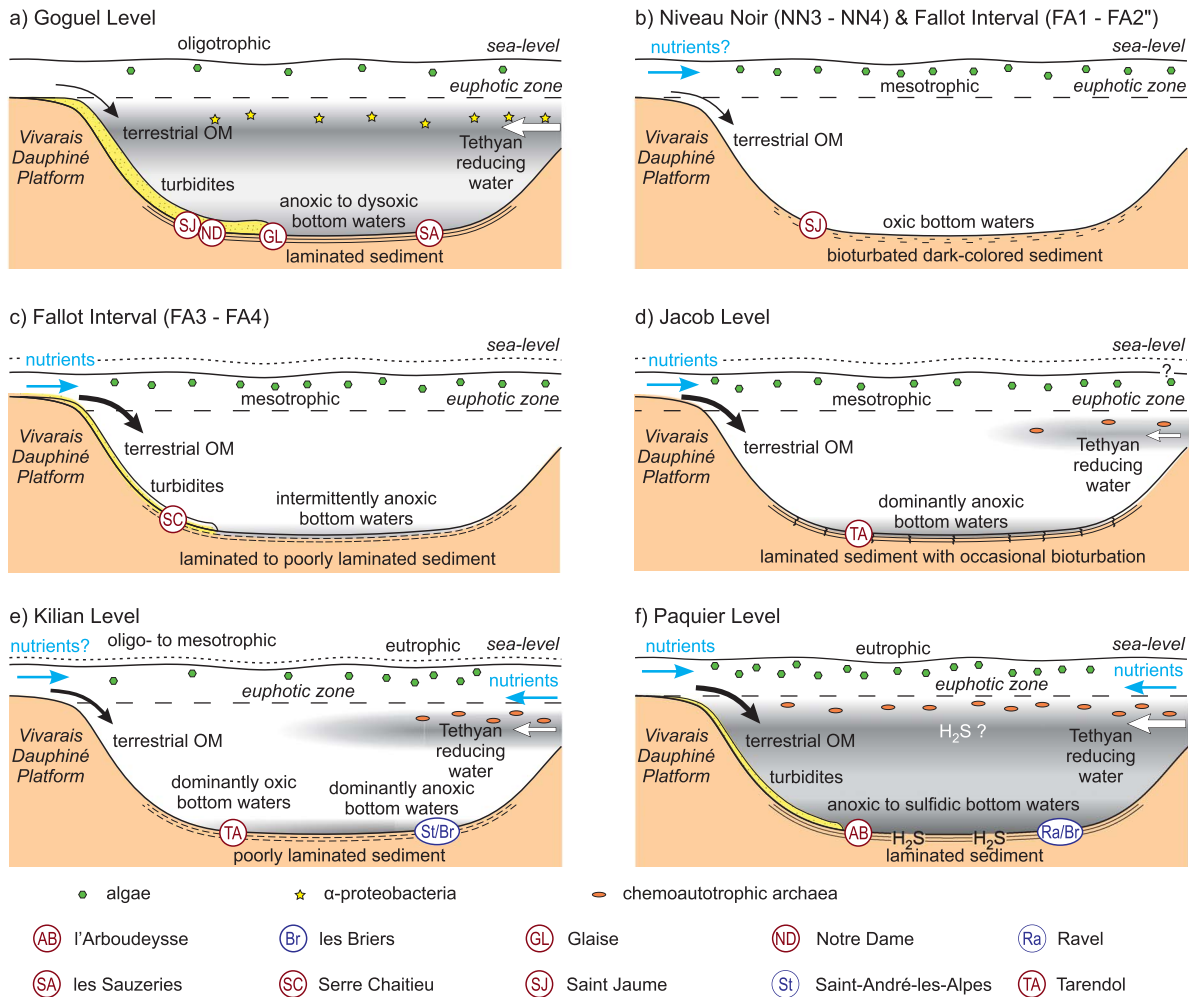


Figure 7. Depositional model for the different Ols.

tio indicates significant input of eukaryotic biomass, including algae producing 4-methyl-steranes. The chain length distribution of steranes in the Niveau Noir is characterized by a high proportion of the C₂₇ compounds (Figure 5). C₂₇ sterols are produced by a variety of marine algae as well as zooplankton [Volkman, 1986], and thus are not specific biomarkers. Nevertheless, cholesterol dominance was observed in the upper sediment or settling particles of several high productivity environments [e.g. Volkman *et al.*, 1987, Colombo *et al.*, 1996]. The high proportion of the C₂₇ steranes in the Niveau Noir could therefore reflect high primary productivity, despite the low enrichment of trace elements sensitive to productiv-

ity [Caillaud *et al.*, 2022]. Consistent with our interpretation, the nannofossil content of the NN4 level indicates higher primary productivity than for the surrounding marls [Herrle *et al.*, 2010].

To summarize, the Niveau Noir resulted from an increase in surface primary productivity (Figure 7b, Supplementary Figure 14), possibly resulting from orbitally induced increases of nutrient delivery associated to continental runoff [Herrle *et al.*, 2010]. Nevertheless, this increase in primary productivity was not sufficient to significantly alter the concentration of oxygen in the water column and sediment (Figure 7b). As a result, OM preservation was ultimately low. The Niveau Noir was deposited during a

high sea level interval [Rubino, 1989, Friès and Parize, 2003], sediment condensation likely also contributed to OM enrichment [Supplementary Figure 14; Caillaud *et al.*, 2022].

4.2.4. *Fallot interval*

The Fallot Interval has no recognised lateral equivalent outside the Vocontian Basin and is considered a local event. Though the biomarker content of the Fallot Interval is dominated by an algo-bacterial signature, the influence of terrestrial OM is more pronounced than in the other OLS. A progressive increase of the terrestrial influence from the base to the top of the Fallot Interval is indicated by the increase of TAR and of the relative abundance of PAHs, mirroring a decrease of the proportions of the marine steroids and of dibenzofuran (Supplementary Table 1). Consistently, several authors consider that the Fallot Interval was deposited during a period of falling relative sea level [Supplementary Figure 14; Rubino, 1989, Friès and Parize, 2003]. The values of the AIR and C₃₅ homohopane ratio, as well as the absence of isorenieratane [Reitner *et al.*, 2015], point to dysoxic to well oxygenated conditions, consistent with the presence of bioturbations and benthic foraminifera in most of the Fallot Interval [Bréhéret, 1995, Friedrich *et al.*, 2003]. The low HI and low abundance of steroids consistently indicate efficient OM degradation. The moderate sterane/hopane ratio suggests a moderate input of eukaryotic biomass, consistent with the mesotrophic conditions indicated by planktic foraminifera [Friedrich *et al.*, 2003]. The latter authors suggested that OM enrichment in the sediment was related to moderately high primary productivity for the lower part of the Fallot Interval, but was linked to water column stagnation in the upper part. The molecular fossil content of the lower part of the Fallot Interval is consistent with the “productivity” model of Friedrich *et al.* [2003] and points to depositional conditions comparable to the Niveau Noir, but with a higher input of terrestrial OM (Figure 7b). Nevertheless, for the second part of the Fallot Interval, the stagnation model [Friedrich *et al.*, 2003] is not supported by the redox proxies. Taking account of the lower hydrocarbon extraction yields from leaves and wood of terrestrial plants compared to algae [e.g. Cranwell *et al.*, 1990, Bush and McInerney, 2013, Jambrina-Enríquez *et al.*, 2018], the

biomarker content likely underestimates the proportion of terrestrial OM in the sediment. Though a detailed palynofacies analysis is needed to further support this hypothesis, the more pronounced terrestrial signature suggests that the upper part of the Fallot Interval results from efficient burial of terrestrial OM (Figure 7b, Supplementary Figure 14), as proposed by Caillaud *et al.* [2022].

4.2.5. *Jacob Level*

The Jacob Level is the first organic-rich deposit associated to OAE1b in the Vocontian Basin [Leckie *et al.*, 2002, Coccioni *et al.*, 2014]. Lateral equivalents of the Jacob Level have been mostly recognised in the Tethys Ocean and in the Pacific Ocean; it could correspond to a global event [see Bodin *et al.*, 2023, for a review].

Debris of higher plants have been described in the Jacob Level [Barale and Bréhéret, 1995], as well as abundant spores and pollen grains in the palynofacies [Bréhéret, 1995, Heimhofer *et al.*, 2006]. Consistent, PAHs, retene and cadalene are relatively abundant. Nevertheless, only the highest sample from the Jacob Level shows a high TAR, and the molecular signature is overall dominated by the algal contribution (Supplementary Table 1). Low proportions of dinosterane and medium values of the triaromatic dinosteroid (TADS, Supplementary text 2) ratio suggest medium to low contribution of dinoflagellates. Average C₂₇ triaromatic steroids (TAS, Supplementary text 2) values also suggest an average productivity of coccolithophorids or prasinophytes. Consistent, the microfaunal content suggests mesotrophic conditions [Erbacher *et al.*, 1998, Heimhofer *et al.*, 2006]. The samples of the Jacob Level plot between the “high HI” and “low HI” trends (Figure 2), which suggests intermediate OM preservation, and is consistent with the variable proportion of amorphous OM in the palynofacies [Heimhofer *et al.*, 2006]. The same conclusion can be reached based on the molecular signature: steranes and hopanes are relatively abundant but the homohopane index is null, suggesting OM degradation in an oxygenated sediment. The presence of benthic foraminifera in the Jacob Level [Erbacher *et al.*, 1998] gives support to this latter interpretation.

A peculiar feature in the extracts of the Jacob Level is the abundance of acyclic and monocyclic isoprenoids. Though PMI and TMI are not observed

in the Jacob Level [this study; Ando *et al.*, 2022, 2017], we consider that the abundant isoprenoids likely derive from lipids of planktic chemoautotrophic archaea. The archaeal biomarkers PMI and TMI have been described in Livello 113, a lateral equivalent of the Jacob Level in Umbria-Marche Basin [Coccioni *et al.*, 2014, Ferraro, 2017]. Livello 113 was deposited as a result of moderate to high primary productivity and anoxia to dysoxia of the bottom water [Coccioni *et al.*, 2014, Sabatino *et al.*, 2015, Ferraro *et al.*, 2020]. Planktic chemoautotrophic archaea could have been driven in the Vocontian Basin through intrusions of anoxic intermediate waters originating from the northern Tethyan margin. The presence of the Tethyan taxon *Nannoconus* in the Jacob Level [Herrle and Mutterlose, 2003], is consistent with this scenario. Nevertheless, the water column was oxygenated in the Vocontian Basin, which led to efficient degradation of the archaeal lipids (Figure 7d).

Previous models have proposed that OM enrichment in the Jacob Level was the result of sediment condensation, low sea level, elevated detrital input, or water column anoxia [Bréhéret, 1995, Erbacher *et al.*, 1998, Heimhofer *et al.*, 2006, Caillaud *et al.*, 2022]. A short episode of temperature increase during this interval is documented in the Umbria-Marche Basin [Ferraro *et al.*, 2020]. Increased continental runoff associated to a more humid climate could have increased the delivery of terrestrial OM, but also favoured primary productivity and bottom water stagnation in the Vocontian Basin [Figure 7d; Heimhofer *et al.*, 2006]. The Jacob Level was deposited during a period of low sea level, which also favoured the delivery of continental OM to the Vocontian Basin [Figure 7d, Supplementary Figure 14; Friès and Parize, 2003]. Nevertheless, the surrection of the west margin of the Vocontian Basin during the late Aptian–early Albian [Ferry *et al.*, 2022] could have further contributed to the increased detrital flux.

4.2.6. *Kilian Level*

The Kilian Level is the second organic-rich deposit associated to OAE1b in the Vocontian Basin [Leckie *et al.*, 2002, Trabucho Alexandre *et al.*, 2011, Coccioni *et al.*, 2014]. The Kilian Level is associated to a negative carbon isotope excursion, which has been recognised in numerous settings [Trabucho Alexandre *et al.*, 2011, Bodin *et al.*, 2023]. It corresponds to a global event.

Two samples from the Kilian Level were analyzed for their biomarker content and they show contrasting results: the lower one is comparable to the marls below, with a marked terrestrial signature (TAR, PAHs) and abundant hopanes, while the second sample has a reduced terrestrial contribution and a more marine affinity, but high abundance of plant terpenes. The relative abundance of steroids in the Kilian Level is low, but is higher than in the surrounding marls. The sterane/hopane ratio is high in the upper sample. Based on TADS values, the dinoflagellate contribution is low in both samples, but higher than in the surrounding marls, and lower than in the Jacob Level (Supplementary Table 1). The C_{27} TAS ratio indicates a contribution of coccolithophorid or prasinophyte comparable in the Kilian Level and surrounding marls. The sterane distribution in the upper sample is dominated by cholestane, interpreted as indicative of increased primary productivity. Despite the differences between the two studied samples, the biomarker content is consistent with the notable occurrence of terrestrial paly-nomorphs in the palynofacies [Herrle *et al.*, 2003b]. It also suggests low to medium primary productivity, consistent with the oligo- to mesotrophic conditions indicated by nannofossils [Herrle *et al.*, 2003b]. No molecular indicators of water column anoxia are observed, though the small and poorly diversified planktic foraminifera suggest water column stratification or deoxygenation [Bréhéret, 1995, Kennedy *et al.*, 2000]. Though the Kilian Level is often laminated, the low C_{35} homohopane ratio indicates a relatively oxygenated sediment, consistent with the presence of benthic foraminifera [Herrle *et al.*, 2003b] and modest enrichments in redox-sensitive trace elements [Caillaud *et al.*, 2022, Wang *et al.*, 2022]. Our observations differ from previous molecular studies of the Kilian Level at Saint-André-les-Alpes, located to the east of the Vocontian Basin, in a more basinal setting (Figure 1). A higher contribution of dinoflagellates was observed [Ando *et al.*, 2017], with a general increase from the Jacob to the Kilian and Paquier Levels. In addition, PMI and TMI were present in significant concentration [Okano *et al.*, 2008b].

In the Umbria-Marche Basin and in the Central Atlantic Ocean, the equivalents of the Kilian Level are dominated by marine OM and resulted from increases in surface productivity [Trabucho Alexandre *et al.*, 2011, Coccioni *et al.*, 2014]. They were de-

posited under anoxic bottom waters, though trace elements are not systematically enriched in the rocks [Trabucho Alexandre *et al.*, 2011, Sabatino *et al.*, 2015]. The Italian equivalent of the Kilian Level contains TMI and PMI, but no isorenieratane [Ferraro, 2017].

Recent studies of les Briers outcrop, located to the east of the Vocontian Basin, suggest that the Kilian Level resulted from an episode of increased primary productivity and OM preservation, associated to pulses of continental runoff in the Vocontian Basin [Bodin *et al.*, 2023]. The molecular data do not conflict with this model, but the presence of archaeal biomarkers in the eastern part of the basin suggest that the Vocontian Basin was also influenced by intrusions of reducing water from the Tethyan margin (Figure 7d, Supplementary Figure 14). These intrusions led to higher surface productivity, high abundance of dinoflagellates, presence of planktic archaea and possibly more reducing conditions in the water column in the eastern part of the Vocontian Basin, but not to the west (Figure 7d). The east–west decrease of TOC content in the Kilian Level [Caillaud *et al.*, 2022, Bodin *et al.*, 2023] and the absence of *Nannoconus* in the Kilian Level at Pré-Guittard and Palluel [Bréhéret, 1995], in the west part of the Vocontian Basin, give support to this scenario.

4.2.7. Paquier Level

The Paquier Level is the most prominent of the organic-rich deposits associated to OAE1b in the Vocontian Basin [Bréhéret, 1995, Coccioni *et al.*, 2014]. Equivalents of the Paquier Level are recognised worldwide, in particular by its marked negative carbon isotope excursion in carbonate [Trabucho Alexandre *et al.*, 2011, Coccioni *et al.*, 2014; also see Bodin *et al.*, 2023 for a review]. The Paquier Level is the only level in the OAE1b that records global ocean deoxygenation [Wang *et al.*, 2022].

The molecular fossil content of the Paquier Level is characterized by the abundance of archaea-derived acyclic and monocyclic isoprenoids (Supplementary text 3). This feature was previously observed in Ravel section, located in a more basinal part of the Vocontian Basin [Vink *et al.*, 1998, Kuypers *et al.*, 2002, Okano *et al.*, 2008b]. The high abundance of archaea-derived phytane in the samples of the Paquier Level explains the low Pr/Ph, which are the lowest of our dataset (Supplementary Table 1). The Paquier

Level is also characterized by a high abundance of steranes, a high sterane/hopane ratio and the highest abundances of *n*-propyl cholestanes, indicative of a high flux of a diversified eukaryotic biomass. The relative abundance of dinosteroids is high, as indicated by the TADS values [Ando *et al.*, 2017], which can be related to the abundance of dinocysts in the palynofacies [Tribovillard and Gorin, 1991, Kennedy *et al.*, 2000]. The chain length distribution of steranes in the Paquier Level is characterized by the dominance of the C₂₇ compounds, which we interpret as indicating high primary productivity. This interpretation is consistent with the microfaunal content indicating eutrophic conditions [Erbacher *et al.*, 1998, Kennedy *et al.*, 2000, Herrle *et al.*, 2003b]. Though the molecular signature of marine organisms is dominant, the terrestrial contribution, indicated by the TAR, abundance of PAHs and of higher plant aromatic terpenoids, is also notable (Supplementary Table 1). These molecular data can be related to the presence of abundant terrestrial palynomorphs in the palynofacies [Tribovillard and Gorin, 1991, Herrle *et al.*, 2003b], and of occasional plant remains in the rocks [Bréhéret, 1995]. The contribution of terrestrial OM in the Paquier Level has been observed in different locations of the Vocontian Basin, and cannot be ascribed to the relatively proximal setting of the studied section.

The high homohopane ratio and the presence of OSCs indicate sulfidic conditions in the sediment, possibly associated with bottom water anoxia (Figure 7f). This is consistent with the rarity of the benthic fauna [Bréhéret, 1995, Erbacher *et al.*, 1998], abundance of amorphous OM in the palynofacies [Tribovillard and Gorin, 1991], and trace metal enrichment in the sediment [Benamara *et al.*, 2020, Caillaud *et al.*, 2022, Wang *et al.*, 2022]. Nevertheless, no indicator of photic zone anoxia was detected, consistent with previous data [Kuypers *et al.*, 2002].

Molecular fossil analyses were performed in several lateral equivalents of the Paquier Level, in the Umbria-Marche Basin [Coccioni *et al.*, 2014], in the Ionian Basin [Tsikos *et al.*, 2004] and in the Central Atlantic Ocean [Kuypers *et al.*, 2002]. All these levels are characterized by the abundance of biomarkers derived from archaeal lipids, including PMI and TMI, and by the absence of isorenieratane [Kuypers *et al.*, 2002, Tsikos *et al.*, 2004, Ferraro, 2017]. While in the Central Atlantic Ocean samples

the steranes are dominated by the C₂₉ compounds and 2-methylhopanes are present [Kuypers *et al.*, 2002], the biomarker content in the Umbria-Marche Basin is more comparable with that of the Paquier Level, with a dominance of C₂₇ steranes and possible absence of 2-methylhopanes [Ferraro, 2017]. These lateral equivalents of the Paquier Level are all characterized by heavy organic carbon isotopic ratios ($\delta^{13}\text{C}_{\text{org}} = -22$ to -17%), indicative of a high contribution of chemoautotrophic archaea [Kuypers *et al.*, 2002, Tsikos *et al.*, 2004, Sabatino *et al.*, 2015]. In the Paquier Level, however, heavy organic carbon isotopic ratios are only observed sporadically [Benamara *et al.*, 2020, Ait-Itto *et al.*, 2023, Bodin *et al.*, 2023], indicating that archaea were rarely dominant in the Vocontian Basin.

Because of the high proportion of terrestrial OM, several authors proposed that the Paquier Level deposited as a result of increased input of nutrient to the ocean associated to a warm, humid climate and continental runoff [Herrle *et al.*, 2003a,b, Benamara *et al.*, 2020, Bodin *et al.*, 2023]. The highest levels of primary productivity and water stratification would have been reached under favourable orbital conditions, at the peak of a long period of progressive warming [Wang *et al.*, 2022, Bodin *et al.*, 2023]. The surrection of the west margin of the Vocontian Basin during the late Aptian–early Albian [Ferry *et al.*, 2022] possibly also contributed to the increased inputs of continental material during this period. The molecular fossil content does not conflict with the influence of terrestrial runoff. Nevertheless, the similarity of biomarker composition in the northern Tethyan margin and in the Vocontian Basin, as well as the abundance of the Tethyan nannofossil *Nannoconus* in certain layers of the Paquier Level [Bréhéret, 1995], are consistent with the establishment of good connections between the Tethys Ocean and the Vocontian Basin (Figure 7f). The Paquier Level is interpreted as a 3rd order maximum flooding surface [Figure 7f, Supplementary Figure 14; Rubino, 1989, Friès and Parize, 2003]. Sediment and bottom water anoxia in the Vocontian Basin could therefore have resulted from the high primary productivity, nevertheless, an expansion of the Tethyan oxygen minimum zone associated to the eustatic rise also seems possible.

5. Conclusion

Basing on sedimentation rate, grain size analysis, Rock-Eval analysis, trace metal content, and preliminary biomarker data, Caillaud *et al.* [2022] came to the conclusion that organic matter (OM) enrichment within the Blue Marls Formation (Aptian–Albian) was only modest because the conditions in the Vocontian Basin were overall not favorable to massive burial of OM. This detailed study of the biomarker content in the Organic Levels confirms that surface productivity fluctuated mainly between oligotrophic and mesotrophic and that bottom waters were rarely reducing. As a result, the OLs of regional extension only show modest OM enrichments, associated to small increases of productivity (Niveau Noir) or of terrestrial OM inputs (Fallot Interval).

Larger-scale events are fundamentally different: the Goguel Level (OAE1a) and Jacob, Kilian, and Paquier Levels (OAE1b) present the same molecular peculiarities (abundance of 2-methylhopanoids and of archaeal lipids, respectively) as coeval deposits located outside the Vocontian Basin. These are strong arguments in favor of good connections between the Tethys Ocean and the Vocontian Basin during the deposition of these levels. In particular, a lateral spreading of the Tethyan oxygen minimum zone into the Vocontian Basin could explain the low sediment oxygenation despite moderate increases of surface productivity. Sea-level variations were previously considered as an important factor influencing OM enrichment, through sediment condensation and water column stratification. The present biomarker study highlights how sea-level variations also impact OM enrichment in a given sedimentary basin, through connections with surrounding basins. Such feature, well known in modern settings, such as the Cariaco Basin off Venezuela, are more difficult to document in ancient sedimentary basins.

Declaration of interests

The authors do not work for, advise, own shares in, or receive funds from any organization that could benefit from this article, and have declared no affiliations other than their research organizations.

Acknowledgements

We thank TOTAL S.A. (now TotalEnergy) for funding this research, M. Gentric for administrative management, M. Delattre and R. Abraham for technical support. P. Adam and P. Schaeffer (Institut de Chimie de Strasbourg) are acknowledged for their help in identifying compounds.

Supplementary data

Supporting information for this article is available on the journal's website under <https://doi.org/10.5802/crgeos.233> or from the author.

References

- Aguado, R., de Gea, G. A., Castro, J. M., O'Dogherty, L., Quijano, M. L., Naafs, B. D. A., and Pancost, R. D. (2014). Late Barremian–early Aptian dark facies of the Subbetic (Betic Cordillera, southern Spain): Calcareous nannofossil quantitative analyses, chemostratigraphy and palaeoceanographic reconstructions. *Palaeogeogr. Palaeoclimatol. Palaeoecol.*, 395, 198–221.
- Aichner, B., Herzsuh, U., and Wilkes, H. (2010). Influence of aquatic macrophytes on the stable carbon isotopic signatures of sedimentary organic matter in lakes on the Tibetan Plateau. *Org. Geochem.*, 41, 706–718.
- Ait-Itto, F.-Z., Martinez, M., Deconinck, J.-F., and Bodin, S. (2023). Astronomical calibration of the OAE1b from the Col de Pré-Guittard section (Aptian–Albian), Vocontian Basin, France. *Cret. Res.*, 150, article no. 105618.
- Ajuaba, S., Sachsenhofer, R. F., Bechtel, A., Galasso, F., Gross, D., Misch, D., and Schneebeli-Hermann, E. (2022). Biomarker and compound-specific isotope records across the Toarcian CIE at the Dormettingen section in SW Germany. *Int. J. Earth Sci.*, 111, 1631–1661.
- Allard, B. and Templier, J. (2000). Comparison of neutral lipid profile of various trilaminar outer cell wall (TLS)-containing microalgae with emphasis on algaenan occurrence. *Phytochemistry*, 54, 369–380.
- Ando, T., Sawada, K., Okano, K., Takashima, R., and Nishi, H. (2017). Marine primary producer community during the mid-Cretaceous oceanic anoxic events (OAEs) 1a, 1b and 1d in the Vocontian Basin (SE France) evaluated from triaromatic steroids in sediments. *Org. Geochem.*, 106, 13–24.
- Ando, T., Sawada, K., Okano, K., Takashima, R., and Nishi, H. (2022). Marine paleoecological variations during the mid-Cretaceous oceanic anoxic event 1a in the Vocontian Basin, southeastern France. *Palaeogeogr. Palaeoclimatol. Palaeoecol.*, 586, article no. 110779.
- Barale, G. and Bréhéret, J.-G. (1995). Discovery of *Cheirolepidiaceae* from the Aptian Marnes bleues of the Vocontian zone, south east basin, France. *C. R. Acad. Sci. Paris*, 321, 433–439.
- Baudin, F., Fiet, N., Coccioni, R., and Galeotti, S. (1998). Organic matter characterisation of the Selli Level (Umbria-Marche Basin, central Italy). *Cretac. Res.*, 19, 701–714.
- Benamara, A., Charbonnier, G., Adatte, T., Spangenberg, J. E., and Föllmi, K. B. (2020). Precession-driven monsoonal activity controlled the development of the early Albian Paquier oceanic anoxic event (OAE1b): evidence from the Vocontian Basin, SE France. *Palaeogeogr. Palaeoclimatol. Palaeoecol.*, 537, article no. 109406.
- bin Abas, M. R., Simoneit, B. R. T., Elias, V., Cabral, J. A., and Cardoso, J. N. (1995). Composition of higher molecular weight organic matter in smoke aerosol from biomass combustion in Amazonia. *Chemosphere*, 30, 995–1015.
- Birgel, D., Thiel, V., Hinrichs, K.-U., Elvert, M., Campbell, K. A., Reitner, J., Farmer, J. D., and Peckmann, J. (2006). Lipid biomarker patterns of methane-seep microbialites from the Mesozoic convergent margin of California. *Org. Geochem.*, 37, 1289–1302.
- Blumenberg, M. and Wiese, F. (2012). Imbalanced nutrients as triggers for black shale formation in a shallow shelf setting during the OAE 2 (Wunstorf, Germany). *Biogeosciences*, 9, 4139–4153.
- Blumer, M., Guillard, R. R. L., and Chase, T. (1971). Hydrocarbons of marine phytoplankton. *Mar. Biol.*, 8, 183–189.
- Bobrovskiy, I., Hope, J. M., Nettersheim, B. J., Volkman, J. K., Hallmann, C., and Brocks, J. J. (2021). Algal origin of sponge sterane biomarkers negates the oldest evidence for animals in the rock record. *Nat. Ecol. Evol.*, 5, 165–168.
- Bodin, S., Charpentier, M., Ullmann, C. V., Rudra, A., and Sanei, H. (2023). Carbon cycle during the late

- Aptian–early Albian OAE 1b: a focus on the Kilian–Paquier levels interval. *Glob. Planet. Change*, 222, article no. 104074.
- Bourbonniere, R. A. and Meyers, P. A. (1996). Sedimentary geolipid records of historical changes in the watersheds and productivities of Lakes Ontario and Erie. *Limnol. Oceanogr.*, 41, 352–359.
- Brassell, S. C., Wardroper, A. M. K., Thomson, I. D., Maxwell, J. R., and Eglinton, G. (1981). Specific acyclic isoprenoids as biological markers of methanogenic bacteria in marine sediments. *Nature*, 290, 693–696.
- Br  h  ret, J.-G. (1994). The mid-cretaceous organic-rich sediments from the vocontian zone of the French southeast basin. In Mascle, A., editor, *Hydrocarbon and Petroleum Geology of France*, Special Publication of the European Association of Petroleum Geoscientists, pages 295–320. Springer, Berlin, Heidelberg.
- Br  h  ret, J.-G. (1995). L’Aptien et l’Albien de la Fosse vocontienne (des bordures au bassin).   volution de la s  dimentation et enseignements sur les   v  nements anoxiques. Th  se de doctorat, Universit   Fran  ois Rabelais—Tours.
- Brocks, J. J. and Schaeffer, P. (2008). Okenane, a biomarker for purple sulfur bacteria (Chromatiaceae), and other new carotenoid derivatives from the 1640Ma Barney Creek Formation. *Geochim. Cosmochim. Acta*, 72, 1396–1414.
- Bush, R. T. and McInerney, F. A. (2013). Leaf wax *n*-alkane distributions in and across modern plants: implications for paleoecology and chemotaxonomy. *Geochim. Cosmochim. Acta*, 117, 161–179.
- Caillaud, A., Quijada, M., Hlohowskyj, S. R., Chappaz, A., Bout-Roumazielles, V., Reynaud, J.-Y., Riboulleau, A., Baudin, F., Adatte, T., Ferry, J.-N., and Tribovillard, N. (2022). Assessing controls on organic matter enrichments in hemipelagic marls of the Aptian-Lower Albian Blue Marls of the Vocontian Basin (France): an unexpected variability observed from multiple “organic-rich” levels. *BSGF—Earth Sci. Bull.*, 193, article no. 2.
- Caillaud, A., Quijada, M., Huet, B., Reynaud, J.-Y., Riboulleau, A., Bout-Roumazielles, V., Baudin, F., Chappaz, A., Adatte, T., Ferry, J.-N., and Tribovillard, N. (2020). Turbidite-induced re-oxygenation episodes of the sediment-water interface in a diverticulum of the Tethys Ocean during the Oceanic Anoxic Event 1a: the French Vocontian Basin. *Depos. Rec.*, 6, 352–382.
- Castro, J. M., de Gea, G. A., Quijano, M. L., Aguado, R., Froehner, S., Naafs, B. D. A., and Pancost, R. D. (2019). Complex and protracted environmental and ecological perturbations during OAE 1a—evidence from an expanded pelagic section from south Spain (Western Tethys). *Glob. Planet. Change*, 183, article no. 103030.
- Charbonnier, G., Boulila, S., Spangenberg, J. E., Vermeulen, J., and Galbrun, B. (2023). Astrochronology of the Aptian stage and evidence for the chaotic orbital motion of Mercury. *Earth Planet. Sci. Lett.*, 610, article no. 118104.
- Coccioni, R., Sabatino, N., Frontalini, F., Gardin, S., Sideri, M., and Sprovieri, M. (2014). The neglected history of Oceanic Anoxic Event 1b: insights and new data from the Poggio le Guaine section (Umbria–Marche Basin). *Stratigraphy*, 11, 245–282.
- Colombo, J. C., Silverberg, N., and Gearing, J. N. (1996). Lipid biogeochemistry in the Laurentian Trough: I—fatty acids, sterols and aliphatic hydrocarbons in rapidly settling particles. *Org. Geochem.*, 25, 211–225.
- Cordova-Gonzalez, A., Birgel, D., Kappler, A., and Peckmann, J. (2020). Carbon stable isotope patterns of cyclic terpenoids: a comparison of cultured alkaliphilic aerobic methanotrophic bacteria and methane-seep environments. *Org. Geochem.*, 139, article no. 103940.
- Cranwell, A., Jaworski, G. H. M., and Bickley, H. M. (1990). Hydrocarbons, sterols, esters and fatty acids in six freshwater chlorophytes. *Phytochemistry*, 29, 145–151.
- Didyk, B. M., Simoneit, B. R. T., Brassell, S. C., and Eglinton, G. (1978). Organic geochemical indicators of palaeoenvironmental conditions of sedimentation. *Nature*, 272, 216–222.
- Dumitrescu, M. and Brassell, S. C. (2005). Biogeochemical assessment of sources of organic matter and paleoproductivity during the early Aptian Oceanic Anoxic Event at Shatsky Rise, ODP Leg 198. *Org. Geochem.*, 36, 1002–1022.
- Dumitrescu, M. and Brassell, S. C. (2006). Compositional and isotopic characteristics of organic matter for the early Aptian Oceanic Anoxic Event at Shatsky Rise, ODP Leg 198. *Palaeogeogr. Palaeoclimatol. Palaeoecol.*, 235, 168–191.

- Eglinton, G. and Hamilton, R. J. (1967). Leaf epicuticular waxes. *Science*, 156, 1322–1335.
- Elvert, M., Suess, E., and Whiticar, M. J. (1999). Anaerobic methane oxidation associated with marine gas hydrates: superlight C-isotopes from saturated and unsaturated C₂₀ and C₂₅ irregular isoprenoids. *Naturwissenschaften*, 86, 295–300.
- Erbacher, J., Gerth, W., Schmiedl, G., and Hemleben, Ch. (1998). Benthic foraminiferal assemblages of late Aptian-early Albian black shale intervals in the Vocontian Basin, SE France. *Cret. Res.*, 19, 805–826.
- Farrimond, P., Eglinton, G., Brassell, S. C., and Jenkyns, H. C. (1990). The Cenomanian/Turonian anoxic event in Europe: an organic geochemical study. *Mar. Pet. Geol.*, 7, 75–89.
- Farrimond, P., Stoddart, D. P., and Jenkyns, H. C. (1994). An organic geochemical profile of the Toarcian anoxic event in northern Italy. *Chem. Geol.*, 111, 17–33.
- Ferraro, S. (2017). *Oceanic Anoxic Event (OAE) 1b (Late Aptian–Early Albian): Evolutionary, Palaeoecological, Palaeoceanographic and Palaeoclimatic Implication*. Università Degli Studi di Urbino Carlo Bo - Urbino, Italia.
- Ferraro, S., Coccioni, R., Sabatino, N., Del Core, M., and Sprovieri, M. (2020). Morphometric response of late Aptian planktonic foraminiferal communities to environmental changes: a case study of *Paraticinella rohri* at Poggio le Guaine (central Italy). *Palaeogeogr. Palaeoclimatol. Palaeoecol.*, 538, article no. 109384.
- Ferry, S., Grosheny, D., and Amédéo, F. (2022). Sedimentary record of the “Austrian” tectonic pulse around the Aptian–Albian boundary in SE France, and abroad. *C. R. Geosci.*, 354, 1–21.
- Föllmi, K. B. (2012). Early Cretaceous life, climate and anoxia. *Cret. Res.*, 35, 230–257.
- Forster, A., Kuypers, M. M. M., Turgeon, S. C., Brumsack, H.-J., Petrizzo, M. R., and Sinninghe Damsté, J. S. (2008). The Cenomanian/Turonian oceanic anoxic event in the South Atlantic: New insights from a geochemical study of DSDP Site 530A. *Palaeogeogr. Palaeoclimatol. Palaeoecol.*, 267, 256–283.
- Friedrich, O., Reichelt, K., Herrle, J. O., Lehmann, J., Pross, J., and Hemleben, C. (2003). Formation of the Late Aptian Niveau Fallot black shales in the Vocontian Basin (SE France): evidence from foraminifera, palynomorphs, and stable isotopes. *Mar. Micropaleontol.*, 49, 65–85.
- Friès, G. (1986). Dynamique du bassin subalpin à l’Apto-Cénomanién. These de doctorat, Paris 6 - Paris.
- Friès, G. and Parize, O. (2003). Anatomy of ancient passive margin slope systems: Aptian gravity-driven deposition on the Vocontian palaeomargin, western Alps, south-east France. *Sedimentology*, 50, 1231–1270.
- Gale, A. S., Bown, P., Caron, M., Crampton, J., Crowhurst, S. J., Kennedy, W. J., Petrizzo, M. R., and Wray, D. S. (2011). The uppermost Middle and Upper Albian succession at the Col de Palluel, Hautes-Alpes, France: An integrated study (ammonites, inoceramid bivalves, planktonic foraminifera, nanofossils, geochemistry, stable oxygen and carbon isotopes, cyclostratigraphy). *Cret. Res.*, 32, 59–130.
- Giger, W., Schaffner, C., and Wakeham, S. G. (1980). Aliphatic and olefinic hydrocarbon in recent sediments of Greifensee, Switzerland. *Geochim. Cosmochim. Acta*, 44, 119–129.
- Giraud, F., Pittet, B., Grosheny, D., Baudin, F., Lécuyer, C., and Sakamoto, T. (2018). The palaeoceanographic crisis of the Early Aptian (OAE 1a) in the Vocontian Basin (SE France). *Palaeogeogr. Palaeoclimatol. Palaeoecol.*, 511, 483–505.
- Golonka, J. (2007). Phanerozoic Paleoenvironment and Paleolithofacies Maps. Mesozoic. *Geologia*, 33, 211–264.
- Goossens, H., de Leeuw, J. W., Schenck, P. A., and Brassell, S. C. (1984). Tocopherols as likely precursors of pristane in ancient sediments and crude oils. *Nature*, 312, 440–442.
- Goossens, H., Rijpstra, W. I. J., Düren, R. R., and de Leeuw, J. W. (1986). Bacterial contribution to sedimentary organic matter; a comparative study of lipid moieties in bacteria and recent sediments. *Org. Geochem.*, 10, 683–696.
- Grabenstatter, J., Méhay, S., McIntyre-Wressnig, A., Giner, J.-L., Edgcomb, V. P., Beaudoin, D. J., Bernhard, J. M., and Summons, R. E. (2013). Identification of 24-*n*-propylidenecholesterol in a member of the Foraminifera. *Org. Geochem.*, 63, 145–151.
- Heimhofer, U., Hochuli, P. A., Herrle, J. O., Andersen, N., and Weissert, H. (2004). Absence of major vegetation and palaeoatmospheric pCO₂ changes associated with oceanic anoxic event 1a (Early Aptian, SE France). *Earth Planet. Sci. Lett.*, 223, 303–318.
- Heimhofer, U., Hochuli, P. A., Herrle, J. O., and Weis-

- sert, H. (2006). Contrasting origins of Early Cretaceous black shales in the Vocontian basin: evidence from palynological and calcareous nanofossil records. *Palaeogeogr. Palaeoclimatol. Palaeoecol.*, 235, 93–109.
- Herrle, J. O., Kössler, P., and Bollmann, J. (2010). Palaeoceanographic differences of early Late Aptian black shale events in the Vocontian Basin (SE France). *Palaeogeogr. Palaeoclimatol. Palaeoecol.*, 297, 367–376.
- Herrle, J. O. and Mutterlose, J. (2003). Calcareous nanofossils from the Aptian–Lower Albian of southeast France: palaeoecological and biostratigraphic implications. *Cret. Res.*, 24, 1–22.
- Herrle, J. O., Pross, J., Friedrich, O., and Hemleben, C. (2003a). Short-term environmental changes in the Cretaceous Tethyan Ocean: micropalaeontological evidence from the Early Albian Oceanic Anoxic Event 1b. *Terra Nova*, 15, 14–19.
- Herrle, J. O., Pross, J., Friedrich, O., Kößler, P., and Hemleben, C. (2003b). Forcing mechanisms for mid-Cretaceous black shale formation: evidence from the Upper Aptian and Lower Albian of the Vocontian Basin (SE France). *Palaeogeogr. Palaeoclimatol. Palaeoecol.*, 190, 399–426.
- Hoefs, M. J. L., Rijpstra, W. I. C., and Sinninghe Damsté, J. S. (2002). The influence of oxic degradation on the sedimentary biomarker record I: evidence from Madeira Abyssal Plain turbidites. *Geochim. Cosmochim. Acta*, 66, 2719–2735.
- Holzer, G., Oró, J., and Tornabene, T. G. (1979). Gas chromatographic—mass spectrometric analysis of neutral lipids from methanogenic and thermoacidophilic bacteria. *J. Chromatogr. A*, 186, 795–809.
- Huang, W.-Y. and Meinschein, W. G. (1979). Sterols as ecological indicators. *Geochim. Cosmochim. Acta*, 43, 739–745.
- Jambrina-Enríquez, M., Herrera-Herrera, A. V., and Mallol, C. (2018). Wax lipids in fresh and charred anatomical parts of the *Celtis australis* tree: insights on paleofire interpretation. *Org. Geochem.*, 122, 147–160.
- Kaneda, T. (1991). Iso- and anteiso-fatty acids in bacteria: biosynthesis, function, and taxonomic significance. *Microbiol. Rev.*, 55, 288–302.
- Karakitsios, V., Tzortzaki, E., Giraud, F., and Pasadakis, N. (2018). First evidence for the early Aptian Oceanic Anoxic Event (OAE1a) from the Western margin of the Pindos Ocean (NW Greece). *Geobios*, 51, 187–210.
- Kennedy, J., Gale, A., Huber, B., Petrizzo, M. R., Bown, P., and Jenkyns, H. (2017). The Global Boundary Stratotype Section and Point (GSSP) for the base of the Albian Stage, of the Cretaceous, the Col de Pré-Guittard section, Arnayon, Drôme, France. *Episodes*, 40, 177–188.
- Kennedy, W. J., Gale, A., Lees, J., and Caron, M. (2004). The Global Boundary Stratotype Section and Point (GSSP) for the base of the Cenomanian Stage, Mont Risou, Hautes-Alpes, France. *Episodes*, 27, 21–32.
- Kennedy, W. J., Gale, A. S., Bown, P. R., Caron, M., Davey, R. J., Gröcke, D., and Wray, D. S. (2000). Integrated stratigraphy across the Aptian-Albian boundary in the Marnes Bleues, at the Col de Pré-Guittard, Arnayon (Drôme), and at Tartonne (Alpes-de-Haute-Provence), France: a candidate Global Boundary Stratotype Section and Boundary Point for the base of the Albian Stage. *Cret. Res.*, 21, 591–720.
- Koopmans, M. P., Köster, J., Van Kaam-Peters, H. M. E., Kenig, F., Schouten, S., Hartgers, W. A., de Leeuw, J. W., and Sinninghe Damsté, J. S. (1996a). Diagenetic and catagenetic products of isorenieratene: molecular indicators for photic zone anoxia. *Geochim. Cosmochim. Acta*, 60, 4467–4496.
- Koopmans, M. P., Schouten, S., Kohnen, M. E. L., and Sinninghe Damsté, J. S. (1996b). Restricted utility of aryl isoprenoids as indicators for photic zone anoxia. *Geochim. Cosmochim. Acta*, 60, 4873–4876.
- Kusch, S. and Rush, D. (2022). Revisiting the precursors of the most abundant natural products on Earth: a look back at 30+ years of bacteriohopanepolyol (BHP) research and ahead to new frontiers. *Org. Geochem.*, 172, article no. 104469.
- Kuypers, M. M. M., Blokker, P., Hopmans, E. C., Kinkel, H., Pancost, R. D., Schouten, S., and Sinninghe Damsté, J. S. (2002). Archaeal remains dominate marine organic matter from the early Albian oceanic anoxic event 1b. *Palaeogeogr. Palaeoclimatol. Palaeoecol.*, 185, 211–234.
- Kuypers, M. M. M., Lourens, L. J., Rijpstra, W. I. C., Pancost, R. D., Nijenhuis, I. A., and Sinninghe Damsté, J. S. (2004a). Orbital forcing of organic carbon burial in the proto-North Atlantic during oceanic anoxic event 2. *Earth Planet. Sci.*

- Lett.*, 228, 465–482.
- Kuypers, M. M. M., van Breugel, Y., Schouten, S., Erba, E., and Damsté, J. S. S. (2004b). N₂-fixing cyanobacteria supplied nutrient N for Cretaceous oceanic anoxic events. *Geology*, 32, 853–856.
- Leckie, R. M., Bralower, T. J., and Cashman, R. (2002). Oceanic anoxic events and plankton evolution: biotic response to tectonic forcing during the mid-Cretaceous. *Paleoceanography*, 17, 13–1–13–29.
- Li, M., Larter, S. R., Taylor, P., Jones, D. M., Bowler, B., and Bjorøy, M. (1995). Biomarkers or not biomarkers? A new hypothesis for the origin of pristane involving derivation from methyltrimethyltridecylchromans (MTTCs) formed during diagenesis from chlorophyll and alkylphenols. *Org. Geochem.*, 23, 159–167.
- Meunier-Christmann, C., Albrecht, P., Brassell, S. C., Ten Haven, H. L., Van Der Linden, B., Rullkötter, J., and Trendel, J. M. (1991). Occurrence of dammar-13(17)-enes in sediments: indications for a yet unrecognized microbial constituent? *Geochim. Cosmochim. Acta*, 55, 3475–3483.
- Moldowan, J. M., Seifert, W. K., and Gallegos, E. J. (1985). Relationship between petroleum composition and depositional environment of petroleum source rocks. *AAPG Bull.*, 69, 1255–1268.
- Naafs, B. D. A., Bianchini, G., Monteiro, F. M., and Sánchez-Baracaldo, P. (2022). The occurrence of 2-methylhopanoids in modern bacteria and the geological record. *Geobiology*, 20, 41–59.
- Neunlist, S. and Rohmer, M. (1985). Novel hopanoids from the methylotrophic bacteria *Methylococcus capsulatus* and *Methylomonas methanica*. (22S)-35-aminobacteriohopane-30,31,32,33,34-pentol and (22S)-35-amino-3 β -methylbacteriohopane-30,31,32,33,34-pentol. *Biochem. J.*, 231, 635–639.
- Okano, K., Sawada, K., Takashima, R., Nishi, H., and Okada, H. (2008a). Depositional environments revealed from biomarkers in sediments deposited during the mid-Cretaceous Oceanic Anoxic Events (OAEs) in the Vocontian Basin (SE France). In Okada, H., Mawatari, S. F., Suzuki, N., and Gautam, P., editors, *Origin and Evolution of Natural Diversity - Proceedings of International Symposium. Presented at the Origin and Evolution of Natural Diversity, Sapporo, Japan*, pages 233–238. Hokkaido University, Hokkaido.
- Okano, K., Sawada, K., Takashima, R., Nishi, H., and Okada, H. (2008b). Further examples of archaeal-derived hydrocarbons in mid-Cretaceous oceanic anoxic event (OAE) 1b sediments. *Org. Geochem.*, 39, 1088–1091.
- Ourisson, G. and Rohmer, M. (1992). Hopanoids. 2. Biohopanoids: a novel class of bacterial lipids. *Acc. Chem. Res.*, 25, 403–408.
- Pancost, R. D., Crawford, N., Magness, S., Turner, A., Jenkyns, H. C., and Maxwell, J. R. (2004). Further evidence for the development of photic-zone euxinic conditions during Mesozoic oceanic anoxic events. *J. Geol. Soc.*, 161, 353–364.
- Peters, K. E. and Moldowan, J. M. (1991). Effects of source, thermal maturity, and biodegradation on the distribution and isomerization of homohopanes in petroleum. *Org. Geochem.*, 17, 47–61.
- Peters, K. E., Walters, C. W., and Moldowan, J. M. (2005). *The Biomarker Guide*. Cambridge University Press, Cambridge, 2nd edition.
- Radke, M., Vriend, S. P., and Ramanampisoa, L. R. (2000). Alkyldibenzofurans in terrestrial rocks: influence of organic facies and maturation. *Geochim. Cosmochim. Acta*, 64, 275–286.
- Raederstorff, D. and Rohmer, M. (1984). Sterols of the unicellular algae *Nematochryopsis roscoffensis* and *Chrysothila lamellosa*: isolation of (24E)-24-n-propylidenecholesterol and 24-n-propylcholesterol. *Phytochemistry*, 23, 2835–2838.
- Reitner, J., Blumenberg, M., Walliser, E.-O., Schäfer, N., and Duda, J.-P. (2015). Methane-derived carbonate conduits from the late Aptian of Salinac (Marne Bleues, Vocontian Basin, France): petrology and biosignatures. *Mar. Pet. Geol.*, 66, 641–652.
- Rubino, J. L. (1989). Introductory remarks on Upper Aptian to Albian siliciclastic/carbonate depositional sequences. In Ferry, S. and Rubino, J. L., editors, *Mesozoic Eustacy on Western Tethyan Margins. Post-Meeting Field Trip in the “Vocontian Trough”*, pages 28–45. ASF Publications Spéciales, Paris.
- Ruebsam, W., Müller, T., Kovács, J., Pálffy, J., and Schwark, L. (2018). Environmental response to the early Toarcian carbon cycle and climate perturbations in the northeastern part of the West Tethys shelf. *Gond. Res.*, 59, 144–158.
- Sabatino, N., Coccioni, R., Salvagio Manta, D., Baudin, F., Vallefucio, M., Traina, A., and Sprovieri, M. (2015). High-resolution chemostratigraphy of the late Aptian–early Albian oceanic anoxic event (OAE 1b) from the Poggio le Guaine section

- (Umbria–Marche Basin, central Italy). *Palaeogeogr. Palaeoclimatol. Palaeoecol.*, 426, 319–333.
- Scalan, E. S. and Smith, J. E. (1970). An improved measure of the odd-even predominance in the normal alkanes of sediment extracts and petroleum. *Geochim. Cosmochim. Acta*, 34, 611–620.
- Schwark, L. and Frimmel, A. (2004). Chemostratigraphy of the Posidonia Black Shale, SW-Germany: II. Assessment of extent and persistence of photic-zone anoxia using aryl isoprenoid distributions. *Chem. Geol.*, 206, 231–248.
- Simoneit, B. R. T. (1984). Organic matter of the troposphere—III. Characterization and sources of petroleum and pyrogenic residues in aerosols over the western United States. *Atmos. Environ.*, 18, 51–67.
- Simoneit, B. R. T. and Mazurek, M. A. (1982). Organic matter of the troposphere—II. Natural background of biogenic lipid matter in aerosols over the rural western United States. *Atmos. Environ.*, 16, 2139–2159.
- Sinninghe Damsté, J. S., Keely, B. J., Betts, S. E., Baas, M., Maxwell, J. R., and de Leeuw, J. W. (1993). Variations in abundances and distributions of isoprenoid chromans and long-chain alkylbenzenes in sediments of the Mulhouse Basin: a molecular sedimentary record of palaeosalinity. *Org. Geochem.*, 20, 1201–1215.
- Summons, R. E. and Capon, R. J. (1988). Fossil steranes with unprecedented methylation in ring-A. *Geochim. Cosmochim. Acta*, 52, 2733–2736.
- Summons, R. E. and Capon, R. J. (1991). Identification and significance of 3 β -ethyl steranes in sediments and petroleum. *Geochim. Cosmochim. Acta*, 55, 2391–2395.
- Summons, R. E., Jahnke, L. L., Hope, J. M., and Logan, G. A. (1999). 2-Methylhopanoids as biomarkers for cyanobacterial oxygenic photosynthesis. *Nature*, 400, 554–557.
- Summons, R. E. and Powell, T. G. (1987). Identification of aryl isoprenoids in source rocks and crude oils: biological markers for the green sulphur bacteria. *Geochim. Cosmochim. Acta*, 51, 557–566.
- Summons, R. E., Volkman, J. K., and Boreham, C. J. (1987). Dinosterane and other steroidal hydrocarbons of dinoflagellate origin in sediments and petroleum. *Geochim. Cosmochim. Acta*, 51, 3075–3082.
- Talbot, H. M., Summons, R. E., Jahnke, L. L., Cockell, C. S., Rohmer, M., and Farrimond, P. (2008). Cyanobacterial bacteriohopanepolyol signatures from cultures and natural environmental settings. *Org. Geochem.*, 39, 232–263.
- ten Haven, H. L., de Leeuw, J. W., Rullkötter, J., and Sinninghe Damsté, J. S. (1987). Restricted utility of the pristane/phytane ratio as a palaeoenvironmental indicator. *Nature*, 330, 641–643.
- ten Haven, H. L., de Leeuw, J. W., and Schenck, P. A. (1985). Organic geochemical studies of a Messinian evaporitic basin, northern Apennines (Italy) I: hydrocarbon biological markers for a hypersaline environment. *Geochim. Cosmochim. Acta*, 49, 2181–2191.
- Trabucho Alexandre, J., Van Gilst, R. I., Rodríguez-López, J. P., and De Boer, P. L. (2011). The sedimentary expression of oceanic anoxic event 1b in the North Atlantic. *Sedimentology*, 58, 1217–1246.
- Tribovillard, N.-P. and Gorin, G. E. (1991). Organic facies of the Early Albian Niveau Paquier, a key black shales horizon of the Marnes Bleues formation in the Vocontian trough (Subalpine Ranges, SE France). *Palaeogeogr. Palaeoclimatol. Palaeoecol.*, 85, 227–237.
- Tsikos, H., Karakitsios, V., Breugel, Y. V., Walsworth-Bell, B., Bombardiere, L., Petrizzo, M. R., Damsté, J. S. S., Schouten, S., Erba, E., Silva, I. P., Farrimond, P., Tyson, R. V., and Jenkyns, H. C. (2004). Organic-carbon deposition in the Cretaceous of the Ionian Basin, NW Greece: the Paquier Event (OAE 1b) revisited. *Geol. Mag.*, 141, 401–416.
- van Aarssen, B. G. K., Alexander, R., and Kagi, R. I. (2000). Higher plant biomarkers reflect palaeovegetation changes during Jurassic times. *Org. Geochem.*, 64, 1417–1424.
- van Breugel, Y., Schouten, S., Tsikos, H., Erba, E., Price, G. D., and Sinninghe Damsté, J. S. (2007). Synchronous negative carbon isotope shifts in marine and terrestrial biomarkers at the onset of the early Aptian oceanic anoxic event 1a: Evidence for the release of ¹³C-depleted carbon into the atmosphere. *Paleoceanography*, 22, article no. PA1210.
- Vink, A., Schouten, S., Sephton, S., and Sinninghe Damsté, J. S. (1998). A newly discovered norisoprenoid, 2,6,15,19-tetramethylcosane, in Cretaceous black shales. *Geochim. Cosmochim. Acta*, 62, 965–970.
- Volkman, J. K. (1986). A review of sterol markers for marine and terrigenous organic matter. *Org.*

- Geochem.*, 9, 83–99.
- Volkman, J. K., Farrington, J. W., and Gagosian, R. B. (1987). Marine and terrigenous lipids in coastal sediments from the Peru upwelling region at 15° S: sterols and triterpene alcohols. *Org. Geochem.*, 11, 463–477.
- Wakeham, S. G., Amann, R., Freeman, K. H., Hopmans, E. C., Jørgensen, B. B., Putnam, I. F., Schouten, S., Sinninghe Damsté, J. S., Talbot, H. M., and Woebken, D. (2007). Microbial ecology of the stratified water column of the Black Sea as revealed by a comprehensive biomarker study. *Org. Geochem.*, 38, 2070–2097.
- Wakeham, S. G., Schaffner, C., and Giger, W. (1980). Polycyclic aromatic hydrocarbons in Recent lake sediments—I. Compounds having anthropogenic origins. *Geochim. Cosmochim. Acta*, 44, 403–413.
- Wakeham, S. G., Turich, C., Schubotz, F., Podlaska, A., Li, X. N., Varela, R., Astor, Y., Sáenz, J. P., Rush, D., Sinninghe Damsté, J. S., Summons, R. E., Scranton, M. I., Taylor, G. T., and Hinrichs, K.-U. (2012). Biomarkers, chemistry and microbiology show chemoautotrophy in a multilayer chemocline in the Cariaco Basin. *Deep Sea Res. Part I*, 63, 133–156.
- Wang, Y., Bodin, S., Blusztajn, J. S., Ullmann, C., and Nielsen, S. G. (2022). Orbitally paced global oceanic deoxygenation decoupled from volcanic CO₂ emission during the middle Cretaceous Oceanic Anoxic Event 1b (Aptian-Albian transition). *Geology*, 50, 1324–1328.
- Westermann, S., Stein, M., Matera, V., Fiet, N., Fleitmann, D., Adatte, T., and Föllmi, K. B. (2013). Rapid changes in the redox conditions of the western Tethys Ocean during the early Aptian oceanic anoxic event. *Geochim. Cosmochim. Acta*, 121, 467–486.
- Zumberge, J. A. (2019). *A lipid biomarker investigation tracking the evolution of the neoproterozoic marine biosphere and the rise of eukaryotes*. PhD thesis, University of California Riverside.



Research article

Tribute to Jean Dercourt

The contrasting origins of glauconite in the shallow marine environment highlight this mineral as a marker of paleoenvironmental conditions

Nicolas Tribovillard^{Ⓢ,*^a}, Viviane Bout-Roumazeilles^{Ⓢ,^a}, Romain Abraham^a, Sandra Ventalon^a, Marion Delattre^a and François Baudin^{Ⓢ,^b}

^a Université de Lille, UMR 8187 LOG – Laboratoire d’Océanologie et de Géosciences, Univ. Lille, CNRS, Univ. Littoral Côte d’Opale, IRD, 59000 Lille, France

^b Sorbonne Université - CNRS, Institut des Sciences de la Terre de Paris, UMR ISTeP 7193, 75005 Paris, France

E-mails: nicolas.tribovillard@univ-lille.fr (N. Tribovillard), viviane.roumazeilles@univ-lille.fr (V. Bout-Roumazeilles), romain.abraham@univ-lille.fr (R. Abraham), sandra.ventalon@univ-lille.fr (S. Ventalon), marion.delattre@univ-lille.fr (M. Delattre), francois.baudin@sorbonne-universite.fr (F. Baudin)

Abstract. Glauconite is an authigenic mineral reputed to form during long-lasting contact between a nucleus (a pre-existing phyllosilicate) and seawater. This protracted contact makes it possible to subtract the ions necessary for the construction of the neoformed phyllosilicate, here, glauconite (a mineral very close to an illite, rich in K and Fe). As a result, glauconite is often associated with sediments deposited in a transgressive context with a strong slowdown in the rate of sedimentation and a relatively large water layer thickness. This is the case of the Cenomanian chalk of Boulonnais (north of France). Being chemically and physically resistant, glauconite is a mineral that is often reworked, like quartz grains. This is frequently the case of the Jurassic deposits of the Boulonnais, where glauconite, almost ubiquitous, either in traces or in significant proportions of the sediments, presents a grain size sorting attesting to its transport and reworking. However, these Jurassic deposits are shallow (shoreface, upper offshore), which supports the idea that the “glauconite factory” was itself in the shallow areas of the Boulonnais. The only identified Jurassic facies of the Boulonnais where glauconite is both relatively abundant, large in size and unsorted (non reworked) are oyster reefs that formed at the outlet of cold seeps linked to a late-Jurassic synsedimentary tectonic (Kimmeridgian, Tithonian). Our work makes it possible to hypothesize that isolated oyster reefs were environments combining the redox conditions and in contact with seawater favoring the authigenic formation of glauconite. The weakly reducing conditions necessary for the formation of glauconite here are attested by the contents of metallic trace elements sensitive to redox conditions (vanadium, germanium, arsenic, in this case). Our work thus adds a new element to the understanding of the mechanisms of formation of glauconite in shallow environments.

Keywords. Jurassic, Cretaceous, Boulonnais, Oyster reefs, Redox-proxies.

Manuscript received 26 August 2022, revised 20 September 2022, accepted 5 October 2022.

1. Introduction

Glauconite and other green minerals (berthierine, odinite, etc.) are authigenic sedimentary minerals

* Corresponding author.

that form slowly at the sediment–water interface or in its immediate vicinity, as is known, especially since the work of Odin and Matter [1981]. The formation and growth of these phyllosilicates require protracted exchanges between a nucleus (usually a pre-existing clay mineral) and seawater. Glauconite is a mineral close to an illite, rich in potassium and iron, present in both Fe^{2+} and Fe^{3+} forms simultaneously. Its formation therefore requires weakly reducing conditions allowing the co-existence of ferrous ions and ferric ions. A case favoring the formation of glauconite may meet the following conditions [Chamley, 2001, Meunier and El Albani, 2007, Velde, 2014, Banerjee *et al.*, 2016a,b, Bennett and Canfield, 2020]: (1) the presence of organic matter is crucial, because its decomposition favors the development of oxygen-poor conditions and, therefore, reducing micro-milieus (fecal pellets, interior of foraminifera tests). Simultaneously, organic decay allows the release of iron initially bound to organic matter. (2) The oxidation of pre-existing pyrite also makes iron available, although this element is usually not abundant in dissolved form in seawater. (3) Finally, a long period of exchange with seawater allows the capture and incorporation of K^+ ion into the crystal lattice during neof ormation (authigenic growth). This mineral is therefore able to undergo and record the paleoenvironmental conditions that prevailed at the sediment–water interface (or at shallow depth beneath it) during its authigenic growth. This character of redox marker is central to the study proposed here. This character has very rarely been studied on the basis of the content of trace elements sensitive to redox conditions [Tribovillard *et al.*, 2021] because, to the best of our knowledge, previous studies focused on the content of major elements [e.g., Baldermann *et al.*, 2022, and reference therein]. This work therefore represents an unprecedented approach to understanding the formation of this mineral that is relatively ubiquitous in time and space on the scale of geological ages. This mineral has been extensively studied but is not fully understood, although a lot is known. Due to its mode of formation, glauconite is reputed to originate mainly from offshore areas of the continental shelf where sedimentation rates can be (extremely) low. This makes it a tool for identifying episodes of marine transgression in sequence stratigraphy patterns [e.g. Amorosi and Centineo, 2000, Hesselbo and Huggett, 2001, Banerjee *et al.*,

2022]. Simultaneously, many studies have shown that glauconite could also appear in proximal environments, possibly estuarine or lagoonal-lacustrine [El Albani *et al.*, 2005].

In the Mesozoic of Boulonnais (Northernmost France; Figure 1), glauconite is very often mentioned in the Jurassic deposits as well as under the base of the Chalk formation (glauconious sandstone of the Aptian-Albian), and in the lower part of the Chalk of Cenomanian age [Mansy *et al.*, 2007]. If the Cenomanian glauconite is interpreted as having formed contemporaneously with the chalk deposition [Amorosi and Centineo, 2000], in connection with the great transgression of the Upper Cretaceous and the concomitant decrease in sedimentation rates (synsedimentary glauconite), the glauconites of the Aptian-Albian sandstones and those of the Jurassic formations studied here show a grain size sorting attesting to their reworking (unpublished results included in this article). Thus, is it possible to consider that these reworked glauconites were initially formed in shallow environments, perhaps estuarine ones? Finally, the Jurassic deposits rich in reworked glauconite being also rich in small oyster shells (*nanogyra*) put in place during storms, the question arises as to whether the sources of glauconite could be the oyster reefs identified in the Kimmeridgian-Tithonian Argiles de Châtillon Formation [Hatem *et al.*, 2014]. Thus, the questions addressed here are: (1) Are oyster reefs the glauconite factory fueling storm deposits? (2) Given that the Upper Jurassic formations were deposited under conditions that were more reducing and more favorable to the accumulation of organic matter than those that prevailed during the deposit of the Cenomanian chalk, it is wondered whether the glauconites—possible markers of the conditions at the sediment–water interface—are enriched in redox-sensitive trace elements in Jurassic deposits compared to what is observed in the chalk.

2. Geological background

2.1. Stratigraphic framework

From the much detailed explanatory note of the geological map of Marquise [Mansy *et al.*, 2007], the stratigraphic framework of this study (Figure 1) can be sketched as follows. The study area extends from Cap de la Crèche (south of the town of Wimereux)

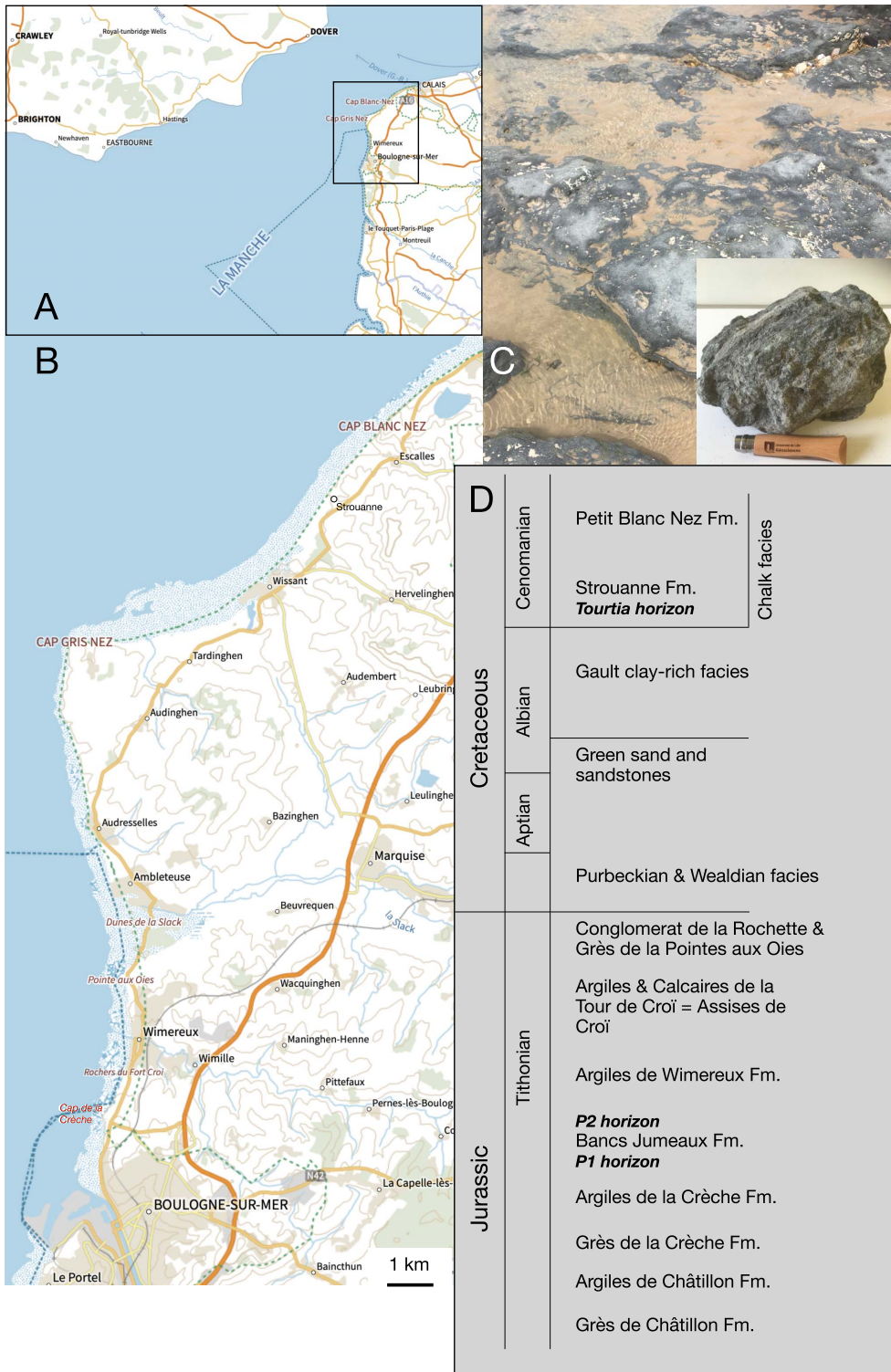


Figure 1. (A) Location of the studied zone within the English Channel. (B) Detail of the coastline of the Boulonnais with the sampling sites mentioned. (C) View of the glauconite-rich basal level of the Cenomanian chalk, the so-called Tourtia level. (D) Stratigraphy of the Upper Jurassic-Cretaceous formations of the Boulonnais.

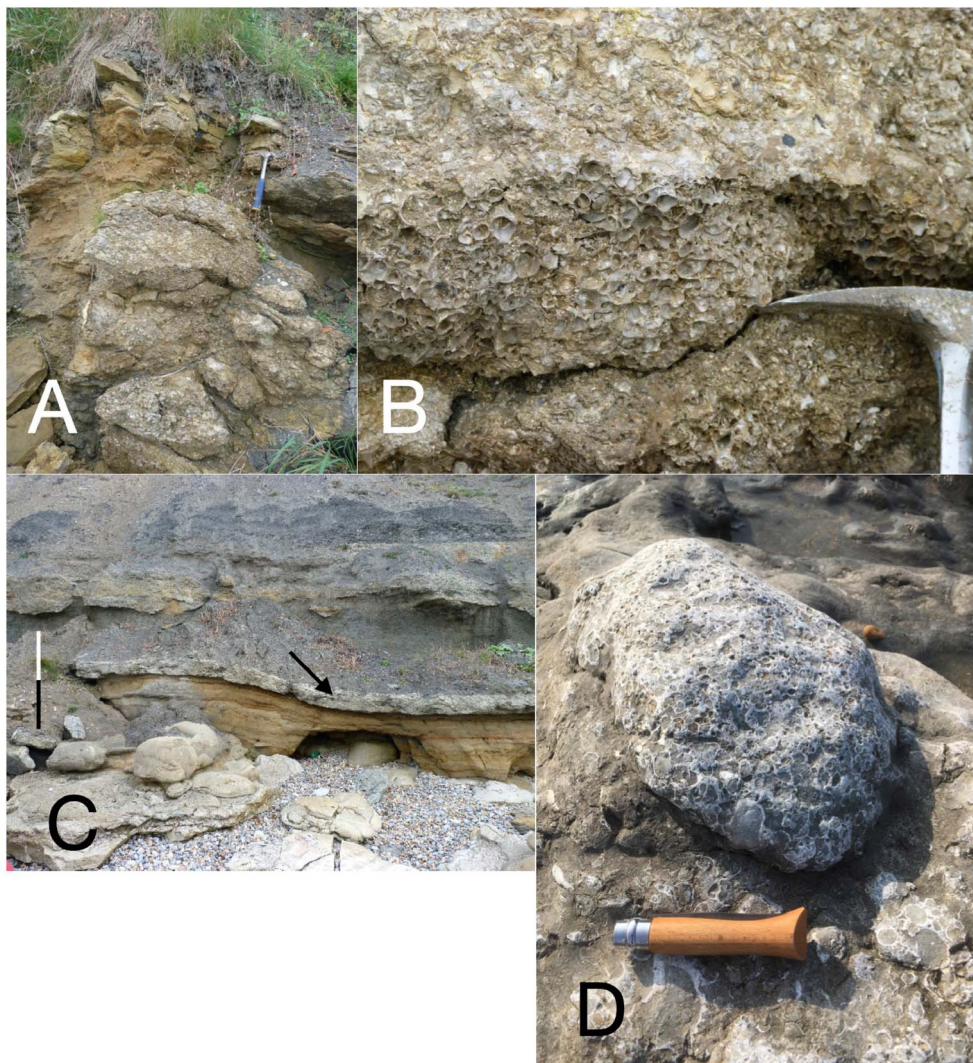


Figure 2. (A) An oyster patch reef on the beach called “La Sirène” at Cap Gris-Nez. (B) Close up view of the oyster reef. (C) The carbonate bed (arrow) separating the Grès de Châtillon Fm. (below) and the Argile de Châtillon Fm. (above). The scale bar is 2 m long. This bed, called the “Boundary Bed”, is colonized by sparse, small dimension, patch reefs (D).

to Cap Blanc Nez (Figure 1) and presents outcrops ranging in age from the Tithonian to the Cenomanian. The geological formations studied in this work start with the upper part of the Grès de Châtillon Formation (Fm.), deposited in a very shallow context. These sandstones are overlain by dark marly formations indicating a greater water depth: the Argiles de Châtillon Fm. (Figure 2). The transition from the Grès de Châtillon to the Argiles de Châtillon is marked by a specific bed containing small oys-

ter patch reefs [the so-called Boundary Bed of Hatem *et al.*, 2016; Figure 2]. The top of the Argiles de Châtillon corresponds to the return to shallow-depth conditions of deposition, with the presence of the Grès de la Crèche Fm. (Supplementary Figure S1). Above, come two marly formations, the Argiles de la Crèche and the Argiles de Wimereux formations. These two formations are separated by a meter-scale alternation of diagenetic limestone beds and marly interbeds: the Bancs Jumeaux Fm. [Tribouvillard

et al., 2012]. This formation is marked at its base and top by two discontinuity surfaces rich in phosphate debris and glauconite, the levels P1 and P2, respectively (Supplementary Figure S2). The end of the Jurassic marine-deposition episode is represented by an alternation of limestone beds and marly interbeds, both facies being glauconious (the Formation des Argiles et Calcaires of the Tour de Croï, a.k.a. Assises de Croï), which are overlain by shallow, detrital deposits showing conglomerates and sandstones with storm structures (Conglomérat de la Rochette and Grès de la Pointe aux Oies; Supplementary Figure S3). The regression that characterizes the transition from the Jurassic to the Cretaceous is echoed by freshwater carbonate stromatolites (Purbeckian facies) overlain by continental deposits (Wealdian facies). The Cretaceous transgression will be marked by the deposition of green sands and sandstones from Aptian to Lower Albian age. The middle and upper Albian is made of clay and marl deposits, sometimes glauconious (the so-called Argiles du Gault, a.k.a. the Saint-Pô and Lottinghen formations). The Cenomanian witnessed the establishment of conditions conducive to the deposition of chalk, which lasted until the end of the Cretaceous. The initial meters of chalk (the Strouanne Fm.) are very rich in glauconite. The basal level of this formation, called Tourtia, is very dark, and remarkably abundant with glauconite (Figure 1). This conspicuous level has a regional extension. The Cenomanian continues with the clayey chalk of the Petit Blanc Nez Fm.; glauconite is only present in small quantities, restricted to certain horizons. This brief presentation is illustrated in Supplementary Figure S4.

2.2. Short presentation of glauconite

Glauconite is a hydrous phyllosilicate rich in iron and potassium with the formula: $(K,Na)(Fe^{3+},Fe^{2+},Al,Mg)_2 3[Si_3(Si,Al)O_{10}](OH)_2,4H_2O$ is a mineral generally interpreted to be of diagenetic origin [Odin and Matter, 1981, Amorosi, 1995, El Albani et al., 2005, Banerjee et al., 2016a,b, López-Quirós et al., 2020]. Some conditions are commonly invoked to account for the formation of glauconite at, or close to, the sediment–water interface: reduced sedimentation rates allowing long-lasting availability of dissolved cations, together with oxygen-depleted,

mildly reducing, conditions [Odin and Matter, 1981, Meunier and El Albani, 2007, Choudhury et al., 2021, Huggett, 2021]. Glauconite usually appears as lobate grains (pellets), with frequent cracked surfaces [Boyer et al., 1977, Bayliss and Syvitski, 1982]. Along with its K_2O concentration, the morphologic characteristics of glauconite are used as criteria to estimate the duration of the authigenic formation of this mineral [Velde, 2014]. Finally, glauconite is commonly used as a tool for reconstructing sea-level variations [e.g., Banerjee et al., 2008, 2016a,b, Amorosi and Centineo, 2000, Hesselbo and Huggett, 2001, Huggett et al., 2017].

3. Materials and methods

Table 1 summarizes the sampling conducted for this study. We completed the chalk sampling [Tribouvillard et al., 2021] with samples from the Tourtia level, very rich in glauconite, taken from two outcrops between Strouanne and Cap Blanc Nez (Figure 1). To examine transgressive episodes of the Upper Jurassic, in order to compare them to the transgression of the base of the Cenomanian chalk, we sampled the transition from sandstone deposited in a very shallow environment to marls that are first sandy/silty and then progressively more clayey upward: the transition from the Grès de Châtillon Fm. to the Argiles de Châtillon Fm. (Figure 2) and the one from the Grès de la Crèche Fm. to the Argiles de la Crèche Fm. (Supplementary Figure S1). In the Argiles de Châtillon, we studied in particular the oyster reefs at the base of the formation (Figure 2), and the levels of tempestites showing a lumachel (a.k.a. coquina bed) facies where the rock is only made of compressed shells of small oysters [dominantly *nanoogyra nana*, *accessorily n. virgula*; Fürsich and Oschmann, 1986; Figure 3]. Several of these tempestites have been examined, in particular the one accompanying the Kimmeridgian/Tithonian boundary that separates the formation of the Argiles de Châtillon in two parts, as well as lenticular lumachels scattered in the claystone level located immediately below the Kimmeridgian-Tithonian boundary. We have also examined shell-rich levels in which oyster shells are abundant but not exclusive as they are in lumachels: levels P1 and P2 of the Bancs Jumeaux Fm. (Supplementary Figure S2) and three levels of

Table 1. Recapitulation of the sampling site along the Boulonnais coastline

Age	Geological formations	Sampled levels	Location (see Figure 1)
Cretaceous	Cenomanian Chalk	Glauconious chalk at the lowermost part of the formation	Beach between Strouanne and Cap Blanc Nez
	Aptian-Albian sandstones	Dark-colored sandstones visible at low tide	Strouanne beach
	Assise de Croï	Two shell-rich carbonate levels and one marly interbed	Pointe aux Oies (N Wimereux)
	Bancs Jumeaux	P1 and P2 levels and each of the marly interbeds	Pointe aux Oies (N Wimereux)
	Argiles de la Crèche	Silty marls at the very base of the formation	Rochers du Fort Croï (S Wimereux)
Jurassic	Grès de la Crèche	Two green-colored marly interbeds of the topmost part of the formation (Tithonian)	Rochers du Fort Croï (S Wimereux)
	Argiles de Châtillon	Coquina beds of the Kimmeridgian-Tithonian boundary and immediately below it	North of Audresselles (Cran du Noirda)
	Argiles de Châtillon	Silty marls at the base of the formation evolving to black shales (Kimmeridgian)	North of Audresselles (Cran du Noirda)
	Argiles de Châtillon	Oyster patch reefs at the base of the formation (the Boundary Bed, Kimmeridgian)	North of Audresselles (Cran du Noirda) and Cap Gris Nez (plage de la Sirène)

See Figure 1 for their location.

the Assises de Croï Fm.: two limestone levels and a marly inter-bed (Supplementary Figure S5).

The glauconite grains were isolated through the following protocol. Samples were digested with HCl to dissolve the carbonate phases before being rinsed. Several rinses were carried out with the necessary time for minerals heavier than clays to settle and to be removed with the supernatant. This operation was repeated at least 25 times, until the liquid kept limpid. What remained in the beakers was grains of glauconite and quartz (plus some accessory minerals and woody fragments). Glauconite was then separated from quartz using a Frantz magnetic separator. The grain size of the glauconite particles was studied using a laser beam-equipped analyzer Malvern MasterSizer [protocol described in Trentesaux *et al.*, 2001]. The glauconite particles were imaged using a scanning electron microscope (SEM) equipped

with a EDS-type analytical probe. The grains were also analysed by X-ray diffraction (XRD) to determine their mineralogy according to the standard protocol described in Bout-Roumzeilles *et al.* [1999] and Tribouvillard *et al.* [2021]. XRD was carried out on both oriented mounts and non-oriented mounts to fully discriminate glauconite from illite. Lastly, the elemental composition (major and trace elements) of the glauconite grains was analysed at the CNRS analytical facility: the Rock and Mineral Analysis Service (SARM), in Vandoeuvre-les-Nancy [see details of the analytical protocol (ICP-OES and ICP-MS) in Carignan *et al.*, 2004]. Some bulk-rock, coquina bed samples were analysed with a Thermo CHNS elemental analyser to determine the abundance of sulfur (pyrite) in this facies.

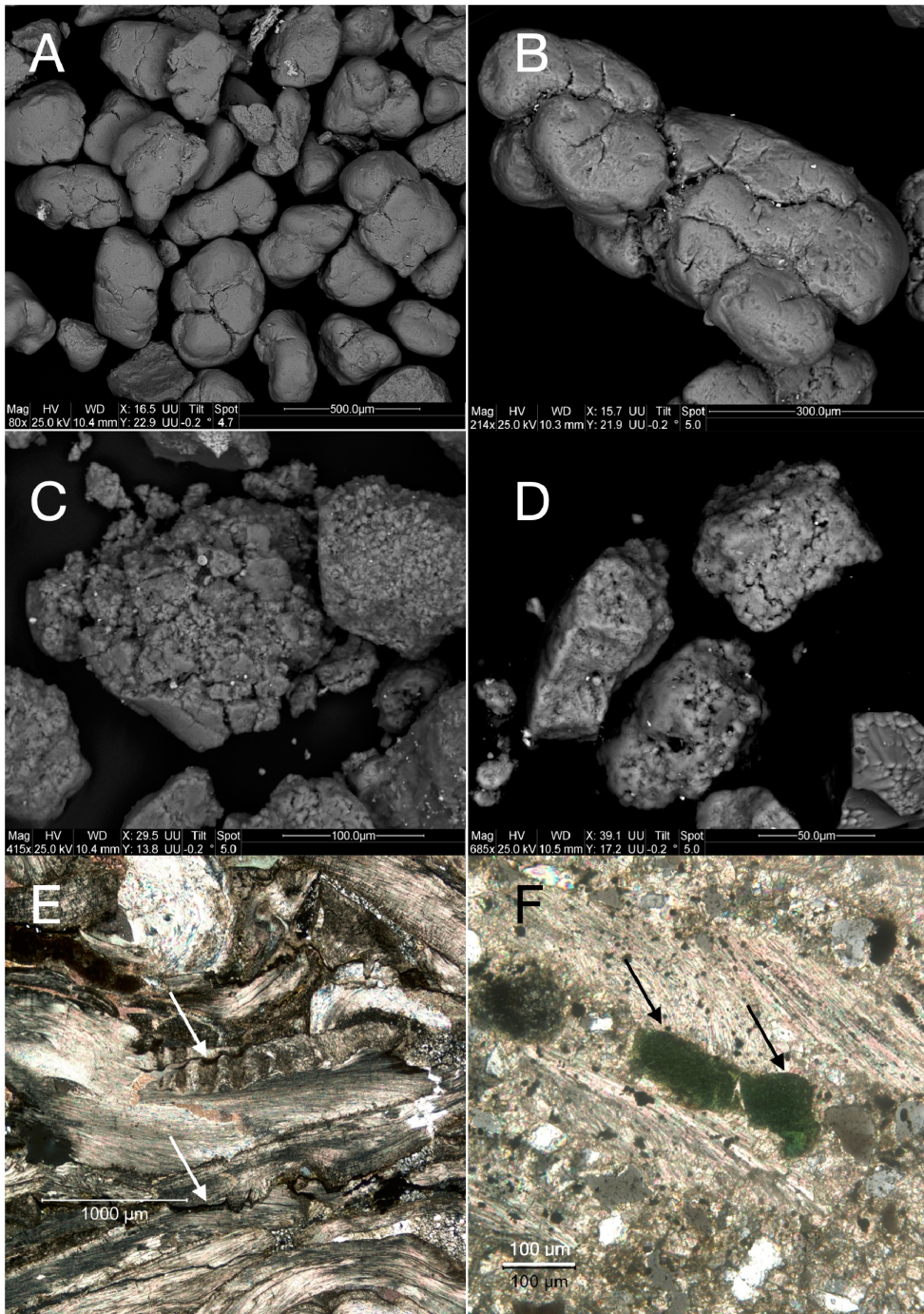


Figure 3. (A,B) Examples of glauconite grains from the oyster reefs. (C,D) Examples of glauconite grains contained in the coquina beds. Note their smaller dimensions and the marked corrosion. (E,F) Thin section observation of a coquina bed showing the dense packing of the oyster shells locally cemented with pyrite (E; white arrow) and containing glauconite grains (F; black arrows).

4. Results

Mineralogical analyses show that the green grains observed in this study are all glauconite. Tribovillard *et al.* [2021] had made this observation for chalk samples and it can be extended to all Jurassic and Aptian-Albian samples studied here. This seems to be a constant of the Mesozoic sedimentary deposits of the Boulonnais. Glauconite is almost omnipresent in our samples, but in very contrasting proportions. It has only been detected in quantities allowing its extraction and analysis in the chalk, the Aptian-Albian sandstones, the oyster reefs, the P1 and P2 levels, the Assises de Croï and the lumachels. In the later, glauconite is present but in variable amounts according to the samples, not always allowing grain size analysis (Figure 4 and Supplementary Figures S6–S8), even when rock samples of 500 g are studied. These lumachels are sometimes very rich in pyrite, seen in the form of cement (Figure 3) and not framboids. Their sulfur content can reach 28 wt%, which is considerable. Moreover, these rocks are very hard under the hammer and are difficult to fragment. It is observed that the richer the lumachels in pyritic cement, the less abundant the glauconite; the glauconite grains seen are of very small size and appear corroded when observed under the microscope (Figure 3).

In all the other samples studied, glauconite grains are systematically present but in insignificant quantities. The grain size analyzes of the samples rich in glauconite make it possible to distinguish two categories of samples, those where the grains of glauconite are poorly sorted (all the samples from the chalk and those from the oyster reefs) and those where the grains of glauconite are well sorted (all others; Figure 4 and Supplementary Figures S6–S8). The poorly sorted glauconite grains are also larger in size than the others. Regarding the samples from the Assises de Croï, where the glauconite is well sorted, the limestone levels show a mode at 78 μm and 65.5 μm , respectively, while the marly inter-bed shows a mode at 34 μm (Supplementary Figure S7).

In the samples where glauconite is well sorted, the grain size distribution of the quartz grains (isolated through magnetic separation) shows an even better sorting. See for instance the P1 and P2 samples or the Aptian-Albian samples (Figure 4). Glauconite being usually a bit denser than quartz (2.40–2.95 g/cm^3

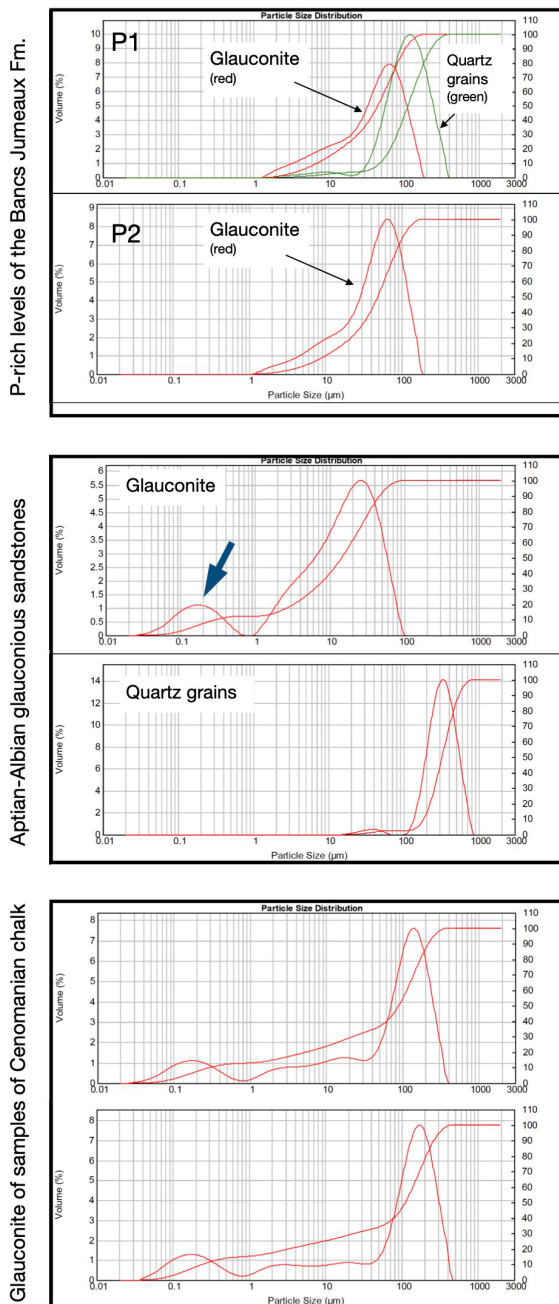


Figure 4. Illustrations of the grain size distribution patterns for glauconite and quartz grains of the P1 and P2 levels of the Bancs Jumeaux Fm., the Aptian-Albian sandstones and the Cenomanian chalk. The arrow points to a clay-sized fraction of glauconite probably released during grain wear induced by the measuring device.

Table 2. Chemical composition of 16 samples from various formations

Samples	As	Co	Cr	Cu	Ge	Ni	U	V	Zn	SiO ₂	Al ₂ O ₃	Fe ₂ O ₃	MnO	MgO	CaO	Na ₂ O	K ₂ O	TiO ₂	P ₂ O ₅	LOI	Total	
	µg/g	µg/g	µg/g	µg/g	µg/g	µg/g	µg/g	µg/g	µg/g	%	%	%	%	%	%	%	%	%	%	%	%	%
Cenomanian Chalk	5.87	25.9	115	3.6	5.0	53.1	0.15	96.2	55.5	50.82	7.81	20.1	< L.D.	4.1	0.31	0.02	8.21	0.05	< L.D.	7.61	98.86	
Tourtia 1 Chalk base	5.55	25.3	110	< L.D.	4.7	49.4	0.10	86.8	46.8	52.52	7.54	19.37	< L.D.	3.82	0.30	0.02	7.85	0.06	< L.D.	7.45	98.92	
Tourtia 2 Chalk base	5.83	25.0	118	< L.D.	5.0	46.7	0.13	90.5	51.6	51.61	7.46	20.15	< L.D.	3.84	0.31	< L.D.	8.3	0.05	< L.D.	7.35	98.80	
ONM 1 Cenom Chalk	5.86	24.3	115	48.8	4.8	53.0	0.13	92.0	54.9	53.03	7.66	19.59	< L.D.	3.98	0.38	0.03	8.19	0.06	< L.D.	7.29	100.20	
ONM 1 Cenom Chalk	6.8	33.3	109	28.8	4.8	64.6	0.09	92.4	50.0	52.45	7.95	19.46	< L.D.	4.18	0.31	0.03	8.39	0.04	< L.D.	7.39	100.20	
ONM 1 Cenom Chalk	5.82	29.2	113	34.2	5.3	68.8	0.10	94.5	58.2	52.51	7.95	19.43	< L.D.	4.27	0.30	0.03	8.48	0.04	< L.D.	7.28	100.29	
ONM 1 Cenom Chalk	6.9	25.4	125	5.4	5.1	52.6	0.15	95.8	54.3	52.31	7.63	20.28	< L.D.	3.97	0.34	0.02	8.25	0.05	< L.D.	7.43	100.28	
Glaucous Sandstone 1	25.1	28.5	218	9.5	5.3	52.5	0.31	322	89.1	51.06	10.34	17.16	0.016	3.59	0.53	0.05	6.98	0.36	< L.D.	8.99	99.07	
Assises de Croi 1	26.8	9.9	139	4.4	8.1	18.0	0.23	132	72.5	47.47	5.44	27.47	< L.D.	2.73	0.20	0.03	8.9	0.05	0.17	7.32	98.96	
Assises de Croi 2	25.2	8.9	138	3.8	8.1	18.8	0.33	126	72.7	47.66	5.50	27.41	< L.D.	2.73	0.20	0.03	8.12	0.05	0.17	7.26	99.13	
Bancs Jumeaux P1	28.4	14.7	302	13.1	8.1	22.8	0.85	150	74.9	49.39	7.34	22.97	0.017	2.42	0.31	0.08	7.6	0.24	0.27	8.99	99.07	
Bancs Jumeaux P2	27.2	12.1	280	11.6	8.6	17.7	0.46	138	71.8	56.14	6.58	19.14	< L.D.	2.10	0.42	0.06	6.30	0.22	0.12	8.16	99.25	
Oyster patch reef 1	26.9	10.0	138	4.3	8.1	18.0	0.13	131	72.0	47.74	5.45	27.74	< L.D.	2.37	0.19	0.03	8.90	0.06	0.18	7.23	99.89	
Oyster patch reef 2	26.0	9.9	139	3.9	8.1	17.8	0.13	128	71.7	47.55	5.42	27.14	< L.D.	2.79	0.20	0.02	8.21	0.04	0.16	7.62	99.15	
Oyster patch reef 3	26.1	29.5	267	23.0	5.3	60.2	0.68	327	99.0	50.89	10.10	16.76	0.021	3.52	0.58	0.06	6.78	0.73	0.13	9.7	98.64	
Oyster patch reef 4	26.9	10.0	143	11.5	8.0	21.1	0.27	130	70.9	47.62	5.48	27.17	< L.D.	2.74	0.19	0.03	8.14	0.05	0.16	7.91	99.50	

Blue: the Jurassic samples; green: the Cretaceous ones, Aptian-Albian glauconious sandstones and Cenomanian chalk.

versus 2.68 g/cm³), the mode of the size distribution pattern expectedly shifts toward smaller particle sizes for glauconite compared to quartz. This shift does not preclude that glauconite and quartz have been deposited simultaneously. Regarding the sandstone-to-sandy claystone transition from the Grès de la Crèche to the overlying Argiles de la Crèche, i.e., formations where glauconite is not significantly present, a well-sorted distribution is observed for the carbonate-free fractions of the sediments. Incidentally, the fallacious green color observed for the marly interbeds of the Grès de la Crèche must be ascribed to the presence of green clays in the absence of glauconite, as evidenced through XRD analysis.

Finally, the particle size analysis of the poorly sorted samples using the Malvern apparatus shows the presence of particles of micrometer size whereas the extraction protocol should have resulted in their

elimination (arrow on Figure 3 illustrating the grain size distribution). After separation and analysis (XRD) of this very fine fraction, it appears to be made of glauconite. We believe that these very fine particles are released during the analysis itself, by wear of the grains circulating into the pipes of the apparatus (see discussion below, in Section 5.3). Badly sorted glauconites are therefore more fragile than those that are well sorted.

The elemental analyses (Table 2) show that the major elements have a homogeneous distribution for all the samples studied. In particular, the K₂O and iron contents are relatively high and indicate that the glauconites can be qualified as mature (or evolved) or very mature (highly evolved), according to the pioneering work of Odin and Matter [1981]. With K₂O concentrations exceeding 8% of the glauconite composition in many samples, the mineral can be said to be highly evolved, which implies that its evolution

may have lasted between 100 ky and 1 My, according to Odin and Matter [1981]. The other samples analysed have K₂O content above 6.8% (evolved glauconite). Trace elements show more contrasting distributions. The chalk samples contain more Co and Ni than those of the Aptian-Albian sandstones and the Jurassic samples. In contrast, the Jurassic and Aptian-Albian samples are all enriched in As, Ge, V and Zn compared to the chalk samples. Among the elements sensitive to redox conditions, while vanadium is enriched, uranium is not and molybdenum is below the detection limit in most samples. Finally, the distribution of rare earth element (REE) shows that little difference is observed in the REE patterns from one sample to another (Supplementary Figure S9). An europium anomaly can be observed on each REE pattern. Thus, REE patterns are not a discriminating factor in the present study.

5. Interpretations

5.1. *Synsedimentary versus reworked glauconite*

We are faced with two contrasting logics, depending on whether we consider the glauconites present in the chalk of the Cenomanian or those present in the sandstones of the Aptian-Albian or in the Jurassic deposits. Previous work [Amorosi and Centineo, 2000, Tribovillard *et al.*, 2021] showed that the glauconite of the Boulonnais chalk responded to the typical logic of formation: very slow sedimentation rate in the “Chalk Sea” in connection with the great transgression of the Upper Cretaceous, prolonged exchanges with seawater at the sediment–water interface, formation of a synsedimentary glauconite rich in iron and potassium, showing relatively large grains and an absence of particle size sorting. The long duration of the exchanges between the seawater and the sediment–water interface could have been caused by the reduced flux of particles or by winnowing induced by currents affecting the seabed [Giresse, 1985, Giresse *et al.*, 2021, see the works of and references therein]. In contrast, the glauconite of the Aptian-Albian sandstones and that of most of the Jurassic deposits studied here show smaller, well sorted grains, which are therefore not synsedimentary but reworked from their source zones. Glauconite being a relatively dense mineral ($d = 2.40\text{--}2.95\text{ g/cm}^3$, most often 2.68 g/cm^3), it cannot be assumed that the

grains were brought up from deeper or more distal zones by ascending marine currents. More probably, the glauconite grains must have been reworked from more proximal source zones with an emplacement linked to the hydrodynamics of the depositional environment [Huggett *et al.*, 2017]. There is, however, a Jurassic facies in which the glauconite grains are not reworked: the oyster reefs observed at Cap Gris Nez and Cran du Noirda at the base of the Argiles de Châtillon Fm. Again, the grains are of relatively large size and do not show particle size sorting (Figures 2 and 3). Many of them have the same morphology as that of the grains observed within the chalk [Tribovillard *et al.*, 2021]. It makes sense to regard them as syndeposit, based on the same reasoning as that used for chalk glauconite.

5.2. *Oyster patch reefs, a glauconite factory?*

In the Jurassic deposits, the base of the Argiles de la Crèche Fm. corresponds to a transgression, with the transition from shoreface sandstones (Grès de la Crèche Fm.) to silty marl being gradually more clayey upward (Argiles de la Crèche Fm.). Yet, unlike the Cretaceous chalk transgression discussed above, the transgressive Jurassic deposits show no glauconite enrichment. Sparse grains of glauconite are present but in very low abundance. The carbonate-free fraction is made up of quartz and clay particles (Supplementary Figure S8) with the exclusion of determinable glauconite.

The same logic did not prevail for the chalk and for the Jurassic deposits; the conditions necessary for the formation of glauconite in significant quantities were not met during the episodes of transgression recorded by the lower part of the Argiles de la Crèche. The simplest hypothesis is that this detrital formation had a significantly higher sedimentation rate than that of the Cenomanian chalk, which prevented protracted exchanges between the sediment–water interface and seawater. On the other hand, glauconite is present in very large abundance in Jurassic facies rich in bivalve shells: levels P1 and P2 of the Bancs Jumeaux, some lumachels of the Argiles de Châtillon, the beds rich in shells of the Assises de Croix and finally, the oyster reefs at the base of the Argiles de Châtillon. This level rich in oyster reefs (the so-called Boundary bed) which marks the transition between the shoreface sandstones of the Grès de Châtillon

lon and the marly to shaly Argiles de Châtillon was studied by Hatem *et al.* [2016]. It is strongly impacted by the precipitation of diagenetic limestone. If we disregard it, we can make the same observation as that which was made herein above for the transition from the Grès de la Crèche to the Argiles de la Crèche: the transgression which caused the evolution of the deposits of sand to silty/clayey/shale deposits was not accompanied by syn-deposit glauconite formation.

Our results show that the glauconite of the oyster reefs at the base of the Argiles de Châtillon, whether at Cap Gris-Nez or Cran du Noirda, is clearly synsedimentary, whereas that of the other shell-rich facies is always reworked. This finding suggests that the reefs were the source of the glauconite. The glauconite formed or accumulated in the oyster reefs, and would have been mobilized at the same time as the shells during storms (or very strong currents), and redeposited in the tempestites (coquina beds) and comparable facies (such as the P1 and P2 levels or the shell-rich bed of the Assises de Croï). Associations between glauconite and oyster or lumachel reefs are mentioned in the literature [e.g., Cloud Jr., 1955, Curtis Jr., 1955, Gardner, 1957, Glenn *et al.*, 1994, Videt, 2003, Gréselle, 2007].

Glauconite can form in living oyster reefs because the conditions conducive to its authigenic formation are met there:

(1) The presence of abundant organic matter (decaying biomass, or necromass, and fecal pellets) promotes the development of low oxygen conditions [Southwell *et al.*, 2017]. These authors report that oysters can withstand conditions of low oxygenation but that then, the development of the reef is limited by a slowed larval recruitment. However, it is commonly observed that suboxic conditions develop locally in such reefs. Such weakly reducing conditions favor the formation of glauconite in which iron is present in the form of Fe^{2+} and Fe^{3+} . More strongly reducing conditions would favor the Fe^{2+} form and, in the presence of sulfide ions generated by the activity of sulfate-reducing bacteria, the precipitation of pyrite would be observed and not that of glauconite [Meunier and El Albani, 2007].

(2) As oyster reefs develop in coastal or estuarine environments, iron may be abundant enough not to be a factor limiting the formation of iron minerals [e.g., Mayer, 1982, Jilbert *et al.*, 2018, Herzog

et al., 2020]. In addition, today's oysters are naturally rich in iron [e.g., Le Gall, 1948]. If this were also true for Jurassic oysters, then reefs would have been an environment particularly favorable to the formation of glauconite. In addition, the upward growth of the reefs helps to combat burial and facilitates protracted exchanges with seawater, allowing time for glauconite to grow.

In lumachels, glauconite is present but in variable proportions, always lower than in oyster reefs. On the other hand, pyrite is very abundant there, not in the form of framboids but in that of cement binding the shells. The presence of this pyrite suggests that reducing conditions may have developed in the coquina beds in response to the activity of sulfate-reducing bacteria feeding on the necromass of the oysters or their excreta. The presence of iron possibly linked to oysters could have favored the formation of pyrite and the conditions must have been too reducing for glauconite to form. The ex-situ formation of glauconite trapped in the coquina beds is attested by the good grain size sorting of the green grains and their very small size, which show that they have been reworked (Figure 3). Additionally, recent work by Toshchakov *et al.* [2018] report that bacteria are able to reduce glauconite *in vitro*. It involves bacteria coupling hydrogenogenic CO oxidation with the reduction of Fe^{3+} minerals to ensure the production of metabolic energy [see also Shapkin *et al.*, 2013, Zavarzina *et al.*, 2016]. If this dissimilatory reduction of structural Fe^{3+} from glauconite can be observed on the time scale of laboratory analyses, this suggests that on the time scale of diagenetic phenomena, a partial destruction of glauconite may occur. This could contribute to explain the low presence of glauconite in the facies of Boulonnais which underwent the most reducing conditions. This would also explain why the glauconite grains in the coquina beds appear unusually small and corroded when viewed under a microscope (Figure 3).

5.3. *In vitro* wear of glauconite grains

Particle size analysis showed that some populations of glauconite grains released extremely fine fractions (micrometer scale) during measurement in the instrument (probable wear of the grains by the rapid current inside the measuring instrument). These are

the glauconite grains from the facies where this mineral was formed authigenically (syndeposit: chalk, oyster reefs). On the other hand, the grains from reworked deposits (coquina beds, Assises de Croÿ, Aptian-Albian sands) do not show this release of micrometer-sized particles. This observation suggests that the reworked grains are more mechanically resistant than the other, as if the reworked grains had already lost their more fragile cortex. However, there are a few exceptions: some samples with well-sorted glauconite show the presence of the clay-sized fraction of glauconite (Figure 4 and Supplementary Figure S7).

5.4. Redox proxy enrichments

A difference is observed in the content of elements sensitive to redox conditions between the chalk samples and those of the other deposits (sandstones of the middle part of the Cretaceous, Jurassic deposits). The Cenomanian Chalk samples show a relatively high content of As and V, but not of U or Mo, as detailed by Tribovillard *et al.* [2021]. The present study confirms these results and shows that the samples other than those of the chalk are even richer in As and V while are not enriched U and Mo. The absence of enrichment in U and Mo in minerals that however formed under slightly reducing conditions is explained by the absence of mineralogical support from glauconite (for U and for Mo) and the limitation of sulfide ions that restricts the capture of Mo [Tribovillard *et al.*, 2021]. On the other hand, V [which is a well-studied redox tracer; e.g., Breit and Wanty, 1991, Wanty and Goldhaber, 1992, Huang *et al.*, 2015, Bian *et al.*, 2022] is known to be easily incorporated into phyllosilicates during diagenesis/authigenesis phases [e.g., Gustafsson, 2019, Bennett and Canfield, 2020, and references therein], and As is known for its affinity for iron [Tribovillard, 2020]. However, as we know, glauconite is an iron-rich phyllosilicate. The presence of As and V is therefore expected, since glauconite forms under slightly reducing conditions. Moreover, these two elements can be transferred from the water column to the sediment in the form of organo-metallic complexes, the abundance of organic matter therefore impacts the distribution of these two elements in the sediments [Tribovillard *et al.*, 2006, Tribovillard, 2020, Gustafsson, 2019, Algeo and Liu, 2020, Bian *et al.*, 2022]. If

the idea that the oyster reefs were the source zone of the glauconite of the Jurassic deposits of the Boulonnais is adopted, then their enrichments in As and V, significantly higher than those of the chalk samples, would reflect that the environmental conditions were more reducing and/or richer in organic matter in the close environment of oyster reefs than at the time of the chalk accumulation. This interpretation is reinforced by the distribution of germanium, a trace element substituting for silicon in silicates, and showing some redox-dependent behavior [Tribovillard *et al.*, 2011]. The comparatively higher Ge enrichment in the Jurassic glauconite is consistent with the interpretation derived above using V and As.

If this result seems logical, it nevertheless shows that the elemental composition of glauconite can be used to reconstruct the redox conditions accompanying authigenesis/diagenesis. In this case, this reasoning can be applied to the glauconite present in very large quantities in the sandstones of the Aptian-Albian at the base of the chalk. This remarkably well-sorted glauconite was emplaced at the same time as the quartz grains of this detrital facies. These two phases are therefore reworked from more proximal zones on the occasion of the initiation of the great transgression of the Upper Cretaceous. This great transgression followed the emersion of the Boulonnais [and more broadly of the whole region; Mansy *et al.*, 2007] that started during the latest Jurassic [leading to the accumulation of the Purbeckian facies; Mansy *et al.*, 2007]. The resumption of marine sedimentation (mid-Cretaceous) induced by the return of the sea was therefore accompanied by the reworking of glauconite from more coastal zones, even estuaries, where the depositional conditions were to be confined. This confinement is attested by the high values of As, V and Ge contents, these values being the highest among those reported in the present study.

5.5. Europium anomaly

According to Jarrar *et al.* [2000], the negative europium (Eu) anomaly, commonly observed for glauconite, is presumably inherited from the source material, that is, the substrate upon which the authigenic growth of glauconite took place. The Eu anomaly reflects the deficiency of this element in the Earth's upper crust, because Eu values low enough to

induce europium reduction in sedimentary milieu is seldom observed [Bau and Möller, 1991]. The REE of glauconites are supplied by lithogenous, clastic material, and the contribution of seawater can be considered to be minimum [Fleet *et al.*, 1980].

6. Conclusion

This work illustrates the diversity of the places where glauconite can form. In the Boulonnais, glauconite is formed in relatively deep environments (the bottom of the Cenomanian Chalk Sea), also formed (or was accumulated) within sparse oyster patch reefs of Jurassic age, and the Aptian-Albian sandstones, linked to an incipient major transgression, collected glauconite probably originating from shallow (estuarine?) environments.

In this work, the emphasis is set upon oyster patch reefs as sites of production of glauconite. The break up of such reefs during storms allowed glauconite to be exported downdip basinward together with shells, accumulating in noticeable proportions in coquina beds or shell-rich beds.

Comparing glauconites formed in contrasting environments teaches us that their V, As and Ge concentrations are a tool for assessing the redox conditions prevailing during authigenesis, in milieu where these conditions were mildly reducing. As a matter of fact, strongly reducing environments favor pyrite precipitation over, or at the expense of, glauconite: in such environments, it may be put forward that glauconite could be (partly) destroyed post-deposition.

Conflicts of interest

Authors have no conflict of interest to declare.

Acknowledgements

We thank Olivier Averbuch, Jean-François Deconinck, François Guillot and Alain Trentesaux for sharing their knowledge of the geology of Boulonnais, as well as the reviewers and the CR Geoscience team, who helped make things possible and better than they were initially. We are grateful to Monique Gentric for her administrative management of the project. Our thanks to undergraduate intern Cynthia

Richard. This project received financial support from the INSU Tellus Syster program. We sincerely thanks the Earth Science Department of University of Lille for its support.

Supplementary data

Supporting information for this article is available on the journal's website under <https://doi.org/10.5802/crgeos.170> or from the author.

References

- Algeo, T. J. and Liu, J. (2020). A re-assessment of elemental proxies for paleoredox analysis. *Chem. Geol.*, 540, article no. 119549.
- Amorosi, A. (1995). Glaucony and sequence stratigraphy: a conceptual framework of distribution in siliciclastic sequences. *J. Sediment. Res.*, B65, 419–425.
- Amorosi, A. and Centineo, M. C. (2000). Anatomy of a condensed section: the lower cenomanian glaucony-rich deposits of cap Blanc-Nez (Boulonnais, Northern France). In Glenn, C. R., Prevot-Lucas, L., and Lucas, J., editors, *Marine Authigenesis: From Global to Microbial*. SEPM Society for Sedimentary Geology, Tulsa, OK.
- Baldermann, A., Banerjee, S., Czuppon, G., Dietzel, M., Farkaš, J., Löhr, S., Moser, U., Scheibelhofer, E., Wright, N. M., and Zack, T. (2022). Impact of green clay authigenesis on element sequestration in marine settings. *Nat. Commun.*, 13, article no. 1527.
- Banerjee, S., Bansal, U., Pande, K., and Meena, S. S. (2016a). Compositional variability of glauconites within the upper cretaceous karai shale formation, Cauvery Basin, India: implications for evaluation of stratigraphic condensation. *Sediment. Geol.*, 331, 12–29.
- Banerjee, S., Bansal, U., and Thorat, U. V. (2016b). A review on palaeogeographic implications and temporal variation in glaucony composition. *J. Palaeogeogr.*, 5, 43–71.
- Banerjee, S., Chakrabarty, S., Choudhury, T. R., *et al.* (2022). The application of glauconite for high-resolution stratigraphic interpretations of eocene succession. In Meghraoui, M. *et al.*, editors, *Advances in Geophysics, Tectonics and Petroleum Geosciences. CAJG 2019*, Advances in Science, Technology & Innovation. Springer, Cham.

- Banerjee, S., Jeevankumar, S., and Eriksson, P. G. (2008). Mg-rich ferric illite in marine transgressive and highstand systems tracts: examples from the Paleoproterozoic Semri Group, central India. *Pre-cambrian Res.*, 162, 212–226.
- Bau, M. and Möller, P. (1991). Rare earth element fractionation in metamorphogenic hydrothermal calcite, magnesite and siderite. *Mineral. Petrol.*, 45, 231–246.
- Bayliss, P. and Syvitski, J. P. M. (1982). Clay diagenesis in recent marine fecal pellets. *Geo-Marine Lett.*, 2, 83–88.
- Bennett, W. W. and Canfield, D. E. (2020). Redox-sensitive trace metals as paleoredox proxies: A review and analysis of data from modern sediments. *Earth-Sci. Rev.*, 204, article no. 103175.
- Bian, B., Chappaz, A., Schovsbo, N. H., and Sanei, H. (2022). A new vanadium species in black shales: Updated burial pathways and implications. *Geochim. Cosmochim. Acta*, 338, 1–10.
- Bout-Roumazeilles, V., Cortijo, E., Labeyrie, L., and Debrabant, P. (1999). Clay-mineral evidence of nepheloid layer contribution to the Heinrich layers in the Northwest Atlantic. *Palaeogeogr. Palaeoclimatol. Palaeoecol.*, 146, 211–228.
- Boyer, P. S., Guinness, E. A., Lynch-Blosse, M. A., and Stolzman, R. A. (1977). Greensand fecal pellets from New Jersey. *J. Sediment. Res.*, 4, 267–280.
- Breit, G. N. and Wanty, R. B. (1991). Vanadium accumulation in carbonaceous rocks: a review of geochemical controls during deposition and diagenesis. *Chem. Geol.*, 91, 83–97.
- Carignan, J., Hild, P., Morel, J., and Yeghicheyan, D. (2004). Routine analysis of trace elements in geochemical samples using flow injection and low-pressure on-line liquid chromatography coupled to ICP-MS: a study of geochemical reference materials BR, DR-N, UB-N, AN-G and GH. *Geostand. Newslett.*, 25, 187–198.
- Chamley, H. (2001). Clay mineralogy. In *Encyclopedia of Ocean Sciences*, pages 462–471. Elsevier, Amsterdam.
- Choudhury, T. R., Banerjee, S., Khanolkar, S., Saraswati, P. K., and Meena, S. S. (2021). Glauconite authigenesis during the onset of the Paleocene-Eocene thermal maximum: A case study from the Khuijala Formation in Jaisalmer Basin, India. *Palaeogeogr. Palaeoclimatol. Palaeoecol.*, 571, article no. 110388.
- Cloud Jr., P. E. (1955). Physical limits of glauconite formation. *Bull. Amer. Assoc. Petrol. Geol.*, 39, 484–492.
- Curtis Jr., N. M. (1955). Paleocology of the viesca member of the weches formation at Smithville, Texas. *J. Paleontol.*, 29, 263–282.
- El Albani, A., Meunier, A., and Fursich, F. (2005). Unusual occurrence of glauconite in a shallow lagoonal environment (Lower Cretaceous, northern Aquitaine Basin, SW France). *Terra Nova*, 17, 537–544.
- Fleet, A. J., Buckley, H. A., and Johnson, L. R. (1980). The rare earth element geochemistry of glauconites and celadonites. *J. Geol. Soc. London*, 137, 683–688.
- Fürsich, F. and Oschmann, W. (1986). Storm shell beds of *Nanogyra virgula* in the upper Jurassic of France. *Neues Jahrb. Geol. Palaontol. Abh.*, 172, 141–161.
- Gardner, J. (1957). Little Stave Creek, Alabama – Paleocologic study. In *Geological Society of America Memoir 67*. Geological Society of America, Boulder, Colorado. Chapter 20.
- Giresse, P. (1985). Le fer et les glauconies au large de l'embouchure du fleuve Congo. *Sci. Géol., Bull.*, 38, 293–322.
- Giresse, P., Bayon, G., Tallobre, C., and Loncke, L. (2021). Neodymium isotopes in glauconite for palaeoceanographic reconstructions at continental margins: a preliminary investigation from Demerara Rise. *Front. Earth Sci.*, 9, article no. 652501.
- Glenn, C. R., Arthur, M. A., Resig, J. M., Burnett, W. C., Dean, W. E., and Jahnke, R. A. (1994). Are modern and ancient phosphorites really so different? In Iijima, A., Abed, A. M., and Garrison, R. E., editors, *Siliceous, Phosphatic and Glauconitic Sediments of the Tertiary and Mesozoic*, pages 159–188. VSP Sci. Publ., Zeist.
- Gréselle, B. (2007). *Impact des variations paléoclimatiques sur la sédimentation carbonatée au Valanginien*. PhD thesis, Université Claude Bernard, Lyon I. Minéralogie. tel-00275099.
- Gustafsson, J. P. (2019). Vanadium geochemistry in the biogeosphere – speciation, solid-solution interactions, and ecotoxicity. *Appl. Geochem.*, 102, 1–25.
- Hatem, E., Tribovillard, N., Averbuch, O., Sanjofre, P., Adatte, T., Guillot, F., Ader, M., and Vidier, D. (2016). Early diagenetic formation

- of carbonates in a clastic-dominated ramp environment impacted by synsedimentary faulting-induced fluid seepage - Evidence from the Late Jurassic Boulonnais Basin (N France). *Mar. Pet. Geol.*, 72C, 12–29.
- Hatem, E., Tribovillard, N., Averbuch, O., Vidier, D., Sansjofre, P., Birgel, D., and Guillot, F. (2014). Oyster patch reefs as indicators of fossil hydrocarbon seeps induced by synsedimentary faults. *Mar. Pet. Geol.*, 55, 176–185.
- Herzog, S. D., Persson, P., Kvashnina, K., and Kritzbeg, E. S. (2020). Organic iron complexes enhance iron transport capacity along estuarine salinity gradients of Baltic estuaries. *Biogeosciences*, 17, 331–344.
- Hesselbo, S. P. and Huggett, J. (2001). Glaucony in ocean-margin sequence stratigraphy (Oligocene-Pliocene, Offshore New Jersey, USA; ODP Leg 174A). *J. Sediment. Res.*, 71, 599–607.
- Huang, J. H., Huang, E., Evans, L., and Glasauer, S. (2015). Vanadium: global (bio)geochemistry. *Chem. Geol.*, 417, 68–89.
- Huggett, J., Adetunji, J., Longstaffe, F., and Wray, D. (2017). Mineralogical and geochemical characterisation of warm-water, shallow-marine glaucony from the Tertiary of the London Basin. *Clay Miner.*, 52, 25–50.
- Huggett, J. M. (2021). Glauconites. In *Encyclopedia of Geology*, pages 334–340. Elsevier, Amsterdam, 2nd edition.
- Jarrar, G., Amireh, B., and Zachmann, D. (2000). The major, trace and rare earth element geochemistry of glauconites from the early Cretaceous Kurnub Group of Jordan. *Geochem. J.*, 34, 207–222.
- Jilbert, T., Asmala, E., Schröder, C., Tiuhonen, R., Myllykangas, J. P., Virtasalo, A., Kotilainen, J. J., Peltola, P., Ekholm, P., and Hietanen, S. (2018). Impacts of flocculation on the distribution and diagenesis of iron in boreal estuarine sediments. *Biogeosciences*, 15, 1243–1271.
- Le Gall, J. V. (1948). *Valeur Nutritive et Valeur Thérapeutique de L'huitre*, volume 2 of *Notes et Rapports de l'Office Scientifique et Technique des pêches maritimes, Nouvelle Série*. Office Scientifique et Technique des Pêches Maritimes.
- López-Quirós, A., Sánchez-Navas, A., Nieto, F., and Escutia, C. (2020). New insights into the nature of glauconite. *Am. Mineral.*, 105, 674–686.
- Mansy, J.-L., Guennoc, P., Robaszynski, F., Amédéo, F., Auffret, J.-P., Vidier, J.-P., Lamarche, J., Lef, D., Sommé, J., Brice, D., Mistiaen, B., Prud'homme, A., Rohart, J.-C., and Vachard, D. (2007). *Notice Explicative, Carte Géologique de la France (1/50 000), Feuille Marquise*. BRGM, Orléans, 2nd edition.
- Mayer, L. M. (1982). Retention of riverine iron in estuaries. *Geochim. Cosmochim. Acta*, 46, 1003–1009.
- Meunier, A. and El Albani, A. (2007). The glauconite–Fe-illite–Fe-smectite problem: a critical review. *Terra Nova*, 19, 95–104.
- Odin, G. S. and Matter, A. (1981). De glauconiarum origine. *Sedimentology*, 28, 611–641.
- Shapkin, A. A., Chistyakova, N. I., Rusakov, V. S., Zhilina, T. N., and Zavarzina, D. G. (2013). Mössbauer study of bacterial iron-reduction processes in natural glauconite and biotite. *Bull. Russ. Acad. Phys.*, 77, 734–738.
- Southwell, M. W., Veenstra, J. J., Adams, C. D., Scarlett, E. V., and Payne, K. B. (2017). Changes in sediment characteristics upon oyster reef restoration, NE Florida, USA. *J. Coast. Zone Manag.*, 20, article no. 442.
- Toshchakov, S. V., Lebedinsky, A. V., Sokolova, T. G., Zavarzina, D. G., Korzhenkov, A. A., Teplyuk, A. V., Chistyakova, N. I., Rusakov, V. S., Bonch-Osmolovskaya, E. A., Kublanov, I. V., and Gavrillov, S. N. (2018). Genomic insights into energy metabolism of *Carboxydocella thermautotrophica* coupling hydrogenogenic CO oxidation with the reduction of Fe(III) Minerals. *Front. Microbiol.*, 9, article no. 1759.
- Trentesaux, A., Recourt, P., Bout-Roumazeilles, V., and Tribovillard, N. (2001). Carbonate grain-size distribution in hemipelagic sediments from a laser particle sizer. *J. Sediment. Res.*, 71, 858–862.
- Tribovillard, N. (2020). Arsenic in marine sediments: how robust a redox proxy? *Palaeogeogr. Palaeoclimatol. Palaeoecol.*, 550, article no. 109745.
- Tribovillard, N., Algeo, T. J., Lyons, T. W., and Ribouleau, A. (2006). Trace metals as paleoredox and paleoproductivity proxies: An update. *Chem. Geol.*, 232, 12–32.
- Tribovillard, N., Bout-Roumazeilles, V., Delattre, M., Ventalon, S., Abraham, R., and Nzié, O. (2021). Syndepositional glauconite as a paleoenvironmental proxy – the lower Cenomanian Chalk of Cap Blanc Nez (N-France). *Chem. Geol.*, 584, article no. 120508.

- Tribouvillard, N., Bout-Roumazielles, V., Riboulleau, A., Baudin, F., Danelian, T., and Riquier, L. (2011). Transfer of germanium to marine sediments: Insights from its accumulation in radiolarites and authigenic capture under reducing conditions. Some examples through geological ages. *Chem. Geol.*, 282, 120–130.
- Tribouvillard, N., Sansjofre, P., Ader, M., Trentesaux, A., Averbuch, O., and Barbecot, F. (2012). Early diagenetic carbonate bed formation at the sediment-water interface triggered by synsedimentary faults. *Chem. Geol.*, 300/301, 1–13.
- Velde, B. (2014). Sediments, diagenesis and sedimentary rocks. In *Treatise Geochemistry*, volume 9, pages 351–364. Elsevier, Amsterdam, 2nd edition.
- Videt, B. (2003). *Dynamique des paléoenvironnements à huîtres du Crétacé Supérieur nord-aquitain (SO France) et du Mio-Pliocène andalou (SE Espagne): biodiversité, analyse séquentielle, biogéochimie*. PhD thesis, Université Rennes 1. tel-00006038.
- Wanty, R. B. and Goldhaber, M. B. (1992). Thermodynamics and kinetics of reactions involving vanadium in natural systems: Accumulation of vanadium in sedimentary rocks. *Geochim. Cosmochim. Acta*, 56, 1471–1483.
- Zavarzina, D. G., Chistyakova, N. I., Shapkin, A. V., Savenko, A. V., Zhilina, T. N., Kevbrin, V. V., Alekseeva, T. V., Mardanov, A. V., Gavrilov, S. N., and Bychkov, A. Yu. (2016). Oxidative biotransformation of biotite and glauconite by alkaliphilic anaerobes: The effect of Fe oxidation on the weathering of phyllosilicates. *Chem. Geol.*, 439, 98–109.



Research article

Tribute to Jean Dercourt

Data and models reveal humid environmental conditions during MIS 3 in two of the world's largest deserts

Anne-Marie Lézine^{Ⓢ,*}, Masa Kageyama^{Ⓢ,b} and Franck Bassinot^{Ⓢ,b}

^a Laboratoire d'Océanographie et du Climat - Expérimentations et Approches Numériques (LOCEAN/IPSL), CNRS UMR 7159, Sorbonne Université, Paris, France

^b Laboratoire des Sciences du Climat et de l'Environnement (LSCE/IPSL), UMR 8212 CEA, CNRS, UVSQ Orme des Merisiers, 91191 Gif-sur-Yvette cedex, France

E-mail: anne-marie.lezine@locean.ipsl.fr (A.-M. Lézine)

Abstract. MIS 3 environmental conditions in Africa north of the Equator and the Arabian Peninsula have long been controversial due to data scarcity and methodological caveats. In this paper we compare 245 continental hydrological records and 11 long and continuous continental and marine cores with results from the IPSL general circulation model to discuss hydrological changes between 59 and 29 ka in North Tropical Africa, North (Mediterranean) Africa and the Arabian Peninsula. Despite a generally glacial context, wet conditions widely expanded giving place to numerous lakes, rivers and wetlands. The major result of our study is to show that humid conditions appeared much earlier and were more prevalent in the Arabian Peninsula than in Africa, due to the conjunction of monsoon rains in summer and Mediterranean rains in winter. The mechanisms driving MIS 3 humidity in our study area involve global cooling factors such as greenhouse concentrations and ice volume, which have impacted available moisture, orbital forcing, which impacts monsoon circulation and amplitude and sensitivity to the state of the Atlantic Meridional Overturning Circulation (AMOC).

Keywords. MIS 3, Tropical Africa, North Africa, Arabian Peninsula, Continental hydrology.

Funding. European Research Council TracSymbols project (Grant agreement no. 249587).

Manuscript received 4 July 2023, revised 9 October 2023, accepted 10 October 2023.

1. Introduction

Increasing archaeological and paleogenetic evidence in desert areas of northern Africa and the Arabian Peninsula shows that the period spanning the time interval 59,000–29,000 years ago (i.e., Marine Isotopic Stage 3) was crucial for human history with important migration waves of *Homo sapiens* from Africa into the Arabian Peninsula and the Levant [e.g., Drake et al., 2013, Gracea, 2016, Timmermann and

Friedrich, 2016]. However, the environmental conditions behind these migrations are poorly known. The time interval corresponding to MIS 3 belongs to the last glacial period (70–15 ka). The paucity of continental records corresponding to this period has been interpreted as indicating the absence of wet phases between MIS 5 and the Holocene throughout the Sahara [Causse et al., 1988]. But that conclusion has been debated ever since. Intense deflation during the last ice age [e.g., Sarnthein, 1978] could have largely destroyed or severely damaged lake or fluvial sediments, which could have reflected climatic conditions favourable to the settlement or migration of hu-

* Corresponding author.

man populations.

In addition to the paucity of paleoenvironmental archives, there is a major methodological limitation: due to the short half-life time of ^{14}C (5730 years) the radiocarbon dating method reaches its limit of use around 50,000 years. Contamination of lake sediments by older carbon from groundwater or detrital material, or recrystallisation process cast doubt on the quality of the dating at the limit of the method [Fontes and Gasse, 1989]. In recent decades, radiocarbon dating has been complemented by the increasing use of U/Th or luminescence methods for dating continental sediments, thereby improving significantly age reconstructions, despite the large uncertainties that can be associated with these methods. Whenever they are available, well-dated and continuous continental and marine records can shed light on the chronology of climatic events which punctuated MIS 3. However, these records are too scarce to provide a global view of the evolution of climatic and environmental conditions over North Africa and the Arabian Peninsula. In particular, they cannot address the geographical spreading and retraction of humid areas. Thus, to complement these few continuous records, we also collected published data to build a comprehensive database of well-dated samples from wet environments (lakes, paleosoils, river terraces, concretions and travertines). We interpret the number of dated samples over 1000-year time windows along the MIS 3 as an indicator of humidity. The likelihood of collecting and dating those wet paleo-environmental archives is higher for time intervals when humid conditions prevailed over North Africa and the Arabian Peninsula, thus resulting in many more sedimentation sites and higher chances that some of these archives have reached us despite the intense deflation of the last ice age. The large dating uncertainties of the continental samples do not allow us to interpret the rapid variations seen in the high-resolution continuous records, nor to confidently discuss leads and lags between climate indicators at different sites. Thus, the main objective of this article is limited to (i) evaluating whether MIS 3 was drier or wetter compared to the pre-industrial period, and (ii) comparing the climatic signals and their evolution over three regions of the northern hemisphere: (1) Tropical Africa, (2) North Africa and (3) East Africa and the Arabian Peninsula (Figure 1). Our reconstructions are compared with past climate

simulations obtained with the climate model from IPSL (IPSLCM5A-LR) in order to discuss the forcings and the mechanisms involved in the climate system.

2. Modern climate conditions

The monsoonal climate of tropical North Africa and the Arabian Peninsula is characterised by seasonal reversal of the atmospheric circulation and migration of the intertropical convergence zone (ITCZ) associated with the tropical rain belt. In summer, southwesterly surface winds carry moisture from the Atlantic and Indian oceans to the adjacent continents. Atlantic monsoon fluxes penetrate far northward over northern Africa to the Tropic of Cancer and eastward to eastern Sudan whereas the easternmost areas of northern Africa are mainly subjected to the Indian monsoon influence. SW Indian monsoon fluxes follow the southern Arabian coasts then penetrate eastward to southern Iran, Pakistan and western India. In winter, the atmospheric circulation reverses with the development of northeasterly winds blowing toward the ocean and resulting in dry conditions over the continents. Wet conditions are observed, however, over the Red Sea and in the Arabo-Persian Gulf corridors owing to the penetration of Mediterranean depressions during winter.

3. The data sets

In order to subdivide our dataset into internally consistent, climate areas, three main regions have been distinguished based on the respective influence of tropical and Mediterranean climates. These three regions are: (1) Tropical Africa (including the Eastern Atlantic) from the Atlantic coast to the eastern border of Sudan which encompass areas under the predominant influence of summer rains from the African monsoon, (2) North Africa influenced by winter rains from the Mediterranean area and (3) eastern tropical Africa (Ethiopia and Dibouti) and the Arabian Peninsula (including the Arabian Sea and the Red Sea), which are influenced by the Indian monsoon, and the Mediterranean rains. Marine records from the eastern Mediterranean are included in sector 3 because they are influenced by the Nile River, whose watershed includes the Ethiopian highlands.

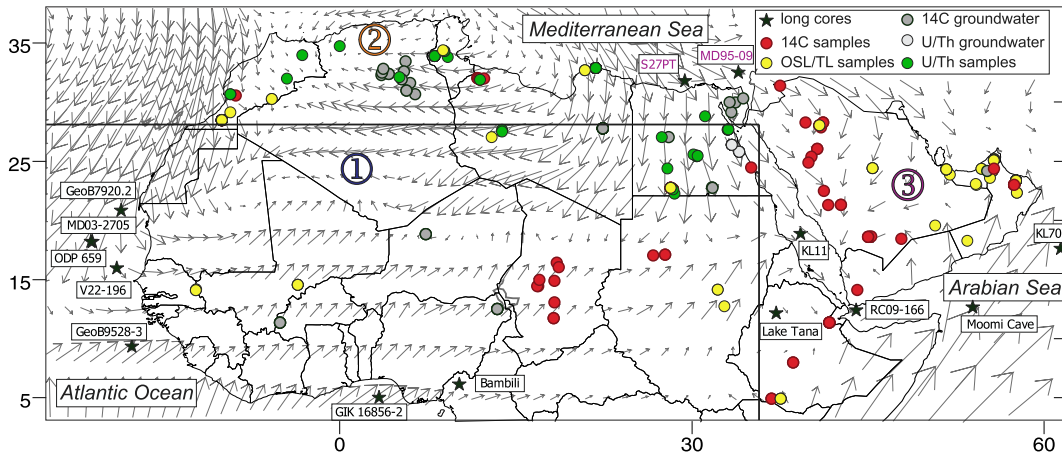


Figure 1. Location map of the MIS 3 dated continental records and long paleoclimatic records cited in the text. Grey arrows indicate the strength and direction of the main 925 hPa monsoonal winds during boreal summer (NCEP-DOE AMIP-II Reanalysis [Kanamitsu et al., 2002]). Numbers refer to (1) Tropical Africa, (2) North Africa and (3) Eastern tropical Africa and the Arabian Peninsula. Continuous paleo-archives from tropical Africa and eastern tropical Africa and the Arabian Peninsula are shown in Figures 4 and 5, respectively.

3.1. Continuous continental and marine records

3.1.1. Tropical Africa, including eastern Atlantic Ocean sites

We selected long, published sequences from West Africa to provide us with vegetation information (pollen, plant waxes, carbon isotopes) and continental hydrology (pollen, sediments). From South to North (Figure 2):

- **Gulf of Guinea:** Pollen data were used to reconstruct phases of forest expansions in cores GIK 16856-2 (4.805 N, 3.40167 E) [Dupont and Weinelt, 1996] and Bambili (5.93369 N, 10.24064 E) [Lézine et al., 2019] located off the mouth of the Niger River and off the nearby Cameroon highlands, respectively.
- **Off the Sahel and the Sahara:** The percentage of C_4 and C_3 vegetation as well as variations in continental humidity were reconstructed from (i) marine records of the $\delta^{13}C$ of plant leaf waxes (*n*-alkanes) obtained on core GeoB9528-3 [9.166 N, 17.6635 W, Castañeda et al., 2009] and ODP site 659 [18.083333 N, 21.033333 W; Kuechler et al., 2013] and (ii) the pollen content of core V22-196 [15.83333 N, 18.95 W; Lézine and

Casanova, 1991]. Continental humidity over the Sahara was reconstructed based on the ratio of hemi-pelagic mud to Aeolian dust in core GeoB7920.2 [20.7515 N, 18.581667 W; Tjallingii et al., 2008].

3.1.2. Eastern Africa, including sites from the Indian Ocean and the Arabian Sea (Figure 3)

- **Eastern Africa:** At Lake Tana in northwest Ethiopia (12 N, 37.25 E) [Lamb et al., 2018] the Ca/Ti ratio was used as a proxy for the lake level change. Off the mouth of the Nile River in the Mediterranean Sea, the Fe content of core MS27PT [31.798333 N, 29.461667 E; Revel et al., 2010] was used to infer the Nile River discharges and wet phases in its watershed including the Ethiopian highlands.
- **The Arabian Sea:** The $\delta^{18}O$ variations recorded in the stalagmite M1-2 from the Moomi Cave on Socotra Island [12.498168 N, 54.209132 E; Burns et al., 2003, 2004, Fleitmann et al., 2004] were used to infer past changes in precipitation in the Arabian Sea area. Past hydroclimatic variations in the Gulf of Aden and the Arabian Sea were also deduced from the stable hydrogen isotopic composition of leaf waxes from marine core

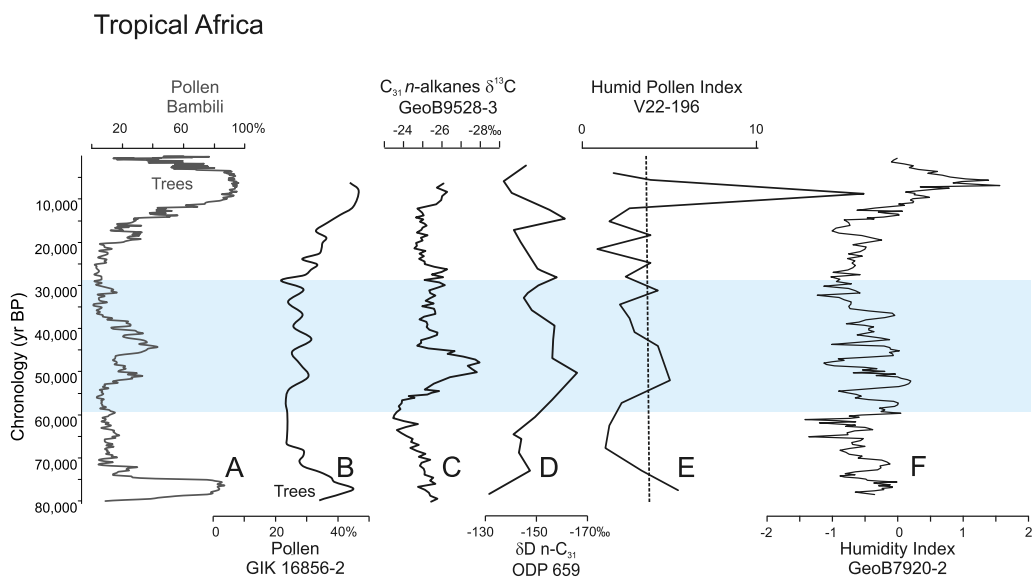


Figure 2. MIS 3 in North Tropical Africa: From left to right (A) tree pollen percentages (Lake Bambili, Cameroon) [Lézine *et al.*, 2019]; (B) tree pollen percentages (Core GIK 16856-2) [Dupont and Weinelt, 1996]; (C) $\delta^{13}\text{C}$ of plant leaf waxes (Core GeoB9528-3) [Castañeda *et al.*, 2009]; (D) $\delta^{13}\text{C}$ of plant leaf waxes (Core ODP 659) [Kuechler *et al.*, 2013]; (E) Humid Pollen Index (Core V22-196) [Lézine and Casanova, 1991]; (F) Humidity Index (Core GeoB7920.2) [Tjallingii *et al.*, 2008]. The blue band indicates the period corresponding to MIS 3.

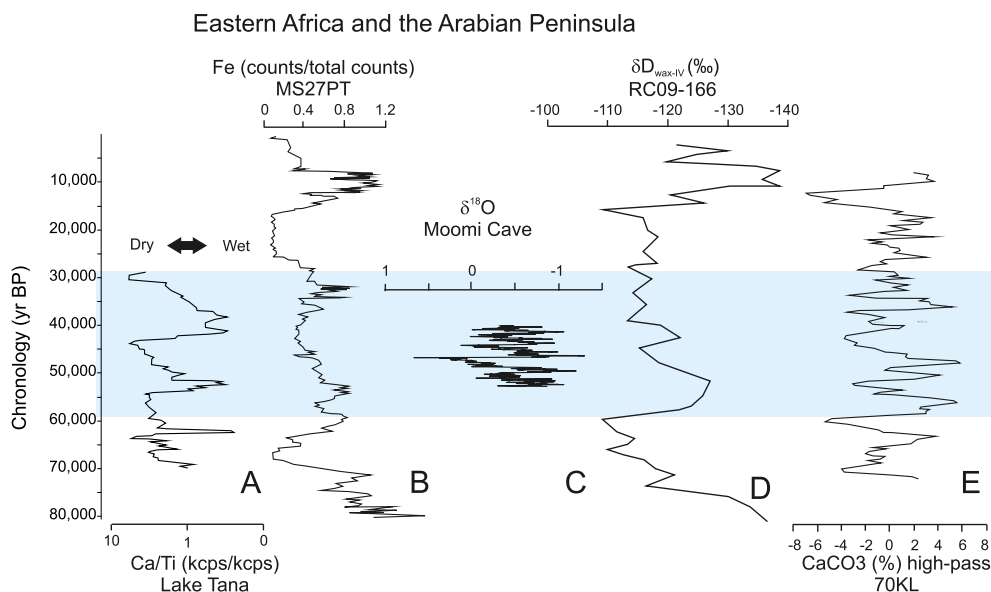


Figure 3. MIS 3 in Eastern Africa and the Arabian Peninsula: (A) Lake Tana (Ethiopia) Ca/Ti ratio [Lamb *et al.*, 2018]; (B) Nile River record from core MS27PT Fe [Revel *et al.*, 2010]; (C) Moomi Cave (Socotra Island) $\delta^{18}\text{O}$ record [Burns *et al.*, 2003, 2004]; (D) Stable hydrogen isotopic composition of leaf waxes from Core RC09-166 [Tierney *et al.*, 2017]; (E) CaCO_3 from Core KL70 [Leuschner and Sirocko, 2000].

RC09-166 [12.25 N, 44.0666667 E; Tierney *et al.*, 2017] and the %CaCO₃ profile of core KL70 [17.5 N, 61.5 E; Leuschner and Sirocko, 2000].

3.2. Continental hydrological samples

Our data set contains 245 dated samples from lake sediments, paleosoils, fluvial terraces, speleothems and travertines/springs collected at 82 localities in North Africa and the Arabian Peninsula and published in the literature (Figures 1 and 4; Supplementary Table 1). We also examined seventy-four dated groundwater samples from 27 localities.

The age control is based on (i) 75 AMS and conventional radiocarbon dates and Electron Spin Resonance dates (ESR) on lake carbonates, remains of aquatic faunas and organic matter (ii) 61 luminescence (OSL, TL, IRSL) dates on quartz grains and (iii) 46 Uranium–Thorium (U–Th) dates on lake, spring and speleothem carbonates. All dates are abbreviated ka BP.

Raw ¹⁴C dates were converted to calendar ages using the CALIB 8.2 software [Stuiver and Reimer, 1993]. Most of these dates originate from isolated samples or discontinuous archives, as is usual under predominantly arid climate conditions [Lézine *et al.*, 2014]. The ¹⁴C dating of North Africa paleoarchives developed following the pioneering work of Gasse [1975] in Djibouti, Street [1979] in Ethiopia and Servant [1983] in Chad. There are total 42 ¹⁴C dates in MIS 3 paleoarchives of north tropical Africa: Egypt (9), Chad (9), Ethiopia (4), Morocco (5), Libya (6), Djibouti (6) and Sudan (3). In Arabia, there are 33 published radiocarbon dates, 23 in Saudi Arabia, 8 in Oman, 1 in the United Arab Emirates and 1 in Yemen. In Africa as in Arabia, the ¹⁴C dates are mainly from lake (47) and river (18) sediments. There are only 5 ¹⁴C dates obtained on palustrine sediments (including paleosoils) and 8 on speleothems. Hereafter in the text, dates were calibrated and abbreviated ka BP.

Regarding the luminescence dating method, only dates on fluvial or fluvio-lacustrine sediments were considered, as Aeolian (dune) sediments from arid periods do not concern our study. It is in the Arabian Peninsula that this method has been mostly used, since Goodall's work [1995] at Sabkhat Matti (United Arab Emirates) (1 date), with 22 additional dates in the same sector, 16 in Oman, 5 in Saudi Arabia and 1

in Yemen. In Africa, after the early work of White *et al.* [1996] at Oued es Seffia (Tunisia) (1) the method has been developed in Morocco (18), Senegal (3), Sudan (4), Mali (4), Ethiopia (3), Egypt (2) and Libya (2).

The MIS 3 sediments dated by the U/Th method are only from Africa (Libya, Morocco, Tunisia, Egypt and Algeria; 46 measurements). The method was first applied to the Wadi Shati lacustrine deposits (Libya) by Gaven *et al.* [1981]. In addition, Rogerson *et al.* [2019] provided an extremely detailed chronology of MIS 3 from 35 U/Th measurements of speleothems in Susah Cave, northern Libya. We also put in our database the ESR dates from the Kharga Oasis (Egypt) obtained on fresh-water gastropod shells [Blackwell *et al.*, 2012].

In addition to the chronological control points listed above, we also collected ¹⁴C and U/Th measurements performed on African and Arabian groundwaters falling within MIS 3. However, the groundwater ages can be biased by the mixing of groundwaters from different layers in the stratified aquifers or the contributions of ancient carbon through the dissolution of carbonate minerals or the oxidation of old organic matter in the soil [Froehlich *et al.*, 2007]. While there are several ways to estimate the initial ¹⁴C activity, those contamination processes remain a major source of uncertainty. Thus, these measurements should be considered with caution.

Raw data were used to construct box-plot diagrams (Figure 4). We also combined the dated hydrological archives over 1000 yr-long time windows (Figure 7). We interpret the number of dates per interval as a proxy of climate humidity (see above).

3.3. IPSL climate model simulations

We have used the Institut Pierre-Simon Laplace (IPSL) Global Climate Model IPSLCM5A-LR [Dufresne *et al.*, 2013]. This model represents the atmosphere, ocean, sea ice and land surface and their interactions, at a resolution of 3.5° × 2.75° in longitude × latitude for the atmosphere [LMDZ model, Hourdin *et al.*, 2013] and land surface [Krinner *et al.*, 2005] and of 2° for the ocean [for which the resolution is refined in key regions, Madec, 2011]. The state of this system is computed as a function of the following external forcings: atmospheric greenhouse gases (CO₂, CH₄ and N₂O), astronomical parameters (eccentricity, precession, obliquity) and

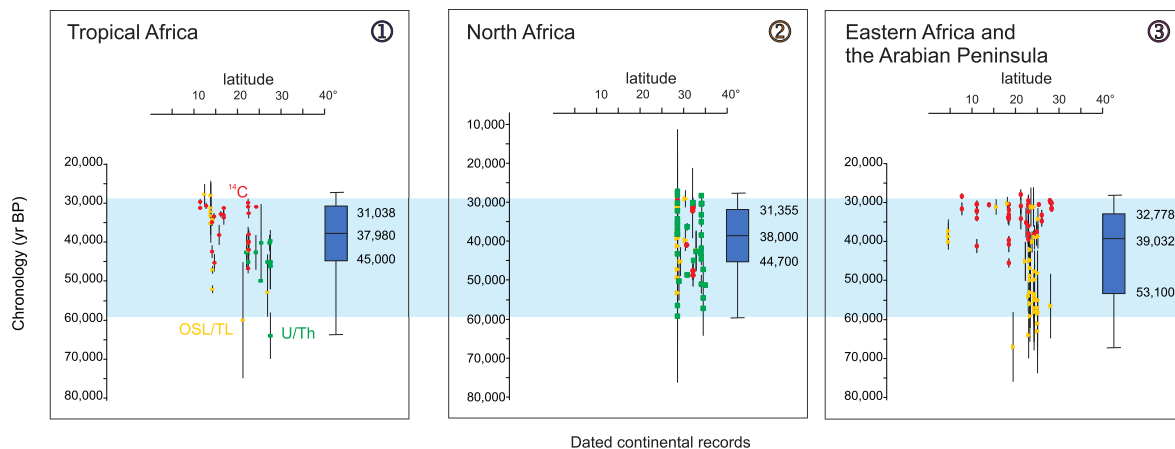


Figure 4. MIS 3 continental data in the three sectors shown in Figure 1. From left to right in each panel: the dated records and corresponding box plot calculated in the mean age (error bars excluded). The colours correspond to the different dating methods used: U/Th in green, OSL/TL in yellow and radiocarbon in red.

boundary conditions: continental distribution, land ice distribution, bathymetry and topography. All simulations were run on supercomputers Mercure and Curie at TGCC (Très Grand Centre de Calcul du CEA). Table 1 summarises the forcing and boundary conditions for the simulations analysed in the present work. The pre-industrial simulation (PI) is described in Dufresne *et al.* [2013] and serves as a reference simulation for past, historical and future climate simulations.

The boundary conditions used for the Last Glacial Maximum run presented here are described in Kageyama *et al.* [2013a]. These are compliant with PMIP3 [Otto-Bliesner *et al.*, 2009, Braconnot *et al.*, 2012] recommendations, in particular in terms of ice sheets [Abe-Ouchi *et al.*, 2015]. The run itself is a continuation of the LGM simulation presented in Kageyama *et al.* [2013a,b], in which a continuous 0.2 Sv fresh water flux is added to the North Atlantic and the Arctic Ocean so as to decrease the Atlantic Meridional Overturning Circulation to a more realistic LGM state (*i.e.* weak).

The boundary conditions used for the MIS 3 runs are described in Woillez *et al.* [2014] and Le Mézo *et al.* [2017]. They used smaller ice sheets than for the LGM (ICE_6G-C 16 ky BP ice sheet reconstructions from Peltier *et al.* [2015] available at the time of running, which corresponded to the same global sea level as MIS 3), and intermediate atmospheric greenhouse values between those known for the pre-

industrial and for the LGM, as documented by ice cores. All these runs use the same boundary conditions but differ in terms of the astronomical and greenhouse gas forcings. The “MIS 3—strong AMOC” and “MIS 3—weak AMOC” runs used 46 ka astronomical parameters and greenhouse gas concentrations while the “MIS 3 60 ka” uses 60 ka astronomical parameters and greenhouse gas concentrations [in Le Mézo *et al.*, 2017, this “MIS 3 60 ka” simulation is named MIS4F, it actually sits at the boundary between MIS 3 and MIS 4]. The “MIS 3—weak AMOC” simulation is obtained by imposing a 0.2 Sv fresh water flux into the North Atlantic and Arctic Oceans to weaken the AMOC which is strong in the “MIS 3—strong AMOC” simulation. Indeed, this simulation was designed to study the sensitivity of the MIS 3 climate to the AMOC state. The AMOC ranges between 20 and 26 Sv in the MIS 3 strong AMOC run, while it stays between 8.5 and 11 Sv in the MIS 3 weak AMOC simulation (Table 1). We have included simulations with a weak and a strong AMOC because MIS 3 is characterised by AMOC instabilities which have been shown to have an impact on the African and Asian monsoons [Zhang *et al.*, 2022]. Even though the resolution of most records does not allow to depict climate changes in relationship with the AMOC instabilities, their potential impact on the recorded continental climate cannot be ignored, hence the approach of considering both states in the experimental design of the numerical experiments.

Table 1. Summary of the boundary conditions, forcings and characteristics of the IPSLCM5A-LR simulations analysed in the present work

Simulation	PI	LGM	MIS 3—strong AMOC	MIS 3—weak AMOC	MIS 3 60 ka
Period	1850	21 ky BP	46 ky BP	46 ky BP	60 ky BP
Ice sheet	Present	PMIP3	ICE_6G-C, 16 ka	ICE_6G-C, 16 ka	ICE_6G-C, 16 ka
Sea level anomaly w.r.t PI (m)	0	−120	−70	−70	−20
Eccentricity	0.016715	0.018994	0.01384268	0.01384268	0.018469
Obliquity (degree)	23.441	22.949	24.3548	24.3548	23.2329
Precession (ω —180°)	102.7	114.42	101.337	101.337	266.65
CO ₂ (ppm)	284	185	205	205	200
CH ₄ (ppb)	791	350	500	500	426
N ₂ O (ppb)	275	200	260	260	230
Initial condition	Previous piControl simulation	Previous 1000+ year-long LGM simulation, with strong AMOC	Previous MIS 3 simulation under same boundary conditions and forcings	MIS 3 AMOC on simulation, year 79	Previous simulations under same boundary conditions and forcings
Run duration (years)	250	350	200	250	210
Years analysed (since start of run)	150–249	300–349	10–189	230–249	110–209
Run reference on supercomputer Joliot-Curie	piControl2 years 2000–2099	lgm11f3 years 3350–3399	MS3I46K2 years 2320–2509	M3I46F02 years 2630–2649	MIS4fB6 years 3100–3199
AMOC (Sv) over the analysed period	7–11.5	2.5–5	20–26	8.5–11	

The AMOC value is defined as the maximum of the meridional overturning stream function along the 30° S vertical section. Minimum and maximum values of the AMOC are indicated.

4. Results

4.1. Tropical Africa and North Africa

4.1.1. Long paleoclimatic records

Marine cores and long continental series from West Africa between 5° and 20° 45 N reveal a coherent picture of higher humidity during MIS 3 than during MIS 4 and MIS 2. Such a higher humidity is responsible for the development of plant cover and is therefore readily seen in pollen and leaf wax records (Figure 2). Lézine and Casanova [1991] and Castañeda *et al.* [2009] observed a wet period between 51 (52) and 44 (45) ka with the expansion of C₃ plants in the Sahel [Castañeda *et al.*, 2009]. In addition, Kuechler *et al.* [2013] noted the expansion of C₄ herbaceous plants in the Sahara, between 61 and 40 ka with a peak at 51 ka. High-resolution analyses show that the climate was highly variable with significant phases of climatic degradation punctuating MIS 3, coeval with the Heinrich events of northern latitudes [Tjallingii *et al.*, 2008]. In the highlands of Cameroon

[Lézine *et al.*, 2019], forest trees around Lake Bambili increased as early as 53 ka and reached a maximum between 46 and 41 ka with a peak at 43.9 ka. The forest phase that extended up to 30.9 ka was punctuated by phases of disruptions at 48–46 ka (H 5), 41–39 ka (H 4), 37–34.5 ka and then 26–30 ka (H 3).

4.1.2. Continental records

Continental data from MIS 3 are extremely rare in tropical Africa west of Chad (Figure 1), which gave substance to the assumption by Causse *et al.* [1988] that there were no wet phases between MIS 5 and the Holocene throughout the Sahara. However, the unique 40 ± 20 a U/Th age initially measured by Gaven *et al.* [1981] at Wadi Shati, Southern Libya, was later confirmed by Armitage *et al.* [2007] who provided an OSL age of 52.8 ± 6.3 ka on lake deposits in the same area. In Senegal and Mali, OSL ages measured on fluvial deposits in the Falémé River [Lebrun *et al.*, 2017, Mayor *et al.*, 2018] and at Ounjougou [Rasse *et al.*, 2004] fall within the interval 38–

25 ka and 52–33 ka, respectively. As expected, given the limitations of the method and the old origin of the data [Gasse, 1975, Street, 1979, Servant, 1983, Pachur and Hoelzmann, 1991, Szabo *et al.*, 1995], the radiocarbon measurements do not extend beyond 47 ka. Two intervals around 40 and 31 ka show a high density of dates obtained in sediments from Chad, Egypt, Sudan and East Africa (Djibouti and Ethiopia). The oldest ages are recorded in Chad (45 ka) and Egypt (47 ka), while the oldest records from Eastern Africa only date from 37.6 ka (Ethiopia) and 41 ka (Djibouti). In Ethiopia, the ^{14}C age provided by Street [1979] in the Ziway-Shala Basin (31.5 ka) is of the same order as those recently provided by Viehberg *et al.* [2018] at Lake Chew Bahir by both ^{14}C (33.8 and 37.6 ka) and OSL methods (40, 38.6 and 37.2 ka). In North Africa (Libya and Morocco), radiocarbon dates clearly show two well-identified periods: an early one in Libya at 48.5–47 ka [Gracea and Giraudi, 2006], and another one common to both countries at 34.5–29.2 ka [Giraudi, 2005, Gracea and Giraudi, 2006, Mercier *et al.*, 2009, Barich *et al.*, 2010]. In addition, Occhietti *et al.* [1994] note an age of 40.7 ka in the Souss river valley (Morocco).

U/Th dating is mainly concentrated in North Africa from Morocco to Egypt and is distributed over the entire MIS 3. The periods where U/Th ages are most concentrated are between 45 and 38 ka [Egypt—Hamdan, 2000; Sultan *et al.*, 1997, Szabo *et al.*, 1989, Churcher *et al.*, 1999; Algeria—Fontes *et al.*, 1992; Tunisia—Causse *et al.*, 1989, 2003; Libya—Macklin *et al.*, 2002, Gaven *et al.*, 1981; Morocco—Mercier *et al.*, 2009] and around 30 ka [Morocco—Boudad *et al.*, 2003, Mercier *et al.*, 2009, Rousseau *et al.*, 2008; Tunisia—Causse *et al.*, 2003; Libya—Barich and Garcea, 2008, Barich *et al.*, 2010]. In addition to these fluvial and lacustrine records, Rogerson *et al.* [2019] published a well-dated U/Th series on a speleothem from northern Libya showing three major periods of speleothem growth at 56, 51 and 36 ka.

OSL dating is divided into four major groups at 53–52 ka [Mali—Rasse *et al.*, 2004; Libya—Armitage *et al.*, 2007; Morocco—Mercier *et al.*, 2009], at 47 ka [Mali—Rasse *et al.*, 2004; Morocco—Mercier *et al.*, 2009; Tunisia—White *et al.*, 1996]; between 42 and 37 ka with a peak at 39 ka [Morocco—Mercier *et al.*, 2009, Weisrock *et al.*, 2006, Thorp *et al.*, 2002; Libya—Macklin *et al.*, 2002] then between 34 and 30 ka [Morocco—Mercier *et al.*, 2009, Weisrock *et al.*, 2006;

Senegal—Lebrun *et al.*, 2017; Mali—Rasse *et al.*, 2004].

4.2. *Eastern Africa, the Arabian Peninsula and the Indian Ocean*

4.2.1. *Long paleoclimatic records*

In Eastern Africa and the Arabian Peninsula, the Ca/Ti ratio at Lake Tana [Lamb *et al.*, 2018] clearly shows two phases of high lake level at 54 ka and then between 42 and 31 ka, which is consistent with the periods of strong Nile River discharges recorded in core MS27TP between 60 and 50 ka and then between 38 and 30 ka [Revel *et al.*, 2010]. A wet period between 53.4 and 40.4 ka also is at the origin of the formation of the Moomi stalagmite on Socotra Island [Burns *et al.*, 2003, 2004]. This early humid phase is also recorded in core RC09-166 showing two wet phases in the Gulf of Aden, between 57.7 and 50.8 ka, then around 41.9 ka [Tierney *et al.*, 2017].

In detail, high-resolution studies of the Arabian Sea [KL70—Leuschner and Sirocko, 2000; Moomi Cave—Burns *et al.*, 2003, 2004] show that environmental variability during MIS 3 is consistent with the Greenland $\delta^{18}\text{O}$ ice record. In these high-resolution records, Dansgaard–Oeschger cycles and Heinrich Events were identified and H 4, in particular, revealed a strong peak in wind activity in the Red Sea [Rohling *et al.*, 2008].

4.2.2. *Continental records*

Regarding continental data, early studies in Arabia, since McClure [1976] [in e.g., Sanlaville, 1992, and reference therein], provided radiocarbon dates for MIS 3 lacustrine deposits distributed across the Peninsula between 18 and 31° N and ranging from 40.5 ka at Mundafan [McClure, 1976] to 27.7 ka at Harrat Nawasif [Zötl, 1984]. The ^{14}C ages obtained on speleothems from Oman by Clark and Fontes [1990] also fall within this interval and range from 39.2 to 29.3 ka. However, most of these ^{14}C dates have probably been subject to contamination processes by younger ^{14}C that would have resulted in considerable age rejuvenation. At Mundafan (Saudi Arabia), Rosenberg *et al.* [2011] obtained OSL dates that challenge the older ^{14}C measurements from McClure [1976, 1978] and place the Pleistocene Lake of Mundafan during MIS 5.

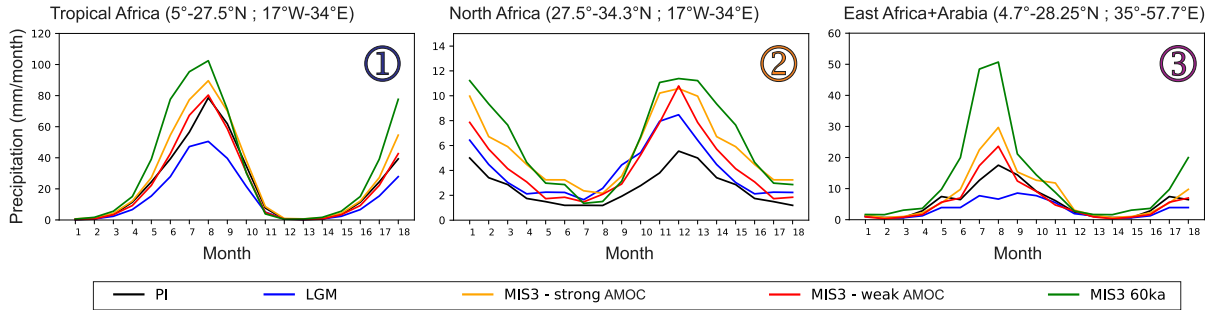


Figure 5. Mean seasonal cycle of continental precipitation (mm/month) over regions 1, 2 and 3, as simulated by the IPSLCM5A-LR climate model for the five sets of forcings and boundary conditions summarised in Table 1. The results for months 13 to 18 replicate those for months 1 to 6, in order to better show the seasonal cycle for region 2, which peaks during the winter season.

OSL ages on fluvio-lacustrine sediments indicate humid environmental conditions between 61–55 ka around the Aqaba paleolake (UAE) [Parton *et al.*, 2013]; and between 59–42 ka at Wadi Mistal (Oman) [Hoffmann *et al.*, 2015]. However, younger ages spanning the radiocarbon period are also recorded in the easternmost sector of the Arabian Peninsula in Al Ain, Liwa [Glennie and Singhvi, 2002] (31 ka) and Jebel Faya [Bretzke *et al.*, 2013] (34 ka) as well as in southern Oman, in the Dhofar region [Rose *et al.*, 2019] (30 ka) and in Yemen at Wadi Dawan [Amirkhanov, 2020] (33 ka).

4.3. Model simulations

The results of the IPSLCM5A-LR climate model simulations show that for all the conditions summarised in Table 1, the seasonal cycles of continental precipitation are characterised by a summer, monsoon-related peak for sectors 1 and 3, which contrasts with no precipitation in December and January, while for sector 2, the cycle is dominated by a wet winter and a dry summer, which still receives some rain.

For all sectors, the amplitude of the wet season is strongly sensitive to the boundary conditions and forcings for the different periods. The driest period is the LGM for all three sectors. In Tropical Africa (sector 1) the precipitation values for the MIS 3—weak AMOC run are close to the PI values, peaking at about 80 mm/month, whereas the MIS 3—strong AMOC run and the MIS 3 60 ka run are much larger than the PI values, in particular during spring and summer. The peak value for the MIS 3 60 ka run reaches

more than 100 mm/month. The largest differences with the PI control simulations are for the month of June, for which the precipitation doubles in MIS 3 60 ka compared to PI (Figure 5). This corresponds to a northward extension of the monsoon region, in particular for the MIS 3 strong AMOC and MIS 3 60 ka simulations (Figure 6).

For East Africa and the Arabian Peninsula (sector 3) all MIS 3 simulations show wetter conditions than for PI, from June to August for the MIS 3 strong and weak AMOC runs, and all year round for the MIS 3 60 ka run. The MIS 3 strong AMOC simulation shows a lengthening of the precipitation season until November. The MIS 3 60 ka results are much wetter than for all other simulations, with a maximum at 50 mm/month for August, w.r.t. between 20 and 30 mm/month for the other MIS simulations, less than 20 mm/month for the PI run and less than 10 mm/month for the LGM run. These wetter conditions in the MIS 3 simulations are due to a northward extension of the monsoon region on both sides of the Red Sea and the southern part of the Arabian Peninsula, as well as a southward extension of the rainbelt extending eastward from the Mediterranean Sea, which results in wetter conditions in the northern part of the Arabian Peninsula (Figure 6). This corresponds to autumn and winter precipitation (not shown).

Over North Africa (sector 2), the precipitation seasonal cycle is dominated by fall, winter and spring rainfall (Figure 5). The maxima are reached in December, with values of 8 mm/month for the PI run, between 10 and 11 mm/month for MIS 3 strong and weak AMOC and between 11 and 12 mm/month for

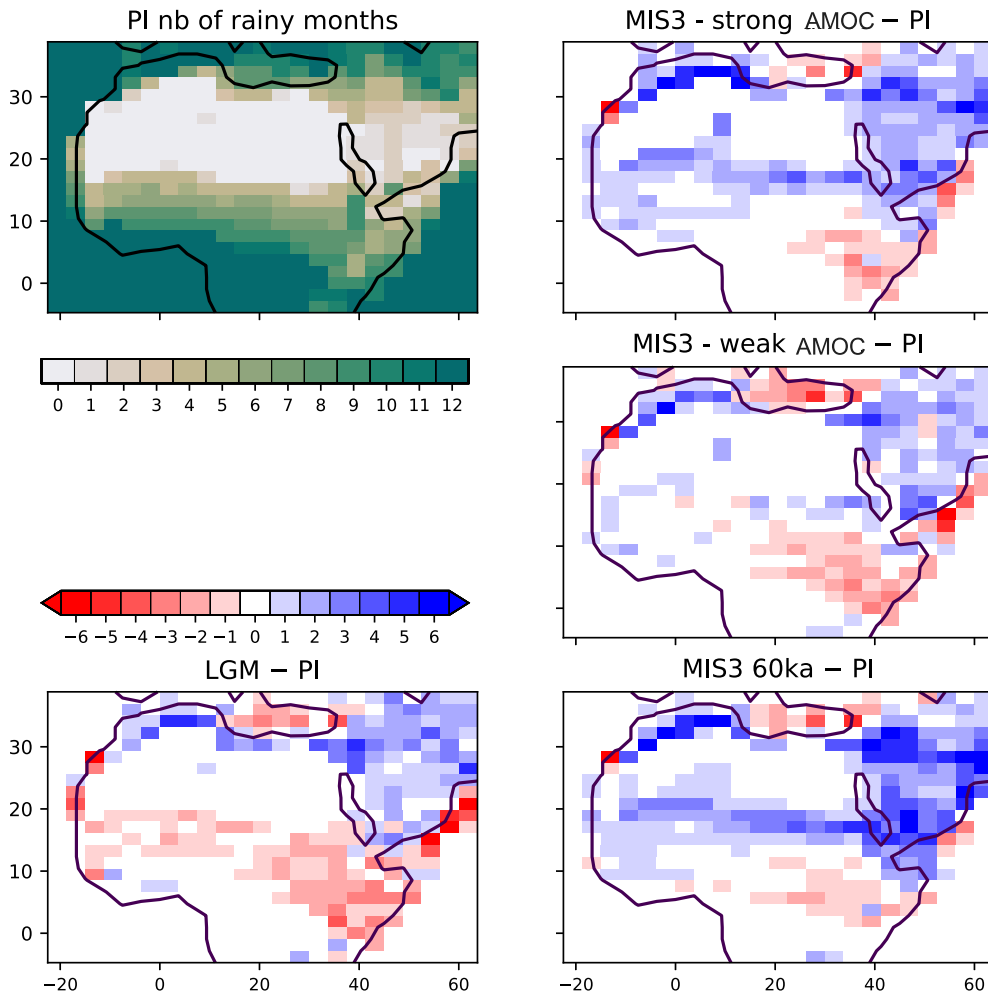


Figure 6. Number of months, in the average seasonal cycle of continental precipitation, with precipitation larger than 3 mm/month. The results are shown in absolute value for the PI simulation (top left) and as anomalies with respect to this reference for all other simulations.

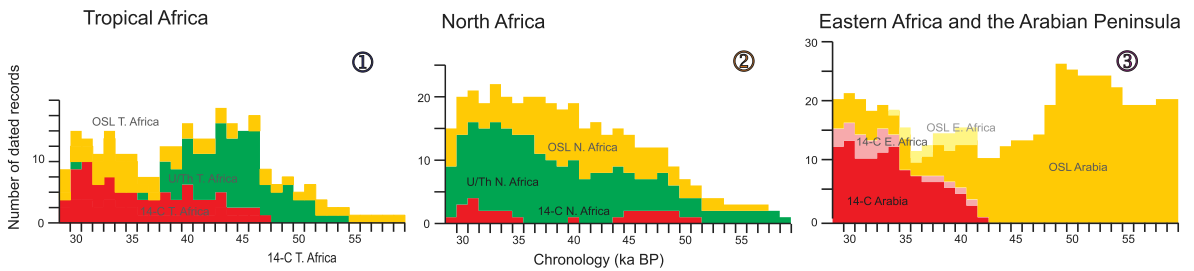


Figure 7. Number of dated records (vertical axis) of humidity during MIS 3 by 1000-year time steps. Ages are considered with their error bars (horizontal axis) in the three sectors shown in Figure 1. Underground waters are not shown in this figure.

MIS 3 60 ka. In addition to showing the strongest winter values, MIS 3 60 ka also displays the longest rainy season in spring. The spring season is the one for which there are most differences between the simulations, with low values for LGM and PI, and higher and higher values for MIS 3 weak AMOC, MIS 3 strong AMOC, and maximum values for MIS 3 60 ka. This longer duration of the rainy season is also illustrated in Figure 6.

5. Discussion

Despite the scattered nature of the records and the large chronological uncertainties, continental sediment dating and long paleoclimate series allow us to identify several key aspects:

(1) Numerous indicators of wetness (lakes, playas, rivers...) are recorded in Africa north of the Equator and in the Arabian Peninsula during MIS 3.

(2) A clearly differentiated distribution of these humid indicators is observed between sector 3 (Eastern Africa and the Arabian Peninsula), on the one hand and the two other sectors of Tropical Africa (sector 1) and North Africa (sector 2), on the other hand (Figure 7).

- In sector 3 the onset of humid conditions during MIS 3 occurred earlier than in sectors 1 and 2, starting at 64 ka in Eastern Arabia and about 10 ka later in tropical and North Africa. Wet conditions were also probably more intense during the first half of MIS 3, as shown by the number of dated records. These wet conditions lasted until the end of MIS 3. These results are consistent with previous observations from Preusser *et al.* [2002] who noticed the absence of aeolian remobilisation in the “Wahiba sands” area (Oman) between 64 and 22 ka reflecting a long, wet period. At Lake Chew Bahir (Ethiopia), Viehberg *et al.* [2018] also noticed a long period of climatic stability between 58 and 32 ka allowing the maintenance of a lake despite intense evaporation. Although our study shows that humid indicators were continuously present throughout MIS 3, this period was climatically far from stable. Two periods of marked humidity emerge: (1) an early wet phase is attested by the peak of

OSL-dated records between 59 and 48 ka; (2) a second wet phase is revealed by the distribution of ^{14}C records from both Eastern Africa and the Arabian Peninsula between 42 and 29 ka with a maximum between 39 and 34 ka. This second wet phase is confirmed by ^{14}C ages on groundwaters at Liwa (South-Eastern Arabian Peninsula) starting from 43 ka and peaking ca. 30 ka [Wood and Imes, 1995]. These results are also consistent with the Lake Tana (Ethiopia) and the eastern Mediterranean records [Lamb *et al.*, 2018, Revel *et al.*, 2010, Langgut *et al.*, 2018] which reveal two periods of enhanced humidity in eastern Africa and the Levant at 54 ka (56–44) then between 42 and 30 ka, bracketing a dry period peaking ca. 44–42 ka. Marine cores from the Arabian Sea and the Red Sea (KL11 and 70KL), as well as the Socotra stalagmite show that climatic variability also occurred at a shorter timescale, resulting in a succession of wet and arid periods that seem to mimic Dansgaard/Oeschger events at high latitudes although chronological uncertainties do not currently allow to correlate them unambiguously [Svensson *et al.*, 2008].

- In Tropical Africa and North Africa (sectors 1 and 2) there is a near absence of dated wet records prior to 53 ka (Figure 7).
- In North Africa, the number of OSL and U/Th dates increases steadily after 52 ka, reaching a peak between 42 and 37 ka (OSL) and 36–32 ka (U/Th). Radiocarbon dates, in limited number, show two humid periods between 51 and 44 ka and then between 35 and 29 ka. These results are consistent with U/Th measurements from Susah Cave in northern Libya [Rogerson *et al.*, 2019]. This record shows that humid conditions started from 53 ka and that the major phase of speleothem growth was dated from 36 ka that closely corresponds to the last period of aquifer recharge in northern Africa [Edmunds and Wright, 1979, Guendouz *et al.*, 1997, Abouel-magd *et al.*, 2014].
- In Tropical Africa, two peaks of humidity are distinctly identified: the first peak is revealed by U/Th and OSL-dated continental deposits at Wadi Shati and in Egypt/Sudan

between 47 and 37 ka, the second peak is observed in the distribution of OSL-dated deposits in Senegal and Mali between 36 and 30 ka, consistent with the ^{14}C records in both Chad and Egypt/Sudan. These results are consistent with groundwater records, which show two major phases of aquifer recharge between 55 and 42 ka in Eastern Egypt, [Sultan *et al.*, 1997, Osmond *et al.*, 1999] and in the Taoudenni basin [Huneau *et al.*, 2011] then between 39 and 29 ka in Niger [Dodo and Zuppi, 1999], Burkina Faso [Huneau *et al.*, 2011], Nigeria [Edmunds *et al.*, 1998] and Egypt [Patterson *et al.*, 2005, Froehlich *et al.*, 2007]. The long sedimentary series from the Sahara and Sahel reveal an increase in humidity and vegetation cover between about 55–53 and 42 ka, coeval with a reduced Aeolian circulation over the Sahara [Core MD03 2705—Matsuzaki *et al.*, 2011]. Near the equator, this wet period lasted until 30 ka, albeit to a lesser degree. There were several variations responsible for the degradation of the forest cover. They are coeval with Heinrich events in northern latitudes (H 5, 4 and 3). High amplitude climate variability in the eastern Atlantic domain during MIS 3 is moreover confirmed by Tjallingii *et al.* [2008].

(3) Modelling results are broadly consistent with the data showing a wet MIS 3 in all three sectors, despite the fact that this period was globally colder and drier than the pre-industrial period. In fact, favourable obliquity (for MIS 3 strong and weak AMOC runs) or precession parameter (MIS 3 60 ka) outweigh the impact of these globally colder and drier environment and favour strong monsoons both over West Africa and East Africa and the Arabian Peninsula. This confirms results obtained by other models for periods close to those analysed here [e.g. Jennings *et al.*, 2015, Singarayer and Burrough, 2015]. The impact of the AMOC strength is clearly visible for both regions, a strong AMOC being favourable to stronger monsoon. This was already shown in several earlier works performed with different types of climate models, e.g. Tjallingii *et al.* [2008] with the CLIMBER Earth System Model of Intermediate Complexity (EMICs), or in the review by Kageyama *et al.* [2013a,b], based

on Global General Circulation models and EMICs. Compared to these works, the simulations presented here, performed with a GCM for different periods within MIS 3, are either more detailed [compared to Tjallingii *et al.*, 2008] or using a more realistic set up for MIS 3 [the experiments analysed by Kageyama *et al.*, 2013a,b used the Last Glacial Maximum as a reference]. Singarayer and Burrough [2015] insist on multiple factors forcing the response of the African monsoon. This is also the case here, with the combined effects of the orbital parameters, ice sheet state and AMOC state which result in the MIS 3 simulation with a weak AMOC showing wetter conditions than for the pre-industrial, for instance. The conditions at the start of MIS 3 are particularly favourable to both monsoons too, in particular for East Africa and the Arabian Peninsula, as found by the previous studies cited above. This brings an explanation for the record of wet conditions for this period compiled here. For Tropical Africa, the model simulates slightly wetter conditions for the beginning of MIS 3 than for the middle of this period, but the differences between the periods are not as large as for East Africa and Arabia. In North Africa, the reasons for MIS 3 being wet are associated with a strengthening of the winter rain and an extension of the rainy season over spring for the wettest periods (MIS 3 strong AMOC and beginning of MIS 3). This could be due to a southern position of the mid-latitude jet stream, which would have to be confirmed by further analyses. All in all, these simulations offer possible explanations for the recorded wet conditions over tropical Africa, northern Africa, East Africa and the Arabian Peninsula during MIS 3. Additional feedbacks (e.g. vegetation and lake cover) could enhance the simulated response to astronomical parameters, greenhouse gas and ice sheets depicted by the simulations shown here.

6. Conclusion

Our results show that, contrary to what had been concluded in previous studies, MIS 3 was a relatively wet period in tropical Africa, North Africa and the Arabian Peninsula compared to MIS 4 and MIS 2. This brings important environmental constraints when trying to understand the migratory waves of *Homo sapiens* from Africa to the Arabian Peninsula and the Levant. Our results show in particular that

there are significant differences between regions, with a clear East–West contrast. The most striking breakthrough of our study is to show that eastern tropical Africa and the Arabian Peninsula were particularly humid from the end of MIS 4 already, thus well ahead of the humidification that took place over western Africa.

Numerical simulations are in agreement with the data and make it possible to specify the processes at work. From a hydrological point of view, MIS 3 in the Arabian Peninsula is characterised by a lengthening of the rainy season due to the combined effects of the Indian monsoon and Mediterranean depressions. These evolutions are, in the first place, linked to the orbital forcing. Model results suggest that precession had a major impact on monsoon intensity through its control of the northern hemisphere, low latitude summer insolation. But the simulations also suggest that obliquity may have played an important role as well, through its impact on the AMOC. The available data do not currently allow us to test this hypothesis but the question of AMOC impact on the precipitation dynamics during MIS 3 will have to be addressed in the years to come.

Declaration of interests

The authors do not work for, advise, own shares in, or receive funds from any organization that could benefit from this article, and have declared no affiliations other than their research organizations.

Acknowledgements

We would like to thank the editors of this special volume in honour of Professor J. Dercourt for inviting us to contribute. The computing time was provided by GENCI (Grand Equipement National de Calcul Intensif) and the simulations were performed using Curie at TGCC (Très Grand Centre de Calcul du CEA). M.-N. Woillez and P. Le Mézo are thanked for taking part in this endeavour, as part of their post-doctoral and PhD projects, respectively. The MIS 3 60 ka simulation was initially run for the European Research Council TracSymbols project led by C. Henshilwood and F. D’Errico (Grant no. 249587).

Supplementary data

Supporting information for this article is available on the journal’s website under <https://doi.org/10.5802/crgeos.240> or from the author.

References

- Abe-Ouchi, A., Saito, E., Kageyama, M., Braconnot, P., Harrison, S. P., Lambeck, K., Otto-Bliesner, B. L., Peltier, W. R., Tarasov, L., Peterschmitt, J.-Y., and Takahashi, K. (2015). Ice-sheet configuration in the CMIP5/PMIP3 Last Glacial Maximum experiments. *Geosci. Model Dev.*, 8, 3621–3637.
- Abouelmagd, A., Sultan, M., Sturchio, N. C., Soliman, F., Rashed, M., Ahmed, M., Kehew, A. E., Milewski, A., and Chouinard, K. (2014). Paleoclimate record in the Nubian sandstone aquifer, Sinai Peninsula, Egypt. *Quat. Res.*, 81(1), 158–167.
- Amirkhanov, H. A. (2020). *Les antiquités primitives de l’Eurasie occidentale : articles de diverses années*. Institut d’archéologie de l’Académie des sciences de Russie, Moscou. ISBN: 978-5-94375-312-1.
- Armitage, S. J., Drake, N. A., Stokes, S., El-Hawat, A., Salem, M. J., White, K., Turner, P., and McLaren, S. J. (2007). Multiple phases of North African humidity recorded in lacustrine sediments from the Fazzan Basin, Libyan Sahara. *Quat. Geochronol.*, 2(1–4), 181–186.
- Barich, B. E. and Garcea, E. A. A. (2008). Ecological patterns in the upper Pleistocene and Holocene in the Jebel Gharbi, Northern Libya: chronology, climate and human occupation. *Afr. Archaeol. Rev.*, 25(1–2), 87–97.
- Barich, B. E., Garcea, E. A. A., Giraudi, C., Lucarini, G., and Mutri, G. (2010). The latest research in the Jebel Gharbi (Northern Libya): environment and cultures from MSA to LSA and the first Neolithic findings. In Fabrizio, S., editor, *The Latest Research in the Jebel Gharbi (Northern Libya)*, pages 1000–1016. Annual of the Department of Archaeology of Libya V, Lybia antiqua.
- Blackwell, B. A. B., Skinner, A. R., Mashriqi, F., Deely, A. E., Long, R. A., Gong, J. J., Kleindienst, M. R., and Smith, J. R. (2012). Challenges in constraining pluvial events and hominin activity: examples of ESR dating molluscs from the Western Desert, Egypt. *Quat. Geochronol.*, 10, 430–435.
- Boudad, L., Kabiri, L., Farkh, S., Falguères, C., Rousseau, L., Beauchamp, J., Nicot, E., and

- Cairanne, G. (2003). Datation par la méthode U/Th d'un travertin quaternaire du Sud-Est marocain : implications paléoclimatiques pendant le Pléistocène moyen et supérieur. *C. R. Géosci.*, 335(5), 469–478.
- Braconnot, P., Harrison, S. P., Kageyama, M., Bartlein, P. J., Masson-Delmotte, V., Abe-Ouchi, A., Otto-Bliesner, B., and Zhao, Y. (2012). Evaluation of climate models using palaeoclimatic data. *Nat. Clim. Chang.*, 2, 417–424.
- Bretzke, K., Armitage, S. J., Parker, A. G., Walkington, H., and Uerpman, H. P. (2013). The environmental context of paleolithic settlement at Jebel Faya, emirate Sharjah, UAE. *Quat. Int.*, 300, 83–93.
- Burns, S. J., Fleitmann, D., Matter, A., Kramers, J., and Al-Subbary, A. A. (2003). Indian Ocean climate and an absolute chronology over Dansgaard/Oeschger events 9 to 13. *Science*, 301, 1365–1367.
- Burns, S. J., Fleitmann, D., Matter, A., Kramers, J., and Al-Subbary, A. A. (2004). Corrections and clarifications. *Science*, 305, 1567.
- Castañeda, I. S., Mulitza, S., Schefuß, E., Lopes dos Santos, R. A., Sinninghe Damsté, J. S., and Schouten, S. (2009). Wet phases in the Sahara/Sahel region and human migration patterns in North Africa. *Proc. Natl. Acad. Sci. USA*, 106(48), 20159–20163.
- Causse, C., Conrad, G., Fontes, J. C., Gasse, F., Gibert, E., and Kassir, A. (1988). Le dernier « humide » pléistocène du Sahara nord-occidental daterait du 80–100.000 ans. *C. R. Acad. Sci., Paris*, 306, 1459–1464.
- Causse, C., Coque, R., Fontes, J. C., Gasse, F., Ben Oueddou, H., and Zouari, K. (1989). Two high levels of continental waters in the southern Tunisian chotts at about 90 and 150 ka. *Geology*, 17, 922–925.
- Causse, C., Ghaleb, B., Chkir, N., Zouari, K., Ouezodou, H. B., and Mamou, A. (2003). Humidity changes in southern Tunisia during the late Pleistocene inferred from U-Th dating of mollusc shells. *Appl. Geochem.*, 18, 1691–1703.
- Churcher, C. S., Kleindienst, M. R., and Schwarcz, H. P. (1999). Faunal remains from a Middle Pleistocene lacustrine marl in Dakhleh Oasis, Egypt: palaeoenvironmental reconstructions. *Palaeogeogr. Palaeoclimatol. Palaeoecol.*, 154(4), 301–312.
- Clark, I. D. and Fontes, J. C. (1990). Paleoclimatic reconstruction in northern Oman based on carbonates from hyperalkaline groundwaters. *Quat. Res.*, 33(3), 320–336.
- Dodo, A. and Zuppi, G. M. (1999). Quaternary climatic variability in the Tarat Aquifer (Arlit, Niger). *C. R. Acad. Sci., Paris*, 328, 371–379.
- Drake, N. A., Breeze, P., and Parker, A. (2013). Palaeoclimate in the Saharan and Arabian Deserts during the Middle Palaeolithic and the potential for hominin dispersals. *Quat. Int.*, 300, 48–61.
- Dufresne, J.-L., Foujols, M.-A., Denvil, S., Caubel, A., Marti, O., Aumont, O., Balkanski, Y., Bekki, S., Bellenger, H., Benschila, R., Bony, S., Bopp, L., Braconnot, P., Brockmann, P., Cadule, P., Cheruy, F., Codron, F., Cozic, A., Cugnet, D., de Noblet, N., Duvel, J.-P., Ethé, C., Fairhead, L., Fichet, T., Flavoni, S., Friedlingstein, P., Grandpeix, J.-Y., Guez, L., Guilyardi, E., Hauglustaine, D. A., Hourdin, F., Idelkadi, A., Ghattas, J., Joussaume, S., Kageyama, M., Krinner, G., Labetoulle, S., Lahellec, A., Lefebvre, M.-P., Lefevre, F., Levy, C., Li, Z. X., Lloyd, J., Lott, F., Madec, G., Mancip, M., Marchand, M., Masson, S., Meurdesoif, Y., Mignot, J., Musat, I., Parouty, S., Polcher, J., Rio, C., Schulz, M., Swingedouw, D., Szopa, S., Talandier, C., Terray, P., Viovy, N., and Vuichard, N. (2013). Climate change projections using the IPSL-CM5 Earth System Model: from CMIP3 to CMIP5. *Clim. Dyn.*, 40, 2123–2165.
- Dupont, L. M. and Weinelt, M. (1996). Vegetation history of the savanna corridor between the Guinean and the Congolian rain forest during the last 150,000 years. *Veg. Hist. Archaeobot.*, 5, 273–292.
- Edmunds, W. M., Fellmann, E., Baba Goni, I., McNeil, G., and Harkness, D. D. (1998). Groundwater, palaeoclimate and palaeorecharge in the Southwest Chad basin, Borno state, Nigeria. In *Isotope Techniques in the Study of Environmental Change. Proceedings of a Symposium, Vienna 1997*, pages 693–707. IAEA, Vienna.
- Edmunds, W. M. and Wright, E. P. (1979). Groundwater recharge and palaeoclimate in the Sirte and Kufra basins, Libya. *J. Hydrol.*, 40, 215–241.
- Fleitmann, D., Matter, A., Burns, S. J., Al-Subbary, A., and Al-Aowah, M. A. (2004). Geology and quaternary climate history of Socotra. *Fauna of Arabia*, 20, 27–44.
- Fontes, J. C., Andrews, J. N., Causse, C., and Gibert, E. (1992). A comparison of radiocarbon and

- U/Th ages on continental carbonates. *Radiocarbon*, 34(3), 602–610.
- Fontes, J. C. and Gasse, F. (1989). On the ages of humid holocene and late pleistocene phases in North Africa—remarks on “Late quaternary climatic reconstruction for the Maghreb (North Africa)” by P. Rognon. *Palaeogeogr. Palaeoclimatol. Palaeoecol.*, 70, 393–398.
- Froehlich, K., Aggarwal, P. K., and Garner, W. A. (2007). An integrated approach in evaluating isotope data of the Nubian Sandstone Aquifer System (NSAS) in Egypt. In *Advances in Isotope Hydrology and its Role in Sustainable Water Resources Management*. IAEA-CN-151/167, pages 31–46. IAEA, Vienna.
- Gasse, F. (1975). *L'évolution des lacs de l'Afar Central (Éthiopie et T.F.A.I.) du Plio-Pléistocène à l'Actuel. Reconstitution des paléomilieux lacustres à partir de l'étude des Diatomées*. Phd thesis, Paris VI University, Paris.
- Gaven, C., Hillaire-Marcel, C., and Petit-Maire, N. (1981). A Pleistocene lacustrine episode in south-eastern Libya. *Nature*, 290(5802), 131–133.
- Giraudi, C. (2005). Eolian sand in peridesert north-western Libya and implications for Late Pleistocene and Holocene Shara expansions. *Palaeogeogr. Palaeoclimatol. Palaeoecol.*, 218(1–2), 161–173.
- Glennie, K. W. and Singhvi, A. K. (2002). Event stratigraphy, paleoenvironment and chronology of SE Arabian deserts. *Quat. Sci. Rev.*, 21, 853–869.
- Goodall, T. M. (1995). *The Geology and Geomorphology of the Sabkhat Matti Region (United Arab Emirates): a Modern Analogue for Ancient Desert Sediments from North-west Europe*. Phd thesis, University of Aberdeen. Unpublished.
- Gracea, E. A. A. (2016). Dispersal out of Africa and back to Africa: modern origins in North Africa. *Quat. Int.*, 408, 79–89.
- Gracea, E. A. A. and Giraudi, C. (2006). Late quaternary human settlement patterning in the Jebel Gharbi. *J. Hum. Evol.*, 51, 411–421.
- Guendouz, A., Moulla, A. S., Edmunds, W. M., Shand, P., Poole, J., Zouari, K., and Mamou, A. (1997). Palaeoclimatic information contained in groundwaters of the Grand Erg Oriental, North Africa. In *Isotope Techniques in the Study of Past and Current Environmental Changes in the Hydrosphere and the Atmosphere. Proceedings of a IAEA Vienna Symposium “Isotope techniques in the study of environmental change”*, pages 555–572. IAEA, Austria.
- Hamdan, M. A. E. (2000). Quaternary travertines of wadis Abu Had-Dib area, Eastern Desert, Egypt: paleoenvironment through field, sedimentology, age and isotopic studies. *Sediment. Egypt*, 8, 49–62.
- Hoffmann, G., Ruppel, M., Rahn, M., and Preusser, F. (2015). Fluvio-lacustrine deposits reveal precipitation pattern in SE Arabia during early MIS 3. *Quat. Int.*, 382, 145–153.
- Hourdin, F., Foujols, M.-A., Codron, F., Guemas, V., Dufresne, J.-L., Bony, S., Denvil, S., Guez, L., Lott, F., Ghattas, J., Braconnot, P., Marti, O., Meurdesoif, Y., and Bopp, L. (2013). Impact of the LMDZ atmospheric grid configuration on the climate and sensitivity of the IPSL-CM5A coupled model. *Clim. Dyn.*, 40, 2167–2192.
- Huneau, F., Dakoure, D., Celle-Jeanton, H., Vitvar, T., Ito, M., Traore, S., Compaore, N. E., Jirakova, H., and Le Coustumer, P. (2011). Flow pattern and residence time of groundwater within the south-eastern Taoudeni sedimentary basin (Burkina Faso, Mali). *J. Hydrol.*, 409(1–2), 423–439.
- Jennings, R. P., Singarayer, J., Stone, E. J., Krebs-Kanzow, U., Khon, V., Nisancioglu, K. H., Pfeiffer, M., Zhang, X., Parker, A., Parton, A., Groucutt, H. S., White, T. S., Drake, N. A., and Petraglia, M. D. (2015). The greening of Arabia: Multiple opportunities for human occupation of the Arabian Peninsula during the Late Pleistocene inferred from an ensemble of climate model simulations. *Quat. Int.*, 382, 181–199.
- Kageyama, M., Braconnot, P., Bopp, L., Caubel, A., Foujols, M.-A., Guilyardi, E., Khodri, M., Lloyd, J., Lombard, F., Mariotti, V., Marti, O., Roy, T., and Woillez, M.-N. (2013a). Mid-Holocene and Last Glacial Maximum climate simulations with the IPSL model—part I: comparing IPSL_CM5A to IPSL_CM4. *Clim. Dyn.*, 40, 2447–2468.
- Kageyama, M., Merkel, U., Otto-Bliesner, B., Prange, M., Abe-Ouchi, A., Lohmann, G., Roche, D. M., Singarayer, J., Swingedouw, D., and Zhang, X. (2013b). Climatic impacts of fresh water hosing under Last Glacial Maximum conditions: a multi-model study. *Clim. Past*, 9, 935–953.
- Kanamitsu, M., Ebisuzaki, W., Woollen, J., Yang, S.-K., Hnilo, J. J., Fiorino, M., and Potter, G. L. (2002). NCEP-DOE AMIP-II Reanalysis (R-2). *Bull. Am. Meteorol. Soc.*, 83, 1631–1643.

- Krinner, G., Viovy, N., de Noblet-Ducoudré, N., Ogée, J., Polcher, J., Friedlingstein, P., Ciais, P., Sitch, S., and Prentice, I. C. (2005). A dynamic global vegetation model for studies of the coupled atmosphere-biosphere system. *Glob. Biogeochem. Cycle*, 19, article no. GB1015.
- Kuechler, R. R., Schefuß, E., Beckmann, B., Dupont, L., and Wefer, G. (2013). NW African hydrology and vegetation during the Last Glacial cycle reflected in plant-wax-specific hydrogen and carbon isotopes. *Quat. Sci. Rev.*, 82, 56–67.
- Lamb, H. F., Bates, C. R., Bryant, C. L., Davies, S. J., Huws, D. G., Marshall, M. H., Roberts, H. M., and Toland, H. (2018). 150,000-year palaeoclimate record from northern Ethiopia supports early, multiple dispersals of modern humans from Africa. *Sci. Rep.*, 8(1), article no. 1077.
- Langgut, D., Almogi-Labin, A., Bar-Matthews, M., Pickarski, N., and Weinstein-Evron, M. (2018). Evidence for a humid interval at ~56–44 ka in the Levant and its potential link to modern humans dispersal out of Africa. *J. Hum. Evol.*, 124, 75–90.
- Le Mézo, P., Beaufort, L., Bopp, L., Braconnot, P., and Kageyama, M. (2017). From monsoon to marine productivity in the Arabian Sea: insights from glacial and interglacial climates. *Clim. Past*, 13, 759–778.
- Lebrun, B., Tribolo, C., Chevrier, B., Lespez, L., Rasse, M., Camara, A., Mercier, N., and Huysecom, E. (2017). Chronologie du Paléolithique ouest africain: premières datations OSL de la Vallée de la Falémé (Sénégal). *L'anthropologie*, 121(1–2), 1–8.
- Leuschner, D. C. and Sirocko, F. (2000). The low-latitude monsoon climate during Dansgaard-Oeschger cycles and Heinrich events. *Quat. Sci. Rev.*, 19(1–5), 243–254.
- Lézine, A. M., Bassinot, F., and Peterschmitt, J. Y. (2014). Orbitally-induced changes of the Atlantic and Indian monsoons over the past 20,000 years: New insights based on the comparison of continental and marine records. *Bull. Soc. Géol. Fr.*, 185(1), 3–12.
- Lézine, A.-M. and Casanova, J. (1991). Correlated oceanic and continental records demonstrate past climate and hydrology of North Africa (0–140 ka). *Geology*, 19, 307–310.
- Lézine, A. M., Izumi, K., Kageyama, M., and Achoundong, G. (2019). A 90,000-year record of Afromontane forest responses to climate change. *Science*, 363(6423), 177–181.
- Macklin, M. G., Fuller, I. C., Lewin, J., Maas, G. S., Passmore, D. G., Rose, J., Woodward, J. C., Black, S., Hamlin, R. H. B., and Rowan, J. S. (2002). Correlation of fluvial sequences in the Mediterranean basin over the last 200 ka and their relationship to climate change. *Quat. Sci. Rev.*, 21, 1633–1641.
- Madec, G. (2011). NEMO ocean engine. User manual 3.3. Note du pôle de modélisation 27. Institut Pierre-Simon Laplace (IPSL), France, ISSN No 1288-1619.
- Matsuzaki, K. M. R., Eynaud, F., Malaisé, B., Grousset, F. E., Tisserand, A., Rossignol, L., Charlier, K., and Jullien, E. (2011). Paleoceanography of the Mauritanian margin during the last two climatic cycles: From planktonic foraminifera to African climate dynamics. *Mar. Micropaleontol.*, 79, 67–79.
- Mayor, A., Douze, K., Lorenzo Martinez, M., Truffa Giachet, M., Aymeric, J., and Bocoum, H. (2018). Dynamiques techniques et environnementales dans la vallée de la Falémé (Sénégal): Résultats de la 20ème campagne du programme « Peuplement humain et paléoenvironnement en Afrique ». In *Fondation Suisse-Liechtenstein Pour Les Recherches Archéologiques à Létranger*, Annual Report SLSA, 2017, pages 157–256.
- McClure, H. A. (1976). Radiocarbon chronology of late quaternary lakes in the Arabian desert. *Nature*, 263, 755–756.
- McClure, H. A. (1978). Ar Rub' Al Khali. In Al-Sayari, S. S. and Zötl, J. G., editors, *Quaternary Period in Saudi Arabia*, volume 1, pages 252–263. Springer, Vienna.
- Mercier, N., Hatté, C., Fontugne, M., Reyss, J. L., Valladas, H., Wengler, L., Brugal, J. P., Ouammou, A., and Weisrock, A. (2009). Chronology of Upper Pleistocene sequences at Sidi Messaoud (wadi Noun, southwestern Morocco) based on ¹⁴C, optical and U-series dating. *Quat. Geochronol.*, 4(4), 326–334.
- Occhiotti, S., Bhiry, N., Rognon, P., and Pichet, P. (1994). Stratigraphie et aminochronologie des formations quaternaires de la vallée moyenne du Souss, Maroc. *Quaternaire*, 5(1), 23–34.
- Osmond, J. K., Dabous, A. A., and Dawood, Y. H. (1999). U series age and origin of two secondary uranium deposits, central eastern desert, Egypt. *Econ. Geol.*, 94, 273–280.

- Otto-Bliesner, B. L., Joussaume, S., Braconnot, P., Harrison, S. P., and Abe-Ouchi, A. (2009). Modeling and data syntheses of past climates. *Eos*, 90, 93.
- Pachur, J. and Hoelzmann, P. (1991). Paleoclimatic implications of late quaternary lacustrine sediments in Western Nubia, Sudan. *Quat. Res.*, 36, 257–276.
- Parton, A., Farrant, A. R., Leng, M. J., Schwenninger, J. L., Pose, J. I., Uerpman, H. P., and Parker, A. G. (2013). An early MIS 3 pluvial phase in Southeast Arabia: climatic and archaeological implications. *Quat. Int.*, 300, 62–74.
- Patterson, L. J., Sturchio, N. C., Kennedy, B. M., van Soest, M. C., Sultan, M., Lu, Z. T., Lehman, B., Purtschert, R., El Alfy, Z., El Kaliouby, B., Dawood, Y., and Abdallah, A. (2005). Cosmogenic, radiogenic, and stable isotopic constraints on groundwater residence time in the Nubian Aquifer, Western Desert of Egypt. *Geochem. Geophys. Geosyst.*, 6(1), article no. Q01005.
- Peltier, W. R., Argus, D. F., and Drummond, R. (2015). Space geodesy constrains ice age terminal deglaciation: The global ICE-6G_C (VM5a) model. *J. Geophys. Res. Solid Earth*, 120, 450–487.
- Preusser, F., Radies, D., and Matter, A. (2002). A 160,000-year record of dune development and atmospheric circulation in Southern Arabia. *Science*, 296(5575), 2018–2020.
- Rasse, M., Soriano, S., Tribolo, C., Stokes, S., and Huysecom, E. (2004). La séquence pléistocène supérieur d'Ounjougou (Pays dogon, Mali, Afrique de l'Ouest): évolution géomorphologique, enregistrements sédimentaires et changements culturels. *Quaternaire*, 15(4), 329–341.
- Revel, M., Ducassou, E., Grousset, F. E., Bernasconi, S. M., Migeon, S., Révillon, S., Mascle, J., Murat, A., Zaragosi, S., and Bosch, D. (2010). 100,000 years of African monsoon variability recorded in sediments of the Nile margin. *Quat. Sci. Rev.*, 29(11–12), 1342–1362.
- Rogerson, M., Dublyansky, Y., Hoffmann, D. L., Luetscher, M., Töchterle, P., and Spötl, C. (2019). Enhanced Mediterranean water cycle explains increased humidity during MIS 3 in North Africa. *Clim. Past*, 15(5), 1757–1769.
- Rohling, E. J., Grant, K., Hemleben, C., Kucera, M., Roberts, A. P., Schmeltzer, I., Schulz, H., Siccha, M., Siddall, M., and Trommer, G. (2008). New constraints on the timing of sea level fluctuations during early to middle marine isotope stage 3. *Paleoceanography*, 23(3), article no. PA3219.
- Rose, J. I., Hilbert, Y. H., Usik, V. I., Marks, A. E., Jaboob, M. M. A., Černý, V., Crassard, R., and Preusser, F. (2019). 30,000-Year-old geometric microliths reveal glacial refugium in Dhofar, Southern Oman. *J. Paleolit. Archaeol.*, 2, 338–357.
- Rosenberg, T. M., Preusser, F., Fleitmann, D., Schwalb, A., Penkman, K., Schmid, T. W., Al-Shanti, M. A., Kadi, K., and Matter, A. (2011). Humid periods in southern Arabia: windows of opportunity for modern human dispersal. *Geology*, 39(12), 1115–1118.
- Rousseau, L., Weisrock, A., Falguères, C., Bahain, J. J., Beauchamp, J., Pozzi, J. P., Ghaleb, B., Mahieux, G., Boudad, L., Bejjit, L., and Bouajaja, M. (2008). Premières datations de travertins d'Imouzzer Idaou Tanane, Oujda, Maroc. <https://shs.hal.science/halshs-00356276>. pp. 209–221.
- Sanlaville, P. (1992). Changements climatiques dans la péninsule arabique durant le Pléistocène supérieur et l'Holocène. *Paléorient*, 18(1), 5–26.
- Sarnthein, M. (1978). Sand deserts during glacial maximum and climatic optimum. *Nature*, 272(5648), 43–46.
- Servant, M. (1983). Evolution du bassin du Tchad au Cénozoïque supérieur. Paris, ORSTOM: Travaux et Documents 159.
- Singarayer, J. S. and Burrough, S. L. (2015). Inter-hemispheric dynamics of the African rainbelt during the late quaternary. *Quat. Sci. Rev.*, 124, 48–67.
- Street, F. A. (1979). *Late quaternary Lakes in the Ziwai-shala Basin, Southern Ethiopia*. Phd thesis, University of Cambridge, Cambridge.
- Stuiver, M. and Reimer, P. J. (1993). Extended ¹⁴C data base and revised CALIB 3.0 ¹⁴C calibration program. *Radiocarbon*, 35(1), 215–230.
- Sultan, M., Sturchio, N., Hassan, F. A., Hamdan, M. A. E., Mahmood, A. M., El Alfy, Z., and Stein, T. (1997). Precipitation source inferred from stable isotopic composition of pleistocene groundwater and carbonate deposits in the western desert of Egypt. *Quat. Res.*, 48(1), 29–37.
- Svensson, A., Andersen, K. K., Bigler, M., Clausen, H. B., Dahl-Jensen, D., Davies, S. M., Johnsen, S. J., Muscheler, R., Parrenin, F., Rasmussen, S. O., Röthlisberger, R., Seierstad, I., Steffensen, J. P., and Vinther, B. M. (2008). A 60 000-year Greenland stratigraphic ice core chronology. *Clim. Past*, 4(1),

- 47–57.
- Szabo, B. J., Haynes, C. V., and Maxwell, T. A. (1995). Ages of quaternary pluvial episodes determined by uranium-series and radiocarbon dating of lacustrine deposits of Eastern Sahara. *Palaeogeogr. Palaeoclimatol. Palaeoecol.*, 113, 227–242.
- Szabo, B. J., McHugh, W. P., Schaber, G. G., Haynes Jr, C. V., and Breed, C. S. (1989). Uranium-series dated authigenic carbonates and Acheulian sites in southern Egypt. *Science*, 243(4894), 1053–1056.
- Thorp, M., Glanville, P., Stokes, S., and Bailey, R. (2002). Preliminary optical and radiocarbon age determinations for Upper Pleistocene alluvial sediments in the southern Anti Atlas Mountains, Morocco. *C. R. Géosci.*, 334, 903–908.
- Tierney, J. E., deMenocal, P. B., and Zander, P. D. (2017). A climatic context for the out-of-Africa migration. *Geology*, 45(11), 1023–1026.
- Timmermann, A. and Friedrich, T. (2016). Late Pleistocene climate drivers of early human migration. *Nature*, 538(7623), 92–95.
- Tjallingii, R., Claussen, M., Stuut, J. B. W., Fohlmeister, J., Jahn, A., Bickert, T., Lamy, F., and Röhl, U. (2008). Coherent high- and low-latitude control of the northwest African hydrological balance. *Nat. Geosci.*, 1, 670–675.
- Viehberg, F. A., Just, J., Dean, J. R., Wagner, B., Franz, S. O., Klasen, N., Kleinen, T., Ludwig, P., Asrat, A., Lamb, H. F., Leng, M. J., Rethemeyer, J., Milodowski, A. E., Claussen, M., and Schäbitz, F. (2018). Environmental change during MIS 4 and MIS 3 opened corridors in the Horn of Africa for Homo sapiens expansion. *Quat. Sci. Rev.*, 202, 139–153.
- Weisrock, A., Wengler, L., Mathieu, J., Ouammou, A., Fontugne, M., Mercier, N., Reyss, J. L., Valladas, H., and Guery, P. (2006). Upper Pleistocene comparative OSL, U/Th and ¹⁴C datings of sedimentary sequences and correlative morphodynamical implications in the South-Western Anti-Atlas (Oued Noun, 29 N, Morocco). *Quaternaire*, 17, 45–59.
- White, K., Drake, N., Millington, A., and Stokes, S. (1996). Constraining the timing of alluvial fan response to late quaternary climatic changes, southern Tunisia. *Geomorphology*, 17, 295–304.
- Wuillez, M.-N., Levavasseur, G., Daniau, A.-L., Kageyama, M., Urrego, D. H., Sánchez-Goñi, M.-F., and Hanquiez, V. (2014). Impact of precession on the climate, vegetation and fire activity in southern Africa during MIS 4. *Clim. Past*, 10, 1165–1182.
- Wood, W. W. and Imes, J. L. (1995). How wet is wet? Precipitation constraints on late quaternary climate in the southern Arabian Peninsula. *J. Hydrol.*, 164, 263–268.
- Zhang, P., Xu, J., Holbourn, A., Kuhnt, W., Xiong, Z., and Li, T. (2022). Obliquity induced latitudinal migration of the intertropical convergence zone during the past ~410 kyr. *Geophys. Res. Lett.*, 49, article no. e2022GL100039.
- Zötl, J. G. (1984). Geochronology and climate of the quaternary. In Jado, A. R. and Zötl, J. G., editors, *Quaternary Period in Saudi Arabia*, volume 2, pages 297–335. Springer, Vienna.

Comptes Rendus

Géoscience

Objet de la revue

Les *Comptes Rendus Géoscience* sont une revue électronique évaluée par les pairs de niveau international, qui couvre l'ensemble des domaines des sciences de la Terre et du développement durable. Ils publient des articles originaux de recherche, des articles de revue, des mises en perspective historiques, des textes à visée pédagogique ou encore des actes de colloque, sans limite de longueur, en anglais ou en français. Les *Comptes Rendus Géoscience* sont diffusés selon une politique vertueuse de libre accès diamant, gratuit pour les auteurs (pas de frais de publication) comme pour les lecteurs (libre accès immédiat et pérenne).

Directeur de la publication : Étienne Ghys

Rédacteurs en chef : Éric Calais, Michel Campillo, François Chabaux, Ghislain de Marsily

Comité éditorial : Jean-Claude André, Pierre Auger, Mustapha Besbes, Sylvie Bourquin, Yves Bréchet, Marie-Lise Chanin, Philippe Davy, Henri Décamps, Sylvie Derenne, Michel Faure, François Forget, Claude Jaupart, Jean Jouzel, Eric Karsenti, Amaëlle Landais, Sandra Lavorel, Yvon Le Maho, Mickaele Le Ravalec, Hervé Le Treut, Benoit Noetinger, Carole Petit, Valérie Plagnes, Pierre Ribstein, Didier Roux, Bruno Scaillet, Marie-Hélène Tusseau-Vuillemin, Élisabeth Vergès

Secrétaire éditoriale : Adenise Lopes

À propos de la revue

Toutes les informations concernant la revue, y compris le texte des articles publiés qui est en accès libre intégral, figurent sur le site <https://comptes-rendus.academie-sciences.fr/geoscience/>.

Informations à l'attention des auteurs

Pour toute question relative à la soumission des articles, les auteurs peuvent consulter le site <https://comptes-rendus.academie-sciences.fr/geoscience/>.

Contact

Académie des sciences
23, quai de Conti, 75006 Paris, France
Tél. : (+33) (0)1 44 41 43 72
CR-Geoscience@academie-sciences.fr



Les articles de cette revue sont mis à disposition sous la licence
Creative Commons Attribution 4.0 International (CC-BY 4.0)
<https://creativecommons.org/licenses/by/4.0/deed.fr>

COMPTES RENDUS DE L'ACADÉMIE DES SCIENCES

Géoscience *Sciences de la Planète*

Volume 355, n° S2, 2023

Special issue / Numéro thématique

Tribute to Jean Dercourt / *Hommage à Jean Dercourt*

Guest editors / Rédacteurs en chef invités

François Baudin (Institut des Sciences de la Terre - Paris (ISTeP), Sorbonne Université), Éric Calais (École normale supérieure, Département de Géosciences, Paris)

François Chabaux (Institut Terre Environnement de Strasbourg (UMR 7063-Unistra-CNRS-ENGEEES), Université de Strasbourg)

Cover illustration / Illustration de couverture

Portraits of Jean Dercourt, from the article “A tribute to Jean Dercourt (1935–2019) — Editorial” by François Baudin, p. 1, © Famille Dercourt and B. Eymann / Académie des sciences, all rights reserved.

François Baudin

A tribute to Jean Dercourt (1935–2019) — Editorial 1-7

Laurent Jolivet

Tethys and Apulia (Adria), 100 years of reconstructions 9-28

Sung-Ping Chang, Manuel Pubellier

Rifting and seafloor spreading in the South China sea: a subduction-related extension on the down-going plate? 29-52

Taniel Danelian, Maria Triantaphyllou, Monique Seyler, Ghazar Galoyan, Arayik Grigoryan, Marc Sosson

Synthesis of micropaleontological age constraints for the reconstruction of the Tethyan realm in the Lesser Caucasus (Armenia, Karabagh) 53-66

Yves-Michel Le Nindre, Denis Vaslet, Bruno Vrielynck, Leopold Krystyn, Jacques Manivit, Abdullah Memesh, Roger Brett Davies

The Middle to Late Triassic of Central Saudi Arabia with emphasis on the Jilh Formation. Part I: lithostratigraphy, facies and paleoenvironments, palaeontology and biostratigraphic age calibration from outcrop studies 67-97

Yves-Michel Le Nindre, Roger Brett Davies, Benoit Issautier, Leopold Krystyn, Denis Vaslet, Bruno Vrielynck, Abdullah Memesh

The Middle to Late Triassic of Central Saudi Arabia with emphasis on the Jilh Formation. Part II: sequence stratigraphy, depositional and structural history, correlations and paleogeography 99-135

Marc Pouljol, Mathilde Mercuzot, Michel Lopez, Sylvie Bourquin, Olivier Bruguier, Erwan Hallot, Laurent Beccaletto

Insights on the Permian tuff beds from the Saint-Affrique Basin (Massif Central, France): an integrated geochemical and geochronological study 137-161

Laurent Beccaletto, Sylvie Bourquin

The Brécly depocenter as part of a new northern Massif Central Carboniferous–Permian Basin (France) 163-190

Armelle Riboulleau, Melesio Quijada, Alexis Caillaud, François Baudin, Jean-Noël Ferry, Nicolas Tribovillard

Molecular fossils of Aptian–Albian blue marls of the Vocontian Basin (France), depositional conditions and connections to the Tethys Ocean 191-212

Nicolas Tribovillard, Viviane Bout-Roumazelles, Romain Abraham, Sandra Ventalon, Marion Delattre, François Baudin

The contrasting origins of glauconite in the shallow marine environment highlight this mineral as a marker of paleoenvironmental conditions 213-228

Anne-Marie Lézine, Masa Kageyama, Franck Bassinot

Data and models reveal humid environmental conditions during MIS 3 in two of the world's largest deserts 229-246

COMPTES RENDUS

DE L'ACADÉMIE DES SCIENCES

Geoscience

VOLUME 355, N° S2, 2023